ISSN 0288-4534
CODEN: KONAE7

粉

KONA

POWDER AND PARTICLE

No. 23 (2005)

Published by Hosokawa Powder Technology Foundation

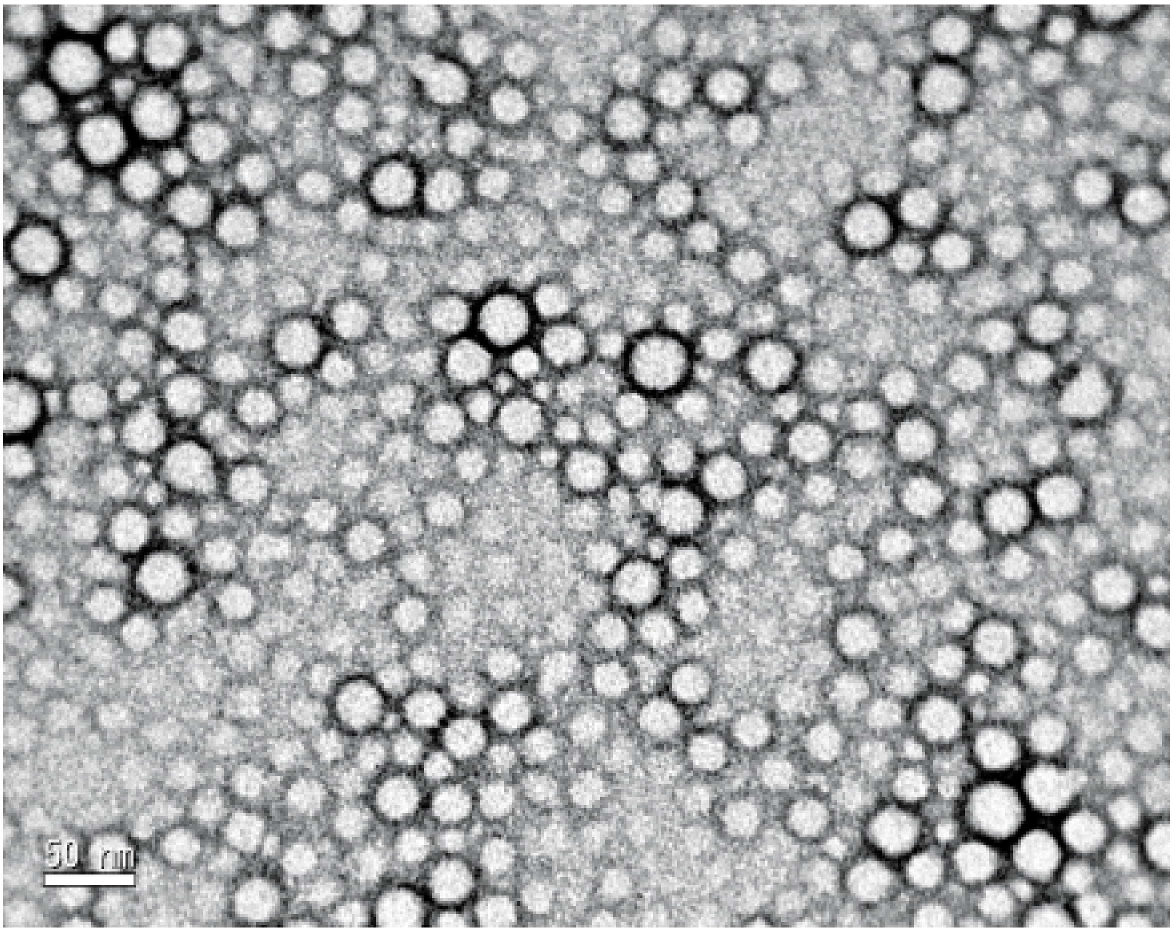

TEM image of biodegradable polymeric PEG-PLGA nano-spheres (See Page 3)

now available online – www.kona.or.jp

KONA

POWDER AND PARTICLE

http://www.kona.or.jp

KONA is a refereed scientific journal that publishes articles on powder and particle sciences and technology. KONA has been published annually since 1983 in Japan. KONA is distributed to researchers, members of the scientific community, universities and research libraries throughout the world.

About the Cover of Journal "KONA"

The Chinese character "粉" is pronounced "KONA" in Japanese, and means "Powder". The hand written "粉" is after the late Mr. Eiichi Hosokawa, founder of the Hosokawa Micron Corporation.

Hosokawa Micron Corporation and its R&D Center

Editorial Board

Y. Tsuji	Editor in Chief (Osaka Univ., JAPAN)
Asia / Oceania Editorial Board	
Y. Kousaka	(Emeritus Professor of Osaka Prefecture Univ., JAPAN)
H. Masuda	(Kyoto Univ., JAPAN)
H. Emi	(Emeritus Professor of Kanazawa Univ., JAPAN)
K. Higashitani	(Kyoto Univ., JAPAN)
K. Nogi	(Osaka Univ., JAPAN)
Y. Fukumori	(Kobe Gakuin Univ., JAPAN)
J. Hidaka	(Doshisha Univ., JAPAN)
M. Takahashi	(Nagoya Institute of Technology, JAPAN)
M. Rhodes	(Monash Univ., AUSTRALIA)
Y. Kang	(Chungnam National Univ., KOREA)
W. Tanthapanichakoon	(National Science and Technology Development Agency, THAILAND)
T. Yokoyama	(Hosokawa Powder Technology Research Institute, JAPAN)
M. Naito	(Osaka Univ., JAPAN)
Secretariat	
T. Kawamura	(Hosokawa Powder Technology Foundation, JAPAN)
Europe / Africa Editorial Board	
E. Forssberg	Chairman (Univ. Lulea, SWEDEN)
W. Peukert	(Univ. Erlangen, GERMANY)
S.E. Pratsinis	(ETH Zürich, SWITZERLAND)
H. Kalman	(Ben Gurion Univ., ISRAEL)
J.F. Large	(Univ. de Tech. de Compiégne, FRANCE)
N.Z. Lyakhov	(Institute of Solid State Chemistry, RUSSIA)
M. Ghadiri	(Univ. of Leeds, UNITED KINGDOM)
Secretariat	
P. van der Wel	(Hosokawa Micron B.V. NETHERLANDS)
P. Krubeck	(Hosokawa Micron GmbH, GERMANY)
Americas Editorial Board	
B.M. Moudgil	Chairman (Univ. of Florida., U.S.A.)
D.W. Fuerstenau	Vice Chairman (Univ. of California, U.S.A.)
R. Flagan	(California Institute of Technology, U.S.A.)
R. Hogg	(Pennsylvania State Univ., U.S.A.)
D.J.W. Grant	(Univ. of Minnesota., U.S.A.)
A.I. Hickey	(Univ. of North Carolina, U.S.A.)
F. Concha	(Univ. of Concepción, CHILE)
S.B. Savage	(McGill Univ., CANADA)
Secretariat	
C.C. Huang	(Hosokawa Micron Powder Systems, U.S.A.)

■ Publication Office

Hosokawa Powder Technology Foundation (Japan) in Hosokawa Micron Corporation
No. 9, 1-chome, Shoudai Tajika, Hirakata-shi, Osaka 573-1132, Japan

■ Notes

○ Hosokawa Powder Technology Foundation has entrusted the editorial duty to the editorial board organized by the Council of Powder Technology, Japan.

(Complimentary Copy)

Printed in Japan

The Letter from the Editor

Yutaka Tsuji
Editor-in-Chief

I am pleased that KONA No.23 has been issued in due course as usual. If you look at the KONA editorial board shown in the back cover, you will find a minor change in the Asian and Oceania members. That is, Prof. Y. Kang (Chungnam National Univ., Korea) and Prof. M. Rhodes (Monash Univ., Australia) have joined us as new editorial board members. Both professors have taken over from Prof. S. H. Kang (Korea) and Prof. P. Arnold (Australia), respectively. I should like to express sincere thanks to Prof. S. H. Kang and Prof. P. Arnolds for their devoted cooperation in KONA for many years.

In this Letter from the Editor, allow me to write something about language problems which many non-native speakers of English have. Research is not completed before writing reports or papers. Needless to say, the language to be in use is English in KONA as in almost all international journals in the world. The language handicap is serious for non-native speakers of English. I myself am non-native of English and so I really understand and feel this handicap.

The language handicap is most apparent in debating in an international meeting where the common language is English. Native speakers and non-native speakers are not in the same position. If you assimilate this handicap to a sport, the situation is similar to the case where a right handed player of tennis is forced to use the left hand in play. Compared with the case of debating, the handicap in writing is lighter, but still the writing skill greatly reduces under the condition that mother language is prohibited. Delicate or sophisticated expressions are difficult for lack of vocabulary. Above all, it takes a long time for them to translate their articles from the mother language to English. Sometimes researchers can not afford to spend much time to translate their papers and are eager to advance in their work. As a result, many researchers of non-native of English are satisfied with writing articles in their mother language different from English. Many good works have not published in English. They remain unknown in other countries.

Fortunately, KONA has an unique editorial system to be a truly international journal. We have three regional editorial boards in the world: American Board, Europe/African Board and Asian/Oceania Board. The three regional boards cover very wide areas in the world. In some areas, English is spoken and in other areas, not spoken. Each board has the responsibility to collect good articles from the region. Good articles which have not written originally in English are published in KONA as translated articles in English. The mission of an international journal is to find out qualified information from every corner of the world and provide such information to other world. As the editor-in-chief, I will endeavor to make KONA continue to perform this important mission.

Y. Tsuji

KONA

GENERAL INFORMATION

HISTORY OF THE JOURNAL

KONA journal has been published by the Council of Powder Technology, Japan. (CPT), from No.1 to No.12 issues, under the sponsorships of Hosokawa Micron Corporation (No.1 to No.9) and Hosokawa Powder Technology Foundation (No.10 to No.12).

The CPT has been established in 1969 as a non-profit organization to enhance the activities of research and development on powder science and technology in Japan under the sponsorship of Hosokawa Micron Corporation. In 1983, the CPT has decided to issue an international journal named “KONA”, which publishes the excellent articles appeared in Japanese journals concerning powder science and technology, after translated into English, throughout the world. After the seventh volume issued in 1989, the CPT has changed its policy to internationalize the “KONA” from the 8th issue (1990) and on by incorporating the monographs originally written in English from the authors throughout the world. Immediately, the present editorial board including Asian, Americas' and European Blocks has been organized.

From the 13th issue and on, the Hosokawa Powder Technology Foundation has taken over the role of KONA publisher from the CPT in 1995 (No.13) and the Foundation has entrusted the editorial duty to the present KONA editorial board organized by the CPT without requesting any shift in our present editorial policies. This switching of publisher has been simply and only to make the aim and scope of the Foundation definite. Essentially no change has been observed in continuously editing and publishing this journal except in the designation on a part of the journal cover.

AIMS AND SCOPE OF THE JOURNAL

KONA Journal is to publish the papers in a broad field of powder science and technology, ranging from fundamental principles to practical applications. The papers discussing technological experiences and critical reviews of existing knowledge in specialized areas will be welcome.

These papers will be published only when they are judged, by the Editor, to be suitable for the progress of powder science and technology, and are approved by any of the three Editorial Committees. The paper submitted to the Editorial Secretariat should not have been previously published except the translated papers which would be selected by the Editorial Committees.

CATEGORY OF PAPERS

- Invited papers
  Original research and review papers invited by the KONA Editorial Committees.
- Contributed papers
  Original research and review papers submitted to the KONA Editorial Committees, and refereed by the Editors.
- Translated papers
  Papers translated into English, which were previously published in other languages, selected by the KONA Editorial Committees with the permission of the authors and / or the copyright holder.

SUBMISSON OF PAPERS

Papers should be sent to each KONA Editorial Secretariat.

- Asia / Oceania Editorial Secretariat
  T. Kawamura
  Hosokawa Micron Corporation Micromeritics Laboratory 1-9, Shoudai Tajika, Hirakata 573-1132 JAPAN
- Europe / Africa Editorial Secretariat
  Dr. P. van der Wel or Mrs. P. Krubeck
  Hosokawa Micron GmbH
  Welserstr. 9-11, 51149 Köln
  P.O. Box 920262, 51152 Köln
  GERMANY
- Americas Editorial Secretariat
  C.C. Huang, Ph.D.
  Hosokawa Micron Powder Systems
  10 Chatham Road, Summit, NJ 07901 USA

PUBLICATION SCHEDULE

KONA is published once a year.

SUBSCRIPTION

KONA is distributed free of charge to senior researchers at universities and laboratories as well as to institutions and libraries in the field throughout the world. The publisher is always glad to consider the addition of names of those who wish to obtain this journal regularly to the mailing list. Distribution of KONA is made by each Secretariat.

Free electronic publication of KONA is available in http://www.kona.or.jp

INSTRUCTIONS TO AUTHORS

(1) Manuscript format

- Two copies should be submitted to the Editorial Secretariat, in double-spaces typing on pages of uniform size.
- Authorship is to give author's names, and the mailing address where the work has been carried out on the title page.
- Abstract of 100-180 words should be given at the beginning of the paper.
- Nomenclature should appear at the end of each paper. Symbols and units are listed in alphabetical order with their definitions and dimensions in SI units.
- Literature references should be numbered and listed together at the end of paper, not in footnotes. Please give information as in the following examples:
  1) Carslaw, H.C. and J.C. Jaeger: “Conduction of Heat in Solids”, 2nd ed., Clarendon Press, Oxford, England (1960).
  2) Howell, P.A.: US Patent, 3,334,603 (1963).
  3) Rushton, J.H., S. Nagata and D.L. Engle: AlChEJ., 10. 294 (1964).
  4) Seborg, D.E.: Ph.D. Dissertation, Princeton Univ., N.J., U.S. A. (1969).
- Original figures with each single copy should be submitted, on separate sheets. Authors' names and figure numbers are marked in the corner.
- Figure numbers and captions are listed on a separate sheet.
- Place of figure insertion is to be indicated in the margin of the manuscript.
- Tables should be typed on separated sheets.
- Author's short biography and photograph should be attached.
- For data and text submissions we accept PC-format floppy and CD-ROM discs with unformatted text files in ASCII code. Files in Microsoft Word format are also acceptable. When submitting images, please insure that the files are compatible with Adobe Photoshop and have a resolution of at least 350 dpi.

(2) Reprints

- The authors shall receive 50 free reprints. Additional reprints will be furnished when ordered with return of galley proofs.

(3) Publication policy

- Original papers submitted for publication become immediately the property of the CPT and remain so unless withdrawn by the author prior to acceptance for publication or unless released by the Editor. The original papers in KONA should not be reproduced or published in any form without the written permission of the CPT. CPT does not claim the copyright for translated papers.

Explanation of the Cover Photograph

Development of deliver system for genes and drugs using PEG-PLGA nano-spheres as a carrier material, prepared by Emulsion Solvent Diffusion (ESD) method

H. Tsujimoto, K. Hara and Y. Tsukada
Beauty Science Laboratory
Hosokawa Powder Technology Research Institute

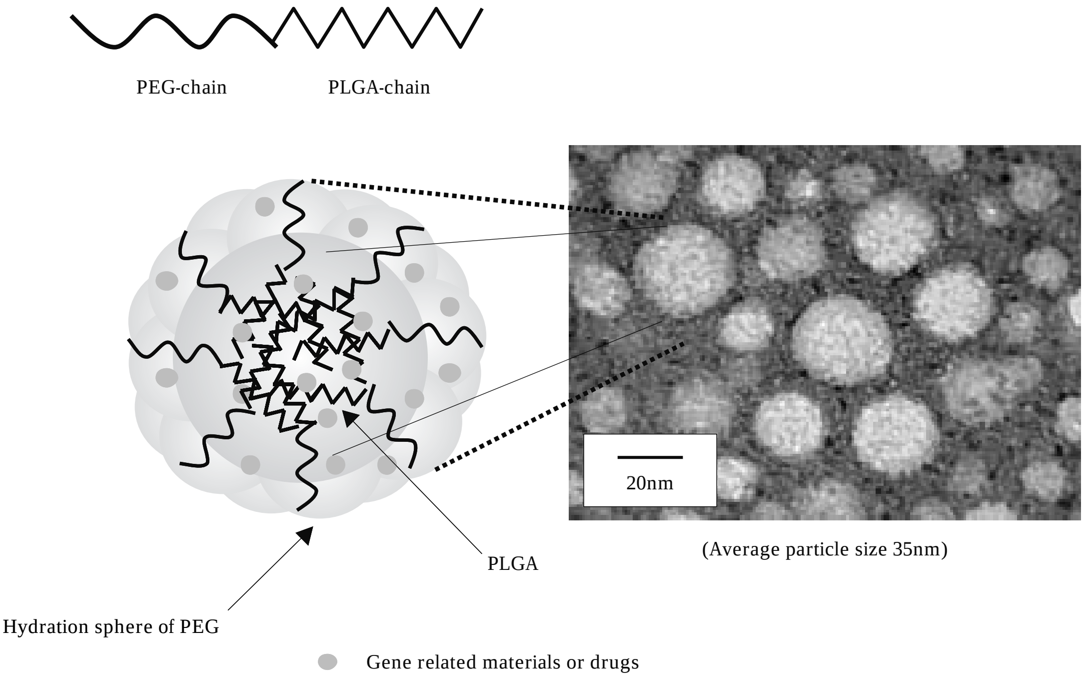

The photograph shows a TEM image of biodegradable polymeric PEG-PLGA nano-spheres, PEGylated poly(lactic-co-glycolic acid), as siRNA carriers having approximately 35nm in average particle size measured by dynamic light scattering method.

The PEG-PLGA nano-spheres having core shell structure as shown in Figure, which could be used to prepare the stealth nano-particles or long-circulating nano-particles for the delivery of genes and drugs, was made by a novel physicochemical process using Emulsion Solvent Diffusion (ESD) method in the aqueous PVA solution with 1 to 5% siRNA, DAN plasmid, GFP plasmid, NFκB Decoy Oligonucleotides or other types of gene related materials loading depending upon the preparation conditions.

We succeeded encapsulating various gene related materials and drugs into the PEG-PLGA nano-spheres prepared by the ESD methods, which can fuse with cell membrane to efficiently introduce genes and drugs into cells. We newly discovered that this nano-spheres become very effective carrier for the delivery of gene related materials both in cytoplasm of cultured cells and in various tissues, which leads to new gene therapy development applied to the intractable human diseases.

The Beauty Science Laboratory of Hosokawa Powder Technology Research Institute has proposed variety types of biodegradable polymeric nano-spheres and devoted itself to the research and development of the advanced gene & drug delivery systems using several nano-spheres' composite technologies.

KONA Powder and Particle No. 23 (2005)

CONTENTS

<**Translated Research Papers**>

<**Translated Review Paper**>

Nanoparticle Technology for the Production of Functional Materials[†]

T. Yokoyama[1]
*Hosokawa Powder Technology Research Institute**
C.C. Huang
*Hosokawa Micron Powder Systems***

Abstract

The nanoparticle technology, relating to the preparation, characterization, processing, and applications of nano-sized particles, plays an increasingly important role in the emerging nanotechnology. Although the nanoparticles have many unique functional properties superior to the coarser particles, they also suffer from dispersion and stability problems because of their strong cohesiveness and high specific surface areas. To make the best use of nanoparticles and solve their application problems, the development of nanomaterial processing techniques is essential.

New chemical synthesis methods for producing nano-sized oxides particles in the gas phase and producing biocompatible polymeric nano-composite particles in the solution phase were elucidated in the paper. In addition, mechanical breakdown method (e.g. nano-grinding) was briefly discussed. Furthermore, newly developed dry particle processing systems for making high performance nanocomposites as well as their applications in Fuel Cells, Drug Delivery Systems, and Cosmetics were introduced.

Key words: Nanoparticles, Nanotechnology, Nanocomposite, Fuel cell, Drug delivery system

1. Introduction

The nanotechnology has drawn much attention since the beginning of this century as the critical technology to advance industrial outputs and to extend human life in the 21st century. Developing commercial applications of nanotechnology, the nano-sized particles play a significant role because of their unique functional properties.

The definition of nanoparticles depends on their applications. In general, nanoparticle refers to the particle having a size smaller than 100 nm. However, it could be, in the narrow sense, less than around 10 nm as its physical properties, such as melting point, differ from those of the bulk solids. On the other hand, particles ranging from nm to one μm could also be called "nanoparticles" in the broader sense. In this paper, the particles less than the shortest wavelength of visible light (around 400 nm) are called "nanoparticles", which are finer than the so-called "submicron particles".

The technology to prepare, characterize, process and apply these nanoparticles is called "Nanoparticle Technology", which is expected to be one of the key technologies to materialize the commercial applications of nanotechnology. In fact, nano-sized particles, such as ink, pigment, carbon black, fine silica etc., are not new to some industries and have been used as additives to improve product structure and qualities. The nanoparticle technology is to bridge the new nanotechnology applications and the traditional powder technology.

In this paper, the nanoparticle technology for the production of nanoparticles and nanocomposites and their applications are to be discussed.

[†] Accepted: August 23, 2005

* 9, Shodai-Tajika 1-chome, Hirakata, Osaka 573-1132, Japan
** 10 Chatham Road, Summit, NJ 07901, USA
[1] Corresponding author
TEL: 072-855-2307 FAX: 072-855-2561
E-mail: tyokoyama@hmc.hosokawa.com

2. Production of nanoparticles and nano-sized composite particles

Nanoparticles can be produced by the break-down (top-down) or the build-up (bottom-up) method. In this paper, the production methods were discussed according to their working environments, i.e. the solid, liquid or gas phase, as shown in **Fig. 1**.

1) Solid phase method

The most popular way to break-down solid materials is the grinding method. The sizes of ground product have been getting finer and finer since long. Thirty years ago or so, the dry grinding limit of mineral materials1) was around few microns. However, the grinding limit was reduced down to the submicron range with the development of compression-shear type ultra-fine grinding mills2) in early 1980's. Furthermore, the nanosized products were reported by using wet grinding with ball media mill3) in late 1990's.

However, it was also understood that the grinding process could reach its finest possible product size (so-called grinding equilibrium), after that the size of the ground product increased with an increase in the grinding time because of particle agglomeration. It was also experimentally proven that the smaller the grinding media and the maximum force exerting on them were, the finer was the grinding equilibrium diameter as shown in **Fig. 2**4), as long as the grinding intensity given by the grinding media was large enough to break the particles. Becker et al. also confirmed this phenomenon in terms of the grinding intensity5). Nowadays, fine ceramic beads below 30 μm are available for nano-grinding applications.

In addition to the grinding intensity, the physico-chemical conditions of the grinding processes could affect the outcomes of nano-griding. **Fig. 3** showed that the size reduction of products stopped at a certain grinding time, but its particle size could further be reduced when the pH value of the slurry was adjusted to better disperse the particles in it. The pH value of the slurry could be controlled by measuring its zeta potential6).

2) Gas phase method

A number of methods are available to prepare the nanoparticles in the gas phase using chemical reactions or physical state changes. The gas phase methods can generally produce higher quality nanoparticles but at a lower capacity in comparison to the solid phase and liquid phase methods because of their extremely low bulk densities. Nearly 20 years ago, we developed a system to produce metallic nanoparticles using the evaporation method with the plasma-arc7). This lab-scale system produced nano-sized metallic particles at a rate of tens of grams per hour for usual metals such as iron and cupper.

The new gas phase method we recently developed is based on the plasma assisted chemical reaction technique. The liquid mixture of raw materials is fed together with the reaction gas into the combustion chamber, where the raw materials are gasified and the nanoparticles are generated by the chemical reaction in the gas phase with the assistance of plasma emission. The critical step of this method is to collect

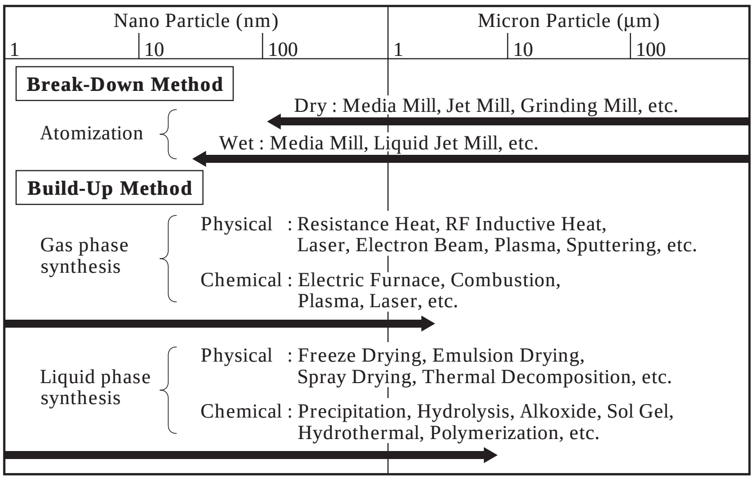

Fig. 1 Production methods for nano particles and micron particles

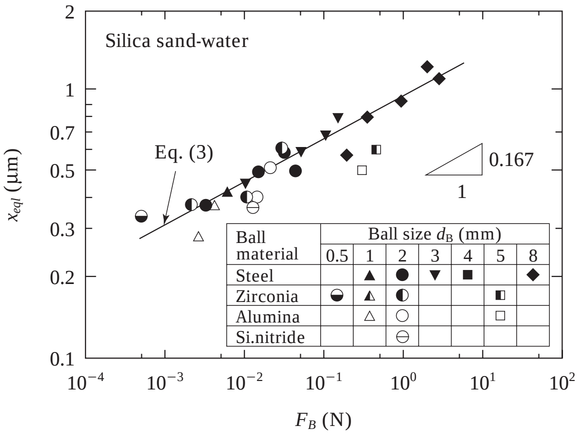

Fig. 2 Correlation between the grinding equilibrium diameter (x_{eql}) and the maximum force exerting on a single grinding ball (F_B) in the planetary ball mill

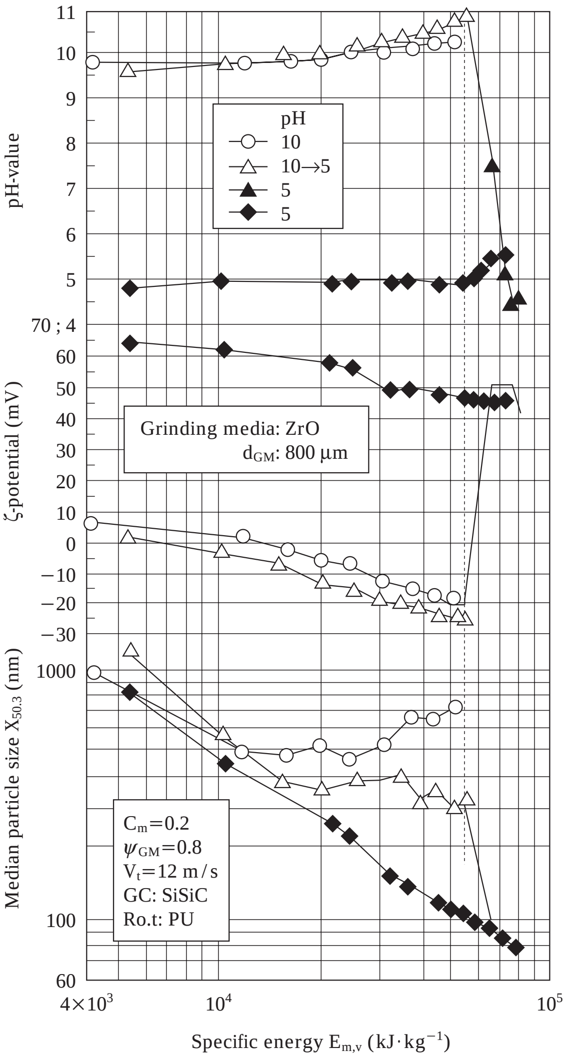

Fig. 3 Change of product particle size, zeta-potential and pH-value with the specific grinding energy

the nanoparticles by rapid quenching before the occurrence of any grain size growth or particle agglomeration. Our pilot-scale system has the advantage of producing various kinds of high-purity nanoparticles at a rate of several kgs per hour, depending on the type of materials and their particle size requirements. Based on the BET specific surface area measurement, nanoparticles in tens of nanometers have been produced by this system. In some cases, nanoparticles, such as ceria, less than ten nanometers could be obtained as well.

The other advantage of the newly developed system is to produce nanoparticles consisting of multi-components with three structural patterns, as shown in **Fig. 4**. The pattern a) is the particle of uniform structure, such as solid solutions or compounds, made of mutually soluble components. The pattern b) is the core-shell structure consisting of the core particles covered by another shell component. The pattern c) is the finely dispersed nanocomposites, where oxide nanoparticles are scattered in the matrix material. In principle, these patterns are formed depending on raw materials and their concentrations during the particle formation. But, the ratio of individual components can be widely varied to optimize the quality of the final products.

3) Liquid phase method

There are also various methods, such as evaporation decomposition, crystallization, precipitation, sol-gel process, polymerization etc., can be used to prepare nanoparticles in the wet phase. Their production rates are normally higher than the gas phase method and suitable for mass production. Many types of nanoparticles, not only ceramics but also organic polymers, can be produced by the liquid phase method. However, the nanoparticles tend to agglomerate during the drying process if dry powder is desirable.

One of the liquid phase methods for nanoparticle production we are recently involved in is the spherical crystallization of polymeric nanoparticles by using emulsion solvent diffusion technique, originally developed by Kawashima et al[8]. With this method, the polymer, such as PLGA (Poly Lactide-co-Glycolide) is first dissolved in a solvent, such as the mixture of acetone and ethanol. The solution is then introduced into

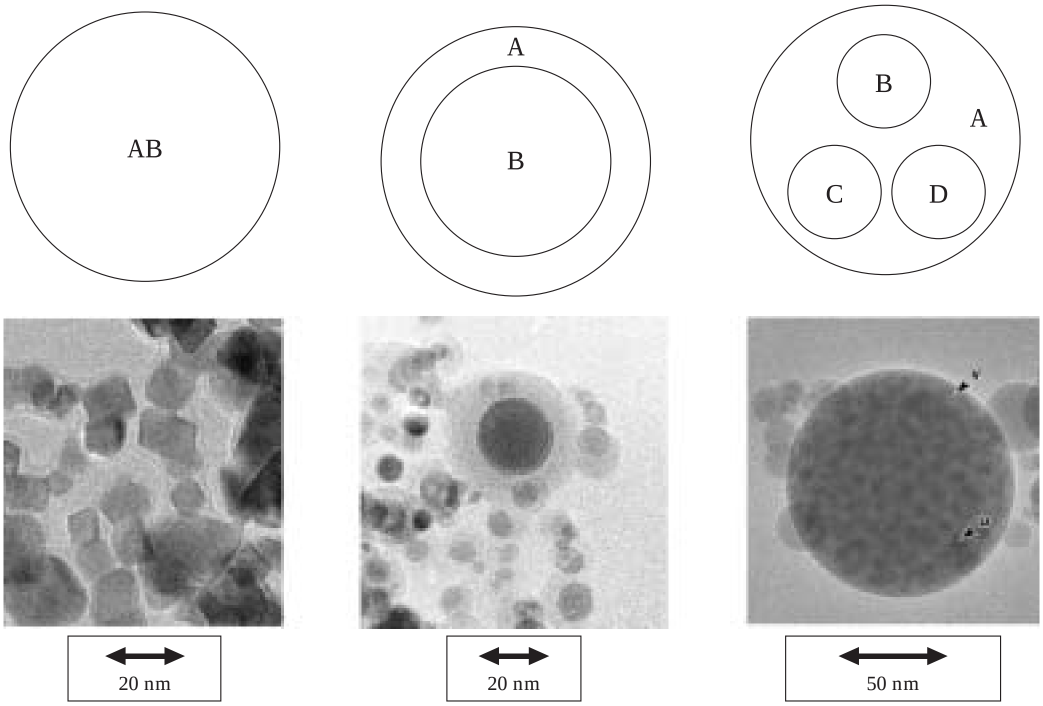

a) Solid solution type (ZrO_2-CeO_2)

b) Core-shell type (ZrO_2-SiO_2)

c) Finely dispersed type (Al-Ca-Ti-Si-Zr oxide)

Fig. 4 Structural patterns of nanocomposite particles

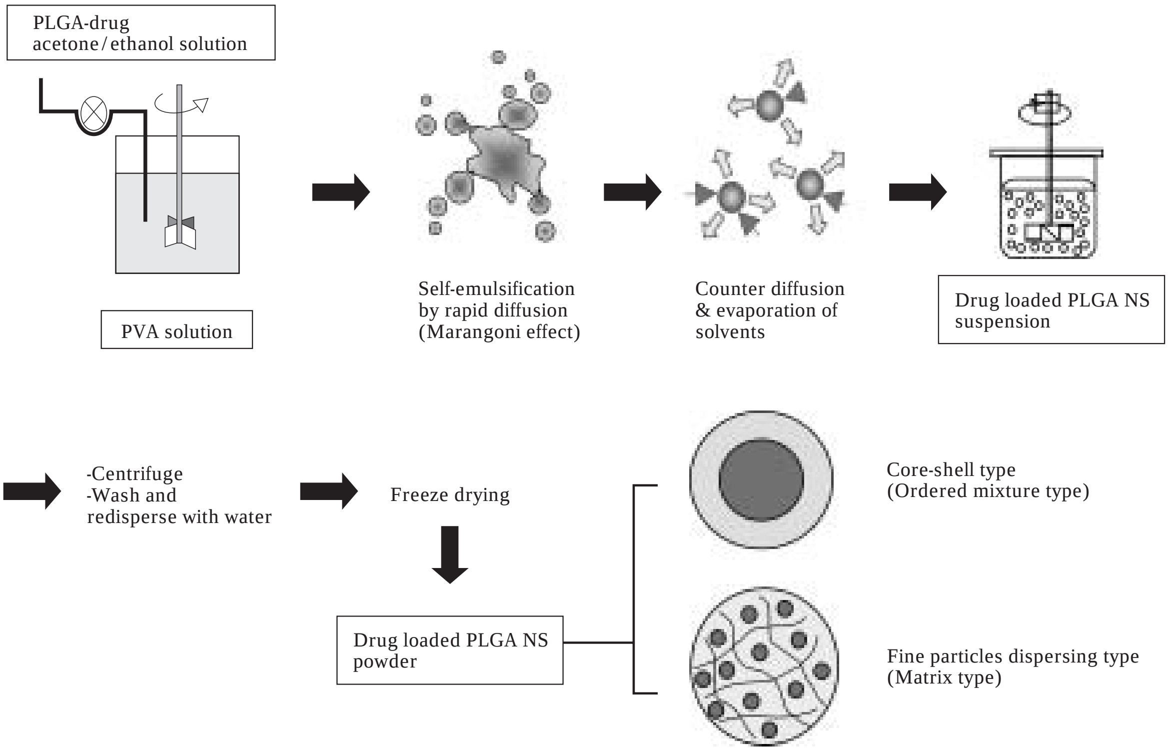

Fig. 5 Process for production of drug encapsulated PLGA NS (nanospheres) by the spherical crystallization method

water with PVA to make polymeric nanoparticles in the suspension by the crystallization mechanism, as shown in **Fig. 5**. The PLGA nanoparticles produced by this method are in the spherical shape and have a narrow particle size distribution with a median diameter of about 200 nm (**Fig. 6**). When a drug is dissolved in the solvent with the PLGA, drug encapsulated biocompatible PLGA nanoparticles can be produced. The applications of these nanoparticles for DDS (Drug Delivery Systems) will be discussed in the later section.

Fig. 6 PLGA nanospheres made by the spherical crystallization method

3. Fabrication of nanocomposites

It is well known that composites can create superior functional and structural properties of materials. **Fig. 7** showed the typical methods to fabricate particle composites[9]. The composites could be made by intercalation in the nanometer scale.

The nanocomposite particles can be prepared by the methods such as gas phase reaction or crystallization as discussed in the previous sections. In those cases, the particle size of the nanocomposites ranges from tens to a few hundreds of nanometers. On the other hand, micron-sized composite particles consisting of nanoparticles can also be produced efficiently by mechanical processing. For example, fluidized-bed granulation method and the like can produce nanocomposite particles from tens of microns to mm.

Although the nanoparticles have unique properties and big potential for many new applications, they are usually difficult to handle because of their strong cohesiveness, low flowability, and low stability. The search for a way to overcome the handling problem becomes a priority in the commercialization of nanoparticles. Making nanocomposites is often a good solution to the problem, because it can modify parti-

Particle size	Production methods		
1 Å	Inclusion in crystal structure	intercalation in layer structure inclusion in porous structure	
	Encapsulation in molecular structure	inclusion in amphiphilic molecule	
1 nm	Doping of fine particles	gas penetration, CVD liquid penetration sol-gel supercritical fluid	
	Surface modification	surface reaction, adsorption surface crystal growth fine particle coating	
1 µm	Mechanical particle bonding	core-shell composites finely dispersed particle composite mechanical alloying	
	Dry/wet agglomeration	powder agglomeration emulsified suspension agglomeration encapsulation	liquid-liquid boundary solid-liquid boundary
1 mm	Melt-extrusion/grinding	polymeric composites, etc.	

Fig. 7 Methods to make composite particles

cle surface properties to improve their flowability or control the particle structure for better functional performance. The nanocomposite production methods can be in the wet or dry phase as described below.

1) Dry method

Nanoparticles have low stability and tend to agglomerate or make aggregates because of their strong cohesiveness and high surface areas. It is usually not easy to disperse them, especially in a solid mixture. Recently, new machines and systems, based on MCB (MechanoChemical Bonding) Technology were developed to address these application problems. The MCB Technology is to create direct solid bonding between fine particles by the mechanical energy without using any binders, which may further be assisted by additional physical energy such as plasma and the like. The plasma has the function of cleaning particle surfaces and enhancing the strength of the solid bonding. The plasma assisted MCB system is called Nanocular, which can make nanocomposite materials continuously. The plasma effect during the mechanical treatment was confirmed by studying the photo-catalytic characteristics of the nano titanium dioxide[10]. **Fig. 8** showed the batch type lab-scale Nanocular for the purpose of research and development of new materials.

Fig. 8 Lab-scale Nanocular for applying MechanoChemical Bonding (MCB) with the plasma assembly

Another system developed based on MCB mechanical treatment alone is called Nobilta[11], which can impose high mechanical energy intensity on the material mixtures. Although the Nobilta is a batch system, it is designed to handle various types of materials.

The degree of particle bonding in the nanocomposites can be evaluated by the particle size analysis, BET specific surface area measurement[12], image analysis of particle cross-section with electron microscope[13], photo-correlation of elements[14], sieving separation of core and guest particles, and so on. The BET measurement is chosen to use in this study, because it is often applied in the nanoparticle characterization. As shown in **Fig. 9**, the raw material mixture consisted of SiO_2 with an average particle size of 26 μm and TiO_2 nanoparticles with a nominal diameter of 15 nm at a mass ratio of 10 to 1. The specific surface area of the powder mixture decreased with the increase of mechanical energy input, which indicated the progression of bonding the nano TiO_2 onto the surface of SiO_2 particles. Particle bonding performances of three different batch types of equipment, as shown in **Fig. 10**, were compared in this study. The Cyclomix is a high-speed powder mixer based on the impact and shearing mechanisms; the MechanoFusion AMS system is a particle-bonding machine having a rotating chamber with stationary press heads; and, the Nobilta is specially designed to give high specific energy input on the powder mixture. The test results showed that the Nobilta could reduce the specific surface area of powder mixture from about 11.0 m^2/g to about 1.0 m^2/g, which was nearly that of starting

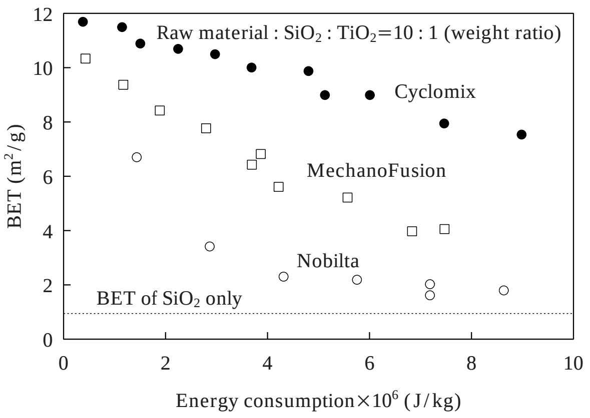

Fig. 9 Effect of particle bonding on the BET specific surface areas of powder mixtures

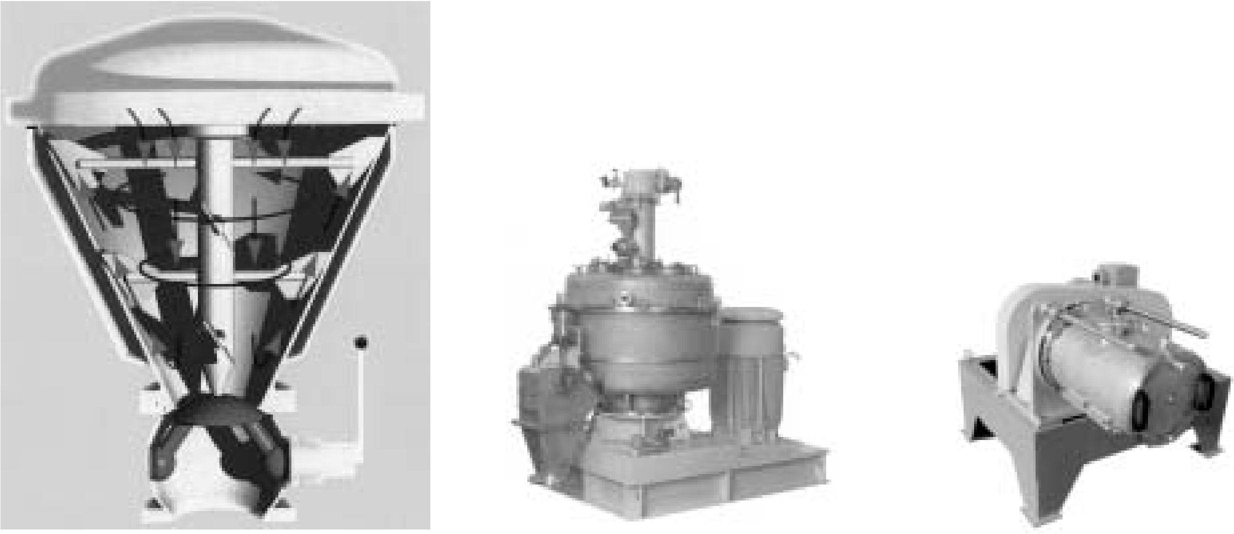

a) High-speed powder mixer, Cyclomix

b) Compression-shearing type particle composing machine, MechanoFusion system

c) A New particle processing machine, Nobilta

Fig. 10 Mechanical processing machines for particle bonding

SiO_2 particles, very quickly and effectively in comparison to the other two machines.

2) Wet method

With this method, nanocomposites are produced from the suspension or slurry containing nanoparticles via a drying process. The dry nanocomposites can be obtained by spray drying of mixed material suspension or by coating the core particles with the suspended materials as the shell particles. In this case, the dispersion of the nanoparticles and homogeneity of the components in each nanocomposite particle are important to insure the product quality. One of the useful machines for this application is the Agglomaster, which is a fluidized-bed type granulator with spray drying assembly[15] and pulse-jet mechanism for better dispersion of particles[16]. Using this machine, granules having an average size of tens of μm with various interesting granule structures can be obtained because of the simultaneous granulation and particle dispersion during the drying process[17]. **Fig. 11** showed an example of composite particles made of platinum-doped nano-sized carbon black and resin using the Agglomaster. This material was successfully used to improve the electro-conductivity and catalytic characteristics of the electrode for high performance fuel cells. This method can modify particle surfaces for various functional applications as well.

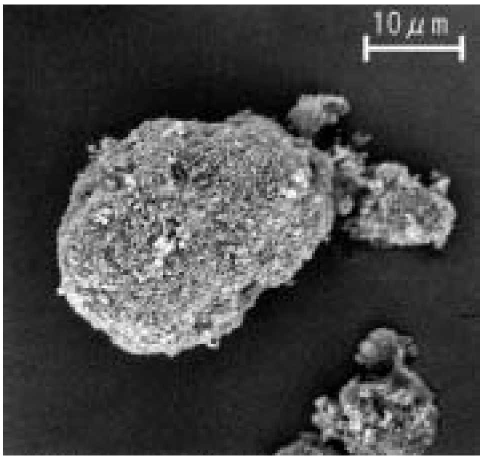

Fig. 11 Example of composite particles made of platinum-doped nano-sized carbon black and resin using the fluidized-bed granulator (Agglomaster)

4. Applications of nanoparticles

The nanoparticles have many unique features comparing to the bulk solids because of their particle size effect and high surface reactivity. They can be used in various applications, such as batteries, sensors, catalysts, paints, inks, films and plastics, cosmetics, nanobiotechnology and so on. A few highlighted examples were discussed below.

1) Fuel cell

Fuel cell is a clean energy generator and expected to use widely in the near future. Among several different types of fuel cells being developed, the SOFC (solid oxide fuel cells) has the highest energy efficiency, but its conventional operating temperatures have been as high as 800 to 1000℃, which requiries expensive seals and insulation materials for the cell construction. The SOFC anode electrode is usually made of YSZ (yttria-stabilized zirconia) − NiO cermet. For developing high performance SOFC, it is necessary to create large reaction area with high reactivity in the electrode and to achieve low internal resistance and good morphological stability of the fuel cell at the elevated temperatures, while securing the passages of gases and liquid reactant. Therefore, porous electrodes made of well-dispersed fine particles is highly desirable. However, sintering “green” anode electrode often causes the grain sizes of fine NiO to grow. This leads to the formation of large Ni particles in the anode and results in inhomogeneous electrode structure. It was experimentally confirmed that bonding the YSZ nanoparticles on the surfaces of NiO particles using the above-mentioned MCB system could suppress the grain size growth of Ni and improve the power density of SOFC and its stability to a great extent$^{17)}$. **Fig. 12** showed the microstructure of the Ni-YSZ cermet anode fabricated from NiO-YSZ composite particles processed by the MCB technology.

In concert with the thin solid electrolyte, the SOFC using MCB treated electrode materials was found to have exceptional performance at 700℃, which could significantly reduce the manufacturing costs of the SOFC. **Fig. 13** showed the performance improvement of our prototype SOFC. As seen in the figure, the anode polarization of MCB treated SOFC was remarkably reduced at 800℃ comparing to that of the conventional SOFC at the same temperature. In addition, it was still better than the conventional one even at 700℃.

2) DDS and cosmetics

Site specific drug delivery has been investigated for a while. One of the recent developments is to use biocompatible PLGA polymeric nanoparticles, as mentioned in the previous section, for the applications of DPI (dry powder inhalation). It is known that the absorbance of nanoparticles in the human body is much higher than that of micron-sized particles, but the nanoparticles tend to agglomerate, stick to the drug capsule, and adhere to the throat and trachea of the patient during pulmonary drug administration. They cannot effectively reach the depth of human lung. Therefore, it is necessary to make coarse agglomerates having a diameter of 30∼50 μm for easy handling while allowing the inhaler to break them down to several μm, suitable for pneumatic-conveying to the lung. The micron-sized agglomerates are fully dispersed to their original nanoparticles in the lung. **Fig. 14** showed an example of the functional compos-

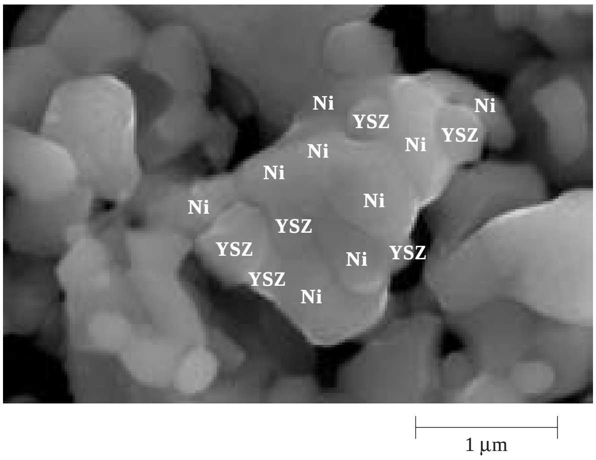

Fig. 12 Ni-YSZ cermet anode fabricated from NiO-YSZ composite particles

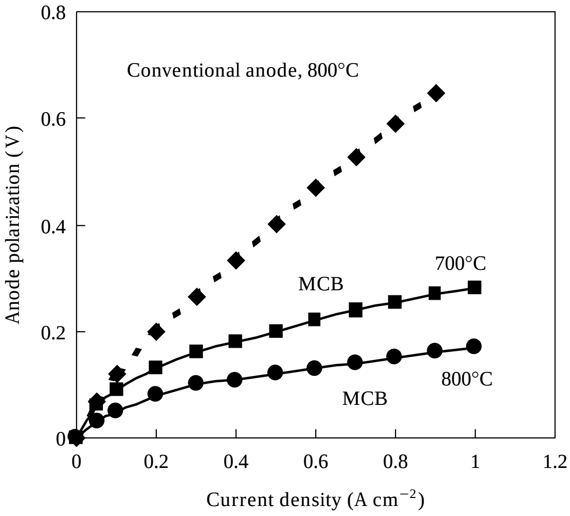

Fig. 13 Performance comparison of SOFC anode fabricated by MCB treated NiO-YSZ composite particles to that by the conventional powder mixture

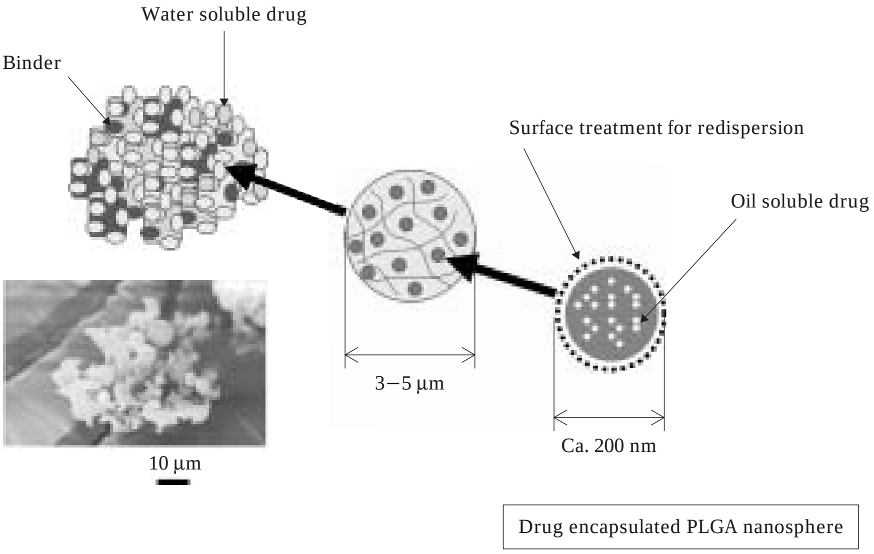

Fig. 14 Structure of functional composite particle consisting of drug encapsulated PLGA nanospheres

ite particles consisting of drug encapsulated PLGA nanospheres and the photo of composite agglomerates. For this application, both dry and wet methods for making nanocomposites as mentioned previously were applied. Test results showed that the respirable fraction of the drug could be improved from less than 10% to over 40% by using PLGA nanocomposites in vitro study with a cascade impactor[18]. In addition, the drug efficacy was found significantly improved with the use of insulin encapsulated PLGA polymeric nanoparticles. **Fig. 15** showed the blood glucose level of rats after introducing insulin via different drug administration methods. The drug efficacy could be evaluated by calculating the area between the initial blood glucose level and that after insulin administration in the figure. It was confirmed that the therapeutic efficacy of using drug encapsulated nanoparticles could be 1.6 times of that applying insulin solution injection[19]. This might attribute to the controlled release effect of the PLGA co-polymer, which gradually decomposed in the water by hydrolysis.

The nanocomposite particles can also be used as transdermal drugs and cosmeceuticals. **Fig. 16** showed the amount of ascorbic acid in the dermis of human skin[20] as a function of time after applying pro-vitamin C. It clearly indicated that applying the pro-vitamin C encapsulated PLGA nanoparticles could produce much more reduced form vitamin C in the dermis than using pro-vitamin C liquid suspension. The reduced form vitamin C is known to prevent the oxidation of biological tissues caused by the UV radiation and to suppress the generation of melanin pigment, which causes black spots on the skin. It also promotes the formation of collagen to reduce the wrinkles for anti-aging applications. The reason for the differences in the vitamin-C absorption attributed

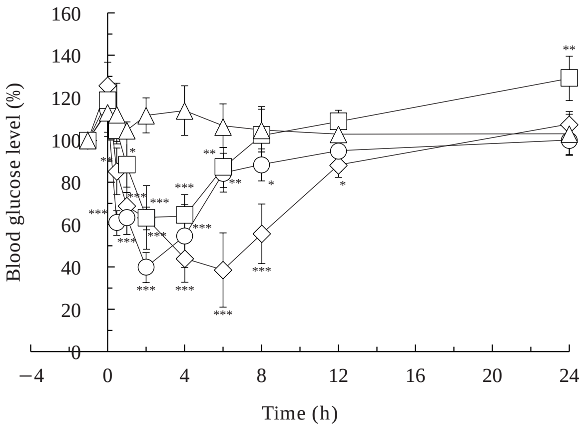

Fig. 15 Change of blood glucose levels by different insulin administration methods (◇): Composite particles with insulin encapsulated PLGA nanospheres, (○): intravenous administered insulin solution, (□): intratracheally administered insulin solution, (△): intratracheally administered saline solution as control group. Dose of insulin: 3.0 IU/rat. N=6, significantly different from control group (*p<0.05, **p<0.01, ***p<0.001, student t-test).

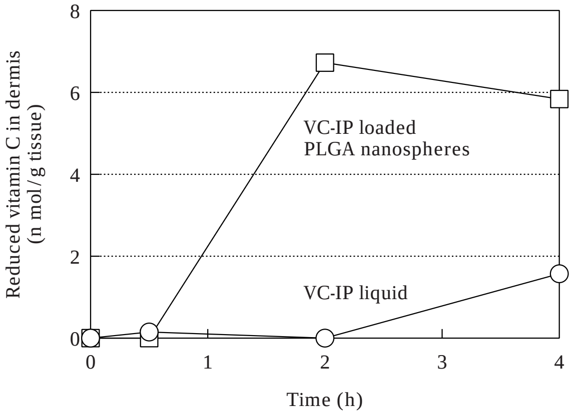

Fig. 16 Comparison of the amount of ascorbic acid in the dermis delivered by the PLGA nanoparticle and liquid suspension

to the excellent skin permeability of PLGA nanosphere, which was used as a carrier of pro-vitamin C. The pro-vitamin C has poor skin permeability because of its hydrophilic characteristics. It was also found in-vitro that the pro-vitamin C encapsulated PLGA nanoparticles could remarkably reduce the DNA damage on the skin caused by the UV radiation.

5. Conclusion

Although nanoparticles have a lot of unique properties and present great potential for many applications, the relationship between the material properties and product performance has to be established to justify their usages. While nanoparticle production had impressive progress in the past few years, the nanoparticle technology is still in its infancy. It is necessary to demonstrate the benefits of nanoparticles to the commercial products before their commercialization. Therefore, the technologies relating to the nanoparticle characterization, design, modification, and processing will play an important role in the nanoparticle commercialization; and, the nanoparticle technology is expected to further develop rapidly in all the industries handling fine particles in the near future.

References

1) G. Jimbo: Funtai no Kagaku (Powder Science), Koudansha, pp.33-34 (1985)
2) T. Yokoyama, K. Urayama, T. Yokoyama: J. Soc. Powder Technol., Japan, 20, 767-771 (1983)
3) M. Inkyo, T. Kitakaze, T. Tahara: Proc. Autumn Symposium, Soc. Powder Tehcnol., Japan, pp.249-253, Kyoto (1995)
4) T. Yokoyama, Y. Taniyama, G. Jimbo, Q.Q. Zhao: J. Soc. Powder Technol., Japan, 28(12), 751-758 (1991)
5) M. Becker, A. Kwade and J. Schwedes: Proceedings of World Congress on Particle Technology 3, p.125 (1998)
6) S. Mende, F. Stenger, W. Peukert, J. Schwedes: Proc. of 10th European Symposium on Commimution, Heidelberg, Germany (2002)
7) K. Fujii, M. Inoki, T. Yokoyama: J. Soc. Powder Technol., Japan, 21(2), 778-782 (1984)
8) Y. Kawashima, M. Okumura and H. Takenaka: *Science*, 216, 1127-1128 (1982)
9) M. Arakawa: Funsai (The Micromeritics), No.33, 60-65 (1989)
10) H. Abe, T. Kimitani, K. Sato, M. Naito, K. Nogi: Preprint of 40th Technical discussion (Tokyo, June 21-22, 2005) pp.57-60
11) M. Inoki: Kinou Zairyo, 24(7), 77-86 (2004)
12) S. Nakajima, T. Koga, M. Senna: Preprint of 30th Summer Symposium (Kannami, July 1994) pp.14-17
13) T. Takahara, M. Iwasaki, Y. Tanihata: Yokogawa giho, 37(2), 45-50 (1993)
14) M. Naito, M. Yoshikawa, T. Tanaka, A. Kondo: J. Soc. Powder Technol., Japan, 29, 434-439 (1992)
15) H. Tsujimoto, T. Yokoyama, I. Sekiguchi: J. Soc. Powder Technol., Japan, 36(5), 368-377 (1999)
16) H. Tsujimoto, T. Yokoyama, I. Sekiguchi: J. Soc. Powder Technol., Japan, 36(10), 756-767 (1999)
17) T. Fukui, K. Murata, S. Ohara, H. Abe, M. Naito, K. Nogi: J. Power Sources, 125, 17-21 (2004)
18) H. Yamamoto, W. Hoshina, H. Kurashima, H. Takeuchi, Y. Kawashima, T. Yokoyama, H. Tsujimoto: J. Soc. Powder Technol., Japan, 41(7), 514-521 (2004)
19) H. Yamamoto, H. Kurashima, D. Katagiri, M. Yang, H. Takeuchi, Y. Kawashima, T. Yokoyama, H. Tsujimoto: Yakuzaigaku, 64(4), 245-253 (2004)
20) H. Tsujimoto, K. Hara, C.C. Huang, T. Yokoyama, H. Yamamoto, H. Takeuchi, Y. Kawashima, K. Akagi, N. Miwa: J. Soc. Powder Technol., Japan, 41(12), 867-875 (2004)

Author's short biography

Toyokazu Yokoyama

Toyokazu Yokoyama graduated in Chemical Engineering from Kyoto University and received M.S. in 1975. Then he spent six years in Europe to study powder technology at Karlsruhe University and to work as an engineer for Hosokawa Europe Ltd. in Cologne and near London. After another six year work in the engineering division and laboratory of Hosokawa Micron Corp. in Osaka, he was engaged in research at Nagoya University, where he received Ph.D. on the subject of fine wet grinding by ball media mills. From 1992 to 2003, he was a manager of Hosokawa Micromeritics Laboratory and since then he has been working for Hosokawa Powder Technology Research Institute. His major interests are particle design and processing for advanced functioning by mechanical composing and granulation methods as well as fine grinding and particle characterization.

C.C. Huang

Dr. C.C. Huang is the director of Research & Development, Nanoparticle Technology and Micron Products at Hosokawa Micron Powder Systems. He leads nanotechnology applications and material business in North America for Hosokawa Micron Group. He holds an M.S. degree in engineering from Illinois Institute of Technology and a Ph.D. degree in chemical engineering from West Virginia University. He has many years' experience in industrial R&D, as well as academia, in the field of powder technology and science. Dr. Huang specializes in powder processing, powder characterization, powder granulation, and fluidization. He has published over 30 articles and 8 patents, chaired several meetings, and continues to be an active member in a number of scientific and engineering societies.

Modelling of Particulate Processes[†]

M. Kraft
Department of Chemical Engineering
University of Cambridge[*]

Abstract

We review models and numerical methods used in flame synthesis of organic and inorganic nanoparticles. We discuss a general model in which particles form in the gas phase and grow through mass-adding surface reactions, condensation, and coagulation. They shrink or reshape by sintering and mass-abstracting surface reactions. The model is formulated in terms of a population balance which can incorporate a range of levels of detail, i.e. a varying number of internal coordinates. These coordinates can not only describe the geometry of a particle but also its chemical composition or age. In the simplest version a particle is modelled as a sphere whereas in the most complicated form a particle is modelled as an agglomerate of smaller or primary particles where the geometrical shape is known exactly. For these population balance models a number of different numerical approaches exist. We review the method of moments, sectional, finite element, and Monte Carlo methods and give examples of their applications in flame synthesis. Different strategies for coupling a population balance to laminar and turbulent flows are reviewed. For turbulent flows the closure problems arising from chemical reactions and the population balance are briefly discussed. We then summarize the literature on nanoparticle modelling from laboratory to industrial scale and highlight important areas for future research.

Key words: Nanoparticles, Modelling, Numerical methods

1 Introduction

In this article we review models of combustion synthesis of nanoparticles and the numerical methods used to solve them. Nanoparticles can be found in everyday life, for example as pigments, reinforcement material, or even in sunscreen. They are produced on a million ton per year scale and the industrial processes are well established. Also, based on recent research efforts, it is believed that nanoparticles hold great promise for future applications. However, there are also major concerns about the environmental and specifically human health effects of nano-particle emissions, for example from diesel engines. To improve yields or product quality and to avoid particle emissions, numerical modelling has been extensively used. In this paper we shall discuss models and numerical methods for two types of nanoparticles.

Organic nanoparticles come in two forms namely carbon black and soot. Carbon black is a name for a well-defined industrially manufactured product which is produced at a rate of several million tons per year. Amongst a variety of applications it is used as filler and reinforcement material with the properties of the individual particles determining their application. There are several production routes which all involve combustion of gases and liquids. The most important is the furnace process in which liquid hydrocarbons are sprayed into the exhaust of a turbulent lean natural gas flame. Soot on the other hand is an unwanted product of combustion, mainly in diesel engines. New emissions regulations make it necessary to reduce the amount of soot formed during combustion drastically.

[†] Accepted: August 23, 2005

[*] Pembroke Street, Cambridge CB2 3RA, United Kingdom
TEL: +44 1223 762784 FAX: +44 1223 334796
E-mail: mk306@cam.ac.uk

The variety of **inorganic nanoparticles** is much greater. Two main routes of synthesis are in use: wet-phase chemistry synthesis and flame synthesis. In many cases flame technology has been identified to be superior as it is a direct, continuous process with little waste and by-product generation[110)]. For this reason we only examine models which have been developed for flame synthesis. Important inorganic nanoparticles are titania, fumed silica, and alumina powders. However there are many others and recently the number of ceramic powders has grown as a result of new applications, for example as catalysts and surface coatings. These powders are mainly produced similar to carbon black by spraying metal oxide precursors into a high temperature reaction zone.

Two very important aims which one hopes to achieve with the knowledge gained through modelling are the improvement of yield and quality of products and the scale-up of new processes from a laboratory or bench scale level to an industrial level. In both cases the model needs to capture the important physics and chemistry of the formation of nanoparticles, their interactions with each other and with the surrounding gas phase, and their transport through surrounding media. This requires detailed models of the chemical reactions, the population of particles and for the mostly turbulent transport. Despite recent progress in some of these areas the predictive power of the current models remains poor.

In the research community it has been recognized that it is necessary to study systems which are simpler than a spray injected into a reactor of complex geometry and in which the flow is turbulent. For this reason a number of laboratory experiments have been developed, the simplest being a shock tube; other experimental configurations include plug flow reactors, jet stirred reactors, premixed flames, counterflow and axisymmetric co-flow diffusion flames. Whereas for industrial applications only simplified models are available there exist detailed models for the laboratory scale experiments. The findings obtained from these experiments and attempts to model them are summarized in a number of text books and review articles. These are excellent sources of further information on nanoparticles and their applications and a selection is discussed below. The books by Seinfeld and Pandis[105)] and Williams and Loyalka[125)] are comprehensive treatises on the transport of aerosols and gas phase chemistry in the atmosphere. Although these books do not treat the industrial application of nanoparticles directly they contain a lot of material which is relevant to their modelling. The book by Friedlander[37)] is also a classic text and is more relevant to nanoparticles as it contains details on population balance modelling, in particular on agglomerate formation and restructuring. A more general text on population balances is the book of Ramkrishna[95)] which describes several numerical techniques for population balance problems each of them relevant for the modelling of nanoparticle population dynamics. Important review articles in the area of soot include the articles by Kennedy[48)] and Bockhorn[19)] which contain comprehensive collections of references but also describe a number of empirical and detailed soot models. In addition, the book on soot formation edited by Bockhorn[18)] is recommended. It contains a collection of papers which address all the important issues concerning the modelling and measurement of soot in a variety of reactors, from lab-scale up to diesel engines. In the area of inorganic nanoparticles, the papers by Pratsinis and co-workers[94, 92, 66)] include a number of interesting references for experimental and modelling work. For educational purposes the article by Rosner[97)], the excellent brochure on carbon black from Degussa[74)] and the chapter on carbon black in Ullmann's Encyclopedia of Industrial Chemistry[120)] are recommended.

The **aim of this paper** is to provide an up-to-date review of the literature which is concerned with modelling of organic and inorganic nanoparticle population dynamics considering both models and numerical methods. A variety of numerical approaches are discussed. A distinction is made between detailed models describing particle inception, their growth, and their change in structure and models which describe particle transport in laminar and turbulent flows.

The paper is structured as follows. First, a general model for a population of nanoparticles is presented which assumes no spatial gradients in any of the physical quantities. Then different numerical approaches for population balances are reviewed. The next section presents different strategies for coupling the population balance equation with the fluid flow equations in laminar and turbulent flows. A number of applications are presented in the next section. Finally, some new areas for future research are identified.

2 Outline of a General Model

We first lay out a general model for the population dynamics of nanoparticles as displayed in **Fig. 1**. We assume that all precursors and particles are in a perfectly mixed control volume which means that there are no gradients in any of the physical quantities contained in this volume. The model is defined as follows:

- Individual nanoparticles may be completely described by elements of some type space E on which addition corresponding to coagulation is defined.
- The nanoparticle population is described at time t by the number $n(t, x)$ per unit volume of particles of type $x \in E$.
- n evolves according to the discrete Smoluchowski coagulation equation:

$$\frac{\mathrm{d}}{\mathrm{d}t}n(t, x)=\left(K_t(x)+\sum_{l\in U}S_t^{(l)}(x)\right)\left(n(t,\cdot)\right)+I(t, x). \qquad (1)$$

In these definitions we make the implicit assumption that E is countable so that summations are meaningful. This assumption is common in the literature but not essential and can be removed by replacing the sums with integrals. The (time dependent and nonlinear) **coagulation** operator K is then defined by

$$K_t(x)\left(n(t,\cdot)\right)=\frac{1}{2}\sum_{y,\,z\in E:y+z=x}K_t(y, z)n(t, y)n(t, z) - \sum_{y\in E}K_t(x, y)n(t, x)n(t, y). \qquad (2)$$

The first sum represents coagulation to form particles of type x and the second loss of particles of type x due to coagulation. $K_t(x, y)$ defines a map from the concentrations of particles of types x and y to their coagulation rate at time t given by $K_t(x, y)n(t, x)n(t, y)$. K is known as the coagulation kernel.

Surface reactions, condensation, and sintering which only involve one physical particle at a time are described by the linear operator S defined by

$$S_t^{(l)}(x)\left(n(t,\cdot)\right)=\sum_{y\in E}\beta_t(y)\mathbb{P}\left(g^{(l)}(y)=x\right)n(t, y)-\beta_t^{(l)}(x)n(t, x), \qquad (3)$$

where $l \in U$. U is an index set for a process or a type of event which is either one element of a set of surface reactions, sintering steps or condensation steps. $\beta_t^{(l)}(x)$ is the rate at which a particle of type x undergoes the change of index l at time t. $g^{(l)}(x)$ is the result of a particle of type x undergoing an event of index l. If a surface reaction removes a particle from the population the function will take the special value 0 in E. We allow for $g^{(l)}$ to be a random function. Note in the deterministic case the probability $\mathbb{P}$ in (3) reduces to an indicator function. For example, in the case of x describing the number of monomers in a particle then the addition of a monomer is given by $g(y)=y+1$. Models for sintering and surface reactions will be discussed below.

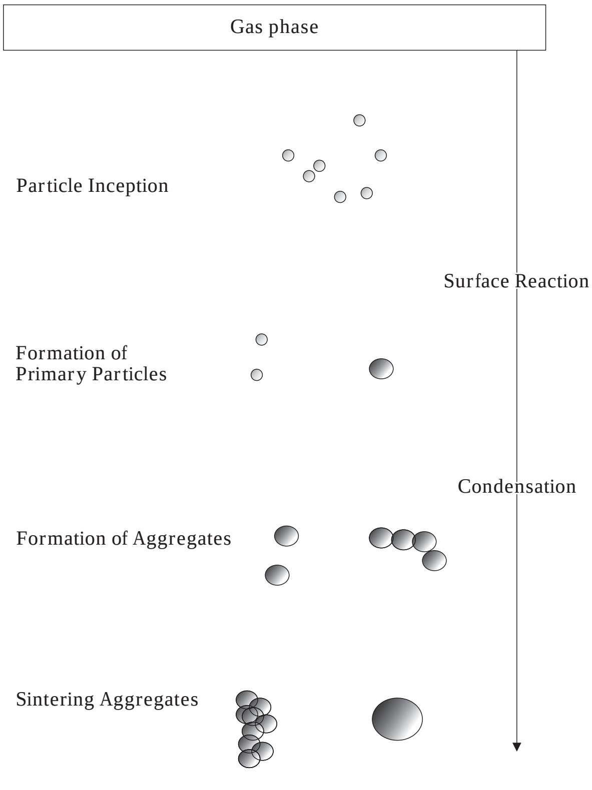

Fig. 1 Schematic of processes in nanoparticle flame synthesis.

The **particle inception** $I(t, x)$ is the rate at which particles of type x enter the system at time t.

As boundary conditions generally we will use $n(0, x)=n_0(x)$ for all $x \in E$.

2.1 Representations of nanoparticles

Nanoparticles can be modelled using different degrees of detail which is specified by the set E. In the following, three examples for the set E are given. The models discussed in this paper will either be identical to or are combinations of the following examples.

The **Primary Particle Model** is the most detailed particle model discussed in the literature. There, a nanoparticle is described as an unordered finite sequence of 'primary particles' and their locations e.g. displacement from the first particle in the list. Primary particles can be characterized as spheres of constant density described by, say, mass but can also contain additional information as for example chemical composition of the surface of a primary particle. The number of internal coordinates is the length of the sequence times the number of particle attributes like distance from the first member in the sequence. Therefore a member of the population of nanoparticles can have several thousand internal coordinates.

The simplest and most widely used model is the **Coalescent Sphere Model** in which all particles are assumed to be spheres of common density. It is then convenient to describe a particle in terms of the number of monomers. Addition is defined just as for the natural numbers: the result of the coagulation of two spheres is a new sphere with volume equal to the sum of the volumes of the initial spheres, i.e. coagulation is completely coalescent. The internal coordinate of the nanoparticle is its volume or number of contained monomers.

A slightly more detailed model with two internal coordinates is the **Surface and Volume Model**. Here we say that a particle is described by volume and surface area. We define addition componentwise, i.e. volume and surface area of the new particle are the sums of the volumes and the surface areas of the interacting particles respectively and hence coagulation is modelled without any coalescence. It is an intermediate stage between the Primary Particle Model and the Coalescent Sphere Model. Processes like sintering, condensation, or surface reactions can transform the volume to surface ratio of an aggregate. The definition of $g^{(l)}$ is non-trivial even with a clear picture of the underlying chemical processes.

2.2 Gas phase chemistry

The gas phase chemistry leading to organic soot and Polycyclic Aromatic Hydrocarbons (PAH) has been subject of research for a long time because the combustion of hydrocarbons is so important for many technical and chemical applications. Gas phase chemistry models used for modelling soot and carbon black can be found in 121, 3, 96).

The gas phase chemistry leading to inorganic nanoparticles is far less well understood and it is very clear that this is an important field of future research. Kinetic data for SiO_2 particles formed from SiH_4 can be found in 60). Reference 113) contains data on the formation of titania particles (TiO_2) made from tetraisopropoxide and reference 93) contains data if $TiCl_4$ is used as precursor. Simple models for the gas phase chemistry describing the formation of Fe_2O_3 particles from $Fe(CO)_5$ can be found in 38, 77).

2.3 Particle inception

Particle inception is probably the most difficult part when modelling nanoparticle synthesis. It is fair to say that it is still not really understood. One approach to model particle inception for inorganic nanoparticles is to apply the theory of homogeneous nucleation of Vollmer-Becker-Döring-Zeldovich which dates back to the early thirties of the last century. In their model supersaturated vapor containing monomers and subcritical clusters of molecules collide to form stable clusters of molecules which exceed a critical radius. This critical radius depends on the surface energy, the volume of the formed structure, the temperature and the degree of supersaturation. The surface energy for clusters of such small size is not known and is usually estimated from bulk properties. These estimates can deviate from the true values by orders of magnitude. Unfortunately surface energies can only be measured for clusters which are significantly larger than the critical size and therefore cannot provide sufficient accuracy. However, molecular dynamics simulation can be used to calculate the properties of a critical cluster, for instance surface tension. These simulations are computationally very expensive and contain significant approximations.

For the simulation of SiO_2 and TiO_2 the critical cluster size has been determined by homogeneous nucleation theory using bulk properties to be not more than one molecule in 60). However in a more recent paper Artelt et al.6) studied the effect of varying surface energy on the critical particle diameter and proposed that the size of critical clusters can exceed one.

The nucleation of organic nanoparticles is believed to be different but also still unknown. The inception species for the first soot particles are polycyclic aromatic hydrocarbons (PAH). The model in 3), also called ABF model, which is widely used in the combustion community, assumes that the first particles form when two pyrene molecules collide. In this model every collision leads to successful formation of a soot particle. Despite the simplicity of this assumption the prediction for number density and soot volume fractions in premixed laminar flames are within an order of magnitude of the experimental observations. A more refined model is that of Frenklach and Wang36) where a population balance of PAHs of different sizes is considered which form a soot particle on collision.

More recently, quantum mechanic calculations have been used to shed light on the problem of particle inception. Appel et al.4) argue that dimers should be stable under flame conditions if the interaction energy in the dimer is larger than the internal energy of the two molecules. The result of their quantum mechanical calculations indicate that PAH dimers larger than the pyrene dimer are sufficiently stable to form a three dimensional structure at temperatures above 1500K. Schuetz and Frenklach[104] make use of molecular dynamics to study the collision of two pyrene molecules and conclude that aromatic dimers of species as small as pyrene can survive long enough to evolve into soot nuclei. Violi[118] combines kinetic Monte Carlo simulations on a mesoscopic level with molecular dynamics simulations to study the formation of the first soot particles from PAHs. She explains successfully the difference in H/C ratio, particle sphericity, and depolarization ratio as a function of the fuel properties. Despite first success of molecular dynamics modelling the time scales on which these calculations are carried out are in the order of nanoseconds which is too short to bridge the time gap necessary to establish the statistics of collision. Fortunately new experimental data on particle size distribution down to very small particle sizes are available for validation[130] and will help in gaining a better understanding of particle inception.

2.4 Coagulation

The model for particle coagulation depends on the choice of the particle model and on the physical conditions like temperature and pressure of the environment the particles are in. The coagulation kernel K determines the rate of collision of two particles. For nanoparticles even in turbulent flows Brownian coagulation is the mechanism with which particles coagulate. In 14) it is shown that for typical flame conditions the Brownian collision frequency is dominating over the Saffman Turner collision frequency which describes the collision frequency of particles due to turbulence. Brownian coagulation is modelled by the Fuchs kernel, e.g.[125, 37, 86] which covers different regimes classified by the Knudsen number, the ratio of twice the gas mean free path to the particle diameter. The free mean path of course depends on temperature and pressure of the particle surrounding gas. The different regimes are the continuum, slipflow, transition, and free molecular regime where at one end of the spectrum, in the continuum regime, particles perform a Brownian motion and on the other end of the spectrum, in the free molecular regime, particles perform a free flow followed by a collision type of movement. In addition to these kinetically derived collision frequencies an enhancement factor due to van der Waals forces between the particles needs to be accounted for 43). These forces lead to coagulation of particles even if they do not collide but get “close enough”.

The collision diameter which appears in the coagulation kernel is unknown except for the very simple Coalescent Sphere Model where all particles are spheres. The collision diameter depends on the fractal dimension of the aggregate which is formed. The fractal dimension can be obtained from Monte Carlo simulations. In the continuum regime the diffusion limited cluster-cluster aggregation model (DLCA) gives a fractal dimension of 1.80. For the free molecular regime, the prevailing in atmospheric flames, the ballistic cluster-cluster aggregation model (BCA) leads to a slightly higher fractal dimension of 1.94.

However, sintering, surface growth, or condensation can change the fractal dimension significantly. Mitchell and Frenklach[75, 76] developed a Monte Carlo method including coagulation and surface growth. Using the BCA model, i.e. assuming a particle sticks rigidly at the first point of contact to a target particle, they performed surface growth on each primary particle in the target particle by integration, losing the discrete nature of the surface events. The collision diameter and fractal dimension was then obtained from the target particle.

In 103) a Monte Carlo simulation of aggregation and sintering is performed. Similar to the approach above a target particle is allowed to coagulate with other particles. The authors then employ a ‘shrinking back backbone’ approach to change the surface to volume ratio and therefore the particles’ fractal dimension.

Very recently Balthasar et al.[10] combine the approach developed in 76) with a Monte Carlo algorithm developed in 40) to simulating for the first time a full population of nanoparticles using the Primary Particle Model for a nonpremixed laminar flame.

The most important result of the above-mentioned simulations is that the fractal dimension of nanoparticles changes in time depending on surface growth, coagulation, and sintering. The detailed simulations can then be used to extract a functional relationship for the change of fractal dimension and therefore collision diameter with the aim to include this information in a simpler Surface and Volume Model.

2.5 Surface reaction

In order to model surface reactions accurately it is necessary to understand the gas-phase chemistry and the chemical composition and area of the surface of the nanoparticles. In many applications surface reactions play a very important role. Along with particle sintering which will be discussed later surface reaction can significantly change the fractal dimension of a particle. Unfortunately the importance on the one hand is reflected by the lack of knowledge about these processes on the other hand.

In the case of carbon nanoparticles the number of active sites has been observed to reduce as a function of the age of a soot particle in a premixed laminar flame. In 3) a measure for surface reactivity was introduced and fitted to a number of experiments. In 107) the surface reactivity has been associated to the age of the soot particles which accounts for the change of the surface chemistry of each particle. However, this very simplistic model needs to be replaced by a more detailed one in which the chemical composition of the particles' surface is known.

In a series of papers[31, 32, 35)] Frenklach and co-workers used a kinetic Monte Carlo technique to study this deactivation of surface reactivity on soot particles. The fluctuations of the spatial structure of PAHs on the surface of the particles are responsible for the deactivation of active surface sites. However these findings have not been implemented in a population balance model.

The number of papers which present models for surface growth of inorganic nanoparticles is quite small (e.g. see 92) and references therein). Here, not only the chemical nature of the active sites needs to be known but also an accurate model for the change of the surface through sintering needs to be in place.

2.6 Condensation

Particle condensation is a process in which a chemical species from the gas phase sticks to the surface of a particle not through chemical reactions but through the weaker van der Waals force. A typical example for condensation is the attachment of PAHs on a soot particle's surface. In the case of soot or carbon black this can be a significant growth process. Typically species that play a role in the particle inception mechanism, like PAHs, are likely to condense on a particle's surface. For laminar flames where the particle inception zone is very thin condensation is less likely to play an important role in particle growth.

2.7 Sintering

The driving force for the sintering of nanoparticles is the reduction of potential energy due to the decrease in surface area. A lot of research has been carried out to understand sintering of metallic particles. However, there are much fewer papers on nanoparticles that simultaneously perform sintering and coagulation.

One of the most widely used sintering models in population balances has been introduced by Koch and Friedlander[49, 128)]. The model is based on the Particle Volume Surface model where a particle with a surface to volume ratio equivalent to an agglomerate of primary particles changes its surface area at a characteristic sintering time to the surface area of a perfect sphere while keeping its density constant. For some nanoparticles, e.g. Si-particles the driving force for this physical mechanism is grain boundary diffusion. This simple model describes only the later stages of the sintering process sufficiently well where the particles are close to spherical. Structural changes are not taken into account.

To obtain deeper understanding of the structural changes, and therefore the changes in fractal dimension over time, Monte Carlo simulations have been performed by a number of research groups. Pratsinis and co-workers[1)] carried out one of the first Monte Carlo simulations considering coagulation with simultaneous restructuring due to sintering. They examined two-dimensional clusters with finite binding energy using random particle walks on the surface of these clusters. This model is able to reproduce at least qualitatively the influence of residence time and temperature on nanoparticles formed in a reactor. Much more recently Schmid et al.[103)] presented a very detailed Monte Carlo simulation of agglomeration and sintering where the particles are shrunk along a common backbone and the overlapping volume is then distributed over the accessible surface. Depending on the sintering time the fractal dimensions vary from 1.86 to 2.99. They established a functional relationship for the change of the fractal dimension over time and used this relationship in a simpler population balance model[5)].

3 Numerical Methods

The numerical solution of equation (1) is a very challenging problem for several reasons. The two most important ones are the large size of the system of ordinary differential equations and the nonlinearity of the coagulation operator (2). For example in the case of the coalescent sphere model the difference between the smallest and largest particle sizes and therefore the size of (1) can easily be several orders of magnitude. Surface reactions and particle inception can also cause severe numerical challenges. In this section we shall discuss different strategies to obtain meaningful numerical solutions to (1) despite these difficulties.

3.1 Method of moments

The method of moments (MOM) is computationally the most efficient approach to obtain a numerical approximation to the moments of a population balance. For this reason this method is often used when simulating problems where transport of particles in a flow with complex geometry is essential. In the area of nanoparticle modelling two techniques have been used so far. The first technique used by Frenklach and co-workers is the method of moments with interpolative closure (MOMIC)[34]. The second approach is based on the quadrature method of moments which is a more recent technique based on the work of McGraw[73].

In the first instance MOMIC has been developed to describe the formation and oxidation of soot particles. In its early form the method is based on a univariate description of spherical soot particles in the free molecular regime, for instance in 36) MOMIC is used to simulate the formation of soot in a burner stabilized premixed ethylene flame where the soot moments are calculated in a post processing step. In this work two sets of moments of the size distribution of PAH and the size distribution of soot particles are solved simultaneously. Some theoretical remarks on the validity of the MOMIC approach can be found in 33). Numerical tests of the accuracy of the interpolative closure are contained in 12) for inorganic and in 41) for organic nanoparticles. For unimodal particle size distributions where no surface reactions that reduce particle size are present MOMIC produces excellent results being accurate and fast. The method has been extended to include coagulation in the transition and the continuum regime and taking into account the aggregate structure of soot particles by introducing a preset size for a primary particle in an agglomerate[47]. In the latest development in MOMIC a shape descriptor, which is related to the surface fractal dimension, is used to model the aggregate structure of soot particles using particle volume and particle surface area[9].

An alternative approach for obtaining the moments of the PSD is the quadrature method of moments (QMOM)[73]. There the moments are calculated assuming the PSD can be represented as weighted multi-dimensional Dirac delta function. The weights and the nodes are then chosen to satisfy the transport equations for the moments of the PSD. The advantage of this approach is that due to the choice of delta functions there exists no closure problem. Rosner and co-workers use this method to simulate uni-variate and bivariate population balances to model alumina nanoaggregate evolution in counterflow diffusion flames. The bivariate model includes coagulation and sintering of the particles. In 98) Rosner uses a Monte Carlo method to validate this approach and discusses the role of mixed moments in QMOM. Despite the success of this method Marchisio and Fox[68] point out two main problems with QMOM. First, the solution of the transport equations for the moments of the PSD makes it difficult to treat systems where the dispersed-phase velocity strongly depends on the internal coordinates and more importantly for multivariate systems the QMOM becomes numerically very challenging. The authors present an improved approach called the 'direct quadrature method of moments' (DQMOM) which is computationally more attractive and allows the extension to more internal variables.

Despite all the computational advantages there are some shortcomings associated with the method of moments. The most significant shortcoming is the non-uniqueness of the reconstruction of the particle size distribution function, i.e. the PSDF is not available. As a consequence, reactions that take place on the particles' surface which lead to decomposition of particles back to the gas phase can only be incorporated with additional model assumptions.

3.2 Sectional methods

Sectional methods (SM) are widely used to solve population balance equations. There the size spectrum is divided into a set of size classes. One distinguishes between zero-order and higher-order methods. Higher-order methods use low order polynomials to represent the particles within each section and can be regarded as a simple form of finite element methods which will be discussed in the next section. They can suffer from stability problems and artificial dispersion whereas zero-order methods are more robust. There the computational domain is divided into rather small intervals in which the solution is approximated by step functions. For each interval one obtains an ordinary differential equation which is coupled to the neighbors depending on the discretization scheme used. Batterham et al.[16] divide the size domain in a geometric series of 2 and derive a numerical scheme which is mass conserving. Hounslow et al.[44] extend this method using a correction to conserve particle number and particle mass. Litster et al.[62] modified this method by introducing an adjustable geometrical size discretization so that higher moments and self-preserving shape of the PSD is correctly predicted. However, there are large numerical errors in the presence of discontinuities and surface growth. To alleviate the problem with numerical diffusion in the presence of surface growth Kumar and Ramkrishna[54, 55, 56] introduced a pivot technique combined with a moving grid as well as the method of characteristics. An additional set of equations is solved to ensure that a chosen set of properties is conserved. All these methods are compared by Vanni[115] for a comprehensive set of test cases. Pope and Howard[89] couple a sectional model to a detailed gas phase mechanism to calculate the soot particle size distribution in a CSTR. Sectional methods have also been developed for bivariate population balance equations. Based on a model by Koch and Friedlander[49] Xiong and Pratsinis[128] present a two-dimensional particle size distribution including particle volume and particle surface as internal variables. The numerical method is based on a sectional approach which conserves volume. Nakaso et al.[79] also use a two-dimensional discrete-sectional representation of the size distribution solving the aerosol general dynamic equation for chemical reaction, agglomeration, and sintering. However, the use of these methods has been limited by their high computational cost. Hence in 78) a number of approximations to the detailed two-dimensional model in 128) are made. The most important being the introduction of constant average coagulation coefficients and employing look up tables. Also a volume correction term was introduced that ensured the conservation of both number and mass.

An alternative to bivariate population balances with volume and surface area as internal coordinates is to average the surface area information for each volume section turning a bivariate population balance into two univariate population balance. Different strategies are used to do this. Tsantilis and Pratsinis[114] proposed a sectional method in which they assumed that particle surface area in a given section decreases monotonically due to sintering and solved two sets of equations for particle volume and surface area using the sectional method developed in 44). This method is applied in 113) to simulate titania particles and compared with the bivariate model. Recently, Jeong and Choi[45] used a single surface fractal dimension to correlate particle volume and area in a given interval to simplify the bivariate model of Xiong and Pratsinis[128] to two sets of one-dimensional equations for particle volume and surface area. A slightly different approach has been developed by Park and Rogak[87] where the agglomerate volume and the number of primary particles within an aggregate is tracked. This model considers the effect of surface growth due to ultrafine particle deposition on the primary particle size. Wen et al.[124] combined this with moving sections as well as the addition of new sections for incepted particles and applied it to model soot formation in a plug flow reactor. In each section the number of soot clusters and the number of primary particles is stored.

3.3 Finite element methods

An alternative to sectional methods are the more sophisticated finite element methods. In the finite element approach the solution of the population balance is expanded in a series of polynomials. For the coefficients of this expansion a set of equations has to be solved which is obtained by inserting the expansion into the population balance equation. Various methods can be derived by a different choice of basis functions, nodes, and time stepping schemes. The mathematical discipline of functional analysis provides the theoretical framework with which errors can be estimated. This is of course a very attractive feature of finite element methods.

In the early 1990s, Deuflhard, Bornemann, and Wulkow at the ZIB in Berlin[25, 24, 20] developed a discrete Galerkin h-p method for the simulation of molecular weight distributions in polymerization reactions. Wulkow commercialized this idea and successfully implemented an algorithm in his software product PREDICI[126].

The structural similarities between the population balances in polymerization and nanoparticle dynamics then led to the development of the software package PARSIVAL, a new dynamic flow sheet simulator especially suited for process units which are modelled by population balance equations. This new approach is based on a fully adaptive Galerkin h-p method with an automatic error control for time discretization as well as for the discretization of the property coordinate. The minimization of the required number of degrees of freedom is combined with an adaptivity in time and internal coordinate. Details of the numerical procedure are given in 127). Recently, PARSIVAL has been extended to solve bivariate population balances but no examples involving the simulation of nanoparticles are available in the open literature.

PARSIVAL and PREDICI are employed not only in industry but also by several research groups. Appel and Bockhorn used the PARSIVAL to simulate soot particle size distributions in laminar premixed flames[4]. Artelt, Schmid, and Peukert[5, 6] have been using PARSIVAL for modelling Si production. They incorporated the mean value of fractal dimension into their model as well as the agglomerate collision diameter and the number of primary particles. Not using PARSIVAL or PREDICI but based on Wulkow's earlier work, Vlasov, Warnatz and co-workers employed a finite element code to simulate the formation of soot in a shock tube[119, 80].

Independent of the work that originated in Berlin, also in the early 1990s, Sabelfeld and co-workers from Novosibirsk in Russia[101, 52] developed a finite element approach using a local set of either B-spline or Hermitian spline basis functions. For the time stepping they employ an explicit scheme with enlarged stability region. This method has been applied to aerosol dynamics describing SiH_4 decomposition in a quartz reactor[85]. Nicmanis and Hounslow in Cambridge developed a finite element method to calculate the steady state of a general population balance equation[81, 82]. In 83) some error estimates are derived for this method. Although this method has not been applied to nanoparticle dynamics the authors make some comparison to sectional methods finding the finite element approach numerically more accurate.

More recently, Liu and Cameron[63] presented a wavelet based approach which has been validated against analytical solutions. Wavelets are a special choice of basis function and provide through their multiresolution properties a number of advantages. They seem particularly suited for modelling bimodal particle size distributions. However, up to now this technique has not been used for modelling nanoparticle population dynamics.

3.4 Monte Carlo methods

An alternative to sectional methods for solving the population balance equation are Monte Carlo (MC) methods. They are easy to implement, can account for fluctuations, and can easily incorporate several internal coordinates. In the case of nanoparticle modelling the number of particles is so large that the fluctuations in particle numbers can be neglected.

Monte Carlo methods used to obtain approximations to the solution of equation (1) are all generalization of the classic Marcus-Lushnikov process[70, 65]. The theory of probabilistic methods related to coagulation is reviewed in 2). One of the first applications of Monte Carlo methods to the solution of the Smoluchowski equation was presented in 39). In this very influential work Gillespie used a Direct Simulation Monte Carlo (DSMC) method to simulate the dynamics of aerosol particles. Around the same time Ramkrishna and co-workers presented a Monte Carlo method for population balance equations[106, 95].

The DSMC algorithm works as follows. First, a normalization volume is chosen; then the solution to the population balance equation is approximated by N particles. The normalization volume plays the role of a numerical approximation parameter and determines the error between the approximation and the solution to (1). This particle system evolves in time mimicking the physical nanoparticle system. For a waiting time τ nothing happens. Then one of the following events, particle inception, coagulation/coalescence, surface growth, or sintering takes place depending on their probability, i.e. on the rate of the corresponding processes. The particle system is modified accordingly and the new probabilities are calculated. Then a new waiting time is determined.

Over the last decade the DSMC has been improved by several research groups in the engineering community. Most of these improvements can be classified as variance reduction techniques. Matsoukas and co-workers developed a constant number algorithm for coagulation[108], coagulation and fragmentation[58], and 59) contains an extension to other source terms and discusses a variation to the constant number approach namely a constant mass approach which is found to be superior. Maisels et al.[67] discuss a particle doubling strategy to reduce variance for simultaneous nucleation, coagulation, and surface growth.

Independently of those efforts MC methods have been developed by mathematicians and physicists mainly to simulate problems arising in nuclear weapon development and space programmes. In Russia probability theory was applied to aerosol transport quite early. In the mid-eighties Sabelfeld and co-workers in Novosibirsk developed a weighted MC method that made use of an acceptance rejection method also called fictitious jumps to speed up the algorithm. The idea is based on the acceptance rejection technique introduced by John von Neumann where the coagulation kernel is replaced by a majorant. This leads to more events/jumps but some of them are rejected to correct the overall number. This method is computationally attractive if the majorant reduces the numerical effort when choosing the collision pairs. In 101) Sabelfeld and co-workers publish in English a variety of techniques that significantly improve the standard DSMC techniques. They not only use a constant majorant kernel but also discuss a more sophisticated version of the particle doubling technique, introduce a weighted particle method for variance reduction and discuss the Nanbu type stochastic algorithm. These methods are nothing else but a mathematically rigorous way of describing what is known in the engineering community as time driven, event driven, constant number and constant volume methods.

An important contribution to the field has been

Fig. 2 Two-dimensional TEM-style projection of a sample particle taken from premixed laminar ethylene flame simulation (Provided by Neal Morgan).

made by Wolfgang Wagner and his student Andreas Eibeck. Motivated by Wagner's work on the Boltzmann equation they refined the method of fictitious jumps by introducing more effective majorants[28] for the coagulation Kernel and, more importantly, managed to prove rigorously the convergence[27, 57] of their stochastic simulation procedure for (1). This algorithm will be called direct simulation algorithm (DSA) in this paper. Other interesting convergence results and algorithms are published[84, 22, 42, 57]. One choice of weighted MC methods deserves more attention. Based on work by Babovsky[7] Eibeck and Wagner developed a mass flow algorithm (MFA)[29] which is in many cases more efficient than DSA[17] and can be generalized to include particle inception, surface growths[23, 77], and sintering[122]. Kolodko and Sabelfeld, now also at WIAS, discuss MFA as a special case of a general class of stochastically weighted algorithms and perform some numerical experiments to compare the different methods[51].

Monte Carlo methods can be easily extended to multiple internal coordinates and for this reason they have been employed to simulate various systems of nanoparticles. Akhtar et al.[1] included two internal coordiantes to describe the restructuring of the particles and showed the time evolution of the mass fractal dimension. Tandon and Rosner studied a very similar system using the technique of fictitious jumps with a constant majorant for the coagulation sintering equation[112]. Methods introduced by Wagner have been applied to inorganic nanoparicle dynamics in 41, 40, 123) and organic nanoparticles in 12, 107).

Monte Carlo methods have also been used to model coating of nanoparticles. For example in 26) the enclosure of Fe_2O_3 by SiO_2 is studied. There a population balance within a population balance is modelled. In 53) a DSMC algorithm is applied to model the coating of particles by aggregation. However, in the paper not much detail on the technique is given.

Monte Carlo methods have also been used to simulate the growth of single aggregates and study the effect of surface growth or sintering on the fractal dimension and other properties of the aggregate. For example, Mitchell and Frenklach[75] developed a Monte Carlo method to study soot agglomeration and surface growth of a single particle. A similar study but for inorganic aggregates which change through sintering has been performed in 103). So far a full simulation of aggregation of thousands of aggregates has to not been feasible due to excessive computational demands. However, for the first time, in 13) efficient majorants[40] and a ballistic MC algorithm including surface growth[76] have been combined to simulate a full population balance of soot particles in a premixed laminar flame. **Fig. 2** shows a two dimensional projection of a soot particle from a premixed laminar ethylene flame simulation.

4 Transport of Nanoparticles

So far we have only discussed models based on the assumption that the physical quantities do not vary in space. In practice this is of course never the case and therefore the models need to include the transport of particles due to convection and diffusion. Simulating reactive flows is a difficult task even if there are no particles present. We distinguish between laminar flow and turbulent flow.

4.1 Laminar flows

Transport of nanoparticles in laminar premixed flames has been modelled using the method of moments and sectional methods. Historically the effect of diffusion has been neglected. For stationary premixed laminar flames the space coordinate can be transformed into a time coordinate so that the zero-dimensional population balance equation (1) can be solved. If transport by diffusion and thermophoretic effects are included then additional equations that either account for the sections or the moments of the population balance have to be solved. The first coupling of a MOMIC approach to flow equations simulating a laminar counterflow diffusion flame was published by Mauss et al.72) and was subsequently used also for premixed laminar flames in 71). Giesen et. al.38) coupled the equations for the moments of the particle sizes and area to the commercial CFD package Fluent to simulate the formation of iron particles in a heated reactor. Marchisio et al. implemented QMOM69) into Fluent taking simultaneous aggregation and breakage into account. Also the sectional approach has been coupled to flow equations by Smooke et al.109) to simulate the formation of soot in a co-flow ethylene diffusion flame. The authors are using a sectional approach which is coupled to a detailed chemical model along with a velocity-vorticity formulation including buoyancy. Sun et al.111) present a fully coupled two-dimensional sectional method where they model the formation of sodium coated carbon particles in a sodium halide diffusion flame. These simulations consume a lot of CPU time even on fast machines, in particular, if the gas phase chemical mechanism is very large, as it is the case for combustion of hydrocarbons leading to soot. A strategy to alleviate this problem is to decouple the fast processes, like the fast chemical reactions in the gas phase, from the slower ones. This was achieved for a laminar co-flow diffusion flame using a flamelet library for the chemical species and the source term of soot volume fraction. In the simulation of the flame only equations for soot volume fraction and mixture fraction had to be solved along with velocity and temperature11). The authors report good agreement with measurements and low CPU times.

4.2 Turbulent flows

As most industrial reactors are turbulent it is important to incorporate a model for nanoparticle transport into a model which describes turbulent flows. Modelling of reactive turbulent flow is a very challenging problem due to its nonlinear, chaotic nature and the magnitude of length scales present in the flow. The books and review articles by Fox30) and Pope90, 91) give an excellent treatment of the physics of turbulent flow and models which are in use. Although it is possible to formulate detailed models for the synthesis of nanoparticles in turbulent flames it is necessary to simplify these models to make them computationally tractable. The most detailed statistical approach is based on the probability density function (PDF) transport equation from which the moments of all physical quantities can be obtained. The PDF transport equation including an empirical model for soot formation and a global chemistry model has been applied to turbulent flames by Kollmann et al.50). Borghi et al. uses a variant of the PDF approach102) also with global chemistry and an empirical expression for soot volume fraction. More recently, a PDF approach with a reduced chemical mechanism with 15 species and 144 reaction, Curl mixing model and a radiation model has been used by Lindstedt and coworkers61). The particulate phase was modelled using the method of moments including detailed surface reaction chemistry.

Almost all PDF based models use Monte Carlo techniques in conjunction with a CFD code and therefore the computational cost is very high. An alternative and much less computationally expensive are stochastic reactor models (SRMs)17) which are based on the assumption that there are no spatial gradients in the PDF of the physical quantities in the computational domain. Because of this gross simplification, detailed reaction chemistry as well as the moments of a particle population can be included in SRMs making them a useful and computationally attractive tool to simulate engines129) and industrial carbon black reactors14). The alternative to SRMs, where the information on the flow field is sacrificed in favor of the chemistry, is to use a very simple chemistry model and solve Reynolds or Favre averaged transport equations using a closure model for the mean reaction rates. For example Lockwood64) used a global chemistry step combined with an empirical model for soot mass fraction and soot number density employing a presumed beta PDF closure.

Soot formation in turbulent flames, gas turbines and diesel engines has also been modelled using a CFD flamelet approach combined with the method of moments. Two methods are used to decouple the chemistry from the flow field. Mauss and co-workers8, 46, 15) use flamelet libraries which contain the species information as well as the source terms for surface growth, particle inception, and condensation. This approach is now implemented in the commercial code STAR-CD. A computationally more demanding but more accurate approach is to transport representative interactive flamelets (RIF) through the computational domain, average over their properties and couple these properties back to the CFD code. This method has been successfully used to simulate diesel engines by Pitsch et al.88).

Nanoparticles in turbulent reactive flow have only been modelled using the method of moments incorporated into a CFD code. However for the transport of aerosols100) and the transport of bubbles in an extraction column116) a population balance has been coupled to a CFD code using Monte Carlo methods. These methods have good potential if it is necessary to couple population balances with several internal coordinates to turbulent reacting flows.

5 Applications

In this section we attempt to collect a list of references which report on numerical models for nanoparticle synthesis. **Table 1** contains a list of applications where the numerical methods described above have been used to simulate nanoparticle population dynamics. As throughout this paper, both organic and inorganic nanoparticles have been treated together. In 48) a more detailed but older list on soot modelling can be found. The entries of the table are ordered with respect to the mathematical complexity of the model. For example, entries in the left column range from a shock tube (ST) to real industrial furnaces, gas turbines (GT), and internal combustion engines (ICE). It is important to note that this table is not complete and cannot be given the vast amount of literature. However, examples for the most important models and numerical methods are included.

6 Future Development

Despite the progress in the last few years at modelling nanoparticle flame synthesis there is clearly a need for further development of models and numerical methods. One important field of future research will be the chemistry of precursors to inorganic nanoparticles. Homogeneous and heterogeneous chemical reactions need to be understood to model particle formation and the change in particle size due to chemical reactions on the particles' surface. Currently, data on the thermodynamic properties of relevant species and reaction mechanisms are either missing or have high uncertainties associated with them. It will be necessary to conduct more high quality experiments in order to determine the relevant data. However, the role of computational chemistry will become more important as computers become more powerful so that thermodynamic properties and reaction kinetics can be obtained.

Another area which will certainly develop further is the coupling of population balances to CFD codes. Here the method of moments seems to be very promising but it is necessary to extend the method so that more internal variables can be tracked. The direct quadrature method of moments seems to be the method of choice at the moment. However, with the increase of computational power coupling Monte Carlo methods to CFD seems also viable. A more fundamental problem is the modelling of turbulent two phase flow which will remain a challenge for a long time to come. Apart from coupling of the population balance to the continuous phase, closure models for chemical reactions and for the turbulent transport terms need to be found. The use of LES in conjunction with flamelets and the PDF transport equations could be a possible but computationally expensive way forward.

An area which is very important is the development of mathematical techniques for estimating parameters in population balance models from experimental data. Recently, a weighted Monte Carlo method for the calculation of parametric derivatives has been developed117). This method has a large potential to determine physical parameters from experimental data in the area of nanoparticles.

In the scientific community only the modelling of homogeneous gas phase nanoparticle synthesis has been studied. However in many applications the precursors of the particles are sprayed into a flame where they then form particles under the appropriate conditions66). This means that the dynamics of the droplets including the precipitation within the droplets needs to be included in the population balance model. Models which have been developed in the area of spray drying are a suitable starting point to achieve this.

There exist a number of applications where nanoparticles are coated or are composites of different types of particles. Models for these processes have not been treated in this paper but will be an important field in the future. First steps have been taken in 111) where the primary size of a particle has been controlled by condensing a sodium fluoride layer on the particles and thus avoiding the formation of hard agglomerates. The authors of that paper used a sectional method with two internal coordinates to model this process. Monte Carlo methods have been used in similar applications26).

Table 1 List of applications.

Reactor	Material	Numerical method						Reference
		a	b	c	d	e	f	
ST	Soot	1	FEM	0	c	d	–	Vlasov and Warnatz[119)]
ST	Soot	1	FEM	0	c	d	–	Naydenova et al.[80)]
PFR	Soot	1, 1	SM	0	c	d	–	Wen et al.[124)]
PFR	SiH_4	1	FEM	0	nc	d	–	Onischuk et al.[85)]
PFR	TiO_2	1	SPM-MFA	0	nc	d	–	Morgan et al.[77)]
PFR	TiO_2	1	SM	0	c	d	–	Tsantilis and Pratsinis[114)]
PFR	TiO_2	2	SM	0	nc	d	–	Nakaso et al.[79)]
PFR	TiO_2	1, 1	FEM	0	nc	d	–	Schmid et al.[6)]
PFR	SiO_2, TiO_2	1, 1	SM	0	nc	d	–	Jeong and Choi[45)]
CSTR	Soot	1	MOMIC	0	c	d	–	Brown et al.[21)]
CSTR	Soot	1	SM	0	c	d	–	Pope and Howard[89)]
PLM	SiO_2	1	SM	0	nc	d	–	Lindaker et al.[60)]
PLM	SiO_2	1	MOMIC	0	nc	d	–	Grosschmidt et al.[41)]
PLM	SiO_2	1	SPM-DSA	0	nc	d	–	Grosschmidt et al.[41)]
PLM	SiO_2	2	SPM-MFA	0	nc	d	–	Wells et al.[123)]
PLM	Fe_2O_3	1	SPM-MFA	0	nc	d	–	Morgan et al.[77)]
PLM	Soot	1	MOMIC	0	nc	d	–	Frenklach and Wang[36)]
PLM	Soot	2	MOMIC	1	c	d	–	Balthasar and Frenklach[9)]
PLM	Soot	1	MOMIC	1	c	d	–	Appel et al.[3)]
PLM	Soot	1	FEM	0	nc	d	–	Appel et al.[4)]
PLM	Soot	1	SPM-DSA	0	nc	d	–	Balthasar and Kraft[12)]
PLM	Soot	1	SPM-DSA	0	nc	d	–	Zhao et al.[130)]
PLM	Soot	2	SPM-DSA	0	nc	d	–	Singh et al.[107)]
PLM	Soot/NaF	2	SM	1	c	d	–	Sun et al.[111)]
PLM	SiO_2/Fe_2O_3	2	SPM-DSA	0	nc	g	–	Efendiev and Zachariah[26)]
PLM	Generic	2	SM	0	nc	g		Mühlenweg et al.[78)]
PLM	Generic	1, 1	SM	3	c	g	CFD	Mühlenweg et al.[78)]
LCF	Alumina	2	QMOM	2	nc	g	CFD	Rosner and Pyykönen[99)]
LCF	Soot	1	MOMIC	1	c	d	CFD	Mauss et al.[72)]
LDF	Soot/Sodium	2	SM	1	c	g	CFD	Sun et al.[111)]
LDF	Soot	1	SM	2	c	d	CFD	Smooke et al.[109)]
LDF	Soot	1	MOMIC	2	c	d	CFD/Flamelet	Balthasar et al.[11)]
TF	Soot	1	MOM	2	c	g	PDF	Kollmann et al.[50)]
TF	Soot	1	MOM	2	c	g	PDF	Borghi et al.[102)]
TF	Soot	1	MOM	1	c	r	PDF	Lindstedt and Louloudi[61)]
TF	Soot	1	MOM	2	c	d	CFDT/Flamelet	Bai et al.[8)]
ICE	Soot	1	MOM	0	c	d	SRM	Yoshihara et al.[129)]
ICE	Soot	1	MOM	3	c	d	CFDT/Flamelet	Pitsch et al.[88)]
ICE	Soot	1	MOM	3	c	d	CFDT/Flamelet	Karlsson et al.[46)]
GT	Soot	1	MOM	3	c	d	CFDT/Flamelet	Balthasar et al.[15)]
Furnace	CB	1	MOM	0	c	d	SRM	Balthasar et al.[14)]
Furnace	Fe	1, 1	MOM	3	c	g	CFDT	Giesen et al.[38)]
Furnace	CB	1	MOM	3	c	g	CFDT	Lockwood and Niekerk[64)]

Reactor: shock tube (ST), plug flow reactor (PFR), continuously stirred reactor (CSTR), premixed laminar flame (PLM), laminar diffusion flame (LDF), laminar counter flow diffusion flames (LCF), turbulent flame (TF), internal combustion engine (ICE), gas turbine (GT), Furnace. Numerical method: (a) internal coordinates, (b) population balance approach, (c) spatial coordinates, (d) coupling between particulate and gas phase (c-coupled, nc-not coupled), (e) chemistry model (d-detailed, r-reduced, g-global), (f) transport model (CFD) Navier Stokes equation, (CFDT) averaged Navier Stokes equation

7 Conclusion

In this paper we reviewed the literature of nanoparticles from flame synthesis and discussed the models and the numerical methods used in this field. We started by describing a general population balance model for nanoparticles in the absence of spatial gradients of the physical quantities. The model is comprised of several submodels which are: a detailed homogeneous gas phase reaction mechanism, a particle inception model, a model for particle agglomeration, surface reactions, condensation, and sintering. References for these submodels were given and their accuracy was discussed. Then the numerical treatment of population balances was reviewed. The literature on the method of moments, sectional, finite element, and Monte Carlo methods was discussed. Special attention was given to the latest developments in the area of Monte Carlo methods. They are very promising for solving population balance models with a very large number of particle properties. Then the coupling of a population balance to laminar and turbulent flow was examined. The method of moments has been identified as a suitable method to efficiently simulate laminar flames. The method of moments is also a good choice to couple a population balance to turbulent flow where several closure problems have to be addressed. The separation of time scales is an important technique when modelling particle synthesis in industrial type combustion chambers. A number of examples were summarized in a table to make the vast amount of literature more accessible. Finally, future areas of research were discussed.

New materials and processes as well as the ever growing computational power will turn modelling of particular processes from specialized software used in research laboratories to a development tool for engineers in industry. This development needs to be accounted for in the education of engineers.

Acknowledgements

The author would like to thank the members of the Computational Modelling Group in Cambridge, in particular my students Neal Morgan, Robert Patterson, Jasdeep Singh, and Sebastian Mosbach.

References

1) M. K. Akhtar, G. Lipscomb, and S. E. Pratsinis. Monte Carlo simulation of particle coagulation and sintering. *Aerosol Sci. Tech.*, 21:83-93, 1994.

2) D. J. Aldous. Deterministic and stochastic models for coalescence (aggregation and coagulation): A review of the mean-field theory for probabilists. *Bernoulli*, 5(1):3-48, 1999.

3) J. Appel, H. Bockhorn, and M. Frenklach. Kinetic modelling of soot formation with detailed chemistry and physics: Laminar premixed flames of C_2 hydrocarbons. *Combustion and Flame*, 121:122-136, 2000.

4) J. Appel, H. Bockhorn, and M. Wulkow. A detailed numerical study of the evolution of soot particle size distributions in laminar premixed flames. *Chemosphere*, 42:635-645, 2001.

5) C. Artelt, H.-J. Schmid, and W. Peukert. On the relevance of accounting for the evolution of the fractal dimension in aerolsol process simulations. *Journal of Aerosol Science*, 34:511-534, 2003.

6) C. Artelt, H.-J. Schmid, and W. Peukert. On the impact of accessible surface and surface energy on particle formation and growth from the vapour phase. *Journal of Aerosol Science*, 36:147-172, 2005.

7) H. Babovsky. On a Monte Carlo scheme for Smoluchowski's coagulation equation. *Monte Carlo Methods and Appl.*, 5(1):1-18, 1999.

8) X. S. Bai, M. Balthasar, F. Mauss, and L. Fuchs. Detailed soot modelling in turbulent jet diffusion flames. *Proc. Comb. Inst.*, 27:1623-1630, 1998.

9) M. Balthasar and M. Frenklach. Detailed kinetic modelling of soot aggregate formation in laminar premixed flames. *Combustion and Flame*, 140:130-145, 2005.

10) M. Balthasar and M. Frenklach. Monte-Carlo simulation of soot particle coagulation and aggregation: the effect of a realistic size distribution. *Proceedings of the Combustion Institute*, 30(1):1467-1475, 2005.

11) M. Balthasar, A. Heyl, F. Mauss, F. Schmitt, and H. Bockhorn. Flamelet modelling of soot formation in laminar ethyne/air diffusion flames. *Proc. Comb. Inst.*, 26:2369-2377, 1996.

12) M. Balthasar and M. Kraft. A stochastic approach to calculate the particle size distribution function of soot particles in laminar premixed flames. *Combustion and Flame*, 133:289-298, 2003.

13) M. Balthasar, M. Kraft, and M. Frenklach. Kinetic Monte Carlo simulations of soot particle aggregation. *Prepr. Pap.-Am. Chem. Soc., Div. Fuel Chem.*, 50(1): 135-136, 2005.

14) M. Balthasar, F. Mauss, A. Knobel, and M. Kraft. Detailed modeling of soot formation in a partially stirred plug flow reactor. *Combustion and Flame*, 128: 395-409, 2002.

15) M. Balthasar, F. Mauss, M. Pfitzner, and A. Mack. Implementation and validation of a new soot model and application to aeroengine combustors. *ASME 2000-GT-0142*, 2001.

16) R. J. Batterham, J. S. Hall, and G. Barton. Pelletizing kinetics and simulation of full scale balling circuits. In *Proceedings of the third international symposium on agglomeration*, page A136, 1981.

17) A. Bhave and M. Kraft. Partially stirred reactor model:

Analytical solutions and numerical convergence study of a PDF/Monte Carlo method. *SIAM J. Sci. Comput.*, 25:1798-1823, 2004.

18) H. Bockhorn, editor. *Soot Formation in Combustion*, volume 59 of *Springer Series in Chemical Physics*. Springer-Verlag, 1994.
19) H. Bockhorn. Ultrafine particles from combustion sources: approaches to what we want to know. *Phil. Trans. R. Soc. London. A*, 358:2659-2672, 2000.
20) F. Bornemann. An adaptive multilevel approach to parabolic equations. ii. variable-order time discretization based on a multiplicative error correction. *IMPACT Computer Science and Engineering*, 3:93-122, 1991.
21) N. J. Brown, K. L. Revzan, and M. Frenklach. Detailed kinetic modelling of soot formation in ethelene/air mixtures reacting in a perfectly stirred reactor. In *Twenty-Seventh Symposium (International) on Combustion*, pages 1573-1580, 1998.
22) M. Deaconu, N. Fournier, and E. Tanre. Rate of convergence of a stochastic particle system for the Smoluchowski coagulation equation. *Methodology and computing in applied probability*, 5(2):131-158, 2003.
23) E. Debry, B. Sportisse, and B. Jourdain. A stochastic approach for the numerical simulation of general dynamics equation for aerosols. *Journal of Computational Physics*, 184:649-669, 2003.
24) P. Deuflhard, U. Novak, and M. Wulkow. Recent developments in chemical computing. *Computers and Chemical Engineering*, 14(11):1249-1258, 1990.
25) P. Deuflhard and M. Wulkow. Computational treatment of polyreaction kinetics by orthogonal polynomials of a discrete variable. *IMPACT Computer Science and Engineering*, 1:269-301, 1989.
26) Y. Efendiev and M. Zachariah. Hierarchical hybrid Monte Carlo method for simulation of two-component aerosol nucleation, coagulation, and phase segregation. *Aerosol Science*, 34:169-188, 2003.
27) A. Eibeck and W. Wagner. Approximative solution of the coagulation-fragmentation equation by stochastic particle systems. *Stochastic Analysis and Application*, 18(6):921-948, 2000.
28) A. Eibeck and W. Wagner. An efficient stochastic algorithm for studying coagulation dynamics and geleation phenomena. *SIAM J. Sci. Comput.*, 22(3): 802-821, 2000.
29) A. Eibeck and W. Wagner. Stochastic particle approximations for Smoluchowski's coagulation equation. *Ann. Appl. Probab.*, 11(4):1137-1165, 2001.
30) R. O. Fox. *Computational Models for Turbulent Reacting Flows*. Cambridge University Press, 2003.
31) M. Frenklach. On surface growth mechanism of soot particles. In *Twenty-Sixth Symposium (International) on Combustion*, pages 2285-2293, 1996.
32) M. Frenklach. Simulation of surface reactions. *Pure & Appl. Chem.*, 70:477-484, 1998.
33) M. Frenklach. Method of moments with interpolative closure. *Chemical Engineering Science*, 57:2229-2239, 2002.
34) M. Frenklach and S. Harris. Aerosol dynamics modeling using the method of moments. *Journal of Colloid and Interface Science*, 118:252-261, 1987.
35) M. Frenklach, C. A. Schuetz, and J. Ping. Migration mechanism of aromatic-edge growth. *Proceedings of the Combustion Institute*, 30(1):1389-1396, 2005.
36) M. Frenklach and H. Wang. Detailed mechanism and modeling of soot particle formation. In H. Bockhorn, editor, *Soot Formation in Combustion – Mechanisms and Models*, pages 165-192. Springer Verlag, 1994.
37) S. K. Friedlander. *Smoke, Dust, and Haze. Fundamentals of Aerosol Dynamics*. Oxford University Press, 2nd edition, 2000.
38) B. Giesen, H. Orthner, A. Kowalik, and P. Roth. On the interaction of coagulation and coalescence during gas phase synthesis of Fe-nanoparticle agglomerates. *Chemical Engineering Science*, 59:2201-2211, 2004.
39) D. T. Gillespie. An exact method for numerically simulating the stochastic coalescence process in a cloud. *Journal of the Atmospheric Science*, 32:1977-1989, 1975.
40) M. Goodson and M. Kraft. An efficient stochastic algorithm for simulating nano-particle dynamics. *Journal of Computational Physics*, 183(1):210-232, 2002.
41) D. Grosschmidt, H. Bockhorn, M. Goodson, and M. Kraft. Two approachs to the simulation of silica particle synthesis. *Proceedings of the Combustion Institute*, 29:1039-1046, 2002.
42) F. Guias. A direct simulation method for the coagulation-fragmentation equations with multiplicative coagulation kernels. *Monte Carlo Methods and Appl.*, 5(4): 287-309, 1999.
43) S. J. Harris and I. M. Kennedy. The coagulation of soot particles with van der waals forces. *Combust Sci Technol*, 59(4-6):4443-454, 1988.
44) M. J. Hounslow, R. L. Ryall, and V. R. Marshall. A discretized population balance for nucleation, growth, and aggregation. *A.I.Ch. E. Journal*, 34:1821-1832, 1988.
45) J. I. Jeong and M. Choi. A sectional method for the analysis of growth of polydisperse non-spherical particles undergoing coagulation and coalescense. *Aerosol Science*, 32:565-582, 2001.
46) A. Karlsson, I. Magnusson, M. Balthasar, and Mauss. Simulation of soot formation under diesel engine conditions using a detailed kinetic soot model. *SAE Transactions, Journal of Engines*, SAE981022, 1998.
47) A. Kazakov and M. Frenklach. Dynamic modeling of soot particle coagulation and aggregation: Implementation with the method of moments and application to high-pressure laminar premixed flames. *Combustion and Flame*, 114:484-501, 1998.
48) I. M. Kennedy. Models of soot formation and oxidation. *Prog. Energy Combust. Sci*, 23:95-132, 1997.
49) W. Koch and S. K. Friedlander. The effect of particle coalescence on the surface area of a coagulating aerosol. *Journal of Colloid and Interface Science*, 140(2):419-427, 1990.
50) W. Kollmann, I. M. Kennedy, M. Metternich, and J.-Y. Chen. Application of a soot model to a turbulent ethyl-

ene diffusion flame. In H. Bockhorn, editor, *Soot Formation in Combustion — Mechanisms and Models*, pages 503-526. Springer Verlag, 1994.

51) A. Kolodko, K. Sabelfeld, and W. Wagner. A stochastic method for solving Smoluchowski's coagulation equation. *Mathematics and Computers in Simulation*, 49:57-79, 1999.

52) K. P. Koutzenogii, A. Levykin, and K. Sabelfeld. Kinetics of aerosol formation in the free molecule regime in presence of condensable vapor. *J. Aerosol Sci.*, 27(5): 665-679, 1996.

53) F. E. Kruis, A. Maisels, and H. Fissan. Direct simulation Monte Carlo method for particle coagulation and aggregation. *AIChE Journal*, 46:1735-1742, 2000.

54) S. Kumar and D. Ramkrishna. On the solution of population balance equations by discretisation I. A fixed pivot technique. *Chemical Engineering Science*, 51: 1311-1332, 1996.

55) S. Kumar and D. Ramkrishna. On the solution of population balance equations by discretisation II. A moving pivot technique. *Chemical Engineering Science*, 51: 1333-1342, 1996.

56) S. Kumar and D. Ramkrishna. On the solution of population balance equations by discretisation III. Nucleation, growth and aggregation of particles. *Chemical Engineering Science*, 52:4659-4679, 1997.

57) C. Lecot and W. Wagner. A quasi-Monte Carlo scheme for Smoluchowski's coagulation equation. *Mathematics of Computation*, 73(248):1953-1966, 2004.

58) K. Lee and T. Matsoukas. Simultaneous coagulation and break-up using constant *n* Monte Carlo. *Powder Technology*, 110:82-89, 2000.

59) Y. Lin, K. Lee, and T. Matsoukas. Solution of the population balance equation using constant-number Monte Carlo. *Chemical Engineering Science*, 57:2241-2252, 2002.

60) D. Lindackers, M. Strecker, P. Roth, C. Janzen, and S. E. Pratsinis. Formation and growth of SiO_2 particles in low pressure $H_2/O_2/Ar$ flames doped with SiH_4. *Comb. Sci. Tech.*, 123:287-315, 1997.

61) R. Lindstedt and S. Louloudi. Joint-scalar transported PDF modeling of soot formation and oxidation. *Proceedings of the Combustion Institute*, 30:775-783, 2005.

62) J. D. Litster, D. J. Smit, and M. J. Hounslow. Adjustable discretised population balance for growth and aggregation. *A. I. Ch. E. Journal*, 41:591-603, 1995.

63) Y. Liu and I. Cameron. A new wavelet-based method for the solution of the population balance equation. *Chemical Engineering Science*, 56:5283-5294, 2001.

64) F. Lockwood and J. Van Niekerk. Parametric study of a carbon black oil furnace. *Combustion and Flame*, 1995.

65) A. A. Lushnikov. Some new aspects of coagulation theory. *Izv. Akad. Nauk SSSR Ser. Fiz. Atmosfer. i Okeana*, 14(10):738-743, 1978.

66) L. Mädler. Liquid-fed aerosol reactors for one-step synthesis of nano-structured particles. *KONA*, 22:107-120, 2004.

67) A. Maisels, F. E. Kruis, and H. Fissan. Direct simulation monte carlo method for simultaneous nucleation, coagulation, and surface growth in dispersed systems. *Chemical Engineering Science*, 59:2231-2239, 2004.

68) D. L. Marchisio and R. O. Fox. Solution of population balance equations using the direct quadrature method of moments. *J Aerosol Sci*, 36(1):43-73, 2005.

69) D. L. Marchisio, R. D. Vigil, and R. O. Fox. Implementaion of the quadrature method of moments in cfd codes for aggregation-breakage problems. *Chemical Engineering Science*, 58:3337-3351, 2003.

70) A. H. Marcus. Stochastic coalescence. *Technometrics*, 10(1):133-148, 1968.

71) F. Mauss, T. Schäfer, and H. Bockhorn. Inception and growth of soot particles in dependence on the surrounding gas phase. *Combustion and Flame*, 99:697-705, 1994.

72) F. Mauss, B. Trilken, H. Breitbach, and N. Peters. Soot formation in partially premixed diffusion flames at atmospheric pressure. In H. Bockhorn, editor, *Soot Formation in Combustion — Mechanisms and Models*, pages 325-349. Springer Verlag, 1994.

73) R. McGraw. Description of aerosol dynamics by the quadrature method of moments. *Aerosol Science & Technology*, 27:255-265, 1997.

74) B. Merkner. What is carbon black. Technical report, Degussa AG, 2000.

75) P. Mitchell and M. Frenklach. Monte Carlo simulations of soot aggregation with simultaneous surface growth — Why primary particles appear spherical. In *Twenty-Seventh Symposium (International) on Combustion*, pages 1507-1514, 1998.

76) P. Mitchell and M. Frenklach. Particle aggregation with simultaneous surface growth. *Physical Review E*, 67:061407, 2003.

77) N. Morgan, C. G. Wells, M. Goodson, M. Kraft, and W. Wagner. A new numerical approach for the simulation of the growth of inorganic nanoparticles. *Journal of Computational Physics*, 211(2):638-658, 2006.

78) H. Mühlenweg, A. Gutsch, A. Schild, and S. E. Pratsinis. Process simulation of gas-to-particle-synthesis via population balances: Investigation of three models. *Chemical Engineering Science*, 57:2305-2322, 2002.

79) K. Nakaso, T. Fujimoto, T. Seto, M. Shimada, K. Okuyama, and M. Lunden. Size distribution change of titania nano-particle agglomerates generated by gas phase reaction, agglomeration, and sintering. *Aerosol Science and Technology*, 35(5):929-947, 2001.

80) I. Naydenova, M. Nullmeier, J. Warnatz, and P. Vlasov. Detailed kinetic modelling of soot formation during shocktube pyrolysis of C_6H_6: Direct comparison with the results of time-resolved laser-induced incandescence (lii) and CW-laser extinction measurements. *Combust. Sci. and Tech.*, 176:1667-1703, 2004.

81) M. Nicmanis and M. J. Hounslow. A finite element analysis of the steady state population balance equation for particulate systems: Aggregation and growth. *Computers & Chemical Engineering*, 20:S261-S266, 1996.

82) M. Nicmanis and M. J. Hounslow. Finite-element methods for steady-state population balance equations. *AIChE Journal*, 44(10):2258-2272, 1998.

83) M. Nicmanis and M. J. Hounslow. Error estimation and control for the steady state population balance equation: 1. an a posteriori error estimate. *Chemical Engineering Science*, 57(12):2253-2264, 2002.

84) J. R. Norris. Cluster coagulation. *Communications in Mathematical Physics*, 209(2):407-435, 2000.

85) A. Onischuk, A. Levykin, V. P. Strunin, K. Sabelfeld, and V. Panfilov. Aggregate formation under homogeneous silane thermal decomposition. *J. Aerosol Sci.*, 31(11):1263-1281, 2000.

86) E. Otto, H. Fissan, S. Park, and K. Lee. The Log-Normal size distribution theory of Brownian aerosol coagulation for the entire particle size range: Part II − Analytic solution using Dahneke's coagulation kernel. *J. Aerosol Sci.*, 30(1):17-34, 1999.

87) S. Park and S. Rogak. A novel fixed-sectional model for the formation and growth of aerosol agglomerates. *Aerosol Science*, 35:1385-1404, 2004.

88) H. Pitsch, H. Barths, and N. Peters. Three-dimensional modeling of NOx and soot formation in DI-diesel engines using detailed chemistry based on the interactive flamelet approach. SAE 962057, 1996.

89) C. J. Pope and J. B. Howard. Simultaneous particle and molecule modeling (SPAMM): An approach for combining sectional aerosol equations and elementary gas-phase reactions. *Aerosol Science and Technology*, 27:73-94, 1997.

90) S. B. Pope. PDF methods for turbulent reactive flows. *Prog. Energy Combust. Sci.*, 11:119-192, 1985.

91) S. B. Pope. *Turbulent Flows*. Cambridge University Press, Cambridge, 2000.

92) S. E. Pratsinis. Flame aerosol synthesis of ceramic powders. *Prog. Energy Combust. Sci.*, 24:197-219, 1998.

93) S. E. Pratsinis, H. Bai, P. Biswas, M. Frenklach, and S. V. R. Mastangelo. Kinetics of titanium(IV) chloride oxidation. *J. Am. Ceram. Soc.*, 73(7):2158-2162, 1990.

94) S. E. Pratsinis and S. Vemury. Particle formation in gases: a review. *Powder Technology*, 88:267-273, 1996.

95) D. Ramkrishna. *Population Balances*. Academic Press, 2000.

96) H. Richter and J. B. Howard. Formation of polycyclic aromatic hydrocarbons and their growth to soot = a review of chemical reaction pathways. *Progress in Energy and Combustion Science*, 26(4-6):565-608, 2000.

97) D. E. Rosner. Combustion synthesis and materials processing. *Chemical Engineering Education*, Fall: 228-235, 1997.

98) D. E. Rosner, R. McGraw, and P. Tandon. Multivariate population balances via moment and monte carlo simulation methods: An important sol reaction engineering bivariate example and "mixed" moments for the estimation of deposition, scavanging, and optical properties for populations of nonspherical suspended particles. *Ind. Eng. Chem. Res.*, 42:2699-2711, 2003.

99) D. E. Rosner and J. J. Pyykönen. Bivariate moment simulation of coagulating and sintering nanoparticles in flames. *AIChE Journal*, 48(3):476-491, 2002.

100) K. Sabelfeld and A. Kolodko. Stochastic Lagrangian models and algorithms for spatially inhomogeneous Smoluchowski equation. *Mathematics and Computers in Simulation*, 61(2):115-137, 2003.

101) K. Sabelfeld, S. Rogasinsky, A. Kolodko, and A. Levykin. Stochastic algorithms for solving the Smolouchovsky[sic] coagulation equation and applications to aerosol groth[sic] simulation. *Monte Carlo Methods and Appl.*, 2(1):41-87, 1996.

102) R. Said, A. Garo, and R. Borghi. Soot formation modeling for turbulent flames. *Combustion and Flame*, 108:71-86, 1997.

103) H.-J. Schmid, S. Tejwani, C. Artelt, and W. Peukert. Monte Carlo simulation of aggregate morphology for simultaneous coagulation and sintering. *Journal of Nanoparticle Research*, 6:613626, 2004.

104) C. A. Schuetz and M. Frenklach. Nucleation of soot: Molecular dynamics simulations of pyrene dimerization. *Proceedings of the Combustion Institute*, 29:2307-2314, 2002.

105) J. H. Seinfeld and S. N. Pandis. *Atmospheric Chemistry and Physics: From Air Polution to Climate Change*. John Wiley & Sons, NewYork, 1997.

106) B. H. Shah, D. Ramkrishna, and J. D. Borwanker. Simulation of particulate systems using the concept of the interval of quiescence. *AIChEJ*, 23:897-904, 1977.

107) J. Singh, M. Balthasar, M. Kraft, and W. Wagner. Stochastic modelling of soot particle size and age distribution in laminar premixed flames. *Proceedings of the Combustion Institute*, 30:1457-1465, 2005.

108) M. Smith and T. Matsoukas. Constant-number Monte Carlo simulation of population balances. *Chemical Engineering Science*, 53(9):1777-1786, 1998.

109) M. Smooke, R. J. Hall, M. Colket, J. Fielding, M. B. Long, C. S. McEnally, and L. Pfefferle. Investigation of the transition from lightly sooting towards heavily sooting co-flow ethylene diffusion flames. *Combustion Theory and Modelling*, 8:593-606, 2004.

110) W. J. Stark and S. E. Pratsinis. Aerosol flame reactors for manufacture of nanoparticles. *Powder Technology*, 126:103-108, 2002.

111) Z. Sun, R. L. Axelbaum, and B. H. Chao. A multicomponent sectional model applied to flame synthesis of nanoparticles. *Proceedings of the Combustion Institute*, 29:1063-1069, 2002.

112) P. Tandon and D. E. Rosner. Monte Carlo simulation of particle aggregation and simultaneous restructuring. *J. Colloid Interface Sci.*, 213:273, 1999.

113) S. Tsantilis, H. K. Kammler, and S. E. Pratsinis. Population balance modeling of flame synthesis of titania nanoparticles. *Chemical Engineering Science*, 57:2139-2156, 2002.

114) S. Tsantilis and S. E. Pratsinis. Evolution of primary and aggregate particle-size distributions by coagulation and sintering. *AIChE Journal*, 46(2):407-415, 2000.

115) M. Vanni. Approximate population balance equations

for aggregation-breakage processes. *Journal of Colloid and Interface Science*, 221:143-160, 2000.

116) A. Vikhansky and M. Kraft. Modelling of a RDC using a combined CFD-population balance approach. *Chemical Engineering Science*, 59:2597-2606, 2004.

117) A. Vikhansky and M. Kraft. A Monte Carlo method for identification and sensitivity analysis of coagulation processes. *Journal of Computational Physics*, 200:50-59, 2004.

118) A. Violi. Modeling of soot particle inception in aromatic and aliphatic premixed flames. *Combustion and Flame*, 139:279-287, 2004.

119) P. Vlasov and J. Warnatz. Detailed kinetic modelling of soot formation in hydrocarbon pyrolysis behind shock waves. *Proceedings of the Combustion Institute*, 29: 2335-2341, 2002.

120) M. Voll and P. Kleinschmit. *Ullmann's Encyclopedia of Industrial Chemistry*, volume A 5, chapter 5, pages 140-163. VCH Weinheim, 1986.

121) H. Wang and M. Frenklach. A detailed kinetic modeling study of araomatics formation in laminar premixed acetylene and ethylene flames. *Combustion and Flame*, 110:173-221, 1997.

122) C. G. Wells and M. Kraft. Direct simulation and mass flow stochastic algorithms to solve a sintering-coagulation equation. *Monte Carlo Methods and Appl.*, 11(2): 175-199, 2005.

123) C. G. Wells, N. Morgan, M. Kraft, and W. Wagner. A new method for calculating the diameters of partially-sintered nanoparticles and its effect on simulated particle properties. *Chemical Engineering Science*, 61(1): 158-166, 2006.

124) J. Z. Wen, M. Thomson, S. Park, S. Rogak, and M. Lightstone. Study of soot growth in a plug flow reactor using a moving sectional model. *Proceedings of the Combustion Institute*, 30(1):1477-1484, 2005.

125) M. Williams and S. Loyalka. *Aerosol Science Theory and Practice*. Pergamon Press, Oxford, 1991.

126) M. Wulkow. The simulation of molecular weight distributions in polyreaction kinetics by discrete galerkin methods. *Macromolecular Theory Simulations*, 5:393-416, 1996.

127) M. Wulkow, A. Gerstlauer, and U. Nieken. Modeling and simulation of crystallization processes using Parsival. *Chemical Engineering Science*, 56(7):2575-2588, 2001. www.cit-wulkow.de/tbcpars.htm.

128) Y. Xiong and S. E. Pratsinis. Formation of agglomerate particles by coagulation and sintering — Part I. a two-dimensional solution of the population balance equation. *J. Aerosol Sci*., 24:283-300, 1993.

129) Y. Yoshihara, A. Kazakov, H. Wang, and M. Frenklach. Reduced mechanism of soot formation — application to natural gas-fueled diesel combustion. In *Twenty-Fifth Symposium (International) on Combustion*, pages 941-948, 1994.

130) B. Zhao, Z. Yang, M. V. Johnston, H. Wang, A. S. Wexler, M. Balthasar, and M. Kraft. Measurement and numerical simulation of soot particle size distribution functions in a laminar premixed ethylene-oxygen-argon flame. *Combustion and Flame*, 133:173-188, 2003.

Author's short biography

MARKUS KRAFT

MARKUS KRAFT is a Reader in Chemical Engineering in the Department of Chemical Engineering at the University of Cambridge. He obtained the academic degree 'Diplom Technomathematiker' at the University of Kaiserslautern in 1992 and completed his PhD studies in the Department of Chemistry at the same University in 1997. His main research interests are in the field of computational chemical engineering. In particular he and his research group develop models and numerical methods for simulating nanoparticle population dynamics.

Relationship between the Structure and Properties of Pharmaceutical Crystals[†]

A.R. Sheth and D.J.W. Grant[1]
Department of Pharmaceutics
College of Pharmacy
University of Minnesota[*]

Abstract

The majority of drug products are solid dosage forms, most of which contain the drug substance in the crystalline state. This review considers the forces responsible for crystal packing, the various types of pharmaceutical crystals, and the methods used to determine the structure of pharmaceutical crystals. These topics provide background for the main thrust, which focuses on the importance of studying the structure of pharmaceutical crystals with particular stress on phase changes of crystal forms of drugs during pharmaceutical processing and implications of different solid forms of drugs on its mechanical properties. The present review does not consider pharmaceutical co-crystals, which could be the subject of another review.

Key words: Mechanical properties, Hydrates/solvates, Amorphous, Clathrates, Crystal-structure, Processing, Polymorphism, Physicochemical properties, X-ray powder diffractometry, Solid state

Introduction

When applied to solids, the adjective, *crystalline*, implies an ideal crystal in which the structural units, termed *unit cells*, are repeated regularly and indefinitely in three dimensions in space. The unit cell, containing at least one molecule, has a definite orientation and shape defined by the translational vectors, a, b, and c. The unit cell therefore has a definite volume, V, that contains the atoms and molecules necessary for generating the crystal.1) Amorphous solids lack the long-range order present in crystals.1)

Each crystal can be classified as a member of one of seven possible crystals systems or crystal classes that are defined by the relationships between the individual dimensions, a, b, and, c, of the unit cell and between the individual angles, α, β, and γ, of the unit cell.2, 3) The structure of the given crystal may be assigned to one of the seven crystal systems, to one of the 14 Bravais lattices, and to one of the 230 space groups.4) All the 230 possible space groups, their individual symmetries, and the symmetries of their diffractions patterns are compiled in the International Tables for Crystallography.5)

Certain space groups occur more frequently than others. According to the Cambridge Structural Database,6, 7) about 76% of all organic and organometallic compounds crystallize in only 5 space groups, $P2_1/c$, $P2_12_12_1$, $P\bar{1}$, $P2_1$, and C_2/c, and about 90% of all organic and organometallic crystal structures are covered by the 17 most common space groups.6)

The present review does not consider pharmaceutical co-crystals, which are solid phases that contain two or more components, such as a drug and an excipient. The preparation and study of co-crystals add appreciable complexity to the topic, which could justify an additional review.

[†] Accepted: August 30, 2005

[*] Weaver-Densford Hall
308 Harvard Street SE
Minneapolis, MN 55455-0343

[1] Corresponding author
TEL: 612-624-3956 FAX: 612-625-0609
E-mail: grant001@umn.edu

Forces responsible for crystal packing

While the intramolecular interactions bond the atoms in a molecule, the intermolecular forces minimize the energy of the molecules in the crystal and are primarily responsible for the formation of organic crystals.[8] A crystal structure therefore corresponds to a free energy minimum that is not necessarily the lowest (so called, global) minimum. The intermolecular forces may be either attractive or repulsive. The attractive interactions consist of three types: non-bonded (sometimes termed non-covalent interactions) such as van der Waals forces (which depend on dipole moments, polarizability, and electronic distribution of the molecules) and hydrogen bonds (which require donor and acceptor functional groups),[9] ionic interactions, and electrostatic interactions. The major attractive interactions in most pharmaceutical crystals are hydrogen bonds and van der Waals interactions.[10, 11] However, in ionic crystals, electrostatic interactions can significantly affect the overall crystal packing energy.[12]

Non-bonded interactions are relatively weak and are generally treated as isotropic, although a more realistic interpretation may require the inclusion of anisotropicity in the treatment.[13] Hydrogen bonds, the energies of which are in the range of 1-10 kcal/mol, are anisotropic and directional.[10] The magnitude of the sum of the forces acting on a molecule, and the energies involved in the interactions of individual atoms of a molecule with atoms of the surrounding molecules, may be estimated from the sublimation energy of the molecular crystal.[14] For most molecular crystals, the sublimation enthalpy is within the range, 10-25 kcal/mol.[15]

The arrangement of molecules in a crystal determines its physical properties and, in some cases, its chemical properties.[16] The physicochemical properties of the solid drug can affect its performance. Thus, an understanding of the crystalline state leads to an understanding of the drug properties, which is crucial for preformulation and formulation in the pharmaceutical industry.

Types of pharmaceutical crystals

The molecules in an organic pharmaceutical crystal may be chiral or achiral. Some pharmaceuticals are salts. Based on its internal structure, a pharmaceutical crystal may be a molecular adduct (hydrate or solvate), or may be one of a group of polymorphs, as shown in **Table 1** and explained below.

Polymorphism, in general, denotes the ability of a substance to exist as two or more crystalline phases that have different arrangements and/or conformations of the molecules in the crystal lattice.[17] Conformationally rigid molecules exhibit orientational, or packing, polymorphism. Conformational polymorphism arises when a flexible molecule adopts different conformations in different crystal structures.[18]

Polymorphs can be classified as enantiotropes or monotropes, depending on whether or not one form can transform reversibly to another.[19] Enantiotropes are members of a pair of polymorphs whose mutual transition temperature is less than the melting point of either polymorph. Each enantiotrope has its own temperature range of stability. Monotropes are members of a pair of polymorphs that have no mutual transition temperature. One monotrope is always more stable than the other polymorph under all conditions in which the solid state can exist.

A crystal is termed a molecular adduct when its lat-

Table 1 Classification of pharmaceutical crystals. Modified from reference[16]

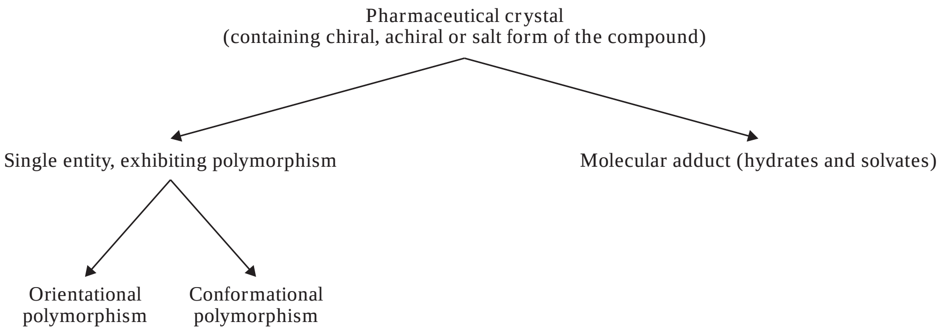

tice consists of more than one chemical component,[16) and includes solvates and hydrates. A solvate is a solid phase containing solid molecules in addition to molecules of the major component in the crystal lattice. When the solvent is water, the solid phase is termed a hydrate. Molecular adducts can be stoichiometric or nonstoichiometric in nature.[16, 20) Clathrates[21) are special types of molecular adducts that consist of two distinct components, a relatively rigid host and a quite mobile guest. Within clathrates, the guest molecules lie trapped in closed, three dimensional cavities or cages formed by the crystalline structure of the host.[22) The term clathration is used instead of solvation when there is no specific interaction between the solvent and solute.[23) Approximately one third of active pharmaceutical substances are capable of forming crystalline hydrates.[24) Solvates and hydrates generally demonstrate different solubilities and consequently different intrinsic dissolution rates (dissolution rates per unit surface area) than their unsolvated counterparts.[3) Moreover, the stability profiles of hydrates and solvates at various temperatures and at different vapor pressures of water or organic solvents differ from those of the unsolvated crystal form.[25) These differences can influence formulation, processing, and stability under various storage conditions of the drug compound, as well as in the pharmaceutical product.

Polymorphism and the formation of molecular adducts are also common among pharmaceutical salts,[26) leading to unique molecular environments and physicochemical properties that differ from those of their respective free acid or base. Polymorphism in a chiral drug[27, 28) can be exhibited by individual enantiomers (for example, carvoxamine[29) and nitrendipine[30)) as well as by racemates (for example, mandelic acid[31)) and can be expressed by the interconversion between different types of racemates, as shown by nicotine derivatives[32) and sodium ibuprofen.[33)

Determination of the structure of pharmaceutical crystals

Methods for determining the structure of pharmaceutical crystals fall into three broad categories (**Table 2**): (1) methods utilizing single crystals, (2) methods utilizing powder X-ray diffraction patterns, and (3) methods that determine crystal structure from molecular structure alone, i.e., *ab initio* methods. Each of these methods may be further subclassified, as in **Table 2**. The salient features of the three methods are outlined below.

Table 2 Classification of methods used to determine structures of pharmaceutical crystals

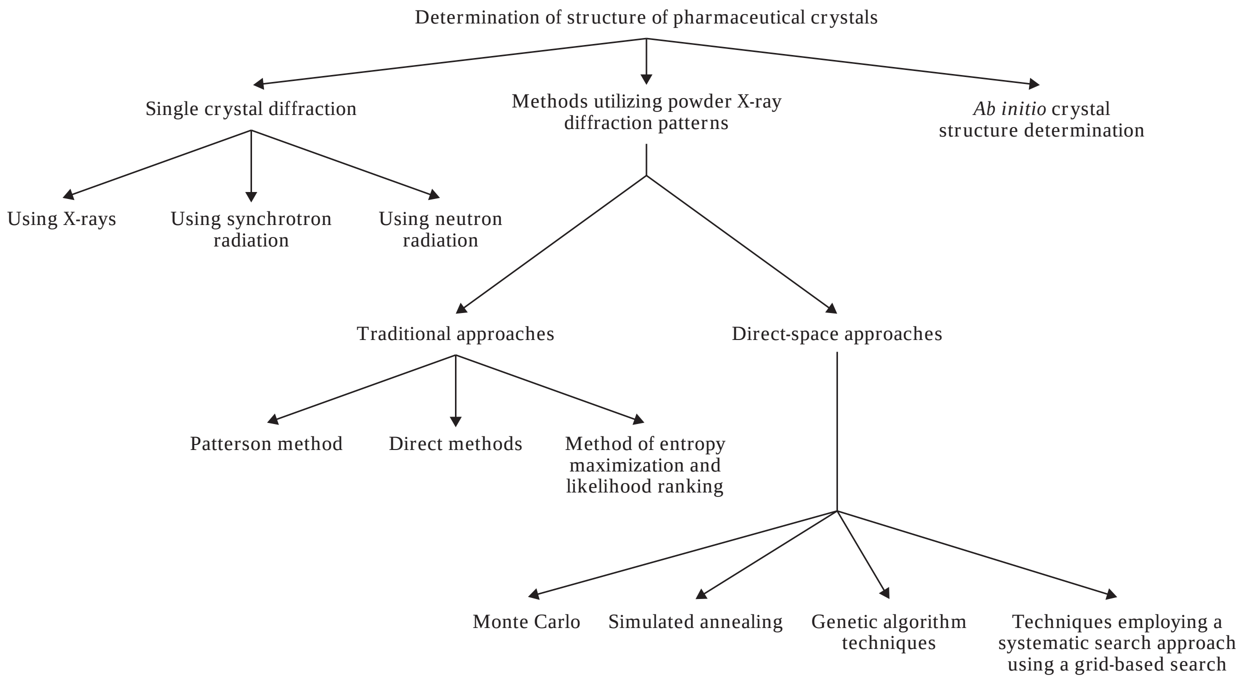

Method utilizing single crystals

This method requires crystals of suitable size and quality.[34, 35] In general, the minimum dimension along each axis should exceed 50 μm for single crystal X-ray diffraction. Although use of synchrotron X-ray radiation has considerably reduced this minimum crystal size, single crystal X-ray diffraction still remains the most commonly used method. The principles and methods of single crystal X-ray diffraction for organic molecules are described in Stout and Jensen.[34]

It is sometimes difficult to obtain the desired compound as single crystals of adequate size and quality. The material may be available only as a polycrystalline powder. Moreover, solving the structure of certain types of crystalline substances may be beyond the capability of single-crystal techniques,[3] even when performing microcrystal diffraction with a synchrotron radiation source. In particular, metastable polymorphic forms that are isolated by rapid crystallization from the melt or that rapidly grow from solution may be highly flawed crystals. Desolvation processes commonly result in crystals that appear to have the same particle size as the crystals from which they were formed; however, upon examination by polarized light microscopy, these crystals are usually composed of microcrystalline aggregates.[3] Twinned crystals have different growth sectors that are related by symmetry to one another. The sectors have different orientations that can be related to one another through applications of twinning laws to relate the orientation matrices of the different growth sectors. However, solving twinning structures by single crystal diffraction is not always a straightforward task.[36]

Crystal structure determination using single crystal diffraction is the most reliable technique. However, when suitable single crystals are not available, techniques utilizing powder X-ray diffractometry[37] and *ab initio* methods can be used.

Methods utilizing powder X-ray diffraction (PXRD) patterns

Methods in this category include traditional methods and direct-space approaches. The traditional approach for crystal structure solution from PXRD data is to extract the integrated Bragg intensities of individual reflections directly from the PXRD pattern.[38] Once the integrated intensities are known, an electron-density map (assuming X-ray radiation) is constructed using the same techniques that have been developed for single-crystal diffraction data. To extract the integrated intensities, various modifications of the Pawley[39] or Lebail[40] methods are commonly used. Variants of this basic idea have been applied successfully to organic systems with up to 31 non-H atoms.[41] Although traditional techniques for structure solution from PXRD data have been applied successfully in several cases,[42, 43] these techniques have certain intrinsic limitations[44] and organic molecular crystals represent a particularly challenging case. Peak overlap can create major difficulties in extracting intensities from PXRD patterns, which limits the complexity of structures that can be solved by traditional methods.[45] Traditional methods have been used to determine the structure of inorganic and/or non-pharmaceutical crystals and include the Patterson method,[46] direct methods,[47] and methods of entropy maximization and likelihood ranking.[48]

Direct-space approaches postulate structural models in direct-space,[43, 49, 50] independently of PXRD data. The suitability of these models is assessed by direct comparison of the PXRD patterns calculated from these models with the experimental PXRD patterns. Most direct-space approaches are stochastic in nature, and so it is recommended that calculation of the structure solution be repeated several times from different random starting populations. Possible methods that can be used to locate the global minimum within direct-space structure solution include Monte Carlo,[50, 51] simulated annealing,[49, 52] genetic algorithm techniques,[53] and techniques employing a systematic search approach using a grid-based search with lattice energy calculations.[54] Besides determination of crystal structures from PXRD, simulated annealing can also be used for improved predictions in *ab initio* crystal structure determination. In general, this approach can be used in conjunction with other techniques for improved predictions.[55] Direct-space approaches were utilized to determine crystal structures of a series of organic compounds.[56] However, in this case, unit cell parameters and space groups were obtained from published work, and only the steps of unit cell refinement and structure solution were performed. Moreover, not all the compounds tested were pharmaceutical crystals. The reader is directed to appropriate references for underlying theory and mathematical treatment on powder-indexing,[57] pattern decomposition and unit cell refinement using the Pawley method,[39] the Monte Carlo method,[58] the Metropolis importance sampling technique,[59] simulated annealing,[60] and structure refinement using the Rietveld method.[45, 61, 62]

Because the PXRD pattern is collected from a sample of crystallites of random orientation, structure solution by this method circumvents the problem of crystal quality and twinning through the nature of this experimental approach.[63] Hence, it is also not necessary to apply the twin laws by the powder method.

Crystal structure determination from PXRD patterns can, however, be complicated. For powder diffraction patterns, the reflections from different crystal planes are averaged over directions and projected onto a single variable, the diffraction angle (2θ). This averaging makes the reconstruction of the underlying crystal structure much more difficult than for single-crystal diffraction patterns.[43] Space group determination on powders is more ambiguous than with single crystal diffraction, because of limitations of the regions in the pattern where systematic absences are free from peaks due to other reflections. Also, poor-quality PXRD patterns preclude their successful indexing. Furthermore, preferred orientation affects the relative intensities of given peaks and hinders the correct solution of the pattern.[64]

Determining crystal structures from PXRD data is an important and emerging discipline. There is still considerable potential for the continued development and improvement of the methodologies in this field.[43] Also, during crystal structure determination by PXRD patterns, other analytical techniques, such as vibrational spectroscopy and solid-state nuclear magnetic resonance spectroscopy, can provide additional structural information complementary to that obtained by PXRD patterns, as in the case of *N*-(*p*-tolyl)-dodecylsulfonamide[65] and acetohexamide form B.[66]

***Ab initio** crystal structure determination*

In more challenging cases, where suitable experimental data are not available, crystal structure determination can be guided by lattice energy calculations instead of powder pattern comparisons, to generate initial models for subsequent Rietveld refinement. Success using this technique is limited[67] and such *ab initio* prediction of crystal structures still remains an admirable long-term goal[68] because of the complexity of the task.[69] Such methods are still plagued by difficulties, including the location of global energy minima, force field accuracy, description of the electrostatic interactions, and inclusion of the entropy term that contributes to the free energy. The ability to determine the crystal structure from the molecular structure of a compound is the ultimate goal of computational crystallography.

Importance of studying the structure of pharmaceutical crystals

An organic molecule, which may be chiral or achiral or a pharmaceutical salt, can, in the crystalline state, exist as polymorphs and/or molecular adducts. Differences in crystal packing forces (i.e. intermolecular forces) lead to differences in long-range periodicity of the molecules. This difference in long-range periodicity in turn leads to differences in energy, and hence, differences in physical reactivity, between the various crystalline forms of the organic molecule. For conformationally flexible molecules, intramolecular forces may also contribute to such differences. The various solid forms of a drug substance can also differ in their chemical reactivity.[70] Hence, the physical (and also chemical) properties of the organic pharmaceutical crystal will depend on its solid form. **Table 3** shows the differences in physical properties that can be shown by the different crystalline forms of an organic molecule.

These differences in physical properties arising from differences in structure of the various crystal forms of an organic pharmaceutical compound has implications in candidate-selection for drug development, processing, formulation, and performance of drug products, regulatory aspects, and intellectual property issues. Differences in solubility and dissolution rate of the various crystal forms can affect drug performance, especially that of BCS Class II drugs.[71] Existence of different solid forms of a drug can also lead to phase transformations during its processing and formulation (e.g. milling, granulation, drying, compaction),[72, 73] as observed in theophylline,[74] chlorpropamide,[75] carbamazepine,[76] phenobarbital,[77] lactose,[78] chlorpromazine hydrochloride,[79] uricosuric agent FR76505,[80] cefixime trihydrate,[81] and pentamidine isethionate.[82] These phase changes can affect the stability of the product and, in some cases, even the bioavailability of the drug.[83] An understanding of the relationship between the solid state properties and crystal structures of the likely phases may be utilized for optimizing operational and formulation strategies and for designing suitable stability protocols to avoid later problems.[17, 84] Additionally, each of the several pharmaceutical excipients utilized in drug formulations can also exist in different solid forms, and the solid nature of the excipients may also influence the final physical form of the tablet,[14, 70] such as tendency to stick,[85] or polymorphic conversion of the active ingredient.[86] Among chiral drugs, it is known that the pharmacological, toxicological, phar-

Table 3 Physical properties that differ among the various crystalline forms of a drug substance[17)]

1. Packing properties	a. Molar volume and density
	b. Refractive index
	c. Conductivity, electrical and thermal
	d. Hygroscopicity
2. Thermodynamic properties	a. Melting and sublimation temperatures
	b. Internal energy (i.e. structural energy)
	c. Enthalpy (i.e. heat content)
	d. Heat capacity
	e. Entropy
	f. Free energy and chemical potential
	g. Thermodynamic activity
	h. Vapor pressure
	i. Solubility
3. Spectroscopic properties	a. Electronic transitions (i.e. ultraviolet-visible absorption spectra)
	b. Vibrational transitions (i.e. infrared absorption spectra and Raman spectra)
	c. Rotational transitions (i.e. far infrared or microwave absorption spectra)
	d. Nuclear spin transitions (i.e. nuclear magnetic resonance spectra)
4. Kinetic properties	a. Dissolution rate
	b. Rates of solid state reactions
	c. Stability
5. Surface properties	a. Surface free energy
	b. Interfacial tensions
	c. Habit (i.e. shape)
6. Mechanical properties	a. Hardness
	b. Tensile strength
	c. Compactibility, tableting
	d. Handling, flow, and blending

macodynamic, and pharmacokinetic properties differ markedly between its opposite enantiomers and racemates.[87)] The molecular environments in each of these solids are unique and impart different physicochemical properties to the crystals.[27)] Among pharmaceutical salts, which can also exist in different crystal forms, the presence of ions influences the physicochemical properties of the crystals, including solubility, dissolution rate, stability, and hygroscopicity.[26)]

The structure of a crystal also affects its mechanical properties, thereby affecting its processability. Thus, theophylline monohydrate, because of the greater number of intermolecular hydrogen bonds in its crystal structure, possesses higher mechanical strength and is also less brittle than anhydrous theophylline.[88)] The presence of water molecules in the crystal structure of the monohydrate of 4-hydroxybenzoic acid facilitates its plastic deformation as compared with its anhydrate.[89)] The term slip refers to the translational motion of lattice planes relative to each other. Such planes are termed slip planes and a family of slip planes, together with the slip direction, is termed a slip system. Knowledge of crystal structure and slip systems can be utilized to model the tableting and compaction behavior of molecular crystals such as the anhydrate and dihydrate forms of L-lysine hydrochloride[90)] and polymorphs I and II of sulfamerazine.[91] The Young's modulus of aspirin has been determined from its crystal structure[92] and the mechanical properties of aspirin, sulphathiazole, carbamazepine, and polymorphs of primidone (forms A and B) can be predicted[93] by applying lattice dynamics to the atom-atom potential model while also taking into account the crystal morphology. Even though it is possible to predict the mechanical properties of a compound from its crystal structure, crystal engineering of pharmaceuticals has not yet resulted in the design of crystals with desired mechanical properties. By developing a molecular basis for the origins and magnitude of mechanical properties, the required controlled modification might by achieved by analysis of the structural and constituent molecular information.[94] The knowledge thus gained might be utilized to design crystals with desired mechanical properties.[95]

Differences in the physical and mechanical properties of the various crystal forms of a drug substance also affect scale up and transfer from laboratory quantities and procedures through pilot plant and full production[91] as equipment changes, variations in heating/cooling rates, variations in stirring procedures,[96] and seeding,[97] can all influence the result of a crystallization procedure and the solid form obtained.[14, 73]

Characterization and understanding of the crystal properties is also important for quality control and regulatory purposes.[98] Information about the various crystal forms of a drug substance is required by the United States Food and Drug Administration (USFDA) in a New Drug Application and a set of decision trees has been provided to assist in the presentation of data for different crystal forms of a drug substance to the USFDA.[99] Guidelines have also been set up the International Committee of Harmonization to address the existence of different crystal forms of a drug substance.[100] Furthermore, the different crystal forms of a drug and processes for preparing them are patentable.[3, 14] Among the frequently cited uses for patenting different crystal forms are improved formulation, handling and stability, reduced hygroscopicity, and improved solubility and bioavailability.[3]

Conclusions

Most marketed pharmaceuticals consist of molecular crystals. Selection of the most suitable crystalline form of a drug in the initial stages of drug development is crucial to save time and cost associated with the drug development process, and, in recent years, much research has focused on achieving this goal. Isolation and thorough characterization of the maximum number of solid forms of a drug substance reduce the possibility of surprises resulting from inadvertent phase changes during processing or from crystallization of previously unknown forms.

For a given crystalline drug substance, the intermolecular and intramolecular interactions in its lattice, manifested by the molecular arrangement, packing and conformation, determine its observed physicochemical properties, including mechanical properties, which may in turn impact even the pharmaceutical properties of the drug product. To better understand, control, and possibly predict, these properties of pharmaceutical crystals, a thorough understanding of the underlying crystal and molecular structures of the maximum number of solid forms of a drug substance is desirable. While single crystal X-ray diffraction unambiguously establishes the crystal and molecular structure, the continuous development of sophisticated computational tools for the ultimate prediction of crystal and molecular structures provides valuable alternatives when single crystal diffraction is not successful.

References

1) Vippagunta SR, Brittain HG and Grant DJW. Crystalline solids. *Adv. Drug Delivery Rev*. **48**: 3-26 (2001).

2) Brittain HG & Byrn SR. Structural aspects of polymorphism. In: Brittain HG, editor. *Polymorphism in Pharmaceutical Solids*. New York: Marcel Dekker. pp. 73-124. (1999).

3) Byrn SR, Pfeiffer RR & Stowell JG. *Solid State Chemistry of Drugs*, 2nd edition. West Lafayette, Indiana: SSCI, Inc. (1999).

4) Cullity BD. *Elements of X-ray Diffraction* 3rd edn. New Jerse: Prentice Hall (2001); Buerger MJ. *Elementary Crystallography*. New York: Wiley Interscience. pp. 253-273. (1963).

5) Han T, editor. *International Tables for Crystallography*, International Union of Crystallography, Boston, MA (1987).

6) Cambridge Crystallographic Data Center, *The Cambridge Structural Database*, University Chemical Laboratory, Cambridge, UK (1996).

7) Allen FH. The Cambridge Structural Database: a quarter of a million crystal structures and rising. *Acta Cryst*. **B**58: 380-388 (2002); Allen FH and Motherwell WDS. Applications of the Cambridge Structural Database in organic chemistry and crystal chemistry. *Acta. Cryst*. **B**58: 407-422 (2002); Bruno IJ, Cole JC, Edgington PR, Kessler M, Macrae CF, McCabe P, Pearson J, and Taylor R. New Software for searching the Cambridge Structural Database and visualizing crystal structures.

Acta. *Cryst*. **B**58: 389-397 (2002).

8) Buckingham AD. In: Seddon KR and Zaworotko M, editors. *Crystal Engineering: The Design and Application of Functional Solids*. NATO Science Series C volume 539. Boston: Kluwer Academic. pp. 49-68. (1999).

9) Pimental GC and McClennan AL. *The Hydrogen Bond*. San Francisco: W.H.Freeman (1960); Scheiner S. *Hydrogen Bonding: A Theoretical Perspective*. Oxford: Oxford University Press (1997); Desiraju GR. Hydrogen bridges in crystal engineering: interactions without borders. *Acc*. *Chem*. *Res*. **35**: 565-573 (2002).

10) Jeffrey GA. *An Introduction to Hydrogen Bonding*. New York, NY: Oxford University Press (1997); Desiraju GR and Steiner T. *The Weak Hydrogen Bond in Structural Chemistry and Biology*. New York, NY: Oxford University Press. pp. 15-47. (1999).

11) Beyer A, Karpfen A, and Schuster P. Energy surfaces of hydrogen complexes in the vapor phase. *Topics Curr*. *Chem*. **120**: 1-40 (1984); Perlstein J. Molecular self-assemblies 4. Using Kitaigorodskii's AufBau principle for qualitatively predicting the packing geometry of semiflexible organic molecules in translation monolayer aggregates. *J*. *Am*. *Chem*. *Soc*. **116**: 11420-11432 (1994).

12) Smith ER. Electrostatic energy in ionic crystals. *Proc*. *R*. *Soc*. *Lond*. *A* **375**: 475-505 (1981).

13) Price SL. Toward more accurate model of intermolecular potentials for organic molecules. *Rev*. *Comput*. *Chem*. **14**: 225-289 (2000).

14) Bernstein J. *Polymorphism in Molecular Crystals*. Oxford, UK: Clarendon Press (2002).

15) Chickos J. Heats of sublimation. In: Liebman JF and Greenberg, editors. *Molecular Structure and Energetics*. Vol. 2. *Physical Measurements*. New York, NY: VCH. pp. 67-150. (1987).

16) Haleblian JK. Characterization of habits and crystalline modifications of solids and their pharmaceutical applications. *J*. *Pharm*. *Sci*. **64**: 1269-1288 (1975).

17) Grant DJW. Theory and origin of polymorphism. In: Brittain HG, editor. *Polymorphism in Pharmaceutical Solids*. New York: Marcel Dekker. pp. 1-33. (1999).

18) Corradini P. X-ray studies of conformation: observation of different geometries of the same molecule. *Chem*. *Ind*. *(Milan)* **55**: 122-129 (1973); Panagiotopoulos NC, Jeffrey GA, LaPlaca SJ, and Hamilton WC. The A and B forms of potassium D-gluconate monohydrate. *Acta Cryst*. *B***30**: 1421-1430 (1974); Bernstein J and Hagler AT. Conformational polymorphism. The influence of crystal forces on molecular conformation. *J*. *Am*. *Chem*. *Soc*. **100**: 673-681 (1978).

19) Haleblian JK and McCrone WC. Pharmaceutical applications of polymorphism. *J*. *Pharm*. *Sci*. **58**: 911-929 (1969); Burger A and Ramburger R. On the polymorphism of pharmaceuticals and other molecular crystals. I. Theory of thermodynamic rules. *Mikrochim*. *Acta* **II**: 259-271 (1979); Burger A and Ramburger R. On the polymorphism of pharmaceuticals and other molecular crystals. II. Applicability of thermodynamic rules. *Mikrochim*. *Acta* **II**: 273-316 (1979); Henck JO and Kuhnert-Brandstaetter M. Demonstration of the terms enantiotropy and monotropy in polymorphism research exemplified by flurbiprofen. *J*. *Pharm*. *Sci*. **88**: 103-108 (1999); Yu L, Reutzel SM, and Stephenson GA. Physical characterization of polymorphic drugs: an integrated characterization strategy. *Pharm*. *Sci*. *Technol*. *Today* **1**: 118-127 (1998); Grunenberg A, Henck JO, and Siesler HW. Theoretical derivation and practical application of energy/temperature diagrams as an instrument in preformulation studies of polymorphic drug substances. *Int*. *J*. *Pharm*. **129**: 147-158 (1996); Yu L. Inferring thermodynamic stability relationship of polymorphs from melting data. *J*. *Pharm*. *Sci*. **84**: 966-974 (1995); Gu CH, Young Jr. VG, and Grant DJW. Polymorph screening: influence of solvents on the rate of solvent-mediated polymorphic transformation. *J*. *Pharm*. *Sci*. **90**: 1878-1890 (2001); Toscani S. An up-to-date approach to drug polymorphism. *Thermochim*. *Acta* **321**: 73-79 (1998).

20) Morris KR. Structural aspects of hydrates and solvates. In: Brittain HG, editor. *Polymorphism in Pharmaceutical Solids*. pp. 125-181. New York: Marcel Dekker (1999).

21) Powell HM. The structure of molecular compounds. Part IV. Clathrate compounds. *J*. *Chem*. *Soc*. pp. 61-73. (1968).

22) Andreeti GD. In: Atwood JL, Davies JED, and MacNicol DD, editors. *Inclusion Compounds*. Vol. 3. pp. 129-146. London: Academic Press (1984); Mandelcorn L. Clathrates. *Chem*. *Rev*. **59**: 827-839 (1959).

23) Lipkowski J. In: Tsoucaris G, Atwood JL, and Lipkowski J, editors. *Crystallography of Supramolecular Compounds* NATO Science Series C. Vol. 480. pp. 265-283. Boston: Kluwer Academic (1996).

24) Stahl PH. In: Braimer DD, editor. *Towards Better Safety of Drugs and Pharmaceutical Products*. Amsterdam: Elsevier/North-Holland Biomedical. pp. 265-280. (1980).

25) Bechtloff B, Nordhoff S, and Ulrich J. Pseudopolymorphs in industrial use. *Cryst*. *Res*. *Technol*. **36**: 1315-1328 (2001).

26) Berge SM, Bighley LD, and Monkhouse DC. Pharmaceutical salts. *J*. *Pharm*. *Sci*. **66**: 1-19 (1977); Neau SH. In: Liu R, editor. *Water-Insoluble Drug Formulations*. pp. 405-425. Buffalo Grove: Interpharm (2000); Puddipeddi M, Serajuddin ATM, Grant DJW, and Stahl PH. In: Stahl PH and Wermuth CH, editors. *Handbook of Pharmaceutical Salts: Properties, Selection, and Use*. pp. 19-38. Weinheim: Wiley (2002); Giron D and Grant DJW. In: Stahl PH and Wermuth CG, editors. *Handbook of Pharmaceutical Salts: Properties, Selection, and Use*. pp. 41-81. Weinheim: Wiley (2002).

27) Li Z and Grant DJW. Relationship between physical properties and crystal structures of chiral drugs. *J*. *Pharm*. *Sci*. **86**: 1073-1078 (1997).

28) Stahl PH and Byrn SR. In: Myerson AS, editor. *Molecular Modeling Applications in Crystallization*. pp. 313-

345. New York: Cambridge University Press (1999); Shah RD and Nafie LA. Spectroscopic methods for determining enantiomeric purity and absolute configuration in chiral pharmaceutical molecules. *Curr. Opin. Drug Discov. Devel.* **4**: 764-775 (2001).

29) Jacques J, Collet A, and Wilen SH. *Enantiomers, Racemates, and Resolutions.* New York: John Wiley and Sons. pp. 3-213. (1981).

30) Burger A, Rollinger JM, and Bruggeler P. Binary system of (R)- and (S)-nitrendipine – polymorphism and structure. *J. Pharm. Sci.* **86**: 674-679 (1997).

31) Kuhnert-Brandstaetter M and Ulmer R. Contribution to the thermal analysis of optical antipodes – mandelic acid. *Mikrochim. Acta* **5**: 927-935 (1974).

32) Langhammer L. Binary systems of enantiomeric nicotine derivatives. *Arch Pharm.* **308**: 933-939 (1975).

33) Zhang GGZ, Paspal SYL, Suryanarayanan R, and Grant DJW. Racemic species of sodium ibuprofen: characterization and polymorphic relationships. *J. Pharm. Sci.* **92**: 1356-1366 (2003).

34) Stout GH and Jensen LH. *X-ray Structure Determination: A Practical Guide.* 2nd edn. New York: John Wiley and Sons (1989).

35) Fagan PG, Hammond RB, Roberts KG, Docherty R, and Edmondson M. In: Myerson A, Green DA, and Meenan P, editors. *Crystal Growth of Organic Materials.* Third International Workshop on Crystal Growth of Organic Materials Conference. pp. 22-27. New York: Oxford University Press (1996).

36) Wang B, Lu ZP, Shi EW, and Zhong WZ. Twinning morphologies and mechanisms of β-BaB2O4 (BBO) crystal grown by TSSG method. *Cryst. Res. Technol.* **33**: 929-935 (1998); Wadhawan VK. A tensor classification of twinning in crystals. *Acta. Cryst.* A**53**: 546-555 (1997).

37) Bond AD and Jones W. Structure prediction as a tool for solution of the crystal structures of metallo-organic complexes using powder X-ray diffraction data. *Acta Cryst. B***58**: 233-243 (2002); Hammond RB, Roberts KJ, Docherty R, and Edmondson RB. In: Ulrich J, editor, *Crystal Growth of Organic Materials* International Workshop 4th edn. pp. 53-60. Aachen: Shaker (1997).

38) Hauptman H and Karle J. *The Solution of the Phase Problem. I. The Centrosymmetric Crystal. ACA Monograph*, No. 3. New York: Polycrystal Book Service (1953); Giacovazzo C. *Direct Methods in Crystallography*. London: Academic Press (1980); Altomare A, Cascarano G, Giacovazzo A, Guagliardi A, Burla MC, Polidori G, and Camalli M. SIRPOW.92 – a program for automatic solution of crystal structures by direct methods optimized for powder data. *J. Appl. Cryst.* **27**: 435-436 (1994); Will G. POWLS: a powder least-squares program. *J. Appl. Cryst.* **12**: 483-485 (1979).

39) Pawley GS. Unit-cell refinement from powder diffraction scans. *J. Appl. Cryst.* **14**: 357-361 (1981).

40) Lebail A, Duroy H, and Forquet JL. Ab initio structure detrmination of $LiSbWO_6$ by X-ray powder diffraction. *Mater. Res. Bull.* **23**: 447-452 (1988); Altomare A, Burla MC, Cascarano G, Giacovazzo A, Guagliardi A, Moliterni AGG, and Polidori G. EXTRA: a program for extracting structure-factor amplitudes from powder diffraction data. *J. Appl. Cryst.* **28**: 842-846 (1995).

41) Knudsen KD, Pattison P, Fitch AN & Cernik RJ. Solution of the crystal and molecular structure of complex low-symmetry organic compounds with powder diffraction techniques: Fluorescein diacetate. *Angew Chem. Int. Ed. Engl.* **37**: 2340-2343 (1998).

42) McCusker LB. Zeolite crystallography. Structure determination in the absence of conventional single-crystal data. *Acta Cryst.* A**47**: 297-313 (1991); Poojary DM and Clearfield A. Application of X-ray powder diffraction techniques to the solution of unknown crystal structures. *Acc. Chem. Res.* **30**: 414-422 (1997).

43) Harris KDM & Tremayne M. Crystal structure determination from powder diffraction data. *Chem. Mater.* **11**: 2554-2570 (1996).

44) Gavezzotti A. Methods and current trends in the simulation and prediction of organic crystal structures. *Nova Acta Leopold* **79**: 33-46 (1999).

45) *The Rietveld Method.* Young RA, Ed. Oxford, UK: Oxford University Press (1993).

46) Patterson AL. A Fourier series method for the determination of the components of interatomic distances in crystals. *Phys. Rev.* **46**: 372-376 (1934); Tremayne M. *Ab initio* structure determination from X-ray powder diffraction data. Ph.D. Thesis. University of St. Andrews, Scotland (1995).

47) Lightfoot P, Glidewell C, and Bruce PG. *Ab initio* determination of molecular structures using high-resolution powder diffraction data from a laboratory X-ray source. *J. Mater. Chem.* **2**: 361-362 (1992).

48) Tremayne M. Lightfoot P, Mehta MA, Bruce PG, Harris KDM, Shankland K, Gilmore CJ, and Bricogne G. *J. Solid State Chem.* **100**: 191 (1992); Gilmore CJ, Henderson K, and Bricogne G. A multisolution method of phas determination by combined maximization of entropy and likelihood. IV. The *ab initio* solution of crystal structures from their X-ray powder data. *Acta. Cryst.* A**47**: 830-841 (1991); Shankland K, Gilmore CJ, Bricogne G, and Hashizume H. A multisolution method of phase determination by combined maximization of entropy and likelihood. VI. Automatic likelihood analysis via the student *t* test, with an application to the powder structure of magnesium boron nitride, Mg_3BN_3. *Acta Cryst.* A**49**: 493-501 (1993).

49) Newsam JM, Deem MW, and Freeman CM. *Accuracy in Powder Diffraction II; NIST Special Publ. No. 846*, p. 80. (1992).

50) Harris KDM, Tremayne M, Lightfoot P, and Bruce PG. Crystal structure determination from powder diffraction data by Monte Carlo methods. *J. Am. Chem. Soc.* **116**: 3543-3547 (1994).

51) Ramprasad D, Pez GP, Toby BH, Markley TJ, and Pearlstein RM. Solid state lithium cyanocobaltates with a high capacity for reversible dioxygen binding: Synthesis, reactivity, and structures. *J. Am. Chem. Soc.*

117: 10694-10701 (1995); Tremayne M, Kariuki BM, and Harris KDM. Structure determination of a complex organic solid from X-ray powder diffraction data by a generalized Monte Carlo method: The crystal structure of red fluorescein. *Angew. Chem., Int. Ed. Engl.* **36**: 770-772 (1997); David WIF, Shankland K, and Shankland N. Routine determination of molecular crystal structures from powder diffraction data. *Chem. Comm. (Camb.)* **8**: 931-932 (1998).

52) Andreev YG, Lightfoot P, and Bruce PG. Structure of a polymer electrolyte poly(ethylene oxide)$_3$: LiN(SO$_2$CF$_3$)$_2$ determined by powder diffraction using a powerful Monte Carlo approach. *Chem. Commun.* 2169-2170 (1996); David WIF, Shankland K, and Shankland N. Routine determination of molecular crystal structures from powder diffraction data. *Chem. Commun.* 931-932 (1998); Gdanitz RJ. Prediction of molecular crystal structures by Monte Carlo simulated annealing without reference to diffraction data. *Chem. Phys. Lett.* **190**: 391-396 (1992).

53) Kariuki BM, Serrano-Gonzalez H, Johnston RL, and Harris KDM. The application of a genetic algorithm for solving crystal structures from powder diffraction data. *Chem. Phys. Lett.* **280**: 189-195 (1997); Harris KDM, Johnston RL, and Kariuki BM. The genetic algorithm: Foundations and applications in structure solution from powder diffraction data. *Acta. Cryst.* A**54**: 632-645 (1998); Kariuki BM, Calcagno P, Harris KDM, Philp D, and Johnston RL. Evolving opportunities in structure solution from powder diffraction data − crystal structure determination of a molecular system with twelve variable torsion angles. *Angew. Chem., Int. Ed. Engl.* **38**: 831-835 (1999); Shankland K, David WIF, and Csoka T. Crystal structure determination from powder diffraction data by the application of a genetic algorithm. *Z. Kristallogr.* **212**: 550-552 (1997); Shankland K, David WIF, Csoka T, and McBride L. Structure solution of ibuprofen from powder diffraction data by the application of a genetic algorithm combined with prior conformational analysis. *Int. J. Pharm.* **165**: 117-126 (1998).

54) Hammond RB, Roberts KJ, Docherty R, and Edmondson M. Computationally assisted structure determination for molecular materials from X-ray powder diffraction data. *J. Phys. Chem. B.* **101**: 6532-6536 (1997).

55) Chin DN. Improving the efficiency of predicting hydrogen-bonded organic molecules. *Trans. Am. Cryst. Assoc.* **33**: 33-43 (1999).

56) Engel GE, Wilke S, Konig O, Harris KDM, and Leusen FJJ. Powdersolve – A complete package for crystal structure solution from powder diffraction patterns. *J. Appl. Cryst.* **32**: 1169-1179 (1999).

57) Visser JW. A fully automatic program for finding the unit cell from powder data. *J. Appl. Cryst.* **2**: 89-95 (1969); Werner PE, Eriksson L, and Westdahl M. TREOR, A semi-exhaustive trial-and-error powder indexing program for all symmetries. *J. Appl. Cryst.* **18**: 367-370 (1985); Boultif A and Louer D. Indexing of powder diffraction patterns for low-symmetry lattices by the successive dichotomy method. *J. Appl. Cryst.* **24**: 987-993 (1991).

58) Hammersley JM and Handscomb DC. *Monte Carlo Methods*. London: Methuen (1964); Allen MP & Tildesley DJ. *Computer Simulation of Liquids*. Oxford: Clarendon Press (1987); Siepmann JI. An introduction to the Monte Carlo method for particle simulations. In: Ferguson DM, Siepmann JI, and Truhlar DG, editors. *Monte Carlo Methods in Chemical Physics*. New York: John Wiley & Sons, Inc. pp. 1-12. (1999); Metropolis N and Ulam S. The Monte Carlo method. *J. Am. Stat. Assoc.* **44**: 335-341 (1949).

59) Metropolis N, Rosenbluth AW, Rosenbluth MN, Teller AH, and Teller E. Equation of state calculations by fast computing machines. *J. Chem. Phys.* **21**: 10-15 (1953).

60) Kirkpatrick S, Gelatt CD, and Vecchi Jr. MP. Optimization by simulates annealing. *Science* **220**: 671-680 (1983); van Laarhoven PJM and Aarts EHL. *Simulated Annealing: Theory and Applications.* Holland: D. Riedel Publishing (1987).

61) McCusker LB, von Dreele RB, Cox DE, Louer D, and Scardi P. Rietveld refinement guidelines. *J. Appl. Cryst.* **32**: 36-50 (1999); Stephenson GA and Young R. Potential applications of Rietveld analysis in the pharmaceutical industry. *Am. Pharm. Rev.* **4**: 46-51 (2001); Kisi EH. Rietveld analysis of powder diffraction patterns. *Mater. Forum* **18**: 135-153 (1994).

62) Rietveld HM. A profile refinement method for nuclear and magnetic structures. *J. Appl. Cryst.* **2**: 65-71 (1969).

63) Hammond RB, Jones MJ, Murphy SA, Roberts KJ, Smith EDL, Klapper H, Kutzke H, Docherty R, Cherryman J, Roberts RJ, and Fagan PG. Determining the crystal structures of organic solids using X-ray powder diffraction together with molecular and solid state modeling techniques. *Mol. Cryst. Liq. Cryst. Science and Technology A***356**: 389-405 (2001).

64) Aakeroy CB, Beatty AM, Tremayne M, Rowe DM, and Seaton CC. A combination of X-ray single crystal diffraction and Monte Carlo structure solution from X-ray powder diffraction data in a structural investigation of 5-bromonicotinic acid and solvates thereof. *Cryst. Growth. Des.* **1**: 377-382 (2001).

65) Rajeswaran M, Blanton TN, Zumbulyadis N, Giesen DJ, Conesa-Moratilla C, Misture SC, Stephens PW, and Huq A. Three-dimensional structure determination of N-(p-tolyl)-dodecylsulfonamide from powder diffraction data and validation of structure using solid-state NMR spectroscopy. *J. Am. Chem. Soc.* **124**: 14450-14459 (2002).

66) Stephenson GA. Structure determination from conventional powder diffraction data: application to hydrates, hydrochloride salts, and metastable polymorphs. *J. Pharm. Sci.* **89**(7): 958-966 (2000).

67) Gavezzotti A. Are crystal structures predictable? *Acc. Chem. Res.* **27**: 309-314 (1994); Gavezzotti A and

Filippini G. Computer prediction of organic crystal structures using partial X-ray diffraction data. *J. Am. Chem. Soc.* **118**: 7153-7157 (1996); Karfunkel R and Gdanitz RJ. Ab initio prediction of possible crystal structures for general organic molecules. *J. Comput. Chem.* **13**: 1171-1183 (1992). Chaka AM, Zaniewski R, Youngs W, Tessier C, and Klopman G. Predicting the crystal structure of organic molecular materials. *Acta Cryst.* B**52**: 165-183 (1996).

68) Leusen FJJ and Engel GE. Computational approaches to crystal structure and polymorph prediction. *J. Pharm. Pharmacol.* **51**: 1 (supplement) (1999).

69) Lommerse JPM, Motherwell WDS, Ammon HL, Dunitz JD, Gavezzotti A, Hofmann DWM, Leusen FJJ, Mooij WTM, Price SL, Schweizer B, Schmidt MU, Van Eijck BP, Verwer P, and Williams DE. A test of crystal structure prediction of small organic molecules. *Acta Cryst, B***56**: 697-714 (2000); Giovannini J, Perrin MA, Louer D, and Leveiller F. Ab initio crystal structure determination of three pharmaceutical compounds from X-ray powder diffraction data. *Mater. Sci. Forum* **2**: 582-587 (2001); Bond AD, Feeder N, Teat SJ, and Jones W. The solid-state structure of 3-hydroxy-4-methyl-2(3H)-thiazolethione: prediction and measurement. *Tetrahedron* **56**: 6617-6624 (2000); Motherwell WDS, Ammon HL, Dunitz JD, Dzyabchenko A, Erk P, Gavezzotti A, Hofmann DWM, Leusen FJJ, Lommerse JFM, Mooij WTM, Price SL, Scheraga H, Schweizer B, Schmidt MU, van Eijck BP, Verwer P, and Williams DE. Crystal structure prediction of small molecules: a second blind test. *Acta Cryst. B* **58**: 647-661 (2002); Price SL. The computational prediction of pharmaceutical crystal structures and polymorphism. *Adv. Drug. Del. Rev.* **56**: 301-309 (2004).

70) Byrn SR, Xu W, and Newman AW. Chemical reactivity in solid-state pharmaceuticals: formulation implications. *Adv. Drug Delivery Rev.* **48**: 115-136 (2001).

71) Amidon GL, Lennernas H, Shah VP, and Crison JR. A theoretical basis for a biopharmaceutic drug classification: The correlation of in vitro drug product dissolution and in vivo bioavailability. *Pharm. Res.* **12**: 413-420 (1995); Yu LX, Amidon GL, Polli JE, Zhao H, Mehta MU, Conner DP, Shah VP, Lesko LJ, Chen M-L, Lee VHL, and Hussain AS. Biopharmaceutics classification system: The scientific basis for biowaiver extensions. *Pharm. Res.* **19**(7): 921-925 (2002).

72) Morris KR, Nail SL, Peck GE, Byrn SR, Griesser UJ, Stowell JG, Hwang S-J, and Park K. Advances in pharmaceutical materials and processing. *Pharm. Sci. Technol. Today* **1**: 235-245 (1998).

73) Morris KR, Griesser UJ, Eckhardt CJ, and Stowell JG. Theroetical approaches to physical transformations of active pharmaceutical ingredients during manufacturing processes. *Adv. Drug Delivery Rev.* **48**: 91-114 (2001).

74) Phadnis NV and Suryanarayanan R. Polymorphism in anhydrous theophylline: implications on the dissolution rate of theophylline tablets. *J. Pharm. Sci.* **86**: 1256-1263 (1997).

75) Otsuka M and Matsuda Y. Effects of environmental temperature and compression energy on polymorphic transformation during tableting. *Drug Dev. Ind. Pharm.* **19**: 2241-2269 (1993).

76) Otsuka M, Hasegawa H, and Matsuda Y. Effect of polymorphic transformation during the extrusion-granulation process on the pharmaceutical properties of carbamazepine granules. *Chem. Pharm. Bull.* **45**: 894-898 (1997); Otsuka M, Hasegawa H, and Matsuda Y. Effect of polymorphic forms of bulk powders on pharmaceutical properties of carbamazepine granules. *Chem. Pharm. Bull.* **47**: 852-856 (1999).

77) Otsuka M, Nakanishi M, and Matsuda Y. Effects of crystalline form on the tableting compression mechanism of phenobarbital polymorphs. *Drug Dev. Ind. Pharm.* **25**: 205-215 (1999); Otsuka M, Onoe M, and Matsuda Y. *Pharm. Res.* **10**: 577 (1993).

78) Otsuka M, Ohtani H, Otsuka K, and Kaneiwa N. Effect of humidity on solid-state isomerization of various kinds of lactose during grinding. *J. Pharm. Pharmacol.* **45**: 2-5 (1993).

79) Wong MWY and Mitchell AG. Physicochemical characterization of a phase change produced during the wet granulation of chlorpromazine hydrochloride and its effects on tableting. *Int. J. Pharm.* **88**: 261-273 (1992).

80) Miyamae A, Kema H, Kawabata T, Yasuda T, Otsuka M, and Matsuda Y. X-ray powder diffraction study on the grinding effect of the polymorphs of a novel and orally effective uricosuric agent: FR76505. *Drug Dev. Ind. Pharm.* **20**: 2881-2897 (1994).

81) Kitamura S, Koda S, Miyamae A, Yasuda T, and Morimoto Y. *Int. J. Pharm.* **87**: 1052-1061 (1998).

82) Chongprasert S, Griesser UJ, Bottorff AT, Williams NA, Byrn SR, Nail SL. Effects of freeze-dry processing conditions on the crystallization of pentamidine isethionate. *J. Pharm. Sci.* **87**: 1155-1160 (1998).

83) Khankari RK and Grant DJW. Pharmaceutical hydrates. *Thermochim. Acta.* **248**: 61-79 (1995).

84) Ghosh S, Ojala WH, Gleason WB, and Grant DJW. Relationships between crystal structures, thermal properties and solvate stability of dialkylhydroxypyridones and their formic acid solvates. *J. Pharm. Sci.* **84**: 1392-1399 (1995); Ojala WH, Khankari RK, Grant DJW, and Gleason WB. Crystal structures and physical chemical properties of nedocromil zinc heptahydrate and nedocromil magnesium pentahydrate. *J. Chem. Crystallog.* **26**: 167-178 (1996); Giordano F, Bettini R, Donini C, Gazzaniga A, Caira M, Zhang GGZ, and Grant DJW. Physical properties of parabens and their mixtures: solubility in water, thermal behavior, and crystal structures. *J. Pharm. Sci.* **88**: 1210-1216 (1999); Zhu HJ, Young Jr. VG and Grant DJW. Crystal structure and thermal behavior of nedocromil nickel octahydrate. *Int. J. Pharm.* **232**: 23-33 (2002).

85) Schmid S, Muller-Goymann CC, and Schmidt PC. Interactions during aqueous film coating of ibuprofen

with Aquacoat ECD. *Int. J. Pharm*. **197**: 35-39 (2000).

86) Kitamura S, Chang LC, and Guillory JK. Polymorphism of mefloquine hydrochloride. *Int. J. Pharm*. **101**: 127-144 (1994).

87) Van Eikeren P. Commercial manufacture of chiral pharmaceuticals. *Chiral Seperations* 9-35 (1997); Gu CH and Grant DJW. In: Eichelbaum M, Testa B, and Somogyi A, editors. *Handbook of Experimental Pharmacology: Stereochemical Aspects of Drug Action and Disposition*. Vol. 153. Berlin: Springer. pp. 113-137. (2003).

88) Abgada CO and York P. Dehydration of theophylline monohydrate powder: effects of particle size and sample weight. *Int. J. Pharm*. **106**: 33-40 (1994).

89) Sun C and Grant DJW. Improved tableting properties of p-hydroxybenzoic acid by water of crystallization — a molecular insight. *Pharm Res.* (in press).

90) Bandopadhyay R and Grant DJW. Plasticity and slip system of plate-shaped crystals of L-lysine monohydrochloride dehydrate. *Pharm. Res.* **18**: 274-280 (2001).

91) Sun C and Grant DJW. Influence of crystal structure on the tableting properties of sulfamerazine polymorphs. *Pharm. Res.* **18**: 274-280 (2001).

92) Payne RS, Roberts RJ, and Rowe RC. The mechanical properties of two forms of primidone predicted from their crystal structures. *Int. J. Pharm*. **145**: 165-173 (1996).

93) Roberts RJ, Payne RS, and Rowe RC. Mechanical property predictions for polymorphs of sulfathiazole and carbamazepine. *Eur. J. Pharm. Sci*. **9**: 277-283 (2000).

94) Roberts RJ, Rowe RC, and Kendall K. Brittle-ductile transitions in die compaction of sodium chloride. *Chem. Eng. Sci*. **44**: 1647-1651 (1989); Roberts RJ and Rowe RC. Determination of the critical stress intensity factor (KIC) of microcrystalline cellulose using radically edge-cracked tablets. *Int. J. Pharm*. **52**: 213-219 (1989); Bassam F, York P, Rowe RC, and Roberts RJ. Young's modulus of powders used as pharmaceutical excipients. *Int. J. Pharm*. **64**: 55-60 (1990).

95) Roberts RJ, Rowe RC, and York P. The relationship between Young's modulus of elasticity of organic solids and their molecular structure. *Powder Technol.* **65**: 139-146 (1991).

96) Genck WJ. The effects of mixing on scale-up — how crystallization and precipitation react. *Chem. Process.* **63**: 47 (2000).

97) Brittain HG and Fiese EF. Effects of pharmaceutical processing on drug polymorphs and solvates. In: Brittain HG, editor. *Polymorphism in Pharmaceutical Solids.* New York: Marcel Dekker. pp. 331-361. (1999); Beckmann W. Seeding the desired polymorph: background, possibilities, imitations, and case studies. *Org. Proc. Res. Dev*. **4**: 372-383 (2000).

98) Brittain HG. The impact of polymorphism on drug development: a regulatory viewpoint. *Am. Pharm. Rev*. **3**(4): 67-68, 70 (2000).

99) Byrn SR, Pfeiffer R, Ganey M, Hoiberg C, and Poochikian G. Pharmaceutical solids: a strategic approach to regulatory considerations. *Pharm. Res.* **12**: 945-954 (1995).

100) Federal Register, United States Government Printing Office, Superintendent of Documents, P.O. Box 37194, Pittsburgh, PA 15250-7954 (2000).

Author’s short biography

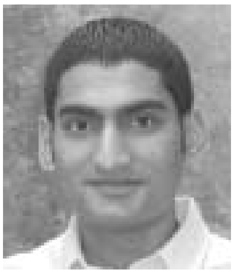

Agam R. Sheth

Dr. Agam R. Sheth is Senior Research Chemist at Merck Research Laboratories in West Point, PA, where his responsibilities include preformulation and basic research support. Dr. Sheth’s research interest lies in solid-state organic chemistry, particularly the structure-property relationship of pharmaceutical crystals. Dr. Sheth is the author of several peer-reviewed publications and has presented at several national and international scientific meetings. Dr. Sheth is a member of the American Chemical Society and the American Association of Pharmaceutical Scientists. He is also a member of the American Pharmacists Association, where he held elected office in 2002-03. Dr. Sheth is a recipient of the 2002 Walter F. Enz Research Award in Pharmaceutics and is a member of the Rho Chi Honor Society. Dr. Sheth obtained his Ph.D. in Pharmaceutics at the University of Minnesota under the guidance of Prof. David J.W. Grant.

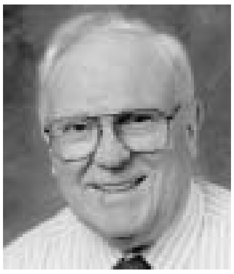

David J.W. Grant

David J.W. Grant is a graduate of Oxford University, UK: B.A. in Chemistry in 1960; D.Phil. in Physical Chemistry in 1963; M.A. (Keble College, 1963); and D.Sc. for recognized published research on the physical chemistry of pharmaceutical systems (October 1990). He has held academic appointments at the University of Nottingham, UK, and University of Toronto, Canada. In 1988, he was appointed to the William and Mildred Peters Chair in Pharmaceutics, University of Minnesota. Since July 1998, he has served as Director of the Drug Delivery Center in the University. Since January 1994, David Grant has served as Associate Editor of the *Journal of Pharmaceutical Sciences*. He is also a member of the Editorial Advisory Board of the journals *Pharmaceutical Development and Technology, Kona Powder and Particle* and *The AAPS Journal*. David Grant teaches the physical chemistry of pharmaceuticals in which he is co-author of an undergraduate text. In 1978 and 1980 he worked on the intermolecular interactions of drugs in solution at the University of Kansas in the laboratory of the late Dr. Takeru Higuchi, with whom he is the co-author of a book entitled, *Solubility Behavior of Organic Compounds*. Since 1978 David Grant has been studying the crystal engineering of drugs and the properties of the solid state, particularly the thermodynamics, solvation, polymorphism, crystallization, compaction, solubility, and dissolution of drugs. He is also studying the effects of doping, hydration, hydrogen bonding, and chirality in the solid state. David Grant’s recent work has focused on the structure and properties of hydrates and the molecular basis of polymorph crystallization and screening. He is the author or co-author of over 200 peer-reviewed scientific articles and reviews and serves as a consultant for numerous companies that manufacture fine chemicals and pharmaceuticals. David Grant is a Fellow of AAAS, AAPS, IUPAC and the Royal Society of Chemistry (Chartered Scientist, UK). He was awarded the PhRMA Foundation Pharmaceutics Award in Excellence in 1999, the European Society of Applied Physical Chemistry Award in 2004, the AAPS Dale E. Wurster Award in Pharmaceutics in 2004, and the Mettler-Toledo Award in thermal analysis from the North American Thermal Analysis Society in 2005. Memberships also include ACA, ACS, AIChE, and the Rho Chi Honor Society.

Modelling the Particle Stress at the Dilute-intermediate-dense Flow Regimes: A Review[†]

Y. Makkawi and R. Ocone[1]
*Chemical Engineering, School of Engineering and Physical Sciences, Heriot-Watt University**

Abstract

Gas-solid flow systems are found in many industrial applications such as catalytic reactions, pneumatic conveying, granulation, crystallisation, mineral classification, etc. The operational hydrodynamics can vary depending on the operation method from fast dilute flow, which is dominated by collisional particle-particle contacts, to dense slow flow, which is dominated by sustained frictional contacts. For many years, the former has been successfully modelled using the classic kinetic theory for granular flow, while the latter has been modelled based on soil mechanics principles. At the intermediate-dense regime, three different modelling approaches are identified: (1) the kinetic-frictional model using an ad hoc patching together of the stress from the two limiting regimes at a specific solid fraction (Johnson and Jackson, 1978; Ocone et al., 1993; Syamlal et al., 1993); (2) the switching from one regime to another using different solid stress formulations (Laux, 1998; Makkawi and Ocone, 2005); and (3) the new emerging fluid mechanic approach which allows for a smooth transition from one regime to another using a unified model (Tardos et al., 2003, Savage, 1998). In this study, a one-dimensional fully developed gas-solid flow model for horizontal flow will be used to review the various treatments of solid stresses, and the sensitivity of the flow predictions to the frictional stress will be assessed.

Key words: Gas-solid flow; Kinetic theory; Frictional stress; Intermediate regime; Hydrodynamic modelling

1. Introduction

The last two decades have seen a growing interest in the modelling of dense gas-solid flow where kinetic, collisional and frictional particle stresses coexist. Various forms of constitutive relations for these stresses have been reported in the literature. In 1984, Lun et al. reported the most widely used comprehensive model for slightly inelastic granular flow supported by the corresponding constitutive relations for the energy balance. The model was developed in analogy with the kinetic theory of gases, and it incorporates kinetics as well as collisional contributions to the particle stress and energy generation, conduction and dissipation. In 1987, Johnson and Jackson introduced a new constitutive frictional-collisional model for plane shearing to account for the slow deformation of particles in dense flow. The model employs a frictional stress formula adopted from the critical state theory of soil mechanics. Accordingly, the resulting particle stress was assumed as the sum of the kinetic and frictional contribution at a hypothetical critical particle concentration. In 1993, Ocone et al. and Syamlal et al. reported further development of this approach. In 1998, Laux developed an alternative frictional stress relation and employed it in the simulation of dense gas-solid flow using a complete switching approach at a critical concentration. Most recently, Tardos et al. (2003) proposed new constitutive relations for the particle shearing and energy dissipation developed for the geometry of a Couette device. These relations were used to simulate the rheological behaviour of powder flow in the so-called "intermediate regime". The model was basically developed to replace the additive approach and presents a smooth merging between rapid-intermediate-dense flows.

[†] Accepted: August 9, 2005

* Edinburgh EH14 4AS, UK

[1] Corresponding author
TEL: 0044 131 451 3777 FAX: 0044 131 451 3129
E-mail: r.ocone@hw.ac.uk

In this study, we present a critical review of the various reported closure equations for particle stress. We begin by writing the mathematical form for each contributing stress; then we show the different approaches for merging these contributions in a unified particle stress constitutive equation. The different approaches for the particle stress along with the corresponding energy balance constitutive equations are then tested in the simulation of gas-particle flow in a horizontal duct using the two-fluid models. Finally, we assess and compare the various predicted hydrodynamics by each model.

2. Modelling the particle stress

2.1 Kinetic stress

At very dilute concentrations, the particles stress is dominated by the rate-dependent "viscous" contribution. According to Lun et al. (1984), this was described as kinetic stress, and its contribution to the total shear stress is given by:

$$\tau_{s-kinetic}=2\mu_{kinetic}S \tag{1}$$

where S is the strain rate and defined as follows:

$$S=\frac{1}{2}\left(\nabla v+(\nabla v)^T\right) \tag{2}$$

and the kinetic viscosity is:

$$\mu_{kinetic}=\left(\frac{5\sqrt{\pi\theta}\rho_s d_p}{96}\right)\left(\frac{1}{\eta(2-\eta)}\left(\frac{1}{g_o}+\frac{8}{5}\eta\alpha(3\eta-2)\right)\right) \tag{3}$$

The kinetic contribution to the total solid pressure is given by:

$$p_{s-kinetic}=\rho_s\alpha\theta \tag{4}$$

2.2 Collisional stress

For moderate concentrations, and because of the slightly inelastic collisions between particles, a second contribution term, designated here as collisional stress, was described by Lun et al. (1984) as follows:

$$\tau_{s-collision}=2\mu_{collision}S \tag{5}$$

where

$$\mu_{collision}=\left(\frac{5\sqrt{\pi\theta}\rho_s d_p}{96}\right)\left(\frac{1}{\eta(2-\eta)}\left(\frac{8}{5}\eta\alpha+\frac{64}{25}\eta^2\alpha^2 g_o(3\eta-2)\right)+\frac{768\alpha^2\eta g_o}{25\pi}\right) \tag{6}$$

The quantity in the first bracket of Eqs. 3 and 6 represents the shear viscosity for perfectly elastic particles. The collisional solid pressure is given by:

$$p_{s-collision}=4\rho_s\eta g_o\alpha^2\theta \tag{7}$$

2.3 Frictional stress

At very high solid concentrations, the grain inertia is negligible and sustained contacts control the flow. The majority of the available friction models are based on the critical state theory of soil mechanics (Atkinson and Bransby, 1978; Syamlal, 1993; Ocone et al., 1993). Here, the shear stress is described in terms of a "frictional viscosity" such that:

$$\tau_{s-friction}=2\mu_{friction}S \tag{8}$$

On the basis of soil mechanics principles, Schaeffer (1978) proposed an equation for the frictional viscosity that satisfies the Coulomb yield condition in dense plane shear such that:

$$\mu_{friction}=\frac{\sqrt{2}p_{s-friction}\sin\phi}{|S|} \tag{9}$$

where ϕ is the angle of internal friction. $|S|$ is the magnitude of the strain rate and is given by:

$$|S|=\left[\left(\frac{\partial u}{\partial x}\right)^2+\left(\frac{\partial v}{\partial y}\right)^2+\frac{1}{2}\left(\frac{\partial u}{\partial y}+\frac{\partial v}{\partial x}\right)^2\right]^{1/2} \tag{10}$$

Johnson and Jackson (1978) proposed a critical state solid frictional pressure that allows for a slight compressibility with very limited particle concentration change, such that:

$$p_{s-friction}=\begin{cases}0 & \text{if } \alpha<\alpha_{\text{critical}}\\ A\dfrac{(\alpha-\alpha_{critical})^n}{(\alpha_{\max}-\alpha)^p} & \text{if } \alpha\geq\alpha_{\text{critical}}\end{cases} \tag{11}$$

where A, n and p are empirical constants depending on the particle properties and specified by Ocone et al. (1993) as 0.05, 2 and 3, respectively. Johnson et al. (1990) and Ocone et al. (1993) specified the critical solid concentration to be 0.5, they assumed this to be the point where the frictional stress becomes significant.

Similarly, Syamlal et al. (1993) developed and implemented the following equation which they used in the Mfix hydrodynamic code:

$$\mu_{friction}=\frac{\sqrt{2}p_{s-friction}\sin\phi}{\alpha|S|} \tag{12}$$

$$p_{s-friction}=\begin{cases}0 & \text{if } \alpha<\alpha_{\text{critical}}\\ A\alpha(\alpha-\alpha_{critical})^n & \text{if } \alpha\geq\alpha_{\text{critical}}\end{cases} \tag{13}$$

where A and n are equal to 10^{25} and 10, respectively. The magnitude of the strain rate is given here by:

$$|S|=\left\{\frac{1}{6}\left[\left(\frac{\partial v_x}{\partial x}-\frac{\partial v_y}{\partial y}\right)^2+\left(\frac{\partial v_x}{\partial x}\right)^2+\left(\frac{\partial v_y}{\partial y}\right)^2+\frac{1}{4}\left(\frac{\partial v_x}{\partial y}+\frac{\partial v_y}{\partial x}\right)^2\right]\right\}^{1/2} \tag{14}$$

Instead of a critical solid concentration of 0.5, here Syamlal et al. (1993) assume that the frictional stress is only important above the critical value of 0.59.

Laux (1998) proposed the following frictional stress viscosity, which is only assumed significant above the critical particle concentration of 0.5:

$$\mu_{friction}=\frac{6\sin\phi}{9-\sin^2\phi}\frac{|I_{11}|}{2\sqrt{3|II_D|}} \tag{15}$$

the invariant I_{11} is defined in terms of the particle pressure and the bulk viscosity such that:

$$II_{11}=3\left(\lambda_s\nabla v-\frac{p_s}{\alpha}\right) \tag{16}$$

the solid pressure, p_s, is defined as the sum of kinetic and collisional contributions (i.e. Eq. 4+Eq. 7). The second invariant of the strain rate, II_D is given by:

$$II_D=-\frac{1}{2}S.S \tag{17}$$

3. Merging the dilute with the intermediate-dense flow

In many gas-solid transport and processes, multi-flow regimes coexist and the particle stress fluctuations may be a result of dominant kinetic, collisional, or frictional stresses or the result of all three mechanisms working together. Different modelling approaches for particle stresses have been developed in the last two decades to provide a unified model covering the whole flow regime. These approaches, which are summarised in **Table 1**, are discussed below in detail.

3.1 Classic kinetic theory approach

The classic kinetic theory was developed to treat the rapid flows of granular material at low and moderate concentrations. In 1984, Lun et al. reported one of the most widely used kinetic-theory-based model for the solid stress, energy flux and collisional dissipation. The theory, which was developed for slightly inelastic particles, incorporates kinetics as well as collisional contributions to the solid stress. Lun et al. (1984) described their theory as "appropriate for dilute as well as dense concentrations of solids".

The classic kinetic theory of Lun et al. (1984) assumes the total particle shear stress as the *ad hoc* patching of the kinetic and collisional contribution described in the previous section:

$$\tau_{s-k}=\tau_{s-kinetic}+\tau_{s-collision} \tag{18}$$

Similarly, the solid pressure is assumed to arise from kinetic and collisional contributions such that:

$$p_{s-k}=p_{s-kinetic}+p_{s-collision} \tag{19}$$

Fig. 1 shows the kinetic and collisional contributions to the total particle stress as a function of concentration. While the kinetic stress decreases and almost vanishes close to the maximum packing condition, the collisional stress shows exactly the opposite behaviour. The simple addition of both limiting

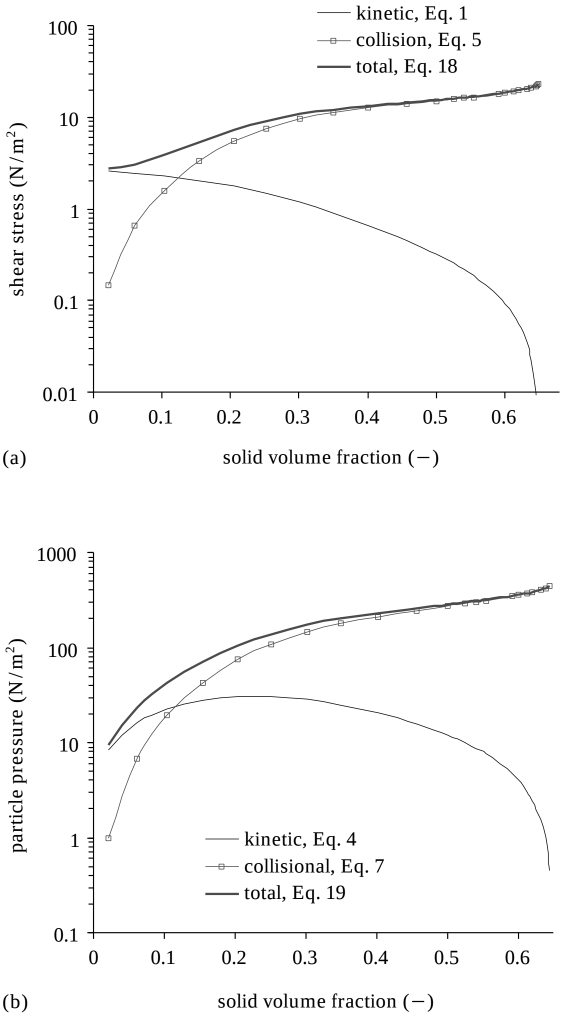

Fig. 1 Classic kinetic stresses as a function of particle concentration (a), shear stresses (b) solid pressure.

Table 1 Summary of particle stress modelling approaches and the corresponding energy balance constitutive relations

Modelling approach	Sources	Equations
Classic kinetic theory	Lun et al. (1984)	$\tau_s=\tau_{s-kinetic}+\tau_{s-collision}$ $p_s=p_{s-kinetic}+p_{s-collision}$ $q_s=q_{s-kinetic}+q_{s-collision}$ $\gamma_s=\frac{48}{\sqrt{\pi}}\eta(1-\eta)\frac{\rho_p}{d}g_o\theta^{3/2}$
Frictional additive	Johnson and Jackson (1978)[a] Ocone et al. (1993)[a]	$\tau_s=\tau_s+\tau_{s-friction}$ $p_s=p_s+p_{s-friction}$ $q_s=q_{s-kinetic}+q_{s-collision}$ $\gamma_s=\frac{48}{\sqrt{\pi}}\eta(1-\eta)\frac{\rho_p}{d}g_o\theta^{3/2}$ $\alpha<\alpha_{critical}\Rightarrow\left.\begin{matrix}\tau_{s-friction}\\ p_{s-friction}\end{matrix}\right\}=0$
	Syamlal et al. (1993)[b]	$\tau_s=\tau_{s-collision}+\tau_{s-friction}$ $p_s=p_{s-collision}+p_{s-friction}$ $q_s=q_{s-collision}$ $\gamma_s=\frac{48}{\sqrt{\pi}}\eta(1-\eta)\frac{\rho_p}{d}g_o\theta^{3/2}$ $\alpha<\alpha_{critical}\Rightarrow\left.\begin{matrix}\tau_{s-friction}\\ p_{s-friction}\end{matrix}\right\}=0$
Switching	Laux (1998)[c]	$\tau_s=\begin{cases}\max\lvert\tau_{s-kinetic},\ \tau_{s-friction}\rvert & \alpha\geq\alpha_{critical}\\ \tau_{s-kinetic} & \alpha<\alpha_{critical}\end{cases}$ $p_s=p_{s-kinetic}+p_{s-collision}$ $q_s=q_{s-kinetic}+q_{s-collision}$ $\gamma_s=\frac{48}{\sqrt{\pi}}\eta(1-\eta)\frac{\rho_p}{d}g_o\theta^{3/2}$
	Makkawi and Ocone (2005)	$\tau_s=\begin{cases}\max\lvert\tau_s,\ \tau_{s-Tardos}\rvert\\ \tau_s\end{cases}$ $q_s=q_{s-kinetic}+q_{s-collision}$ $p_s=Hydrostatic\ pressure$ $\gamma_s=\gamma_{s-Tardos}$
Smooth Transition	Tardos et al. (2003)[d]	$\tau_s=p_s\sin\phi\tanh\left(\frac{\sqrt{K\pi}}{2}\right)$ $q_s=q_{s-kinetic}+q_{s-collision}$ $\gamma_s=\sqrt{\frac{\pi}{2}}p_s\sigma\sin\phi\left[\frac{1}{\sin\phi}+\sec h^2\left(\frac{\sqrt{K\pi}}{2}\right)\right]$

(*a*) $\alpha_{critical}=0.5$
(*b*) $\alpha_{critical}=0.59$
(*c*) $\alpha_{critical}=0.5$
(*d*) This is tested here using the particle pressure estimated by the classic kinetic model.

stresses produces a smooth stress curve covering the whole range of particle concentration. However, this approach has a serious drawback in the simulation of very dilute flow close to empty duct condition and very dense flow close to maximum packing condition. In the former case, the total shear stress does not reduce towards the characteristic shearing behaviour of very dilute flow (i.e. zero particle shearing); in the latter case, because of neglecting frictional shearing stress, the model fails to capture the characteristic feature of slow flow of enduring contacts (i.e. abruptly increasing stress at close to maximum packing condition). In the next section, we will review further research efforts directed towards resolving this deficiency.

3.2 Kinetic-frictional approach

3.2.1 Critical additive approach

This approach is based on the assumptions of Savage et al. (1983, 1998), which assume that the solid stress arises from kinetic, collisional and frictional contributions with each source acting separately. However, the frictional stress is only considered important at high particle concentration such that:

$$\tau_s=\begin{cases}\tau_{s-k} & \text{if } \alpha<\alpha_{\text{critical}}\\ \tau_{s-k}+\tau_{s-friction} & \text{if } \alpha\geq\alpha_{\text{critical}}\end{cases} \tag{20}$$

and similarly,

$$p_s=\begin{cases}p_{s-k} & \text{if } \alpha<\alpha_{\text{critical}}\\ p_{s-k}+p_{s-friction} & \text{if } \alpha\geq\alpha_{\text{critical}}\end{cases} \tag{21}$$

where τ_{s-k} and p_{s-k} are the sum of the kinetic and collisional contributions as described by the classic kinetic approach.

Ocone et al. (1993) employed this approach for the simulation of gas-solid flow in inclined ducts. Syamlal et al. (1993) employed the same approach for the simulation of bubbling bed behaviour; but due to the dense nature of the flow, they neglected the kinetic contribution to the particle stress as well as its contribution to the energy balance. **Fig. 2** shows the variation of particle stress as a function of particle concentration using the frictional additive approach of Ocone et al. (1993). The models show abruptly increasing frictional stress at the critical concentration. At the same point, it is also interesting to note the same behaviour in the classic kinetic stresses contribution, but this time in a decreasing manner. This is mainly related to the considerable increase in particle stresses, which tends to shift the material towards the packing condition. This in turn results in stiff contact between particles and considerable decrease in collisional stresses. Here, the frictional stress compensates for the loss in particle stress and increase of the shearing rate. This approach ensures a smooth transition from the dominant collisional regime to the slow frictional regime.

As described by many researchers, this simple *ad hoc* approach has no strong physical justification; however, it has shown limited success in the simulation of spouted and bubbling beds (Huilin et al., 2004, Patil et al., 2005). Another critical weakness of this approach lies in the hypothetical assumption of a critical concentration at which transition occurs. The exact value of the critical particle concentration, $\alpha_{critical}$, remains without any experimental proof. On the other hand, as stated by Campbell (2002), “the solid concentration at which this transition occurs as well as the magnitude of the stresses in the elastic regimes are strong functions of the particle surface friction”, thus casting extra doubts on the generalisation of a critical concentration value.

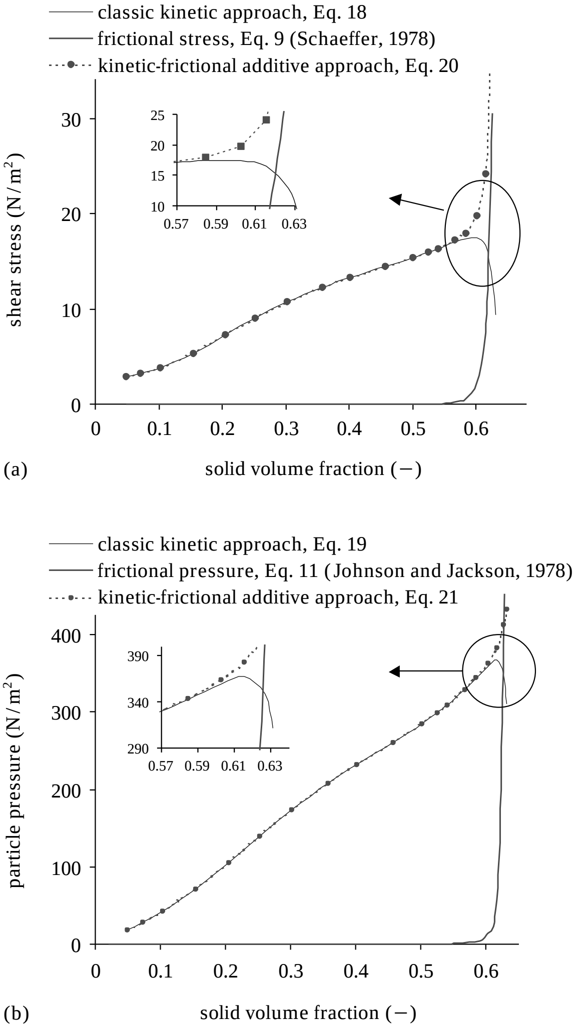

Fig. 2 Critical additive approach of particle stresses (a) shear stresses (b) particle pressure.

3.2.2 Switching approach

This method employs switching from the classic kinetic approach to a complete frictional model when the latter is proved dominant. This is done by selecting the maximum of the two acting stresses. Laux (1998) incorporated a frictional stress model in the simulation of dense gas-solid flow, but only considered the maximisation analysis after reaching the critical solid fraction. This is described mathematically as follows:

$$\tau_s=\begin{cases}\tau_{s-k} & \text{if } \alpha<\alpha_{\text{critical}}\\ \max\left|\tau_{s-k},\ \tau_{s-friction}\right| & \text{if } \alpha\geq\alpha_{\text{critical}}\end{cases} \tag{22}$$

This approach was tested by Laux (1998) and Patil et al. (2005) assuming $\alpha_{critical}=0.5$ with the frictional viscosity $\mu_{s-friction}$ given by Eq. 15. It is justified by the fact that after reaching the critical state, the particles experience long-term contacts with a very limited chance of collisional and kinetic stress taking place due to the limited free space and considerable drop in the kinetic temperature. Although this approach is backed up by strong physical justification, the precise switching point must be selected with some caution.

We have recently employed a similar switching approach for the gas-solid flow in a horizontal duct. The model allows for a smooth switching between the classic kinetic approach and the intermediate flow shear model of Tardos et al. (2003) (see next section) without the need to specify a critical switching point. The predicted variation of shear stress as a function of the particle concentration is shown in **Fig. 3**.

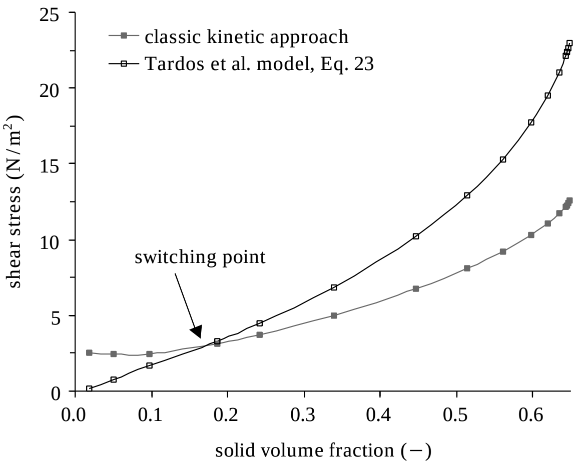

Fig. 3 Switching between classic kinetic and Tardos et al. (2003) shear stress expression, a modelling approach employed by Makkawi and Ocone (2005).

3.3 Smooth transition approach

To avoid the critical additive or switching approach, Tardos et al. (2003) proposed a new approach for the average solid shear stress that smoothly merges the slow-intermediate regime with the rapid flow regime. The basic assumption of this approach, which is a generalisation of Savage's (1998) approach, is that stresses during particle flow are not constant but fluctuate around an average value $\langle\tau_s\rangle$. The average particle stress was developed and tested for granular flow in a Couette device and, for 2D flow, is as follows:

$$\langle\tau_s\rangle=\frac{p_s\sqrt{\pi}\,\sin\phi\,\exp(-K)}{2\sqrt{2}\sigma}\left[I_o(K)+I_1(K)\right]\langle S\rangle \tag{23}$$

where σ is the standard deviation of the strain rate and related to the granular temperature, θ, such that $\sigma=\omega\sqrt{\theta}/d_p$. I_o and I_1 are the modified Bessel functions of the first kind. K is a parameter defined in terms of the average strain rate and its fluctuation such that:

$$K=\left[\frac{\langle S\rangle}{2\sigma}\right]^2 \tag{24}$$

The coefficient ω was calculated by Savage to be approximately equal to 1/4. Tardos et al. (2003) also provided further theoretical development for the energy dissipation that smoothly merges the long-term frictional and rapid flow dissipation such that:

$$\gamma_s=\frac{p_s\alpha\sqrt{\pi}\,\sin\phi\,\exp(-K)}{\sqrt{2}}\left[\frac{1}{\sin\phi}+I_o(K)-I_1(K)\right]\langle S\rangle \tag{25}$$

Makkawi and Ocone (2005) tested a simplified version of Tardos' formulation in the simulation of horizontal duct flow using the particle hydrostatic pressure for the pressure term p_s; this is given by:

$$p_s=\rho_s g\int_y^H \alpha\, dy \tag{26}$$

where y is the distance measured from the lower wall towards the top wall and H is the duct's width (see **Fig. 6**). Surprisingly, further analysis using the classic kinetic pressure of Eq. 19 instead of the hydrostatic pressure showed the same results with negligible differences at the dilute flow region (see **Fig. 4**). Therefore, in the rest of this review, we used the classic kinetic pressure with the above formulations of Tardos et al. (2003).

Fig. 5 shows the variation of shear stress predicted by Eq. 23 as a function of the particle concentration. A specially developed subroutine was used in the simulation code to compute the modified Bessel functions

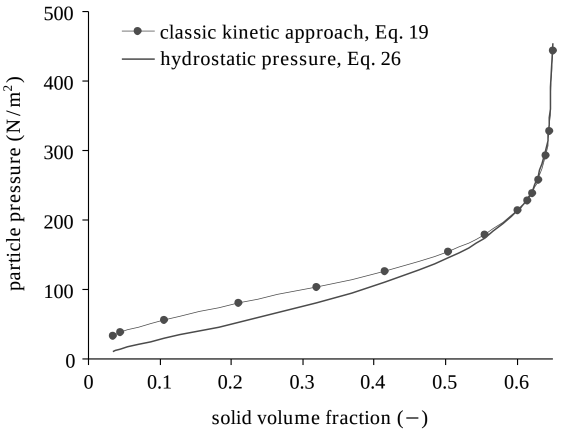

Fig. 4 Comparison between the hydrostatic pressure and classic kinetic model predictions.

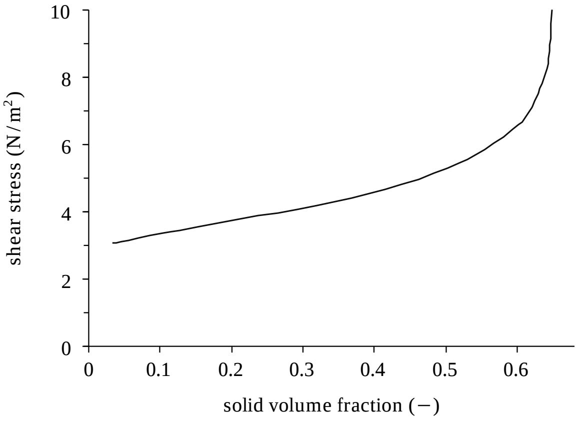

Fig. 5 Predicted particle shear stress using Eq. 24 of Tardos et al. (2003).

I_o and I_1. Similar to the classic kinetic theory predictions, here we note a linear increase in the shear stress up to the point of solid fraction ~0.5, whereas at the other extreme of close packing, the shear increases sharply independently of the solid concentration. In between these two limits a smooth transition is evident. This seems to prove the principal hypotheses of the original work of Savage (1984) and the recent development of Tardos et al. (2003). Qualitatively, this approach reduces to the same behaviour as that of the frictional additive approach for dense flow as discussed in Section 3.2; however, it has the advantage of smooth merging between the limiting stress without the need for specifying a critical transition point.

4. Simulation tests

To test the various particle stress modelling approaches discussed in Section 3, we incorporated those in the numerical model reported in Makkawi and Ocone (2005) and summarised here in **Table 2**. Briefly, this is a two-fluid model for the simulation of one-dimensional particle-gas flow in a horizontal duct. Because Eqs. 23 and 25 are mathematically difficult to use in the numerical solution of the flow momentum equation, Tardos et al. (2003) proposed a simplified version that reduces to the same solution of Eqs. 23 and 25 (see **Table 1**). These simpler forms will be used in the rest of this review. The schematic diagram of the flow geometry is shown in **Fig. 6** and the parameters used in the simulation test are summarised in **Table 3**.

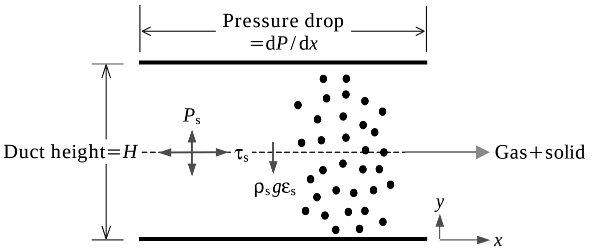

Fig. 6 Schematic diagram of the simulation test geometry and orientation.

Table 2 Model equations for one-dimensional steady flow in a horizontal duct

Gas phase	X-momentum	$\frac{\partial \tau_g}{\partial y}-\frac{\partial P_g}{\partial x}-\beta(u-v)=0$
Particle phase	X-momentum	$\frac{\partial \tau_s}{\partial y}+\beta(u-v)-\frac{\partial P_g}{\partial x}=0$
	Y-momentum	$\frac{\partial p_s}{\partial y}+\alpha\rho_s g=0$
Energy balance		$\tau_s\frac{\partial v}{\partial y}-\frac{\partial}{\partial y}\left(k_s\frac{\partial \theta}{\partial y}\right)-\gamma_s=0$

Table 3 Parameters used in the simulation test

Duct width, H	0.03 (m)
Particle diameter, d_p	150 (µm)
Particle density, ρ_p	2500 ($kg \cdot m^{-3}$)
Gas density	1.2 ($kg \cdot m^{-3}$)
Molecular gas viscosity	0.18×10^{-4} ($kg \cdot m^{-1} \cdot s^{-1}$)
Maximum allowable solid fraction, α_{max}	0.65 (−)
Particle-particle restitution coefficient, e_p	0.9
Particle-wall restitution coefficient, e_w	0.9
Angle of internal friction, ϕ	28°

4.1 Flow operational map:

Fig. 7 shows the solid-gas flow map predicted for a pressure gradient of $dP_g/dx = -200$ N/m^3. Each curve predicts an increasing solid flow rate to a maximum value, which then decreases rapidly as the solid loading increases. This behaviour is a classic feature of horizontal gas-solid flow at increasing solid loading.

The model by Ocone et al. (1993) predicts exactly the same curve as that of the classic kinetic approach except at high particle concentration, where a slight deviation is noticed and the model terminates earlier due to the incorporation of the frictional stress contribution to the total solid stress close to packing condition ($\alpha > 0.5$). The switching approach of Makkawi and Ocone (2005) shifts away from the classic kinetic predictions due to switching to the model of Tardos et al. (2003) at the intermediate regime. This approach also experiences numerical difficulties as the flow becomes much denser, and hence terminates at an earlier stage. The models of both Syamlal et al. (1993) and Tardos et al. (2003) show critical differences when compared with the classic kinetic approach; they both fail to provide a solution for dilute flow at low particle loading (i.e. close to empty duct condition). This is probably related to the kinetic stress contribution which is the dominant contribution in dilute flow. Syamlal (1993) neglects this component in order to ensure zero particle shearing at zero particle concentration (i.e. empty duct flow). On the other hand, the particle stress of Eq. 23 by Tardos et al. (2003) ideally should reduce to the "fluid-like behaviour" when the parameter K tends towards zero (i.e. particle fluctuation tends towards infinity or granular temperature tends towards zero). Since in reality such conditions cannot be fulfilled, Eq. 22 may not correctly predict the rapid flow behaviour at $\alpha < 0.1$.

At the other end of dense flow, the models of both Syamlal et al. (1993) and Ocone et al. (1993) terminate at a lower particle loading when compared to the classic kinetic approach; this is related to the consid-

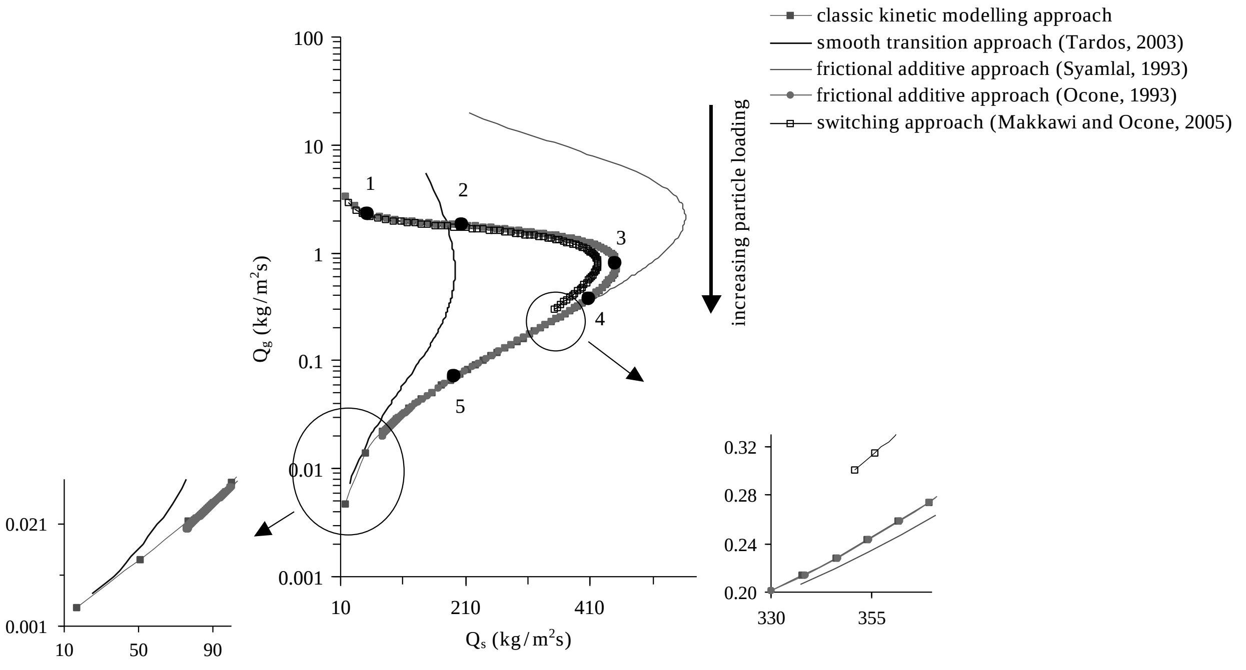

Fig. 7 Gas-solid flow map predicted by various modelling approaches.

erably high increase in particle stress due to the inclusion of frictional stress. Although the proposed frictional stress model of Syamlal et al. (1993) kicks off at a higher particle concentration (at $\alpha > 0.59$), the simulation fails at a much lower particle loading compared with the model by Ocone et al. (1993). This is because the additive frictional solid pressure of Syamlal et al. (1993) (Eq. 13) increases abruptly and reaches unrealistically high values at or just above the critical particle concentration. Detailed comparison between the hydrodynamic features of the flow predicted by each model presented in Section 3 will be discussed below.

4.2 Particle shear stress

Fig. 8 compares the predicted dimensionless shear stress, $\tau_s^* = \tau_s / \rho_p d_p^2 (dv/dy)^2$, as a function of the particle concentration for the different treatments of particle shear stress. Generally, all models show a linear increase in τ_s^* at the intermediate range between $0.1 < \alpha < 0.5$, but the Tardos model predicts a higher shearing stress. The model by Tardos et al. (2003) is mainly based on the assumptions that both collisional and frictional stresses coexist at the intermediate regime. Hence it is not surprising to see a higher stress in this range when compared with other models which mainly retain the dominant collisional stress only (kinetic stress is almost negligible at the intermediate dense flow). At the dilute region of $\alpha < 0.1$, unlike the classic kinetic model predictions, both models of Tardos et al. (2003) and Syamlal et al. (1993) show a decrease in τ_s^* as α decreases. This is physically justifiable as the flow approaches the empty duct flow condition; however, such an approach causes numerical difficulties and the model fails to converge, thus limiting the applicability of these two models to intermediate-dense flow. The classic kinetic model shows an increase in τ_s^* when approaching the zero particle concentration. Lun et al. (1984) discussed this in detail, and they attributed this to the monotonic increase in granular temperature as α approaches zero, and hence results in an undesirable increase in the dominant kinetic shear component at this limit.

To clarify this behaviour, we must discuss it in the context of energy balance formulation. In the classic kinetic theory model of Lun et al. (1984), the energy dissipation is only associated with particle-particle collision and hence, in the absence of collisional dissipation and increasing energy generation due to particle fluctuation, the increase in granular temperature is not surprising. This problem was resolved in the model by Tardos et al. (2003) by the inclusion of a continuous energy dissipation model (Eq. 25) which tends to predict high and constant energy dissipation at the dilute regime. Similarly, the model by Syamlal et al. (1993) shows the same trend as a result of neglecting the kinetic contribution to the energy conduction and generation. These features are shown in **Fig. 9**. The classic kinetic model shows a loop in the predicted energy dissipation at the region of high shear rate, the turning point in the loop at the maximum shearing is a result of an increasing contribution

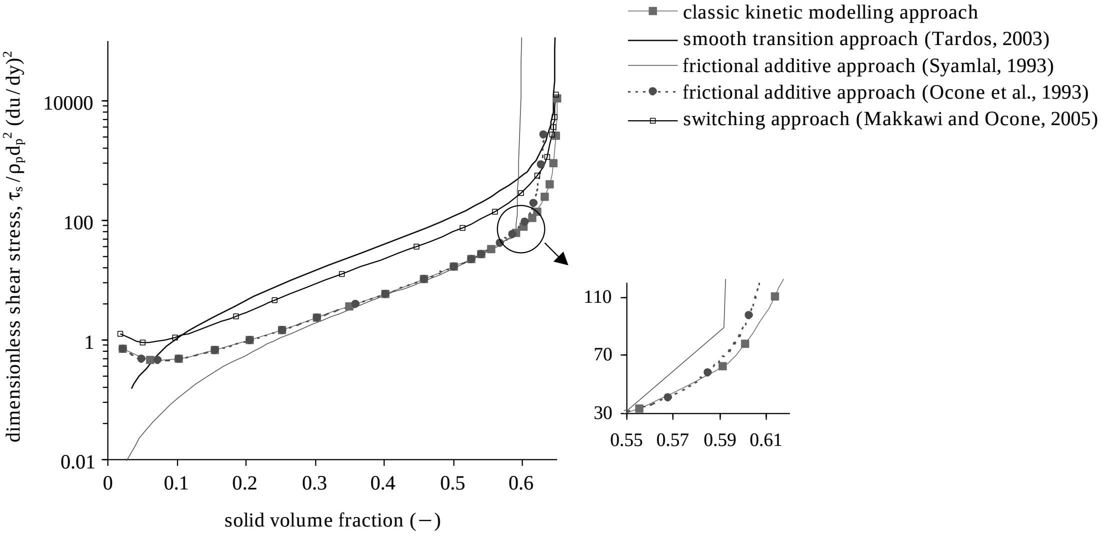

Fig. 8 Dimensionless shear stress as a function of particle concentration predicted by different modelling approaches.

of collisional stress as the flow gets denser, then as the shear rate decreases further, the dissipation starts to reduce due to the limited space available for any further collisions. It must be noted that the comparison with the predictions in the model by Ocone et al. (1993) is omitted here because inclusion of the additive frictional stress shows a negligible effect in energy dissipation with respect to the classic kinetic prediction.

Fig. 10 shows the shear stress to particle pressure ratio, $\delta=\tau_s/p_s$, as a function of the particle concentration α. Within the range of $\alpha<0.3$, all models predict a decrease in δ with increasing α. Qualitatively, this agrees with the results reported by Lun et al. (1984) for small values of α. Within the range of $0.3<\alpha<0.59$ and for all models, δ decreases slightly (i.e. almost independent of the variations in α). Beyond this range, both models of Syamlal et al. (1993) and Ocone et al. (1993) behave differently when compared with the classic kinetic predictions. As discussed earlier, this is attributed to the different treatment of kinetic stress contribution at the dilute flow and of frictional stress at the other extreme of dense flow. The approach by Makkawi and Ocone (2005) employing the smooth transition shear deviates from all other models with a lower value of δ which decreases sharply when approaching the extreme end of close packing condition. According to observations made by Campbell and Brennen (1982) and Lun et al. (1984), the latter approach seems to predict the correct shearing to solid pressure ratio at large α and this is detailed as follows. Campbell and Brennen (1982) observed that at $\alpha>0.3$, the particles tend to rearrange in the form of distinct shear layers. Collisions between particles then become limited due to the limitation of free space, and particle interaction becomes restricted to (a) front and back collisions between particles in the same layer, and (b) top and bottom collisions between sheared layers. Such forms of particle-particle interaction make no effective contribution to the particle shearing but can considerably increase the solid pressure perpendicular to the shearing layer. In fact, Lun et al. (1984) clearly admit that the increase in δ at large particle concentration is “no doubt a failure” in the kinetic theory model formulation for the shear stress at this limit.

4.3 Particle velocity, granular temperature and concentration profiles

In this section, we compare the various predicted hydrodynamic features of the flow using the different modelling approaches described in Section 3. These results will be discussed according to five different flow categories: very dilute; dilute; intermediate; dense; very dense. Since the momentum transport properties of solid-gas are strong functions of the granular temperature, the different treatment of energy balance will be discussed first.

In the classic kinetic theory of Lun et al. (1984), the energy balance incorporates both the kinetic and collisional contributions to the energy generation and conduction. The frictional additive approach of

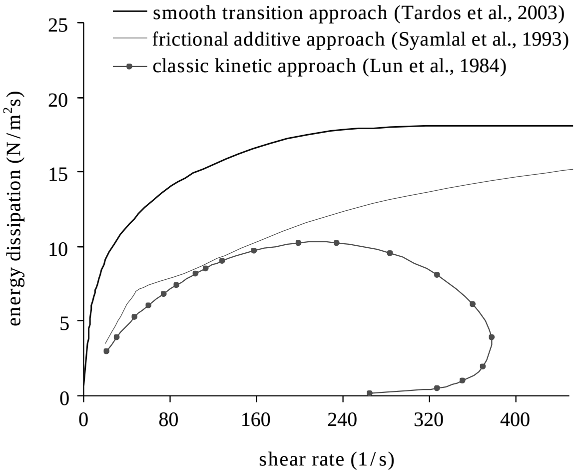

Fig. 9 Variation of energy dissipation as a function of shearing rate predicted by various modelling approaches.

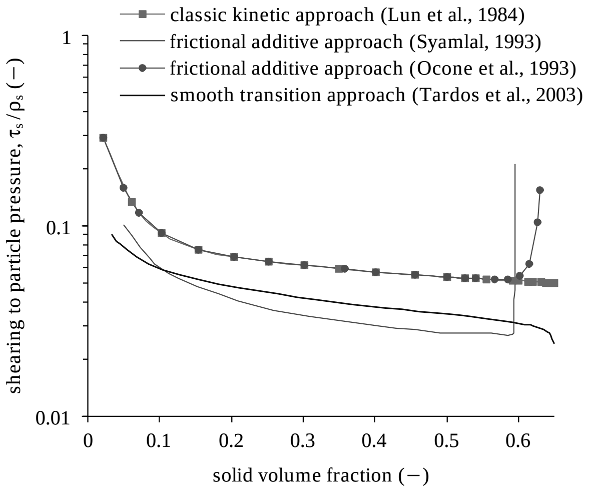

Fig. 10 Shearing to particle pressure ratio as a function of concentration predicted by different modelling approaches.

Syamlal et al. (1993) neglects the kinetic contribution, while Ocone et al. (1993) follow the original classic kinetic theory and retain both of the kinetic and collisional contribution to the energy balance. However, both approaches neglect the effect of the additive frictional shearing on the energy balance at the limit of large particle concentration, and no further theoretical development for the frictional dissipation was considered. It must be noted that in employing the smooth merging models, we also considered the effect of possible frictional energy generation and dissipation by incorporating the simplified shear stress and the energy dissipation formulas of Tardos et al. (2003) in the energy balance equation. The particle conductivity coefficient was estimated from the existing classic kinetic theory model.

Fig. 11 shows a comparison of the predicted granular temperature, θ, as a function of the particle concentration using various test models. Generally, all models predict a decreasing θ as α increases. Within the intermediate range of $0.3<\alpha<0.59$, the additive approach of Ocone et al. (1993) and Syamlal et al. (1993) shows no difference with respect to the kinetic theory predictions. The smooth transition approach of Tardos et al. (2003) consistently predicts a lower θ, mostly due to the increase in energy dissipation. Syamlal et al. (1993) deviate from the classic kinetic predictions at dilute flow due to neglecting the kinetic contribution. At the other dense end, while all models reasonably agree when approaching the maximum packing condition, this model also clearly deviates with a very sharp decrease in granular temperature due to the inclusion of the frictional stress at $\alpha>0.59$.

A comparison between the various modelling approach predictions for the particle velocity, granular temperature and concentration profiles is shown in **Fig. 12** and is discussed in the following.

*Very Dilute flow (**Fig. 12a**):*

This corresponds to $Q_s/Q_g=33$ (point 1 in the classic kinetic curve of **Fig. 7**). In this range of flow, it is widely believed that the classic kinetic theory captures the hydrodynamic feature of the flow with a reasonable level of accuracy. Therefore, the result produced from the classic kinetic model is used here as a benchmark for comparison with other model predictions. At this dilute flow, the frictional stress is absent and therefore the model by Ocone et al. (1993) yields identical results to that produced from the classic kinetic theory. The model by Syamlal et al. (1993) clearly overestimates the granular temperature and particle velocity for the reasons discussed in Section 4.2 above. Tardos et al. (2003) reasonably predict the various hydrodynamic features with a better level of accuracy. All models seem to predict almost the same concentration profile.

*Dilute flow (**Fig. 12b**):*

This corresponds to $Q_s/Q_g=120$ (point 2 in the classic kinetic curve of **Fig. 7**). The predictions in the model of Tardos et al. (2003) and the classic kinetic theory model are in good agreement to a great extent. Again, the model of Syamlal et al. (1993) that assumes negligible kinetic contributions to the parti-

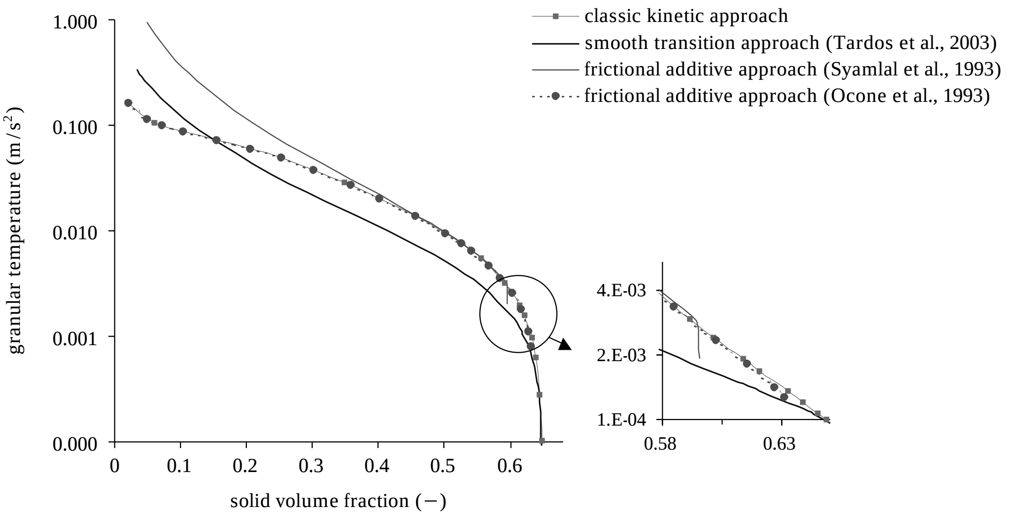

Fig. 11 Variation of granular temperature as a function of concentration predicted by various modelling approaches.

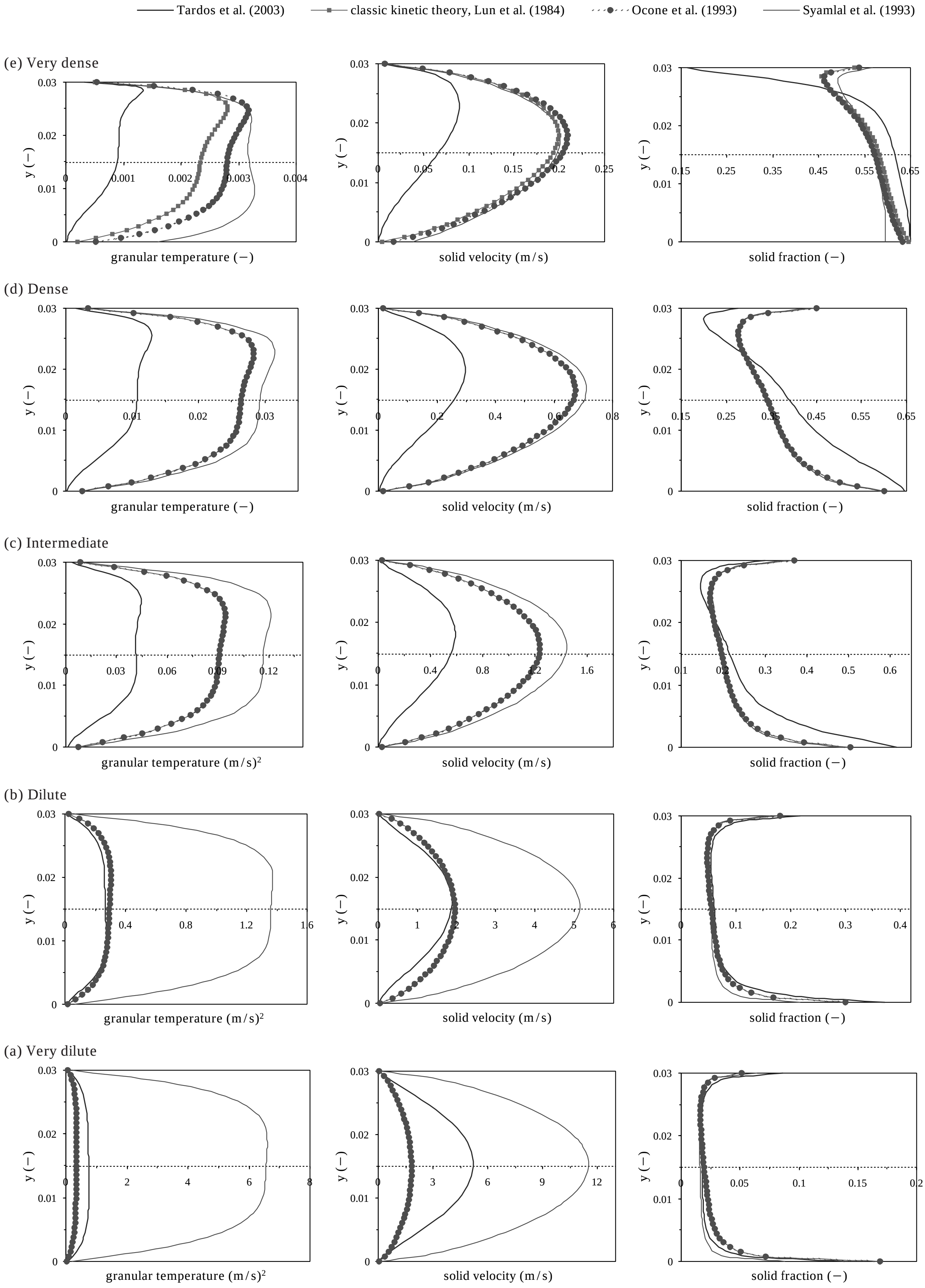

Fig. 12 Hydrodynamic predictions of a wide range of gas-solid flow in a horizontal duct predicted by different shear modelling approaches.

cle stress and energy balance clearly overestimates the granular temperature and particle velocity. Also due to the small particle concentration, we do not expect to see any effect of frictional stress in this flow range. The predicted particle concentrations seem to be insensitive to the various applied shearing models in this range.

*Intermediate flow (**Fig. 12c**):*

This corresponds to Q_s/Q_g=114 (point 3 in the classic kinetic curve of **Fig. 7**). Here it appears that with a further increase in particle loading, each model starts to behave differently. In this range of flow, collisional effects dominate the particle stresses, and hence the predictions by the model of Syamlal et al. (1993) come closer to the classic kinetic theory model results. On the other hand, the model by Tardos et al. (2003) starts shifting away from the other models with lower predicted granular temperature and particle velocity, and most important, a clear tendency towards asymmetric behaviour. This is mainly due to the fact that this new mechanistic approach was originally developed to take into consideration both the collisional and frictional contribution to the particle stress at the intermediate regime, while the frictional additive approach of Ocone et al. (1993) and Syamlal et al. (1993) neglects the frictional contribution at this flow limit. The asymmetric behaviour is due to the migration of particles towards the lower wall as a result of increasing gravity besides the possible increase in shear stress at the denser lower part of the duct.

*Dense flow (**Fig. 12d**):*

This corresponds to Q_s/Q_g=1060 (point 4 in the classic kinetic curve of **Fig. 7**). Here, the frictional additive approach of Syamlal et al. (1993) and Ocone et al. (1993) appears to have no significant effect on the general hydrodynamic behaviour of the flow when compared with the classic kinetic model. The smooth transition model of Tardos et al. (2003) stands alone with significantly reduced granular temperature and particle velocity. Moreover, the particle concentration profile shows well-pronounced segregation behaviour as a result of particle migration towards the lower wall; this in turn is probably a result of the frictional contribution to the particle stress, which tend to slow down the particles' velocity in the lower half of the duct.

*Very dense flow (**Fig. 12e**):*

This corresponds to Q_s/Q_g=2660 (point 5 in the classic kinetic curve of **Fig. 7**). In this limit, the additive frictional stress of the models by Ocone et al. and Syamlal et al. appears to play a role in the rheology of the dense flow. It is here where these two models deviate slightly from the classic kinetic predictions due to the incorporation of dense frictional effect. It is also interesting to note that with the frictional stress taken into consideration, these models predict a higher granular temperature. This is because both models do not allow for the possible energy dissipation resulting from the high frictional stress. The predicted profiles in the model by Tardos et al. (2003) confirm a slow moving layer close to the upper wall, while most of the lower part of the duct is almost stationary with the particle concentration reaching the maximum packing condition.

5. Conclusions

In this study, we reviewed different treatments for the particle stress in gas-solid flow. These models were tested in the simulation of gas-solid flow in a horizontal duct covering the whole range of dilute-intermediate-dense flows. The limitations and applicability of each modelling approach are discussed and supported with the predicted profiles of the hydrodynamic features of the flow. The superiority of any of these modelling approaches over the other within the range of its applicability is a matter of open debate and further experimental validation.

Acknowledgement

The authors thank the UK's Engineering and Physical Science Research Council (*EPSRC*) [grant *GR/R85778*].

Notation

A	Parameter defined in Eqs. 11 and 13	$(-)$
d_p	Particle diameter	(m)
e_p, e_w	Particle-particle and particle-wall restitution coefficient, respectively	$(-)$
g	Gravity acceleration constant	$(\mathrm{m \cdot s^{-2}})$
g_o	Radial distribution function	$(-)$
H	Duct width	(m)
I_o, I_1	Modified Bessel functions of the first kind	
II_{11}	Invariant of particle pressure, defined in Eq. 16	$(\mathrm{N \cdot m^{-2}})$
II_D	Second invariant of the deviator of particle strain rate, defined in Eq. 17	$(\mathrm{s^{-2}})$
k_s	Effective thermal conductivity of particles	$(\mathrm{kg \cdot m^{-1}\, s^{-1}})$

K	Parameter defined in Eq. 24	$(-)$
n	Parameter defined in Eqs. 11 and 13	$(-)$
p	Parameter defined in Eq. 11	$(-)$
p_s	Particle pressure	$(\mathrm{N/m^2})$
P_g	Gas pressure	$(\mathrm{N/m^2})$
q_s	Pseudothermal energy flux gas flow rate	$(\mathrm{kg \cdot s^{-3}})$
Q_g	Gas flow rate	$(\mathrm{kg \cdot m^{-2} \cdot s^{-1}})$
Q_s	Solid flow rate	$(\mathrm{kg \cdot m^{-2} \cdot s^{-1}})$
S	Strain rate tensor	$(\mathrm{s^{-1}})$
u	Gas velocity	$(\mathrm{m \cdot s^{-1}})$
v	Solid velocity	$(\mathrm{m \cdot s^{-1}})$
x	Axial coordinate	(m)
y	Radial coordinate	(m)

Greek symbols

α	Solid volume fraction	$(-)$
μ	Viscosity	$(\mathrm{N \cdot m^{-2} \cdot s})$
ρ	Density	$(\mathrm{kg \cdot m^{-3}})$
β	Gas-particle interphase drag coefficient	$(-)$
τ	Shear stress	$(\mathrm{N \cdot m^{-2}})$
τ_s^*	Dimensionless particle shear stress, $=\tau_s/\rho_p d_p^2 (dv/dy)^2$	$(-)$
η	Parameter function of particle-particle restitution coefficient$=(1+e_p)/2$	$(-)$
γ_s	Dissipation of granular energy	$(\mathrm{kg \cdot m^{-1} \cdot s^{-3}})$
ϕ	Angle of internal friction for the particle	(degrees)
θ	Granular temperature	$(\mathrm{m^2 \cdot s^{-2}})$
σ	Standard deviation of strain rate	$(\mathrm{s^{-1}})$
ω	Coefficient, $=1/4$	$(-)$
δ	Particle shearing to pressure ratio, $=\tau_s/p_s$	$(-)$

Subscripts

g	Solid phase
s	Solid phase
max	Maximum
k	Classic kinetic theory

References

1) Atkinson, H. and Bransby, L., 1978. The Mechanics of solids: An introduction to critical state soil mechanics, McGraw-Hill, UK.
2) Campbell, C.S., 2002. Granular shear flows at the elastic limit. Journal of fluid mechanics, 261-291.
3) Campbell, C.S. and Brennen, C.E., 1982. Computer simulation of shear flows of granular material. Proceeding of the 2nd U.S.-Japan seminar on new models and constitutive relations in the mechanics of granular flow.
4) Huilin, L., Yurong H., Wentie, L., Ding, J., Gidaspow, D., Bouillard, J., 2004. Computer simulations of gas-solid flow in spouted beds using kinetic-frictional stress model of granular flow. Chemical Engineering Science 59. 865-878.
5) Johnson, P.C., Nott, P., Jackson, R., 1990. Frictional-collisional equations of motion for particles flows and their application to chutes. Journal of fluid mechanics 210, 501-535.
6) Lun, C.K., Savage, S.B., Jeffrey, D.J., 1984. Kinetic theories for granular flow: inelastic particles in coquette flow and slightly inelastic particles in a general flow field. Journal of Fluid Mechanics 140, 223-256.
7) Laux, H., 1998. Modelling of dilute and dense dispersed fluid-particle flow. Ph.D Thesis, NTNU Trondheim, Trondheim, Norway.
8) Makkawi, Y. and Ocone, R., 2005. A model for granular flows in a horizontal dust with a smooth merge of rapid-intermediate-dense flows. Chemical Engineering Science. Under revision.
9) Ocone, R., Sundaresan, S., Jackson, R., 1993. Gas-particle flow in a duct of arbitrary inclination with particle-particle interaction. Fluid Mechanics and Transport Phenomena 39, 1261-1271.
10) Patil, D.J., Annaland, M., Kuipers, J., 2005. Critical comparison of hydrodynamic models for gas-solid fluidized beds- Part I: Bubbling gas-solid fluidized bed operated with a jet. Chemical Engineering Science 60, 57-72.
11) Savage, S.B., 1998. Analysis of slow high-concentration flows of granular materials. Journal of Fluid Mechanics 377, 1-26.
12) Savage, S.B., 1983. In Jenike, J.T., Satake (Eds.). Proceedings of the US-Japan seminar on new models and constitutive relations in the mechanics of granular materials. Elsevier, Amsterdam, P. 261.
13) Schaeffer, D.G., 1978. Instability in the evolution equations describing incompressible granular flow. Journal of Differential Equations 66, 61-74.
14) Syamlal, M., Rogers, W.A., O'Brien, T.J., 1993. MFIX documentation and theory guide, DOE/METC94/1004, NTIS/DE94000087.
15) Tardos, G.I, McNamara, S., Talu, I., 2003. Slow and intermediate flow of frictional bulk powder in the coquette geometry. Powder Technology 131, 23-39.
16) Johnson, P.C. and Jackson, R., 1987. Frictional-collisional constitutive relations for granular materials, with application to plane shearing. Journal of Fluid Mechanics 176, 67-93.

Author’s short biography

Yassir Makkawi

Yassir Makkawi received his PhD in Chemical Engineering from Heriot Watt University in 2003, MSc from KFUPM in 1995 and BSc from Khartoum University in 1991. Before his PhD, he worked as a process engineer for 8 years serving the oil and gas industry sectors in the Middle East. Currently he is a Research Associate at Heriot Watt University. He has extensively applied the Electrical Capacitance Tomography (ECT) technique in the analysis of fluidization hydrodynamics. He is now working on theoretical modelling of gas-solid flows and CFD simulation of fluidization. His research interest also includes the application of tomography imaging in multiphase flow and the utilisation of fluidization process for energy conversion from renewable resources.

Raffaella Ocone

Raffaella Ocone received her Laurea in Chemical Engineering from the University of Naples, Italy, and her MA and PhD from Princeton University, USA. She holds the Chair of Chemical Engineering in the School of Engineering and Physical Sciences at Heriot Watt University where she is the Academic Head of Chemical Engineering. Before joining Heriot Watt University, she was a Reader in Chemical Engineering in the Department of Chemical Engineering at Nottingham, Lecturer at the University of Naples, Italy, and twice Visiting Professor at Louisiana State University, USA. She has more than 18 years of experience in modelling complex systems, spanning from the hydrodynamics of solid/gas suspensions, to complex reaction networks. Recent work includes the modelling of biological systems.

An Overview of Nanotechnology in Thailand[†]

Wiwut Tanthapanichakoon
National Nanotechnology Center
National Science and Technology
Development Agency
Ministry of Science and Technology[*]

Abstract

On August 13, 2003, the Cabinet of Thailand approved the setup of National Nanotechnology Center (NANOTEC) under National Science and Technology Development Agency (NSTDA), Ministry of Science and Technology (MOST). One of its urgent tasks is the preparation of the 10-year National Strategic Framework in Nanotechnology for submission to the Cabinet via the recently established National Nanotechnology Policy Committee. The task and framework are in line with the National Strategic Framework in Science and Technology approved by the Cabinet in 2004. What follow is an overview of the recent status and development of nanotechnology in Thailand and a brief introduction of the Nanotechnology Framework, including the R & D direction and human resources development (HRD) of Thailand.

Key words: Nanotechnology, Thailand, National strategic framework, Infrastructure, R & D programs

Introduction

Covering essentially all branches of basic and applied sciences, nanotechnology is hyped as the most important emerging, trans-disciplinary technology in the 21st century. Nowadays, nanotechnology is recognized world-wide as revolutionary manufacturing technology capable of making wildest, occasionally weirdest dreams come true. Drugs, electronic chips, automobiles, consumer products and what not will radically be transformed by the potential reach of nanotechnology. 'Nanotechnology will reverse the damages caused by the Industrial Revolution' – asserted Chemistry Nobel Laureate Dr. Richard Smalley, co-discoverer of the Bucky ball. The USA, European Union and Asia-Pacific countries have all set up national nanotechnology initiatives (NNI). Similarly, the government of Thailand is determined to promote and accelerate nano science and technology as a crucial instrument of sustainable economic growth and international competitiveness.

Current Status of Nanotechnology in Thailand

Science and technology research, development and application are recognized by the present government under the leadership of Prime Minister Thaksin Shinawatra as one of the indispensable key strategies of Thailand to make her economy and society more robust and competitive. The low-key establishment of a brand new National Nanotechnology Center (NANOTEC) under the umbrella of the National Science and Technology Development Agency (NSTDA) was approved by the Cabinet of Thailand on August 13, 2003. The mission of NANOTEC covers but is not limited to the following:

1. Prepare a national road map on nanotechnology for Thailand.
2. Act as secretariat of the recently established National Nanotechnology Policy Committee (NNPC) chaired by PM Thaksin Shinawatra. Under NNPC there will be 7 national sub-committees, such as Industrial Clusters Promotion

---

[†] Accepted: July 25, 2005

[*] 111 Paholyothin Rd., Klong Luang, Pathumthani 12120 Thailand
E-mail: wiwut@nanotec.or.th

and Development, Human Resources Development, Research & Development Planning, Infrastructural Capacity Building, Safety and Ethics, Public Understanding and Awareness, and Supervision and Evaluation Sub-committees. NANOTEC will fully support the work of all 7 sub-committees.

3. Set up collaborative research networks and centers of excellence (COE) in nanotechnology in all regions of Thailand by assembling and producing a critical mass of high-caliber researchers and educators on nanotechnology.
4. Disseminate, promote and transfer innovative and useful knowledge in nanotechnology to the industrial and public sectors.
5. Carry out in-house and collaborative research projects in selected core areas of nanotechnology.
6. To accommodate nanotechnology research needs, set up and provide analytical and testing services that provide access to expensive advanced analytical instruments and fabricating devices at reasonable charges.

National Strategic Framework in Nanotechnology

As of now, NNPC is expected to approve the revised 10-year National Strategic Framework in Nanotechnology 2006 – 2015 prepared by NANOTEC in collaboration with numerous experts and stakeholders from the academic institutions, governmental agencies and private sector. After obtaining NNPC's approval, the Framework will be submitted to the Cabinet for endorsement and deployment. **Fig. 1** shows the main concept and inter-relationship among the 5 major strategies in the Framework (1). Since they are self-explanatory, the author will elaborate only on the proposed R & D and HRD areas in the Framework. Details of the key measures, expected outcomes, etc. will be released after the Framework has gained the Cabinet's approval.

Nanotechnology R & D in Thailand

In Thailand, several governmental agencies are actively involved in implementing and/or funding S & T research and development, for examples, NSTDA (Ministry of Science and Technology (MOST)), the Commission on Higher Education (CHE, Ministry of Education), National Innovation Center (NIA, MOST), the National Research Council of Thailand (NRCT), and Thailand Research Fund (TRF). Besides NANOTEC, NSTDA has three other full-fledged national technology centers as follows:

- National Metal and Materials Technology Center (MTEC)
- National Electronics and Computer Technology Center (NECTEC), and
- National Genetic Engineering and Biotechnology Center (BIOTEC).

Fig. 1 Concept and inter-relationship among main national strategies in nanotechnology

These national centers along with the Asian Institute of Technology (AIT), National Synchrotron Center (MOST), many national and several private universities are conducting a significant number of R & D projects in, or closely related to, Nanotechnology. However, there has been a lack of coordinated synergistic national research direction in nanotechnology.

Typical examples of the proposed national research programs in the Framework are as follows:

– Advanced drug delivery systems
– Nanoparticle synthesis and applications
– Coating and thin film technology
– Diagnostic or monitoring devices, such as carbon nanotube based gas sensors and arrays
– Fundamental R & D in nanobiomaterials
– Nanocomposite materials
– Smart fabric and functional textiles
– New generation solar cells
– Fuel cell technology

In addition to MOST, CHE recently promoted the establishment of Collaborative Research Networks (CRN) in selected S & T fields, including Cleaner Technology, Catalysis, Biomedical Engineering, Neuroscience and Nanotechnology. Meantime, the main objectives of TRF, which does not conduct any in-house research but mainly acts as a granting agency, include the capacity building of professional researchers and strengthening the research community. TRF offers several types of research grants such as Research Team Award (Senior Research Scholar) grants, Research Scholar grants and Post-doctoral Research grants. Some recent TRF's grants are earmarked for nanotechnology-related projects.

HRD in Nanotechnology

Our latest survey could only come up with less than 200 professed nanotech researchers in Thailand, though the true number may be more numerous or fewer depending on the exact definition of nanotechnology and the individual levels of research activities. Accelerated human resources development in S & T in general and nanotechnology in particular is indispensable to the knowledge-based economy and industrial development of Thailand. The population of S & T researchers in Japan is reportedly around 70.7 per 10000, whereas the corresponding number in Thailand is around 3.3. Since the population of Japan is double that of Thailand, the number of man-years contributable annually by Japan is 42 times that of Thailand. Evidently, trying to catch up with Japan is *mission impossible*, except in certain niche areas of the wide-ranging nanotechnology that Thailand has some significant inherent advantages or lie outside the strategic interest of Japan and other developed countries.

Accepting the first batch of students this June 2005, the Faculty of Engineering, Chulalongkorn University, is the first Thai institution to pioneer an undergraduate program in Nanoengineering delivered entirely in English. Generally all ordinary educational programs are taught in Thai. At present a number of national universities such as Chulalongkorn, Chiangmai, and Khonkaen Universities are considering the establishment of new graduate programs in Nanoscience and/or Nanotechnology at the Master and/or Doctoral levels.

To create synergism via networking, it has been proposed that NSTDA (NANOTEC) collaborates with universities in the implementation of their nanotechnology curricula, thereby combining the strengths of NSTDA in terms of R & D capability and research facilities, and leading universities in terms of coursework, human resources and degree granting authority. In 2003 the Cabinet approved a second-phase 5-year plan of MOST to provide 1,500 full-expense scholarships for Thai students to go abroad to advance their study in S & T. The plan also earmarks nearly 200 S & T scholarships for NSTDA, including 48 for NANOTEC to recruit students in the various fields of nanotechnology as well as additional nanotechnology scholarships for the national universities. To be cost effective and directly contribute to S & T capability build-up of Thailand, more scholarships should also be provided to graduate programs offered by national and private universities.

Infrastructural Capacity Build-up

Since 2003 several universities such as Mahidol, Khonkaen, Chiangmai, Kasetsart and Chulalongkorn Universities have set up new research centers specializing in nanotechnology. At present there are at least 40 laboratories in Thailand doing research closely related to nanotechnology. However, there is still a severe shortage of nanofabricating apparatuses as well as analytical and characterization instruments in nanotechnology such as high-resolution Transmission Electron Microscopy (TEM), Atomic Force Microscopy (AFM), Surface Probe Microscopy (SPM), etc. The national Framework calls for the investment of upwards of 2 billion baht (50 million USD) nationwide to build up an array of sophisticated instruments and equipment.

Future Direction of Nanotechnology Development

The ninth 5-year National Social and Economic Development Plan (2002-2006) sets a combined R & D investment goal of 0.40% of the gross domestic production (GERD/GDP) by the public and private sectors, compared to the actual 0.26% in 2003. Optimistic forecast by the government for 2006 predicts the GDP will reach 6 trillion baht, which at 0.4% should translate to research investment of at least 24 billion baht. However, this hard-to-achieve value is still significantly less than those of the advanced industrial countries, percentage-wise and in absolute number. Recently a prominent Deputy Prime Minister has declared that the national R & D budget should be jacked up to a more respectable 1% within the near future. Unfortunately, he failed to specify the target date. In the Nanotechnology Framework, it is proposed that the target of overall annual investment in nanotechnology in Thailand should reach 12 billion baht (roughly 300 USD) in 2015 with 30% coming from the private sector. No matter what, Thailand's limited R & D budget must be spent in the most appropriate and effective manners to achieve reasonable impacts.

Roles of NANOTEC

Meanwhile, NANOTEC itself is strengthening its organizational structure while recruiting additional high-caliber management staffs and researchers. As of July 2005 it has 30 full-time staffs, over 40% of which have PhDs. It is pushing for the creation of more effective strategic alliance with its sister national centers, other national research centers and universities. **Fig. 2** shows scenarios from the National S & T Week held in October 2004 and attended by *more than 4 million* visitors. HM The King, HRH Princess Sirindhorn, PM Thaksin, and many high-ranked government officials as well as the general public expressed keen interest in the Nanotechnology Zone planned and organized by NANOTEC. **Fig. 3** displays selected activities carried out by NANOTEC in 2004.

Another key strategy is to make full use of international and regional cooperation in nanotechnology. NSTDA has recently established and strengthened its alliance with Japan (AIST, Tokyo Institute of Technology, etc.), the USA, Australia (CSIRO), Taiwan (ITRI etc.), Korea (KRIBB) etc. **Fig. 4** illustrates the alliances NANOTEC is seeking and building upon. NANOTEC is also a key founding member of the Asian Nanotechnology Forum (ANF) set up at a sum-

Thailand S&T Week (October 2004)


HM the King and HRH Princess inaugurated the event
HM the King, HRH Princess and PM visited Booth NANOTEC
Thousands of children waited to enter the exhibition
A crowd of visitors at Booth NANOTEC

Fig. 2 Scenarios from the National S & T Week held in October 2004

Other Events in 2004


Asia Nano Forum Summit (ANFoS) in Phuket (May '04)
A group photo of ANFoS participants with Minister of MOST
Speakers at CEO Nanobusiness Forum, Bangkok (May '04)
PM Thaksin visited Booth NANOTEC during NSTDA Annual Conference (June '04)

Fig. 3 Photos of selected activities carried out by NANOTEC in 2004

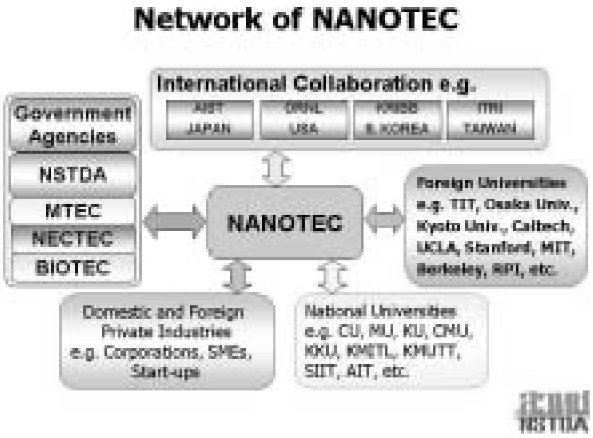

Fig. 4 Schematic of national and international alliances of NANOTEC

mit co-hosted by NANOTEC and AIST in Phuket in May 2004. Currently ANF has 12 member economies, including China, Korea, India, Singapore, Malaysia, Indonesia, Hong Kong, Taiwan, Australia and New Zealand.

Conclusion

As a latecomer to the rapidly evolving fields of Nanotechnology, Thailand has no alternative but to put in a huge amount of critical investments and efforts if it does not want to fall further and further behind. Hopefully, after the adoption of the proposed National Strategic Framework, Thailand would be able to urgently develop its HR and infrastructure in nanotechnology, identify and develop certain niche areas and products, and reap as much potential benefits of nanotechnology as possible. Tangible progresses in nanotechnology development are expected to contribute not only to stable high economic growth but also to sustainable national development, including better environment and higher quality of life.

Reference

National Nanotechnology Policy Committee, Government of Thailand: *National Strategic Framework in Nanotechnology* (draft), July 2005.

Author’s short biography

Wiwut Tanthapanichakoon

Wiwut TANTHAPANICHAKOON obtained his PhD (U of Texas at Austin) and B. Eng. (Kyoto U) in chemical engineering. At present he is the founding Director of the National Nanotechnology Center (NANOTEC) under the umbrella of National Science and Technology Development Agency, Ministry of Science and Technology, Concurrently, he is Professor Emeritus of Chulalongkorn University (CU) and Chair Professor in Particle Technology, Faculty of Engineering, CU. Since NANOTEC serves as Secretariat of the National Nanotechnology Policy Committee chaired by the Prime Minister of the Royal Thai Government, Dr. Wiwut is directly involved with the policy formulation and promotion of nanotechnology in Thailand. His life-long research interest covers particle technology, aerosol engineering (dust collection technology, air pollution control), process analysis and simulation, drying technology, energy technology, and nanotechnology.

Advances in On-line Monitoring and Control of the Morphological and Polymorphic Forms of Organic Crystals Grown from Solution[†]

X.Z. Wang[1], J.C. De Anda and K.J. Roberts
Institute of Particle Science and Engineering, School of Process Environmental and Materials Engineering, The University of Leeds[*]
R.F. Li, G.B. Thomson and G. White
School of Engineering and Physical Sciences, Heriot-Watt University[**]

Abstract

Organic crystals grown from solution are known to exhibit multiple morphology as well as habits which are of great importance to the end-use property of the product such as the bioavailability and the downstream processing such as in filtration and drying. The crystal morphology can also dictate other quality measures such as the size. Compared with the great amount of research work that has been done on the on-line measurement of other quality measures such as the size and concentration using various spectroscopy techniques, the literature on the on-line measurement and manipulation of crystal morphology is scarce. Attempts were made in the past to use laser diffraction and ultrasound spectrometry for shape monitoring. These methods have not proved to be very successful due to the difficulty in extracting detailed shape information from the signals corrupted by noise and multiple scattering. In this paper, we describe a new approach for on-line crystal morphology measurement and control which is based on the integration of on-line imaging, multi-scale image analysis and crystal morphology modelling, and present the results obtained on applying the approach to the batch crystallisation of (L)-glutamic acid. On-line imaging proved capable of capturing high fidelity crystal shapes and polymorphic transitions in real time. A multi-scale image analysis method was proposed to extract the crystals from the image background and to calculate shape descriptors which were then used for shape recognition and to derive monitoring charts showing the ratios of different polymorphs in real time as well as the relative average growth rates of facets of crystals. Calculating crystal growth rates and estimating kinetics parameters for needle-shaped crystals was also investigated. Finally, a methodology called 'camera model' for integrating on-line imaging and crystal morphology modelling was presented.

Key words: Crystal morphology, Crystal polymorph, On-line imaging, Image analysis, Morphology modeling, Morphology control, Glutamic acid

Introduction

High value-added speciality chemicals such as pharmaceuticals are often manufactured in batch crystallisation processes. The shape, size and polymorphic form are properties of great importance to crystalline drug products. It is known that certain crystal morphological forms and habits have been related to difficulties in the dissolution rate, process hydrodynamics, solid-liquid separations, drug tableting, storage and handling, or in milling and grinding. The control of a product in crystallographic form is important in industrial production in that different polymorphs often exhibit different physicochemical properties

---

[†] Accepted: July 26, 2005

[*] Leeds LS2 9JT, UK

[**] Edinburgh EH14 4AS, UK

[1] Corresponding author
TEL: +44 113 343 2427 FAX: +44 113 343 2405
E-mail: x.z.wang@leeds.ac.uk

implying variability in product performance, e.g. via a different solubility and hence bioavailability for a drug compound.

In the past, a significant effort has been devoted to the development of on-line analytical techniques for monitoring deterministic operating variables including the concentration using attenuated total reflectance Fourier transform infrared spectroscopy (ATR-FTIR)[1-3], to monitor the crystallographic structure using X-ray diffraction (XRD) and Raman spectroscopy[4, 5], and the crystal size distribution (CSD) using laser diffraction[5], ultrasonic spectroscopy[6] and light scattering techniques[7-9]. In contrast, the literature on monitoring crystal morphology is scarce[10].

In addition to the ultimate objective of morphology control in manufacture, the on-line monitoring of crystal morphology can also help the development of crystal morphology modelling and prediction techniques. This has not yet come to the level of being able to consider the simultaneous effect of all engineering factors or operating conditions critically related to product morphology such as solvents and cooling rates or heat transfer effects[11], despite the significant progress and the availability of commercial software systems such as HABIT[12] and CERIUS2[13]. It is known that minor changes in supersaturation, cooling rates, reactor hydrodynamics, pH and the presence of impurities can have a significant impact on the crystal product. In addition, there are unexpected factors which can become deterministic such as wall effects on heat transfer, baffles, and impeller materials and types[14]. As a result, on-line measurement and real-time classification of crystal polymorphous is important because it can partially compensate the inability in modelling the morphology and shape. On the other hand, being able to measure morphology on-line in real time will no doubt provide a tool that can help the development and validation of new and more sophisticated crystal morphology prediction models.

This paper reviews the previous efforts on the on-line sensing of crystal morphology and presents recent advances in developing an enabling technique for the real-time measurement and manipulation of the morphology of growing crystals through integrating imaging, image analysis and morphology modelling.

Previous Work

Laser diffraction techniques were investigated previously for the recognition of non-spherical particles, but only limited success has been achieved in this area. The main difficulty has been in obtaining a single-particle pattern in mixtures due to problems associated with partial scattering of the particles[15-17]. Mougin et al.[6, 18, 19] attempted to interpret the ultrasound attenuation spectra in order to identify dynamic changes in polymorphs during the crystallisation of an organic compound. A correct interpretation was found possible though some additional information needs to be provided which is not always readily available. Studies have also been made to produce crystals with different size and shape properties through supersaturation control using ATR-FTIR[3]. The modification of temperature to maintain supersaturation values during nucleation and crystal growth helps produce uniform size and shape properties, nevertheless no information on particle shape is obtained during the experiment. This practice requires concentration and supersaturation models for the compound to crystallise obtained from calibrations, and the temperature range for control may be limited.

In laboratory studies, photo-microscopy has been the most widely used method for analysing crystal morphology. Samples are taken periodically from the reactor and observed using a photo-microscope imaging system. Software systems are also often available for quantitatively analysing the images. Patience and Rawlings[20] reported an interesting approach for automating this process using a flow cell in a laboratory study of the crystallisation of sodium chlorate. The flow through the cell was periodically stopped to allow a photo-microscope to capture images after the crystals had settled down at the bottom of the flow cell. In this way, the crystals of the compound were lying on a habit face and showing a particular shape to be characterised by a commercial image analysis software. They also developed an automatic control system by manipulating the impurity in the feed. The system has some limitations. Firstly, the sampling period is from 20 to 30 seconds, whereas significant morphological events in crystallisation might take only a few seconds. In addition, the use of a flow cell is clearly not ideal for many industrial processes. The flow cell configuration requires a pump to circulate the solution, and this might cause crystal breakage, as discovered by Mougin[18]. The on-line image analysis approach reported by Patience and Rawlings employs boxed-area and aspect-ratio to describe the crystal shape along with predefined cluster regions for the classification of the two studied shapes, square and triangle. Their strategy for crystal recognition does not allow detection of any new crystal shapes existing within the reactor, and requires the assumption of some shapes and calibration to predefine the corresponding classification regions for the shapes. In addition, the regions are fixed throughout the whole process, meaning that changes in morphology due to, for example, the crystal growth of each face or unexpected impurities may lead to a low amount of crystals being detected or may mislead the process control. Lasentec Inc, USA, developed a Particle Vision Measurement (PVM) probe which can be used for visualisation of the process in-situ. The PVM uses a charged coupled device camera with light sources fitted into the probe[21]. Barrett and Glennon[10] used the PVM probe to visualise the crystals in the determination of the meta-stable zone of an inorganic compound. Patience[21] made an attempt to analyse images obtained by the PVM probe in the crystallisation of sodium chlorate. He encountered difficulties in the analysis of the images using a commercial image analysis software tool. More recently, Wilkinson et al.[22, 23] reported an approach using video imaging and image analysis for the on-line measurement of particle length and circularity in the crystallisation of drug compounds. Their approach uses a threshold method for the segmentation of the crystals from the images, and a low lens magnification for achieving a high measurement rate of the crystals.

The Framework

Fig. 1 depicts the structure of the work. It mainly consists of three parts: (a) use of an on-line video-imaging system for monitoring batch crystallisation; (b) obtaining quantitative information from images through image segmentation and image analysis to calculate shape descriptors and perform polymorph and morphology recognition; and (c) calculating crystal growth rates and estimating growth kinetics parameters.

Experiments

Experiments were carried out using a glass-jacketed reactor of 500 ml, a data interface board and a PC running WinISO process control software provided by Hazard Evaluation Laboratory Ltd. (**Fig. 2**)[24, 25]. To control the temperature, a Julabo FP50-HD thermostatic bath was employed. A reflux condenser was used to circulate water at 6℃ to minimise solvent loss at the higher reactor temperatures. Reactor stirring was performed using a pitched-blade stirrer rotating at a constant speed of 200 rpm. The temperature was measured using a platinum resistance thermometer (PT100), turbidity was measured with an in-house-built turbidimetric fibre-optic probe system. Both signals along with pH values were logged into the computer system. Observation and recording of the process were carried out in real time using on-line imaging with an instrument developed by the pharmaceutical manufacturer GlaxoSmithKline, UK. For off-line image analysis, the PVS830 described below

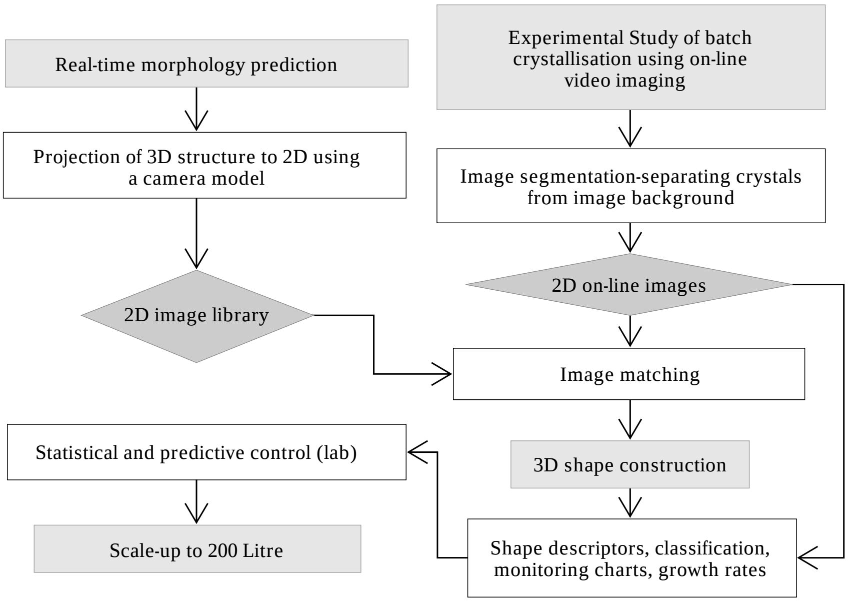

Fig. 1 The framework

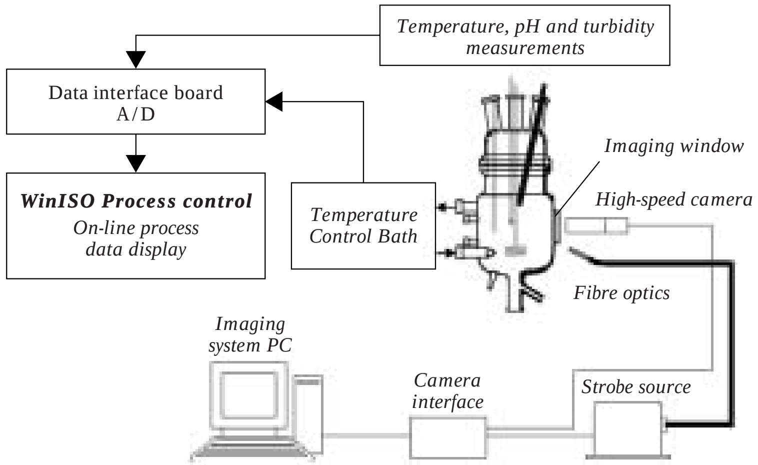

Fig. 2 The experimental system

was employed, using a pipette to take samples from the reactor solution at several instances during the process. The samples were quickly placed and covered on the sample glass slide of the previously calibrated PVS830, and images were captured and analysed. The time from taking a sample until the off-line image analysis was from 10 to 20 seconds.

The on-line imaging instrument employed in the experiments is a high-speed CCD camera system which has a maximum frequency of thirty images per second with a typical pixel resolution of 480×640 and a field of view from 140 μm to 16 mm. The camera is situated just outside the reactor wall and an imaging window is attached to the external reactor wall to avoid convexity effects on the images (**Fig. 3**). To provide illumination, a strobe light source is used and the light is conducted using a fibre-optic guide. Camera acquisition and flashing light are synchronised to freeze the moving particles by using a camera interface box developed by scientists at the pharmaceutical manufacturer GSK[22, 23]. The captured images are sent to a PC running VideoSavant software (IO Industries, Inc.) for acquisition, storage and management of frames.

To enhance the contrast of particles from the image background, two fibre-optic light guides can be used, both adjustable in angle and distance. The system allows the visualisation and recording in real time of every event occurring throughout the process, thus capturing the complete history of the crystallisation.

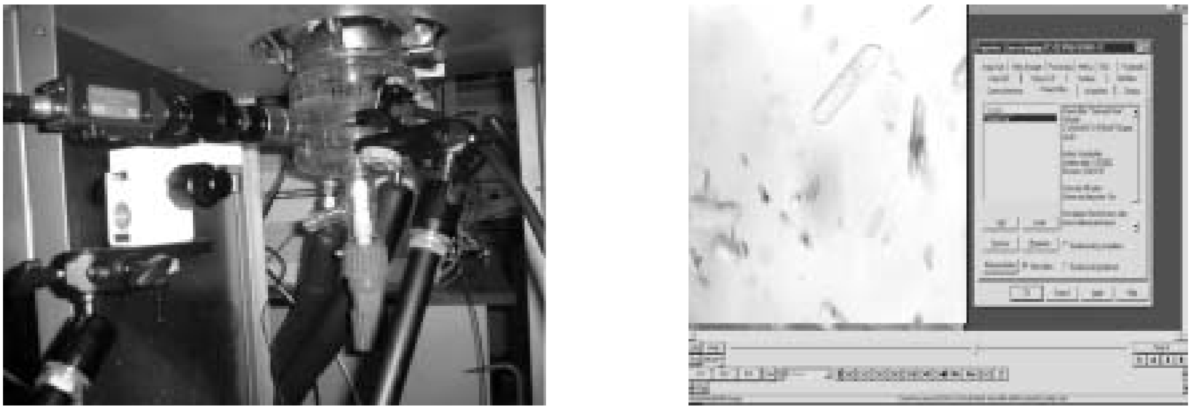

(a) (b)

Fig. 3 (a) the on-line imaging system applied to a 5 Litre reactor; (b) images captured and the image acquisition

For an estimation of the particle size, the camera is calibrated with a glass micrometer scale (Agar Scientific Ltd.), using Mitutoyo objective lenses with Navitar Precise Eye lenses for different magnifications, allowing observations down to 5 µm.

An off-line imaging system, the PharmaVision System 830 (PVS830) from Malvern Instruments Ltd.[26], was also used in the study. It is an automatic vision system for the analysis of the size and shape of particles. A zoom lens allows particles between 0.5 and 2000 µm to be analysed. The instrument automatically calibrates itself prior to an analysis by the measurement of both light intensity and precision grating with a known number of lines per millimetre. To perform the analysis, the sample is placed on a sample tray under a CCD video camera. A linear actuator connected to a PC moves the camera across the sample tray and the camera takes digitised video images. Particles from the images are automatically segmented by embedded computer software, thus obtaining a variety of shape parameters such as length, width, mean diameter and roundness, and supported by images of all particles for further visual understanding. The performance of the instrument is verified by reference slides which are certified and traceable to standards issued by the National Institute of Standards and Technology.

Solutions of 33.3 g of L-glutamic acid (purchased from Aldrich Chemicals) dissolved in 500 ml of fresh distilled water were prepared. The solutions were heated up to 95℃ and kept constant at this temperature until everything was dissolved, then linearly cooled down to 15℃, keeping this temperature until the end of the experiment. Different linear cooling rates of 1, 0.5 and 0.25℃/min were investigated. The concentration and temperatures of the experiments were chosen to be close to those used in an industrial-scale operation. It was found that for the experiment employing a cooling rate of 0.25℃/min, the images revealed that the crystals were at first growing with a rhombic shape, an α-form (**Fig. 4 (a)** and **4 (b)**). Transformation into a β-form was observed at a temperature of 60℃, as illustrated in the real-time image of **Fig. 5 (a)** and **(b)**. For the experiment using a cooling rate of 0.5℃/min, α-form crystals were also first found and the transition to a β-form was also observed, but at a much later stage corresponding to a temperature of 30℃. No transition from α to β was observed when a cooling rate of 1℃/min was used. The results confirmed and helped explain the crystallisation mechanisms[24].

During the onset stage, the crystallisation experi-

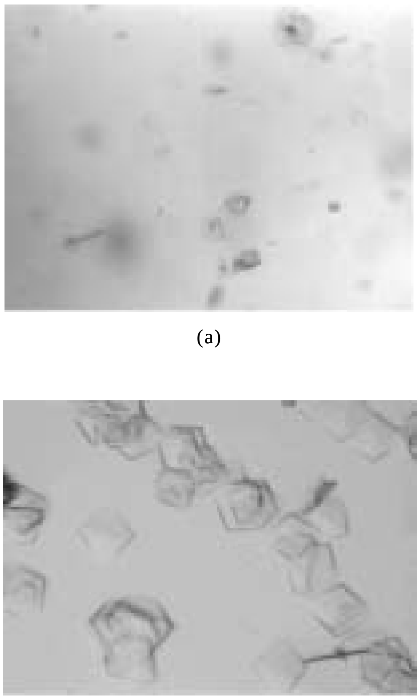
(a)

(b)

Fig. 4 Observed crystals at 63℃ and cooling rate 0.25℃/min in real-time (a), and in the PVS830 (b)

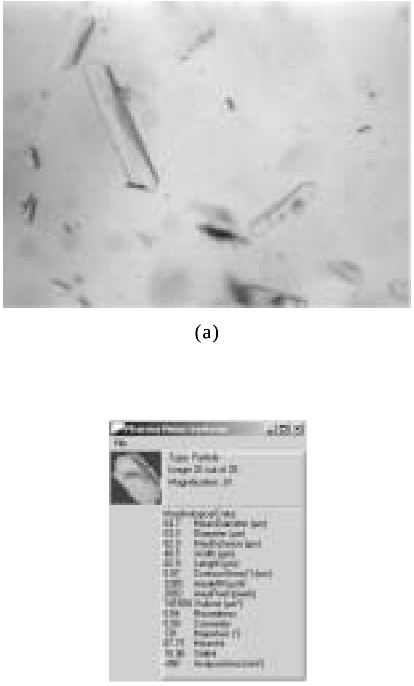
(a)

(b)

Fig. 5 Real-time image for the cooling rate 0.25℃/min at 60℃ (a) and shape dimension obtained from a sample at 60℃ (b) ments were carefully followed by the on-line imaging system. The onset point is said to occur when the first crystals start appearing in the solution, which is sometimes called the 'cloud point'. Looking at the real-time images, we were able to identify a number of appearing particles instants before the fibre-optic turbidity probe could show a pronounced reduction in light transmittance at the cloud point. The temperature at the onset points obtained by on-line imaging corresponding to the three cooling rates are summarised in **Table 1**. The results were found to be either earlier or at the same time as turbidity results[24].

Table 1 Crystallisation onset values obtained from on-line imaging

Cooling rate	Temperature onset	Cooling time
1℃/min	54.10℃	42 min
0.5℃/min	59.74℃	55 min
0.25℃/min	69.95℃	47 min

Image Analysis, Shape Classification and Monitoring Charts

To obtain quantitative information from the images for subsequent monitoring and control purposes, a major challenge is the availability of methods for image analysis that need to be not only tolerant of the quality of on-line images, but also accurate, fast and robust. A literature survey of the various techniques and tools led to the same conclusion as Patience[21] had come to, i.e. that the existing methods do not work effectively for the on-line images obtained from crystallisation reactors. Images of slurries with particles suspended in a solution are much more complex than images of purely solid particles, and the major challenges lie in the fact that the slurries in a stirred reactor are in continuous motion, and that the variation of the distance between the camera lens and the particles captured in a snapshot makes the edges of some particles more vague than others. In addition, the light effect and temporal changes of hydrodynamics within the reactor may lead to varied intensity in the background.

As a result, and as part of the research, a new multi-scale approach based on the Canny[27] and wavelet functions[28, 29] was developed which proved to be very promising in extracting the crystals from the image backgrounds[25, 28, 30]. The image segmentation method involves several steps: edge detection over two scales (so called multi-scale), mathematical morphological closing and opening to remove noises and small objects, to ultimately obtain the segmented crystal objects. **Fig. 6** shows an example of analysing a poor-quality image (to choose a low-quality image to demonstrate the capability of the method). **Fig. 7** shows the analysis results for images obtained using the Malvern Instruments PVS830 and the PVM system of Lasentec. The processing time for a typical image with a resolution of 640×480 obtained by the GSK system is between seven and ten seconds using a PC of 2 GHz. No significant difference in processing time was observed when analysing images from the PVS830 with a resolution of 756×548.

Following image segmentation, the next step is to classify the shapes and extract morphological data[31]. The shape can be defined by the object features that maintain invariance under *similarity transformations*, the transformations including rotation, translation and size scaling[32, 33].

There are two major groups of methods for the use of descriptors to represent a shape. The first group includes techniques that provide a detailed representation and preserve information of the object boundary and thus can enable reconstruction of the original shape from the descriptor values. These types of descriptors usually consider a shape as being a periodic mathematical function which can be represented, for example, as an expansion or as a high-order polynomial. The second group includes global shape descriptors which can also be used to characterise the region boundary, albeit not preserving details of the original shape for reconstruction. These types of descriptors include, for example, critical distances, ratios or shape factors. For the latter, we use the software of a PVS830 imaging system from Malvern Instruments Ltd. to make the calculations, which give the key shape descriptors, while for the former, we use Fourier descriptors.

An extensive review on shape description techniques was made by Zhang and Lu[34]. They concluded that Fourier descriptors based on spectral transforms provide robust performance, accuracy, compact features and low computation complexity, as well as being the most promising method to overcome noise. Fourier descriptors have been used by several researchers for the contour analysis of particles[35, 36]. This technique is popular due to its invariance under two-dimensional transformations, i.e. rotation translation and scaling, and its ability to describe a region

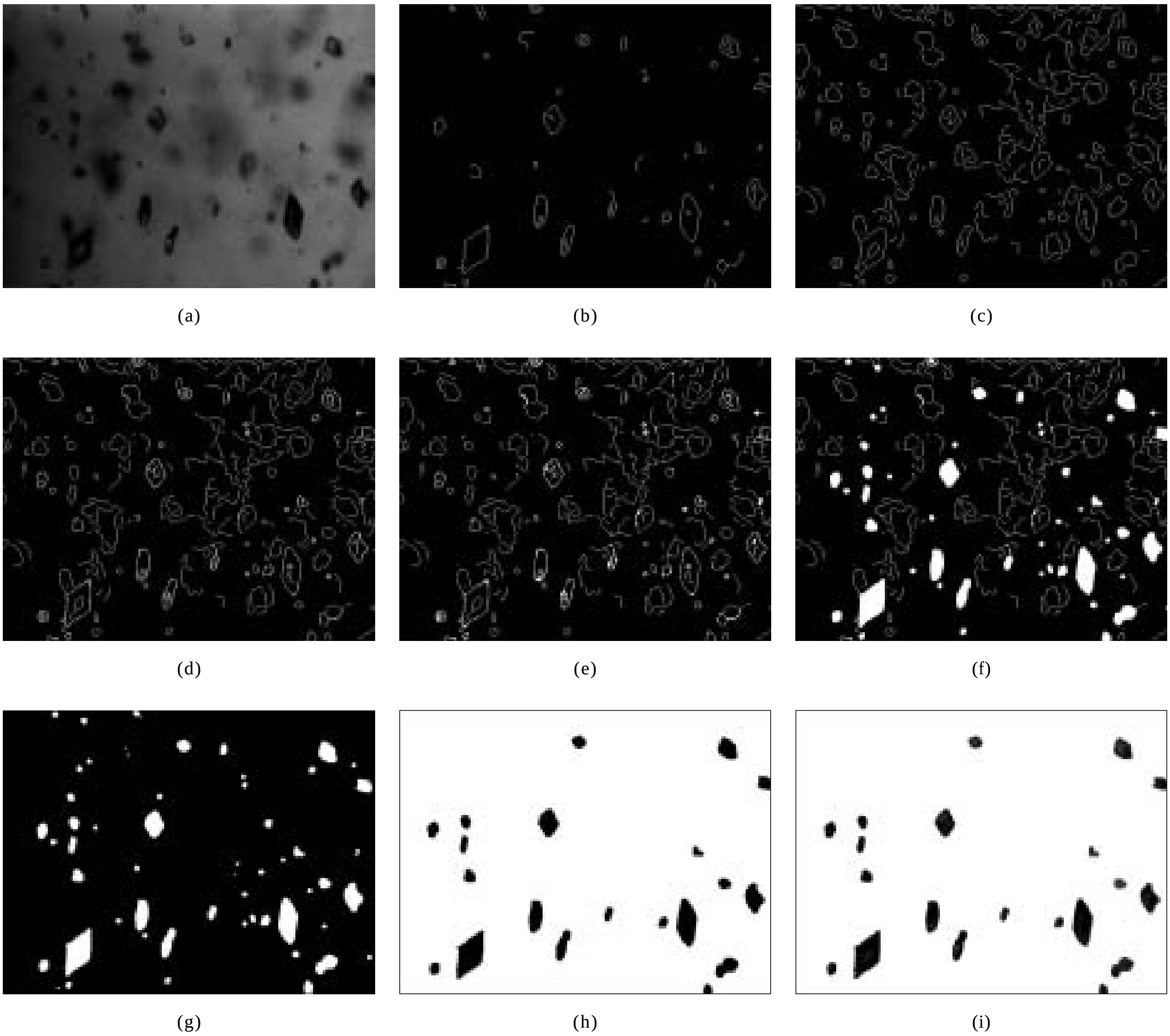

(a) (b) (c)

(d) (e) (f)

(g) (h) (i)

Fig. 6 The segmentation method applied on a sample in-situ image with highly irregular pixel intensity. (a) Original image, (b) edges detected at the first scale, (c) edges detected at the second scale, (d) edges of first and second scales, (e) morphological closing on image *(d)*, (f) region-filling on image *(e)*, (g) morphological opening on image *(f)*, (h) segmented particles after removing those with less than 200 pixels from image *(g)*, (i) segmented particles with the original grey-scale intensity superimposed

boundary in detail, preserving shape information for reconstruction. The calculated Fourier shape descriptors were then used by a shape classification algorithm, the adaptive resonance theory (ART2)[37, 38] for classification purposes. ART2 is a neural network that adopts a learning mechanism that is both unsupervised and recursive. Since it is unsupervised learning, unlike back propagation neural networks that require training using pairs of predefined shape clusters and descriptors[36], ART2 automatically determines the number of clusters and the assignment of data patterns in a way that patterns in a cluster are more similar than those in a different cluster. The recursive learning feature is a mechanism that can continuously update the knowledge with new data available, without corrupting the existing knowledge already learned using previous data and without the need to make up the new data with previous data for re-training or re-learning, also very important for on-line use (in some literature it is called incremental learning). Being recursive is extremely useful for on-line use since new data are continuously made available.

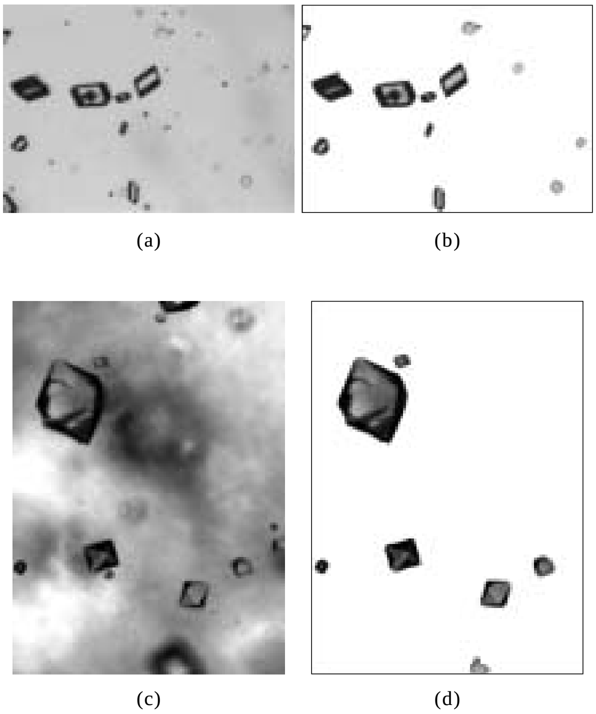
(a) (b)

(c) (d)

Fig. 7 Examples of analysis results for image obtained using PVS830 of Malvern Instruments, (a) and (b); and using PVM of Lasentec, (c) and (d). **Fig. 7** (a) is by courtesy of Lasentec[10)]

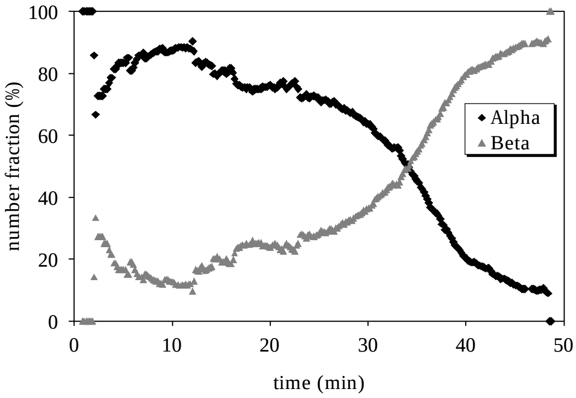

Fig. 8 2-D crystal polymorphic transition charts in number percentage for the polymorphs alpha and beta. Each point represents the previous ten minutes. (Onset at $t=0$)

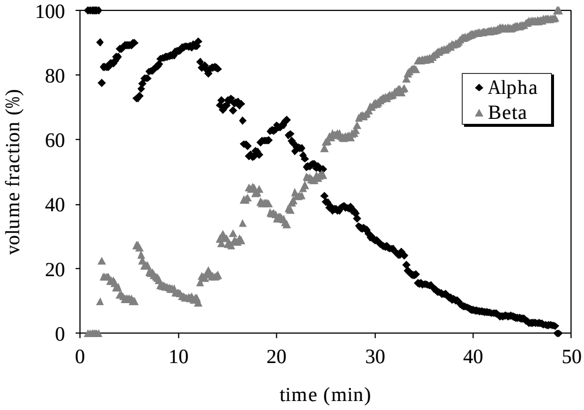

Fig. 9 2-D polymorphic transition for the polymorphs alpha and beta. Each point represents the previous ten minutes. (Onset at $t=0$)

The methodology for image segmentation, descriptor calculation and shape recognition was applied to the on-line raw images obtained during cooling crystallisation of (L)-glutamic acid. The number and volume of the crystals captured in the frame over a fixed time interval were used to estimate the number and volume fractions between the two polymorphs, alpha and beta.

For estimation of the ratios between the prismatic and needle shapes, each time point in **Fig. 8** and **9** represents 60 images taken in the last 10 minutes. **Fig. 8** shows the relative percentage of the number of the two polymorphic forms, alpha and beta, plotted against time, from crystallisation onset throughout the polymorphic transition. The trends illustrate that the number of crystals with prismatic alpha shape became a minority at around 30 minutes from crystallisation onset. This type of chart is very useful to process engineers and operators to obtain the quantitative information about the polymorphic transitions inside the reactor. Due to the natural progress from onset through growth of the crystals, images of the first instants during onset contain only a few crystals compared to images of subsequent stages. As a result, clearer and less fluctuating shape trends are obtained as the time progresses and the amount of crystals detected increases. Nevertheless, the broad features of the polymorphic transformation are still evident through detecting the changes in crystal shape.

Due to the differences in particle size, a volume fraction can provide a better idea of the amount of compounds in solid state with a particular shape. The crystal shape patterns in volume fraction based on the last ten minutes is shown in **Fig. 9**. It is worth noting that in the volume fraction plot, the crossing-over is observed earlier than in the number fraction plots, meaning that the amount of (L)-glutamic acid beta-form becomes predominant in the solid state at the crossing-over in **Fig. 9**, albeit at the same time-point the amount of crystals with prismatic shape, alpha-form, still constitute the majority.

The dynamic change in crystal shape can also be depicted in **Fig. 10**, which illustrates the values of shape roundness of alpha- and beta-form crystals as crystallisation in the reactor progresses. Each point represents a single crystal, and its corresponding roundness value can be read from the vertical axis. As expected, alpha-form crystals have higher values of roundness, while beta-form crystals have low roundness values, and the crystals are clearly separated into two clusters due to the difference in roundness values, with the upper cluster representing alpha-form crystals and the lower cluster corresponding to beta. The plot reveals that at the very early stages of crystallisation, many more crystals have high roundness values than low roundness values, a reflection of the fact that there are more alpha- than beta-form crystals. As time progresses (accompanied with reactor cooling), more crystals have low roundness values (beta-form), and few have high roundness values (alpha-form), indicating the transition from alpha- to beta-form.

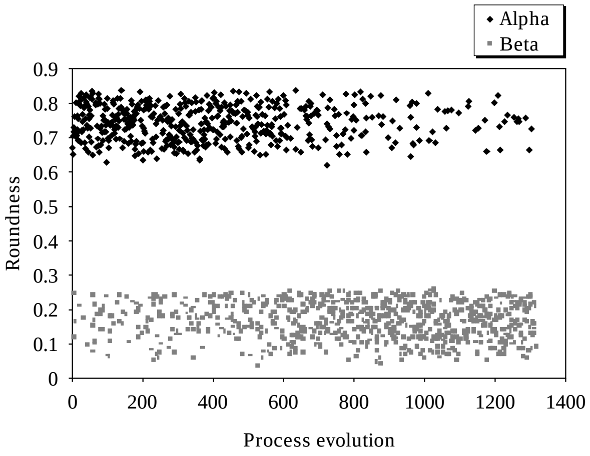

Fig. 10 Evolution of roundness values for the crystal shapes detected as alpha and beta forms

Fig. 11 (a) and **(b)** show the evolution of length, width and equivalent diameter of the crystals for alpha- and beta-forms, respectively. For both cases, a clear relationship is observed between the patterns of crystal length and width. Nevertheless, differences can be observed. For instance, the beta-form crystals show a low difference in crystal width from the first to the last minutes, whereas the crystal length values rise from around 110 μm with more pronounced fluctuations to values of nearly 250 μm during the period of phase transition. In contrast, for the alpha-form crystals, although there are also differences in the crystal length and width patterns, they present more similarities compared with the needle-shaped crystal patterns. This reflects the actual differences in growth rate for the different crystallographic faces. In the beta-form crystals, the [101] crystallographic face clearly has a predominant growth rate compared with the other faces of the crystals, therefore leading to the characteristic needle shape. The crystal habit of the alpha-form, on the other hand, maintains the prismatic ratio as a result of similar growth rates of the crystallographic faces.

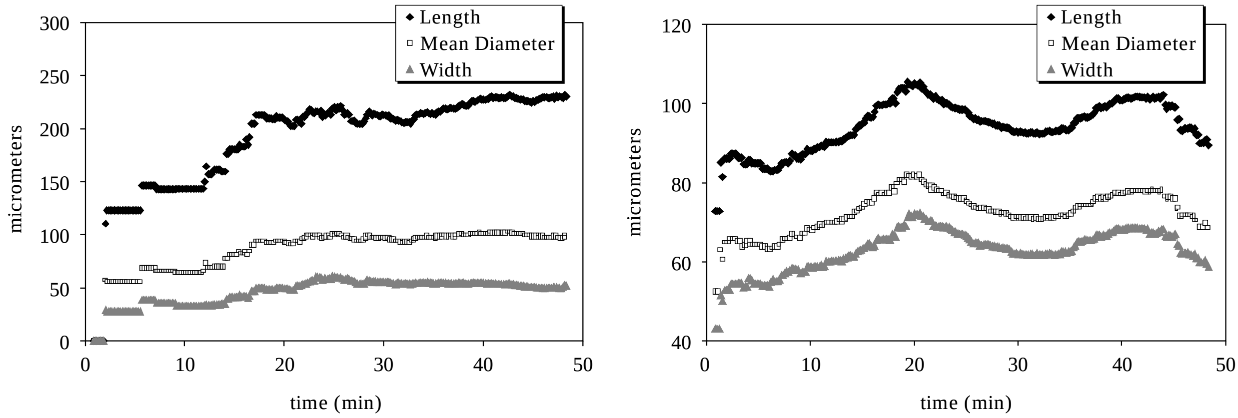

(a) **(b)**

Fig. 11 Evolution of morphological parameters for the crystal shapes detected as (a) beta and (b) alpha forms

In contrast to other on-line techniques for measuring the crystal size that can only provide a value similar to the equivalent diameter, the present monitoring charts obtained from image analysis show the trends of changes in crystal size in more detail. For instance, in our studies, the image analysis results make evident that oscillations in crystal size in needle-shaped crystals mainly correspond to crystal length with minor changes in crystal width, whereas the morphological dimensions of the prismatic crystals oscillate with similar trends.

Crystal Growth Rates and Kinetics

The information obtained from imaging and image analysis was also used to estimate the crystal growth rates[25]. This was conducted for cooling (0.1°C/min) crystallisation of LGA which produced needle-shaped β LGA. As an example, **Fig. 12** shows the mean values of length along with supersaturation, temperature and turbidity. Each point is the average of the previous 60 seconds containing 300 images. **Table 2** gives growth rate values estimated for both the length and width, and the literature result for the same chemical.

Comparing the estimated growth rate values with the literature, the growth rates of different faces of beta-form crystals of glutamic acid have been investigated previously by Kitamura and Ishizu[39] using the single crystal method. The literature reported that the growth rate value at the relative supersaturation of 0.5 is lower compared with the values obtained here in the same direction, the crystal length, in the supersaturation range from 0.47 to 0.51. This difference is consistent with the difference in temperature. Clearly, higher growth rates are obtained at higher temperatures. Other factors within the crystalliser vessel are also associated such as the existing hydrodynamics or collisions that promote crystal surface dislocations which enhance the growth, compared with the conditions of measurement in a single crystal. Although it is expected that at higher temperatures the values of growth rate will also be higher, it is observed in **Table 2** that, for length, the growth rate tends to increase under the (simultaneous) effect of supersaturation increase.

Kitamura and Ishiza[39] also reported that for the width, the growth rate was too small to be measured. Here, the measurements of crystal width involve a combination of the faces and the estimated growth rates for the width are 4 to 6 times smaller than those for the crystal length.

The capability to measure crystal growth rates could, in principle, be used in the estimation of para-

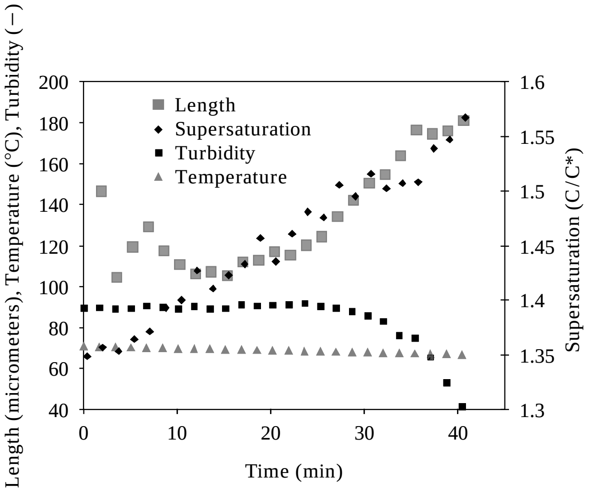

Fig. 12 Evaluation of crystal length along with supersaturation, temperature and turbidity. Each point represents the average of previous 60 seconds

Table 2 Estimated growth rate values for length and width of needle-shaped crystals

Temperature average, T (°C)	Relative supersaturation $\sigma = S - 1$	Length growth rate $R_L \times 10^8$ (m/s)	Width growth rate $R_W \times 10^9$ (m/s)
68.34	0.471	2.440	5.575
68.18	0.478	2.561	5.838
68.01	0.485	3.136	5.852
67.84	0.492	2.837	6.044
67.68	0.502	2.997	5.526
67.51	0.512	2.995	5.019
25	**0.5**	**1.3* (literature[39])**	−

meters associated to the kinetics of growth, in this case image analysis providing the possibility of estimating the kinetics in different morphological directions of the crystals. Here, although the conditions are of cooling temperature, it is tempting to try to fit the growth rates obtained from imaging data to a kinetic model. Due to the low relationship found between width growth rates and supersaturation it was considered that for the case of width, it would not lead to a sensible estimation. Therefore, only the estimation of kinetic parameters associated with the crystal length was attempted.

To estimate the parameters, that is the growth kinetic constant k and the order n, a semi-empirical kinetic model was used

$$R = k\sigma^{n}$$

which can be re-written in logarithmic form to estimate the parameters from a linear regression (**Fig. 13**)

$$\ln R = n \ln\sigma + \ln k$$

Strictly speaking, the value of k is dependent on temperature following the Arrhenius equation[40]. Here, although the variation of temperature is relatively low for the studied points, the estimation was made above all to investigate the potential of using imaging in the estimation of growth kinetics, with the possibility of using the technique in future research in isothermal experiments. **Table 3** summarises the obtained values.

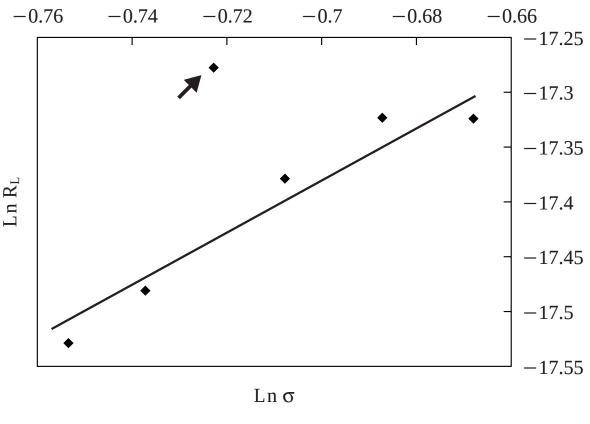

Fig. 13 Data plot for the estimation of kinetic parameters, k and n, of growth in crystal length (r^2=0.95). The arrow indicates an outlier

Looking at the obtained value of the exponent, the estimation suggests that the growth in length is close to a dislocation controlled BCF mechanism. However, one needs to bear in mind that the semi-empirical kinetic model used is in fact describing the growth in the direction of a (100) face, which for this particular morphology is non-existent. The growth in the crystal length is mainly driven by the {101} family of faces, being aware of the existence of an angle between the growth rate in length and the growth rate of the (101) face. Due to the rotation of the crystals in the three-dimensional space in the solution, it is difficult to provide a precise estimation of the growth rates for the face (101), $R_{(101)}$, which would be given by the equation

$$R_{(101)} = R_{L} \cos 36° \tag{6.3}$$

Nevertheless, for the crystal morphology of the beta-form crystals, it is reasonable to assume that the growth rate in length is very close to the growth rate of the faces {101}.

The present results are encouraging. They clearly show that in the current state, the technique can provide a very close approximation of the growth rates and kinetics associated to some particular crystal faces. And they also show that if the rotation of the crystal in the solution can be quantified, the results provided by the imaging technique can lead to estimation of the same parameters of crystal growth of facets with high accuracy.

The Camera Model: Integration of Imaging and Crystal Morphology Modelling

The integration of crystal morphological modelling with in-situ shape measurement using on-line microscopy provides a potentially useful instrument for crystallisation study, for example, for validation of morphology prediction models, for constructing 3-D shapes from on-line 2-D images, as well as for classification of the polymorphic and morphological forms.

Table 3 Estimated kinetic parameters of growth in length for needle-shaped beta-form crystals

Temperature range (℃)	Relative supersaturation, σ	Kinetic growth constant, k×10^7 (m/s)	Kinetic order n
67.51< T< 68.34	0.471< <0.512	1.761	2.61

An approach for the integration called *camera model* was proposed by Li et al[41, 42]. It involves a means of generating a library of 2-D images through rotating a 3-D crystal in the multidimensional space, and a method for matching the 2-D images in the library to those 2-D images obtained on-line.

The first step involves generating a 2-D library by rotating the 3-D crystals, which can be explained using **Fig. 14**. If the camera is placed at a point on the **X** axis, as shown in **Fig. 14**, the rotation around **X** axis will not result in different 2-D shapes, but only change the orientations of the same 2-D shape. As a result, the rotation around the **X** axis can be ignored. Since the crystal is a facetted object, when rotating around an axis, either **Y** or **Z**, from one angle to another at a very small step, for example, around the **Y** axis, the 2-D shapes corresponding to the two positions may only change in a very minor way. **Fig. 15** shows some 2-D shapes when rotating a crystal at different angles, i.e. 1°, 2°, 3°, 4°, 5°, 6°, 7°, 8°, 9°, 10°, and 11° around the **Y** axis, from which it is clear that even when rotating the crystal 11° from the initial position, the 2-D shape does not change very much. This means that the number of 2-D shapes with a significant difference to each other is limited. Here, the words "significant difference" though are vague, and can be defined by the users. For instance, it can be defined as that as long as the number of edges in the projected 2-D images changes (increases or decreases), then it is considered a new 2-D image with a significant difference from its last image. It is worth pointing out that the minimum degree at which the crystal needs to rotate is dependent on the complexity of the 3-D crystal and the initial position of rotation.

Two methods of rotation can be used. One approach is to use a constant rotation angle to continuously rotate the crystal. In this case, the value of the angle must be small enough so that the similarity distance between two 2-D shapes corresponding to any two neighbouring orientations is smaller than a predefined threshold value. An alternative approach of rotation is to use variant rotation angles. In this approach, when rotating the crystal around an axis from one position to the next, the angle between the two positions is chosen so that the similarity distance of the two 2-D shapes corresponding to the two positions is larger than a threshold value sd_1 and smaller than another threshold value sd_2 ($sd_1 < sd_2$). The advantage of this rotation method is that it can reduce the size of the 2-D image library generated.

Fig. 16 shows some examples of 2-D images gen-

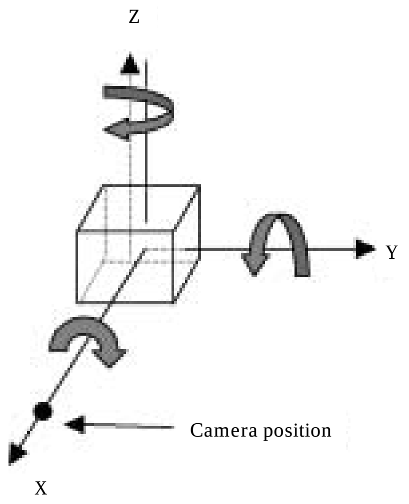

Fig. 14 Crystal rotation method

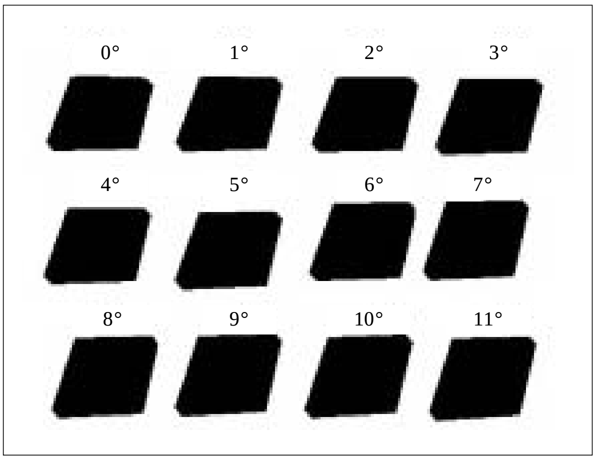

Fig. 15 2D shapes obtained through rotating a crystal at different angles

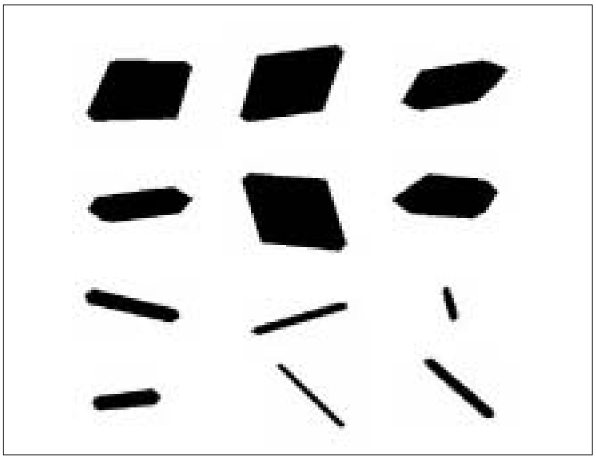

Fig. 16 Some image examples in the generated image library

erated in a library. **Fig. 17** shows an example of online images which has undergone the segmentation procedure. **Table 4** shows the identification of crystals in **Fig. 17** by matching the 2-D crystals with those in the 2-D library generated by the camera model.

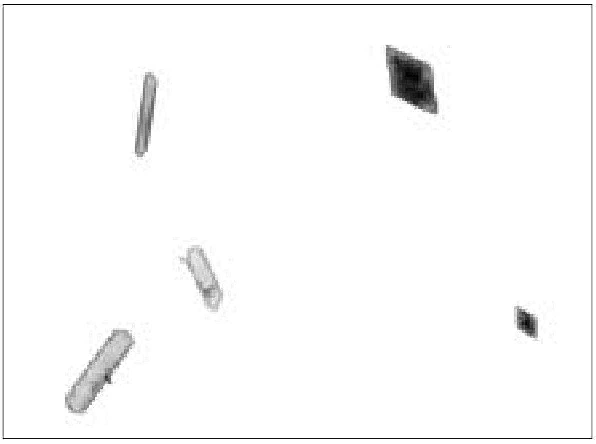

Fig. 17 Segmented on-line crystal images

Final Remarks and Future Work

In the past, pharmaceutical manufacturers have been hesitant to introduce new equipment, instruments and control techniques due to regulatory uncertainties which could lead to longer approval times and high costs43). As part of the FDA initiative to encourage innovation and efficiency of manufacturing process design and control and quality assurance44), the Process Analytical Technology (PAT) framework45) is an important move decided on jointly by the regulatory authority and the industry, which could potentially lead to a revolutionary change in the manufacture of pharmaceuticals that requires all materials properties including concentration, size, shape, morphology and surface properties of feedstocks, intermediates and products at nano-, micro- and macro-scales, to be measured on-line or at-line. In addition, the measurements will not only be used for display purposes, but will also be analysed using advanced sensor and PAT data mining techniques to gain a fundamental understanding of the process and product behaviour

Table 4 The image matching results for crystals of **Fig. 17**

Online Images	Retrieved Reference	Similarity Distance	Polymorph
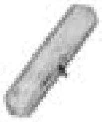	BetaM042182	1.40	β
	BetaM112182	1.44	β
	BetaM112358	1.48	β
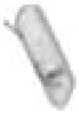	BetaM280330	0.88	β
	BetaM104030	0.89	β
	BetaM284330	0.96	β
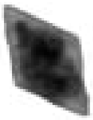	AlphaM176054	0.87	α
	AlphaM356126	0.88	α
	AlphaM176234	0.88	α
	BetaM022228	0.46	β
	BetaM022048	0.51	β
	BetaM320134	0.52	β
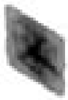	AlphaM356018	0.65	α
	AlphaM354198	0.68	α
	AlphaM004016	0.68	α

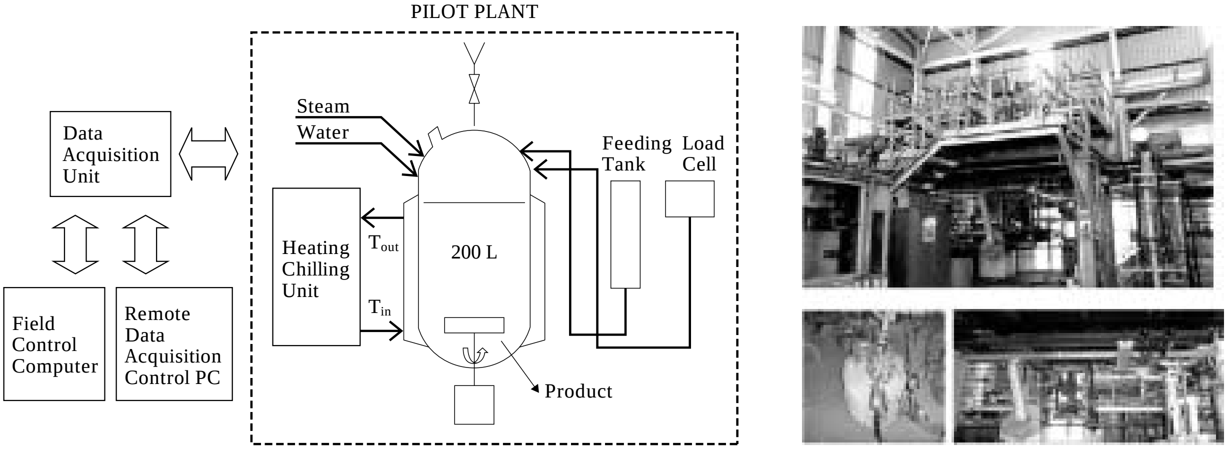

(a) Schematic diagram

(b) The original pilot plant

Fig. 18 A 200 litre pilot plant donated by AstraZeneca is being installed which will be used in the scale-up study.

needed to achieve product quality control and assurance.

The results presented in this paper demonstrate that the integration of advanced on-line imaging sensors and multi-scale image analysis techniques provides great potential for implementing real-time techniques to manipulate the crystal growth and control the morphology of crystals. The work also can potentially lead to full integration of morphology modelling, measurement, control and optimisation techniques. The work reported in this paper was obtained with a laboratory-scale reactor. In the future, it is planned to extend the study to an industrial-scale 200-litre reactor (**Fig. 18**) donated by AstraZeneca which is being installed in the pilot plant of the Institute of Particle Science and Engineering, at the University of Leeds.

Acknowledgements

This work has been carried out as part of Chemicals Behaving Badly, a collaborative project funded by the UK Engineering and Physical Sciences Research Council (GR/R43860, GR/R43877) together with support from an industrial consortium including ANSYS Europe Ltd., AstraZeneca, Bede Scientific Instruments Ltd., British Nuclear Fuel Limited, Clairet Scientific Ltd., GlaxoSmithKline, HEL Ltd., Malvern Instruments Limited, Pfizer and Syngenta. The academic partners are Leeds, Heriot-Watt and Newcastle universities. We gratefully acknowledge all these sponsors and all members of this academic/industrial team and the industrial coordinator of the project, Professor L.J. Ford. We would like to extend our thanks to Duncan Roberts, David Watson and Rob Norris from Malvern Instruments Ltd., who provided the PVS830 system on loan for the study, and to GlaxoSmithKline for providing the imaging system, particularly Kevin Jennings, Mike Wilkinson, Kaz Wood-Kaczmar and David Lee at GSK. The second author acknowledges the Council of Science and Technology in Mexico (CONACYT) for providing the PhD scholarship. The first author thank Malvern Instruments Ltd. for sponsoring his readership. New research is being conducted under the support of EPSRC (EP/C009541) and Malvern Instruments Ltd.

References

1) Nagy Z.K., Chew J.W., Fujiwara M., Braatz R.D.: ADCHEM – 7th International Symposium on Advanced Control of Chemical Processes, IFAC, Hong Kong, 2004.
2) Dunuwila D.D., Berglund K.A. 1997. ATR FTIR spectroscopy for in situ measurement of supersaturation. J Cryst Growth 179(1-2):185-193.
3) Gron H., Borissova A., Roberts K.J. 2003. In-process ATR-FTIR spectroscopy for closed-loop supersaturation control of a batch crystallizer producing monosodium glutamate crystals of defined size. Ind Eng Chem Res 42(1):198-206.

4) Togkalidou T., Fujiwara M., Patel S., Braatz R.D. 2001. Solute concentration prediction using chemometrics and ATR-FTIR spectroscopy. J Cryst Growth 231(4): 534-543.
5) Ono TtH, J.H., Jansens, P.J. 2004. Quantitative measurement of the polymorphic transformation of L-glutamic acid using in-situ Raman spectroscopy. Cryst Growth Des 4(3):465-469.
6) Mougin P., Thomas A., Wilkinson D., White G., Roberts K.J., Herrmann N., Jack R., Tweedie R. 2003. On-line monitoring of a crystallisation process. Aiche J 49(2): 373-378.
7) Hukkanen E.J., Braatz R.D. 2003. Measurement of particle size distribution in suspension polymerization using in situ laser backscattering. Sens Actuator B-Chem 96(1-2):451-459.
8) Ruf A., Worlitschek J., Mazzotti M. 2000. Modeling and experimental analysis of PSD measurements through FBRM. Part Part Syst Charact 17(4):167-179.
9) Barrett P. 2002. In-situ monitoring of crystallisation processes. Department of Chemical Engineering, ed.: PhD thesis, University College Dublin, Ireland.
10) Barrett P., Glennon B. 2002. Characterizing the metastable zone width and solubility curve using lasentec FBRM and PVM. Chem Eng Res Des 80(A7):799-805.
11) Gron H., Mougin P., Thomas A., White G., Wilkinson D., Hammond R.B., Lai X.J., Roberts K.J. 2003. Dynamic in-process examination of particle size and crystallographic form under defined conditions of reactant supersaturation as associated with the batch crystallisation of monosodium glutamate from aqueous solution. Ind Eng Chem Res 42(20):4888-4898.
12) Clydesdale G., Roberts K.J., Docherty R. 1996. HABIT95 — A program for predicting the morphology of molecular crystals as a function of the growth environment. J Cryst Growth 166(1-4):78-83.
13) Accelrys webpage, http://www.accelrys.com/
14) Liang J.K. 2002. Process scale dependence of L-glutamic acid batch crystallised from aqueous solution in relation to reactor internals, reactant mixing and process conditions. Department of Chemical Engineering, ed.: PhD thesis, Heriot-Watt University, UK.
15) Ma Z.H., Merkus H.G., de Smet J., Heffels C., Scarlett B. 2000. New developments in particle characterization by laser diffraction: size and shape. Powder Technol 111(1-2):66-78.
16) Ma Z.H., Merkus H.G., Scarlett B. 2001. Extending laser diffraction for particle shape characterization: technical aspects and application. Powder Technol 118(1-2):180-187.
17) Yamamoto H., Matsuyama T., Wada M. 2002. Shape distinction of particulate materials by laser diffraction pattern analysis. Powder Technol 122(2-3):205-211.
18) Mougin P. 2001. In situ and on-line ultrasonic attenuation spectroscopy for particle sizing during the crystallisation of organic fine chemicals. ed.: PhD thesis, Heriot-Watt University, UK.
19) Mougin P., Wilkinson D., Roberts K.J. 2002. In situ measurement of particle size during the crystallisation of L-glutamic acid under two polymorphic forms: Influence of crystal habit on ultrasonic attenuation measurements. Cryst Growth Des 2(3):227-234.
20) Patience D.B., Rawlings J.B. 2001. Particle-shape monitoring and control in crystallisation processes. AIChE J 47(9):2125-2130.
21) Patience D.B. 2002. Crystal engineering through particle size and shape, monitoring, modeling and control. ed.: PhD thesis, University of Wisconsin-Madison, USA.
22) Wilkinson M.J., Jennings K.H., Hardy, M. 2000. Non-invasive video imaging for interrogating pharmaceutical crystallisation processes. Microscopy and Microanalysis 6(2):996-997.
23) Wilkinson M.J., Jennings K.H., Plant R., Logan R., Drayson B. Particulate Systems Analysis-2003, Harrogate, UK, 2003.
24) Calderon De Anda J., Wang X.Z., Lai X., Roberts K.J., Jennings K.H., Wilkinson M.J., Watson D., Roberts D. 2005. Real-time product morphology monitoring in crystallisation using imaging technique. AIChE J 51(5):1406-1414.
25) Calderon De Anda J. 2005. Real-time particle morphology monitoring in crystallisation using on-line microscopy imaging and image analysis. Institute of Particle Science and Engineering, Leeds: PhD thesis, University of Leeds.
26) Malvern Instruments Ltd., http://www.malvern.co.uk/.
27) Canny J. 1986. A computational approach to edge detection. IEEE Trans Patt Recog and Mach Intell 36:961-1005.
28) Chen J., Wang X.Z. 2005. A wavelet method for analysis of droplet and particle images for monitoring heterogeneous processes. Chem Eng Commun 192(4):499-515.
29) Wang X.Z., Chen B.H., Yang S.H., McGreavy C. 1999. Application of wavelets and neural networks to diagnostic system development, 2, an integrated framework and its application. Comput Chem Eng 23(7):945-954.
30) Calderon De Anda J., Wang X.Z., Roberts K.J. 2005. Multi-scale segmentation image analysis for the in-process monitoring of particle shape with batch crystallisers. Chem Eng Sci 60(4):1053-1065.
31) Calderon De Anda J., Wang X.Z., Lai X., Roberts K.J. 2005. Classifying organic crystals via in-process image analysis and the use of monitoring charts to follow polymorphic and morphological changes. Journal of Process Control 15(7):785-797.
32) Kindratenko V.V. 2003. On using functions to describe the shape. J Math Imaging Vis 18(3):225-245.
33) Abbasi S., Mokhtarian F. 2001. Affine-similar shape retrieval: Application to multiview 3-D object recognition. IEEE Trans Image Process 10(1):131-139.
34) Zhang D., Lu G. 2004. Review of shape representation and description techniques. Pattern Recognition 37(1): 1-19.
35) Xu K., Luxmoore A.R., Deravi F. 1997. Comparison of shape features for the classification of wear particles. Eng Appl Artif Intell 10(5):485-493.

36) BernardMichel B., Rohani S., Pons M.N., Vivier H., Hundal H.S. 1997. Classification of crystal shape using Fourier descriptors and mathematical morphology. Part Part Syst Charact 14(4):193-200.
37) Carpenter G.A.G., S. 1987. ART2: self-organisation of stable category codes for analogue input patterns. Applied Optics 26:4919-4930.
38) Wang X.Z., Chen B.H. 1998. Clustering of infrared spectra of lubricating base oils using adaptive resonance theory. J Chem Inf Comput Sci 38(3):457-462.
39) Kitamura M., Ishizu T. 2000. Growth kinetics and morphological change of polymorphs of L-glutamic acid. J Cryst Growth 209(1):138-145.
40) Mullin J.W. 2001. Crystallisation. 4th edition ed., USA: Butterworth-Heinemann.
41) Li R.F., Thomson G.B., White G., Calderon De Anda J., Wang X.Z., Roberts K.J. 2005. A methodology for integration of morphological modeling and in-situ shape measurement using on-line microscopy in pharmaceutical crystallisation. AIChE J., in press.
42) Li R.F., Thomson G.B., White G., Calderon De Anda J., Wang X.Z., Roberts K.J. 7th World Congress of Chemical Engineering, Glasgow, Scotland, July 2005.
43) Narhi M., Nordstrom K. 2005. Manufacturing, regulatory and commercial challenges of biopharmaceuticals production: a Finnish perspective. European Journal of Pharmaceutics and Biopharmaceutics 59:397-405.
44) FDA 2004. Department of Health and Human Services, Pharmaceutical cGMPs for the 21st century – a risk-based approach final report. http://wwwfdagov/cder/gmp/gmp2004/GMP_fi-nalreport2004htm.
45) FDA 2004. Department of Health and Human Services, Guidance for Industry: PAT – a framework for innovative pharmaceutical development, manufacturing, and quality assurance. http://wwwfdagov/cder/guidance/6419fnlhtm.

Author's short biography

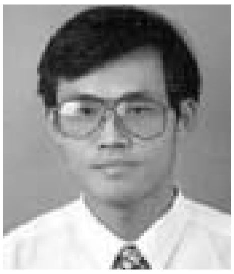

X.Z. Wang

Dr Xue Z. Wang is the Malvern Reader in Intelligent Measurement and Control in the Institute of Particle Science and Engineering, School of Process Environmental and Materials Engineering at the University of Leeds. His research focuses on the investigation of advanced mathematical, knowledge-based as well as data-driven techniques in order to exploit the potential for improved process performance offered by the integration of on-line measurement, control and information systems. The most recent research projects can be grouped into the three areas: process sensor and PAT data mining, on-line PAT measurement and control for particulate products at micron, sub-micron and nano-scale, and eco-toxicity prediction of mixtures of chemicals using quantitative structure – activity relationships and data mining.

J. Calderon De Anda

Jorge Caderon De Anda received his PhD degree in 2005 from the Institute of Particle Science and Engineering, School of Process Environmental and Materials Engineering at the University of Leeds. His PhD thesis is entitled 'Real-time particle morphology monitoring in crystallisation using on-line microscopy imaging and image analysis'. His PhD work won the prestigious BNFL Peter Wilson Prize and Medal in 2005.

Author's short biography

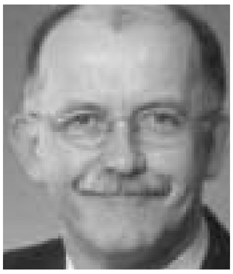

Kevin J. Roberts

Professor Kevin J. Roberts is a Brotherton Professor of Chemical Engineering in the Institute of Particle Science and Engineering, School of Process Environmental and Materials Engineering at the University of Leeds. His research interests are directed towards understanding, predicting and manipulating the properties of solid-form chemical products, and the interfaces associated with their formation, when operating under realistic thermodynamic conditions of temperature and pressure. This synergistic perspective encompasses both theoretical and experimental studies, integrated within a strong underpinning molecular engineering framework, associated with both fundamental and strategic research programmes, with the latter involving substantial industrial collaboration and support.

R.F. Li

Dr Ruifa Li is currently a postdoctoral research fellow in the Institute of Particle Science and Engineering, School of Process Environmental and Materials Engineering at the University of Leeds, working on a project funded by EPSRC. His research interests include multivariate statistical process control, data mining and crystal morphology modelling.

G.B. Thomson

Dr Gillian Thomson is an ExxonMobil Fellow and lecturer in the Department of Chemical Engineering, School of Engineering and Physical Sciences, Heriot-Watt University, whose research is directed towards molecular modelling, crystallisation and process analytics.

G. White

Dr Graeme White is a lecturer in the Department of Chemical Engineering, School of Engineering and Physical Sciences, Heriot-Watt University. His research interests are in computational fluid dynamics, crystallisation and crystal morphology modelling.

Aerogels: Tailor-made Carriers for Immediate and Prolonged Drug Release[†]

I. Smirnova[1], S. Suttiruengwong and W. Arlt
Chair for Separation Science & Technology
Friedrich-Alexander-Universität Erlangen-Nürnberg[*]

Abstract

The potential of inorganic polymeric materials – silica aerogels – as tailor-made drug carriers is discussed. It is shown that the dissolution rate of poorly soluble drugs can be significantly changed through the adsorption on silica aerogels. Adsorption takes place in supercritical CO_2 and allows distribution of the drugs inside the aerogel matrix on the molecular level. The drug concentration in the aerogel is explicitly determined by the temperature, bulk concentration of the drug in the supercritical phase and the properties of the aerogel (density, pore size distribution and surface area). The release rate of the drug depends on the hydrophobicity of the aerogel. In the case of hydrophilic aerogels, an extremely fast release – even compared with nanocrystals – of drugs is achieved, which is especially advantageous for poorly water-soluble drugs. Hydrophobic aerogels exhibit a slower release which is governed by diffusion.

In addition, the possibility of generating organic microparticles inside the pores of the aerogels by precipitation from supercritical solutions is discussed.

Key words: Aerogels, Drug carriers, Adsorption, Supercritical fluid

Introduction

Aerogels are low-density solid materials with a fine, open-pore structure. An aerogel is composed of individual primary particles only a few nanometres in size which are linked in a three-dimensional structure. This microstructure causes characteristic properties of aerogel materials: fine pores (5–100 nm), very high surface areas (200–1000 m^2/g) and low densities (0.003–0.15 g/cm^3). Aerogels can be synthesized from silicon oxide (silica aerogels), and also from different organic and inorganic precursors, for example titanium oxide, aluminium oxide, carbon, gelatine, etc. Silica aerogels are usually synthesized by hydrolysis and the subsequent condensation of tetraalkylorthosilicates. The condensation leads to the formation of a gel phase. To convert a gel into an aerogel, the solvent is removed by extraction with supercritical CO_2 or by the direct conversion of the solvent in supercritical state in order to prevent the structure collapse caused by capillary forces [Fricke 1986]. The chemistry of aerogel materials is relatively flexible: their pore size and surface area can be tailored during the synthesis by changing the solvent and catalysts [Rao et al. 1993, Pajonk 1998, Stolarski et al. 1999]. Furthermore, different functional groups can be implemented in the structure of silica aerogels by surface modification or by reaction during sol-gel processes [Husing and Schubert 1997, Husing et al. 1998]. The hydrophobicity of silica aerogels varies from completely hydrophilic aerogels, whose structure collapses immediately in water, to hydrophobic samples, which float on water for many hours without being wetted.

The combination of an extensive range of unusual solid material properties enables the application of aerogels in many different areas of technology. Overviews about already existing and potential applications of aerogels were given by several authors

---

[†] Accepted: August 19, 2005

[*] Egerlandstr. 3, D-91058 Erlangen, Germany

[1] Corresponding author
TEL: +49-9131-8527638 FAX: +49-9131-8527441
E-mail: Irina.Smirnova@cbi.uni-erlangen.de

[Schmidt and Schwertfeger 1998], [Rolison et al. 2001], [Pajonk 2003], [Akimov 2003]. At present, an interest has grown in the field of aerogel applications in life sciences. The high porosity of aerogels can be exploited to incorporate pharmaceuticals and biomolecules as was done for other sol-gel materials (e.g. xerogels). Silica aerogels are especially suitable for this purpose, since they are chemically inert and not harmful to the human body. The high temperature resistance of silica aerogels (up to 500°C) allows sterilization by high temperature according to the requirements of pharmaceutical products. *Biocatalysis* with a lipase enzyme represents one of the advanced silica aerogel research studies. It was shown that the catalytic activity of several non-specific lipases in liquids and supercritical media could be significantly improved by the *in-situ* encapsulation of an enzyme into the silica aerogel during the sol-gel process [Buisson et al. 2001, El Rassy et al. 2004, Novak et al. 2003]. The immobilization of three further enzymes (PGA, thermolysin and chymotrypsin) in silica aerogels was also demonstrated by Basso et al. (2000). Recently, it was shown that proteins (cytochrom c) can be stabilized in an aerogel matrix using the so-called “nanogluing” [Wallace et al. 2003, Wallace et al. 2004], which implies the formation of a stable protein superstructure around gold nanoparticles. The resulting composites show better stability at a greater range of temperatures than previously reported for biocomposite xerogels, and exhibit extremely rapid sensing of the compounds in the gas phase [Wallace et al. 2004]. The principal application of silica aerogels as *biosensors* was demonstrated by the encapsulation of bacteria *Escherischia coli* and the subsequent use of the doped aerogel as an aerosol collector to detect bacteriophages [Power et al. 2001]. The high adsorption capacity of silica aerogels allows their use for adsorption of pharmaceutical compounds. Since aerogels have an extremely large surface area, it is expected that the drug dispersed or adsorbed in the aerogel can obtain improved dissolution characteristics. Both hydrophobic and hydrophilic silica aerogels were loaded with pharmaceuticals by means of adsorption from corresponding liquid solutions [Schwertfeger et al. 2001]. Ambient-dried aerogels with a relatively high density ($\rho > 0.1\ g/cm^3$) were used for this purpose. The authors mixed the aerogels with a solution of the target drug, allowed the mixture to reach equilibrium and then filtered it to get the loaded aerogel. The resulting powder was dried and could be used as a drug delivery system (DDS) [Schwertfeger et al. 2001]. Berg et al. (1995) claim a similar procedure for the loading of organic (resorcinol-formaldehyde) aerogels with testosterone adipate and 5-fluorouracil. However, the adsorption of drugs from liquid solutions leads to the partial collapse of the aerogel structure, especially for hydrophilic aerogels. To avoid this, two different methods can be applied: loading aerogels with drugs during the sol-gel process, as was done with enzymes and proteins as described above, or replacing the liquid solution by supercritical fluids to prevent shrinkage. Lee and Gould (2001) loaded organic aerogels with the drugs methadone and naltrexone by the co-gelling method before supercritical drying. It was proposed to use the resulting aerogel powder as a part of the aerosol for inhalation since the low density of the product allows the particles to be carried by the aerosol stream. It was possible to incorporate 5-fluorouracil into resorcinol-formaldehyde aerogels in this way as well [Berg et al. 1995]. Nevertheless, such a kind of loading implies the stability of drugs at the sol-gel conditions (reaction of drugs with chemicals used for sol synthesis should be avoided). Since it cannot be guaranteed in all cases, the second method, i.e. adsorption from supercritical fluids, is worth investigating. Our group has studied the adsorption of different drugs on silica aerogels from supercritical solutions and the subsequent release of drugs [Smirnova et al. 2003 (a), Smirnova et al. 2004, Smirnova and Arlt 2004]. It was shown that this method allows a homogeneous distribution of the drug in silica aerogel samples. The drying step which is needed if the loading is carried out from liquid solutions is also avoided since CO_2 is removed by simple pressure reduction. The use of hydrophilic aerogels as drug carriers promotes the very fast release of drugs [Smirnova et al. 2004]. For one of the studied drugs, griseofulvin, it was demonstrated that the release rate of the drug adsorbed on aerogels is even much faster than that of drug nanoparticles [Smirnova et al. 2005]. An additional advantage compared with the nanoparticles is the fact that the drug particles being adsorbed or crystallized in the solid aerogel matrix have a lower tendency to agglomerate and are better protected from the environment. Thus silica aerogels not only allow achievement of a significant acceleration of the dissolution rate of poorly soluble drugs, but they also increase their stability. In this work, we demonstrate the possibility of tailoring the release kinetics of drugs by the properties of the aerogels. Two different methods of loading aerogels with organic substances are described: adsorption and crystallisation from supercritical solutions.

Experimental

Aerogels

Silica aerogels were produced using a two-step sol-gel process. First, tetramethoxysilane (TMOS) was mixed with methanol, water, and hydrochloric acid in the ratio 1 mol TMOS:2.4 mol MeOH:1.3 mol H_2O:10^{-5} mol HCl. After 30 min. of stirring, additional water and ammonia solution were added, so that the following molar ratio was obtained: 1 mol TMOS:2.4 mol MeOH:4 mol H_2O:10^{-5} mol HCl:10^{-2} mol NH_4OH.

The mixture was then diluted with acetonitrile and poured into cylindrical moulds with a volume of 5 ml and aged for 72 h. The amount of acetonitrile is calculated to ensure that a certain volume of the gel solution and thus the desired target density is achieved. In order to dry the cylindrical gels, the autoclave was previously filled with 60–80 ml of acetonitrile. The gels were then transferred to the autoclave and the solvent and pore liquid were extracted by supercritical CO_2 during 24 hours at 40℃ and 100 bar. The density of the resulting monolith silica aerogels was calculated by weighing a sample and measuring its volume. The surface area and pore size of the samples were determined by nitrogen adsorption (BET method). The aerogels produced in this way were initially hydrophilic. For hydrophobization, silica aerogels were placed in a reactor and heated to 220℃. Methanol vapour was passed through the reactor for 13 h. The resulting aerogels were extremely hydrophobic, and were able to float on water for several hours without being wetted.

Loading of aerogels with drugs

To deposit a drug on a silica aerogel, a weighed amount of the drug and an aerogel sample (0.1–0.2 g) were separately wrapped in filter paper and placed in an autoclave. Carbon dioxide was added until a desired pressure was reached. The system was stored under constant pressure and temperature until the adsorption equilibrium was reached (24–72 h). The CO_2 was vented and the loaded aerogel samples were weighed and milled in a porcelain mortar. To determine the drug concentration in the sample, a part of the aerogel powder was dispersed in acetonitrile. The solution was stirred for at least 60 min. to ensure complete dissolution of the drug. The concentration of the drug in acetonitrile was determined using UV-spectrometry (UV-V is spectrometer Specord 200, Analytic Jena). The results were additionally verified by CHN elemental analysis. The drug concentration in CO_2 in equilibrium was calculated as follows:

$$C_{drug} = \frac{m_{drug\ initial} - m_{drug\ adsorbed}}{m_{drug\ initial} - m_{drug\ adsorbed} + m_{CO_2}} \qquad (1)$$

where $m_{drug\ initial}$ is the amount of drug placed in the autoclave, $m_{drug\ adsorbed}$ is the mass of drug adsorbed on silica aerogels (as defined by UV and CHN methods), m_{CO_2} is the mass of CO_2 in autoclave.

All samples were characterized by IR spectroscopy and X-ray diffraction spectrometry. For IR measurements, the samples were milled and compressed with KBr in order to obtain thin homogeneous pellets. The absorption spectra (600–4000 cm^{-1}) were recorded by an IR Spectrometer “Magna System 750”. X-ray diffraction patterns of the samples were obtained by means of a Siemens D5000 powder diffractometer with monochromated Cu Kα1 radiation, a flat silicon sample holder, and a position-sensitive detector.

Investigation of drug release kinetics

The assembly for drug-release measurements was designed according to the recommendation for the dissolution test [FIP 1996]. It consists of a covered glass vessel, a motor, a metallic drive shaft with a six-bladed agitator, and a cylindrical basket. The sample (drug crystals or loaded aerogel powder) was weighed and placed in the basket. The amount of the drug was chosen so that the final concentration was equal to 10% of the maximal solubility of this drug in 0.1 N HCl (sink conditions). The basket was fixed on the agitator and immersed into the vessel containing 900 ml of 0.1 N HCl at 37℃. The stirring speed was 100 rpm. Aliquots of 2 ml were withdrawn at predetermined time intervals, filtered through a 0.45-μm nylon filter and analysed by UV-spectrometry.

Results and Discussion

Loading of aerogels with drugs

The loading of hydrophilic aerogels with different drugs was studied. The maximal possible loading that could be achieved by adsorption from a saturated drug solution in supercritical CO_2 at given experimental conditions (180 bar, 40℃) is presented in **Table 1**. The concentration of every drug was chosen so that the bulk CO_2 phase was saturated with the corresponding drug. Aerogels with a density of 0.03 g cm^{-3} were used.

The loading of aerogels with drugs depends on different process parameters. One of the most important is the concentration of the drug in the bulk phase (supercritical CO_2), which is limited by the solubility of the drugs in supercritical CO_2. In many applica-

Table 1 Loading of hydrophilic aerogels from saturated solutions in CO_2 at 180 bar, 40℃

Drug	Loading of drug in aerogel [wt %]
Ketoprofen	30
Griseofulvin	6.3
Miconazol	60
Dithranol	4.4
Flurbiprofen	18
Ibuprofen	73

tions, a high loading of the carrier with the drug of interest is important. As can be seen in **Table 1**, hydrophilic aerogels can adsorb a relatively large amount of ketoprofen, miconazol and ibuprofen. In contrast, dithranol and griseofulvin show an extremely low affinity for the aerogels because of their poor solubility in the supercritical gas. There are several methods that allow a higher solubility to be attained: higher pressure can be used in order to reach a higher CO_2 density and thus a better solubility; an entrainer such as ethanol or acetone can also be applied.

To observe the possible changes of the drug structure during the loading procedure, the identity of the drugs was analysed using X-ray analysis and IR spectroscopy. It was found that all drugs adsorbed on silica aerogels exhibited an amorphous structure. As an example, the XRD patterns of ketoprofen (which exhibits a good adsorption on the aerogels) and griseofulvin (poor adsorption on the aerogels) adsorbed on silica aerogels are given in **Fig. 1** in comparison with the patterns of original drugs. Both griseofulvin and ketoprofen show several diffraction peaks typical for crystalline powder. In contrast, no corresponding diffraction peaks could be found in drug-aerogel formulations (the only peak, at 28 degrees in all patterns, comes from the silicon sample holder), leading to the conclusion that no crystallites of either drug are present. Also, the SEM pictures taken for all drug-aerogel formulations confirm this statement.

The amorphisation of ketoprofen was additionally proven by IR spectroscopy [Smirnova et al. 2004]. The IR spectra of drug-aerogel formulations were recorded and compared with that of the original drugs in their crystalline form and of a simple mixture of ketoprofen crystals and untreated silica aerogel powder (**Fig. 2**). The characteristic absorption bands of ketoprofen (717, 1455 and 1655 cm^{-1}) appear in the spectra of drug-aerogel formulations (**Fig. 2A**). Furthermore, all spectra show the acid dimer peak at 1697 cm^{-1} and the peak at 1654 cm^{-1} attributed to the benzoyl carbonyl group [Florey 1981]. One can see that the benzoyl carbonyl peak in the case of the aerogel formulation is broader and the acid dimer peak is much smaller than the corresponding peaks in the physical mixture (**Fig. 2B**). This is in agreement with the results of Gupta et al. (2003), who observed similar changes of the IR spectrum of ketoprofen adsorbed on magnesium silicate. The corresponding changes of the spectra are associated with the amorphisation of ketoprofen during the adsorption process [Gupta et al. 2003]. Except for the changes caused by amorphisation, no further changes in the IR spectrum of ketoprofen and all other drugs after the loading procedure were found. The chemical nature of the respective drugs seems not to change during the

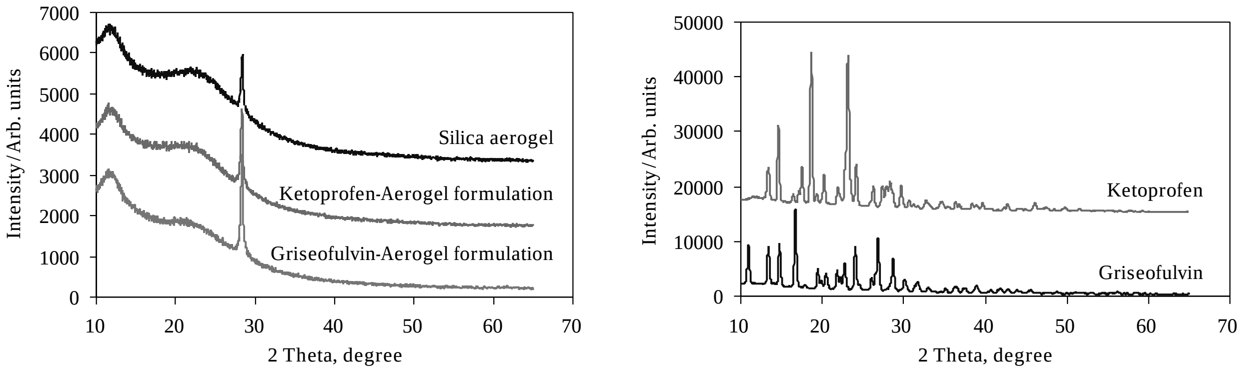

Fig. 1 X-ray diffraction patterns of a) silica aerogel and drug-aerogel formulations; b) crystalline ketoprofen and griseofulvin

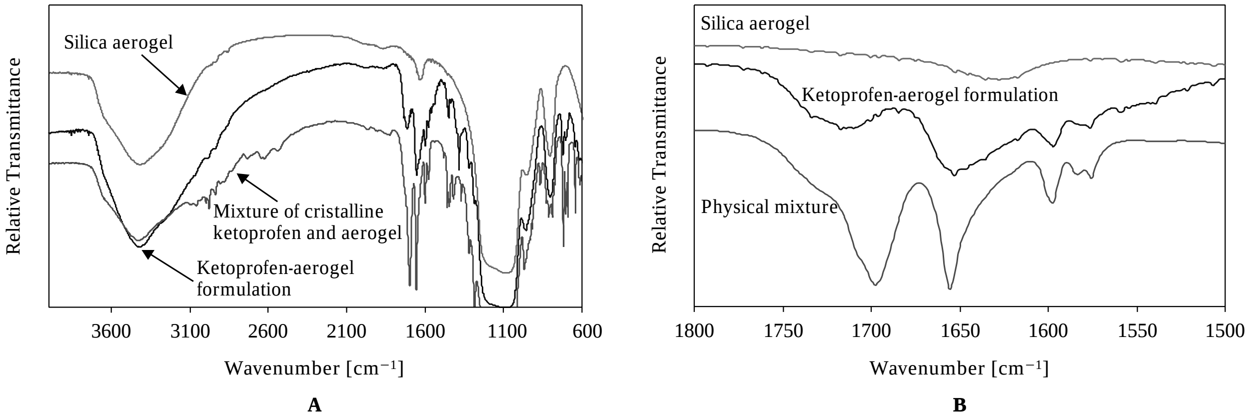

Fig. 2 IR spectra of silica aerogel and ketoprofen-aerogel formulation

loading. The long time chemical stability of the drugs was evaluated for a period of 2 years, with no observed changes in the X-ray patterns and IR spectra of the drugs.

Not only the loading conditions, but also the properties of the aerogel itself influence the drug loading and their further release from the aerogel matrix. To prove this, one of the studied drugs, ketoprofen, was adsorbed on different aerogel samples and both adsorption and drug release processes were studied as a function of the aerogel properties. The aerogels were synthesized as discussed before and their properties are given in **Table 2**. A part of the aerogel samples was hydrophobized before the adsorption experiments took place. The corresponding samples were labelled "S1pb-S4pb". The structural properties (density, pore size) were not significantly influenced by hydrophobization.

Fig. 3 shows the BJH pore size distribution of aerogel samples. All samples show the presence of both micro- and mesopores. In the mesoporous range, a broad distribution is found in aerogels S1 and S2 centred at approximately 40 nm and 35 nm, respectively, whereas samples S3 and S4 have a narrow distribution centred at around 32 nm.

The adsorption of ketoprofen on these aerogel samples was studied at three different concentrations of ketoprofen in the bulk phase. All other parameters (pressure, temperature, loading time) were kept constant. In order to get an idea of how the drug could be arranged on the aerogel's surface, the size of the ketoprofen molecules was estimated by quantum chemistry methods at 402.5 Å^2 (Hyperchem program). Taking into account BET surface areas of the aerogel samples, the number of adsorption layers could be estimated. Clearly, the real orientation of drug molecules on the aerogel surface is unknown, so the calculation made in this way is no more than a rough estimate, but it helps to understand the adsorption process. An estimated monolayer calculated in this way is given in all figures. As can be seen from **Fig. 4A**, at a low bulk concentration of ketoprofen in

Table 2 Characteristics of silica aerogels

Sample	ρ_{bulk} (g/cm^3)	S $_{BET}$ (m^2/g)	Average pore size (nm)	Total pore volume, V_p (cm^3/g)	Remarks on pore size distribution (Table 3)
S1	0.077	572	26.9	3.84	pore diameter: broad maximum at 20−30 nm pore volume (cm^3/g-nm) at maximal pore diameter=0.033
S2	0.10	744	19.4	3.60	pore diameter: broad maximum at 20−30 nm pore volume (cm^3/g-nm) at maximal pore diameter=0.060
S3	0.17	891	17.2	3.82	pore diameter: narrow maximum at 32 nm pore volume (cm^3/g-nm) at maximal pore diameter=0.088
S4	0.22	877	14.0	3.06	pore diameter: narrow maximum at 32 nm pore volume (cm^3/g-nm) at maximal pore diameter=0.085

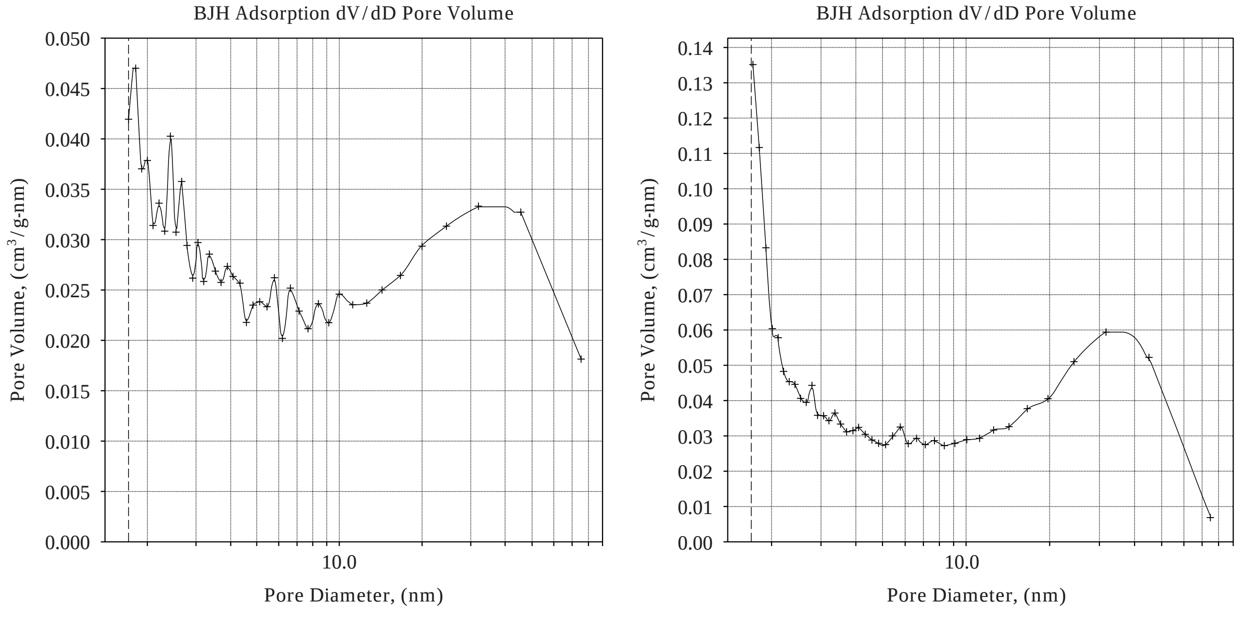

Sample S1 **Sample S2**

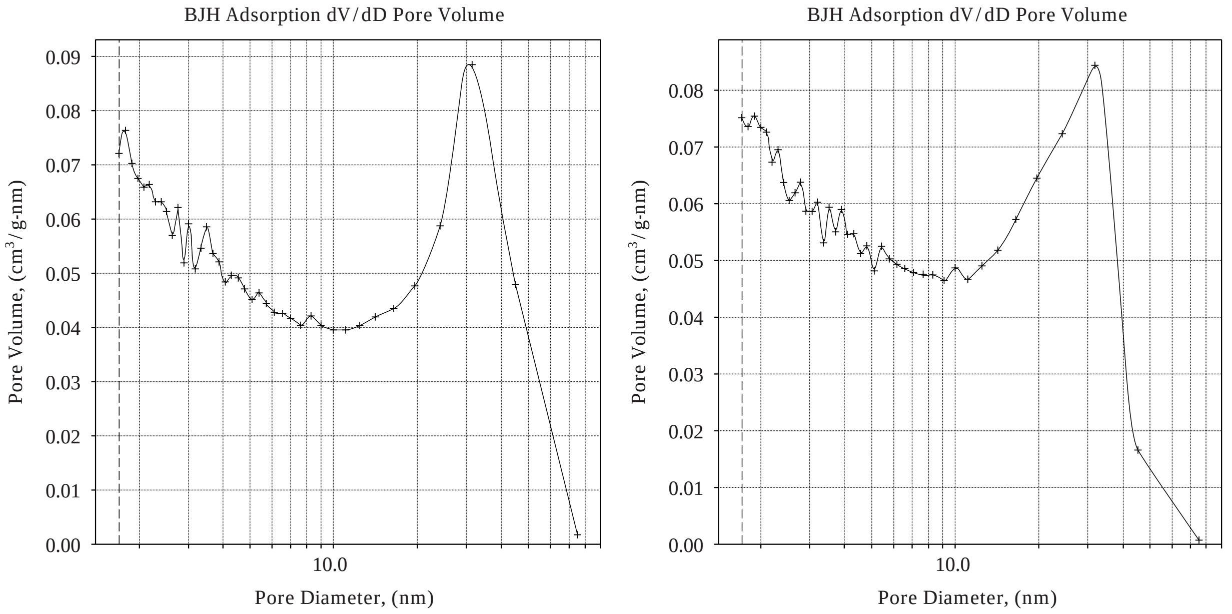

Sample S3 **Sample S4**

Fig. 3 Pore size distribution of aerogel samples (BJH method)

CO_2 (0.001 wt %), ketoprofen molecules are adsorbed equally, independent of the aerogel density. These loading values lie in the range of the estimated monolayer values (see **Fig. 4A**). At larger bulk concentrations of ketoprofen in CO_2, the loading starts to increase with increasing aerogel density. This can be explained by an increase in the specific surface area of the aerogel with increasing density (see **Fig. 4B**). However, if the surface area was the only factor which influences the loading, the plotting of the area-normalized adsorption (loading divided by the surface area) against density would show a straight line. Since this is not the case (see **Fig. 4C**), another factor must influence the adsorption as well. The pore size distribution plays an important role in the adsorption process. As seen in **Table 2**, the pore volume in the mesoporous region increases in the range S1<S2<S3≈S4. The area-normalized adsorption increases in the same sequence. The adsorption in large mesopores is probably more effective than in smaller ones due to better diffusion. A similar effect was observed by Shen et al. (2003), who studied the adsorption of dyes on different activated carbons. They showed that the samples with a larger mesopore content exhibit a higher adsorption rate and a larger loading compared with activated carbons with a smaller mesopore content. Aerogels S3 and S4 have a similar mesopore content and a similar surface area, thus similar loadings may be expected.

The same effect is observed if ketoprofen is adsorbed on hydrophobic aerogels (**Fig. 5**), although the values of loading themselves are much lower than those of hydrophilic aerogels at a similar bulk concentration of ketoprofen in CO_2.

The decrease of the loading values compared with hydrophilic samples should be due to the lack of OH groups in hydrophobic aerogels. Furthermore, in contrast to hydrophilic aerogels, the loading of hydrophobic aerogels depends on the aerogel's density even at a very low ketoprofen concentration where the monolayer is still not achieved. Assuming the adsorption is favoured by the interactions of ketoprofen with the OH groups on the aerogel surface, one can say that the hydrophobic aerogel with the same surface area provides less active sites for adsorption. Therefore, the effective surface area available for adsorption is smaller. So the values of the estimated monolayer have different meanings for hydrophobic and hydrophilic aerogels. The surface of hydrophobic samples is saturated with drugs faster than that of hydrophilic samples, so actually the monolayer should be reached at smaller concentrations of ketoprofen.

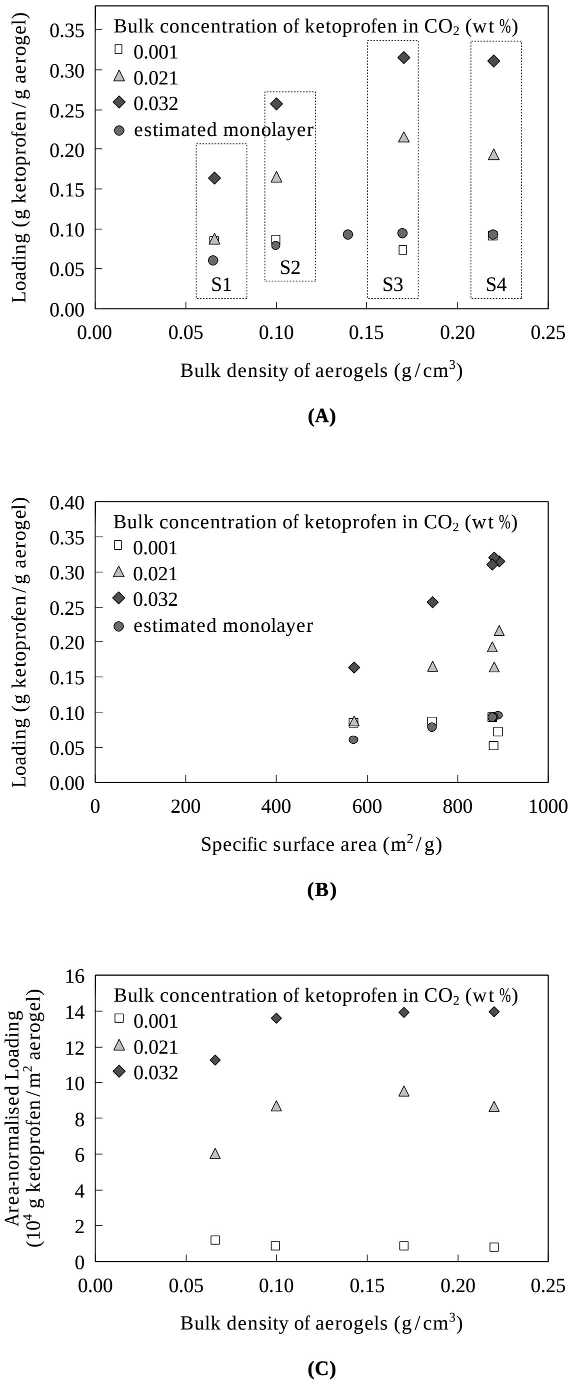

(A)

(B)

(C)

Fig. 4 Adsorption of ketoprofen on hydrophilic aerogels: (A) Loading as a function of density; (B) Loading as a function of aerogels' surface area; (C) Area-normalized loading as a function of density of the aerogel

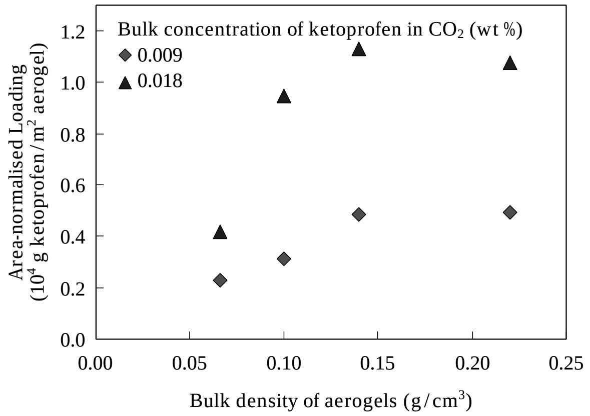

Fig. 5 Area-normalised loading of hydrophobic aerogels as a function of density

Drug release from silica aerogels

In our previous studies, it was shown that the release of the drugs adsorbed on hydrophilic silica aerogels is much faster than that of the crystalline drug form [Smirnova et al. 2004; Smirnova and Arlt 2004; Smirnova et al. 2003 b]. This is demonstrated in **Fig. 6** for the drug ketoprofen. Experimental points were fitted with two common dissolution models ("First order model" and "Peppas model" [Stricker 1989]).

Several effects play a role in release enhancement. Firstly, the specific surface area of ketoprofen is significantly enlarged due to the adsorption on silica aerogel. Secondly, the hydrophilic silica aerogel rapidly collapses in water. The reason for this collapse are capillary forces which are exerted by the surface tension when liquid water enters a nanometre-scale pore of the aerogel. As a result, the solid silica backbone is fractured completely and the aerogel loses its solid integrity. So the drug molecules adsorbed as single molecules on the aerogel network are immediately surrounded by water molecules, and thus dissolve faster. Finally, as discussed above, the drug adsorbed on the aerogel does not have a crystalline structure, so no energy is needed to destroy the crystal lattice of the drug, as in the case for dissolution of the crystalline form of the drug. Only the energy of the desorption of drug molecules from the silica surface (enthalpy of desorption) should be considered. Going by this mechanism, the release rate of the drug should not depend on the physical properties of the hydrophilic aerogels such as density or surface area. This suggestion was confirmed experimentally, as shown in **Fig. 7**. The dissolution rate of ketoprofen adsorbed on hydrophilic aerogels does not change with the density of the hydrophilic aerogel.

A different effect is observed if ketoprofen is adsorbed on hydrophobic silica aerogels (**Fig. 7**). At the beginning of the dissolution process, the drug dissolves from the surface of the hydrophobic aerogel (burst effect) and then later diffuses from its pores. Because the structure of hydrophobic aerogels is much more stable in water than that of hydrophilic samples, the release process from hydrophobic aerogels is governed to a greater extent by the slower influx of water, which leads to a slower release. Hydrophobic aerogels of higher density (0.08 g/cm^3) and thus smaller pore size show a slightly slower release rate than those of lower density (0.03 g/cm^3), as given in **Fig. 7**. It is therefore not only the loading of aerogels with drugs but also the drug release rate that can be influenced by the properties of silica aerogels in this case. These findings allow the release rate to be adjusted to some extent according to the desired application by adjusting the properties of the aerogels.

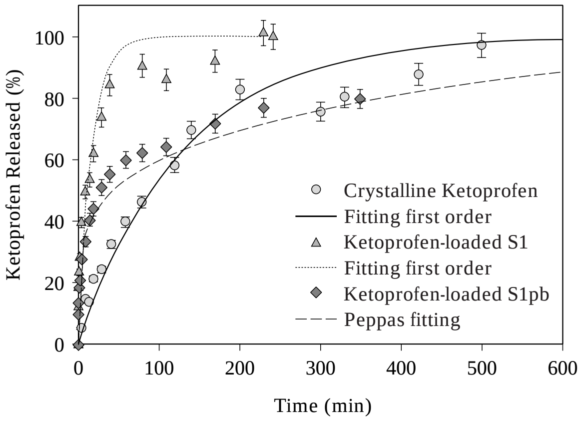

Fig. 6 Release kinetics of different ketoprofen formulations in 0.1 N HCl at 37°C

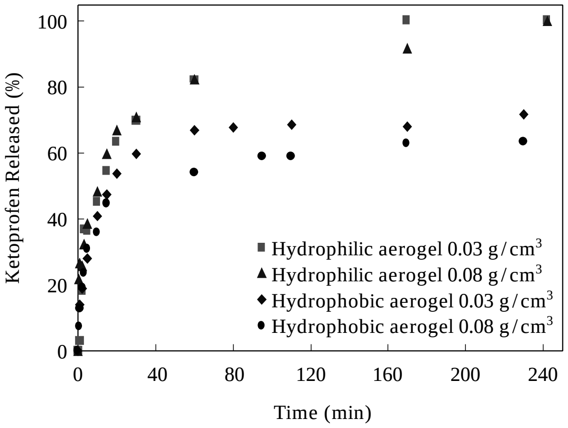

Fig. 7 Release of ketoprofen from hydrophilic and hydrophobic aerogels of different densities in 0.1 N HCl at 37°C

Crystallisation of organic compounds in silica aerogels

Adsorption on the aerogel surface is not the only way to load aerogels with chemicals. Another possibility is the precipitation of drug crystals or particles in the pores of aerogels. Precipitation might lead to much higher loadings than the adsorption. The formation of inorganic nanocrystals in silica aerogels was studied by several research groups [Yao et al.

2000, Merzbacher et al. 1999, Goodwin et al. 1996, Lorenz et al. 1998], however, the formation of drug nanoparticles in an aerogel matrix has not been reported. Since the typical pore size of the aerogel varies from 2 to 50 nm, it can be expected that the crystal growth is limited by the pore size and leads to the formation of nanoparticles inside the aerogel, as was observed for the wet silica gels [Yoda et al. 2001, Sanz et al. 2000]. The final product, silica aerogels with drug nanoparticles inside, would have several advantages. First, drug nanoparticles inside the pores of the aerogel are less sensitive to oxidation and less reactive than original drug nanoparticles. Second, the agglomeration of drug nanoparticles – the main problem of nanoparticles in general – is prevented in this case because the particles are separated from each other. So the aerogels might be used as a "packing material" for drug nanoparticles. The drug "packed" in this way can be applied directly with the carrier. Also in this case, the release kinetics can be regulated by the hydrophobicity of the aerogel (both immediate and prolonged release can be achieved).

The first precipitation experiments were carried out with a model substance – naphthalene and supercritical CO_2. The experimental procedure is identical to that of the adsorption experiments, but the flow rate during the pressure release is significantly higher: from 350 to 4000 l/h (calculated at 1 bar, 25°C). Fast expansion is needed to achieve a high supersaturation of the solution and thus to initiate the crystallisation. Several types of particles are thereby formed: (a) in the bulk phase inside the autoclave (crystallisation from bulk supercritical CO_2), (b) in the vessel in which the expanding gas is flowing, and (c) inside the aerogel (target product). In the case of (a), large hexagonal naphthalene crystals were obtained (**Fig. 8**), similar to those obtained by Tai et al. (1995) during bulk crystallisation from supercritical CO_2. The size of the crystals depends on the supersaturation and varies from 100 µm to 8 mm.

In the case of (b), spherical particles of approximately 100 µm were obtained. The particles precipitated inside the aerogel (case c), as shown in **Fig. 9**. Particle size varies from 100 nm to 2 µm. As soon as the particle size is larger than the average pore size, we conclude that in the case of naphthalene precipitation, the particle growth leads to the partial destruction of the aerogel pores. As expected, the particle size decreases with increasing expansion rate. The concentration of naphthalene in aerogel samples varies from 30 to 77 wt %.

These first results demonstrate the principal possibility of producing micro- and nanoparticles of organic substances inside the aerogel body by precipitation from supercritical solutions. In our further investigations, the precipitation process must be studied systematically in order to optimize the process parameters such as pressure, temperature and depressurization rate. Later on, the experiments will be extended to the drug substances.

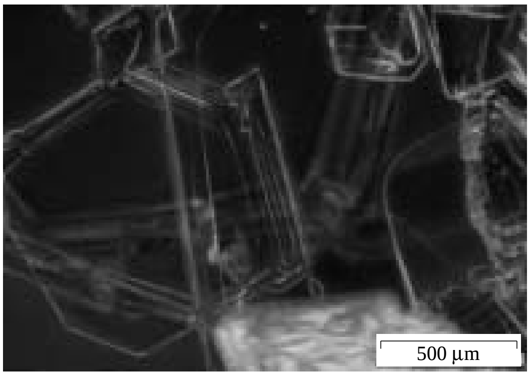

Fig. 8 Naphthalene crystals obtained from the bulk solution

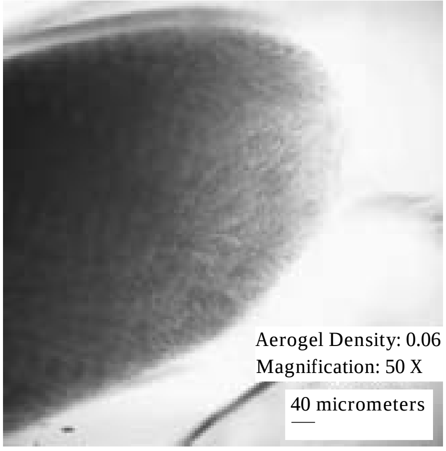

Fig. 9 Naphthalene crystals inside the transparent aerogel matrix

Conclusions

In this work, the possibility of controlling the dissolution rate of poorly soluble drugs by adsorption on silica aerogels with different properties is demonstrated. The loading procedure (adsorption from supercritical gas) allows the homogeneous distribution of the drugs inside the aerogel matrix on the molecular level. The resulting formulations are stable and no chemical degradation of drugs is observed. The drug concentration in the aerogel is explicitly determined by the temperature, bulk concentration of the drug in the supercritical phase and the properties of the aerogel. For a given drug (ketoprofen), the loading increases with the increasing surface area and with the volume of the mesopores of the aerogel, whereas hydrophilic samples have higher loading rates than hydrophobic ones in all cases. The release rate of the drug from the drug-aerogel formulations is significantly influenced by the hydrophobicity and pore size of the aerogels. In the case of hydrophilic aerogels, an extremely fast release – even compared with nanocrystals – of drugs is achieved, which is especially advantageous for poorly water-soluble drugs. This effect is based on the collapse of the structure of hydrophilic aerogels in aqueous solutions due to the surface tension inside the pores. Hydrophobic aerogels exhibit a slower release which is governed by diffusion, since they are more stable in water. Thus, it is possible to tailor the release kinetics of drugs by changing the aerogel's properties. Furthermore it is shown that organic microparticles can be generated inside the pores of the aerogels by precipitation from supercritical solutions. This technique makes it possible to protect the particles from agglomeration. As a model substance, naphthalene led to a very high loading of the aerogel (50–70 wt %). Further investigations of drug precipitation in silica aerogels and the influence of the process parameters thereof are under way.

Acknowledgements

The authors acknowledge the financial support of DFG (Project SM82/1-1).

References

1) Akimov, Y.K. Fields of Application of Aerogels (Review). Instruments and Experimental Techniques (Translation of Pribory i Tekhnika Eksperimenta) (2003), 46(3), 287.
2) Basso, A.; De Martin, L.; Ebert, C.; Gardossi, L.; Tomat, A.; Casarci, M.; Rosi, O.L. A Novel Support for Enzyme Adsorption: Properties and Applications of Aerogels in Low Water Media. Tetrahedron Letters (2000), 41, 8627.
3) Berg, A.; Droege, M.W; Fellmann, J.D.; Klaveness, J.; Rongved P. Medical use of organic aerogels and biodegradable organic aerogels. WO Patent 95/01165, (1995).
4) Buisson, P.; Hernandez, C.; Pierre, M.; Pierre, A.C. Encapsulation of Lipases in Aerogels. Journal of Non-Crystalline Solids (2001), 285, 295.
5) El Rassy, H.; Perrard, A.; Pierre, A.C. Application of lipase encapsulated in silica aerogels to a transesterification reaction in hydrophobic and hydrophilic solvents: Bi-Bi Ping-Pong kinetics. Journal of Molecular Catalysis B: Enzymatic (2004), 30(3-4), 137.
6) FIP Guidelines for Dissolution Testing of Solid Oral Products. Final Draft. Drug Information Journal. (1996), 30, 1071.
7) Florey, K., Ed. “Analytical Profiles of Drug Substances: Ketoprofen”, Academic Press, (1981), 10, 443.
8) Fricke, J., Ed. “Aerogels,” Springer, Berlin, (1986).
9) Goodwin, T.J.; Leppert, V.J.; Smith, C.A.; Risbud, S.H.; Niemeyer, M.; Power, P.P.; Lee, H.W.H.; Hrubesh, L.W. Synthesis of nanocrystalline gallium nitride in silica aerogels. Applied Physics Letters (1996), 69(21), 3230.
10) Gupta, M.K.; Vanwert A.; Bogner, R.H. Formation of physically stable amorphous drugs by milling with neusilin. J.Pharm. Sci. (2003), 92(3), 536.
11) Husing, N.; Schubert, U. Organofunctional Silica Aerogels. Journal of Sol-Gel Sci. & Techn. (1997), 8, 807.
12) Husing, N.; Schubert, U.; Misof, K.; Fratzl, P. Formation and Structure of Porous Gel Networks From Si(OMe)(4) in the Presence of A(CH2)(n)Si(OR)(3) (A=Functional Group). Chemistry of Materials (1998), 10, 3024.
13) Lee, K. and Gould, G. Aerogel powder therapeutic agents. WO Patent 02/051389 A2, (2001).
14) Lorenz, C.; Emmerling, A.; Fricke, J.; Schmidt, T.; Hilgendorff, M.; Spanhel, L.; Muller, G. Aerogels containing strongly photoluminescing zinc oxide nanocrystals. Journal of Non-Crystalline Solids (1998), 238(1,2), 1.
15) Merzbacher C.I., Barker J.G., Long J.W., Rolison D.R. The Morphology of Nanoscale Deposits of Ruthenium Oxide in Silica Aerogels. Nano Structured Materials. (1999), 12, 551.
16) Novak, Z.; Habulin M.; Krmelj, V.; Knez, Z.J. of Supercritical Fluids (2003), 23, 169.
17) Offenlegungsschrift DE 19653758 A1, issued in December 1996.
18) Pajonk, G.M. Transparent Silica Aerogels. J. Non-Cryst. Solids (1998), 225, 307.
19) Pajonk, G.M. Some applications of silica aerogels. Colloid and Polymer Science (2003), 281(7), 637.
20) Power, M.; Hosticka, B.; Black, E.; Daitch, C.; Norris, P. Aerogels as Biosensors: Viral Particle Detection by Bacteria Immobilized on Large Pore Aerogel. Journal of Non-Crystalline Solids (2001), 285, 303.
21) Rao, V. and Parvathy, N.N. J. Mat. Sci. (1993), 28, 3021.
22) Rolison, D.R.; Dunn, B.J. Mat. Chem. (2001), 11, 963.
23) Sanz, N; Baldeck, P.L.; Ibanez, A. Organic nanocrystals embedded in sol-gel glasses for optical application. Synthetic Metals. (2000), 115, 229.
24) Shen, W.Z.; Zheng, J.T.; Zhang Y.L.; Wang J.G.; Qin Z.F. The effect of pore structure of activated carbon on the adsorption of Congo red and vitamin B12. Stud Surf Sci Catal. (Nanotechnology in Mesostructured Materials)

(2003), 146 , 779.

25) Schwertfeger, F.; Zimmermann, A.; Krempel. H. Use of inorganic aerogels in pharmacy. US Patent 6,280,744, 2001.
26) Schmidt M. and Schwertfeger, F.J. Non-Cryst. Solids, (1998), 225(1), 364.
27) Smirnova, I.; Mamic, J.; Arlt, W. Adsorption of Drugs on Silica Aerogels, Langmuir (2003 a), 19(20), 8521.
28) Smirnova, I.; Suttirüngwong, S.; Arlt, W. Release of active substances from aerogel-active substance formulations. Chemie Ingenieur Technik (2003 b), 75(8), 1075.
29) Smirnova, I.; Suttirüngwong, S.; Seiler, M.; Arlt, W. Dissolution Rate Enhancement by Adsorption of Poorly Soluble Drugs on Hydrophilic Silica Aerogels. Pharmaceutical Development and Technology (2004), 9(4), 443.
30) Smirnova, I. and Arlt, W. Synthesis of silica aerogels and their application as drug delivery system. Supercritical Fluids as Solvents and Reaction Media (2004), 381.
31) Smirnova, I.; Türk, M.; Wischumerski, R; Wahl M.A. Comparison of different methods to enhance the dissolution rate of poorly soluble drugs: case of griseofulvin, CIT Eng. Life Sci. (2005), 5(3), 277.
32) Stolarski, M.; Walendziewski, J.; Steininger, M.; Pnia, B. Appl. Cat. A 177,139 (1999).
33) Stricker, H. *Physikalische Pharmazie*. Wissenschaftliche Verlagsgesellschaft mbH: Stuttgart, (1998).
34) Tai, C.Y. and Cheng, C.S. Growth of Naphthalene Crystals from Supercritical CO_2 Solution. AIChE J. (1995), 41, 10, 2227.
35) Wallace, J.M.; Rice, J.K.; Pietron, J.J.; Stroud, R.M.; Long, J.W.; Rolison, D.R. Silica Nanoarchitectures Incorporating Self-Organized Protein Superstructures With Gas-Phase Bioactivity. Nano Letters (2003), 3, 1463.
36) Wallace, J.M.; Stroud, R.M.; Pietron, J.J.; Long, J.W.; Rolison, D.R. The effect of particle size and protein content on nanoparticle-gold-nucleated cytochrome c superstructures encapsulated in silica nanoarchitectures. Journal of Non-Crystalline Solids (2004), 350, 31.
37) Yao, L.Z.; Mo, C.M.; Ye, C.H.; Cai, W.L.; Zhang, L.D. Study of crystallization and spectral properties of PbS nanocrystals doped in SiO_2 aerogel matrix. J Crystal Growth. (2000), 216, 147.
38) Yoda, S.; Ohtake, K.; Takebayashi, Y.; Sugeta, T.; Sako, T. Mater. Chem. (2000), 10, 2151.
39) Yoda, S.; Otake, K.; Takebayashi, Y.; Sugeta, T.; Sato, T. Effects of supercritical impregnation conditions on the properties of silica-titania aerogels. J. Non-Cryst. Solids. (2001), 285, 8.

Author’s short biography

Irina Smirnova

Irina Smirnova graduated from the Chemical Faculty of the St. Petersburg State University (Russia) with a degree in Physical Chemistry in 1998. In 2002 she completed her PhD in Chemical Engineering at the Technical University of Berlin and became an Assistant Professor at the Chair of Prof. Arlt. She followed Prof. Arlt to Erlangen and continued her carrier as an assistant Professor at the Chair of Separation Science and Technology in the University of Erlangen-Nuremberg. Research interests of Dr. Smirnova are aerogels, drug delivery systems and thermodynamics of drug partitioning.

Supakij Suttiruengwong

Supakij Suttiruengwong has received his Batchelor Science degree in Chemical Engineering at Silpakorn University (Thailand) in 1994 and his Master Degree at the University of Wales in 1997. Currently he works on his PhD project with Prof. Arlt at the University of Erlangen-Nuremberg. His research interests are aerogels and hyperbranched polymers as drug delivery systems.

Wolfgang Arlt

Wolfgang Arlt has obtained his first degree at the University of Dortmund. After getting his PhD in the same university with Prof. Onken, he worked at Bayer Co. for 11 years in the filed of thermal separation processes and later for production of the polymer poly-phenylensulfide. In 1992 he became a full professor at the Technical University of Berlin. Since 2004 he continues his academic carrier in the University of Erlangen-Nuremberg as a Head of the Chair of Separation Science and Technology. The topics of his research interests include separation processes (distillation, chromatography), general thermodynamics (equation-of-state, a-priori prediction, reacting systems), drug delivery, process simulation, prediction of thermophysical properties and environmental systems/climate change. He has numerous publications in these fields including patents on the recovery of polymer waste, chromatography and separation processes. Prof. Arlt is an active member of several German and international societies of chemical engineering.

Nanoparticles Surface Engineering of Ultradispersed Polytetrafluoroethylene[†]

S.P. Gubin[1], I.P. Dotsenko, G.Yu. Yurkov,
D.A. Baranov and N.A. Kataeva
N.S. Kurnakov Institute of General and Inorganic
Chemistry, Russian Academy of Sciences[*]
A.K. Tsvetnikov
Institute of Chemistry, Far East Division,
Russian Academy of Sciences, pr. Stoletiya[**]
V.M. Bouznik
Boreskov Institute of Catalysis, Siberian Division,
Russian Academy of Sciences, pr. Akademika[***]

Abstract

In this work we demonstrate that it is possible to create new optical and magnetic materials based on metal-containing nanoparticles stabilized on the surface of polytetrafluoroethylene (PTFE) nanogranules. The magnetic and optical properties of these materials have been investigated. The materials were prepared by a method of thermal decomposition of metal compounds in the heated polytetrafluoroethylene-oil system. Transmission electron microscopy data show that the diameter of the particles is 3−6 nm. Magnetic studies show that for the obtained nanoparticles, the blocking temperature and the magnetic anisotropy is highest for homometallic nanoparticles; this fact makes it promising material for the different magnetic applications. The optical properties of nanomaterials CdS/nanogranules of PTFE are specified. The size and core-shell structure of the nanomaterials has been confirmed by TEM and X-ray diffraction.

Key words: Nanostructures, Nanomaterials, Polymer-matrix composites, Magnetic and optical properties.

Introduction

Nanoparticles are good building blocks for the fabrication of nanomaterials that vary in composition, structure and properties. From this point of view they are universal, ideally suitable for the design of functional nanomaterials and different sensory and electroluminescent devices, magnetic and fluorescent labels, in bioresearches[1, 2)], electronics, as diodes[3)] and lasers[4, 5)], in catalyses[6)], etc.

Materials that contain different types of nanoparticles have attracted the special attention of investigators in recent years. The unique properties of nanoparticles are determined first of all by the fact that many atoms in a nanoparticle belong to its surface[7)]. Thus, the properties of nanoparticles differ greatly from the corresponding bulk materials.

The creation of the nanomaterials from the nanoparticles is the most perspective for a number of reasons. First of all, it is connected with an infinite variety of the sizes, forms, composition and structure of nanoparticles, obtained by “chemical” methods. It allows the preliminary definition and variation of the physical properties of nanoparticles before using them as “building blocks” for the creation of nanoma-

---

[†] Accepted: July 26, 2005

[*] Leninsky av. 31, Moscow, 119991 Russia.

[**] Vladivostoka 159, Vladivostok, 690022 Russia.
E-mail: tsvetnikov@ich.dvo.ru

[***] Lavrent’eva 5, Novosibirsk, 630090 Russia.
E-mail: bouznik@ngs.ru

[1] Corresponding author
TEL: +7 (095) 954-71-36 FAX: +7 (095) 954-12-79
E-mail: gubin@igic.ras.ru

terials.

Unfortunately, there is only a limited number of methods leading to the creation of materials from nanoparticles. Agglomeration of the nanoparticles, as a rule, leads to loss of the majority of unique characteristics. More often than not, the nanoparticles are entered into matrixes of various types. Thus it is observed that the surface atoms can interact with the matrix where they are embedded. From this point of view, a matrix should have an essential influence on the properties of nanoparticles[8)]. The investigation of the properties of such materials is of both fundamental and practical interest. Polymer matrixes containing nanoparticles constitute an important class of nanostructured materials[9)]. These materials are especially important for practical applications, since the polymer technology allows the fabrication of samples with various forms and mechanical properties[10)].

There is another way to engineer nanomaterials; during the recent past, the tendency to fix small (2–10 nm) nanoparticles on the surface of microobjects of spherical form – nanospheres (0.2–20.0 microns) – was outlined. **Fig. 1** presents the schematic of that composite microgranule-nanoparticle material. Such combined micro-nano objects possess a number of advantages. Nanoparticles, being localized on a surface, lose the ability to agglomerate remain at the same time accessible for the interaction with external reagents and keep the basic complex of physical characteristics. At the same time it is possible to create "homogeneous" dispersions – sols and aerosols, and to form materials – films, coverings, three-dimensional samples, from such microgranules with the nanoparticles on its surface. The methods of construction of structures from microgranules are better developed. They are easier to manipulate than small nanoparticles that promote the creation of nanomaterials where the arrangement of nanoparticles will be highly organized. Also, the interest in such particles is connected by the fact that the covering of microgranules by the nanoparticles can essentially change their physical and chemical properties; it can lead to new practical applications in electronics[11)], the creation of displays[12)], the decision of power problems[13, 14)] and others task[15-17)].

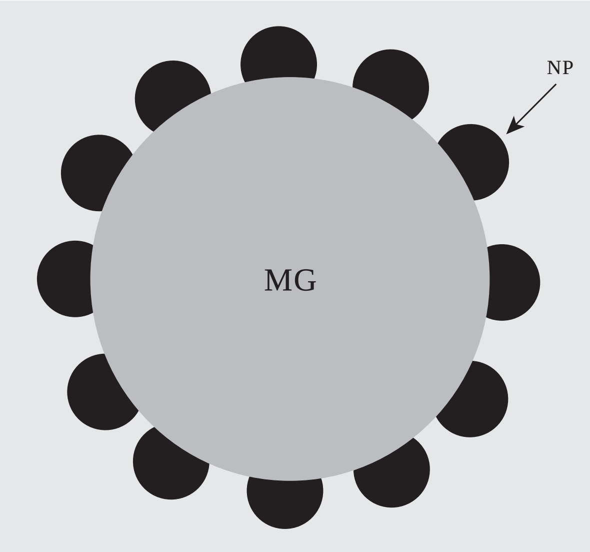

Fig. 1 Schematic of the "polymer core/nanoparticles shell" composite nanomaterials.

Most works concentrate on nanoparticulate core/polymer shell systems with SiO_2, Au and other cores[18, 19)]. There are less works on polymer core/nanoparticle shell systems, clearly because most polymers are difficult to prepare in the form of nanodispersions[20)]. Therefore, the development of new techniques for stabilizing metallic nanoparticles on the surface of polymer cores is a challenging branch of nanotechnology[21)]. One of the most perspective carriers in this direction is polytetrafluoroethylene.

The polytetrafluoroethylene possesses a set of properties, many of which are unique[22)].

At the present time, the thermogas dynamic method is available which allows the industrial production of nanogranules of polytetrafluoroethylene with sizes that do not exceed 500 nanometers[23-27)]. The pictures of nanogranules of polytetrafluoroethylene obtained by this method are shown in **Fig. 2**. The microphotographs were obtained using transmission electronic microscopy (TEM), atomic-force microscopy (AFM) and scanning electronic (SEM) microscopy.

In our research work, polytetrafluoroethylene (PTFE) nanogranules of 100–500 nm in diameter are used to immobilize the nanoparticles. On the surface of such granules, we can stabilize nanoparticles of magnetic materials, nanoparticles of selenides and sulfides of metals (so-called quantum dots) and nanoparticles of rare-earth and noble metals.

In this article, the synthesis of magnetic (Fe, Co) and semiconducting (CdS) nanoparticles localized on the granules of polytetrafluoroethylene and their unique physical properties will be considered.

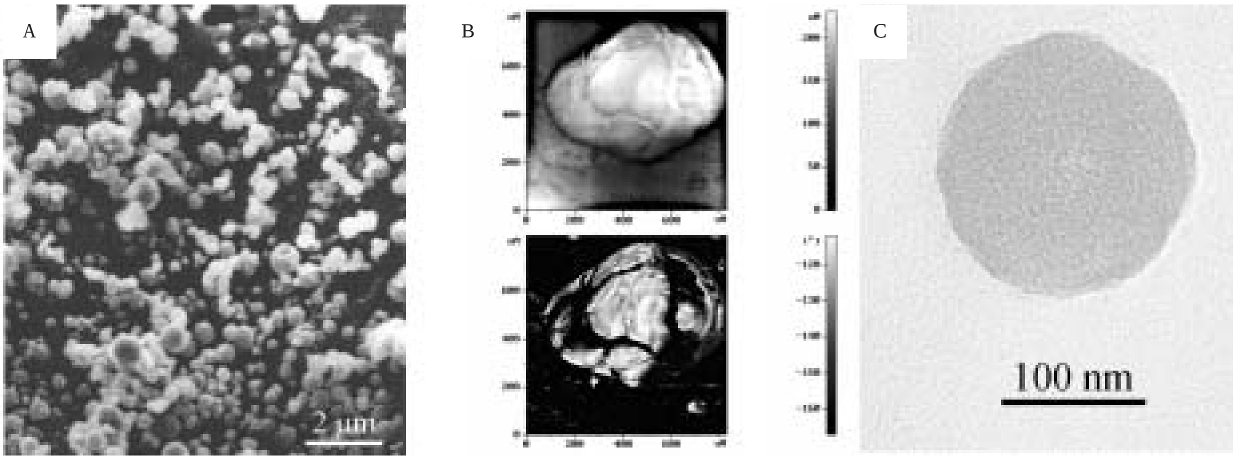

Fig. 2 Microphotographs of polytetrafluoroethylene nanogranules. (A,B,C, – SEM, AFM, TEM images, respectively).

Experiment

Early on, a universal method which allows the fabrication of large amounts of nanocomposites with metal-containing nanoparticles stabilized in polymer matrixes was developed[28-30]. The encapsulation was done by the thermal decomposition of metal-containing compounds (MRn; M=Cr, Mo, W, Ti, Zr, Fe, Co, Ni, Pd, Pt, Cu etc; R=CO, HCOO, CH_3COO, C_2O_4, $C_6H_5CH_2$) in solution/melt of polymer (polyethylene, polypropylene, polyamide, polyacrylate, polycarbonate, polystyrene, polyesters, polyphenyleneoxide, siloxane)[29, 30]. In this work, this method was used to immobilize nanoparticles on the surface of ultradispersed polytetrafluoroethylene (PTFE) nanogranules.

Metal-containing nanoparticles on the surface of UPTFE were formed by the thermal decomposition of cobalt acetate ($Co(CH_3COO)_2 \cdot 4H_2O$), cobalt formate ($Co(HCOO)_2 \cdot 2H_2O$) or iron carbonyl ($Fe(CO)_5$) in a dispersion system of PTFE nanogranules in mineral oil[31]. An appropriate amount of metal-containing compounds was added to the high-temperature dispersed system. We discovered that granules of UPTFE make a fluidized bed on the surface of mineral oil[31, 32]. We used this effect for the nanometallization of nanogranules. Firstly, metallization of nanogranules occurs in the upper area of the fluidized bed. As the concentration of adsorbed metal-containing nanoparticles on the surface of PTFE increases, nanogranules move to the lower areas of oil and are removed from the reaction. The mineral oil was removed by washing with benzene in a Sohxlet apparatus. The resultant powder was dried in vacuum and stored in the air. The optimum conditions were developed for the decomposition of metal-containing compounds in order to introduce highly reactive nanoparticles onto the polymer matrix with a concentration of 3–5 wt. %.

Nanoparticles of cadmium sulfide stabilized on the surface of polytetrafluoroethylene nanogranules were obtained by analogy with an earlier-described technique for the nanometallization of ultradispersed polytetrafluoroethylene[31, 32]. Semiconductor nanoparticles of CdS were formed by a method of chemical modification, using barbotage of hydrogen sulfide through heated oil mixture of cadmium chloride nanoparticles on the surface of polytetrafluoroethylene nanogranules. Also, nanoparticles were doped by ions of manganese. It was carried out by the addition of manganese (II) acetate to the reaction mix.

The size of the nanoparticles was determined by transmission electron microscopy (TEM) studies using a JEOL JEM-100B microscope. The accelerating voltage was 80 kV. Samples were dispersed in the solvent using an ultrasonic oscillator. A drop of the solution was sputtered onto an amorphous carbon film deposited on a copper grid. After evaporation of the liquid, the samples were placed into the microscope.

X-Ray diffraction (XRD) measurements were made on powder samples with a DRON-3 diffractometer (CuKα radiation, λ=1.54056 Å, scan speed of 2°/min). Peak positions were determined with an accuracy of ±0.1°.

The temperature and field dependencies of magnetization were measured with the help of the vibrating sample magnetometer (model PARC-155, Princeton Applied Research) with a flow helium cryostat and a home-made high-temperature insert. The magnetometer sensitivity is better than 5×10^{-5} emu. The magnetic measurements were carried out in the temperature range from 4.2 up to 380 K and in magnetic fields up to 7 kOe. Measurements of hysteresis loops were made by the first saturating of the sample in the field of 7 kOe.

Transmission and reflection spectra for the samples were fixed by means of a standard two-beam spectrophotometer CARY 2415 (VARIAN, USA). For elimination of spatial dependence of reflected and last light intensity measurement were studies using integrating sphere concerning the standard consisting from dispersed $BaSO_4$. In view of the small sizes of samples, an entrance window of integrating sphere was blind.

Results and discussion

In order to confirm the presence of nanoparticles in the material and to determine their dimensions, we used transmission electron microscopy (TEM). **Fig. 3** shows a TEM microphotograph of the sample containing 3.9 and 5.53 wt. % of Co (from different precursors) on the surface of the PTFE nanogranule. According to the TEM data, the average size of the particles is 4.7 and 3.0 nm. **Fig. 4** shows a sample with Fe-containing nanoparticles stabilized on the surface of PTFE. The average size is 6.0 nm. The shape of Co- and Fe-containing nanoparticles is almost spherical. Elemental analysis showed that the cobalt content in the sample is ≈3.9 and 5.53 wt. % and the iron content is ≈4.1 wt. %.

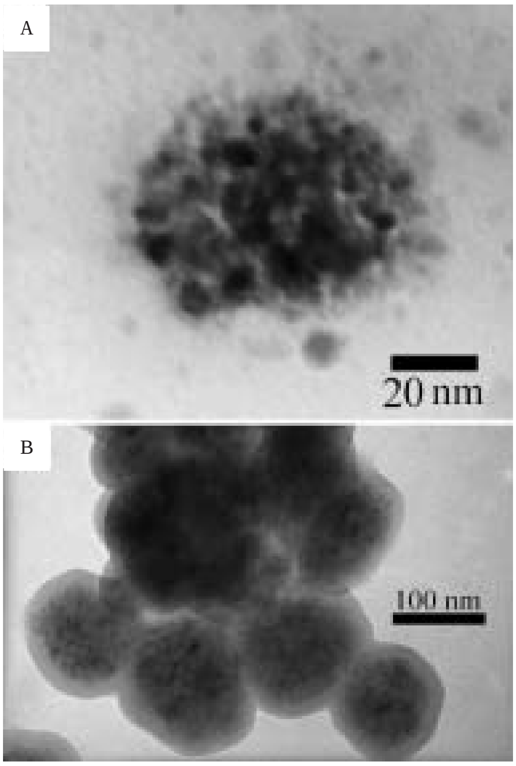

Fig. 3 TEM microphotograph of the sample containing 3.9 and 5.53 wt. % of Co nanoparticles (A, B, – from acetate and formate, respectively) on the surface of PTFE nanogranules.

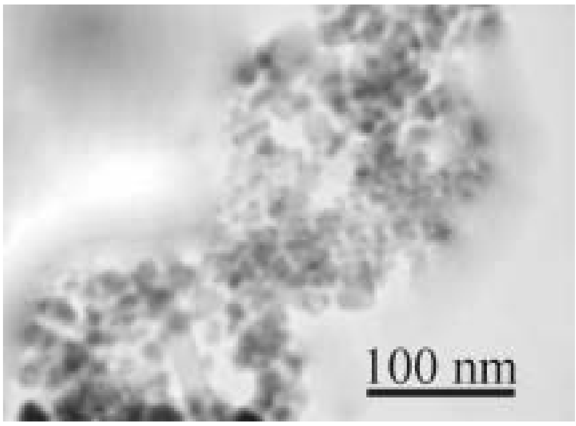

Fig. 4 TEM microphotograph of the Fe-containing nanoparticles stabilized on the surface of PTFE nanogranules.

The particles were analysed using XRD analysis and both diffraction patterns (**Fig. 5 a, b**) indicate the strong peaks of PTFE. **Fig. 5 (a)** shows a diffraction pattern for the sample containing 4.1 wt. % of Fe. There are characteristic peaks of α-Fe, γ-Fe_2O_3, Fe_3O_4, FeF_3 and Fe_3C. For Co-containing nanoparticles on the surface of PTFE, the diffraction pattern in **Fig. 5 (b)** shows hexagonal Co, CoO, Co_3O_4 and CoF_2 phases. XRD studies show that the obtained nanoparticles have a complex composition. That fact may be connected not only with conditions of synthesis but also with interaction between matrix and nanoparticles.

Fig. 6 (a) shows that at room temperature, the coercive force of the sample containing 3.9 wt. % of Co on the PTFE is 300 Oe and increases under cooling reaching the value of 600 Oe at 4.2 K, and the highest magnetization is about 0.4 emu/g (at 6 kOe). **Fig. 6 (b)** presents the temperature dependency of the magnetic moment (M) of the sample. The sample was cooled from 300 K down to 4.2 K without applied magnetic field (ZFC procedure). The magnetic field was then applied and a heating procedure was performed. Above ≈25 K, the temperature behavior of

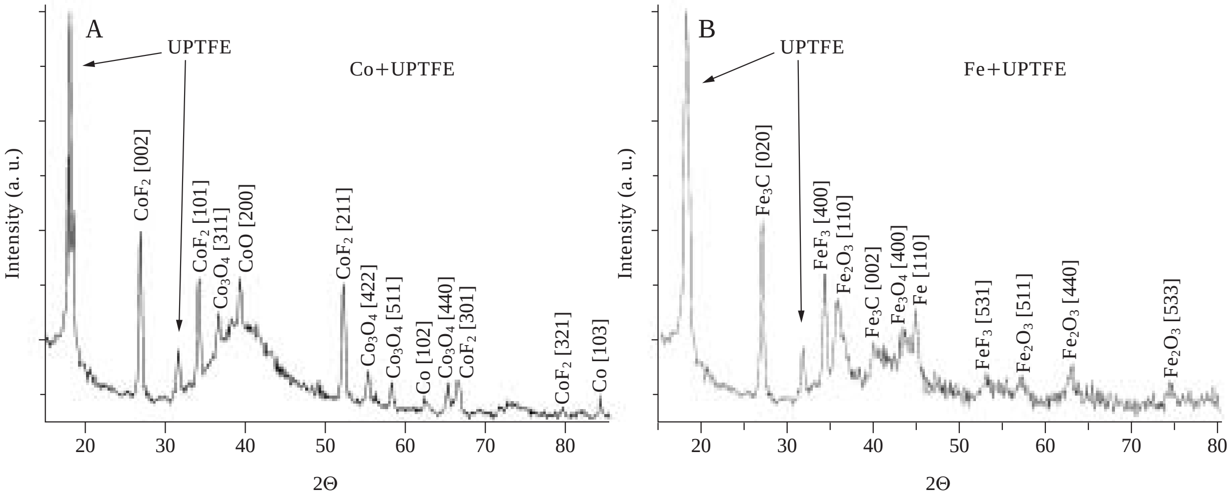

Fig. 5 Diffraction patterns for composite materials Co+UPTFE (a) and Fe+UPTFE (b).

the magnetic moment was typical of ZFC experiments for magnetic single-domain nanoparticles: the magnetic moment grew with temperature increase and reaches a maximum value at a temperature T_{max}. If nanoparticles obey the log-normal size distribution, the temperature of the maximum magnetic moment is approximately equal to the average blocking temperature $<T_B>$. In our case, $T_{max} \approx 270$ K. We can estimate the magnetic anisotropy as $K_V \approx 30\ k_BT/V \approx 5 \cdot 10^6$ J/m^3 (for bulk Co$\approx 10^6$ J/m^3 [33]).

Below 25 K, the magnetic moment demonstrates unusual behavior (**Fig. 6**). We cannot exclude that the sharp increase of M(T) with temperature decreasing might be due to the very small size of nanoparticles, which behave paramagnetically even at low temperatures. Another possible reason is the presence in our nanoparticles of the phase CoF_2. It was found[34] that in bulk CoF_2, the perpendicular magnetic susceptibility significantly grows below the Néel temperature ($\approx$38 K). The magnetic properties of nanoparticles CoF_2 are still unknown, but the general tendency of decreasing the critical magnetic temperatures in nanoparticles in comparison with bulk counterparts does not contradict this hypothesis. **Fig. 6 (c)** shows that at room temperature, the coercive force of the sample containing 5.3 wt. % of Co (from cobalt formate) on the UPTFE is 800 Oe and increases under cooling reaching the value of 1050 Oe at 77 K, and the highest magnetization is about 153 emu/g (at 5 kOe). The received values of coercivity and magnetization are the highest for homometallic nanoparticles.

Fig. 7 (a) shows hysteresis loops at 5 and 300 K for the sample containing 4.1 wt. % of Fe on UPTFE. According to magnetic measurements, Fe-containing nanoparticles demonstrate a typically ferromagnetic behavior. The coercive force at room temperature is $\approx$150 Oe and $\approx$700 Oe at 5 K, and the highest magnetization is about 0.58 emu/g (at 7 kOe). The increase of coercive force under cooling was justified on the basis of the blocking state model. **Fig. 7 (b)** presents the ZFC procedure for Fe+UPTFE sample. The temperature behavior of the magnetic moment was typical for ZFC experiments on magnetic single-domain nanoparticles: the magnetic moment grew with temperature increase and after extrapolation, the average $<T_B>$ is $\approx$765 K. We can estimate the magnetic anisotropy as $K_V \approx 2.3 \cdot 10^7$ J/m^3 (for bulk Fe $K_V \approx 4.5 \cdot 10^6$ J/m^3 [33]).

Fig. 8 shows EPR spectra measured at different temperatures. The spectra have a complex structure, comprising at least from the three components: (1) a typical low-field ferromagnetic resonance (FMR) signal, (2) a relatively narrow line at $g=2.05$ with a peak-to-peak width $DH_{pp} \approx 7 \cdot 10^4$ A/m, and (3) a very broad, poorly resolved line extending up to $6 \cdot 10^5$ A/m. This shows that the nanoparticles are quite uniform in size, the complex structure of the EPR spectrum suggests that the nanoparticles consist of several components. Based on the X-ray diffraction results on the percentages of iron, iron carbide and iron fluoride, we suppose that the relatively narrow EPR signal is due

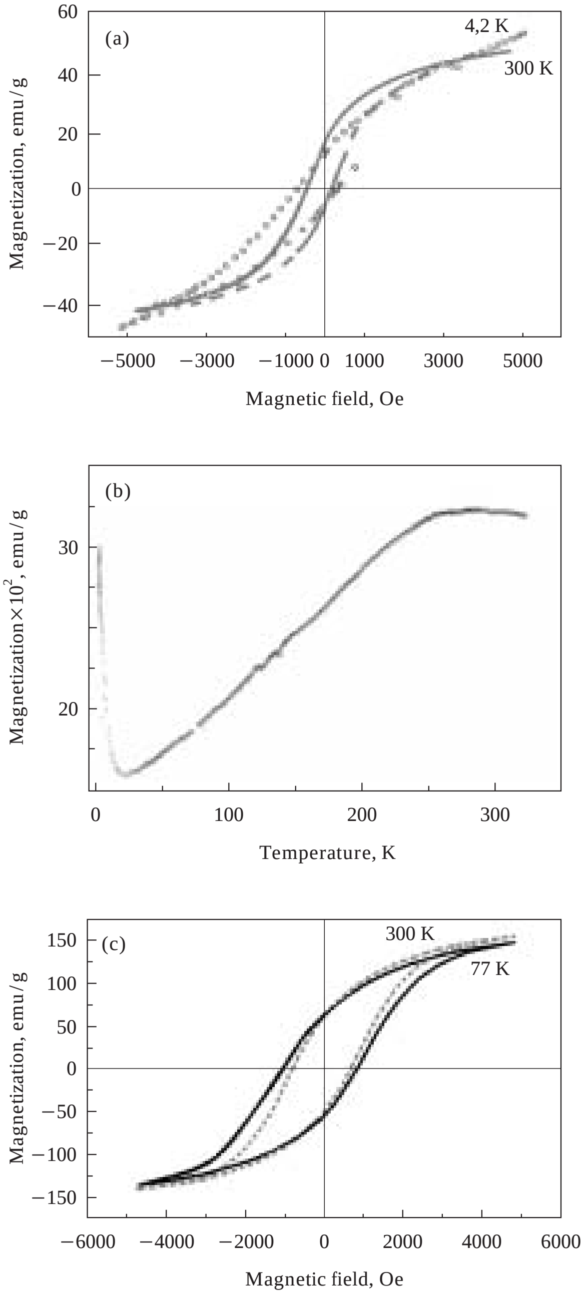

Fig. 6 (a, c) Hysteresis loops and (b) Variation of the magnetic moment with temperature of the Co+UPTFE synthesized from acetate (a, b) and formate (c).

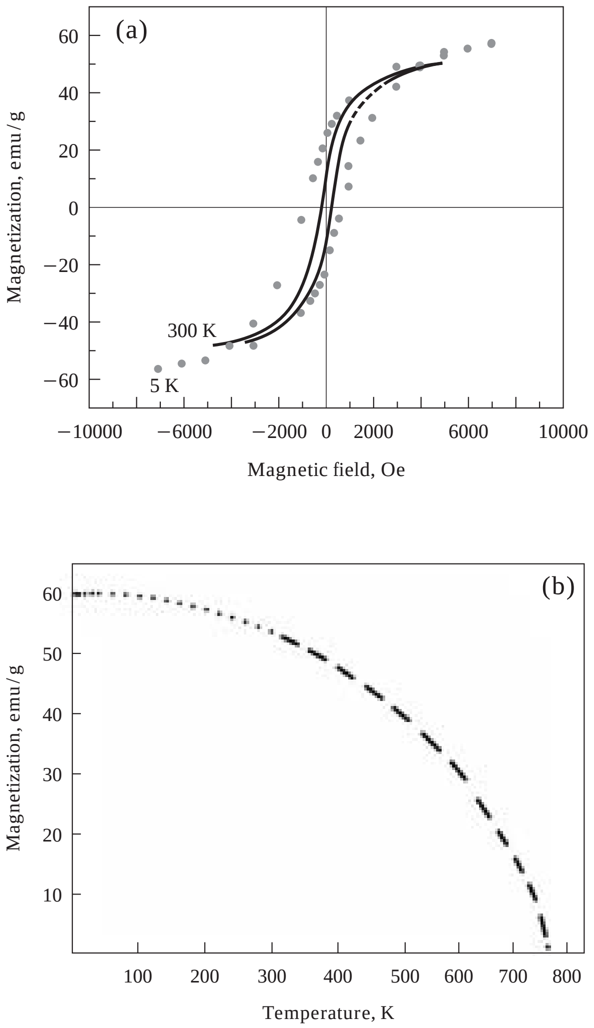

Fig. 7 (a) Hysteresis loops and (b) Variation of the magnetic moment with temperature of the Fe-containing materials.

to iron oxide (which is present in a small amount and, hence, the corresponding regions of the particles are small in size), and that the low-field FMR signal arises from iron carbide (the largest volume fraction in each particle). The broad EPR line is attributable to iron fluoride (since this line was missing in the spectra of Fe nanoparticles in polyethylene[35]), where no fluorine could be present) or a-Fe, which is characterized by a very broad EPR signal[36]). With increasing temperature, the central EPR line becomes even narrower, DH_{pp}≈5·10^4 A/m at 355 K, which is typical of the EPR spectra of nanoparticles. The low-field FMR signal becomes sharper with increasing temperature (**Fig. 8**). **Fig. 9** shows the EPR spectra measured in a magnetic field that was first gradually increased to 4·10^5 A/m and then reduced to zero. Before measurements, the sample was shaken violently to eliminate its initial magnetic moment. It can be seen on **Fig. 9** that, in the course of sample magnetization, the derivative microwave absorption signal does not revert

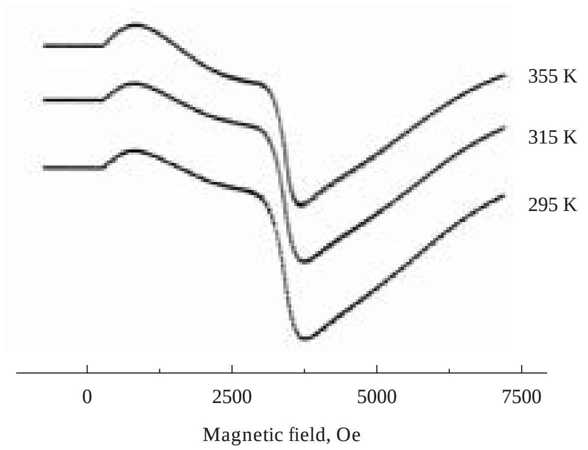

Fig. 8 EPR spectra measured at different temperatures for Fe-containing samples.

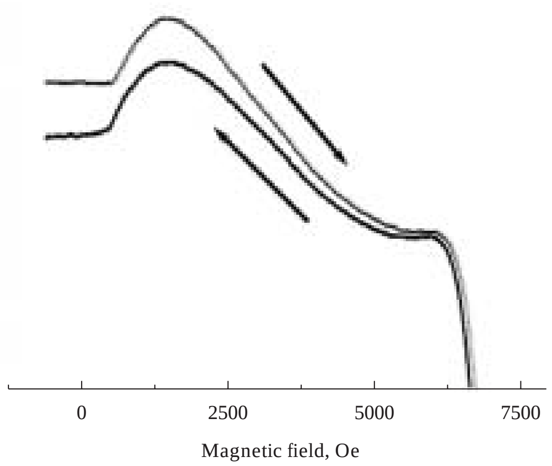

Fig. 9 Microwave absorption hysteresis for Fe-containing samples at room temperature. The arrows indicate the field-sweep direction.

back to its initial level. This attests to a nonzero remanent magnetization $M\mathrm{r}$. Using the method described previously[37)], we obtained $M\mathrm{r}\approx 4\cdot 10^5$ A/m.

The quantum size effect in semiconductor nanoparticles has attracted much attention within the last few years. Besides the research of magnetic properties[38)], proper attention and much time was found for studying the optical properties of semiconductor nanoparticles immobilized in various matrixes[39, 40)]. Therefore, the nanomaterials consisting of nanogranules of PTFE with nanoparticles of cadmium sulfide and cadmium sulfide doped by manganese were also synthesized and investigated during our work. We have been exploring successfully our oil method for the immobilization of such nanoparticles on the surface of PTFE microgranules.

Fig. 10 shows a TEM microphotograph of the sample containing CdS nanoparticles on the surface of PTFE nanogranules. The average size of the particles is 5.0 nm.

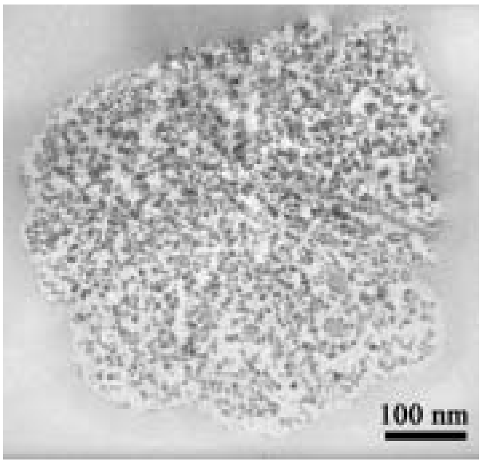

Fig. 10 TEM microphotograph of the sample containing CdS nanoparticles on the surface of PTFE nanogranules.

The particles were analysed using XRD analysis and both diffraction patterns (**Fig. 11**) indicate strong peaks of PTFE. **Fig. 11** shows the diffraction pattern of the sample containing 14.0 wt. % of CdS. There are characteristic peaks of hexagonal CdS. The changes in the absorption spectrum of CdS with changing particle size or with their introduction into the matrix are now well documented[41)].

In **Fig. 12**, a comparison of the variation of the refractive index for nanomaterials on the base of CdS-PTFE nanogranules with a concentration of 14 wt. % of CdS and for bulk crystals of cadmium sulfide are presented. These spectra unambiguously provide evidence that the particles of CdS have a crystalline structure and a good quality from the optical point of view at the same time. In contrast to bulk crystals of CdS[42)] for which the refractive index has a normal character, nanomaterials on the base of CdS-PTFE nanogranules possess an abnormal character in the same spectral range. The detailed interpretation of this result is partially hindered by averaging out the inhomogeneous distributions of size, shape and sur-

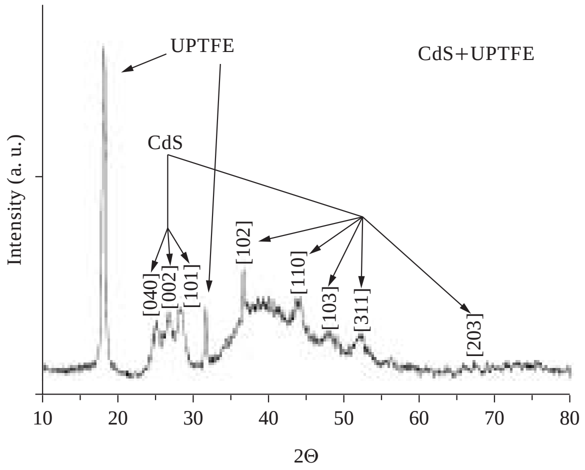

Fig. 11 Diffraction pattern of the sample containing CdS nanoparticles on the surface of the PTFE nanogranules.

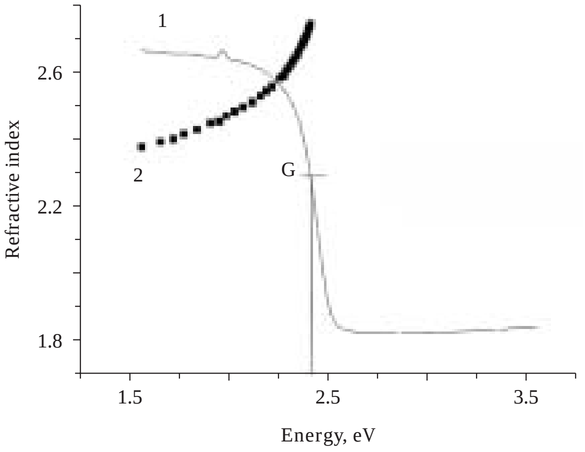

Fig. 12 Comparison of the variations of refractive index for nanomaterials CdS(14 wt. %)-PTFE nanogranules (1) and for bulk crystal of cadmium sulfide (2).

face composition of nanoparticles.

Fig. 13 demonstrates the variations of the refractive index and absorption spectrum of the CdS-PTFE composite. The spectrum shows that a doping by manganese in a quantity up to 2 wt. % from weight of CdS does not change the spectral characteristics as a whole, but leads to a small shift of the absorption edge to the shorter optical wave length.

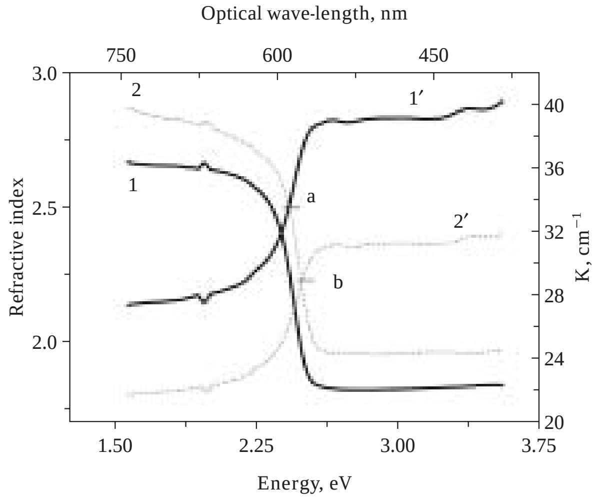

Fig. 13 Absorption spectra and variations in the refractive index of CdS-PTFE composite.

Conclusions

As a result, we made composite materials based on the magnetic and semiconducting nanoparticles stabilized on the surface of PTFE nanogranules.

The obtained magnetic nanoparticles are 4.7 and 3.0 nm in size for Co and 6.0 nm for Fe-containing nanoparticles. Magnetic measurements show that the Fe-based composite material has a rather high blocking temperature ≈765 K and a coercive force of about 700 Oe at 5 K. Co-based materials have a rather high coercive force ≈600 Oe at 4.2 K for the sample synthesized from cobalt acetate, and 1050 Oe at 77 K for the sample obtained from cobalt formate. The received values of coercivity are the highest for homometallic magnetic nanoparticles. All these facts clearly demonstrate that the created nanomaterials with unique magnetic characteristics can be used in the same way as novel composite magnetic materials in which the unique properties of PTFE are supplemented by a high magnetic property.

The obtained semiconducting (CdS) nanoparticles are 5.0 nm in size. The spectral characteristics in visible and near IR regions of spectrum were specified. The influence of doping of nanoparticles by manganese ions on the absorption edge of nanomaterials was investigated. It was shown that such doping increases the width of the forbidden zone of a material on 0.1±0.01 eV. In comparison with bulk cadmium sulfide, the optical dispersion of nanomaterials has an abnormal character, and the ratio of frequency of the optical transition "zone-zone" to width of a line of absorption was 3.56, i.e. much less than for bulk materials. The measured index of refraction of nanomaterials containing 14 wt. % of CdS on the surface of PTFE nanogranules was 2.3, that practically agrees with an index of refraction of the bulk cadmium sulfide. Thus, by means of spectroscopy, the important properties of synthesized nanomaterials were specified. It is shown that semiconductor high-quality nanoparticles can be grown on the surface of a PTFE dielectric matrix. The obtained microgranule-nanopowders can be used as engineered nanopowders to meet the needs for new nanomaterials in biotechnology, sensors, optical transistors, optical switches, optical computing, photovoltaics, light emitting diodes (LEDs), shielding from UV-radiation, lasers or many other nano applications.

Acknowledgements

The experimental and theoretical analysis of the magnetic and optical properties of nanoparticles is the result of a close collaboration with Dr. Yu.A. Koksharov and Prof. N.M. Ushakov, respectively. The authors would like to acknowledge them.

This work was financed by the Russian Foundation for Basic Research (grant nos. 04-03-32090, 05-03-32083), «Russian Science Support Foundation», the President of Russian Federation grant MK-2733. 2005. 3, the Russian Academy of Sciences through the basic research program «Critical Issues in the Physics and Chemistry of Nanoscale Systems and Nanomaterials» and «The directed synthesis of inorganic substances with the set properties and creation of functional materials on their basis».

References

1) Cao, Y.W.C.; Jin, R.C. and Mirkin C.A.: Science, 297. 1536 (2002).
2) Alivisatos, A.P.: Nat. Biotechnol., 22. 47 (2004).
3) Tessler, N.; Medvedev, V.; Kazes, M.; Kan, S.H. and Banin, U.: Science, 295. 1506 (2002).
4) Klimov, V.; Mikhailovsky, A.; Xu, S.; Malko, A.; Hollingsworth, J.A.; Leatherdale, C.A.; Eisler, H.J. and Bawendi, M.G.: Science, 290. 314 (2000).
5) Kazes, M.; Lawis, D.Y.; Ebenstein, Y.; Mokari, T. and Banin, U.: Adv. Mater., 14. 317 (2002).
6) Yin, Y.; Rioux, R.M.; Erdonmez, C.K.; Hughes, S.; Somorjai, G.A. and Alivisatos, A.P.: Science, 304. 711 (2004).
7) Martin, J.I.; Nogues, J.K.L.; Vicent, J.L. and Schuller, I.K.: J. Mag. Mag. Mater., 256. 449 (2003).
8) Kryszewski, M. and Jeska, J.K.: Synth. Met., 94. 99 (1998).
9) Park, I.W.; Yoon, M.; Kim, Y.M.; Kim, Y.; Kim, J.H.; Kim, S. and Volkov, V.: J. Mag. Mag. Mater., 272-276. 1413 (2004).
10) Respaud, M.; Broto, J.M.; Rakoto, H.; Fert, A.R.; Thomas, L.; Barbara, B.; Verelst, M.; Snoeck, E.; Lecante, P.; Mosset, A.; Osuna, J.; Ould Ely, T.; Amiens, C. and Chaudret, B.: Phys. Rev. B, 57. 2925 (1998).
11) Fitz-Gerald, J.M.; Singh, R.K.; Gao, H. and Pennycook, S.J.: Kona, no. 17. 173 (1999).
12) Igarashi, T.; Kusunoki, T.; Ohno, K.; Isobe, T. and Senna, M.: Mater. Res. Bull., 36. 1317 (2001).
13) Ramesh, S.; Sominska, E. and Gedanken, A.: Utrason. Sonochem., 9. 61 (2002).
14) Sun, Y.-K.; Lee, Y.-S.; Yoshio, M. and Amine, K.: Electrochem. Solid-State Lett., 5. A99 (2002).
15) Fu, X. and Qutubuddin, S.: Colloids Surf. A., 178. 151 (2001).
16) Diaz, G.; Perez-Hermandez, R.; Gomez-Cortes, A.; Benaissa, M.; Mariscal, R. and Fierro, J.L.G.: J. Catal., 187. 1 (1999).
17) Deraz, N.M.: Colloids Surf. A, 190. 251 (2001).
18) Xuegang, L.; Gongying, L.; Zhanbo, S. and Wei, Z.: Materials Science and Engineering B, 117. 147 (2005).
19) O'Connor, C.J.; Sims, J.A.; Kumbhar, A.; Kolesnichenko, V.L.; Zhou, W.L. and Wiemann, J.A.: J. Mag. Mag. Mater., 226-230. 1915 (2001).
20) Jordan, J.; Jacob, K.I.; Tannenbaum, R.; Sharaf, M.A. and Jasiuk, I.: Materials Science and Engineering A, 393. 1 (2005).
21) Tianbo, L.; Burger, C. and Chu, B.: Progress in Polymer Science, 28. 5 (2003).
22) Panshin, Yu.A.; Malkevich, S.G. and Dunaevskaja, Ts.S.: "Ftoroplasty", Khimija, Leningrad, Russia (1978).
23) Tsvetnikov, A.K.; Uminskii, A.A. and Tsarev V.A.: RU Patent 1763210.
24) Tsvetnikov, A.K.: RU Patent 2035308.
25) Tsvetnikov, A.K. and Uminskii, A.A.: RU Patent 1775419.
26) Tsvetnikov, A.K.; Bouznik, V.M. and Matveenko, L.A.: RU Patent 2100376.
27) Bouznik, V.M.; Fomin V.M.; Alhimov A.P. et al.: Matallopolimernye nanokompozity (poluchenie, stroenie, primenenie). Izdatelstvo SO RAS, Novosibirsk, Russia (2005).
28) Kosobudskii, I.D. and Gubin, S.P.: Vysokomol. Soedin., 27. 689 (1985).
29) Gubin, S.P.; Yurkov, G.Yu. and Kosobudsky, I.D.: International Journal of Materials and Product Technology, 23. 2 (2005).
30) Gubin, S.P.; Spichkin, Yu.I.; Yurkov, G.Yu. and Tishin, A.M.: Russian Journal of Inorganic Chemistry, 47 (suppl. 1). 32 (2002).
31) Gubin, S.P.; Korobov, M.S.; Yurkov, G.Yu.; Tsvetnikov, A.K. and Bouznik, V.M.: Doklady Chemistry, 388. 44 (2003).
32) Gubin, S.P.; Yurkov, G.Yu.; Korobov, M.S.; Koksharov, Yu.A.; Kozinkin, A.V.; Pirog, I.V.; Zubkov, S.V.; Kitaev,

V.V.; Sarichev, D.A.; Bouznik, V.M. and Tsvetnikov, A.K.: Acta Materialia, 53. 1407 (2005).
33) Skomski, R.: J. Phys.: Condens. Matter, 15. R841 (2003).
34) Lines, M.E.: Phys. Rev. 137. A982 (1965).
35) Koksharov, Yu.A.; Gubin, S.P.; Kosobudsky, I.D.; Beltran, M.; Khodorkovsky, Y. and Tishin, A.M.: J. Appl. Phys., 88. 587 (2000).
36) Grinstaff, M.W.; Salamon, M.B. and Suslick, K.S.: Phys. Rev B, 48. 269 (1993).
37) Koksharov, Yu.A.; Blyumenfel'd, L.A.; Tikhonov, A.N. and Sherle, A.I.: Zh. Fiz. Khim., 73. 1856 (1999).
38) Gubin, S.P.; Koksharov, Yu.A.; Khomutov, G.B. and Yurkov, G.Yu.: Russian Chemical Reviews, 6. 1 (2005).
39) Gubin, S.P.; Kataeva, N.A. and Khomutov, G.B.: Russian Chemical Bulletin, 4. 1 (2005).
40) Klimov, A.: J. of Luminescence, 70. 1 (1996).
41) Yoffe, A.D.: Adv. in Phys., 42. 173 (1993).
42) Shakolskaia, M.P.: Acoustical crystals. Izdatelstvo Nauka, Moscow, Russia (1982).

Author's short biography

S.P. Gubin

Sergey Pavlovich Gubin was born in 1937 in Moscow. He is a professor and head of the Nanomaterials Chemistry lab of the N.S. Kurnakov Institute of General and Inorganic Chemistry of Russian Academy of Sciences, Moscow, Russia. He received his BSc and PhD degrees from the Chemical Department of M.V. Lomonosov Moscow State University and his DSc degree from the A.N. Nesmeianov Institute of Organo-Element Compounds of the Russian Academy of Sciences, Moscow, Russia. His research has been reported in more than 400 primary publications and summarized in 10 review articles and four books and 6 inventions. Professor Gubin's current research focuses on clusters, nanoparticle chemistry and nanomaterials.

I.P. Dotsenko

Dotsenko Ivan Petrovich was born in 1984 in Moscow (Russia). In 2001, he completed his school studies with an in-depth study of foreign languages and simultaneously attended the evening school of the Moscow Chemical Lyceum. In 2001, he entered the Higher Chemical College of the Russian Academy of Sciences and in 2005, he received his bachelor of science degree (chemistry). He is now studying for his master's degree. From February of 2002 till the present, he has been working as a senior laboratory assistant in the Nanomaterials Chemistry Laboratory of the N.S. Kurnakov Institute of General and Inorganic Chemistry, Russian Academy of Sciences. Science interests: metal-containing nanoparticles, magnetic and electrophysical properties of nanomaterials. Ivan P. Dotsenko is an author of 3 articles and a number of abstracts for international conferences.

G.Yu. Yurkov

Gleb Yurjevich Yurkov was born in 1976 in Grozny. In 1998, he graduated from the N.G. Chernishevsky Saratov State University. He received his PhD in inorganic chemistry in 2002 at the N.S. Kurnakov Institute of General and Inorganic Chemistry, Russian Academy of Sciences under the supervision of Professor S.P. Gubin. He is currently a senior researcher at the Nanomaterials Chemistry Laboratory at the N.S. Kurnakov Institute of General and Inorganic Chemistry, Russian Academy of Sciences. His main research interests include inorganic chemistry, the stabilization of nanoparticles, the synthesis and investigation of gomo- and getero-metallic nanoparticles and composite materials on the basis of nanoparticles and polymer matrixes. His research has been reported in more than 30 articles in international and Russian scientific journals and in 1 invention.

Author's short biography

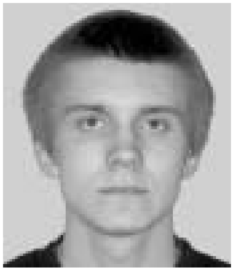

D.A. Baranov

Baranov Dmitry Alexandrovich was born in 1986 in Obninsk (Russia). In 2003, he completed his school studies. In 2003, he entered the Higher Chemical College of the Russian Academy of Sciences. From January of 2004 till the present, he has been working as a senior laboratory assistant in the Nanomaterials Chemistry Laboratory of the N.S. Kurnakov Institute of General and Inorganic Chemistry, Russian Academy of Sciences. Science interests: core-shell nanoparticles, magnetic and optical properties of nanomaterials. Dmitry A. Baranov is an author of 3 articles and a number of abstracts for international conferences.

N.A. Kataeva

Kataeva Nadezhda Anatolievna was born in 1975 in Syktyvkar. In 1997, she graduated from the Chemical-biological Faculty of the Syktyvkar State University. She received her PhD in inorganic chemistry in 2002 at the N.S. Kurnakov Institute of General and Inorganic Chemistry, Russian Academy of Sciences. She is currently a researcher at the Nanomaterials Chemistry Laboratory at the N.S. Kurnakov Institute of General and Inorganic Chemistry, Russian Academy of Sciences. Her main research interests include inorganic chemistry, nanoparticles, the chemistry of new inorganic functional materials. Nadezhda A. Kataeva is the author of more than 10 articles in scientific journals.

A.K. Tsvetnikov

Tsvetnikov Alexander Konstantinovich was born in 1950 in Khabarovsk. He has been a head of the Fluorine of Carbon Materials Group of Institute of Chemistry FEB RAS, Vladivostok, Russia since 1992. In 1971, he graduated from the Far East State University, Vladivostok. He became an employee of the Institute of Chemistry FEBRAS in 1974. He received his PhD in inorganic chemistry in 1998 at the Institute of Chemistry FEB RAS, Vladivostok, Russia. Alexander K. Tsvetnikov is the author of more than 40 articles in scientific journals and book chapters and 30 inventions. He is also the author of technology and the head of pilot production nanofluoropolymers FORUM®.

V.M. Bouznik

Bouznik Viacheslav Mikhailovich was born in 1945. In 1967, he graduated from the State University of Tomsk. He received his PhD in physics and mathematics in 1972; his doctor of sciences in chemistry in 1985; became a corresponding member of RAS in 1994; and a full member of RAS in 1997. He worked in scientific organizations of the Krasnoyarsk Science Center of the Siberian Branch of RAS: Institute of Physics, Institute of chemistry and chemical technology from 1968 to 1990, Krasnoyarsk. He was director of the Institute of Chemistry of the Far Eastern Branch of RAS from 1990 to 1995, Vladivostok. He was a member of the Presidium of FEB RAS from 1995 to 1996, Vladivostok. Since 1996, he has been chairman of the Presidium of Khabarovsk Science Center FEB RAS and head of the fluoride materials laboratory in the Institute of Chemistry FEB RAS – Chemistry of inorganic materials. He is a specialist in the physical chemistry of inorganic materials and in nuclear-spectral methods of research. Scientific interests: nuclear-spectral methods of investigation of materials, sustainable development, small hi-tech business, small forms of production in scientific organizations. His research has been reported in more than 200 articles in international and Russian magazines, among these are 3 monographs and 10 inventions.

The Influence of Force Control Agents on the Cohesive-Adhesive Balance in Dry Powder Inhaler Formulations[†]

P. Begat and R. Price[1]
Pharmaceutical Technology Research Group
Department of Pharmacy & Pharmacology
*University of Bath**
H. Harris, D.A.V. Morton
and J.N. Staniforth
*Vectura Ltd.***

Abstract

The aim of the study was to investigate the specific influence of force control agents (FCAs) (leucine, lecithin and magnesium stearate) on the interfacial properties of a salbutamol sulphate-lactose dry powder inhaler formulation. The influence of FCAs on the cohesive and adhesive force balance was directly assessed via an atomic force microscopy (AFM) colloid probe technique, with a recently developed cohesive-adhesive balance (CAB) graphical analysis procedure. Co-processing of constituent particles was conducted by a novel dry mechanical fusion method (Mechanofusion). The ***in vitro*** *deposition profile of the model salbutamol sulphate formulations was investigated using a Monohaler® DPI device with a next generation impactor (NGI) apparatus. The CAB-graph analysis of a salbutamol sulphate-lactose binary system suggested a predisposition for an interactive mixture. However, the reduced intermixing coefficient ($F_{drug\text{-}lactose}/F_{drug\text{-}drug}$) suggested that a significant amount of energy would be required to overcome the strong adhesive interaction for efficient dispersion of the drug from a lactose surface. The processing of lactose with leucine, lecithin or magnesium stearate, prior to formulating with the drug, significantly reduced the adhesive interactions of the salbutamol with modified lactose samples. The CAB analyses indicated that the reduced intermixing coefficients shifted to such an extent that cohesive drug interactions dominated. These dramatic shifts in the balance of forces were shown to lead to poor blend homogeneity and potential for significant segregation between drug and carrier particles. Conversely, the conditioning of salbutamol sulphate with leucine, lecithin and magnesium stearate, which modified both the adhesive and cohesive interactions, formed homogenous interactive blends with advantageously weaker drug-lactose interactions. Formulations with pre-conditioned drug, in contrast to conditioned lactose, offered the best drug delivery performances. The use of the colloid AFM technique in combination with the cohesive-adhesive balance (CAB) approach provided a very accurate means of predicting dry powder formulation behaviour and the specific influence of particulate interactions on aerosol performance.*

Key words: Inter-particulate, AFM, Magnesium stearate, DPI, Inhalation, Aerosols, Mechanofusion, Nanotechnology

INTRODUCTION

Dry powder inhalers (DPIs) represent a significant advance in pulmonary drug delivery, mainly by overcoming patient related issues of co-ordination with conventional pressurised metered dose inhaler systems. The fluidisation, de-aggregation and dispersion of a dry powder formulation are achieved via the patient's inspiratory action. Arguably more so than

---

[†] Accepted: August 12, 2005

* Bath, BA2 7AY, UK
** 1 Prospect West, Chippenham, SN14 6FH, UK
[1] Corresponding author
TEL: +44 (0) 1225 383644
FAX: +44 (0) 1225 386114
E-mail: r.price@bath.ac.uk

other drug delivery platforms, the characteristic properties of the dry powder formulation are critically important to the effective performance of a DPI system[1, 2].

The formulation should exhibit good flow properties to aid metering, fluidisation and avoid excessive device retention. Meanwhile, the fluidised powder must disperse into a fine aerosol (Ø·5·m) for efficient drug delivery[3, 4]. This leads to the well-known paradox that respirable sized particles tend to be highly cohesive, which causes entrainment problems due to their poor flowability and limits the dispersibility into an aerosol cloud[5, 6]. In addition, strong cohesion forces hinder the handling of the powder during manufacture.

To overcome the highly cohesive nature of respirable powders, the drug is commonly co-processed (blended) with larger carrier particles of an inert excipient to aid flowability and drug re-dispersion. This carrier based formulation approach is limited by the restrictive availability of excipient materials. The only widely approved excipients for use as carriers are lactose and glucose. Thus, the development of a dry powder formulation is a highly specialised, complex and unpredictable operation. A formulation is typically required to go through several iterative and optimisation steps before a product specification can be achieved, and even then variability over time and between batches is common.

By blending a micronised drug with a carrier, the shear forces generated may be sufficient to overcome the cohesive (drug-drug) interactions in forming an interactive mixture. Drug particles need to be sufficiently attracted to the carrier during mixing to support blend homogeneity, device filling and formulation stability. Yet the active ingredient must be readily detached from the carrier upon activation to form a fine particle cloud. Thus, the balance of inter-particulate forces within the carrier-based formulation is critically important.

Numerous techniques have been applied to modify particulate interactions in dry powder formulations. The majority have targeted the physical properties of the carrier. These include modifying the shape[7], size[8], or surface features such as rugosity[9-12] of the excipient. Other methods involve the manufacture of more uniform respirable drug particulates by particle engineering technologies such as spray drying[13] or supercritical fluid precipitation[14]. One of the most simple and popular advances is via the addition of a ternary agent, such as fine particles of lactose. For these complex blends, it is proposed that the ternary agent occupies high energy sites on the carrier particles, such as clefts and areas of increased molecular disorder[15, 16]. As a consequence, only low energy sites remain available for drug-carrier adhesive interaction. The possibility of a marked reduction in particle adhesion would facilitate more effective drug detachment upon device actuation. Extensive work on the use of fines in dry powder formulations and their influence on delivery performances have been reported[17-19].

In addition to passifying active sites, researchers have shown that the addition of fine ternary particles may lead to the formation of fine particle multiplets or metastable agglomerates[20]. The critical formation of agglomerate particles, which remain adhered to the coarse carrier lactose during processing and handling, may dramatically reduce the inspirational energy requirements in elutriating and de-aggregating drug particles upon aerosolisation.

The co-processing of carrier particles with low surface free energy materials has also been reported as a possible means of increasing the aerosolisation efficiencies of dry powder inhaler formulations[19, 21, 22]. The primary role of these materials is to modify the interfacial properties of the excipient particles to decrease drug-excipient adhesion. These force control agents (FCAs) preferably exhibit anti-adherent and/or anti-friction properties. Typical FCAs include amino acids such as leucine, phospholipids such as lecithin or fatty acid derivatives such as magnesium stearate (MgST)[23].

To optimise the efficiency of a carrier based formulation, the force control agent must be specifically introduced into the dry powder formulation to selectively target the particle interactions to be modified. In this study, the FCA was mechanically fused via a highly intensive co-processing system termed “Mechanofusion” to ensure a nanometre thick coating of the specific components of the formulation[24]. This approach was recently developed by Staniforth and Morton for inhalation powders[25]. In contrast to other low energetic mixing or even intensive mixing, this dry coating process is designed to provide a relatively complete ultra thin coating onto the host particles via the application of high shear forces (**Fig. 1**). Succinctly, a Mechanofusion mixer is composed of a large rotor with rounded blades revolving in a steel vessel at very high speed (typically of the order of 5000rpm). The gap size between the rotor blades and the vessel wall can be adjusted in order to vary the mixing energy delivered to the powder blend. As a result, the particles experience very high shear

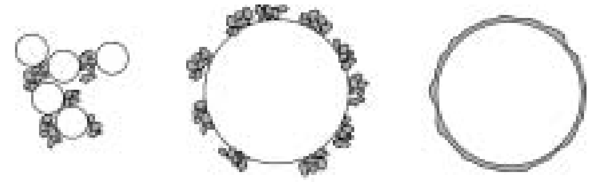

Fig. 1 Schematic representation of Mechanofusion particle mixing mechanisms.

forces as they are compressed between the inner drum wall and the rotor.

The aim of this study was to investigate the specific influence of force control agents (leucine, lecithin and magnesium stearate) on the interfacial properties of a salbutamol sulphate-lactose dry powder inhaler formulation. The influence of the FCAs on the cohesive and adhesive force balance was directly assessed via an AFM colloid probe technique, with a recently developed CAB-graph analysis procedure. This novel procedure allows quantification of cohesive-adhesive balances (CAB) in a dry powder formulation[26], and, thus, can be directly utilised to highlight their specific affect on formulation behaviour and delivery characteristics[27]. The *in vitro* deposition profile of the model salbutamol sulphate formulations was investigated to elucidate any correlation between the cohesive and adhesive nature of the modified formulations with their aerosol delivery performance.

MATERIALS AND METHODS

Materials

Micronised salbutamol sulphate, donated by Vectura Ltd., and Sorbalac 400 lactose (Meggle, Wasserburg, Germany) were used as supplied. The use of Sorbalac 400 lactose particles (<10μm) with respect to more conventional carrier sizes (63-90μm) was dictated by the need to minimise the potential influence of larger carrier particles over fluidisation and de-aggregation processes of particle agglomerates. L-Leucine was supplied from Ajinomoto Co. (batch number 601FK72, Tokyo, Japan), lecithin from Lipoid GmbH (batch number 25661113-1/14, Ludwigshafen, Germany) and magnesium stearate from Avocado (batch number H1028A, Heysham, UK). All materials were used as supplied. Ultra pure water was produced by reverse osmosis (MilliQ, Millipore, Molsheim, France).

Preparation of powder formulations

Powder mixing was achieved in two successive steps involving different energetic processes. Preblends of salbutamol sulphate and FCA (5% w/w) or lactose and FCA (5% w/w) were prepared using a Mechanofusion system. (Hosokawa-Alpine, Augsburg, Germany). Powders to be processed were sealed into the Mechanofusion system core. Cold-water circulation was applied using an incorporated water jacket to dissipate localised heating. Samples were mixed at 5000rpm for 10 minutes to achieve the required process intensity and mechanically fuse the FCA to the host particles.

The formulations were subsequently prepared by geometrically mixing 1g of pre-blend and 1g of either lactose or drug depending on the nature of the preblend in 100mg increments via a Whirlimixer (Fisons Scientific Apparatus, Loughborough, UK). The resulting mixture was further mixed in a Turbula (Glen Creston Ltd., Middlesex, UK) at 46rpm for 30 minutes. This blend design was not intended to reflect any commercial available or relevant DPI powder formulation. This formulation was selected solely to suit the objectives of the study of the cohesive-adhesive balance between drug and lactose components.

Preparation of compressed powder substrates

Model surfaces of the powder formulations were prepared by high-pressure compression (TA HDI Texture analyser, Stable Micro Systems, Surrey, UK). Approximately 250mg of material was weighed into a 10mm stainless steel die and compacted over 3min, with a load of 500kg.

Scanning electron microscopy

The morphology of the various powder formulations of was investigated using a scanning electron microscope (SEM) (Jeol 6310, Jeol, Tokyo, Japan). Samples were gold-coated (Edwards Sputter Coater, Crawley, UK) prior to imaging.

Force measurements by atomic force microscopy (AFM)

Prior to force measurements, salbutamol sulphate, lactose and the corresponding conditioned particles ($n=3$ for each material) were fixed onto standard V-shaped tipless cantilevers (DNP-020, Digital Instruments, CA, USA) using an epoxy resin glue (Araldite, UK). The spring constant (k) of the cantilevers was determined by the thermal noise method ($k=0.282 \pm 0.039$N/m)[28, 29].

The AFM was housed in an environmental chamber to maintain constant temperature of 25℃ (±0.2℃) and relative humidity of 35% RH (±3%). The partial water vapour pressure was controlled via a custom-built perfusion unit coupled to a highly sensitive humidity sensor (Rotronic AG, CH). The interaction forces were measured by recording the deflection of the AFM cantilever as a function of the substrate displacement (z) by applying Hooke's law ($F=-kz$). Individual force curves ($n=4096$) were conducted over a 10μm×10μm at a scan rate of 4Hz and a compressive loading of 10nN. These parameters were kept constant throughout the study.

Cohesive-adhesive balance (CAB) graphs

The wealth of information from AFM measurements of the interparticulate forces were analysed using a recently developed cohesive-adhesive balance procedure. Detailed information regarding the CAB graphical analysis is described elsewhere[26]. Briefly, the construction of a CAB-graph requires a set of probes (n·3) and well-defined substrates of each respective material to investigate all possible interactions (drug-drug, drug-excipient and excipient-excipient).

The adhesive force measurements between drug and excipient are plotted on the X-axis; the related cohesive forces of the respective materials are plotted on the Y-axis. The relative position of the aligned plots with respect to the bisector indicates an affinity for the probe material to develop adhesive interactions (below the bisector.) or a dominancy of cohesive properties (above the bisector).

To express the affinity of the drug (material 1) to interact with the carrier (material 2), the reduced intermixing coefficient (Λ_{12}) was introduced. The Λ_{12} corresponds to the ratio of the adhesive interactions (F_{12}) and cohesive interactions (F_{11}) of two interacting materials and can be directly calculated from the slope:

$$\Lambda_{12}=\frac{F_{12}^{ad}}{F_{11}^{co}}=\frac{1}{k_{12}} \qquad (1)$$

The position of Λ_{12} with respect to unity is a direct indication of the predisposition ($\Lambda_{12}>1$) or the reluctance ($\Lambda_{12}<1$) for the drug particles to blend with another material.

For direct visualisation of the influence of the addition of the FCA on the interfacial behaviour of drug and excipient interactions, the CAB graphs for the virgin and treated surfaces have been superimposed. The graph in the foreground corresponds to the interactions observed between the micronised drug (●) and lactose (▼) probes and the virgin substrate surfaces of the drug and excipient (**Fig. 1**). The background graph corresponds to the interaction measurements when a ternary agent was processed either with the drug (○) or the lactose (▽).

Content uniformity measurements

The content uniformity of the salbutamol sulphate-lactose blends was measured by analysing the quantity of active in 10mg±0.5mg samples (×10). Relative standard deviation between samples was calculated to assess the homogeneity of the different blends. Drug content was analysed by UV-spectrometry (CECIL instruments, CE7200, Cambridge, UK). Salbutamol sulphate was analysed using a 0.06M NaOH solvent and a UV detection wavelength set at 295nm.

In vitro aerosol deposition studies

Approximately 10mg of the carrier formulations was accurately weighed into a gelatine capsule to be loaded into a Monohaler® device (Miat SpA, Milan, Italy). *In vitro* deposition investigations were performed using a next generation impactor (NGI) (Copley Scientific, Nottingham, UK). The loaded device was connected to the throat of the NGI via a moulded mouthpiece. *In vitro* analysis was performed upon each actuation of the device ($n=3$). Testing was performed at 60L.min^{-1} flow rate with a 5 second exposure. Each NGI plate was rinsed with solvent and the subsequent solution was collected in a 50ml volumetric flask. Statistical analysis of the data was performed using one-way ANOVA. The levels of significance are indicated in the legend of the respective graphs.

RESULTS & DISCUSSIONS

Previous studies have emphasized the relative strength of the adhesive salbutamol sulphate-lactose adhesive forces with respect to salbutamol sulphate cohesive forces[26]. The initial part of this study was to investigate possible variations in formulation behaviour upon modifying the cohesive and adhesive bonds, quantified by AFM measurements, via the introduction of a force control agent. This was achieved by first conditioning the lactose with various force control agents using a Mechanofusion system, prior to mixing with the drug.

The CAB-graph obtained for a salbutamol sulphate-lactose binary system, without the presence of a FCA, is shown in **Fig. 2**. The relative position of the data below the bisecting line indicated a stronger affinity

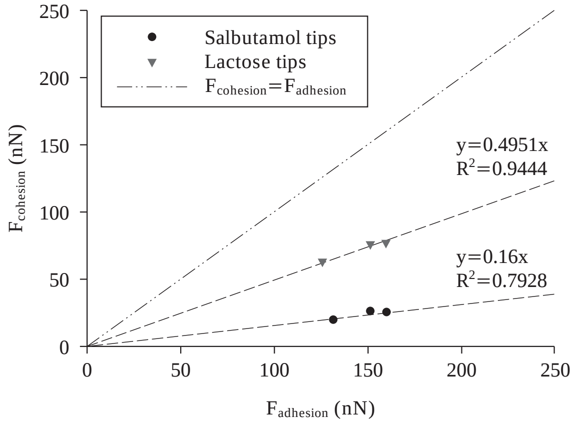

Fig. 2 CAB-graph of a salbutamol sulphate lactose binary system (with the use of compressed tablet substrates).

between salbutamol sulphate and lactose than their cohesive forces. This suggested a predisposition for an ordered blend. However, the quantitative measurement of the relative strength of the cohesive-adhesive ratio indicated that the adhesive salbutamol sulphate-lactose interaction was approximately six times greater ($\Lambda_{12}=6.25$) than the cohesive salbutamol sulphate bond. It should be stressed that previous assessments performed with model crystal substrates revealed a salbutamol sulphate-lactose reduced intermixing coefficient of 16.88[27]. This disparity may be explained by the inevitable increase in surface roughness by using compressed powder substrates in contrast to smooth crystalline substrates. This would have a considerable effect on both van der Waals forces and capillary forces[30, 31]. Nevertheless, both studies revealed a consequent adhesively led system, suggesting that a significant amount of energy would be required to overcome the adhesive interaction for efficient dispersion of the drug from a lactose surface.

Thus, the introduction of a FCA was intended to advantageously lower the adhesive interactions between drug and excipient to facilitate the detachment of the drug particles from the carrier upon aerosolisation provided that an adhesive-led system is maintained.

1. Carrier-based formulations with conditioned lactose

The CAB-graphs obtained for the interaction of salbutamol sulphate probes and conditioned lactose probes with leucine, lecithin and MgST are shown in **Fig. 3A**, **3B** and **3C**, respectively. As expected,

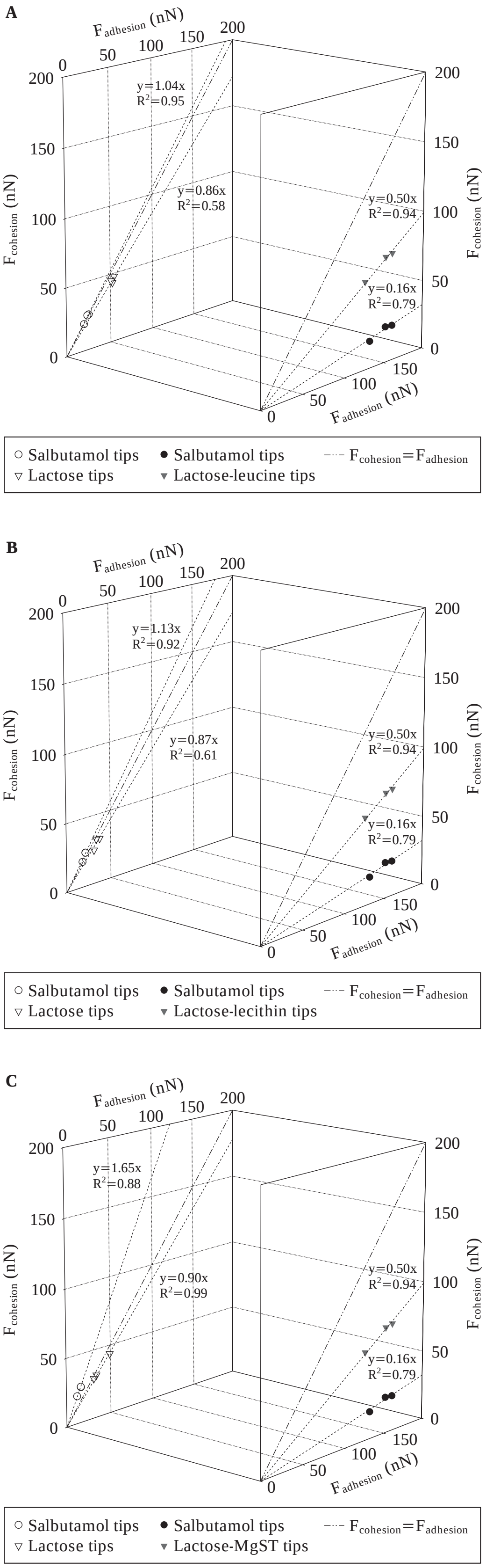

Fig. 3 Influence of the coating of lactose with a force control agent on the cohesive-adhesive balances in a salbutamol sulphate-lactose system.

the addition of FCAs significantly modified the salbutamol-lactose interactions. In all cases, the introduction of the ternary agent significantly reduced the adhesive interactions of the salbutamol probe with the various modified lactose substrates. However, particle adhesion decreased to such an extent that the reduced intermixing coefficient ($F_{drug\text{-}lactose}/F_{drug\text{-}drug}$), calculated from the gradient of the CAB plots, was below 1 (**Table 1**). This shift moved the CAB system to one synonymous of a cohesive-led system. The conditioning of lactose with MgST resulted in the lowest intermixing coefficient value ($\Lambda_{12}=0.61$) while the addition of leucine and lecithin reduced the intermixing coefficient to 0.96 and 0.88, respectively. Thus, the pre-conditioning of lactose particles with leucine, lecithin or MgST transformed a system which was dominated by the adhesive drug-lactose forces into a cohesive system. Such lowering of the interactions between drug and excipient via the introduction of the FCAs may possibly lead to an unstable formulation, subjected to undesirable segregation.

Consequently, to highlight the influence of the modifications of the intermixing coefficient on the blending characteristics via the introduction of FCAs, scanning electron microscopy and drug content uniformity analyses of the blends were investigated. Representative SEM images of formulations of salbutamol sulphate mixed with lactose-leucine, lactose-lecithin and lactose-MgST conditioned particles are shown in **Fig. 4A**, **4B** and **4C**, respectively. As anticipated from the intermixing coefficient measurements, scanning electron micrographs highlighted a high degree of drug segregation resulting from introduction of the FCAs. A very limited adhesive interaction was apparent between agglomerated salbutamol sulphate particles and conditioned lactose-leucine (**Fig. 4A**). However, large quantities of drug particles were present as loose agglomerates. This segregation was even more pronounced for lecithin (**Fig. 4B**) and MgST (**Fig. 4C**) conditioned lactose particles. Virtu-

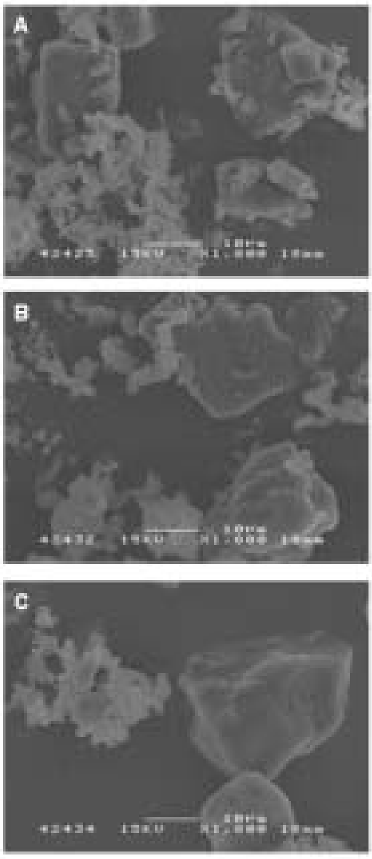

Fig. 4 Representative scanning electron micrographs of ternary mixtures of salbutamol sulphate and lactose pre-conditioned with leucine (A), lecithin (B) or magnesium stearate (C).

Table 1 Mixing sequences of salbutamol, lactose, force control agent formulations and resulting reduced intermixing coefficients and content uniformities.

Conditioning	Mixing	Reduced intermixing coefficient (Λ_{12})	Content uniformity
Mechanofusion, 10min @ 5200rpm	Turbula, 30min @ 46rpm		(% RSD)
Salbutamol sulphate (non conditioned)	Sorbalac 400	6.25	4.20
Sorbalac 400 + Leucine	Salbutamol sulphate	0.96	8.92
Sorbalac 400 + Lecithin	Salbutamol sulphate	0.88	9.31
Sorbalac 400 + MgST	Salbutamol sulphate	0.61	15.51
Salbutamol sulphate + Leucine	Sorbalac 400	1.89	2.92
Salbutamol sulphate + Lecithin	Sorbalac 400	2.13	3.00
Salbutamol sulphate + MgST	Sorbalac 400	1.52	3.62

ally no interaction was observed between drug and the conditioned lactose surfaces, which resulted in the formation of large drug agglomerates. Interestingly, the mechanofused Sorbalac 400 lactose particles appeared to be smoother after pre-conditioning with leucine, lecithin or magnesium stearate, compared to the as supplied Sorbalac[27]. This suggested a smooth continuous coating of the FCAs over the surface of the lactose particles.

As anticipated, dose content uniformity measurements revealed an increase in the relative standard deviation of salbutamol sulphate of each blend. The RSD of 4.2% for micronised salbutamol sulphate mixed with lactose increased to 8.92% with the conditioning of lactose with leucine, 9.31% for lactose-lecithin and 15.51% for lactose-MgST. These observations suggested a good correlation between the reduction of the intermixing coefficients, which were all significantly below 1, and the content uniformity measurements of salbutamol sulphate in the corresponding carrier-based formulations.

The de-agglomeration and dispersion behaviour of the salbutamol sulphate particles from the model carrier based formulations are shown in **Fig. 5**. The emitted dose of the salbutamol sulphate-lactose formulation via the low resistance Monohaler® device was quite high (76.57%). However, a significant percentage of the drug was recovered in the throat and the first stage of the NGI apparatus. These results were in accordance with a previous *in vitro* study conducted with a Rotahaler® and Turbuhaler® DPI devices[2]. This study suggested that the observed deposition pattern was due to the limited detachment of the drug from the carrier upon actuation caused by the highly adhesive salbutamol sulphate-lactose interactions.

The mechanical fusion of leucine with lactose resulted in a similar drug emission efficiency to the conventional blend. However, the amount of salbutamol sulphate recovered in the first stage of the NGI significantly increased with respect to the non coated lactose blend. The coating of lactose with either lecithin or MgST slightly reduced the device retention of the active ingredient from 23.43% to 18.73% and 18.99%, respectively. Although the interaction between drug and coated lactose surfaces were significantly decreased, a large amount of drug was still recovered on the upper stage of the *in vitro* apparatus.

These results were consistent with the assessment from the CAB-graphs. The CAB analysis indicated that the energy of interaction between the drug and coated lactose would reduce to such an extent that the adhesively led salbutamol sulphate-lactose formulation would shift to an unfavourable cohesive system. The aerosolisation performances of the modified lactose carrier-based formulations may have not improved since the dramatic shift in the force balance was shown to lead to poor blend homogeneity and the

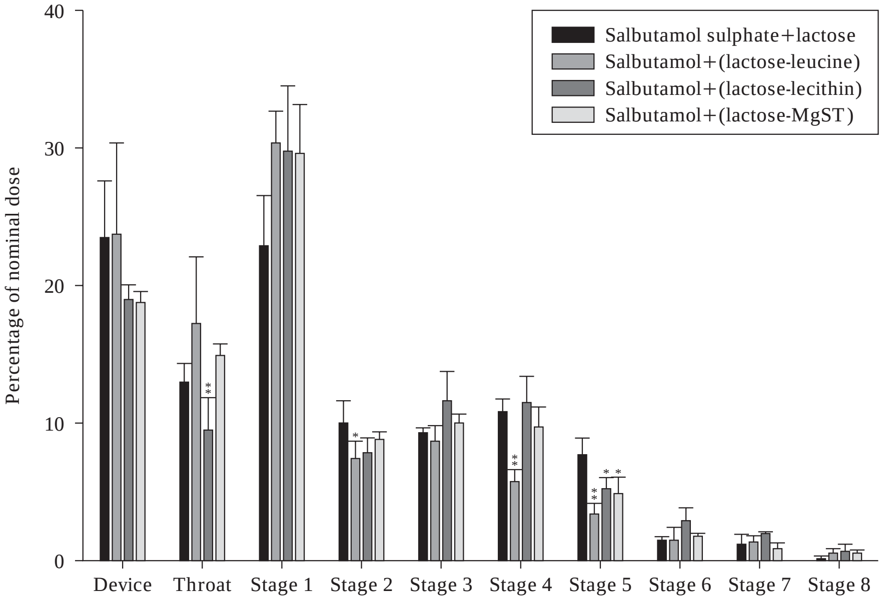

Fig. 5 *In vitro* deposition of salbutamol sulphate carrier-based formulations with conditioned lactose (mean±S.D., n=3).
* $p<0.05$, ** $p<0.01$, *** $p<0.001$: significant difference compared to without force control agent by ANOVA one-way.

potential for significant segregation between drug and carrier particles.

2. Carrier-based formulations with conditioned drug

The conditioning of excipient particles with a FCA modified the adhesive interaction between drug-carrier and excipient-excipient interactions. In contrast, the processing of the micronised drug particles with the FCA would alter both the cohesive (drug-drug) and adhesive (drug-lactose) interactions. To further investigate the possibility of selectively modifying both these interactions within a carrier based formulation, the drug was mechanofused with the FCAs.

The CAB-graphs obtained for the interaction between conditioned salbutamol sulphate with leucine, lecithin or MgST and lactose are shown in **Fig. 6A**, **6B** and **6C**, respectively. The balance remained adhesive for all three systems, although the drug-lactose forces decreased by more than a half of its original value. The conditioning of salbutamol sulphate with leucine, lecithin and MgST led to an intermixing coefficient of 1.89, 2.13 and 1.52, respectively. These mixtures would therefore be expected to form homogenous interactive blends with advantageously weak drug-lactose interactions. As expected, the lactose force balance transformed from an adhesive to a cohesive system. Nevertheless, it can be speculated that this shift should not greatly affect the formulation properties as this change of behaviour is predominately due to a decrease of the adhesive (drug-lactose) forces and not in an increase of the lactose cohesive bonds.

Representative scanning electron micrographs of the lactose particles blended with conditioned salbutamol sulphate-leucine, salbutamol sulphate-lecithin, and salbutamol sulphate-MgST are shown in **Fig. 7A**, **7B** and **7C**, respectively. In contrast to the ternary mixture of drug and conditioned lactose shown in **Fig. 4**, the conditioned drug particles strongly interacted with the lactose particles for all three FCAs. This suggested an effective adhesive disposition, in agreement with the CAB data analyses. The corresponding content uniformity measurements of the ternary mixtures reflected an adhesive led system with low relative standard deviations for lactose mixed with salbutamol sulphate-leucine (2.92%), salbutamol sulphate-lecithin (3.00%) and salbutamol sulphate-MgST (3.62%) conditioned particles.

These observations suggested good correlation between the reduced intermixing coefficients and the characteristics of the respective carrier-based formu-

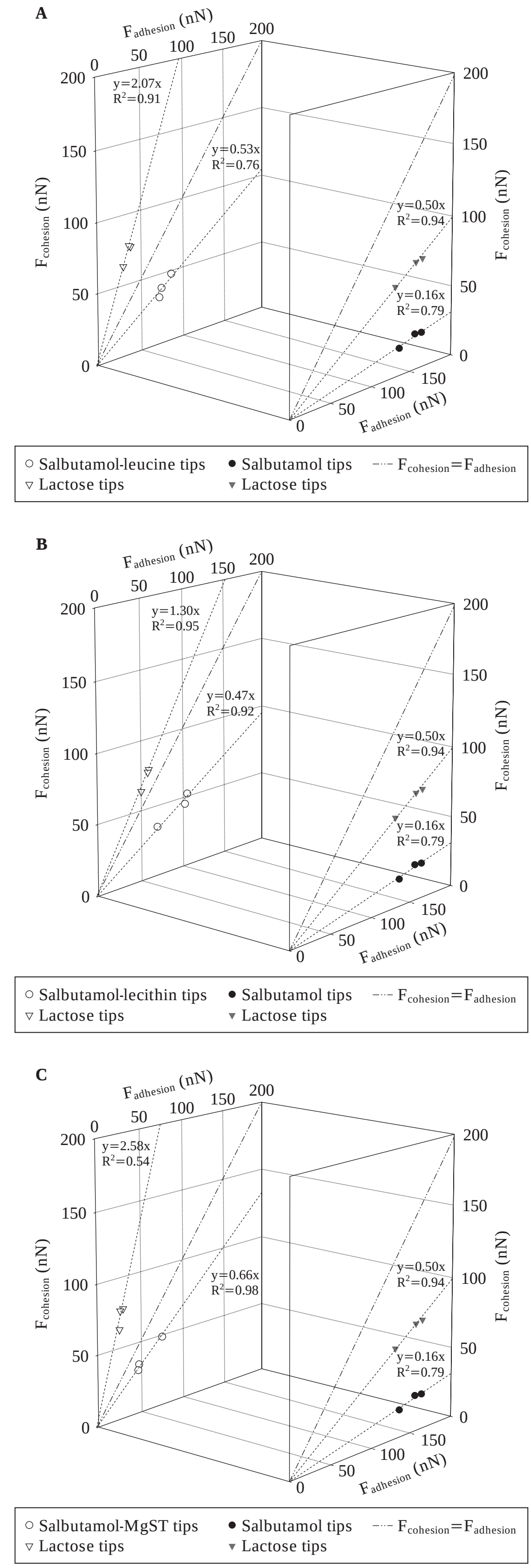

Fig. 6 Influence of the coating of salbutamol sulphate with a force control agent on the cohesive-adhesive balances in a salbutamol sulphate-lactose system.

lations. Such formulations would be expected to be stable during handling and storage, and may lead to a greater de-agglomeration and dispersion efficiency of the respirable particles.

The *in vitro* deposition profile of conditioned salbutamol sulphate carrier-based formulations are shown in **Fig. 8**. The Mechanofusion of the force control agents to the salbutamol sulphate particles resulted in a significant decrease in device retention from 23.42% for the FCA free formulation to 12.51% with leucine, 14.52% with lecithin and 8.23% with MgST. These results suggested a lubrication effect of the FCA and subsequent reduction in interaction between the powder bed and the capsule, while the formulation conserved its metastability as suggested by the CAB analyses. More dramatic was the significant decrease of the percentage of drug deposited on the first stage (cut off diameter·8.06·m) of the NGI apparatus. Stage 1 deposition decreased from 22.89% to 6.16% for the conditioning of salbutamol sulphate with leucine, 9.20% for salbutamol sulphate-lecithin and 7.99% for salbutamol sulphate-MgST. This indicated a greater de-agglomeration efficiency of the coated salbutamol sulphate particles in the carrier based formulations. This was further highlighted by the increase deposition of the active ingredient in the lower stages of the *in vitro* apparatus. These data clearly indicated that the characteristic properties of carrier based formulations can be controllably

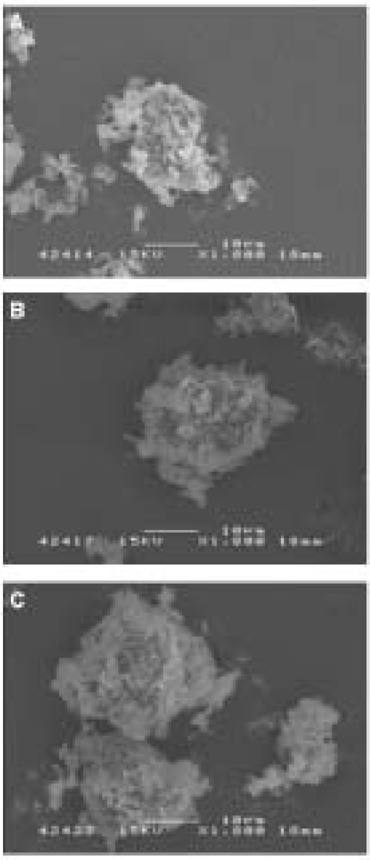

Fig. 7 Representative scanning electron micrographs of ternary mixtures of lactose and salbutamol sulphate pre-conditioned with leucine (A), lecithin (B) or magnesium stearate (C).

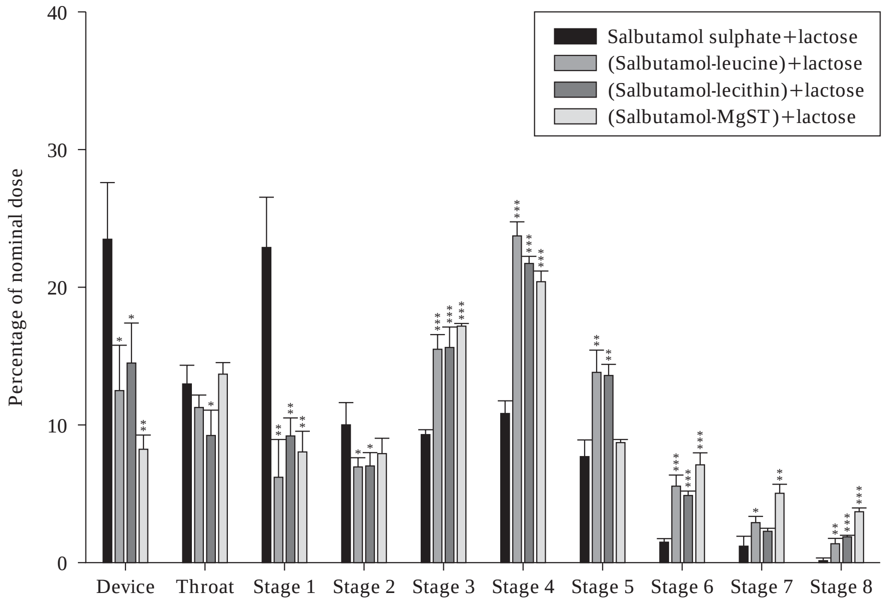

Fig. 8 *In vitro* deposition of salbutamol sulphate carrier-based formulations with conditioned drug (mean±S.D., n=3). * $p<0.05$, ** $p<0.01$, *** $p<0.001$: significant difference compared to without force control agent by ANOVA one-way.

enhanced by judicious selection of the interparticulate interactions to be modified by the introduction of the FCAs.

A summary of the device retention, fine particle fraction (% respirable particle of the emitted dose) and total fine particle fraction (% respirable particle from total recovered dose) of the salbutamol sulphate carrier-based formulations is shown in **Fig. 9**. A clear pattern of formulation performance was observed depending on whether the force control agent was fused either with the drug or the lactose. Formulations with pre-conditioned drug, in contrast to conditioned lactose, offered the best drug delivery performances. It is suggested that the conservation of an adhesive system for the pre-conditioned drug particles directly led to the increased de-aggregation performance. Meanwhile, the selective decrease of the drug-lactose interfacial interaction for conditioned lactose particles led to a dominant cohesive (drug-drug) system, which resulted in poor blend homogeneity and poor fluidisation. The highest %FPF of the emitted dose was obtained for formulations with leucine and lecithin coated salbutamol sulphate particles (73.72% and 71.87%, respectively). The low drug retention of salbutamol sulphate-MgST conditioned particles (8.23% device retention) contributed to deliver an equivalent total fine particle dose as for leucine and lecithin (64.43% for leucine, 61.41% for lecithin and 63.79% for MgST).

CONCLUSIONS

The influence of force control agents on the properties and performances of model salbutamol sulphate carrier based formulations was investigated. The cohesive and adhesive dependencies were controlled by conditioning either the drug or the carrier before mixing in order to create selective modifications of the inter-particulate interactions within a dry powder formulation. The conditioning of these fine inhalation powders was conducted via a Mechanofusion system. This new technique was intended to enable effective particle covering with a nano-scale coating, a process which is difficult to achieve via conventional approaches.

The colloid probe AFM technique together with the novel cohesive-adhesive balance (CAB) analysis procedure was utilised to measure the variations in inter-particulate forces of binary and ternary blends. The CAB-graph method successfully predicted substantial modifications in the behaviour of the formulations, dependant on whether the FCAs were conditioned with the drug or the lactose. This novel approach of applying FCA to the drug is in contrast to previous work in this area where force control agents have traditionally been applied to carrier particles.

This work emphasized that the CAB analysis method can be utilised for pre-formulation studies and in the design of new formulation systems for dry powder inhalers. The work also confirmed the poten-

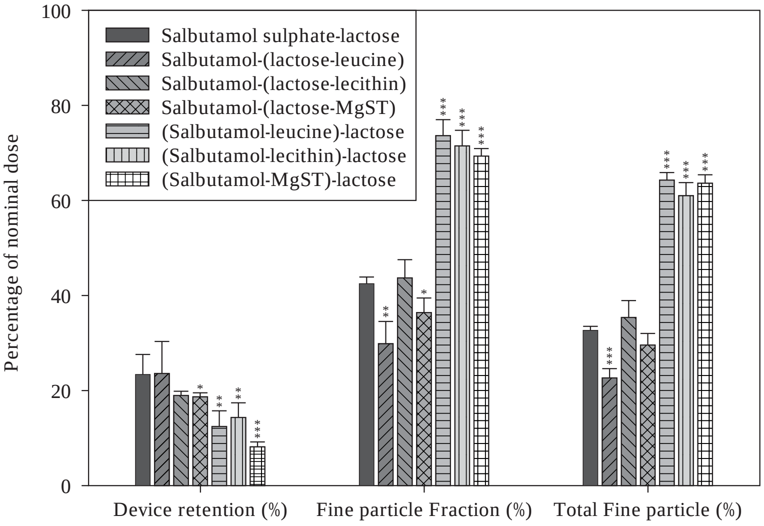

Fig. 9 Fine particle fraction and emission efficiency of salbutamol sulphate carrier-based formulations (mean±S.D., n=3). * $p<0.05$, ** $p<0.01$, *** $p<0.001$: significant difference compared to without force control agent by ANOVA one-way.

tial value of the use of force control agents together with the Mechanofusion process in DPI formulations.

REFERENCES

1) D. Ganderton and N. M. Kassem. *Advances in Pharmaceutical sciences*., Academic Press, London, 1992.
2) A. R. Clark. Medical Aerosol Inhalers – Past, Present, and Future. *Aerosol Science and Technology* **22**: 374-391 (1995).
3) D. Ganderton and T. Jones. *Drug Delivery to the Respiratory Tract*., Camelot Press, Southampton, 1987.
4) W. C. Hinds. *Aerosol technology: Properties, Behaviour and measurements of airborne particles*, Wiley, New York, 1999.
5) J. C. Feeley, P. York, B. S. Sumby, and H. Dicks. Determination of surface properties and flow characteristics of salbutamol sulphate, before and after micronisation. *International Journal of Pharmaceutics* **172**: 89-96 (1998).
6) X. M. Zeng, G. P. Martin, and C. Marriott. *Particulate Interactions in Dry Powder Formulations for Inhalation*, Taylor & Francis, London, 2001.
7) X. M. Zeng, G. P. Martin, C. Marriott, and J. Pritchard. The influence of crystallization conditions on the morphology of lactose intended for use as a carrier for dry powder aerosols. *Journal of Pharmacy and Pharmacology* **52**: 633-643 (2000).
8) X. M. Zeng, G. P. Martin, S. K. Tee, A. Abu Ghoush, and C. Marriott. Effects of particle size and adding sequence of fine lactose on the deposition of salbutamol sulphate from a dry powder formulation. *International Journal of Pharmaceutics* **182**: 133-144 (1999).
9) R. Price, P. M. Young, S. Edge, and J. N. Staniforth. The influence of relative humidity on particulate interactions in carrier-based dry powder inhaler formulations. *International Journal of Pharmaceutics* **246**: 47-59 (2002).
10) M. D. Louey and P. J. Stewart. Particle interactions involved in aerosol dispersion of ternary interactive mixtures. *Pharmaceutical Research* **19**: 1524-1531 (2002).
11) M. D. Louey, P. Mulvaney, and P. J. Stewart. Characterisation of adhesional properties of lactose carriers using atomic force microscopy. *Journal of Pharmaceutical and Biomedical Analysis* **25**: 559-567 (2001).
12) Y. Kawashima, T. Serigano, T. Hino, H. Yamamoto, and H. Takeuchi. Effect of surface morphology of carrier lactose on dry powder inhalation property of pranlukast hydrate. *International Journal of Pharmaceutics* **172**: 179-188 (1998).
13) L. Yu. Amorphous pharmaceutical solids: preparation, characterization and stabilization. *Advanced Drug Delivery Reviews* **48**: 27-42 (2001).
14) P. York. Strategies for particle design using supercritical fluid technology. *Pharmaceutical Science and Technology Today* **2**: 430-440 (1999).
15) X. M. Zeng, K. H. Pandhal, and G. P. Martin. The influence of lactose carrier on the content homogeneity and dispersibility of beclomethasone dipropionate from dry powder aerosols. *International Journal of Pharmaceutics* **197**: 41-52 (2000).
16) N. Islam, P. J. Stewart, I. Larson, and P. G. Hartley. Lactose surface modification by decantation: Are drug-fine lactose ratios the key to better dispersion of salmeterol xinofate from lactose interactive mixtures? *Pharmaceutical Research* **21**: 492-499 (2004).
17) S. K. Tee, C. Marriott, X. M. Zeng, and G. P. Martin. The use of different sugars as fine and coarse carriers for aerosolised salbutamol sulphate. *International Journal of Pharmaceutics* **208**: 111-123 (2000).
18) S. K. Tee, G. P. Martin, A. R. Leeds, C. Walker, A. Kicman, D. A. Cowan, and C. Marriott. The influence of a tertiary component on the in vivo disposition of salbutamol isomers aerosolised from a dry powder inhaler formulation. *Thorax* **56**: P51 (2001).
19) X. M. Zeng, G. P. Martin, S. K. Tee, and C. Marriott. The role of fine particle lactose on the dispersion and deaggregation of salbutamol sulphate in an air stream in vitro. *International Journal of Pharmaceutics* **176**: 99-110 (1998).
20) P. Lucas, K. Anderson, and J. N. Staniforth. Protein deposition from dry powder inhalers: Fine particle multiplets as performance modifiers. *Pharmaceutical Research* **182**: 562-569 (1998).
21) M. J. Clarke, M. J. Tobyn, and J. N. Staniforth. The formulation of powder inhalation systems containing a high mass of nedocromil sodium trihydrate. *Journal of Pharmaceutical Sciences* **90**: 213-223 (2001).
22) J. N. Staniforth. Improvement in dry powder inhaler performance: surface passivation effects. *Proceedings of Drug Delivery to the Lungs VII* 86-89 (1996).
23) P. Begat, M. Green, D. A. V. Morton, A. Whittock, and J. N. Staniforth. PowderHale: A Novel High Performance Dry Powder Inhaler Formulation Technology for Targeted and Systemic Drug Delivery. *Drug Delivery to the Lung XII* 119 (2001).
24) R. Pfeffer, R. N. Dave, D. G. Wei, and M. Ramlakhan. Synthesis of engineered particulates with tailored properties using dry particle coating. *Powder Technology* **117**: 40-67 (2001).
25) J. N. Staniforth and D. A. V. Morton. Powder Technology Research Leading to Improvements in Inhaler Products. *Powder Science and Engineering* **34**: 60-64 (2002).
26) P. Begat, D. A. V. Morton, J. N. Staniforth, and R. Price. The cohesive-adhesive balances in dry powder inhaler formulations I: Direct quantification by atomic force microscopy. *Pharmaceutical Research* **21**: 1591-1597 (2004).
27) P. Begat, D. A. V. Morton, J. N. Staniforth, and R. Price. The cohesive-adhesive balances in dry powder inhaler formulations II: Influence on fine particle delivery characteristics. *Pharmaceutical Research* **21**: 1826-1833 (2004).
28) J. L. Hutter and J. Bechhoefer. Calibration of Atomic-

Force Microscope Tips. *Review of Scientific Instruments* **64**: 1868-1873 (1993).

29) T. J. Senden and W. A. Ducker. Experimental-Determination of Spring Constants in Atomic-Force Microscopy. *Langmuir* **10**: 1003-1004 (1994).

30) R. Price, M. Tobyn, and J. N. Staniforth. Variation in Particle Adhesion Due to Capillary and Electrostatic Forces. *Respiratory Drug Delivery VII* (2000).

31) J. C. Hooton, C. S. German, S. Allen, M. C. Davies, C. J. Roberts, S. J. B. Tendler, and P. M. Williams. An atomic force microscopy study of the effect of nanoscale contact geometry and surface chemistry on the adhesion of pharmaceutical particles. *Pharmaceutical Research* **21**: 953-961 (2004).

Author's short biography

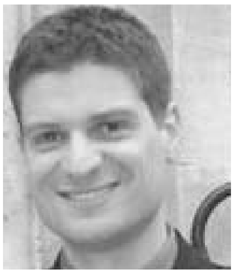

Philippe Begat

Dr Philippe Begat is currently an Inhalation Project leader at Pfizer Inc. Philippe has an MSc in Chemistry. He joined Vectura Ltd in 2001, working on the optimization of PowderHale^{TM} technology. In 2002, he joined the pharmaceutical surface science research group at the University of Bath, as an Experimental Officer, to develop novel methods for characterizing and improving dry powder formulations. He was awarded his PhD in 2005. Philippe has since joined Pfizer Inc. to manage the development of new drug products for their dry powder inhaler programmes.

Robert Price

Dr Robert Price is a senior lecturer at the Department of Pharmacy and Pharmacology at the University of Bath. He gained a BSc in Physics and a PhD in Physical Chemistry from Cardiff University. He leads the pharmaceutical surface science research group, investigating physico-chemical properties governing inter-particulate interactions, surface stability issues of processes particles and the general area of particle engineering and crystal growth. He has published a series of original research articles in the areas of surface electrochemistry, crystal growth, atomic force microscopy and pharmaceutical technology.

Haggis Harris

Haggis is currently a postgraduate student at Bath University in the Department of Pharmacy and Pharmacology investigating inter-particle interactions in dry powder inhaler formulations.

Prior to studying at Bath University, Haggis was employed at Vectura for four years where his primary focus was research and development of high intensity blending techniques to be used in dry powder inhaler formulation.

David A.V. Morton

Dr David Morton is currently Head of Intellectual Property and Technology at Vectura Group plc. He gained a PhD from Bristol University in Structural Chemistry. In 1997, David joined the Centre for Drug Formulation Studies at the University of Bath to manage their dry powder inhaler product development programmes. In 1999, this group spun out into the drug delivery company Vectura, and David was appointed Head of Pulmonary Research, where he co-developed the emerging PowderHale^{TM} technology. He is also known in the inhalation field for his lead role in organising the Aerosol Society 'Drug Delivery to the Lung' conference series.

Author's short biography

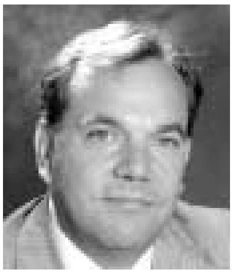

John N. Staniforth

Professor John Staniforth is Chief Scientific Officer and a Founder of Vectura Group plc. He has a BSc in Pharmacy and a PhD in Pharmaceutical Technology. He became Professor of Pharmaceutical Technology and Head of Pharmaceutics at the University of Bath, Department of Pharmacy. In 1999, he led the spin-out of two groups based at the University to establish Vectura. John is a registered Pharmacist and a Chartered Chemist. He has been elected a Fellow of a number of international scientific societies, including the American Association of Pharmaceutical Scientists and is a Member of the Royal Pharmaceutical Society of Great Britain.

Separation of Ink Particles from Waste Paper by Fine-bubbles[†]

H. El-Shall[1], B.M. Moudgil, and A. El-Midany
Engineering Research Center for Particle
Science and Technology,
Department of Materials Science and Engineering,
University of Florida[*]

Abstract

This article describes the research leading to the development of a new process for flotation deinking of waste paper, including old newsprint (ONP), magazines, etc. The technique involves a simple reagent scheme (ammonium hydroxide or sodium bicarbonate) that can be used at room temperature to generate fine bubbles at the ink/fiber/water interface that help in the ink particle detachment as well as in rendering ink particles hydrophobic. The reagents also act on desorbing organic species (oil) from oil-based ink, thereby stabilizing the bubbles. A self-aeration flotation machine could be used to enhance flotation kinetics. Experimental studies have been conducted to evaluate different operating conditions, including reagent dosage, flotation time, recycling flotation water, etc. The efficiency of the process is evaluated in terms of yield of clean pulp, brightness, and reagent consumption.

Key words: De-inking, Flotation, Ammonium hydroxide, Soda ash.

INTRODUCTION

In modern times, with the ecological concerns about conservation of raw materials and the rapid decline of available landfill space, it has become increasingly necessary to recover and recycle used raw materials. Thus, recovered wastepaper represents a valuable source of raw material for the paper industry. Therefore, the wastepaper must be treated to remove any ink particles and non-ink contaminants (Bridle, 1984). Conventional de-inking is accomplished by converting the wastepaper to pulp and contacting the pulp with an alkaline aqueous de-inking medium containing chemicals that play important roles in the ink separation and removal processes. The physical pulping and the alkalinity of the aqueous medium cause the partial removal of ink from the pulp fiber. The added chemicals complete this removal and produce a suspension and/or dispersion of the ink particles that have been removed from the pulp. The resulting mixture is subsequently treated by flotation or washing to separate the suspended ink from the pulp. Examples of the chemicals used in the conventional de-inking plants include alkali metal hydroxides, alkali metal silicates, oxidative bleaches, and surfactants at temperatures in the range of from 30° to 50℃. Anionic and/or non-ionic surfactants, such as soaps or ethoxylated alkylphenols are mainly used as surface-active agents (Chamblee and Greenwood, 1991).

Much of the previous research on de-inking wastepaper has been directed towards the development of de-inking agents. For instance, Poppel et al. (1986) described a process involving the treatment of the wastepaper in a pulper at an alkaline pH with alkali silicate, an oxidizing bleaching agent, a fatty acid containing more than ten carbon atoms, and a dispersing agent. The acid and dispersing agent are added as an oil-in-water emulsion. Other agents include thiol ethoxylate compounds proposed by Poppel et al. (1986), a mixture of C^8 to C^{16} alkanols and alcohol ethoxylates suggested by Wood and Fried (1986), or compounds capable of liberating multivalent cations as reported by Wood and Wood (1985). In addition, DeCeuster and Dupriz (1982) used pine oil and a soap-making fatty acid, and a hydrolyzed copolymer

---

[†] Accepted: August 30, 2005
[*] Gainesville, FL 32611, USA
[1] Corresponding author
TEL: 352-846-1194 FAX: 352-846-1196
E-mail: helsh@mse.ufl.edu

of dimetyldiallyl ammonium chloride and acrylamide was adopted by Bridle (1984).

Other efforts have addressed washing or flotation methods of separating ink particles from wastepaper fibers (Chamblee, 1991, Dingman, 1999, El-Shall, 2003, Eriksson, 1997, Forsberg, 1994, Haynes, 1998, Miller, 1982, Nanda, 1985, Norman, 1994, Pfalzer, 1981, Renders, 1993, Robertson, 1998, Schwinger, 1994, Shiori, 1988, and Tefft, 1988).

In recent years, however, ink formulations have become more and more complex and involve an increasing use of a wide variety of synthetic resins and plasticizers. Many of the new ink formulations incorporate new pigments, dyes, and toners that are difficult to remove by the conventional aqueous de-inking chemicals. The challenges that the pulp and the paper industry is trying to meet today in the recycling area are to: (1) economically produce quality paper that meets the consumer needs while satisfying legislative demands for the content of recycled paper; and (2) increase the process efficiency in order to facilitate use of recovered paper that currently cannot be processed economically. There exists a need for new recycling processes that are more economical and can handle a wider range of recovered paper. One of the most important steps in recycling the recovered paper is de-inking. There also exists a need for methods of de-inking that can handle (1) a wider variety of printed material (newsprint to high quality glossy magazine paper) and (2) a higher pulp density than the conventional processes.

This paper discloses a new reagent scheme for flotation de-inking of a mixture of old news print (ONP) and old magazine print (OMP). The performance and reagent consumption of the process is discussed in comparison to published data by conventional alkaline process.

MATERIALS AND METHODS

Pulping

The wastepaper, 30% old magazines (OMG) and 70% old news print (ONP), was used in these experiments. The pulp stream is mixed with 0.5–1.0 wt. % hydrogen peroxide and 0.1 wt. % ammonia as ammonium hydroxide (or 1–3 wt. % sodium bicarbonate or sodium carbonate). All reagents are related to dry-paper weight. The pH in this stage is about 9.5–10.0. The reagents are added during the pulping stage, which is carried out at room temperature in a Hamilton Beach 16 speed blender running at the highest speed for 1–2 minute pulping time at 10% solids by weight (pulp consistency).

Flotation

After pulping, the pulp is then transferred to the flotation machine, which could be a flotation column or a mechanical flotation cell. In this study, a Denver flotation machine (4.0 liter cell) is used. In some tests polypropylene glycol (400 or 4000 molecular weight) was added as a frother. Dosages are indicated in the results section. Unlike the conventional reagent schemes, which can handle only 1.0–1.2% solids loading during flotation, this method can handle up to 2.0% solids loading efficiently. Flotation was done for different times. The froth was collected and periodically scraped off the top of the flotation cell with a small paddle. The ink and pulp deposited on the sides of the cell and the stand pipe were frequently washed down with water. Water was continuously added to keep the froth level constant and at the lip of the cell. This is needed for efficient froth removal. It should be mentioned that the amount of added water was kept as low as possible (about 3–5% of the cell volume) to minimize dilution of the chemicals present in the suspension. Floated ink particles were discarded and pulp left in the cell was separated from the water using 35 mesh screen. The separated water (containing pulping chemicals) was used for testing recycled water. The pulp was then washed on the same screen using fresh water. **Fig. 1** shows the flow diagram of the deinking process used in this study.

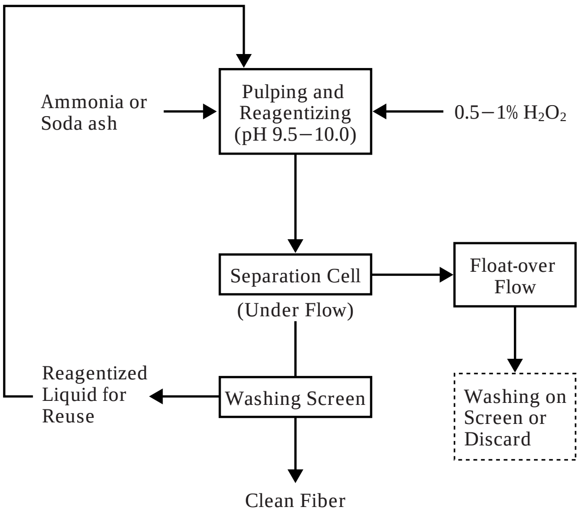

Fig. 1 Flow Diagram of University of Florida (UF) Flotation De-inking Process

Preparation of Handsheets

After screening the pulp, vacuum filtration was done using a 15.0 cm diameter funnel under 15 inches of Hg vacuum. A Whatman filter paper No. 40, 15 cm dia., was placed into the funnel to avoid fiber passing through the funnel pores. Another filter paper was placed at the top of the pulp in the funnel. Filtered pulp was pressed between two flat surfaces to form a uniform cake. After pressing, the cake was completely dried in an oven. The mass of dried pulp was used to calculate the yield. Some samples were sent to a specialized lab to measure the ash content before and after de-inking.

Brightness Measurement

The brightness tests were used to measure ink removal. Brightness of formed cake (pad) was measured using hand held Technidyne Technibrite™ TB-1C. The brightness meter was calibrated using calibration plates of known brightness. The brightness readings were averaged of 5 readings for each sample.

RESULTS AND DISCUSSION

In this study, ammonium hydroxide, sodium bicarbonate, and sodium bicarbonate were used in combination with hydrogen peroxide during the pulping stage. Data obtained in these systems are discussed below.

1. Testing Ammonium Hydroxide

Effect of Flotation Time

Effect of flotation time on brightness of pulp is shown in **Table 1**. The data show that ink floats even after five minutes, as indicated by increasing brightness values of the produced pulp. Extending flotation time to eight minutes improves brightness to a higher value, as shown in **Table 1**. It is worthy to mention that the (ONP) waste paper (without printing) has a brightness value of 56%. The choice of flotation time depends on many factors, including costs (capital and operating), desired quality, and economical yield values.

It is interesting to note that ash content decreases with time, as shown in **Fig. 2**, indicating that filler particles are also floated with the ink particles. One disadvantage, however, of using longer flotation time is the loss of pulp leading to lower yield values as shown in **Fig. 3**. The yield decreases markedly when flotation is continued longer than five minutes.

Table 1 Effect of flotation time on brightness of produced pulp ($0.5\% H_2O_2$, $0.1\% NH_4OH$, 2 minute pulping)

Flotation Time, min	Brightness, % ISO
1	43
2	44
3	49
4	50
5	51
6	54
8	55.5

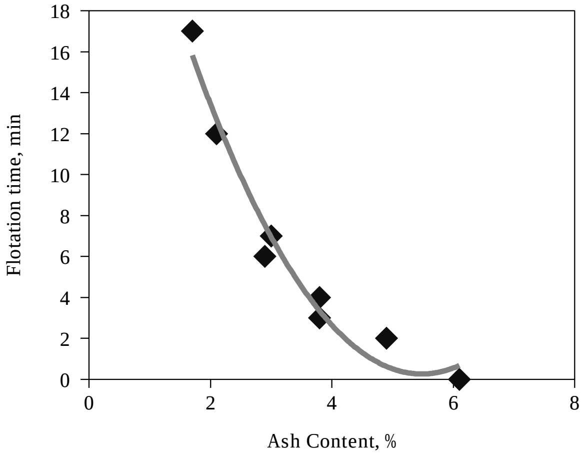

Fig. 2 Effect of flotation time on ash content of de-inked pulp ($0.5\% H_2O_2$, $0.1\% NH_4OH$, 2 minutes pulping)

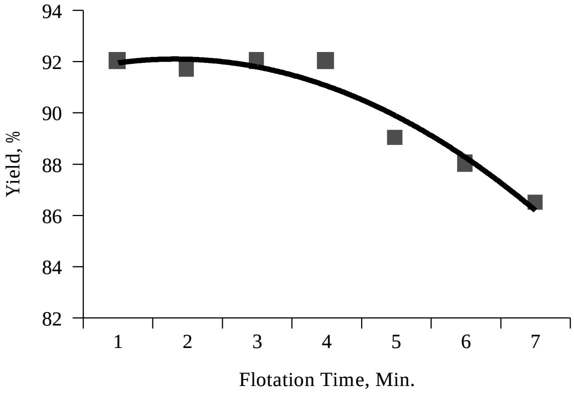

Fig. 3 Effect of flotation time on yield of de-inked pulp ($0.5\% H_2O_2$, $0.1\% NH_4OH$, 2 minutes pulping)

These results may be attributed to bubble formation due to reactive peroxide and soluble alkaline agents may react in the presence of the pulp that dislodge the ink particles of the fiber and help in floating the ink and filler particles. Using ammonium hydroxide, ammonia gas nucleates at the fiber / solution interface. The reaction may be speculated to proceed according to the following scheme:

$$2NH_4OH+H_2O_2 \rightarrow NH_3\uparrow +2H_2O+O+NH_4^+ +OH^- \tag{1}$$

It should be mentioned that no gas bubbles are observed in absence of pulp. The reasons for activation of such reaction in the presence of pulp are still not clear. Nevertheless, the liberated ammonium gas floats the ink and filler particles to the surface. Hydrogen peroxide bleaches the pulp and contributes to the product brightness. In all results shown below, however, a self-aerated flotation machine was used where air was sparged into the system to enhance flotation kinetics of the filler and ink particles.

Effect of Recycling Process Water

Recycling water for reuse in process industries is important to cost effectiveness of the process as well as reduction of discharge to the environment of possibly contaminated water. Thus, it is important to evaluate the effect of water recycling on the performance of the deinking process and the quality of the de-inked pulp. Interestingly, the brightness of the product increases with the number of recycling stages as seen in **Fig. 4**. It is important also to note that a yield value of 88 +/−1% was obtained in all of these tests. In other words, recycled water does not have detrimental effect on pulp recovery or ink removal.

The brightness improvement may be attributed to two reasons. First is due to the bleaching effect of hydrogen peroxide. Second is stabilization of formed gas bubbles by the released oil due to the action of the hydrogen peroxide. Release of oil is evidenced by a decrease in surface tension of water as shown in **Fig. 5**. Interestingly, it is found that further decrease in surface tension and increase in total carbon content are obtained by recycling water.

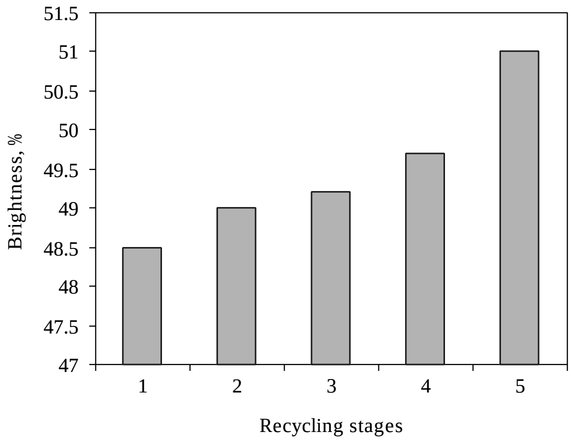

Fig. 4 Effect of water recycling on brightness of de-inked pulp ($0.5\%\ H_2O_2$, $0.1\%\ NH_4OH$, 2.0 minutes pulping, 4.0 minutes flotation time)

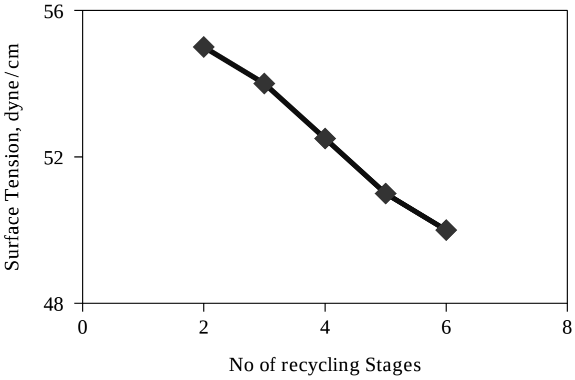

Fig. 5 Effect of recycled water on surface tension ($0.5\%\ H_2O_2$, $0.1\%\ NH_4OH$, 2.0 minutes pulping, 4.0 minutes flotation time)

Further testing of this process utilizing higher dosage of reagents and addition of polypropelyne glycol with Molecular weight of 400 has shown a dramatic improvement in the brightness of de-inked pulp. The obtained brightness values for ONP and magazines have reached a level close to original values (Papers without print). These results are discussed in another publication (El-Shall et al. (2003)).

2. Testing Sodium Bicarbonate/Sodium carbonate

Sodium bicarbonate or sodium carbonate was used instead of ammonia in the pulping stage. In these systems, the following reactions may take place:

$$NaHCO_3+2H_2O_2 \rightarrow Na^+ +OH^- +2H_2O+O_2+CO_2\uparrow \tag{2}$$

$$Na_2CO_3+3H_2O_2 \rightarrow 2Na^+ +2OH^- +2H_2O+O_2+O+CO_2\uparrow \tag{3}$$

The liberated carbon dioxide bubbles would (similar to the ammonia gas) dislodge the ink particles of the fiber surface and help float them to the surface of the suspension. In this case, the formed molecular oxygen would function as an additional flotation agent.

It is expected that processes utilizing combinations of alkaline agents and peroxides, which do not react with each other to liberate gas bubbles, the process is much less efficient. For example, where alkali metal hydroxides and hydrogen peroxide are utilized, the reagents react according to the scheme:

$$NaOH + H_2O_2 \rightarrow 2Na^+ + OH^- + H_2O + O \qquad (4)$$

Although hydrogen peroxide aids in brightening the pulp, no gas bubbles are formed to float the ink particles to the surface of the pulp stream.

In **Fig. 6**, the experimental data show (as in the case of ammonium hydroxide) the brightness increases as flotation time and reagent dosage increase. It should be mentioned that the flotation time might represent the time needed for the bubbles loaded with ink particles to float. Thus, the type of reagent used may not be of significance during the flotation stage.

On the other hand, the effect of dosage can be explained on the bases of the increased number of fine generated CO_2 bubbles, which are responsible for dislodging the ink particles from the fiber surface during the pulping stage.

Most importantly, several tests were conducted using sodium carbonate (less expensive reagent) instead of the bicarbonate. The results indicated that the sodium carbonate could be used to produce a pulp with brightness more than 55% after flotation. Therefore, it may be cost effective to use soda ash instead of ammonia or sodium bicarbonate during the flotation deinking process.

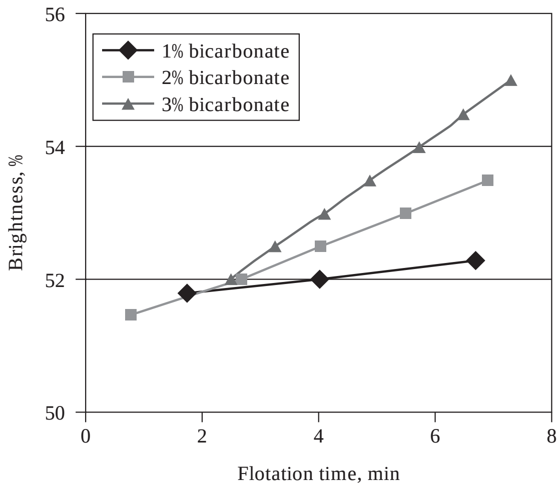

Fig. 6 Effect of Flotation time on deinked pulp Brightness (1% H_2O_2, 2 minutes pulping time, different bicarbonate dosages)

REAGENT CONSUMPTION AND PERFORMANCE COMPARISONS

The recommended reagents to be used in this process to produce pulp of high brightness (over 54% for ONP and over 80% for magazines) are listed in **Table 2**. The dosages of these reagents are also listed in the same table together with that used in conventional alkaline pulping as described by Dingman and Perry (1999). The data show that few reagents at lower dosages are used in the developed process. In addition, the process could be more cost effective, especially when a less expensive reagent such as soda ash is used. An added advantage of this process is the high pulp (2%) consistency in flotation as compared to (1.0−1.25% normally used by the industry). This represents over 60% increase in plant capacity. Another important point to remember is that all pulping and flotation are done at room temperature instead of the high temperature conditions (over 40 degrees C) used in conventional de-inking plants (Dingman et al. (1999)).

Table 2 Comparison between Recipes and Reagent Consumption for Conventional and the Developed Deinking processes

Process	Additive	Dosage (#/ton)
Conventional Alkaline	Sodium hydroxide Hydrogen peroxide Chelant Sodium silicate	12 16 4 20
UF Process-1	Hydrogen peroxide Ammonium hydroxide PPG	20 4 0.5
UF Process-2	Hydrogen peroxide Sodium carbonate PPG (400 MW)	10 10 0.5

CONCLUSIONS

A simple and effective deinking process involving pulping and flotation steps was developed. The process depends on adding reagents in the pulping stage that lead to formation of fine bubbles at ink/fiber/water interface. The results of preliminary tests showed that brightness more than 55% could be obtained from a mixed stock containing 30% old magazines (OMP) and 70% old newsprint (ONP). The process has several features such as, few chemicals such as hydrogen peroxide and Alkali reagent (e.g., Ammonium hydroxide, Sodium bicarbonate and sodium carbonate) are used, and high yield of good quality (brightness) product. From a practical and economic view points, this process may prove to be more economical due to low reagent's consumption, operating at room temperature, increased plant capacity by floating higher solid content pulp, and possibility of water recycling. Further testing at larger scale is recommended to verify the potential of this process.

Acknowledgement

Financial support from the following institutions is acknowledged and greatly appreciated: the Particle Engineering Research Center (PERC) at the University of Florida; the National Science Foundation (NSF), under grant EEC-94-02989; and the Industrial Partners of the ERC.

References

1) Bridle, P., U.S. Patent No. 4,483,742 on "Liquid Soaps Comprising Pine Oil and Soap-making Acid for use in Paper-recycling", Nov. 1984.
2) Chamblee, J.W., Greenwood, B.F., (1991) Evaluation of High Though Put High Consistence Deinking Technology, TAPPI Pulping Conference, Nov. 4-7.
3) DeCeuster, J., and Dupriz, P., U.S. Patent No. 4,343,679 on "Process for Reclaiming Waste Paper", Aug. 1982.
4) Dingman, Daniel J., and Perry, Christopher, D., "Caustic-Free Repulping For Newsprint Production – Part I", Presented at the 1999 TAPPI Pulping Conference and published in www.Buckman.com
5) El-Shall, H., and Moudgil, B., U.S. Patent No. 6,217,706 on "Method of De-inking and Other Cellulosic Materials", April 2001.
6) El-Shall, H., El-Midany, A., and Moudgil, B., "A New Cost-Effective Deinking Technology", Proceedings of the 6th. International Conference on Pulp & Paper Industry, new delhi, India (Dec. 2003) pp. 307-316.
7) Eriksson, T.P., McCool, M.A., 1997. In: Doshi, M.R., Dyer, J.M. (Eds.), A Review of Flotation Deinking Cell Technology, Paper Recycling Challenge, Vol. II. Doshi and Associates.
8) Forsberg, P.M., and Genco, J.M., *Tappi J.* **77**(3): 253(1994).
9) Haynes, D., Roring, A., "What are the Benefits and Barriers of Neutral Deinking?" *Progress in Paper Recycling*, Vol. 7, No. 3, May 1998.
10) Miller, J.D., Van Camp, M.C., 1982. Fine coal flotation in a centrifugal field with an air-sparged hydrocyclone. Mining Engineering, pp. 1575-1580.
11) Nanda, A, Silveri, L., McCool, M., U.S. Patent No. 4,548,673 on "Method and Apparatus for Deinking", Oct. 1985.
12) Norman, J.C., Sell, N.J., and Danelski, M., *Tappi J.* **77**(3): 151(1994).
13) Pfalzer, L., and Fischer, S., U.S. Patent No. 4,277,328 on "Flotation Apparatus for Separating Impurities from a Fiber Suspension", July 1981.
14) Poppel, G., and Ulubay, H., U.S. Patent No. 4,586,982 on "Process for the De-inking of Printed Waste Paper", May 1986.
15) Renders, A, *Tappi J.* **76**(11): 156(1993).
16) Robertson, N., Patton, M., and Pelton, R., 1998. Washing the Fibers from Foams for Higher Yields in Flotation Deinking. *Tappi J.* **81** 6, pp. 138-142.
17) Schwinger, K.; Schmid, H., "Flotation Deinking in Neutral pH Range", *1st International Conference and Exhibition on Paper and Board Recycling*, Preprints, Page 1, London, UK (1994).
18) Shiori, A., Isobe, Y., and Hayano, K., U.S. Patent No. 4,749,473 on "Process for Removing Ink from Wastepaper", June 1988.
19) TAPPI Test Method T 213 om-89, Dirt in Pulp. TAPPI Press, Atlanta, 1990.
20) Tefft, E., U.S. Patent No. 4,786,364 on "DMDAAC/AM Copolymers as Deinkers", Nov. 1988.
21) Wood, D., and Fried, H., U.S. Patent No. 4,618,400 on "Wastepaper Deinking Process", Oct. 1986.
22) Wood, D.L., and Wood, D.C., U.S. Patent No. 4,561,933 on "Xerographics Deinking" Dec. 1985.

Author's short biography

Hassan El-Shall

Dr. El-Shall is Associate professor of Materials Science and Engineering and Associate Director for Research at The Particle Engineering Research Center of University of Florida. He has been at UF since 1994. He also served as Associate Director for beneficiation research at the Florida Institute of Phosphate Research from 1986-1992. Before that he has served as assistant professor of Mineral Processing at Montana Tech from 1980 to 1986. Dr. El-Shall's major research interests include interfacial phenomena and its applications in medicine, mineral industry, and waste treatment in various industries.

Brij M. Moudgil

Dr. Brij M. Moudgil is a Distinguished Professor and Alumni Professor of Materials Science and Engineering, and Director of the Particle Engineering Research Center at the University of Florida, Gainesville, Florida. Dr. Moudgil also serves as the Director of the UF Mineral Resources Research Center. He is scheduled to serve as SME (Society for Mining, Metallurgy and Exploration, Inc.) President in 2006. His research and professional leadership accomplishments are recognized by several major awards including his election to the National Academy of Engineering (NAE), the highest honor accorded to an Engineer in the USA. His current research interests include Flotation and Selective Flocculation (Polymer and Surfactant Adsorption), Dispersion and Aggregation of Fine Particles.

Ayman El-Midany

Dr. El-Midany is a research associate at University of Florida. He graduated with a Ph.D. in Materials Science and Engineering from University of Florida in December, 2004. He also has an appointment as researcher at Central Metallurgical Research and Development Institute (CMRDI), Cairo, Egypt. His research interests are into mineral beneficiation, flotation, and applied surface chemistry.

Characterization of Low-Level, Oversize Particles in Abrasive Powders[†]

T.F. Dumm
Diamond Innovations[*]

Abstract

Abrasive powders are used in fine grinding and polishing applications many of which require defect-free surfaces. Scratching is a primary defect that can be caused by very low levels (less than 10 ppm) of large, oversize particles in the powders. Powders containing low levels of oversize particles can escape the scrutiny of quality control efforts because particle size analysis techniques have detection and sensing limits that prevent detection and quantification. This paper describes several common size analysis techniques with special regard to the limits of detecting oversize particles. Recommendations are described for measuring and quantifying low levels of oversize particles in powder size ranges of greater than and less than 10 microns.

Key words: Diamond, Abrasives, Powders, Size analysis, Oversize

1. Introduction

Many of the abrasive powders that are used for grinding, lapping or polishing are derived from crushing and/or milling larger particles into finer sizes. These powders include silicon carbide, aluminum oxide, boron carbide, cubic boron nitride and diamond. Fine abrasives are usually manufactured by crushing and grinding; followed by size classification methods that include screening, air classification or some form of sedimentation. Although the size reduction operation is important for obtaining the finer sizes from a coarser feed material, it is the size classification process that creates the narrow size fractions that are important for proper performance of abrasive grains in a surface modification application such as lapping or polishing. If the surface modification requires a surface finish that is free of scratching, i.e., no obviously large, deep grooves created by substantially larger particles in a set of narrowly graded particles, then special care must be taken to ensure that these particles are not present in the powder. Scratching is a serious visual and technical defect in applications like gem or crystal glass polishing, chemical mechanical planarization (CMP) of micro-electronic circuitry[1)], precision wire sawing of semi-conductor ingots[2)] and in computer hard drive media[3)]. Unfortunately, the inherent nature of oversize particles is that the concentration needed to cause serious damage to a surface is well below the detection limits or capability of most modern size analysis methods.

On the fine side of the size distribution curve, it is equally possible to have low levels of fine-size particles that suffer from the same detection limitations as those on the coarse side. If present in low levels, these particles usually have no effect on the performance of the abrasive. When present in larger quantities, and depending on the relative fineness of the size, undersize particles can have greater impact on characteristics like dispersion, tendency of forming agglomerates or packing behavior.

Another important factor is particle shape. The effect of particle shape on polishing performance is not as well understood as size effects. Many size measurement techniques are sensitive to shape and particles having very high aspect ratios or have a plate-like shape can appear as oversize particles. However, in many applications using abrasive particles for lapping or polishing, the high aspect ratio or plate-like particles will behave differently from oversize particles with more equi-axial or blocky shapes. In general, the

---

[†] Accepted: August 30, 2005

[*] 6325 Huntley Road
Worthington, OH 43085, USA
TEL: (614)438-2903 FAX: (614)438-2829
E-mail: timothy.dumm@abrasivesnet.com

blocky oversize particles tend to be more problematic because they resist breakage under load and survive longer than those with irregular shapes. This paper will focus on the effects of oversize particles only.

A number of processes are used for reducing or eliminating oversize particles in powders or slurries. These include: sieving, filtration, elutriation, sedimentation and various forms and modifications of these. However, in order for any process to be controlled with confidence, it is necessary to measure the attribute that one is classifying or modifying. In the case of oversize particles, this becomes quite difficult because of the difficulty in measuring them. A number of size standards exist for defining various grades of abrasive powders; for example in the diamond abrasive industry: Federation Europeenne des Fabricants de Produits Abrasifs (FEPA)[4], American National Standards Institute (ANSI)[5] and Industrial Diamond Association (IDA)[6].

There are two factors that make it difficult to control the level of oversize particles in a powder where the term oversize refers to particles substantially coarser than the median size of the powder. The first is the ability of **detecting** the particles with a certain degree of certainty. The second factor is applying the proper metric that adequately **quantifies** the level of oversize particles in a powder. The size attributes of powders are normally measured using particle size analysis techniques such as sieves, microscopic methods, sedimentation, electrical or optical sensing zone, laser light scattering techniques and others. Although each of these techniques employ different definitions of particle size, the distribution of sizes within a powder are measured and quantified using statistical terms such as the mean, median or mode size, standard deviation or percentile points on a cumulative curve of the total size data. These metrics serve quite well for describing the bulk properties and general performance of powders. However, these metrics are not useful for describing low levels, on the order of a few parts per million or even parts per billion, of oversize particles that can cause severe problems in surface modification processes.

This paper will describe the limitations that are associated with most of the modern techniques used for measuring the bulk size characteristics of powders. Additionally, semi-qualitative techniques are described which allow evaluation of oversized particles for very fine powders that are the most difficult to quantify by other techniques.

2. Effect of Oversize Particles

In applications that use abrasives for 2 or 3-body lapping or polishing, the ideal mode of operation is that uniformly sized particles are spread onto a lapping plate or polishing cloth using a liquid carrier. When the substrate being lapped or polished is placed in contact with the slurry on the plate, the particles are forced into a single layer between the plate and substrate (See **Fig. 1**). Only those particles that contact the workpiece and lapping plate provide the action that abrades or polishes the substrate. Where more compliant lapping surfaces are used, like polymeric films or cloths, there is more particle contact with the workpiece, but the pressures exerted by larger particles can exceed those of the smaller ones that are not pushed as far into the lapping cloth. In either case, narrow particle size distributions provide the highest level of particle contact, uniformly support the load placed on the substrate and polish or abrade with the highest material removal rate and best (defect free) resulting surface finish.

When oversize particles are present within a powder, even at levels that are not detected by most size analysis techniques, a considerable amount of surface damage can be caused from the lapping and polishing process. **Fig. 2** shows the effect of a few large particles among millions of smaller narrow-sized particles. When the large particles are between the lapping

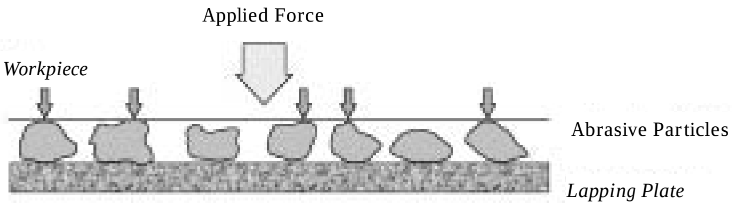

Fig. 1 Schematic of graded particles in a lapping or polishing application showing how uniformly sized particles bear the applied load.

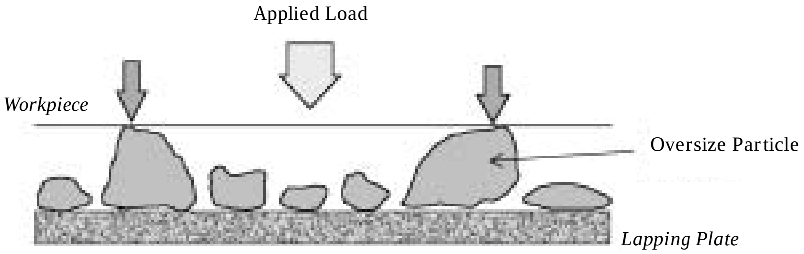

Fig. 2 Schematic of graded particles in a lapping or polishing application showing how A few oversized particles bear a disproportionate amount of the applied load.

plate and substrate, they will support a disproportionate amount of the load placed on the workpiece. The smaller particles around the large particle will bear no load and therefore be rendered useless. If the oversize particles support the pressure placed upon them without fracturing, the result will be relatively deep scratches on the workpiece.

3. Definition of Oversize Particles

The concept of an "oversize" particle has the most relevance with relationship to a "narrow" size distribution. In powders having broad size distributions, the definition and effect of oversize is more vague and less pronounced and for purposes of this discussion, we will limit the definition to narrowly graded powders or those having a median size to standard deviation ratio of 5 or larger (for example a powder having a median size of 15 microns and standard deviation of 2.5 microns will have a ratio of 6).

There are two magnitudes of oversize particles that can exist within a set of particles: Near-oversize refers to solid particles which are present in a distribution with a high degree of statistical probability and occur with enough frequency that they are detected and accounted for within a size distribution. These are the particles that make up the coarse "shoulder" of a distribution curve (see **Fig. 3**) and are generally 1.5 to 2 times larger than the median and are represented within the 90th to the 99th percentiles on a number

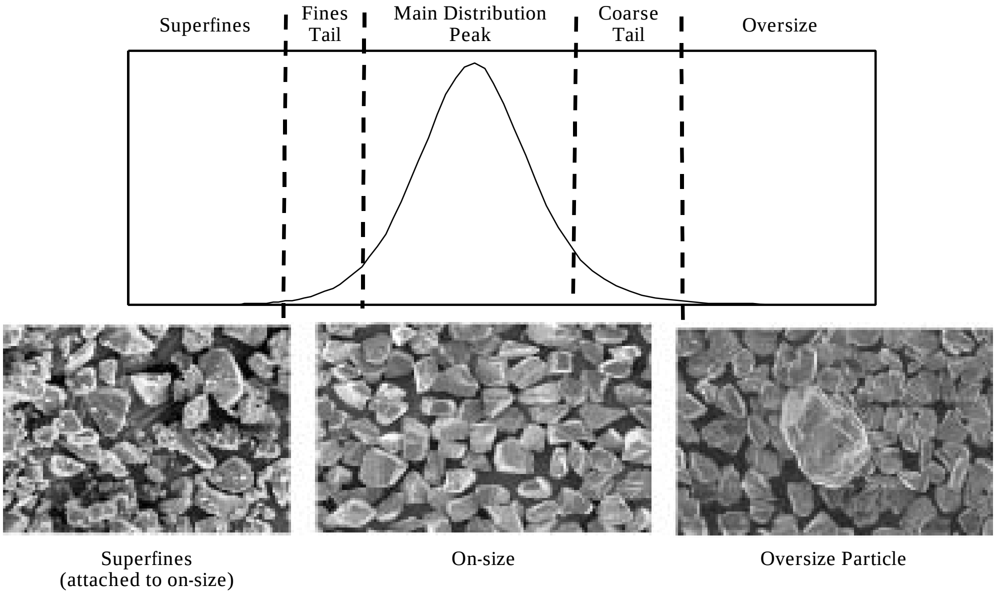

Fig. 3 Schematic of a typical particle size distribution curve showing the major zones that affect powder performance.

basis. For narrowly graded powders, these particles do not generally lead to scratching problems.

Gross-oversize particles that may be present in a distribution usually occur as rogue particles that were not removed from the powder due to process inefficiencies or contamination during handling or storage. In this case, gross-oversize particles are defined as solid particles whose size lies above the coarse shoulder of the particle size distribution curve and are statistical outliers from the rest of the population. Gross-oversize particles are generally 2 to 5 or more times larger than the median size. As little as 0.25 mg of 10 micron particles in as much as 80 kg of 1 micron mean size powder may be enough to allow one 10 micron particle to be included in as little as 60 mg of the bulk powder. Because it is the very largest particles in a powder that cause the scratching problems described in the introduction, for the remainder of this discussion, we will refer to gross-oversize particles as oversize particles.

In many cases, agglomerates of individual median-sized or near-sized particles will behave as oversize particles. The extent with which they can scratch or cause defects depends upon how tightly bound the individual particles are within an agglomerate. Tightly bound agglomerates, that occur with more frequency as the median size of a powder decreases, can behave as solid particles. Agglomerates that are held together with less cohesive force may behave as solid particles initially, then break apart under the applied load.

4. Characterization of Oversize Particles

The common size analysis techniques used for measuring particle size distributions of powders are: sieving, sensing zone methods (electrical and optical), laser light scattering, sedimentation, photon-correlation spectroscopy and microscopy. Each of these methods is based on fundamental principles that are well understood and each technique has advantages over others in specific size ranges, materials and applications. When employed properly, the size analysis techniques generate statistically significant size data for the bulk of the population of powders or particles that are being measured. Bulk size properties include mean, median, standard deviation, skewness factors, and percentiles that are statistically significant.

Table 1 lists the features of the common size analysis techniques with respect to their ability for detecting and quantifying oversize particles. The techniques are listed with respect to the lower detection limit. As can be seen by the table, the sieving technique, which actually performs a physical separation of the particles based on sieve-size, has a tremendous capacity for “measuring” billions of particles in relatively short timeframes. Given that the sieving time is sufficiently long enough to provide each particle with opportunity to fall through the sieve mesh or be retained, the process of determining whether a particle is above or below the sieve size has a high degree of resolution.

Table 1 Comparison of Size Analysis Techniques for Measuring Oversize Particles in Powders

Technique	Particle-by-Particle Counter	Particle Detection Mechanism	Sample Size, grams	Particle Counts per minute*	Resolution	Oversize Detection Level	Lower Practical Size Limit
Sieving	No (for data)	Sieve Opening	1 to 1000	10^3 to 10^{12}	Excellent at sieve size	PPB	10 um
Sensing Zone	Yes	Aperture or Detection Zone Single Particle$^+$	0.005 to 0.5	10^4 to 10^5	Very Good	Several PPM	2-5 um
Light Scattering	No	Detection Zone Field Response	0.05 to 1	10^6 to 10^9	Fair	0.5%	0.1 um
Sedimentaion Bulk Line Start	No	Detection Zone Field or Bulk Response	1 to 10	10^6 to 10^9	 Poor Fair	 0.5% 0.5%	0.1 um
Microscopy Optical Electron	Yes	Single Particle Detection	0.0005 to 0.05	10^3 to 10^4	Excellent	PPM	 1 um 0.05 um
Photon Correlation	No	Detection Zone Field Response	0.005-0.05	10^6 to 10^9	Poor	1%	0.005 um

* Particle counting statistics increase per time increment as size of powder decreases.
\+ Single-particle detection response only if samples are sufficiently diluted.

In the case of using a sieve for detecting oversize particles, a single sieve is employed rather than nesting a series of sieves. The sieve is chosen so that the size of the openings represents an arbitrary definition of oversize so that any particles retained on the sieve would be classified as such. Although no detailed size information is obtained on the bulk of the distribution, the particles that are retained on the sieve can be easily quantified by counting or weighing or other means. The added bonus of using sieves for measuring oversize particles is that these particles are actually removed from the powder and a value-added function has been performed.

Although sieving seems like the ideal method for measuring and detecting oversize particles, there are practical limitations for its use across all products and sizes. With the development of ultrasonic sieving technology, the ability of sieving powders through very fine mesh sizes has improved significantly. Wire mesh screens are made as fine as 635 mesh (20 microns) and electroformed screens as fine as a few microns. Electroformed sieves finer than 10 microns are expensive and fragile. At this size, it becomes difficult and time consuming for even ultrasonic energy to encourage the fine particles to fall through the sieve openings. Therefore 10 microns is near the practical limit of the sieving technique. Other concerns with using the sieving technique are the selection of sieve size with respect to the coarse shoulder of the distribution: if the sieve size is too close to the shoulder, many "near-size" particles will be present on the sieve cloth (see **Fig. 3**). These particles require long sieving times to orient and fall through the sieve and can cause the sieve cloth to blind. If the sieve is much coarser than the coarse shoulder of the distribution, the powder will fall through more easily, but oversize particles that are near the sieve size, and fall through, would not be accounted for. Given that sieves are usually available only in standard size ranges, there may be little flexibility in matching the sieve size based on the coarse shoulder of the size distribution. Finally, sieves must always be thoroughly inspected for holes or tears before being used for size analysis.

Another popular technique for measuring particle size distributions is the electrical sensing zone or optical sensing zone. Particles are sampled into these devices in dilute suspensions so that they can pass through the sensing zone one at a time and are therefore counted individually. As the particles enter into or through a zone, they trigger or disrupt either an electric current or a light beam. A sensor detects, quantifies the intensity of the signal and records the data in a size channel. The resolution of the "size" that is measured is a function of the sensitivity of the sensors, which in modern electronic systems are quite good.

In principle, it would seem that the sensing zone techniques are ideal for measuring and detecting oversize particles. In practice however, this technique is limited by several factors for the ability of measuring oversize crystals. In the case of electrical sensing zone methods, particles suspended in an electrolyte are drawn through an orifice. Particles can only be detected and measured if they pass through the orifice. This of course, requires that the orifice be larger than the coarsest particles in the sample. If there are particles in the sample that are coarser than the orifice, they will not be detected and can also cause plugging of the orifice. Another significant limitation of the sensing zone techniques is the counting statistics related to measuring dilute samples. For electrical sensing zone techniques the count rate is controlled by the concentration of particles in suspension and the suction applied through the aperture. An optimum count rate exists whereby too low of a rate results in inefficient use of time and exacerbation of background noise, whereas too many particles can result in coincidence effects; two or more particles entering the sensing zone simultaneously. When this happens, the analyzer detects these as single, larger particles. In practice, an optimum count rate is approximately 50,000 particles per minute. If oversize particles are present in concentrations of several parts per million, then it is possible that one oversize particle may be present in the population that is sampled in one or more minutes of analysis time.

Other limitations with electrical sensing zone technique occur from the background "noise" that is generated from the electrolyte solution. There are two forms of "noise" that are generated from the electrolyte: the first is a high frequency noise that usually occurs in the finest size channels and is more prevalent as the aperture size decreases. This noise can be accounted for by making an analysis of clear electrolyte having no particles in suspension and subtracting these background counts from the data obtained with the particles. The biggest effect of this noise is that it limits the use of the electrical sensing zone technique to sizes down to about 2 to 5 microns. The second form of noise is low frequency noise that can occur randomly in any size channel. Small bubbles, suspended contamination, particle build-up near the aperture inside the orifice tube, voltage fluctuations or electrical interruptions caused from loose electrical connections or the stirring motor, etc. **Fig. 4** shows the effect of 'noise' that resulted from analyzing a 40 micron mean sized powder that had been sieved three times through a 270 mesh (53 um) sieve to remove any oversize particles. As can be seen, counts still occurred in the coarser channels. Filtering the electrolyte and keeping connections clean can reduce this form of noise, but it cannot be completely eliminated. Both high frequency and low frequency forms of noise can result in counts that appear as coarse particles.

In general, electrical sensing zone techniques are suitable for measuring oversize particles only when the oversize particles are smaller than the aperture size, when the analysis is performed with minimal coincidence effects and when no low frequency noise is present during the analysis. Even when all of these criteria are met, the technique is best suited for powders with mean sizes greater than 5 microns.

Microscopy techniques performed either manually or coupled with digital image analysis equipment, are popular size analysis methods that can also reveal information on particle shape, composition and other features not possible with higher speed analysis techniques. As **Table 1** describes, size analysis using optical microscopy methods is applicable for sizes down to about 1 micron and electron microscopes are suitable for sizes down to about 0.05 microns. Although the resolution associated with microscopy is excellent, the trade-off is that the data collection schemes are considerably slower than other size analysis methods resulting in poorer counting statistics for a given analysis time. When used for measuring bulk powder attributes, especially for narrow size distributions, the data from several thousand particles is usually adequate. However, for detecting and measuring oversize particles, especially those that exist in the parts per million ranges, the microscopy techniques do not lend themselves to scanning millions and millions of particles. Despite the quantitative limitations, the practice of scanning prepared slides of particles under a microscope looking for rogue oversize particles is quite common.

Laser light scattering size analysis methods, based on forward and right angle light diffraction principles are very popular for measuring size distributions. These methods are very appealing because they cover wide size ranges (0.1 to 1000 microns), require small sample quantities (less than 1 gram), generate reproducible data, and are fast and easy to operate. Commercially available systems can analyze powders dispersed in a liquid (usually water) or dry powders that have been aerosolized. In either case, the laser beam passes through a field of particles to a detector or series of detectors. The light passing through the field of particles is scattered at various angles and

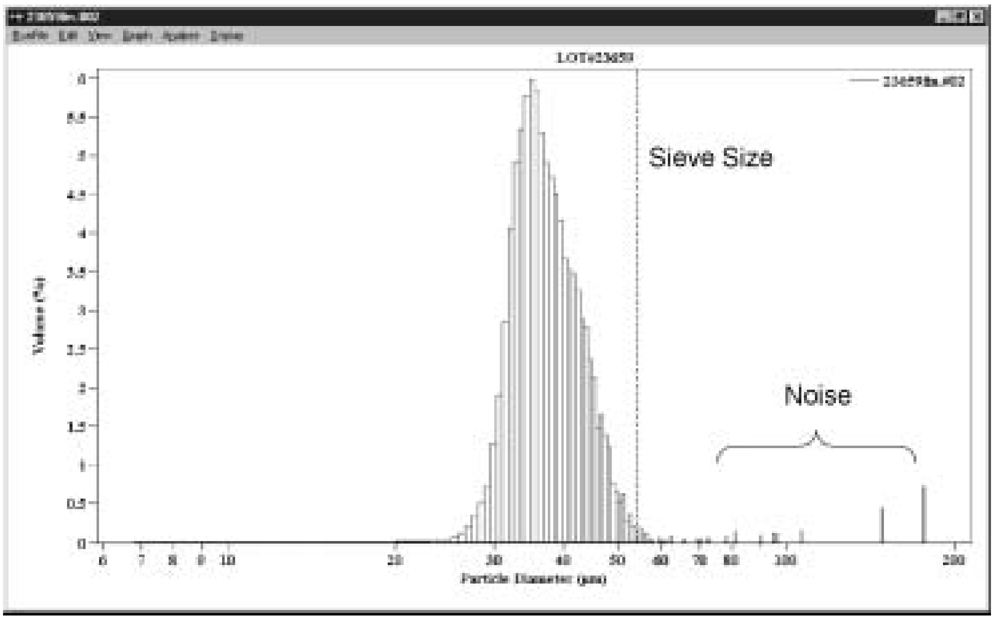

Fig. 4 Example of a particle size distribution from a powder that has been sieved three times to completely eliminate any gross-oversize particles. Subsequent analysis using an electrical sensing zone technique still shows counts that appear in coarser channels.

forms a diffraction pattern that is unique to the size distribution of the powder. The detectors are arranged at fixed angles that relate to a given size or size channel and the intensity of scattered light that falls onto each detector determines the percentage (typically by volume) of those particles in the distribution. The sensitivity of these detectors is such that it requires the cumulative amount of light scattered from many particles simultaneously to achieve the minimum level of light that the detectors can sense. It is the sensitivity limit of the light detectors that limits the ability of this technique for measuring oversize particles in a powder.

A few oversize particles dispersed among millions of particles are simply undetectable by this technique. **Fig. 5** describes this effect. In example A, a 1 micron mean size powder contains less than 0.01 percent by mass of oversize particles generally in the 10 micron or coarser size range. This powder produces an extremely poor surface finish when used for lapping or polishing glass substrates. In spite of the obvious presence of oversize crystals, the laser light scattering technique did not detect these. In fact, example B shows a powder with essentially the same size distribution as example A, but the sample B powder does not contain any oversize particles and performs as expected.

Sedimentation methods of particle size analysis can be performed using homogeneous suspensions in either a gravitational or centrifugal field. In either case, particle size is based on the differential settling rates of particles based on Stokes' Law. The determi-

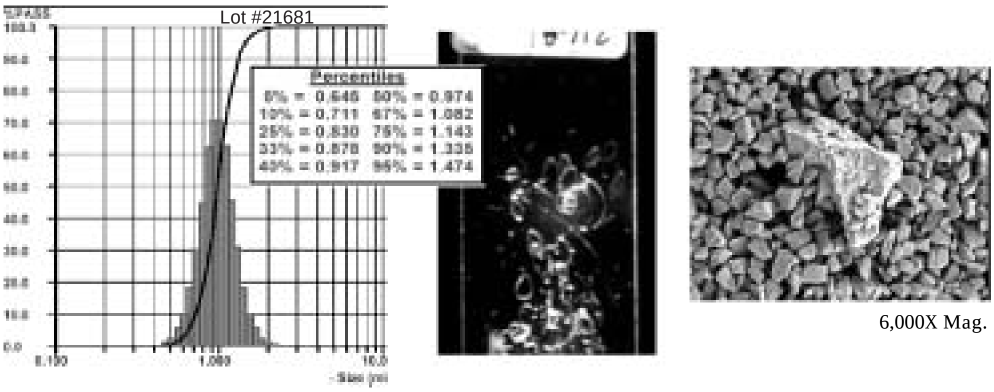

6,000X Mag.

A.) Diamond powder with low-level oversize particles that are undetected by laser light scattering but cause severe scratching.

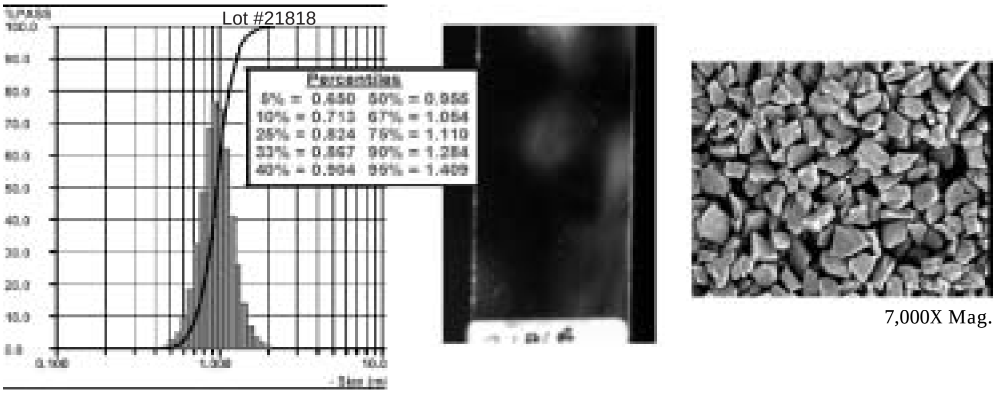

7,000X Mag.

B.) Diamond powder with similar bulk size distribution as A, but with no oversize particles.

Fig. 5 Examples of 1 micron mean size powders having A.) low levels of oversize particles that are undetected using a laser light scattering technique, but clearly causing scratches in lapping application; and B.) powder of similar size distribution having no oversize particles present and producing uniform surface finish in a lapping application.

nation of weight or volume fraction of particles within a size fraction is made in several ways: by physically collecting a sample of suspension and weighing the solids, by measuring the attenuation of an x-ray source through the suspension or by measuring the attenuation of a light or laser beam. If employing the cumulative weight measurement method, the ability of the sedimentation technique for detecting oversize particles is very limited simply because the weight of even a few oversize particles is well below the sensitivity of most weighing balances. If using radiation attenuation, the technique is limited in the same way that laser light scattering techniques are: by the lack of sensitivity of the detectors.

Photon correlation size analysis techniques are applicable to particles in the size range of 0.005 to 1 micron. Particle size is based on the response of a laser beam to particles vibrating in a liquid. Although the physics of the laser response to the particles is somewhat different than in laser light scattering systems, the basic limitations for detecting low-level oversize particles are essentially the same: the photodetectors simply do not have the sensitivity of detecting the response of a few larger particles within the field of on-size particles.

5. Oversize Measurement Recommendations

For powders with mean sizes coarser than 10 microns, sieving is clearly the preferred and most reliable method of measuring and detecting low levels of oversize particles. If the bulk size distribution of the powder is known, then a single sieve with sieve openings that are above the coarse tail of the distribution can be selected. Depending on the size of the powder, a known quantity of powder can be placed on top of a clean sieve (having been pre-inspected for holes and tears), and vibration and/or ultrasonic energy can be used for sieving the material through the openings. Sieving is complete after some point in time such that: 1.) No material resides on the sieve cloth or, 2.) A steady amount of residual material resides on the sieve cloth for a fixed period of time. As an added measure of accuracy, any residual material on the sieve cloth and sidewalls of the sieve can be washed through the sieve with water or alcohol.

If residue is present on the sieve, and it represents enough material for accurate weighing, then the residue can be carefully transferred to weighing paper and weighed. In some cases, there may not be a sufficient amount of material for weighing, then, a visual inspection of the sieve cloth under a stereo microscope would allow an estimate of the number of oversize particles retained. Microscopic analyses of this residue would also allow an estimate of the size of the oversize particles. The visual analysis of retained particles on a sieve cloth is aided by using smaller diameter sieves, such as a 3-inch diameter sieve. Smaller sieves help concentrate any oversize particles that may be present in a smaller area. Using this technique, it is indeed possible to find and measure a single oversize particle in a relatively large quantity (representing billions of particles) of powder.

For particles in the 0.1 to 10 micron mean size range, sieving techniques become less practical unless one knows beforehand that the oversize particles are larger than the sieve size that would retain them. Because of the limitations described above for the sensing zone techniques, these methods are not reliable for detecting low levels of oversize particles primarily because one cannot know with any certainty if counts that occur above the 99th percentile of a distribution are coincidence effects, noise or, in fact, really particles.

One technique that can be used for isolating and ultimately quantifying oversize particles in this size range is a modified sedimentation technique. As discussed above, the resolution of sedimentation technique is not suitable for detecting low levels of oversize particles when measuring a full distribution of particles and when using on-line radiation attenuation techniques. However, it is possible to utilize the technique for repeatedly fractionating a suspension at a single Stokes' diameter that would be chosen based on the known size distribution of the powder. In this technique, a known amount of powder is weighed and dispersed into a suspension at 1 to 5 weight percent solids. The dispersion technique would normally employ de-ionized water containing 0.1 to 0.5% of a surfactant in addition to pH adjustments so that the zeta potential of the dispersed solids is sufficiently high that adequate stability of the suspension is achieved. A combination of mechanical and ultrasonic agitation usually provides enough energy for breaking up any agglomerates that may act as oversize particles. For the very finest size powders, i.e., those less than 0.5 microns, longer agitation times will usually be required.

For powders with mean sizes greater than 1 micron, the sedimentation fractionation technique can be performed using gravity settling in a clean glass beaker. Using Stokes' Law, one can calculate the settling time required for the finest oversize particle to settle from the top of the liquid level to the bottom (or near the bottom) of the beaker. When the suspension is thoroughly mixed and dispersed, the beaker is allowed to stand for the calculated time while the particles settle. At the designated time, a pipette or pump is used for withdrawing the suspension down to a level near the bottom of the beaker. The withdrawn suspension can be saved or discarded, but is not required for further analysis. As the sediment always includes *all* of the oversize plus *some* of the bulk material, several decantation cycles must be performed. Therefore, after the first decantation, the beaker is filled again with “clean” de-ionized water that has been treated with surfactant and pH modifier. The retained suspension, which is now more dilute, is stirred and ultrasonically agitated. The suspension is then allowed to stand again for the calculated time until the oversize particles settle to the bottom and the suspension is decanted again. The process of diluting and decanting is repeated until the settled suspension contains a minimum level of on-size particles. The number of cycles required for isolating any oversize particles will also depend on the concentration of the initial solids loading in the suspension. For example, for the oversize particles to be more than 50% of the sediment, you would need 10 decantation cycles if the oversize particles are twice the median size and 4 cycles at 5 times the median, for 1 ppm oversize. For 1 ppb, it comes out to about 15 cycles and 6 cycles.

When the fractionation process is completed and if residue is present at the bottom of the beaker, and it represents enough material for accurate weighing, then the residue can be carefully dried, transferred to weighing paper and weighed. In some cases, there may not be a sufficient amount of material for weighing, then, a visual inspection of the settled particles under a stereo microscope would allow an estimate of the number of oversize particles in the powder. Microscopic analyses of this residue would also allow an estimate of the size of the oversize particles.

In powders having a mean size less than 1 micron, the same process as described above can be used however, centrifugal sedimentation can reduce the settling times. Whether one uses gravitational or centrifugal sedimentation, it is imperative that one minimizes the risk of external contamination of particles from mixers, probes, decant tubes, etc. In the case of gravity settling, the process can generally be scaled up to accommodate larger quantities of powder if necessary.

6. Summary

Levels of oversize particles may exist within narrowly graded abrasive powders at levels that are in the parts-per-million to parts-per-billion range. The presence of these particles can have a serious and deleterious effect on the performance of these powders especially in abrasive lapping, polishing and precision wire sawing applications. Although abrasive powders are manufactured to stringent size controls for the bulk distribution and measurement techniques are quite effective at characterizing the bulk of the distribution, the ability of detecting the low-levels of oversize particles remains a challenge. These low levels of particles are below the detection limit of most modern, high-speed size analysis techniques. The limitations of some of the most popular techniques are described with respect to their ability for detecting rogue oversize particles.

For powders with mean sizes at or above 10 microns, a sieve analysis technique is described that can be used for detecting and quantifying oversize particles with considerable resolution. For powders that are finer in size, a sedimentation technique can be used for isolating any oversize particles that may be present. The sedimentation method can be performed using either gravity or centrifugal sedimentation techniques.

References

1) Doyen, L., et. al. “Analyzing Large Particles in CMP Slurries,” Semiconductor International, Reed Elsevier (2002).
2) Fisher, G., “Challenges for 300 mm Polished Wafer Manufacturers,” Semiconductor International, Reed Elsevier (1998).
3) Cerutti, D., “Optimizing Systems for Media Texturing,” Proceedings of Industrial Diamond Association Symposium,” Vancouver, British Columbia (2001).
4) “Standard for Diamond Micron Powder Sizes,” Federation Europeenne des Fabricants de Produits Abrasifs, 1977.
5) “Characterization of Diamond and cBN Powders in Sub-Sieve Sizes,” ANSI-B74.20-1997, American National Standards Institute.
6) “IDA Graded Powder Standard,” Industrial Diamond Association of America, Inc. (1985).

Author’s short biography

Timothy F. Dumm

Dr. Timothy F. Dumm graduated from the Pennsylvania State University in 1989 with a degree in Mining Engineering and doctorate in Mineral Processing. He has worked with the industrial diamond division of the General Electric Co. and Diamond Innovations Co. in Worthington, OH for the past 16 years. He has developed milling, classification and characterization techniques for fine diamond and other superabrasive powders. He is currently involved in developing new applications for diamond in a broad range of industries including oil & gas drilling, electronics, plastics, glass, paints & coatings, ceramics and semiconductors.

Hydrogen Storage Characteristics of Nickel Nanoparticle Coated Magnesium Prepared by Dry Particle Coating[†]

D. Cooper and C.Y. Wu[1]
Department of Environmental Engineering Sciences
University of Florida
D. Yasensky and D. Butt
Department of Materials Science and Engineering
University of Florida
M. Cai
Research & Development Center
General Motors

Abstract

On-board hydrogen storage is an important obstacle to the development of a sustainable, ultra-low emission transportation system. A dry particle coating technique was used to coat micron-sized magnesium powders with Ni nanoparticles for hydrogen storage. Three parameters were explored in this study: powder size, nickel loading, and processing time. The composite materials were evaluated based upon a number of criteria, including the degree to which the nanoparticles were distributed over the Mg surface, the improvement in kinetics for hydrogen absorption, and the increased amount of hydrogen absorbed and desorbed. Comparisons were made between the bulk Mg powders and those coated with Ni. Due to the high shear forces it created, the dry particle coating system effectively distributed Ni nanoparticles onto the Mg powder surface. A coating process that required 48 hours using traditional ball milling was reduced to 90 minutes with the dry particle coating system. Magnesium powder with a mean diameter of 44 microns and a nickel loading of 2 atomic weight percent was the most kinetically active for hydrogen absorption under the conditions studied. Hydrogen absorption began at 150°C, and desorption started at 250°C. The dry particle coating system, however, did not alter the magnesium microstructure during 90 minutes of processing and did not produce the large surface areas generated by ball milling.

Key words: Hydrogen Storage Materials, Mechanical Alloying, X-Ray Diffraction, Metals, Nanoparticles

INTRODUCTION

Motor vehicles operating in the United States account for 65% of the oil consumption, 78% of all carbon monoxide emissions, 45% of nitrogen oxide emissions, and 37% of the volatile organic carbons (VOCs), as reported by the Environmental Protection Agency1). On average, the internal combustion engine is only 19% efficient in converting fuel into useful work2). Fuel cell vehicles, which rely on the electrochemical reaction of hydrogen instead of combustion, provide an attractive alternative. For example, proton exchange membrane fuel cells (PEFCs) are 40 – 45% efficient and emit only water vapor and heat when hydrogen gas, obtained from renewable sources, is used as a source of fuel3).

Providing a safe, reliable, efficient and continuous source of hydrogen to the PEFC is one of the most important technological obstacles to overcome before fuel cell vehicles become a viable alternative4). Automakers can choose to store hydrogen directly onboard as a liquid, gas, or hydride, or produce it onboard by refining a fossil fuel; however, it was

---

[†] Accepted: August 30, 2005

[1] Corresponding author
PO Box 116450
Gainesville, FL 32611-6450
TEL: 352-392-0845
FAX: 352-392-3076
E-mail: cywu@ufl.edu

found that vehicles operating on direct sources of hydrogen were simpler in design, lighter weight, more energy efficient, lower cost, and more environmentally benign than those operating with onboard fuel processors5). Solid storage in the form of metal hydrides has several advantages over other direct storage options, including improved safety and a higher hydrogen storage density (6.5×10^{22} H atoms/cm^3 for MgH_2) than hydrogen gas (0.99×10^{22} H atoms/cm^3) or liquid hydrogen (4.2×10^{22} H atoms/cm^3)4). Owing to its high hydrogen capacity, low weight, abundance in nature, and low environmental impact, magnesium is a favorable material for storage6), and thermodynamics favor the formation of the hydride at room temperature. Unfortunately, slow kinetics, resulting in high absorption and desorption temperatures (∼400℃) for MgH_2, limit its potential application7).

Many researchers have attempted to improve the hydrogen absorption/desorption kinetics through mechanical ball milling of bulk magnesium metal, alloying with transition metal catalysts and destabilizing the magnesium-transition metal-hydrogen matrix. Mechanical ball milling can improve hydrogenation rates over those of the bulk material due to its ability to affect changes in the microstructure of the magnesium6). Milling produces a nanocrystalline microstructure that provides an abundance of defects and grain boundaries near the surface6, 8). These fissures serve as passages for hydrogen diffusion, along with improving hydride nucleation and hydrogen atom penetration9). Planetary milling also increases the number of defects in the interior of the materials, while enlarging the specific surface area9). Particle size, also largely affected by mechanical milling, plays an important role in hydriding and dehydriding rate improvements. Mechanical milling is generally used to produce powders in the range of 60 − 100 μm6, 10). The smaller size increases the surface area to volume ratio of the powders and creates more active sites for hydrogen penetration.

Dehydrogenation properties are largely dependent upon the particle's microstructure11). Iwakura's group reported improvement in hydrogenation-dehydrogenation and charge-discharge characteristics resulting from the formation of a nanocrystalline or amorphous structure12). Particles with nano-crystalline structure (grain size 10 nm or less) increase the density of grain boundaries, resulting in easier activation11). A large fraction of hydrogen in the Mg_2Ni-H system occupies the deformed inter-grain regions and not the intra-grain regions13). Iwakura et al.12) postulated that hydrogen stored in the amorphous region was thermodynamically less stable than that stored in inter- and intra-grain regions, resulting in lower temperatures for desorption. When compared to the crystal hydride, the amorphous phase is less stable, which is reflected by the ease of hydrogen solubility in the amorphous phase14).

Alloying bulk magnesium powder with transition metal catalysts has drastically improved hydrogen absorption and desorption kinetics. Holtz and Imam10) reported improved hydrogen discharge rates with the addition of as little as 0.1 atomic weight percent (at %) nickel to the surface of the magnesium. Hydrogen molecules have a strong affinity for nickel and readily dissociate and adsorb onto surface-layer nickel clusters15, 16). Through the addition of 1 at % of nickel to magnesium, Holtz and Imam10) achieved a 50% increase in hydrogen capacity, a decrease of 100℃ in the temperature for the onset of hydrogenation and a lowering of the dehydrogenation onset temperature from for 50℃.

The uniform distribution of catalytic nickel on the surface also allows hydrogen absorption and desorption to occur in the presence of oxides and hydroxides6). Boulet and Gerard17) attributed the ability to absorb hydrogen in the presence of an oxide layer to a modification of the magnesium surface by the catalyst. Transition metal catalysts dissociate H_2 molecules into H atoms, which are able to diffuse along grain boundaries between the magnesium and the additive material. Hydrogen atoms are more easily absorbed by magnesium or magnesium compounds than H_2 molecules18). The interface between the magnesium and the catalyst acts as an active nucleation site for the hydride phase.

Elemental selection for metal hydride production must take into account chemical bonds between atoms. Yukawa et al.19) found that hydrogen interacts more strongly with hydride non-forming elements, B (e.g. Ni and Fe) than it does with hydride forming elements, A (e.g. La, Ti, Mg). However, the B-H interaction was only dominant in the presence of A elements20). Therefore, when designing an alloy for hydrogen storage, it is important to include both A and B elements. For pure metal hydrides (i.e. MgH_2), the interactions between the A and H atoms are strongly ionic, owing to the relatively wide energy gap between them. This results in a charge transfer from the A to the H atom and the formation of a stronger bond. In hydrogen storage alloys (i.e. Mg_2NiH_4) the valence band of the B element occurs in the intermediate energy range between the hydrogen and A element. The result is a covalent interaction between B and the hydrogen atoms, caused by the hybridization of the atomic orbitals to form molecular orbitals. By mixing both A and B elements, the B-H interaction is enhanced while the A-H interaction is weakened[19]. The weaker covalent bond allows for easier activation of the hydrogen desorption process[19, 20].

The objective of this research was to explore a new dry particle coating technique to produce composite materials of magnesium and nickel for hydrogen storage. The dry particle coating system was chosen as an alternative to ball milling because of its ability to disperse nanoparticles in a fraction of the time. Results of the literature review illustrate the important role powder composition and Mg microstructure play in improving hydriding kinetics. Magnesium was selected for study because of its high hydrogen storage capacity and the large volume of work available for comparison. Additions of catalytic amounts of transition metals to the magnesium surface lower the temperature of hydrogen absorption and desorption. Nanosized nickel was chosen for this study because it remains catalytically active even after the formation of oxides. Given that metal oxides readily form upon exposure of the pure metal to air, the ability to remain catalytically active is a valuable asset. Experiments were carried out to evaluate three parameters: Mg powder size, Ni loading and coating time. Hydrogenation studies were performed on the as-processed samples in order to determine the ideal parameters for maximizing hydrogen absorption. Having selected the most effective parameters, further analyses were performed to quantify the amount of hydrogen desorbed from the materials. Results of this study were compared to similar studies that utilized ball milling.

METHODOLOGY

Dry Particle Coating System

Samples containing Mg powder (300 µm, Fisher Scientific; 44 µm, Alfa Aesar; 4 µm, Reade Advanced Materials) and Ni nanoparticles (primary particle size: 72±30 nm, surface area: 6 m^2/g, bulk density: 0.66 g/cm^3, Argonide) in varying concentrations (0, 0.5, 1, or 2 at %) were mechanically processed using a dry particle coating system. Nickel loading in excess of 2 at % was not considered because the resultant loss in hydrogen capacity by weight rendered the materials less competitive for onboard storage. Coating runs lasted 30 or 90 minutes. A rotor speed of 4600 rpm, vessel speed of 70 rpm, gap-size of 1 mm, and Mg mass of 10 g were used to process all powder samples. **Table 1** lists the experimental conditions.

Consisting of an elliptic rotor encased in an elliptical vessel, the dry particle coating system (**Fig. 1**) utilizes a dry coating technique to produce the powder composites[21-25]. The rotor operates at high revolution while the vessel rotates at low speeds in the opposite direction. This applies strong compression and shear forces to the particles when they pass through a narrow gap between the rotor and vessel wall. Smaller gap-sizes increase the forces on the powders and should affect the microstructure of the powders, in addition to creating more cracks and irregular surfaces. The process also more evenly distributes the nickel nanoparticles onto the magnesium surface. A stainless steel vessel and stainless steel rotors capable of maintaining an inert atmosphere were used.

All handling was conducted in a glove box (Plas

Table 1 List of experimental conditions

Set Number	Dry Particle Coating System			Hydrogenation[a]	
	Mg powder size[b] [µm]	Ni loading (x)[c] [at %]	Coating time [min]	Mg-x at % Ni [g]	H_2 gas [%]
1	300	0, 0.5, 1, 2	30, 90	0.1	100
2	44	0, 0.5, 1, 2	30, 90	0.1	100
3	44	0, 1, 2	30, 90	1.8	100
4	4	1, 2	90	1.8	100
5	4, 44	2	90	1.8	100
6	44	2	90	1.8	100[d]

[a] The chamber was heated to 200℃ over approximately 1 hour and maintained for 150 minutes, unless otherwise noted

[b] 10 g of Mg were used for all sets; set 5 used 5 g of each powder size

[c] Ni loading of 0.5, 1, or 2 at % is equivalent to 0.1205, 0.2410, or 0.4820 g, respectively

[d] Chamber was quickly heated (<20 min) to 200℃ and then maintained for 150 minutes

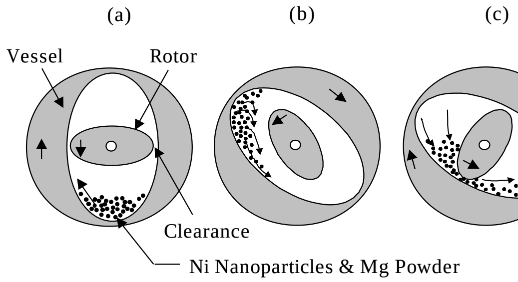

Fig. 1 Schematic of Dry Particle Coating System

Labs, Inc. Model 855-AC) under argon because of the potential reactivity of Mg with air and water. An oxygen analyzer (Cambridge Sensotec, Ltd. Rapidox 3000) was used to monitor the oxygen level in the glove box, which was maintained at lower than 500 ppm.

Hydrogenation System

Hydrogen absorption studies were carried out using a custom designed hydrogenation system (**Fig. 2**). The core of the system was a custom-made stainless steel reaction chamber, 180 cm^3 in volume. High temperature heating tape (Barnstead/Thermolyne, BIH101040) was used to heat the chamber. The chamber was pressurized with pure hydrogen (high purity grade) using a special high-pressure regulator (Concoa, Inlet No. 3124321-01-350). Argon (Praxair, high purity grade) was used to flush the system and remove any contaminants. Pressure was monitored using an electronic pressure transmitter (Omega, PX880) connected to a process panel meter (Omega, DP25B-E). Temperature was measured via a thermocouple (Omega) attached to the outside of the chamber under the heating tape.

Hydrogenation experiments were performed with various Mg powder sizes and Ni loadings to evaluate their effects on hydrogen storage capacity and absorption rates. Initial pressure and temperature readings were taken and recorded prior to heating the chamber. Samples were slowly heated to 200℃ (~60 min) under an initial H_2 pressure of 145 psi and maintained at that temperature for 150 minutes. Experiments were also performed with Mg-2 at % Ni,

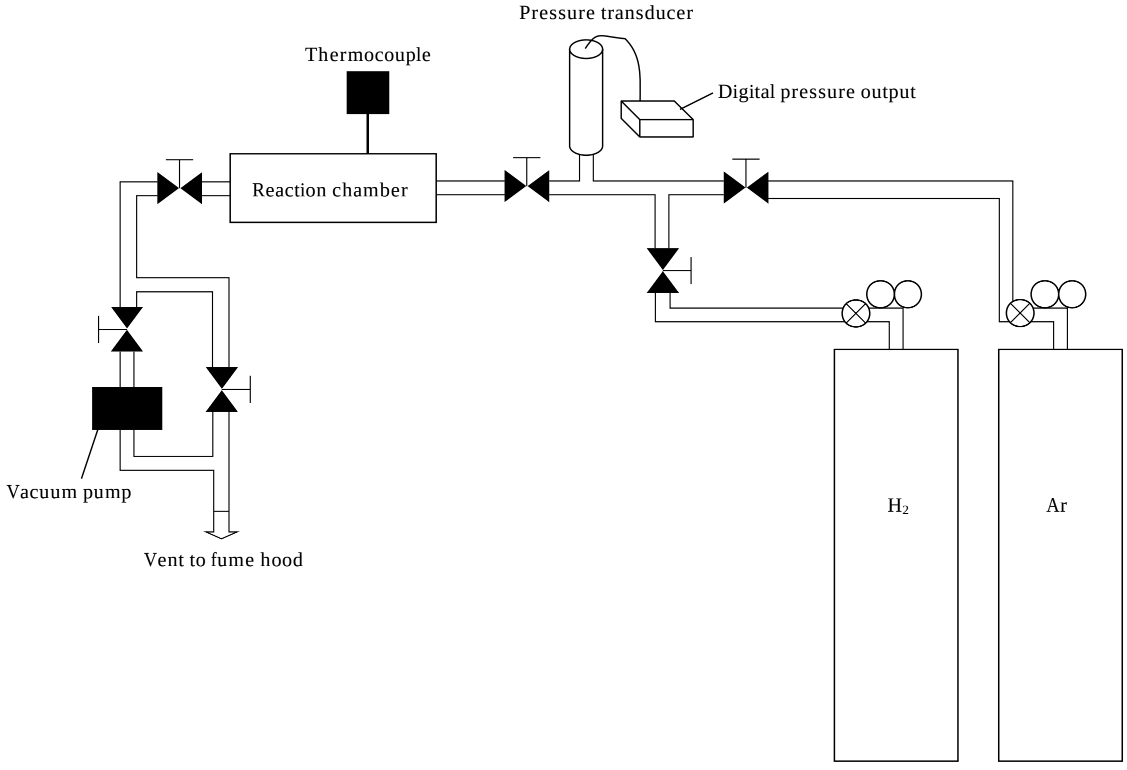

Fig. 2 Schematic of the hydrogenation system

after 90 minutes of processing following a different heating regimen: the chamber was quickly heated (<20 minutes) to 200℃, which was then maintained for 150 minutes. Reaching higher temperatures faster, it was hypothesized, would increase the rate of hydrogen diffusion and minimize the formation of impenetrable surface layers of hydrogen.

Hydrogen Desorption

Desorption studies were performed using a Thermogravimetric analyzer (TGA 2050, TA Instruments) with a sensitivity of 0.2 μg. A small amount (~50 mg) of MgH_2-2 at % Ni was placed on a platinum pan and the system was set to ramp to 350℃ at 2℃/min; after ramping, the system was cooled to room temperature over 60 minutes. Throughout the run, Ar was flowing at a rate of 90 cm^3/min over the sample surface in the furnace and 10 cm^3/min was flowing into the furnace to maintain a positive pressure in the region of the balance. A baseline was generated by performing a similar analysis with a sample of the Mg-2 at % Ni that had not been exposed to hydrogen. The difference in mass loss between the baseline and the hydrogenated samples would be attributable to hydrogen desorbed from the sample. Similar desorption experiments were performed for Mg-2 at % Ni processed for 30 minutes and Mg-1 at % Ni processed for 30 and 90 minutes.

Powder Characterization

X-ray diffraction (XRD, Phillips APD 3720) with Cu Kα radiation was used to identify the compounds present in the mechanically coated powders before and after hydrogenation. The main compounds of interest were Mg, Ni, MgH_2, Mg_2Ni, MgO, MgNi and $MgNi_2$. Reference scans for all of the compounds were obtained from JCPDS[26)] values for diffraction data using PCPDFWIN software. XRD was also used to identify the crystalline structure of the powders. Broadening of the peaks following coating would indicate the formation of nanocrystalline or amorphous structures.

Scanning electron microscopy (SEM, JEOL JSM 6400) was used to examine the surface of the magnesium powders before and after coating. Secondary electron images of the pure magnesium powder and coated materials were compared to evaluate the extent to which the Ni nano-catalyst had been distributed over the Mg surface. SEM was also used to qualify any changes in the appearance of the Mg grains (i.e. evidence of cracking or formation of surface defects). Backscatter electron imaging returned an image with atomic number contrast, which allowed for the identification of the Ni powders. Energy dispersive spectroscopy (EDX) was used to determine the elemental composition on the surface of the sample. Analysis of the resulting spectrum of energy versus relative count allows for a quantitative and qualitative assessment of the sample constituents.

RESULTS AND DISCUSSIONS

Color Change

Prior to processing in the dry particle coating system, the 300 μm Mg powders were silver in color and the Ni nanoparticles were black. Following 90 minutes of processing with Ni, the powders lost their luster and acquired a dull-gray color. The 44 μm powders were darker initially than the larger powders and processing with Ni served to darken them further. No change in color was observed for the 4 μm powders. This color change suggested that the dry particle coating system had sufficiently coated the Ni nanoparticles onto the Mg powder for the two larger sizes. Following exposure to hydrogen, the 44 μm powders were significantly darkened, with the original color returning after one desorption cycle in the TGA. Qualitatively, this provided evidence of hydrogen absorption and desorption.

Powder Size, Ni Loading, and Processing Time

Hydrogen absorption studies were first carried out for 300 μm Mg powders processed in the dry particle coating system for 90 minutes. Each 2 g coated sample (0.5, 1 and 2 at % Ni) was hydrogenated under a starting hydrogen pressure of 145 psi. For comparison purposes, a 2 g sample of pure, unprocessed Mg powder was examined using the same protocol. Both samples were characterized by XRD before and after exposure to hydrogen (not shown).

Good agreement between the intensity of the Ni peak ($°2\theta=45$) and the amount of Ni added to the system (i.e., 2 at %>1 at %>0.5 at %) was observed. This was indicative of successful Ni coating onto the Mg surface. The characteristic MgH_2 peaks ($°2\theta=28$ and 36) were present for these coated materials; however, the relative intensity of the hydride peaks to the Mg peaks ($°2\theta=32$, 34, 37) was small. Results of these hydrogenation studies revealed only a minimal amount of hydrogen absorbed by the 300 μm particles, likely a surface layer of hydride[16, 27, 28)]. Considering how little of the Mg-x at % Ni was converted to the hydride phase, it was concluded that Mg powders with particle sizes in the 300 μm size range were not suitable for hydrogen storage applications using this technique. Because of their large diameter and low surface to volume ratio, diffusion of the hydrogen across the hydride layer into the bulk magnesium core was most likely the barrier to absorption. Neither increased Ni loading nor longer processing time were capable of dramatically improving hydride formation.

Experiments performed with the 44 µm (Sets 2 and 3) powders showed a significant increase in the formation of the hydride phase relative to the similarly prepared 40 − 80 mesh powder samples. This is reflected by the significant increase in the MgH_2 peak (°2θ=28) intensity relative to the Mg (°2θ=37) peak intensity. **Fig. 3** shows the XRD patterns for the 44 µm samples. Given that the intensity of each component's main peak is proportional to the amount present[29)], more of the hydride phase was formed in the 44 µm powder.

Increasing the Ni loading clearly enhanced the quantity of hydrogen absorbed by the 44 µm powders. As shown in **Fig. 3**, with increased Ni loading, the ratio of the Mg peak intensity (°2θ=37) to the MgH_2 peak intensity (°2θ=28) also increased. This indicates that chemisorption of H_2, the process that can be improved by transition metal additions, was the limiting factor for hydride formation in this size range.

The effect of processing time on the 44 µm particles was examined by hydrogenating powders with a reduced processing time (30 minutes) in the dry particle coating system. The intensity peak ratios are 0.21, 0.30 and 0.38 for Mg-x at % Ni (x=0.5, 1, and 2), respectively. Comparing the results for Mg-2 at % Ni at different processing times, the product with a longer processing time of 90 minutes had absorbed significantly more hydrogen. Conceivably, 30 minutes is not long enough to effectively distribute the nanocatalyst. It is interesting to note that powders coated with 0.5 at % Ni absorbed more hydrogen when processed for a shorter period of time. Increasing the processing time for the samples with 0.5 at % Ni loading may have actually embedded the already coated nanoparticles into the Mg surface. Once embedded, less of the Ni surface area would be exposed to H_2, leading to a reduction in the catalytic effects.

Secondary electron images of the 44 µm Mg powder, following 90 minutes of processing with and without 2 at % Ni, are shown in **Fig. 4**. The powders are very smooth and relatively free of surface defects in addition to being uniform in size and shape. Ball milling, in contrast, produces irregularly shaped powders with numerous surface defects and a very rough surface[6, 30)]. Processing in the dry particle coating system does not appear to impart any physical change on the Mg powders under the conditions studied.

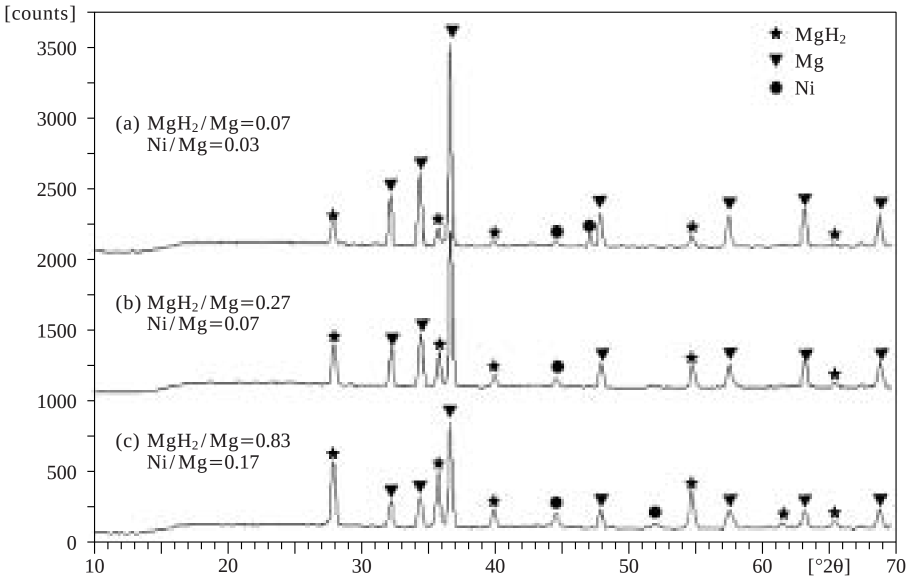

Fig. 3 XRD patterns for 44 µm powder samples of (a) MgH_2-0.5 at % Ni, (b) MgH_2-1 at % Ni, and (c) MgH_2-2 at % Ni processed for 90 minutes. Peak intensity ratios of MgH2/Mg and Ni/Mg for each sample are indicated

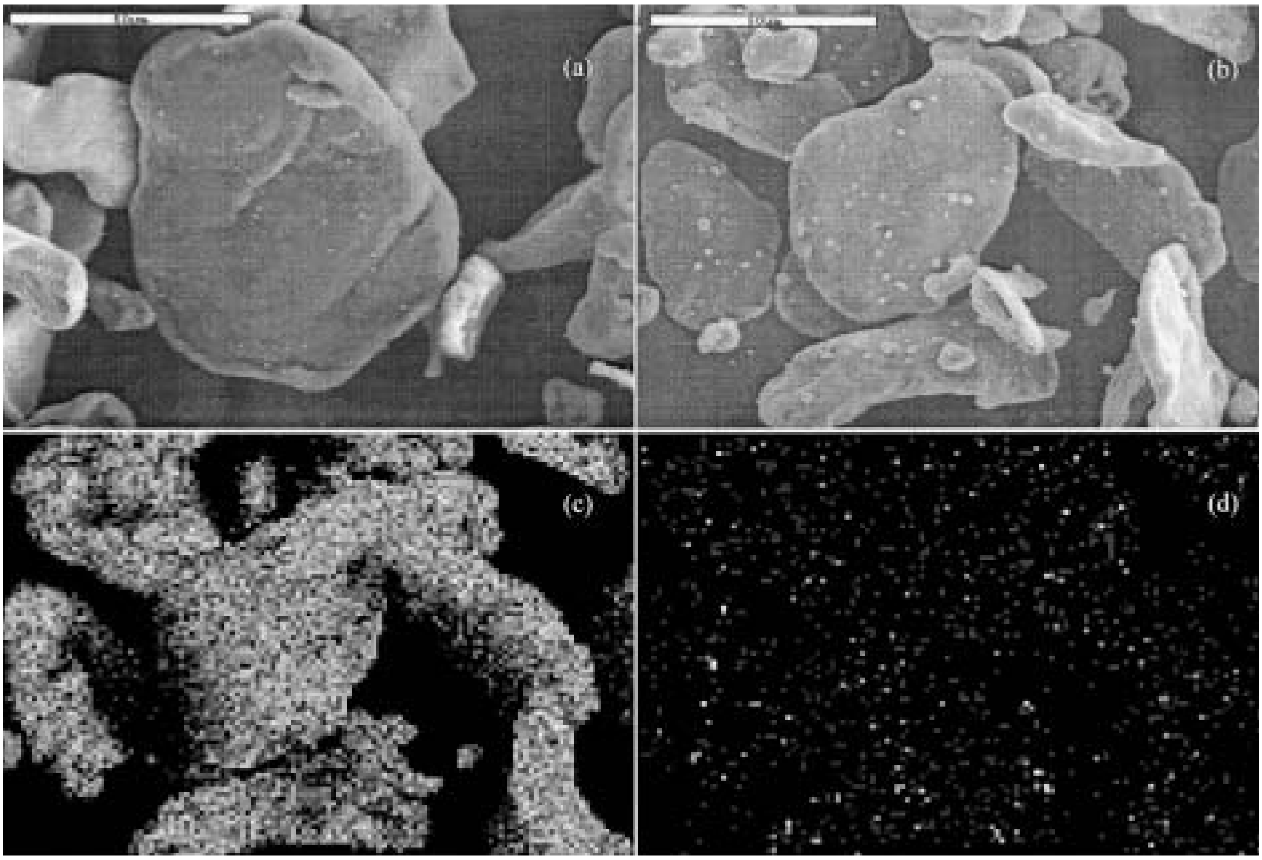

Fig. 4 SEM images of (a) pure Mg (44 μm) processed for 90 minutes and (b) Mg-2 at % Ni processed for 90 minutes; EDX mapping of (c) Mg and (d) Ni for Mg-2 at % Ni

EDX mapping of Mg-2 at % Ni is also shown in **Fig. 4**. The bright spots in image (c) are from Mg Kα X-ray emissions and those in image (d) are for Ni Kα radiation. Although present in only a small amount, the Ni appears to be evenly distributed over the Mg surface: there are no localized regions of intensity. Small levels of oxygen were present in both samples, an expected result given that magnesium readily forms surface layers of hydroxides, oxides, and carbon-oxygen compounds.

The comparison of the 300 μm and 44 μm results agreed with earlier studies (e.g. Zaluska et al.6)) that concluded smaller sizes (<50 μm) eliminate the problem of a compact hydride layer blocking further hydrogen absorption. Diffusion through this hydride layer is slow – many orders of magnitude slower than in Mg – and becomes the rate-limiting step in the hydride formation process31, 32). Higuchi et al.14) reported that hydrogen penetrated to an average depth of 30 μm and stopped. For a spherical particle, this correlates to a diameter of no more than 60 μm. Limiting powders to this size will reduce kinetic barriers associated with slow hydrogen penetration through the hydride layer33).

Experiments were also carried out for 4 μm powders (Set 4). It was hypothesized that the increased surface to volume ratio would improve hydrogen capacity; however, these samples absorbed significantly less hydrogen than the 44 μm powder samples and nearly the same amount as the 300 μm powders. Most likely, the poor performance was a result of ineffective coating with the Ni nanoparicles due to adhesion of the 4 μm Mg powders to the sides of the dry particle coating system vessel during processing. This agrees with the observation reported in the "Color Change" section. Clearly, hydrogen absorption depends not only on powder size but also on the effectiveness of the catalyst coating onto the Mg surface.

Experiments were then carried out with mixtures of the 44 μm and 4 μm powders (Set 5). The hypothesis was that 44 μm powders would improve the flow of the 4 μm powders in the dry particle coating system, thus reducing the amount of powder adhered to the vessel walls and increasing hydride formation. Although hydride formation improved, the combined sizes absorbed less hydrogen than the 44 µm powders alone. Again, the effective dispersion of the Ni particles onto the 4 µm powders may not have occurred, thus preventing them from absorbing hydrogen under the conditions of this study.

Hydrogen Absorption

The above studies were performed to elucidate the most desirable combinations of Mg powder size, Ni loading, and processing time for maximizing hydride formation. Additional experiments were performed to measure the amount of H_2 absorbed by these samples and to determine the onset temperature for absorption. Plots in **Fig. 5** are temperature and pressure profiles for hydrogenation runs of (A) the background, (B) Mg-1 at % Ni – 30 min, (C) Mg-1 at % Ni – 90 min, (D) Mg-2 at % Ni – 30 min and, (E) Mg-2 at % Ni – 90 min. The higher pressures for curve A are a result of the higher temperatures. Although the same procedure was followed for all runs, there were some minor differences in temperature profiles due to the variation in the heating tape wrapping. **Fig. 6** shows the XRD profiles for these runs; there is a clear difference in the amount of hydride formed. The powder coated with 2 at % Ni and processed for 90 minutes absorbed the most H_2 under the conditions studied.

Curves for 90 minutes of processing (C, E) have a similar shape, as do the curves for 30 minutes of processing (B, D), which is indicative of similar mechanisms for H_2 absorption for each processing time. Materials processed for 90 minutes were still absorbing hydrogen after 150 minutes at ~200℃, as evidenced by their maintaining the same slope. Absorption rates for powders processed for 30 minutes, however, were leveling off after 120 minutes. Extended processing in the dry particle coating system improved the hydrogen storage capacity and absorption rate for powders with the same Ni loading. Longer processing times (90 minutes) may increase the number of active absorption sites by more evenly distributing the Ni nanoparticles over the Mg surface. Shorter processing times (30 minutes) may not sufficiently disperse agglomerates on the surface, resulting in only localized catalytic enhancement. Also of note are the lower temperatures required for powders with 2 at % Ni loading to begin hydrogen absorption (where the slope of the pressure curve changed significantly). For example, Mg-2 at % Ni (90 min) began to absorb hydrogen at 170℃ (marked by arrow). Nickel was effective at lowering the high temperature required for the onset of hydrogenation in pure Mg.

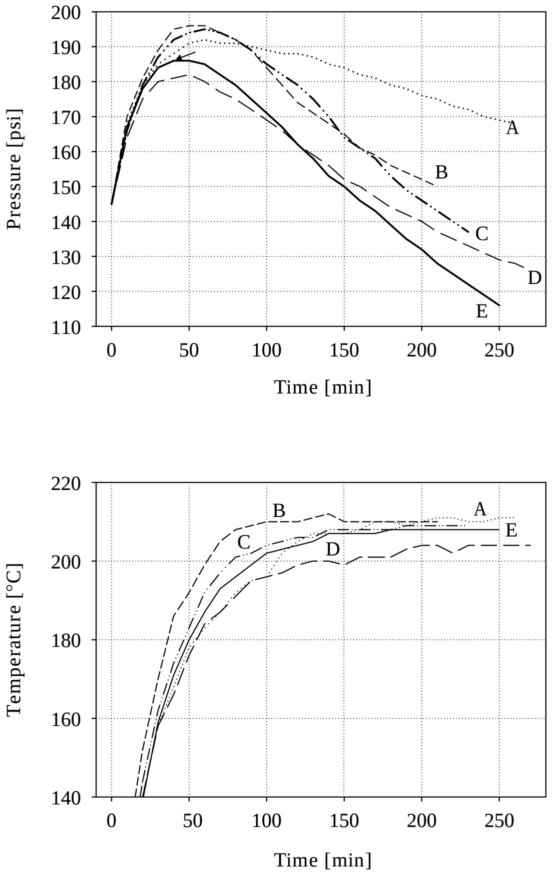

Fig. 5 Profiles for hydrogenation runs: (A) without material, (B) with Mg-1 at % Ni – 30 min, and (C) with Mg-1 at % Ni – 90 min, (D) with Mg-2 at % Ni – 30 min, and (E) with Mg-2 at % Ni – 90 min. The initial temperature was 24℃

XRD scans in **Fig. 6** clearly show that combining longer processing times with increased Ni loading improves hydrogen absorption capacity for these alloys. Whether longer processing time or increased Ni loading is more effective at improving hydrogen absorption is not as clear. A sample processed for 30 minutes with 2 at % Ni absorbed nearly the same amount of hydrogen as a sample processed for 90 minutes with only 1 at % Ni. The longer processing time provides better dispersion of the low Ni loading, which produces effects equivalent to a higher loading with poorer dispersion due to the shorter processing time.

The Mg-2 at % Ni powder processed for 90 minutes

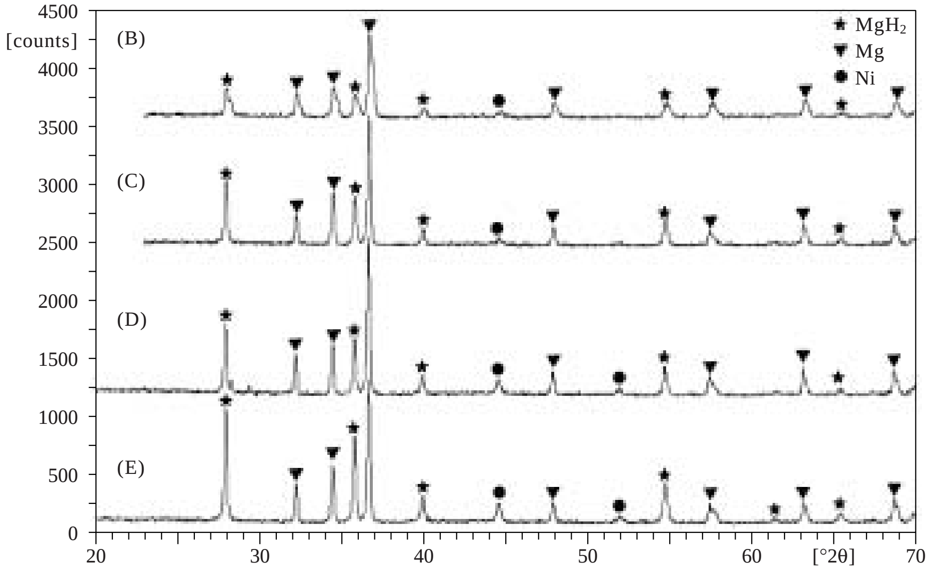

Fig. 6 XRD patterns for (B) MgH_2-1 at % Ni - 30 min, (C) MgH_2-1 at % Ni - 90 min, (D) MgH_2-2 at % Ni - 30 min and (E) MgH_2-2 at % Ni - 90 min. Stoichiometric amounts of Mg-x at % Ni and hydrogen were used for the absorption runs

was shown to absorb the most hydrogen; therefore, it was selected for further study. Experiments were conducted with very slow heating (<1℃/min) in order to determine the temperature required for the onset of hydrogen absorption. The results showed that absorption began at 150℃ and continued for 3 hours to a final temperature of 170℃. This material appeared to have absorbed about the same amount of hydrogen (XRD spectra not shown) as the Mg-1 at % Ni powder processed for 90 min (**Fig. 6C**); however, less of the hydride phase was formed than for the same material (Mg-2 at % Ni, 90 minute) heated to 200℃ at a rate of 3℃/min and maintained at that temperature (**Fig. 6E**). As evidenced, higher temperatures help overcome the slow diffusion kinetics and are required to hydrogenate these powders more completely.

Comparing the XRD spectra for pure Mg and those processed for 30 and 90 minutes shows no evidence that longer processing times affected the crystalline structure of the Mg powders. Neither peak broadening nor reductions in intensity are observed. Their presence would have indicated a reduction of the crystalline size to the nanometer range or the formation of amorphous powders. Additionally, Mg_xNi_y alloys were not observed. In contrast, ball milling affects the Mg microstructure, producing nanocrystalline and amorphous powder alloys. This increases the number of grain boundaries that improves hydrogen diffusion rates[7, 30, 34]. Given that the presence of surface defects and grain boundaries improves hydrogen absorption, the absence of these defects in the processed samples might be responsible for the slower absorption rates witnessed. In this study, the addition of Ni nanoparticles improved chemisorption; however, hydrogen diffusion was the rate limiting step because dry particle coating does not affect the Mg microstructure.

Hydrogen Desorption

Hydrogen desorption studies were performed using TGA. A background scan was first carried out for an Mg-2 at % Ni sample that had not been exposed to hydrogen. The results are shown in **Fig. 7**; a weight change of 0.2547 wt % was observed, which resulted from the loss of any surface impurities (i.e., hydroxides and carbon oxygen compounds). This background loss was applied to subsequent studies performed with the hydrogenated powders to determine the amount of hydrogen desorbed. The four samples examined in the absorption study were analyzed ((B) Mg-1 at % Ni − 30 min, (C) Mg-1 at % Ni − 90 min, (D) Mg-2 at % Ni − 30 min, (E) Mg-2 at % Ni − 90 min), and the results are shown in **Fig. 7**. The powders with 2 at % Ni loading processed for 90 minutes in the dry particle coating system desorbed the most hydrogen: 2.825 wt %. The onset of desorption started at ~200℃ and proceeded rapidly between 225

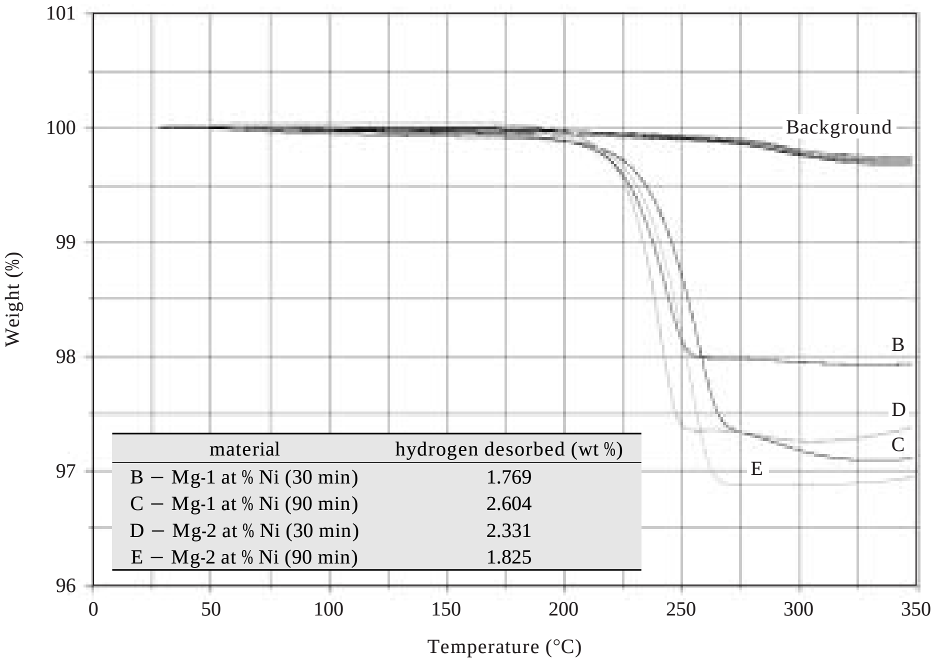

Fig. 7 Weight change from TGA desorption

and 250℃. The major desorption for all samples was completed by 275℃. XRD scans of Mg-2 at % Ni, prior to hydrogenation, and MgH_2-2 at % Ni, prior to and after desorption, showed that following desorption with the ramping profile, all of the hydride phase was converted to pure Mg.

It should be noted that the material regained 0.42 wt % from 325 to 350℃. The weight gain was most likely caused by the absorption of impurities in the Ar gas flow. It is interesting to note that the background sample showed no evidence of weight gain at higher temperatures. One possible explanation is that having been exposed to hydrogen, the surface of the dehydrogenated powders was more active for absorption. Prior to activation, oxide and hydroxide surface layers are barriers to hydrogen absorption and conceivably could have prevented the background sample from absorbing impurities. Future work can focus on identifying the absorbed impurities and determining if they enhance or hinder subsequent hydrogen absorption. Furthermore, the desorbed gas stream should be collected and analyzed as impurities in the stream could affect the performance of the fuel cell$^{35)}$.

CONCLUSIONS

Replacing fossil fuel powered transportation with zero emission fuel cell vehicles could drastically reduce the contribution of vehicular exhaust to ambient air quality problems. Hydrogen storage, however, remains a significant barrier to the wide-scale implementation of hydrogen-powered vehicles. To explore a potential solution to this pressing problem, nickel coated magnesium powders were prepared using a dry particle coating system and the hydrogen absorption/desorption properties were examined.

Magnesium powders of 44 µm in diameter processed with 2 at % Ni for 90 minutes were found to absorb hydrogen at a pressure of 145 psi starting from as low as 150℃. Furthermore, the hydrogenated powders desorbed 2.857±0.0003 wt % H_2 in 20 min between 225 and 265℃. Hydrogen absorption improved with increased processing time or increased Ni nanoparticle loading. Magnesium powders with sizes of 300 and 4 µm, prepared under similar conditions, absorbed only minimal amounts of hydrogen. While the 300 µm powders were coated successfully, the large diameter limited mass transfer. It was hypothesized that the small 4 µm powder would be free of the mass transfer problem, but it was not coated well in this process.

When compared to ball milling, the dry particle coating system can coat and distribute Ni nanocatalysts on Mg powders in a drastically shorter time. However, extensive ball milling affects the morphology of the Mg powders, resulting in nanocrystalline and amorphous structures that improve the kinetics for hydrogenation and dehydrogenation. The dry particle coating system, in contrast, did not yield an observable change in crystalline structure under the conditions of this study. Ball milled samples of Mg-1 at % Ni absorbed 6.13 wt % H_2 after 50 hours of milling compared to 2.6 wt % for samples processed by dry particle coating for 90 minutes. Samples prepared by ball milling completely desorbed H_2 in 20 minutes at 350℃, although they began to desorb hydrogen at 275℃10). Powders processed by the dry particle coating system completely desorbed in 20 minutes, between 220 to 265℃. The future work should examine how the coating process affects the particle characteristics (e.g. size distribution and specific surface area) that may shed new light on how to further improve the hydrogen absorption/desorption capabilities.

ACKNOWLEDGEMENT

This work was supported by General Motors under Contract No. ND0284600. The authors are grateful for the technical support of Tokuju Corp and Dr. Satoru Watano at Osaka Prefecture University, Japan, and the Major Analytical Instrumentation Center at University of Florida. David Cooper acknowledges partial financial support from Dr. Dale Lundgren in the form of USEPA Air Pollution Training Grant.

REFERENCES

1) EPA, Light-Duty Automotive Technology and Fuel Economy Trends 1975 Through 2001. In Advanced Technology Division, Office of Transportation and Air Quality: 2001.
2) Rocky Mountain Institute, Energy: Fuel Cells and Hydrogen. In Rocky Mountain Institute: 2002; Vol. 2002.
3) Fuel Cells 2000 The Online Fuel Cell Information Center.
http://www.fuelcells.org/index.html (August 2002),
4) Becker, L. Hydrogen Storage.
http://www.csa.com/hottopics/hydrogen/overview.php#n1 (November 2002),
5) Ogden, J. M., Developing an Infrastructure for Hydrogen Vehicles: A Southern California Case Study. *International Journal of Hydrogen Energy* **1999**, 24, (8), 709-730.
6) Zaluska, A.; Zaluski, L.; Ström-Olsen, J. O., Nanocrystalline magnesium for hydrogen storage. *Journal of Alloys and Compounds* **1999**, 288, 217-225.
7) Yang, J.; Ciureanu, M.; Roberge, R., Hydrogen Storage Properties of Mg and Zr-Ni-Cr Alloys. *Materials Letters* **2000**, 43, 234-239.
8) Orimo, S.; Fujii, H., Hydriding Properties of the Mg_2Ni-H System Synthesized by Reactive Mechanical Grinding. *Journal of Alloys and Compounds* **1996**, 232, L16-L19.
9) Song, M. Y., Effects of Mechanical Alloying on the Hydrogen Storage Characteristics of Mg-xwt% Ni (x=0, 5, 10, 25 and 55) Mixtures. *International Journal of Hydrogen Energy* **1995**, 20, (3), 221-227.
10) Holtz, R. L.; Imam, M. A., Hydrogen Storage Characteristics of Ball-Milled Magnesium-Nickel and Magnesium-Iron Alloys. *Journal of Materials Science* **1999**, 34, 2655-2663.
11) Hong, T.-W., Dehydrogenation Properties of Nano/Amorphous Mg2NiHx by Hydrogen Induced Mechanical Alloying. *Journal of Alloys and Compounds* **2000**, 312, 60-67.
12) Iwakura, C.; Inoue, H.; Nohara, S.; Shin-ya, R.; Kurosaka, S.; Miyanohara, K., Effects of Surface and Bulk Modifications on Electrochemical and Physiochemical Characteristics of MgNi Alloys. *Journal of Alloys and Compounds* **2002**, 330-332, 636-639.
13) Fujii, H.; Orimo, S.; Ikeda, K., Cooperative Hydriding Properties in a Nanostructured Mg_2Ni-H System. *Journal of Alloys and Compounds* **1997**, 235-254, 80-83.
14) Higuchi, K.; Kajioka, H.; Toiyama, K.; Fujii, H.; Orimo, S.; Kikuchi, Y., In Situ Study of Hydriding-Dehydriding Properties in Some Pd/Mg Thin Films with Different Degree of Mg Crystallization. *Journal of Alloys and Compounds* **1999**, 293, 484-489.
15) Baer, R.; Zeiri, Y.; Kosloff, R., Hydrogen Transport in Nickel (111). *Physical Review B* **1997**, 55, (16), 952-974.
16) Bloch, J.; Mintz, M. H., Kinetics and Mechanisms of Metal Hydride Formation — A Review. *Journal of Alloys and Compounds* **1997**, 253-254, 529-541.
17) Boulet, J. M.; Gerard, N., The Mechanism and Kinetics of Hydride Formation in Mg-10 wt % Ni and CeMg12. *Journal of the Less Common Metals* **1983**, 89, 151-161.
18) Zeppelin, F.; Reule, H.; Hirscher, M., Hydrogen Desorption Kinetics of Nanostructured MgH_2 Composite Materials. *Journal of Alloys and Compounds* **2001**, 330-332, 723-726.
19) Yukawa, H.; Nakatsuka, K.; Morinaga, M., Design of Hydrogen Storage Alloys in View of Chemical Bond Between Atoms. *Solar Energy Materials & Solar Cells* **2000**, 62, 75-80.
20) Morinaga, M.; Yukawa, H.; Takagi, M., Roles of Constituent Elements and Design of Hydrogen Storage Alloys. *Journal of Alloys and Compounds* **2002**, 330-332, 20-24.
21) Coowanitwong, N.; Wu, C. Y.; Nguyen, J.; Cai, M.; Ruthkosky, M.; Rogers, J.; Feng, L.; Watano, S.; Yoshida, Y., Surface Enhancement of Al_2O_3 Fiber with Nanosized Al_2O_3 Particles Using a Dry Mechanical Coating Process. *Journal of Engineering Materials and Technology* **2003**, 125, 163-169.
22) Watano, S.; Imada, Y.; Miyanami, K.; Wu, C. Y.; Dave, R. N.; Pfeffer, R., Surface Modification of Food Fiber by Dry Particle Coating. *Journal of Chemical Engineering Japan* **2000**, 33, (6), 848-854.

23) Iwasaki, T.; Koga, T.; Satoh, M., Analysis of Compressing and Shearing Behavior of Powders in High Speed Elliptical-Rotor-Type Powder Mixer (HEM). *Journal of Chemical Engineering Japan* **2000**, 33, (3), 499-506.
24) Iwasaki, T.; Satoh, M.; Ito, T., Determination of Optimum Operating Conditions Based on Energy Requirements for Particle Coating in a Dry Process. *Powder Technology* **2002**, 123, 105-113.
25) Pfeffer, R.; Dave, R. N.; Wei, D.; Ramlakhan, M., Synthesis of Engineered Particulates with Tailored Properties using Dry Particle Coating. *Powder Technology* **2001**, 117, 40-67.
26) JCPDS, *International Center for Diffraction Data*. 1996.
27) Hampton, M. D.; Lomness, J. K.; Giannuzzi, L. A., Surface Study of Liquid Water Treated and Water Vapor Treated $Mg_{2.35}Ni$ Alloy. *International Journal of Hydrogen Energy* **2002**, 27, 79-83.
28) Holtz, R. L., *Basic User's Guide for NRL 6323 Hydrogen Storage System*. Naval Research Laboratory: Washington, DC, 1996.
29) Klug, H. P.; Alexander, L. E., *X-Ray Diffraction Procedures: For Polycrystalline and Amorphous Materials*. 2nd ed.; John Wiley & Sons: New York, 1974.
30) Liang, G.; Huot, J.; Boily, S.; Van Neste, A.; Schulz, R., Hydrogen Absorption Properties of a Mechanically Milled Mg-50 wt % $LaNi_5$ Composite. *Journal of Alloys and Compounds* **1998**, 268, 302-307.
31) Friedlmeier, G.; Groll, M., Experimental Analysis and Modeling of the Hydriding Kinetics of Ni-Doped and Pure Mg. *Journal of Alloys and Compounds* **1997**, 253-254, 550-555.
32) Sastri, M. V. C.; Viswanathan, B.; Srinivasa Murthy, S., *Metal Hydrides*. Narosa Publishing House: New York, NY, 1998.
33) Schrøder Pederson, A.; Jensen, K.; Larsen, B.; Vigeholm, B., The Formation of Hydride in Pure Magnesium Foils. *Journal of the Less Common Metals* **1987**, 131, 31-40.
34) Liang, G.; Huot, J.; Boily, S.; Van Neste, A.; Schulz, R., Mechanical Alloying and Hydrogen Absorption Properties of the Mg-Ni System. *Journal of Alloys and Compounds* **1998**, 267, 302-306.
35) Narusawa, K.; Hayashida, M.; Kamiya, Y.; Roppongi, H.; Kurashima, D.; Wakabayashi, K., Deterioration in Fuel Cell Performance Resulting from Hydrogen Fuel Containing Impurities: Poisoning Effects by CO, CH_4, HCHO and HCOOH. *JSAE Review* **2003**, 24, (1), 41-46.

Author's short biography

David Cooper

David Cooper is an analyst with Abt Associates, one of the largest for-profit government and business research and consulting firms in the world. At Abt Associates, Mr. Cooper primarily works on projects for the Environmental Protection Agency (EPA) that promote voluntary pollution prevention approaches to environmental protection. As part of EPA's Design for the Environment Program, Mr. Cooper is currently performing a life-cycle assessment (LCA) for the Wire and Cable Partnership that will evaluate the environmental and health impacts of an established cable formulation versus emerging cable formulations. He also works on projects that evaluate the effects of voluntary EPA programs. Mr. Cooper holds a Master of Science in Environmental Engineering Sciences from the University of Florida and a Bachelor of Science in Chemistry from Washington and Lee University.

Chang-Yu

Dr. Chang-Yu Wu is an Associate Professor in the Department of Environmental Engineering Sciences at University of Florida. He received his BS from Mechanical Engineering at National Taiwan University, both MS and PhD from Environmental Engineering at University of Cincinnati. His teaching and research interests include air pollution control, aerosol processes, nanoparticles and catalysis/photocatalysis. He has more then 30 referred journal publications, 110 conference presentations, 12 invited lectures and 1 patent. He received 6 awards for his achievement in research and engineering education in the past 5 years.

Author's short biography

David Charles Yasensky

David Yasensky was born and raised in Clearwater, FL, where he attended Countryside High school. He attended college at the University of Florida in Gainesville and earned his Bachelor of Science in 2004 with a major in Materials Science and Engineering (electronic materials specialty) and a minor in Physics. He is currently working towards a MS at UF in Materials Science and Engineering. His research interests include melting and solidification of alloys and his current project involves the kinetics of solutal melting.

Darryl Butt

Dr. Butt is a Professor of Materials Science and Engineering at Boise State University. He received his PhD in Ceramic Science and B.S. in Ceramic Science and Engineering from the Pennsylvania State University in 1991 and 1984, respectively. He has held several research, management and academic positions at A. P. Green Industries, Ceramatec Inc., Los Alamos National Laboratory, and the University of Florida. Much of Dr. Butt's research has been in the area of environmental effects on materials, particularly the thermodynamics and kinetics of gas-solid reactions.

Mei Cai

Dr. Mei Cai is a Staff Research Engineer at Chemical & Environmental Sciences Lab, GM Research and Development Center. Her current research interests include nanostructured materials, nanocomposite materials, surface and structure of ceramic materials for automotive applications. She has been granted 7 US patents with additional 8 pending during 10 years tenure at GM R&D Center. She had also worked in the area of industrial processing design for two years in China. Dr. Cai obtained her B.S. degree in Chemical Engineering from Tshinghua University (China) in 1988. She received a M.S. in 1993 and a Ph.D. in 1999, both in Chemical Engineering from Wayne State University.

Numerical Simulation of Mechanical Alloying in a Shaker Mill by Discrete Element Method[†]

W. Chen, M. Schoenitz, T.S. Ward,
R.N. Dave[1] and E.L. Dreizin
Mechanical Engineering Department
New Jersey Institute of Technology[*]

Abstract

Modeling of Mechanical Alloying (MA), which is a solid-state powder processing technique, is carried out by examining one widely used laboratory scale milling device, the SPEX 8000 shaker mill. It is a vibratory mill; its vial is agitated at a high frequency in a complex cycle that involves motion in three orthogonal directions. In this work, a popular dynamic simulation technique, Discrete Element Modeling, is applied to examine dynamics of a SPEX 8000 shaker ball mill based on the movement of milling balls. The computational results for energy dissipation rate inside the mill are calculated for different ball sizes and varied total ball to powder mass ratios (charge ratios). The computational results are well correlated with the experimental results tracking milling dose (used to define the degree of milling) as a function of ball sizes and charge ratios. Moreover, the numerical (theoretical) milling dose that correlates well with its experimental analog was found to depend on the energy dissipation rate of the head-on ball collisions. The numerical simulations also indicated that the milling progress is most significantly affected by milling media collisions with the energy within a specific threshold, while the collisions with smaller and greater energies are less effective. Finally, discussion shows how this novel approach of correlating specific scaling terms between experiments and simulations can be applied to other powder processing equipment.

Key words: Mechanoalloying, Discrete Element Modeling (DEM), Simulations, Milling progress, Shaker mill

1. Introduction

Mechanical Alloying (MA) is a solid-state, high-energy ball milling technique used to produce powders with unique microstructures. Mechanical Alloying process has been widely employed in industry to synthesize a variety of commercially useful and scientifically interesting materials[1)]. Generally, in MA process, a mixture of powder is loaded into a high-energy mill along with a suitable grinding medium (milling balls). Powder particles trapped between colliding media are constantly subjected to deformation, resulting particle flattening, coalescence (cold welding) and/or fragmentation.

MA is a complex process. Aspects of the events that occur in MA process have been described qualitatively[2)]. However, modeling the MA process is a difficult task, since a large number of variables need to be considered. Despite its complexity, modeling of the process has been actively pursued during the last 10 − 15 years, e.g.,[3)]. In general, modeling of MA approaches can be classified in either local or global terms. Local modeling describes effects (thermal and mechanical) and events (deformation, fracture and welding) when powder particles are entrapped between colliding or sliding media surfaces[4-6)], while global modeling considers aspects such as distribution of impact velocity, impact angles as well as heterogeneity of powder within the mill[7)]. Attempt has been made to incorporate local and global approaches to examine mechanics of MA process[8)]. While mod-

---

[†] Accepted: August 30, 2005

[*] Newark, NJ 07102, USA

[1] Corresponding author
TEL: 973-596-5860 FAX: 973-642-7088
E-mail: dave@njit.edu

erate success has been achieved in modeling the mechanics of the MA process based on a simplified mill[7)], the mechanics of MA remain incompletely understood. In the present work, a novel approach is considered where a parametric description of the milling progress of mechanical alloying in SPEX 8000 shaker mill is investigated in a manner such that experimental and theoretical results can be correlated. This paper describes the numerical modeling method used to develop theoretical description of the milling progress.

The SPEX 8000 series shaker mill is widely used in laboratories throughout the world. It allows relatively rapid milling of small (<20 g) quantities of material, and has become a de-facto standard piece of equipment. Focusing on this type of mill will enable subsequent comparison of the computations with experimental results published by other researchers. Validation of the numerical approach for this type of mill is the first step required for transition to larger-scale industrial equipment.

The SPEX 8000 shaker mill is a vibratory mill, where its vial is agitated at a high frequency in a complex cycle that involves motion in three orthogonal directions. **Fig. 1** shows the schematic of a SPEX 8000 mill device that is used in our lab. The center of vial vibrates in two-dimensional mode with the same frequency and different amplitude, and its slanted axis rotates around the third direction. The movement of rotation and vibration has the same frequency. In this paper, a popular dynamic simulation technique, Discrete Element Modeling, is applied to 3D simulation of the SPEX 8000 shaker ball mill based on the interactions of balls with other balls as well as the vial boundaries. The purpose of the study is to examine dynamic impact inside this milling device and develop a correlation between the numerical results and the experimental data. As it is known, the driving force for the milling process is the countless impacts between ball and ball and ball and vial. Energy dissipation during the impact directly contributes to any changes in the milled powder, as powder is trapped between impacting surfaces. The cumulative work performed on the powder is described by the milling dose D_m, quantified later in the paper. Therefore, through detailed simulations, energy dissipation rate inside the system is calculated and based upon that a numerical (i.e., theoretical) milling dose is defined. Calculations are carried out for different ball sizes and total ball-to-powder mass ratios (ball mass, m_b, to powder mass, m_p, the ratio is also called the charge ratio, C_R). This numerical milling dose is correlated with a suitably determined experimental milling dose to evaluate the milling progress.

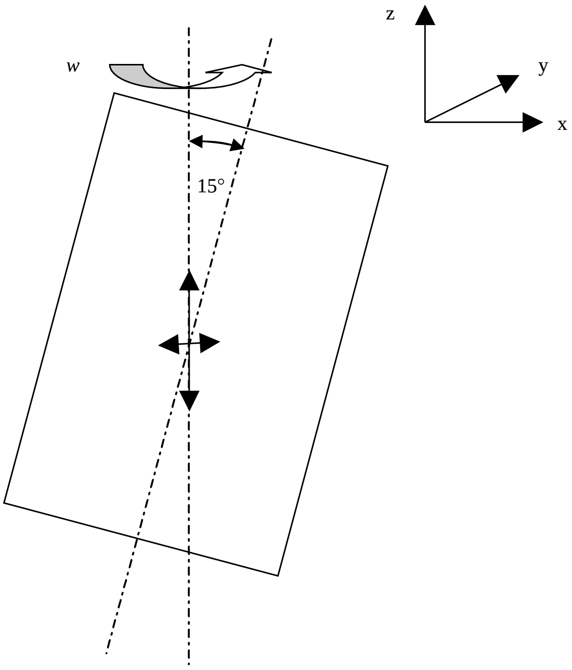

Fig. 1 Schematic of SPEX 8000 mill.

2. Description of the Numerical Model

Most particle dynamic simulations use the Discrete Element Method (DEM). The term "discrete element" refers to the fact that the simulation models the particles as a system of individual element (called discrete elements)[9)]. In other words, this technique simulates systems consisting of discrete particles in which motion of each individual particle is controlled by its interactions with other particles and with the system boundaries, which are also treated as discrete elements. Therefore, in a DEM simulation, discrete elements include particles and boundaries. For numerical simulation of the SPEX 8000 system by DEM, the boundary of the system is disassembled into three elements; one is represented as cylindrical boundary and the other two are represented as bounded top and bottom flat surfaces. In the modeling, the movements of boundary elements are described according to the actual motion of the SPEX 8000 vibrating mill during the experiments. Referring to **Fig. 1**, these include rotation of the vial, which is itself tilted around z-axis, and linear vibratory motion of vial center in x and y directions. As per its design and subsequent operating conditions, the value of rotation frequency is the same as that of vibration. Hence, the vibration movement in x and y directions can be expressed by the following simple equations,

$$\begin{cases} x=A_x \sin \omega t \\ y=A_y \cos \omega t \end{cases} \qquad (1)$$

where, A_x and A_y are the amplitudes of motion in x and y directions respectively, and ω is the frequency of vibratory motion.

For dynamic simulation of a particulate system by DEM technique, the computation time is a critical issue, which is governed by the number of particles and size of the smallest particle in the system. In a given experiment, the physical size of powder to be mechanically alloyed is very small, and the size varies significantly, while the number of particles is very large. This poses a formidable computational challenge, and hence it is impractical to include individual powder particles in the modeling. The main purpose of this work is to compute useful information based on ball-ball and ball-boundary interactions in order to understand the mechanics of the SPEX 8000 mill. Therefore, it is not necessary to exactly model all the powder particles which are being milled, and only the milling media balls along with the vial motion are modeled. Although this is a standard practice as reported in the literature, e.g.[6-7], there is always some effect of powder on ball-ball and ball-boundary interactions, and therefore it is taken into consideration by allowing a change in certain properties of the ball particles. This is done based on the strategy suggested by Kano et al., through proper selection of restitution coefficient[10]. Moreover, previous systematic study has shown that the impact velocity, thickness and strength of the powder layer coating the balls and the ball size contribute to the variation in restitution coefficient[11]. The trends reported earlier were supported by our experimental evaluation of restitution coefficient between the ball and vial surface for a clean ball versus a milled powder coated ball[12]. Therefore, in our study (here as well as in Ref.[12]), it is assumed that under the same amount of powder loading, restitution coefficient is inversely proportional to surface coverage of milling balls and changes within the range of 0.5 – 0.8 under different operating conditions. In our numerical simulation, Walton-Braun soft sphere model[13-15] is applied to ball-ball and ball-boundary interactions. The detailed description of the force model and the numerical implementation can be found in[16].

The time step, Δt, is an important quantity that affects the total computational time required for the simulation, and is calculated by the following expression[13-15],

$$\Delta t=\frac{\pi e\sqrt{m_i/2K_1}}{n} \qquad (2)$$

where e is the restitution coefficient of the milling balls, m_i is the mass of one ball, K_1 is the spring stiffness during the loading (i.e., approach during the contact) and n is the desired number of time steps for one contact. This number is typically chosen to be between 20 and 60, and for this simulation $n=40$. Equation (2) shows that the time step of the calculation is proportional to the ball mass.

The normal stiffness of the milling balls K_1 has been estimated to fall within the recommended guidelines[13-15], allowing for a maximum deformation of 1 % of the ball diameter during a collision. The normal stiffness has thus been calculated using the following equation,

$$K_1=0.01\pi \mathrm{E}\ \mathrm{r_i} \qquad (3)$$

where E is Young's modulus and r_i is the ball radius.

3. Simulation Approach

As mentioned before, because of the large difference between the particle size of the powder being milled and the size of the milling balls, only milling balls were considered. This simplification is reasonable; it allows focusing on the high-energy interactions between milling balls as well as milling ball and milling vial walls, which are responsible for mechanical alloying in a ball mill. During the simulation, energy dissipation in the system, which arises from ball-ball and ball-wall collisions, is calculated in the term of the energy dissipation rate by the following equation,

$$E_d=\sum_{k=1}^{N_c}\frac{\Delta E_k}{t_s}=\sum_{k=1}^{N_c}\frac{(E_1-E_2)_k}{t_s} \qquad (4)$$

where E_1 and E_2 are the energies of a binary impacting system before and after a collision, respectively; k is the collision index, and N_c represents the total number of collisions during the time interval t_s. For a ball-ball collision, the energy of the impacting system is calculated by:

$$E_{1,2}=\frac{1}{2}m_i v_i^2+\frac{1}{2}I_i\omega_i^2+E_{p_i}+\frac{1}{2}m_j v_j^2+\frac{1}{2}I_j\omega_j^2+E_{p_j} \qquad (5)$$

where subscripts *1*, *2* refer to the impact energy before (E_1) and after the collision (E_2), respectively; *i*, *j* are indices of two colliding balls, *v* is the translational velocity, and ω is the rotational speed of each impacting ball; *m* is the mass and *I* is the moment of inertia of the ball; and E_p is the potential energy of the ball under gravity ($E_p=mgh$, where *h* is height of mass center, and *g* is the gravitational acceleration); and for a ball-boundary interaction,

$$E_{1,2}=\frac{1}{2}m_i\Delta v_i^2+\frac{1}{2}I_i\omega_i^2+E_{p_i} \qquad (6)$$

where Δv_i is the relative impact velocity between the ball *i* and the boundary it is colliding with.

Table 1 lists the parameters and their values or variation ranges used in the simulation and in the corresponding experimental study[12)]. The parameters related to the milling vial geometry and movement come from empirical measurements for a specific SPEX 8000 series shaker mill used in experiments[12, 17)]. Milling ball sizes and loadings are also the same as for the corresponding experimental investigation. Milling balls used in the study are made of hardened steel (density, $\rho=7.86\mathrm{g/cm^3}$) with four different sizes.

Table 1 Input parameters of simulation

Size of vial (mm)	$\phi 38\times57$
Angle of vial axis with rotating axis (°)	15
Rotation speed (rpm)	1054
Vibration frequency (Hz)	17.6
Vibration amplitude A_x, A_y (mm)	25, 6
Diameter of milling ball (mm)	2.36, 3.16, 4.76, 9.52
Total mass of milling balls (g)	12.5, 25, 50
Young Modulus of steel (GPa)	200
Friction coefficient	0.4
Restitution coefficient	0.5 – 0.8

4. Numerical Results

Numerical simulations are carried out to represent closely the experimental studies of the effect of milling ball size and ball loading, represented by C_R (total ball mass to powder mass, termed as the charge ratio), on the milling time. According to the experimental study, three values of C_R, i.e., $C_R=2.5$, 5 and 10 are used for each ball size. As stated in the previous sections, because of the computational limitation, powder particles are not considered directly in the numerical analysis. However, the effect of powder to ball-ball and ball-wall interactions is taken into consideration by the appropriate selection of the restitution coefficient. It is assumed that under the same powder loading, the restitution coefficient is inversely proportional to the surface coverage of the milling balls, varying in the range of 0.5 – 0.8. For the milling process, the required milling time is correlated with the impact energy consumption rate, i.e., the energy dissipation rate. The larger the energy consumption rate, the shorter will be the milling time required to achieve the same state in the milled powder. The dynamics of the SPEX 8000 shaker mill is studied in detail in terms of the distribution of energy dissipation per impact and the impact angle. **Fig. 2** represents the histograms of impact energy dissipation inside the system corresponding to four different ball sizes with $C_R=5.0$, and $m_p=2$ g. The vertical scale is the fraction of all impacts occurring at a given energy dissipation level. For the system loaded with the smallest balls considered ($d=2.36$ mm), the value of energy dissipation for most impacts is less than 10e-5 J. For the two ball diameters, $d=3.16$ mm and $d=4.76$ m, most impacts involve energy dissipation at the similar energy levels that do not exceed 10e-2 J. For the system loaded with the largest ball size ($d=9.52$ mm), some impacts involve the energy levels exceeding 10e-2 J. **Fig. 3** illustrates distribution of the dissipated energy as a function of collision angles for the systems with different milling ball sizes. Generally, for all ball sizes, most collisions occur at an angle that is in range 80 – 90°. Such impacts can be classified as oblique or glancing impacts. However, a trend can be noticed that with the increased ball size, the fraction of the energy dissipated in the collisions occurring at smaller angles increases. For the largest milling balls ($d=9.52$ mm), the fraction of the energy dissipation from the collisions occurring at the angles less than 30° (which can be called head-on collisions) approaches 10%. These observations made through numerical simulations show that the processing of powder in a SPEX 8000 mill involves a large fraction of glancing impacts. Relatively few impacts are accompanied with high levels of energy dissipation. These conclusions are in good agreement with previously observed experimental results[2)], suggesting that this numerical simulation strategy can capture the experimental phenomena reasonably well.

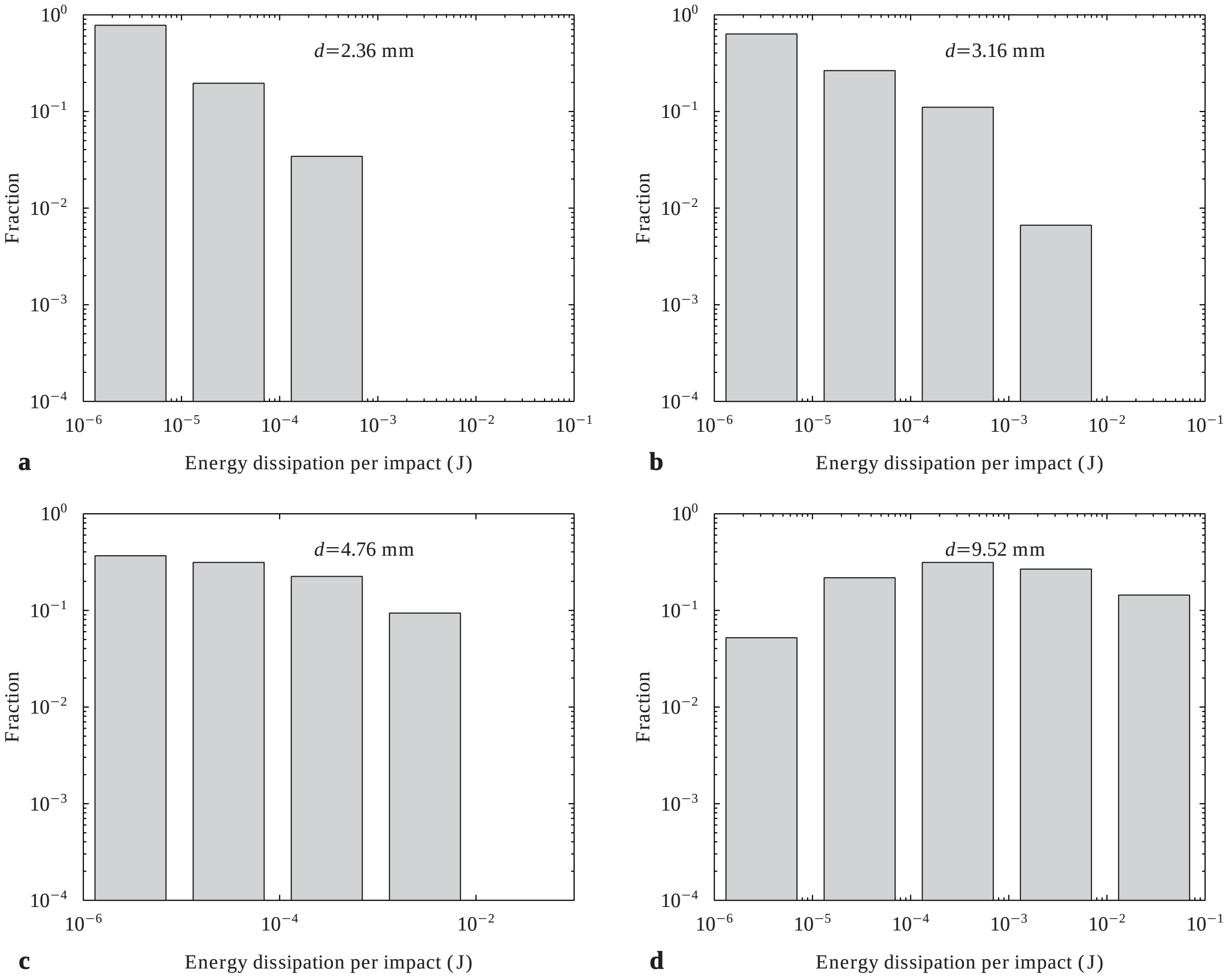

Fig. 2 Histograms of the fraction of energy dissipation per impact for different impact energies for the systems with different ball diameters, d: a. d=2.36 mm; b. d=3.16 mm; c. d=4.76 mm, and d. d=9.52 mm.

Discussing further the results of the numerical simulations, one can consider the frequency of collisions as a function of the number of balls loaded in the milling vial for different ball sizes. The results are plotted in **Fig. 4**. It is observed that the collision frequency inside the SPEX 8000 mill is approximately proportional to the number of balls. This trend remains valid for different ball sizes, allowing some generalization of this result followed from the numerical modeling. **Fig. 4** also shows that the number of collisions per second is quite large, and that the collision frequency remains linearly related to the number of balls while the number of balls increases in a wide range, as illustrated by the log-log plot. Although it is not shown explicitly, the number of collisions per ball increases dramatically as the total number of balls within a system increases. While this is a useful result, it is unclear whether an increase in the number of balls within the same size milling vial would be advantageous for the milling progress. Hence, there is a need to develop parametric information that can allow generalization as well as consolidation of the results for different operating parameters such as ball size and number of balls, and can allow for an easy comparison with the experimental results.

One such function that can be formulated and subsequently studied through simulations is proposed in terms of the energy dissipation rate, E_{d}, and the charge ratio, C_R, of the system, and is expressed as $C_R\cdot m_p/E_d$12). The powder mass, m_p is incorporated in the function as a scaling factor to correlate with the experimental study and characterize the energy dissi-

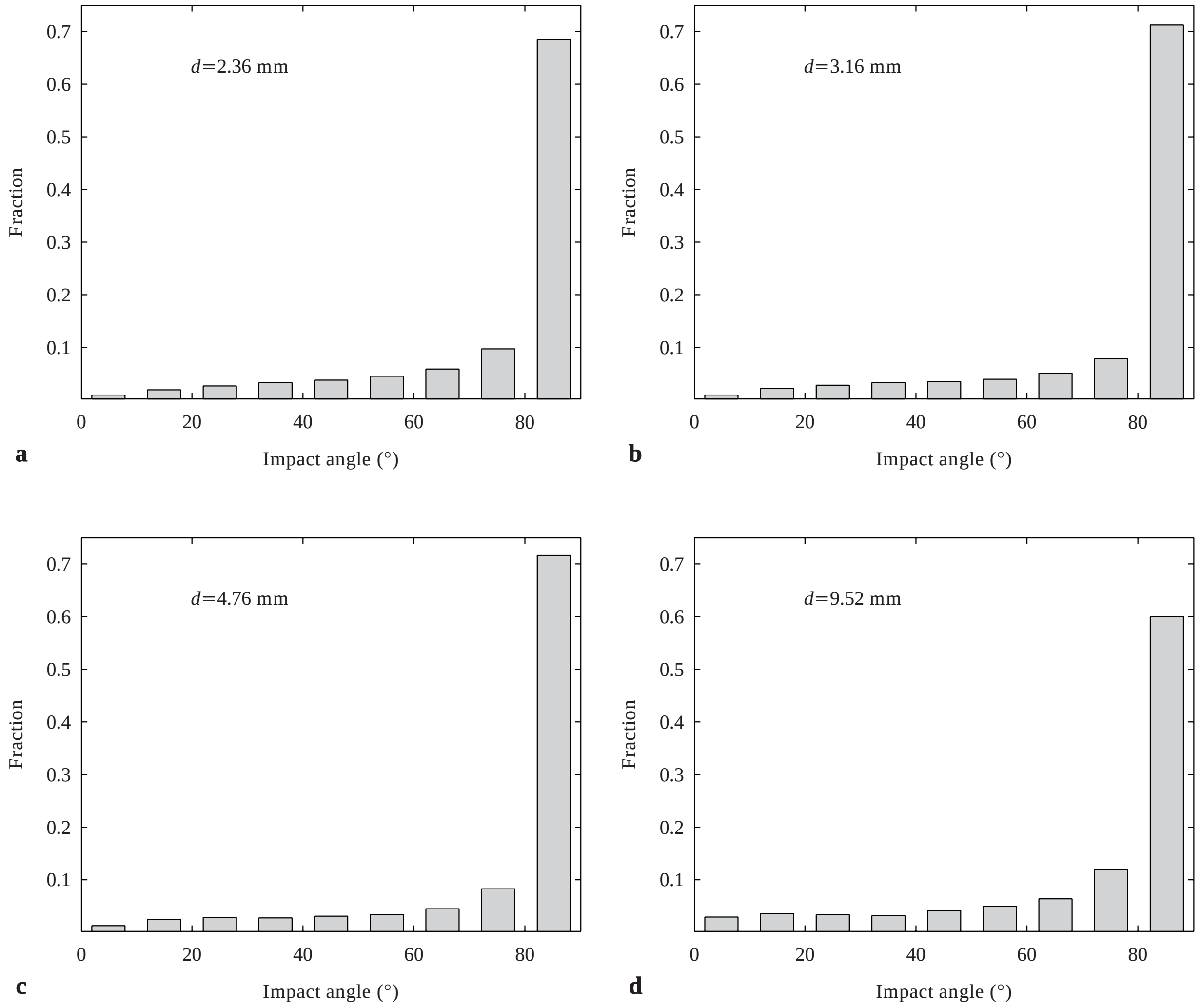

Fig. 3 Distribution of the fraction of energy dissipation per impact as a function of the collision angle for the systems with different ball sizes: a. d=2.36 mm; b. d=3.16 mm; c. d=4.76 mm, and d. d=9.52 mm.

pation per unit mass of powder. **Fig. 5** shows that the function $C_R \cdot m_p / E_d$ is almost constant for four different ball sizes and three charge ratios with two different powder loadings. Noting that C_R is the ratio of the total ball mass to the powder mass, the function can be expressed as, $C_R \cdot m_p / E_d = m_b / E_d$, so that the result shown in **Fig. 5** can be interpreted as $m_b / E_d = const.$ This means that the collision energy dissipation rate E_d is proportional to the total ball mass m_b, and is nearly independent of the ball size. This result is further supported by our simulation data shown in **Fig. 6**.

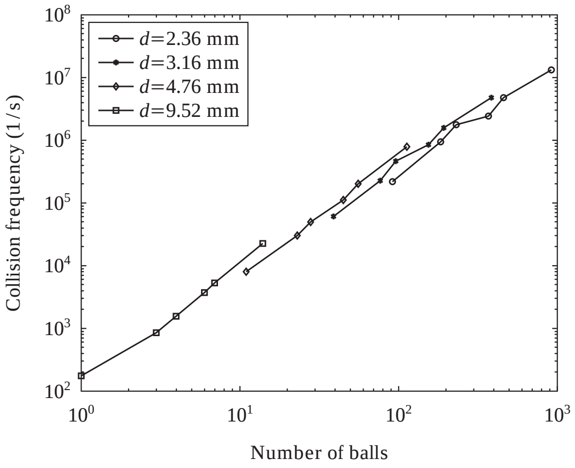

Fig. 4 Collision frequency (1/s) in the system as a function of number of milling balls for different ball sizes.

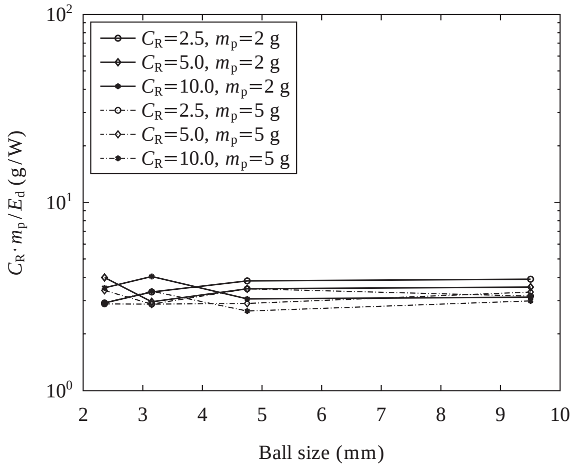

Fig. 5 Computed changes of the function $C_R \cdot m_p / E_d$ for different ball sizes and different charge ratios.

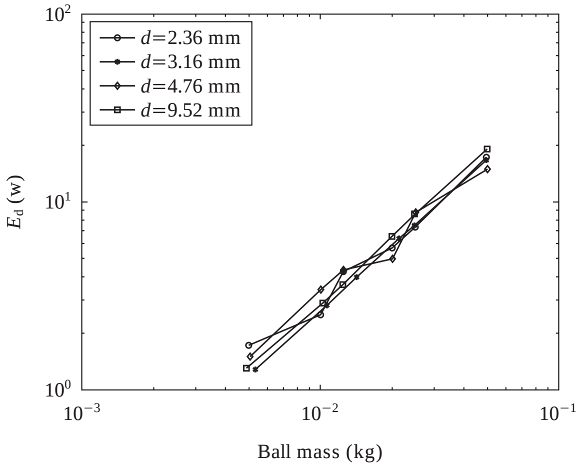

Fig. 6 Simulation results showing the energy dissipation rate as a function of the ball mass for different ball sizes.

5. Parametric Investigation of Mechanical Alloying

Recent experimental studies[12, 17)] on reactive milling using a SPEX 8000 mill suggested that the milling progress can be described using the specific milling dose, D_m given by:

$$D_m = \frac{W}{m_p} \tag{7}$$

where W is the work performed on the powder, and m_p is the powder mass.

The studies involved milling of reactive materials such as thermites, where a self-sustaining reaction is triggered after a certain period of milling. For the purpose of the comparison of experimental and numerical results, it was assumed that the self-sustaining reaction is triggered when a specific degree of refinement of the powder components was achieved. The work performed on the powder in the milling system can be expressed through the energy dissipation rate, E_d, i.e., $W = E_d t_{init}$, where t_{init} is the milling time required to initiate (or trigger) the reaction[12, 18)]. This leads to,

$$D_m = \frac{W}{m_p} = \frac{E_d t_{init}}{m_p} \tag{8}$$

From DEM simulations, it was observed that E_d is proportional to the mass of the milling balls m_b, hence,

$$D_m = \frac{E_d t_{init}}{m_p} \propto \frac{m_b t_{init}}{m_p} = C_R t_{init} \tag{9}$$

This equation provides an easy method for experimental measurements of the milling dose for a specific milled material. Based on the experimental results for milling of $2Al+Fe_2O_3$ thermite[12, 17)], the product of the measured milling time (leading to initiation of the self-sustained reaction) and the charge ratio, $D_m = C_R t_{init}$, is plotted in **Fig. 7** as a function of the ball size for different charge ratios. The plots of $C_R t_{init}$ for different C_R values are similar to one another, especially for the intermediate ball sizes, and the overall value of D_m does not change significantly. Therefore, the experimentally determined milling dose shows the behavior that is qualitatively similar to its numerically calculated equivalent, cf. **Fig. 5**.

However, the experimentally determined milling dose is not always constant, particularly for smaller and larger ball sizes. While the deviations may be explained qualitatively by collective ball motions or vial size limitations, further details could be determined from the numerical simulations. For instance, in the numerical simulation, the effect of the collision impact angle on the milling progress can be readily examined. Following the initial analysis presented in **Fig. 3**, the collisions occurring at different impact angles can be classified, in the first approximation, as head-on impacts (the impact angle is less than 30°) and glancing impacts (the impact angle is greater than 30°). Therefore, the energy dissipation rates for each type of collisions can be computed and respective milling progress functions can be considered and

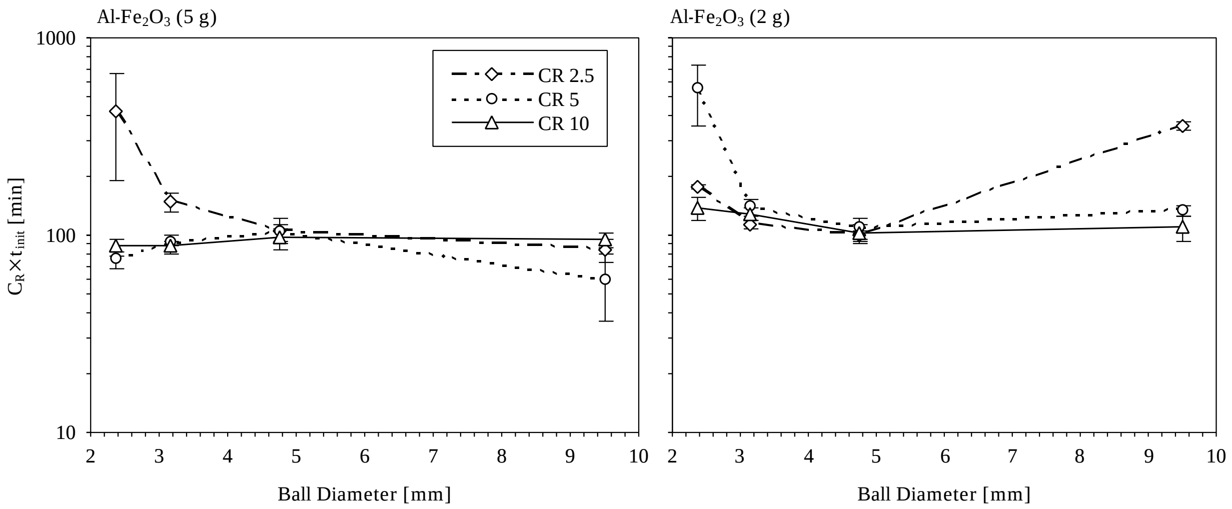

Fig. 7 Experimental data on reactive milling of 2Al+Fe$_2$O$_3$ composition presented as the product of the charge ratio and milling time plotted versus ball size for different charge ratios.

compared to the experimental data shown in **Fig. 7**. The sum of the head-on and glancing energy dissipation rates is the total energy dissipation rate, shown in **Figs. 5** and **6**. In contrast, **Fig. 8** illustrates numerical milling dose, D'_m based on the energy dissipation rate from the head-on collisions only as a function of ball sizes for a series of charge ratios corresponding to the experimental data in **Fig. 7**. For comparison, a similar plot for the numerical milling dose based on energy dissipation rate in glancing impacts only is shown in **Fig. 9**.

The numerical milling corresponding to the total E_d, shown in **Fig. 5**, reveals a relatively constant milling dose as a function of ball size, while the milling dose based on the head-on energy dissipation rate shows a different trend which correlates better with the experimental milling dose as shown in **Fig. 7**. Conversely, the calculation based on the glancing energy dissipation reveals different value of milling dose upon different powder loading, where larger loading results in smaller milling dose, which is not supported by the experimental results. The numerical milling dose based on the head-on dissipation energy rate has a divergence similar to the experimental milling dose for small diameter balls, but demonstrates a less efficient milling (shown as larger average milling dose value) for C_R=10 rather than C_R=2.5 as the experimental results. For the intermediate ball sizes (d=3.16 mm and d=4.76 mm), which generate collisions with very similar levels of energy dissipation (c.f. discussion in section 4 for **Fig. 2**), the numerical milling dose agrees well with the experimental milling dose. This may imply that the specific range of dissipation energies is critical for reactive milling and, by implication, for the progress in mechanical alloying.

The validity of experimental milling dose and numerical milling dose based on the energy dissipation rate for the head-on collisions is also well represented

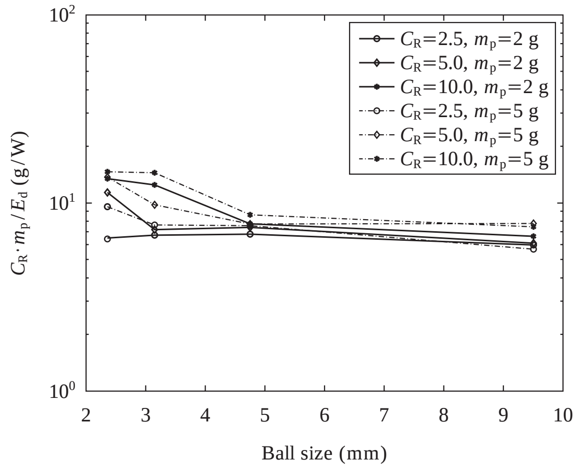

Fig. 8 Theoretical/numerical milling dose D_m based on the head-on energy dissipation rate as a function of ball size.

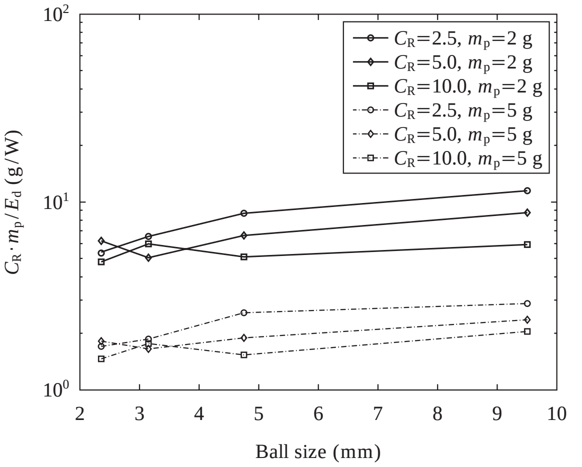

Fig. 9 Theoretical/numerical milling dose based on the glancing energy dissipation rate as a function of ball size.

in the DEM results with a near constant milling dose for 4.76 mm balls among all charge ratios. This intersection point represents the most efficient milling condition for the examined charge ratios. Therefore, head-on collisions are found to be more significant in defining the milling progress. This finding agrees with reports stating that the glancing impacts do not contribute significantly to the deformation, coalescence, and fragmentation[4, 7].

The results shown so far indicate that this methodology of combined numerical and experimental study can be used for the analysis of mechanical alloying suitable for the further process development and scale-up. The numerical (or theoretical) milling dose, although expressed in terms of energy, behaves similarly to the experimental milling dose which is expressed in terms of time. This demonstrates the DEM methodology's ability to capture the physical interactions during milling. In a scaled up operation, the optimal conditions, observed here for 4.76 mm balls, may actually occur at a different ball size, but in general, numerical modeling can be expected to identify the optimal ball size and help identify the additional parameters required for successful production. The same idea could be applied to the analysis of other dynamic systems, such as mechanofusion, where a parameter similar to milling dose can be used to evaluate the coating degree. That topic will be discussed in a future paper.

6. Conclusions

The numerical study of the mechanical alloying in a SPEX 8000 shaker mill is carried out by DEM technique. The movement of the vial is implemented into the modeling according to the experimental measurements. During the simulation, the energy dissipation rate of the system is calculated for four different ball sizes and three charge ratios. The numerical milling dose is thereafter constructed based on the energy dissipation rate and correlated with the experimental milling dose, which is a useful indicator of the milling progress for reactive milling. There is a good agreement between numerical simulation and experimental data indicating a trend for a constant milling dose for a specific material. Furthermore, the numerical milling dose based on the energy dissipation rate from head-on impacts demonstrates a better correlation with the experimental milling dose than the similarly defined milling dose calculated considering the energy dissipation rates for all or only glancing impacts. This classification of the energy dissipation rate according to head-on and glancing impacts can only be accomplished by numerical simulation, emphasizing its importance for the analysis of the actual milling mechanism. Particularly good description of the milling progress by both the experimental milling dose and its numerical analog is found for intermediate ball sizes, which result in collisions within a specific range of energies. The collisions with energies which are higher or lower than the observed threshold, and which occur when larger or smaller balls are used, appear to be less effective in achieving the milling progress. Because the numerical simulation successfully predicts the trends observed in the experiments, it is suggested that the model can accurately describe the progress of mechanical alloying and reactive milling, and is useful for further scale-up studies.

References

1) C. Suryanarayana, "*Mechanical Alloying*", ASM Handbook, **7**, 80-90 (1998).
2) R. M. Davis, B. McDermott and C. C. Koch, "*Mechanical Alloying of Brittle Materials*", Metallurgical Transactions A, **19A**, 2867-2874 (1988).
3) D. R. Maurice and T. H. Courtney, "*The Physics of Mechanical Alloying: A First Report*", Metallurgical Transactions A, **21A**, 289-303 (1990).
4) D. Maurice and T. H. Courtney, "*Modeling of Mechanical Alloying: Part I, Deformation, Coalescence, and Fragmentation Mechanisms*", Metallurgical and Materials

Transactions A, **25A**, 147-158 (1994).

5) D. Maurice and T. H. Courtney, "*Modeling of Mechanical Alloying: Part II. Development of Computational Modeling Programs*", Metallurgical and Materials Transactions A, **26A**, 2431-2435 (1995).
6) M. Abdellaoui and E. Gaffet, "*The Physics of Mechanical Alloying in A Modified Horizontal Rod Mill: Mathematical Treatment*", Acta Materialia, **44**, No. 2, 725-733 (1996).
7) D. Maurice and T. H. Courtney, "*Milling Dynamics: Part II, Dynamics of a SPEX Mill and a One-Dimensional Mill*", Metallurgical and Materials Transactions A, **27A**, 1973-1979 (1996).
8) D. Maurice and T. H. Courtney, "*Milling Dynamics: Part III. Integration of Local and Global Modeling of Mechanical Alloying Devices*", Metallurgical and Materials Transactions A, **27A**, 1981-1986 (1996).
9) P. A. Cundall and O. D. L. Strack, "*A Discrete Numerical Model for Granular Assemblies*", Geotechnique, **29**, 47-65 (1979).
10) J. Kano, M. Hiroshi and F. Saito, "*Correlation of Grinding Rate of Gibbsite with Impact Energy of Balls*", Particle Technology and Fluidization, **46**, No. 8, 694-1697 (2000).
11) H. Huang, M. P. Dallimore, J. Pan, P. G. McCormik, "*An investigation of the effect of powder on the impact characteristics between ball and a plate using free falling experiments*", Materials Science and Engineering. **A241**, 38-47 (1998).
12) T. S. Ward, W. Chen, M. Schoenitz, R. N. Dave and E. Dreizin, "*A study of Mechanical Alloying Processes using Reactive Milling and Discrete Element Modeling*", Acta Materialia, **53**, 2909-2918 (2005).
13) O. R. Walton and R. L. Braun, "*Viscosity and Temperature Calculations for Assemblies of Inelastic Frictional Disks*", J. Rheology, **30**, No. 5, 949-980 (1986).
14) O. R. Walton, "*Numerical Simulation of Inclined Chute Flows of Monodisperse, Inelastic, Frictional Spheres*", Mech. of Materials, **16**, 239-246 (1993).
15) O. R. Walton, "*Numerical Simulation of Inelastic, Frictional Particle – Particle Interactions*", in Part Two – Phase Flow, M. C. Roco (eds), Butterworth – Heinemann, Boston, pg. 885 (1993).
16) W. Chen, R. N. Dave, R. Pfeffer and O. Walton, "*Numerical Simulation of Mechanofusion System for Dry Particle Coating Process*", Powder Technology, **146**, No. 1-2, 121-136 (2004).
17) T. S. Ward, W. Chen, M. Schoenitz, E. Dreizin, and R. Dave, "*Nano-Composite Energetic Powders Prepared by Arrested Reactive Milling*", American Institute of Aeronautics and Astronautics Northeast Regional Student Conference, Boston, Massachusetts, April 3, 2004.
18) F. Delogu, R. Orrhu and G. Cao, Chemical Engineering Science, **58**, 815-821 (2003).

Author’s short biography

Wenliang Chen

Dr. Wenliang Chen is a Postdoctoral Researcher in New Jersey Center of Engineered Particulates (NJCEP). Dr. Chen received her PhD degree from New Jersey Institute of Technology in 2002. Her major research interest is numerical simulation of dynamic systems and linear stability analysis of multi-phase fluidized beds.

Mirko Schoenitz

Dr. Mirko Schoenitz received his PhD in Geosciences/Materials Science from Princeton University in 2001. He is currently a research professor in the Department of Mechanical Engineering at New Jersey Institute of Technology. His research interests include metal-ceramic matrix compositesm structural analysis, calorimetry, advanced nano-composite materials, and mechanical alloying.

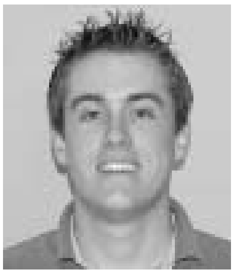

Trent Ward

Trent Ward received his Masters degree in Mechanical Engineering from New Jersey Institute of Technology in 2001. He currently works on development of advanced energetic materials at NAVSEA China Lake, California.

Rajesh N. Dave

Dr. Rajesh N. Dave is Professor of the Department of Mechanical Engineering, at New Jersey Institute of Technology, and holds a joint faculty appointment with Otto York Chemical Engineering, NJIT. His main research interests are in the areas of particle technology and fuzzy pattern recognition. He is also the founding Director of New Jersey Center for Engineered Particulates, a Centre of Excellence funded by numerous federal grants and also works on applied research related to industries such as pharmaceuticals, food, cosmetics, ceramics, defense, electronics and specialty chemicals.

Edward L. Dreizin

Dr. Edward L. Dreizin received his PhD in applied physics from Odessa University, Ukraine in 1992. He is a professor of Mechanical Engineering at New Jersey Institute of Technology. His research interests include metal combustion, high-energy density materials, solid propellants and fuels, combustion and transport phenomena in microgravity, physics and chemistry of arc plasmas, micro-joining, and metal surface treatment.

The Influence of Particle Characterizations of Inner-Constraining Layer upon Constrained Sintering Shrinkage[†]

S. Nakao[1], M. Kojima
and K. Tanaka
Murata Manufacturing Co. Ltd.[*]

Abstract

Constrained sintering of a substrate with a sandwich structure, which was the laminated inner-constraining alumina layer between the glass-alumina mixed layers, has been studied. The influence of specific surface area of the particles and porosity of inner constraining particle layer upon sintering shrinkage was investigated. Specific surface area of the alumina powder for the inner constraining particle layer could be changed by grinding and blending two different particle size powders. As for the debinded sheet used with ground alumina powder, the pore distribution was sharp, and the bending strength was proportional to the specific surface area. In the case of inner constraining particle layer used with ground alumina powder, penetration length of molten glass from glass-alumina mixed layers obeyed Kozeney-Carman's equation. On the other hand, as for the debinded sheet with particle size blended powder, the effects of specific surface area on the bending strength and the penetration length of molten glass differed from the results of the grounded one. Sintering shrinkage in X-Y direction of the sandwich substrate was basically related to the bending strength of debinded alumina powder sheet for inner constraining particle layer in both cases.

Key words: Constrained sintering, Sandwich substrate, Inner-constraining layer, Penetration, Particle size, Pore distribution, Bending strength

1. Introduction

Recently, electronic equipment has become ever smaller, reflecting the growing demand for more compact, lower-profile electronic components and higher density electronic component packaging applications.

In the field of ceramic multi-layer substrates, a method for manufacturing LTCC (Low Temperature Co-fired Ceramics) substrates, whereby silver or copper electrode materials of relatively low electric resistance are fired together with ceramic powder, is gathering attention, and research work is underway to constrain sintering shrinkage to improve the dimensional accuracy of LTCC substrates.

Some of this research proposes methods to reduce sintering shrinkage in the X-Y direction on substrate[1-6]. According to these methods, a particle layer with a high melting point material, such as alumina, is laminated and fired on the surface of a formed member. Any of these methods can be used to produce an LTCC substrate with higher dimensional accuracy.

As a compound material consisting of glass and ceramic, LTCC substrates have a lower bending strength compared with conventional alumina substrates, etc.[7]. However, including a larger proportion of ceramic powder within the LTCC substrate composition does facilitate bending, although a higher sintering temperature is required. As a result, if electrodes are to be fired together with glass and ceramic powders, the potential amount of ceramic powder to be blended is limited[8].

---

[*] 2-26-10, Tenjin, Nagaokakyo-shi, Kyoto 617-8555

[1] Corresponding author
Materials Research & Development Center, 2288 Ohshinohara, Yasu-shi, Shiga 520-2393
TEL: +81-77-586-8325
E-mail: s_nakao@murata.co.jp

[†] This report was originally printed in J. Soc. Powder Technology, Japan, **41**, 730-737 (2004) in Japanese, before being translated into English by KONA Editorial Committee with the permission of the editorial committee of the Soc. Powder Technology, Japan.

The authors have attempted to develop a substrate manufacturing process that is dissimilar to conventional equivalents of the non-shrinkage variety. With our substrate manufacturing process, a high melting point ceramic particle layer, which is not sintered at the normal glass material sintering temperature, is formed within the multi layer substrate in order to constrain sintering shrinkage in its horizontal direction. Namely, during the sintering process, the molten glass penetrates into the pores among the particles in the ceramic particle layer to form a low-porosity compound solid member consisting of glass and ceramic. The authors have proven that this method, combined with inhibition of LTCC substrates' sintering shrinkage, can improve the bending strength of LTCC substrates[9, 10].

The authors have investigated the effects of a ceramic particle layer, which is not sintered at the normal glass material sintering temperature used in the authors' process, on the constraint of sintering shrinkage and densification of the substrate.

2. Experimental Method

2.1 Starting materials

The glass powder used for our experiment was a Si-Ca-Al-Mg-B-O based material available on the market; with a glass transition temperature of 933K, a thermal expansion coefficient of 4.4×10^{-6}/K and a specific gravity of 2.48. Low soda alumina powder was added to this glass powder at an amount of 40% by weight to prepare the glass-alumina mixture layer.

For the alumina particle layer, two alumina powder types with mean particle sizes of 0.4 and 1.5 μm respectively were used as starting materials. These powders were blended, taking their particle sizes into consideration, to provide particle-size blended powder types. At the same time, other powder types were prepared by grinding an alumina powder with a mean particle size of 1.5 μm. These powder types were each used as an alumina particle layer.

2.2 Experimental conditions

The alumina powder, with a mean particle size of 1.5 μm, was ground in a dry media agitating mill. For each grinding run, 2 kg of alumina powder and 12.5 kg of PSZ grinding balls, 5 mm in diameter, were loaded into an agitating tank with an internal volume of 5 L. The agitating speed was set to 4.17 s^{-1}, and the grinding durations were 30, 120 and 320 min respectively. The sheets for the glass-alumina and alumina particle layers were formed using a doctor blade technique. The slurries for the sheets were prepared using an experimental compact ball mill through blending at a speed of 4.58 s^{-1} for 2 hours. 1.75 kg of PSZ balls, 5 mm in diameter, was loaded into a resin pot with an internal volume of 1 L. The slurries for glass-alumina layer were each prepared by loading 0.24 kg of glass powder, 0.16 kg of alumina powder, 0.15 kg of ethanol and 0.06 kg of butylal-based binder into the resin pot respectively.

The slurries for the alumina particle layer were each prepared by loading 0.5 kg of alumina powder, 0.15 kg of ethanol, and 0.06 kg of butyl alcohol based binder into the resin pot.

The particle size blended powders for the alumina particle layer were obtained by blending an alumina powder with a mean particle size of 1.5 μm and an alumina powder with a mean particle size of 0.4 μm at mass ratios of 100:0, 75:25, 50:50, 25:75 and 0:100.

The glass-alumina mixture slurries were dried and formed into 180 μm sheets, while the alumina slurries were dried and formed into 12 and 40 μm sheets.

These sheets were laminated to constitute the sandwich structure shown in **Fig. 1** and then compressed into a solid member. More specifically, a 180 μm-thick glass-alumina mixture sheet was laminated on either side of a 12 or 40 μm-thick alumina sheet respectively, following which the laminates were compressed using a single-axis press.

Each compressed member was punched into pieces of specific dimensions, and each piece was then debinded by heating, with a temperature increase rate of 1K/min and a maximum temperature of 827K. Sintering was performed in air using a batch oven; the heat increase rate was 7K/min, the sintering temperature was 1153K, and the retention time was 60 min. The process chart of the experiment is shown in **Fig. 2**.

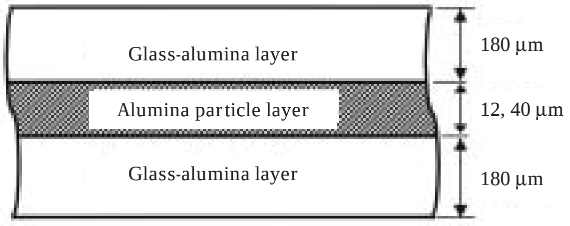

Fig. 1 Schematic drawing of layer structure of substrate before sintering

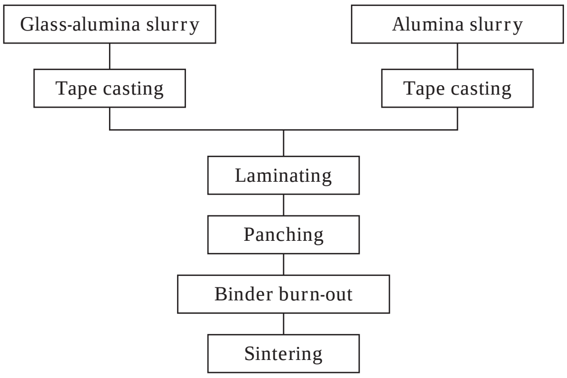

Fig. 2 Process chart of experiment

2.3 Method for measurement

2.3.1 Powder characteristics of alumina powder and alumina particle layer

The particle size distribution of each ground alumina powder was measured using a laser diffraction/dispersion particle size distribution analyzer (LA-700: Horiba).

As for the alumina powders having undergone particle size blending, the formed sheets were debinded by heating at 773K for 60 min, prior to the measurement of particle size distribution on these sheets using the aforementioned analyzer. The surface area of these alumina powders was measured using a BET technique (Monosorb: Yuasa Ionics).

2.3.2 Porosity and pore size distribution of alumina particle layer

The porosity and pore size distribution of the alumina particle layer were measured using a mercury porosimeter (Model 2000: Carlo Erba). The samples used were debinded sheets that were prepared by laminating 40 alumina green sheets, each one formed 40 μm-thick, compressing them together at 110 MPa and heating them at 773K for 60 min.

2.3.3 Bending strength of alumina particle layer

40 alumina green sheets, each one formed 40 μm-thick, were laminated; the green sheets were compressed together at 110 MPa and punched to provide a formed member measuring 5.0×30.0×1.5t mm.

The formed member was debinded by heating at 773K for 60 min, before then being subjected to a three-point bending test with a fulcrum span of 25 mm and a cross head speed of 0.1 mm/s. The bending strength σ_B of the formed body was determined with Eq. (1).

$$\sigma_B=(3F_BL)/(2Wt^2) \qquad (1)$$

where, F_B is the load at which the sample was broken, W, the width of the sample, t, the thickness of the sample, and L, the fulcrum span. A total of 10 identical samples were used for testing.

2.3.4 Penetration length of glass into alumina particle layer

A 180 μm-thick glass-alumina layer was forcibly bonded to each side of the 40 μm-thick alumina particle layer; then the resultant formed member was punched into 35×35 mm square samples, and the cross-section of samples analyzed for Al and Si mapping using a wave-length dispersion X-ray micro analyzer WDX (JXA-8800: JEOL). Based on the Al mapping diagram, the thickness of the alumina particle layer was measured, and then from the Si (a component of the glass) mapping diagram, the penetrating depth of glass into the alumina particle layer was measured. Hence, based on the difference between the thickness of the alumina particle layer and the penetrating depth of the glass, the glass packing depth into the alumina particle layer was determined.

2.3.5 Shrinkage percentage

A 180 μm-thick glass-alumina layer was forcibly bonded to each side of a 40 μm-thick alumina particle layer; the resultant formed member was then punched into 35×35 mm square samples, and the longitudinal and lateral dimensions of the compressed and sintered samples were measured. The shrinkage percentage was determined for the longitudinal, lateral and thickness directions of the samples; based on the proportion of the difference in dimensions before and after sintering.

3. Experimental Results and Discussion

3.1 Characteristics of alumina particle layer consisting of ground material

Fig. 3 provides particle size distribution curves obtained from powders that were prepared by grinding alumina powder of mean particle size 1.5 μm using a dry media agitating mill and respective grinding durations of 30, 120 and 300 min. The longer the grinding time, the smaller the proportion of large size particles. As a result, the particle size of each powder sample decreased as grinding proceeded, meaning the form of particle size distribution curves varied from a two-peak to a single-peak pattern. With a short

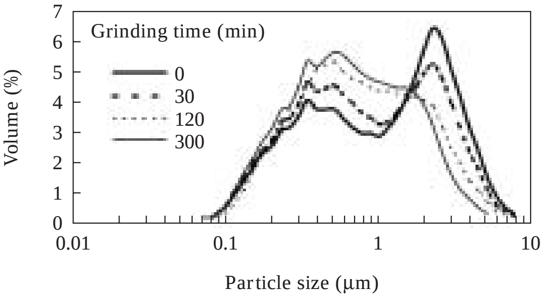

Fig. 3 Effect of grinding time on particle size distribution

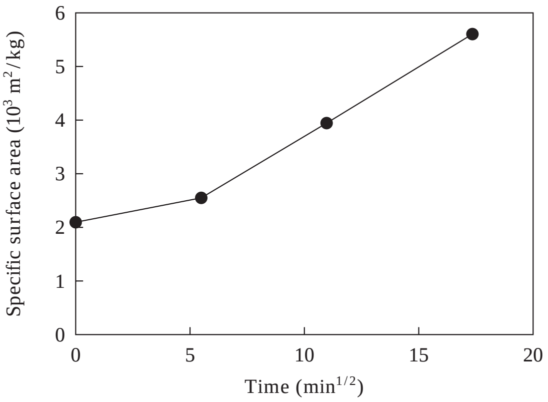

Fig. 4 Relation between specific surface area and grinding time

grinding time of 30 min, the ground powder was seen to peak at around 2.3 µm, with particle size distribution similar to that of a starting material, and a high volume percentage of large size particles in the ground powder. With longer grinding times (i.e. 120 and 300 min), the peak at 2.3 µm disappeared and the percentage of particles sized at around 0.5 µm increased. **Fig. 4** summarizes the tendency of the specific surface area of ground powder that is dependent on the grinding time[11]. With a grinding time of 30 min or longer, the specific surface area increases proportional to the square root of the grinding time. However, the gradient gently increases within the time span from 0 to 30 min, meaning that the grinding speed is low. The reason for this seems to be the time lag before the aggregated starting powder material starts dispersion. **Fig. 5** illustrates the relation between the surface area and porosity with the debinded sheets; prepared using powders that were ground for 30, 120 and 300 min respectively. **Fig. 5** reveals the fact that the porosity remains unchanged, regardless of the specific surface area values. **Fig. 6** meanwhile shows the relation between the specific surface area of powder material before grinding and the bending strength of the debinded member that was heated at 773K for 60 min. **Fig. 6** shows that the bending strength of the debinded member increases proportional to the specific surface area of the powder material after grinding.

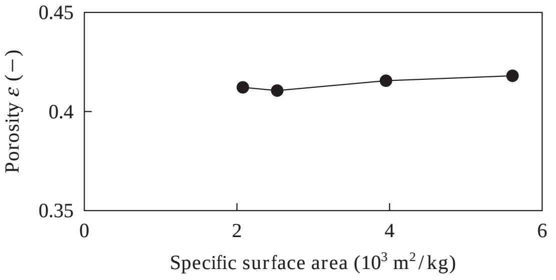

Fig. 5 Relation between specific surface area and porosity of ground alumina particle layer after heat treatment at 827K

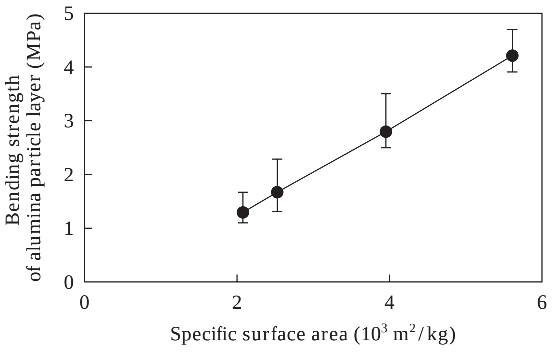

Fig. 6 Bending strength of ground alumina particle layer after heat treatment at 827K as a function of specific surface area

The relation between the three-point bending strength and the characteristics of the particle layer summarized here can be considered as follows: The issue of three-point bending strength can be treated as bending of a cantilever beam, the center of which is exposed to a concentrated load between both fulcrums. According to a bending strength formula derived from the Bernoulli-Euler assumption, maximum amounts of tensile and maximum compression stresses are exerted onto the outer skin of beam[12]. The compression breakage strength exceeds the tensile breakage strength and during a three-point bending test, breakage starts from the outer skin location exposed to the maximum tensile stress test. The three-point bending stress is considered to be equivalent to the tensile breakage strength.

It has been reported that the tensile breakage strength of a particle layer is affected by the interparticle adhesive force and the number of contact points[13-15]. Based on **Fig. 5**, since the porosity remains unchanged, regardless of the specific surface area, the coordination number of the particles seems to also remain virtually the same[16]. However, it appears that as the surface area of a powder increases, the number of particles in the unit area on the breaking face does the same. As a result, the number of contact points does likewise, which enhances the bending strength.

3.2 Characteristics of particle size blended alumina particle layer

Fig. 7 summarizes the relation between the blend proportions and specific surface areas resulting from samples prepared by particle size blending with alumina powders of which the mean particle sizes are 1.5 and 0.4 μm respectively. Based on **Fig. 7**, it is apparent that as the proportion of the large size particles increases, the resultant specific surface area linearly decreases.

Fig. 8 reveals particle size distribution curves with blend percentages of large size particles of 0%, 25%, 50%, 75% and 100% respectively and with each sample exhibiting a two-peak particle size distribution pattern. Judging from the trend in **Fig. 8**, no peak shift occurred, even though the alumina powder was ground in a ball mill. This appears to result from the synthesis of particle size distribution curves of two alumina powders used for particle size blending.

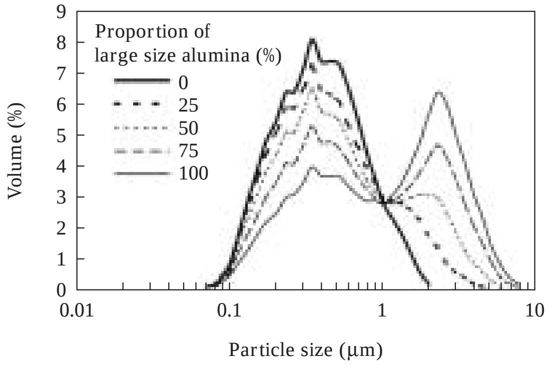

Fig. 8 Particle size distribution as a function of particle size blended powder

Fig. 9 illustrates the relation between the proportion of large size alumina particles and the porosity of the alumina particle layer. **Fig. 9** reveals that when the proportion of large size alumina particles is 25%, the porosity is minimized and when the proportion of large size alumina particles exceeds 25%, it increases. **Fig. 10** shows the pore size distribution curves of the particle size blended powder samples. When the proportion of large size particles is 0% (A), a sharp peak is present at an R_P of 0.05 μm. When the proportion of large size particles is 25% (B), a peak occurs at R_P of 0.06 μm, meaning a slight shift in this peak. When the proportion of large size particles is 50% (C), two peaks are present on the pore size distribution curve; namely one at 0.06 μm and the other at 0.1 μm. When the proportion of large size particles is 75% (D), there is no peak at 0.06 μm while peaks are present at 0.1 and 0.20 μm. The latter peak, at 0.20 μm, is also pre-

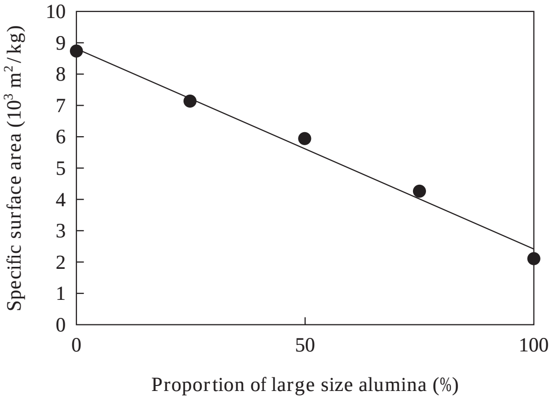

Fig. 7 Effect of particle size blended powder on specific surface area

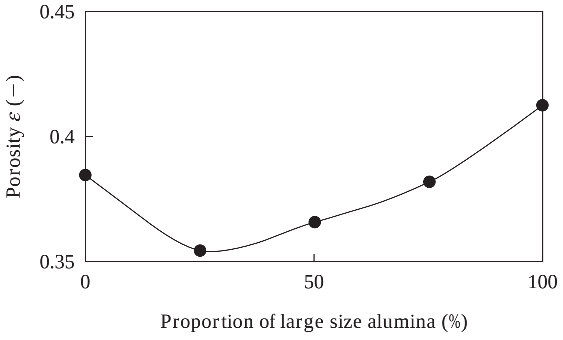

Fig. 9 Effect of particle size blended powder on porosity of alumina particle layer after heat treatment at 827K

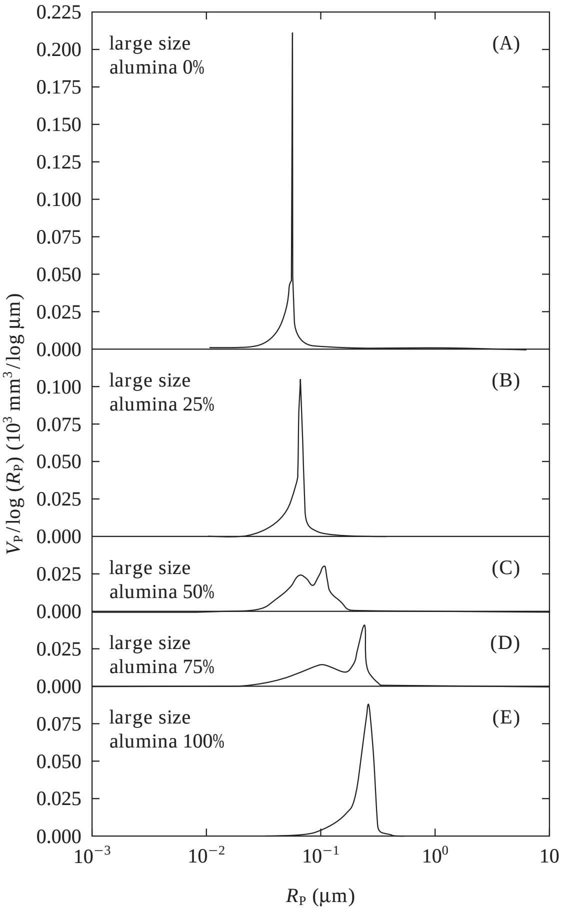

Fig. 10 Variation in pore size R_P distribution for particle size blended powder

sent when the proportion of large size particles is 100% (E). It appears that the peak at 0.22 µm shows a slight tendency to shift to the smaller particle size side.

From these findings, it seems that the pores are present in several clear-cut size groups and that small pores are present among finer particles, large pores are present among larger particles, and there is also the presence of medium-sized pores. The medium-sized pores are considered to be pores that occur following disordered arrangement of fine particles situated near the large particles within an alumina layer packed with arranged fine particles.

Fig. 11 illustrates the relation between the proportion of large particle alumina powder and the pore radii R_{P90}, R_{P50} and R_{P10}; measured using a mercury porosimeter. The pore radius R_{P50} increases in correlation with an increase in the proportion of large size alumina particles. The pore radius R_{P90}, however, remains virtually constant up to the blending proportion of large size particles of 75%, and rapidly increases when the proportion of large size particles is 100%. The pore radius R_{P10} increases until the proportion of large size particles reaches 50%, and becomes virtually constant when the proportion of large size particles is 75% or higher.

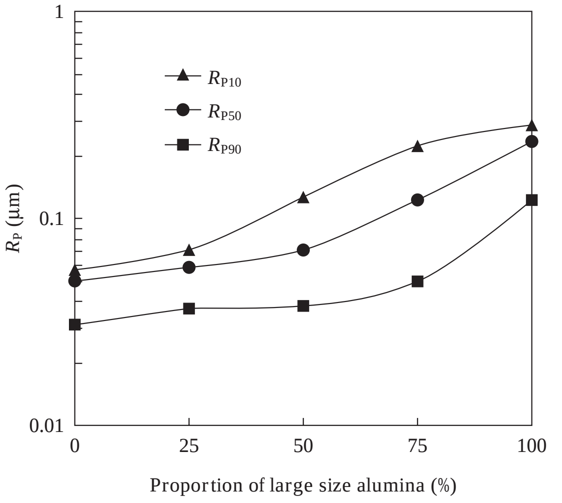

Fig. 11 Variation in pore size R_P for particle size blended powder

Fig. 12 provides the relation between the specific surface area of ground and size blended alumina particles and the bending strength of the alumina particle layer. The ○ marks in the diagram represent the results obtained from alumina particle layers made from size blended alumina particles, while the ● marks indicate the results obtained from alumina particle layers made from ground alumina particles. Though the porosity of the alumina particle layers made from size blended alumina particles exceeds

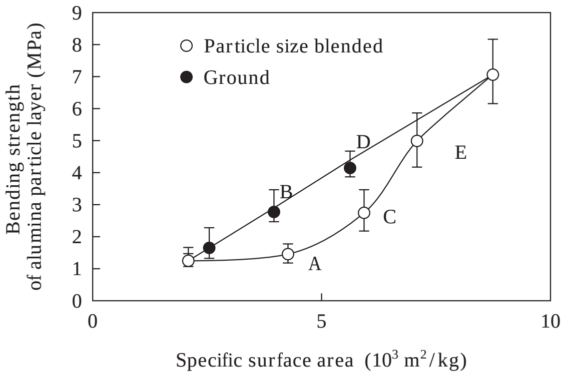

Fig. 12 Bending strength of alumina particle layer after heat treatment at 827K as a function of specific surface area for particle size blended powder

that of the alumina particle layers made from ground alumina particles, the bending strength of the former layers is lower than that attained by the latter that are made from ground alumina particles and have a lower porosity. An alumina particle layer comprising 75% of large size particles (Point A) and one composed of particles ground for 120 min (Point B) each exhibit a specific surface area of approximately 4×10^3 m^2/kg. From this diagram, the bending strength of alumina particle layers comprising size blended particles can be considered to have degraded, due to the blending of particles of a smaller specific surface area. The bending strength values at Points A and B are 1.5 and 2.8 MPa respectively; with the latter twice as large as the former. Likewise, at Points C and D, each exhibiting a specific surface area of 6×10^3 m^2/kg, the bending strength values are 2.8 and 4.2 MPa; with the latter 1.5 times the former.

In addition, the bending strength of the alumina particle layer with 75% of large size particles (Point A) is equivalent to an alumina particle layer composed of 100% of large size particles. The possible reason is considered to be as follows: With size blended particles, the pores formed among large size particles are packed with fine particles, resulting in a higher packing density. If a smaller amount of fine particles is present, virtually all of them fill the pores among those of a larger size; hence the bending strength of the alumina particle layer is governed by the contact points between the large size particles.

Seemingly, as the proportion of small size particles increases, the inter-particle distance between the large size particles does the same; the number of contact points among the small size particles rapidly increased, as did the bending strength of the alumina particle layer.

3.3 Effect of alumina constrained layer onto substrate characteristics

3.3.1 Effect on shrinkage of substrate

Sandwich substrates, each consisting of a 12 μm alumina particle layer sandwiched between 180 μm glass layers, were prepared, where the 12 μm alumina particle layer was formed using ground or size blended particles. **Fig. 13** illustrates the relation between the bending strength and shrinkage in the horizontal directions (X-Y) of these substrates. The ○ marks represent alumina particle layers made from size blended particles while the ● marks stand for those made from ground particles. As **Fig. 13** reveals, the results from all starting materials can be plotted on a single curve. Although the horizontal shrinkage is extremely large when the bending strength of the alumina particle layer is 1.8 MPa or lower, conversely, when the bending strength is 1.8 MPa or higher, the shrinkage is as low as 0.5%.

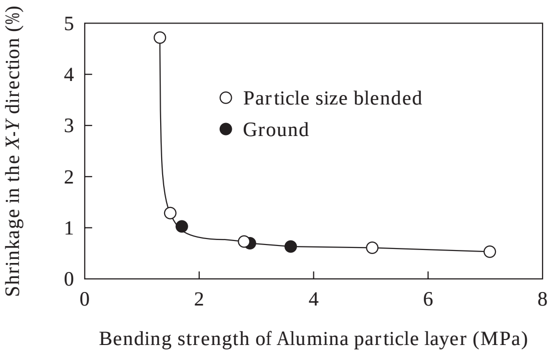

Fig. 13 Shrinkage in the X-Y direction as a function of bending strength of alumina particle layer for particle size blended and ground powder

Glass layers on both sides of a constrained layer shrink when the substrate is fired, and a compression stress is exerted onto both faces of the constrained layer. Assume that the constrained layer is separated in its mid section. A bending moment will occur on each constrained layer toward the glass-alumina layer[12)]. When the alumina particle layer can no longer withstand this moment and fails to maintain the layer structure, the shrinkage value climbs. Therefore, it is important to increase the bending strength of the alumina particle layer in order to decrease the sintering shrinkage.

3.3.2 Effect on substrate porelessness

To be able to produce a poreless ceramic substrate, molten glass must penetrate into its alumina particle layer during the sintering process. Hence, the authors investigated the effect of the packing structure of alumina particle layer onto the distance of glass penetration. Crystallization of the glass was inspected on a glass-alumina layer, which was sintered at 1153K with a X-ray diffraction technique. As a result, no peak other than that for alumina was found. This means that crystallization of the glass did not occur.

Generally, when liquid penetrates into a particle layer, the distance of penetration can be defined with the Kozeny-Carman formula[17)].

$$l^2 = \{\varepsilon^3 \cdot \Delta P \cdot T\}/\{K\,(1-\varepsilon)^2 S_W^2 \cdot \eta\} \qquad (2)$$

where, l is the distance of liquid penetration into a particle layer, ΔP, the difference in pressure that is a motive force for penetration, T, the time needed for penetration, and η, the viscosity of the liquid. K, meanwhile, is a constant known as the Kozeny constant. The difference in pressure ΔP that is a motive force for penetration is considered to be a value equivalent to a capillary suction force P_C of a particle layer. When the radius of the capillary is r_C, the capillary suction pressure P_C can be expressed using the following formula:

$$P_C = 2\sigma_s \cdot \cos\theta / r_C \qquad (3)$$

where σ_s is the surface tension of liquid, and θ the contact angle of wetting between the liquid and particle layers. The hydraulic radius r_H used to derive the Kozeny-Carman formula can be defined by the following formula:

$$r_H = \{\varepsilon / (1-\varepsilon)\}\{1/(S_W \rho)\} \qquad (4)$$

When γ_H is substituted for the capillary radius γ_C in Eq. (3), and P_C is substituted for ΔP, then Eq. (2) can be represented by Eq. (5).

$$l^2 = \{2 \cdot \rho \cdot \varepsilon^2 \cdot \sigma_s \cos\theta \cdot T\} / \{K(1-\varepsilon) S_W \eta\} \qquad (5)$$

From the formula above, it can be understood that the square of distance of glass penetration l into a particle layer is proportional to $\varepsilon^2/\{(1-\varepsilon) \cdot S_W\}$.

Fig. 14 shows the effect of the distance of glass penetration onto $\varepsilon^2/\{(1-\varepsilon) \cdot S_W\}$ when sintering was performed at 1153K for 60 min.

In **Fig. 14**, the ○ marks represent alumina particle layers made from size blended alumina particles and the ● marks stand for alumina particle layers made from ground alumina particles. In the case of alumina particle layers made from ground alumina particles, the square of the penetration distance varies in proportion with $\varepsilon^2/\{(1-\varepsilon) \cdot S_W\}$ according to the Kozeny-Carman formula. Incidentally, with alumina particle layers made from size blended alumina particles, glass readily penetrated into the alumina particle layer in comparison with those made from ground alumina particles. As the pore size distribution curves in **Fig. 10** indicate, the alumina particle layers made from size blended alumina particles, unlike those made from ground alumina, exhibit two clear-cut peaks. From Eq. (5), it also appears that glass selectively penetrated into larger sized pores. Because larger sized pores appear to govern the penetration of glass, the relation between R_{P10} and the penetration distance was plotted in **Fig. 15**. The pore size R_{P10} and distance of penetration exhibit a linear relation. For this reason, larger pore sizes are considered to greatly affect the distance of glass penetration. Additionally, the peak in the large size particles in the alumina particle layer made from particle size blended alumina particles appears to be greatly affected by the packing structure around the larger particles.

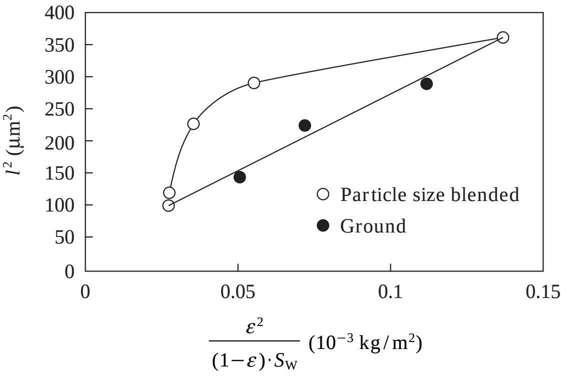

Fig. 14 Penetration length as a function of $\varepsilon^2/\{(1-\varepsilon)\cdot S_W\}$, that is parameter specific surface area and porosity followed by Kozeny-Carman Eq.

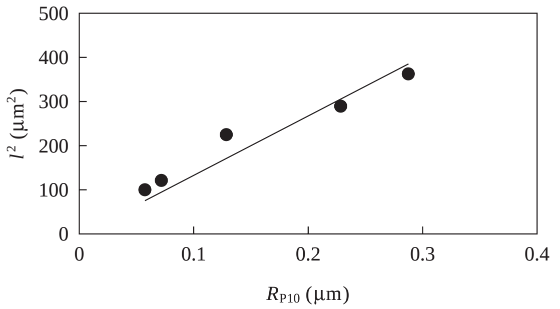

Fig. 15 Penetration length as a function of pore size R_{P10} for particle size blended powder

4. Conclusion

The authors investigated low temperature-fired substrates using a glass-alumina mixture, and more specifically, the effect of the packing structure of an alumina constrained layer on the substrate, wherein the alumina constrained layer, which is not sintered at a sintering temperature for the substrate materials, is provided in the middle of the substrate.

The results obtained from the investigation are summarized below:

1) As the bending strength of an alumina sheet to be used as a constrained layer increases after debinding, the shrinkage of the substrate in horizontal directions decreases. In addition, the relation between the bending strength and shrinkage in hori-

zontal directions of the substrate can be plotted on the same curve, regardless of whether the constrained layer is made from ground alumina or size blended alumina particles.

2) When the constrained layer is made from ground alumina particles and assuming the porosity of the particle layer remains constant, the bending strength is proportional to the specific surface area.
3) When the constrained layer is made from size blended alumina particles, the pore size distribution curves each exhibit a two-peak pattern, and the bending strength of an alumina particle layer made from size blended alumina particles was lower than that obtained from any alumina particle layer made from ground alumina particles. This fact seems to result from a decrease in the number of contact points around the large particles, which led to a loss in bending strength.
4) The distance to which the glass penetrates the alumina particle layer made from ground alumina particles conforms to the Kozeny-Carman formula. In the case of an alumina particle layer made from size blended alumina particles, glass penetrates more readily into the alumina particle layer. With an alumina particle layer consisting of size blended alumina particles, two peaks occur on the pore size distribution curve owing to the presence of large size particles, and the penetration distance is dependent on the larger pore size of the two peaks.

Nomenclature

D_p	: particle diameter	(μm)
D_{SW}	: specific surface area diameter	(μm)
F_B	: bending force	(N)
K	: constant for Eq. (2)	(−)
L	: fulcrum span	(m)
l	: distance of penetration	(μm)
P_C	: capillary suction pressure	(MPa)
R_P	: pore size	(μm)
r_C	: radius of capillary	(μm)
r_H	: hydraulic radius of powder bed	(μm)
S_W	: specific surface area	(m^2/kg)
T	: time of penetration	(s)
t	: thickness of the substrate	(m)
V_L	: proportion of large size alumina	(%)
W	: wideness of the substrate	(m)
ΔP	: difference of pressure	(MPa)
ε	: porosity	(−)
η	: viscosity	(Pa·s)
ρ	: density of particle	(kg/m^3)
σ_B	: bending strength	(MPa)
σ_s	: surface tension	(N/m)

References

1) Mikeska, K. R. and R. L. Brown : “Method for reducing shrinkage during firing of ceramic bodies”, U. S. Pat. No. 5254191 (1993)
2) Mikeska, K. R. and R. L. Brown : “Method for reducing shrinkage during firing of ceramic bodies”, U. S. Pat. No. 5474741 (1994)
3) Bordia, R. K. and A. Jagota : “Crack Growth and Damage in Constrained Sintering Filmes”, *J. Am. Ceram. Soc.*, **76** [10] 287-292 (1993)
4) Lin, Y. C. and J. H. Jean : “Constrained Densification Kinetics of Alumina / Borosilicate Glass+Alumina / Alumina Sandwich Structure”, *J. Am. Ceram. Soc.*, **85** [1] 150-154 (2002)
5) Tzeng, S. Y. and J. H. Jean : “Stress Development during Constrained Sintering of Alumina / Glass / Alumina Sandwich Structure”, *J. Am. Ceram. Soc.*, **85** [2] 335-340 (2002)
6) Bang, J. and G. Q. Lu : “Constrained-Film Sintering of a Borosilicate Glass : In-Situ Measurement of Film Stress”, *J. Am. Ceram. Soc.*, **78** [3] 813-815 (1995)
7) Nishigaki, S. and T. Nonomura : “Multilayer Substrate of Ceramics Sintered at Low Temperature”, *J. Semiconductor World.*, **6** [12] 71-81 (1987)
8) Minowa, T. and K. Kawakami : “Low-Temperature Fired Multilayer Substrate”, *Electronic Ceramics.*, **18** [87] 9-16 (1987)
9) Nakao, S. and H. Kameda : “Hybrid Laminate and Manufacturing Method Therefor”, U. S. Pat. No. 6306511 (2001)
10) Nakao, S., M. Kojima and K. Tanaka : “Constrained sintering of the sandwich substrate with inner-constraining fine particles layer”, *J. Soc. Powder Technol., Japan*, **41**, 350-355 (2004)
11) Tanaka, K., I. Inada, K. Wakino and I. Uei : “Submicron Grinding of Low-soda Alumina by Ball Milling”, *Zairyo*, **37** [11] 1319-1325 (1988)
12) Sekiya, S. and S. Sumi : “Zairyo Rikigaku Gaiyo”, 2nd ed. pp. 90-94, Izumi Syobou (1980)
13) Kosaka, Y. et al. (ed) : “Funtai Kogaku Binran”, 2nd ed. pp. 223-229, Nikkankogyo Shinbunsha (1998)
14) Jinbo, G., S. Asakawa and N. Soga : “Measurement of Adhesion Force of Powder Particles by Powder Bed Tensile Strength Method”, *Zairyo*, **17** [6] 541-545 (1968)
15) Tsubaki, J. and G. Jinbo : “Theoretical Analysis of the Tensile Strength of Powder Bed”, *Powder Technol.*, **37**, 219 (1984)
16) Suzuki, M., S. Makino, S. Yamada and K. Iinoya : “A Study of Coordination Number in Random Packed System of Monosized Spheres”, *Kagaku Kogaku Ronbunshu*, **6**, 59-64 (1980)
17) Kubo, K. et al. (ed) : “Funtai Riron to Ohyo”, 2nd ed. pp. 530-531, Maruzen (1985)

Author's short biography

Shuya NAKAO

Shuya NAKAO received his B. Eng. in 1986 and M. Eng. in 1988 from the Department of Chemical engineering at Hiroshima University. He has been working at Murata Manufacturing Co. Ltd. since 1988.

Masaru KOJIMA

Masaru KOJIMA has been working at Murata Manufacturing Co. Ltd. since 1968.

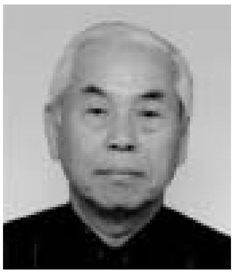

Kenji TANAKA

Kenji TANAKA received his B. S. in 1966 and M. S. in 1968 from the Kyoto Institute of Technology. He has been working at Murata Manufacturing Co. Ltd. since 1968. He received his Ph. D. from Kyoto University in 1990. He got the Technology Award of the Ceramic Society of Japan in 1992 and the Technology Progress Award of the Japan Society of Powder and Powder Metallurgy in 1993, for his establishment of a submicron grinding technique. He is a consultant engineer.

Rapid Size Classification of Ultrafine Particles Using Surface Characteristics†

K. Wakabayashi[1], S. Sekita[2],
H. Hayashi[3], H. Sasaki[4]
*Department of Environment, Resources and Materials Engineering, Waseda University**

Abstract

Size classification of ultrafine particles is one of the most difficult techniques in materials processing. We developed a novel ultrafine particle classification method based on heterocoagulation phenomena of colloidal particle. In this paper, rapid size classification of silica particles (median diameters of 100nm and 300nm) from their mixed suspension was examined in various solution chemistries by column bed packed with ferro-nickel slag (FS) as a fibrous collector medium. Many of 100nm-silica particles selectively attached to the FS surface during passing through the FS-packed column, while 300nm-silica remained in an outlet suspension. Newton's efficiency depended on pH and ionic strength; optimal classification was attained at pH3.5 in 10mM KNO_3*. These results were qualitatively explained by DLVO-type interaction energy curve, indicating that interfacial interaction of both particle and collector determined the classification efficiency. Furthermore, particle concentration and superficial velocity had an influence on classification efficiency. This method proved to be simple, rapid and cost-effective for classifying ultrafine particles in aqueous media.*

Key words: Size classification, Zeta potential, Silica particle, Fibrous slag, DLVO theory

1. Introduction

Increasing demand to introduce nanotechnology in various fields of industry encourages the development of producing, processing and handling technique for ultrafine particles in aqueous media. It is desirable to have the suspended phase consisting of homogeneous particles of uniform size and shape because monodispersed particulate suspensions offer many advantages. Conventional size classification of suspended particles involves the mechanical phenomena such as screening, sedimentation and centrifugation. However, the physical property itself becomes undominant in the particle size range below 1μm; it does not seem promising to perform ultrafine particle classification by mechanical technique. One of our authors proposed a novel method based on surface characteristics as an alternative method for rapid size classification of ultrafine particles. This method is essentially based on heterocoagulation phenomenon of colloidal domain. While passing through the column bed packed with solid collector media, part of the particles dispersed in liquid can approach and successively adhere to collector surface if the interfacial forces between particle and collector are favorable for attachment. On the other hand, if the interfacial forces are unfavorable, particles remain in the effluent suspension. From the Derjaguin-Landau-Verwey-Overbeek theory for colloid stability, surface electrical potential, solution's pH, ionic concentration as well as particle size, have influences on the interaction forces. Therefore, these physicochemical parameters affect selectivity of particle adhesion to collector media, that is, efficiency of particle classification. In the previous study, Sasaki *et al.*[1)] carried out the size classification of polydispersed ultrafine hematite particles (median diameter of 200nm) by passing their suspension through col-

---

* 3-4-1 Okubo, Shinjyuku-ku, Tokyo 169-8555, Japan
[1] Ministry of Welfare, Health and Labor
[2] Shiseido Co. Ltd.
[3] Corresponding author
Central Research Institute of Mitsubishi Materials Co., Ltd.
E-mail: akhaya@mmc.co.jp
[4] Faculty of Science and Engineering
E-mail: hisasaki@waseda.jp

† This report was originally printed in J. Soc. Powder Technology, Japan, **39**, 175-182 (2002) in Japanese, before being translated into English by KONA Editorial Committee with the permission of the editorial committee of the Soc. Powder Technology, Japan.

umn bed packed with glass beads and demonstrated that larger particles selectively obtained in the outlet. Ogawa *et al.*[2)] also investigated the classification of ultrafine hematite using fibrous collector medium. These studies suggested that the performance of size classification were in general agreement with the DLVO interaction energy between particle and collector surface.

In view of the above findings, this study attempts to carry out the rapid size classification of silica particles having median diameters of 100nm and 300nm by column bed packed with fibrous collector and to elucidate its relevance to interfacial interaction energy between particle and collector surface. The fibrous collector employed here was a fibrous ferro-nickel slag (FS), which is a solid waste material from ferro-nickel electrosmelting process. FS has received much attention as a collection media for suspended particles due to its large specific surface area, chemical stability and cheap cost. Effect of suspension's pH and ionic concentration, which is considered to affect the surface electrical properties of both particle and collector, on the particle classification efficiency is experimentally examined.

2. Materials and Methods

2.1 Colloidal silica particles

Two types of monodispersed colloidal silica particles were obtained by chemical reaction of alcoholic solutions containing tetraethylorthosilicate and annmonia catalyst, as described by Stöber *et al.*[3)]. Conditions for preparation and both characteristics are listed in **Table 1**. Silica sol was centrifuged and the supernatant solution was decanted, followed by dispersed in doubly distilled water. After sonicated five minutes, silica sol was centrifuged again to remove the residual reagents completely. This procedure was repeated until the conductivity of the supernatant reached 10μS/cm. The stock suspensions were stored in Pyrex container and were agitated in an ultrasonic bath before use. The hydrodynamic median diameters of two types of particles were determined to be 100nm (small) and 300nm (large) by dynamic light scattering (ELS-800, Otsuka Electronics, Japan). SEM observation showed that both were spherical and monodispersed. Mixed suspension of 100nm- and 300nm- silica particles were used in the size classification experiment. **Fig. 1** shows size distribution of the prepared suspension.

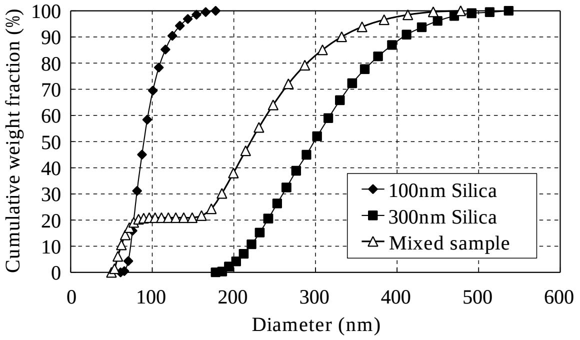

Fig. 1 Size distribution of silica particles used in the experiment.

2.2 Collector for particle adhesion

The collector medium for silica particles was fibers of ferro-nickel slag (FS) from Pacific Metals Co., Japan. FS was byproduct from ferro-nickel electrosmelting process and produced by a high speed spinning technique. The chemical composition determined by a fluorescence X-ray analyzer (X'UNIQUE, PHILIPS, U.S.) is listed in **Table 2**. An individual fiber had a mean diameter of 3 − 8μm and length of 2 − 3mm. Scanning electron micrograph showed that an individual fiber had a completely smooth surface with no surface structure. The specific surface area of FS was determined to be $0.17m^2 \cdot g^{-1}$ by BET method using a surface area measurement apparatus (ASAP2010, micromeritics, U.S.). Previous study indicated that the dissolution of FS was quite negligible in the pH range from 4 to10 at 25℃.

Table 1 Particle characteristics used in the experiment

Samples	Reagents	Hydrodynamic diameter (DLS measurement)	Morphology (SEM observation)
small particle	TEOS* 10mL ethanol 250mL + ammonia 11.5mL	100nm	spherical
large particle	TEOS 10mL methanol 125mL + buthanol 125mL + ammonia 20mL	300nm	spherical

* Tetraethyl orthosilicate

Table 2 Chemical composition of fibrous ferro-nickel slag

Components	SiO_2	MgO	Al_2O_3	CaO	Fe_2O_3
Weight percentage	52.9	22.2	18.6	1.66	1.13

2.3 Zeta potential measurement

Zeta potential measurements of silica particle and FS were carried out using an electrophoretic light scattering spectrophotometer (ELS-800, Otsuka Electronics). Mechanically ground slag powder was used as FS sample because its chemical composition was uniform. Supporting electrolyte was KNO_3. A droplet of HNO_3 or KOH that had the same ionic concentration as the sample suspension was added for pH adjustment. Samples were dispersed in an ultrasonic bath for five minutes and quickly supplied to the measurement.

2.4 Size classification experiment

All tests were performed by column bed method packed with FS. **Fig. 2** illustrates the experimental apparatus. A cylindrical column made of glass had an inner diameter of 25mm and a height of 200mm. To support the FS, a stainless steel screen disk was clamped at the constricted part of column. Three grams of FS were soaked in water for 10minutes and then packed onto the screen disc, yielding a void volume fraction of 0.91. The bed was conditioned with a solution of the same ionic strength and pH as the suspension. That treatment ensured complete removal of fragments of destroyed or unfastened FS and of any adherent microbubbles of air. Silica suspensions which had a desired particle concentrations, pH and ionic concentration were continuously fed from the top of the column into the bed after dispersed in an ultrasonic bath for 5minutes. Each 100mL effluent sample was taken and silica concentration was determined by ICP-AES after complete dissolution of silica by KOH. Also size distribution of silica particle in both influent and effluent was analyzed by dynamic light scattering. Collection efficiency of the silica particles was evaluated by Si ratio analysis of inlet and outlet suspension.

All chemicals were of analytical reagent grade and were used without further purification. Water was doubly distilled, the second distillation being carried out in an all-Pyrex apparatus. The temperature was kept constant at 25±2℃ in all experiment.

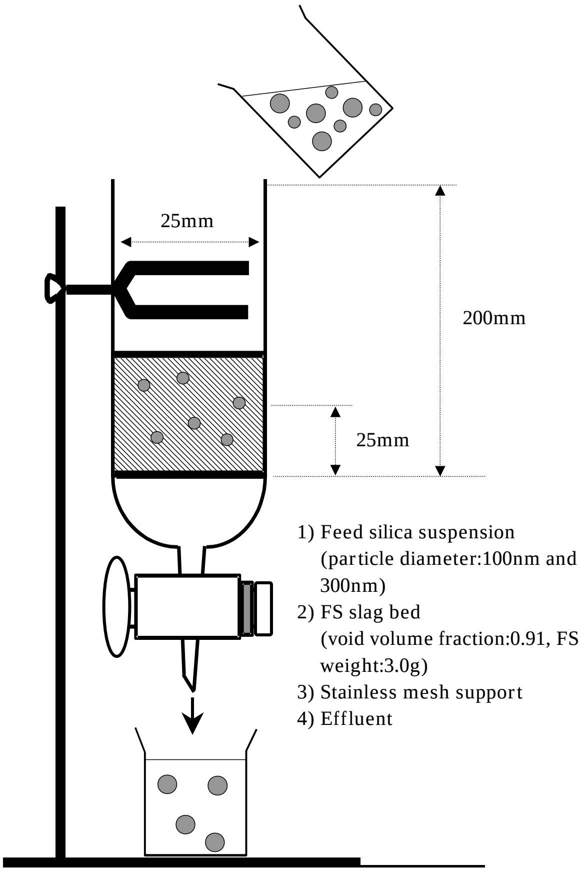

1) Feed silica suspension (particle diameter:100nm and 300nm)
2) FS slag bed (void volume fraction:0.91, FS weight:3.0g)
3) Stainless mesh support
4) Effluent

Fig. 2 Illustration of FS-packed column bed system.

3. Results and Discussion

3.1 Zeta potential measurement

Fig. 3 shows the results of zeta potential measurements of silica and FS in 10mM KNO_3. Both silica particles had negative value ranging from −2 to −60mV and 300nm-silica had more negative zeta potential than 100nm-silica. The gap in the zeta poten-

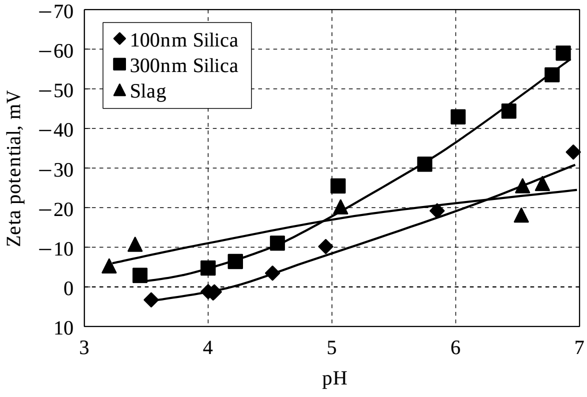

Fig. 3 Zeta potential measurement of silica and slag as a function of pH in 10mM KNO_3.

tial for 100nm- and 300nm-silica particles became larger as the pH increased. The isoelectric points were estimated to be 4.0 for 100nm-silica, 3.2 for 300nm-silica and 2.9 for FS, respectively.

3.2 Size classification tests

3.2.1 Influence of solution chemistry

Fig. 4 shows the recovery of total silica as a function of effluent volume at various pH values in 10mM KNO_3. The vertical line is normalized silica collection ratio $(C_0-C_t)/C_0$, where C_0 and C_t represent inlet and outlet silica concentration, respectively. Silica collection ratio showed maximum value of 0.62 at the effluent volume of 100mL when pH was 4.0. Silica collection ratio decreased in accordance with the increase of pH; silica collection ratio was 0.22 at pH5.0. This trend was explained by the fact that the increase of magnitudes of negative potential of silica and FS caused strong repulsive forces, which contributed to inhibit particle adhesion to FS. The suspension's pH was fixed at 4.0 in the following size classification tests.

Fig. 5 shows the scanning electron microscopic images of the FS surface after passing through column bed. Many 100nm-silica particles were observed, whereas few 300nm-silica adhered to FS. This indicated that 100nm-silica selectively adhered to FS. Also, **Figs. 6 (a)** and **(b)** show SEM images of particles in the inlet and outlet suspension. Comparing the proportion of small and large particles, a substantial number of 100nm-silica particles disappeared from the inlet suspension; 100nm-silica particles selectively deposited on FS surface. In the conventional filtration, the larger particle size is the easier to deposit on collector media, because particle deposition usually occurs by mechanical straining, interception and gravitational settling. Experimental finding was to the contrary; in fact, this was unique to particle processing technique based on heterocoagulation phenomenon. More detailed explanation in connection with interaction energy is discussed later.

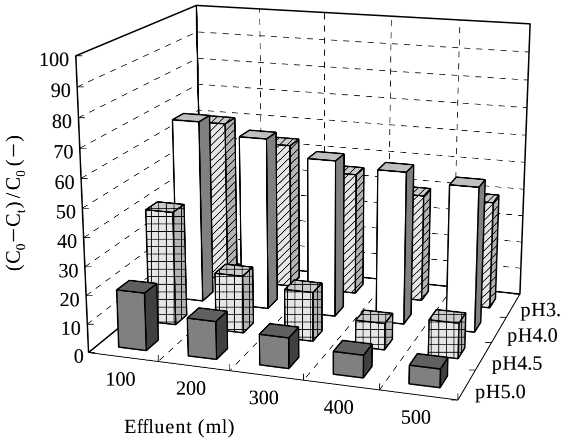

Fig. 4 Recovery of total silica particles as a function of effluent volume at various pH values. Experimental conditions were KNO_3 concentration of 10mM, silica concentration of 26mg/L, and superficial velocity of 1.7mm/s.

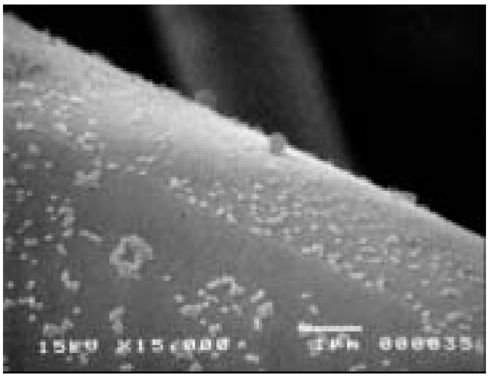

Fig. 5 Scanning electron microscopic images of silica particles deposited on FS surface.

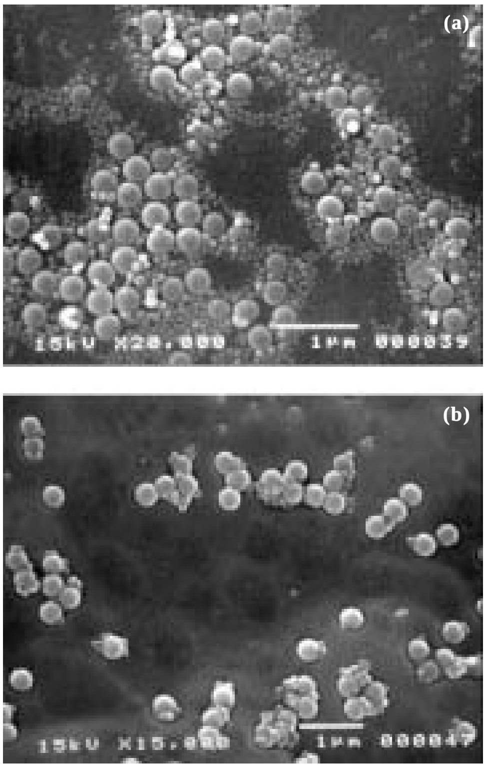

Fig. 6 Scanning electron microscopic images of silica particles in the (a) influent and (b) effluent samples.

Fig. 7 shows the Newton's efficiency as a function

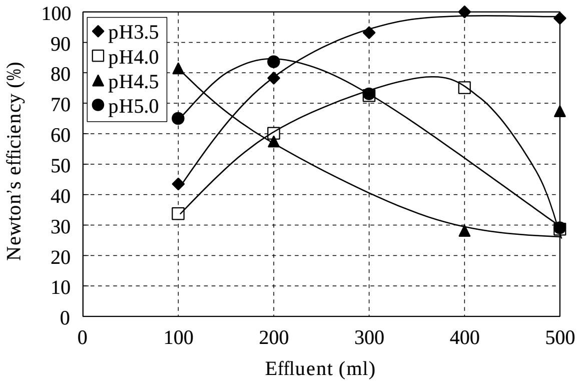

Fig. 7 Newton's efficiency as a function of effluent volume at various pH values. Experimental conditions were KNO_3 concentration of 10mM, silica concentration of 26mg/L, and superficial velocity of 1.7mm/s.

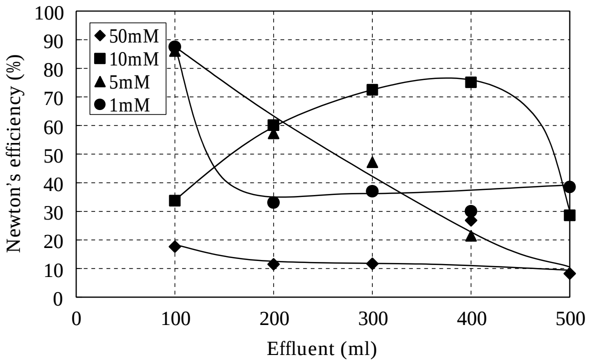

Fig. 8 Newton's efficiency as a function of effluent volume at various ionic strength. Experimental conditions were pH4.0, silica concentration of 26mg/L, and superficial velocity of 1.7mm/s.

of effluent volume at various pH values. If we are targeting at 100nm-silica, Newton's efficiency η is defined in the following form[4].

$$\begin{aligned}\eta &= [(\text{collection ratio of 100nm silica}) \\ &\quad -(\text{entrainment ratio of 300nm silica})]\times 100 \\ &= \left[\left(\frac{\text{number of 100nm silica attached to FS}}{\text{number of 100nm silica in influent}}\right)\right. \\ &\quad \left.-\left(\frac{\text{number of 300nm silica attached to FS}}{\text{number of 300nm silica in influent}}\right)\right]\times 100 \qquad (1)\end{aligned}$$

Newton's efficiency reached 100% in the effluent volume of 400mL when suspension pH was 3.5. Newton's efficiency decreased at pH4 where collection efficiency of total silica particles reached maximum. This was probably due to the fact that both 100nm- and 300nm-silica were able to deposit on FS, thereby causing little selectivity in FS attachment. The position of optimal Newton's efficiency shifted to the larger effluent volume as the pH became lower.

Fig. 8 shows the Newton's efficiency as a function of effluent volume at various KNO_3 concentrations ranging from 1 to 50mM. When KNO_3 concentrations were 1mM and 5mM, Newton's efficiency showed 90% in effluent volume of 100mL. Relatively high Newton's efficiency observed at KNO_3 concentration of 10mM. Newton's efficiency decreased as the total silica collection got higher. This was also due to the low selectivity in particle attachment to FS. The position of optimal Newton's efficiency shifted to the large effluent volume in accordance as the KNO_3 concentration decreased.

3.2.2 Influence of particle concentration and superficial velocity

Fig. 9 shows Newton's efficiency as a function of effluent volume at several silica concentrations. When silica concentration was 64mg/L, Newton's efficiency reached 76% in effluent volume of 200mL. Similarly, optimal Newton's efficiency was attained to be 70% in effluent volume of 400mL at silica concentration of 24mg/L. The position of the optimal Newton's efficiency shifted to the larger effluent volume in accordance with the decrease of silica concentration. On the other hand, Newton's efficiency was generally low when silica concentration was 90mg/L.

Fig. 10 shows Newton's efficiency as a function of effluent volume at various superficial velocities ranging from 0.85 to 11.3mm/s. Optimal Newton's

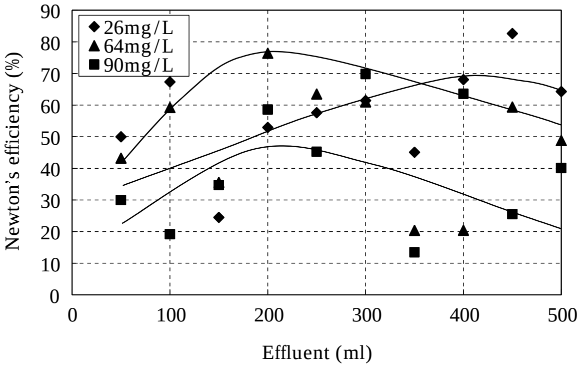

Fig. 9 Newton's efficiency as a function of effluent volume at various silica concentrations. Experimental conditions were pH4.0, KNO_3 concentration 10mM, and superficial velocity 1.7mm/s.

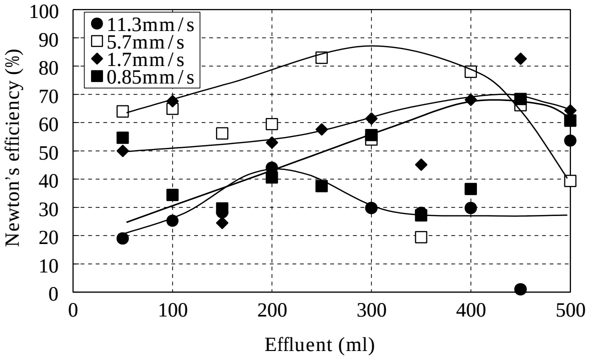

Fig. 10 Newton's efficiency as a function of effluent volume at various superficial velocity. Experimental conditions were pH4.0, KNO_3 concentration 10mM, and silica concentration 26mg/L.

efficiency 68% was observed in effluent volume of 450mL at superficial velocity of 0.85mm/s. Newton's efficiency maximum reached 84% in effluent volume of 200mL at superficial velocity of 5.7mm/s. It was found that the position of the optimal Newton's efficiency shifted to the larger effluent volume in accordance with the decrease of superficial velocity. On the other hand, Newton's efficiency generally decreased when superficial velocity was 11.3mm/s.

3.3 Discussion of DLVO-type interaction energy between particle and collector

Colloidal particles approach at the neighborhood of the collector surface by convection and Brownian diffusion, followed by the interfacial interaction that determines the fate of the particle attachment. If the interaction is favorable for particle attachment, spontaneous and irreversible attachment occurs. On the other hand, if unfavorable for attachment, collector repels particle deposition. The process that silica particles adhered to the fibrous collector was regarded as the *heterocoagulation phenomena*; adhesion of colloidal particle onto macroscopic substratum. The possibility of attachment of colloidal particle to solid surface is discussed by summation of interfacial forces which is mainly the contribution of both electrical double layer interaction and London-van der Waals forces based on DLVO theory[5]. In particular, electrical double layer interaction, which largely depends on electric potential, ionic concentration and so forth, plays a decisive role in particle coagulation phenomenon.

Assuming that the size of the FS was by far larger than the silica particle, it was reasonable to use the sphere-plate model. The linear approximated electrical double layer interaction energy V_e between sphere and plate is derived by Hogg, Healy and Fuerstenau[6] and written in the following form,

$$V_e=\frac{\varepsilon a(\Psi_1^2+\Psi_2^2)}{4}\left[\frac{2\Psi_1\,\Psi_2}{(\Psi_1^2+\Psi_2^2)}\ln\left\{\frac{1+\exp(-\kappa h)}{1-\exp(-\kappa h)}\right\}+\ln\{1-\exp(-\kappa h)\}\right],\ \kappa=\sqrt{\frac{8\pi c e^2 z^2}{\varepsilon k_B T}} \tag{2}$$

where ε is the dielectric constant of the medium, h is the shortest distance, a is a radius of particles, Ψ_1 and Ψ_2 are surface potentials and κ is the Debye reciprocal length, e is the elementary charge, k_B is the Boltzmann constant, c is an ionic concentration, z is a valency of ions and T is absolute temperature. The unretarded London-van der Waals attraction potential[7] V_A is given as,

$$V_A=-\frac{A_{132}a}{6h} \tag{3}$$

where A_{132} is the overall Hamaker constant for the system sphere1-medium3-collector2 which can be approximated by,

$$A_{132}=\sqrt{A_{131}\cdot A_{232}} \tag{4}$$

where A_{131}, A_{232} are the Hamaker constant for the sphere and collector in the medium3, respectively. Hamaker constant was obtained from the tabulation by Visser[8]. The values of A_{131}, A_{232} used in the calculation are listed in **Table 3**. The total interaction energy V_T between particle and collector system is written as follows.

$$V_T=V_e+V_A \tag{5}$$

We discuss the influence of particle size a on the total interaction energy V_T. From Eq. (5), V_T is arranged as follows.

$$\begin{aligned}V_T&=a\left[\frac{\varepsilon a(\Psi_1^2+\Psi_2^2)}{4}\left\{\frac{2\Psi_1\,\Psi_2}{(\Psi_1^2+\Psi_2^2)}\ln\left\{\frac{1+\exp(-\kappa h)}{1-\exp(-\kappa h)}\right\}+\ln\{1-\exp(-2\kappa h)\}\right\}-\frac{A}{6h}\right]\\&=a\cdot\Phi(\Psi_1,\Psi_2,\kappa,A,h)\end{aligned} \tag{6}$$

Table 3 Hamaker constants used in the calculation

$A_{SiO_2-H_2O-SiO_2}$	0.46×10^{-20} J
$A_{SiO_2-H_2O-SiO_2}$	0.96×10^{-20} J
$A_{SiO_2-H_2O-SiO_2}$	0.66×10^{-20} J

It is found that magnitude of V_T is proportional to particle radius if the physicochemical parameters Ψ_1, Ψ_2, κ and Hamaker constant are the same values, namely, the identical materials. During approaching a collector surface, if both particle and collector have negative charges, there exists interaction potential energy maximum at several nanometer distances from the surface of collector. This maximum, called potential energy barrier, is regarded as the activation energy for particle adhesion to solid surface. Equation (6) suggests that the height of potential energy barrier is proportional to the particle radius; the smaller a particle size is, the more favorable for particle attachment. **Fig. 11** illustrates the conceptual explanation for selective particle attachment using the difference of interfacial interaction.

To calculate the total interaction energy curves in the experimental systems, the surface potential was approximated as the measured zeta potential obtained from **Fig. 1**. **Figs. 12** and **13** show the calculated total interaction energy V_T curves as a function of the separation distance between the silica and FS at various pH values. There is no potential energy barrier for 100nm-silica; hence spontaneous attachment is expected. On the other hand, potential energy barrier are observed for 300nm-silica. Thus selective attachment of 100nm-silica was more probable compared with 300nm-silica.

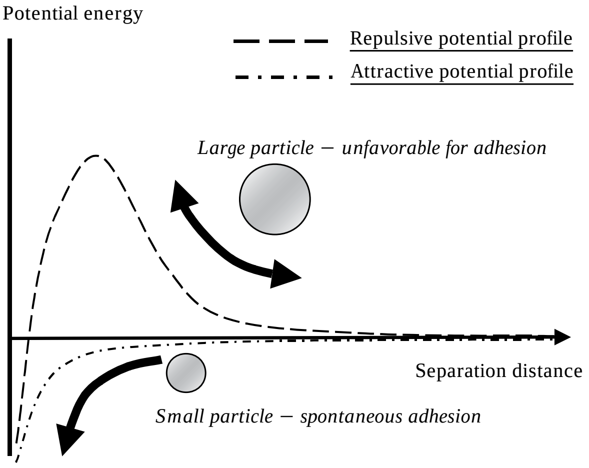

Fig. 11 Illustration of potential curves and their influence on particle adhesion to solid substratum.

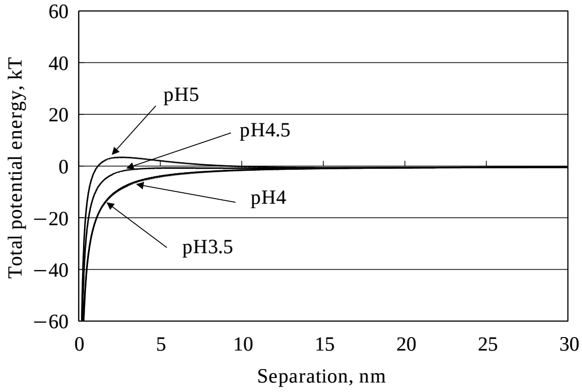

Fig. 12 Total potential energy curves between 100nm silica and FS system as a function of separation distance. The curves from top to bottom are for pH5, 4.5, 4, 3.5, in that order.

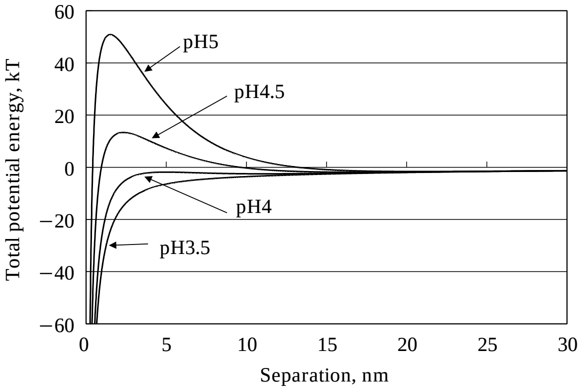

Fig. 13 Total potential energy curves between 300nm silica and FS system as a function of separation distance. The curves from top to bottom are for pH5, 4.5, 4, 3.5, in that order.

3.4 Particle deposition efficiency onto the cylindrical collector

Spielaman and Friedlander[9] presented a theoretical analysis describing a deposition of Brownian particles which interact with collector through potential force. Dimensionless particle collection efficiency by cylindrical collector medium is expressed by the following form.

$$R=2.2955179A_c^{\frac{1}{3}}\left(\frac{Ua_c}{D}\right)^{-\frac{2}{3}}f(V_T),\quad D=\frac{k_BT}{6\pi\mu a} \qquad (7)$$

Here, A_c is a porosity dependent parameter, U is velocity of approaching particle, a_c is radius of a cylindrical collector, D is diffusion coefficient of particle, $f(V_T)$ is a function of total interaction energy, k_B is Boltzmann constant, T is absolute temperature, μ is viscosity of fluid, and a is particle radius. From **Figs. 12** and **13**, the difference of total interaction energy between 100nm- and 300nm-silica is negligibly small when pH was below 4.0. In those cases, dimensionless particle collection efficiency R is a function of diffusion coefficient of particle D because the other parameters are identical. Dimensionless particle collection efficiencies for 100nm- and 300nm-silica particles are represented by R_{100} and R_{300}, respectively. A ratio of R_{100} and R_{300} is arranged as follows.

$$R_{100} : R_{300} = 100^{-\frac{2}{3}} : 300^{-\frac{2}{3}} \cong 2 : 1 \qquad (8)$$

This suggests that particle collision rate for 100nm-silica is preferable to that of 300nm-silica even if interfacial forces for both particles were favorable for attachment.

4. Conclusion

Rapid size classification of mixed silica particles was examined in various solution chemistries by column bed packed with fibrous collector medium. Smaller silica particle whose median diameter was 100nm selectively attached to the collector surface during passing through the FS-packed column. On the other hand, larger silica particle having a median diameter of 300nm remained in an effluent suspension. Newton's efficiency depended on pH and ionic strength; optimal classification was attained at pH3.5 in 10mM KNO_3. These results were qualitatively explained by DLVO-type interaction energy curve, indicating that interfacial interaction of both particle and collector medium determined the Newton's efficiency. Particle concentration and superficial velocity also had an influence on Newton's efficiency. This method proved to be simple, rapid and cost-effective for classifying ultrafine particles in aqueous media.

Nomenclature

A	: Hamaker constant	[J]
A_c	: porosity dependent parameter of Happel's model	[−]
a	: particle radius	[m]
a_c	: radius of a cylindrical collector	[m]
C_0	: particle concentration of influent	[mg/L]
C_t	: particle concentration of effluent	[mg/L]
c	: ionic concentration	[mol/m^3]
D	: diffusion coefficient of particle	[m^2/s]
e	: elementary electric charge	[C]
h	: the closest approach distance between particle and collector	[m]
k_B	: Boltzmann constant	[J/K]
R	: single collector efficiency	[−]
T	: absolute temperature	[K]
U	: velocity of approaching particle	[m/s]
V_A	: London-van der Waals potential	[J]
V_e	: electrical double layer interaction energy	[J]
V_T	: total interaction energy	[J]
z	: valency of ion	[−]
e	: permittivity of the medium	[F/m]
η	: Newton's efficiency	[−]
κ	: Debye reciprocal length	[m^{-1}]
μ	: viscosity of fluid	[Pa·s]
Ψ_1	: electric potential of particle	[V]
Ψ_2	: electric potential of collector	[V]

References

1) Sasaki, H., E. D. Grace and T. Sugimoto: "Separation and Classification of Fine Hematite Particles Using a Glass Bead Column Bed", Powder Technol., 78, 137-142 (1994)
2) Ogawa, Y., K. Wakabayashi, H. Hayashi and H. Sasaki: "Size Classification of Ultrafine Hematite Using Fibrous Slag", Proc. Annual Meeting of MMIJ, pp. 45-46 (2000)
3) Stöber, W., A. Fink, E. Bohn: "Controlled Growth of Mono-dispersed Silica Spheres in Micron Size Range", J. Colloid and Interface Sci., 26, 62-69 (1968)
4) Miwa, S.: "Huntai Kougaku Tsuron", Nikkan Kogyo, pp. 185-189 (1987)
5) Usi, S.: "Progress in Surface and Membrane Science", 5, Academic Press (New York), pp. 223-263 (1972)
6) Hogg, R. I., T. W. Healy and D. W. Fuerstenau: "Mutual Coagulation of Colloidal Dispersions", Trans. Faraday Soc., 162, 1638-1651 (1966)
7) Hunter, R. J.: "Foundation of Colloid Science", 1, Oxford Press (Oxford), pp. 180-184 (1985)
8) Visser, J.: "A Comparison between Hamaker Constants and Lifshitz-Van Der Waals Constants", Adv. Colloid and Interface Sci., 3, 331-361 (1972)
9) Spielman, L. A. and S. K. Freidlander: "Role of the Electrical Double Layer in Particle Deposition by Convective Diffusion", J. Colloid and Interface Sci., 46, 22-31 (1974)

Author's short biography

Kazuya Wakabayashi

Kazuya Wakabayashi obtained his Batchelor Degree (1999) and Master Degree (2001) in Resources Engineering at Waseda University, Tokyo. He is now working at Ministry of Welfare, Health and Labor.

Sonoko Sekita

Sonoko Sekita obtained her Batchelor Degree (2000) and Master Degree (2002) in Resources Engineering at Waseda University, Tokyo. She is now working at Shiseido Co., Ltd., Japan.

Hiroshi Hayashi

Dr. Hiroshi Hayashi obtained his Bachelor Degree (1997) and Master Degree (1999) in Resources Engineering and his Doctor's Degree (2003) in Chemical Engineering at Waseda University, Tokyo. He received a research fellowship for young scientists from the Japan Society for the Promotion of Science (JSPS) in 2002-2003. He is currently worked at Central Research Institute of Mitsubishi Materials Co., Ltd., Omiya. His interests involve: ultrafine particle separation, electrokinetic property of bacterial cell surface, analysis of biofilm formation phenomenon, cell immobilization, and water treatment engineering.

Hiroshi Sasaki

Professor of Waseda University, Dr. of Engineering.
Faculty of Science and Engineering, Graduate School of Resources and Environmental Engineering. Former Professor of Tohoku University, Institute for Advanced Materials Processing and Vice President of MMIJ (Institute of Mining and Material Processing of Japan).

A Fast Algorithm for the Discrete Element Method by Contact Force Prediction[†]

C. Tokoro[1]
Department of Resources and Environmental Engineering, Waseda University[*]
K. Okaya and J. Sadaki
Department of Geosystem Engineering, Graduate School of Engineering, The University of Tokyo

Abstract

The discrete element method (DEM) takes enormous calculation time because it requires a very small time step, one small enough to represent the large frequency in the contact dynamic model. In general, the equations of motion of particles are solved using the second-order Adams-Bashforth method, which estimates the values of contact force in the following calculation time by linear extrapolation, or by multi-step methods such as the predictor-corrector method. Inspired by these two conventional methods, we propose a Contact Force Prediction Method that makes a larger time step possible. Our method uses the predicted values of contact force at every contact point, which are exact solutions or numerical solutions of differential equations that represent two particle contacts. It has been confirmed experimentally that the proposed method gives reasonable results of packing and discharge simulations, and accelerates DEM calculation 3−8 times.

Keywords: Discrete Element Method, Calculation Time, Time Step, Numerical Integration, Fast Algorithm

1. Introduction

Discrete Element Method (DEM) simulations on a number of granular systems have reported positive results since this method can estimate many effects at particle level[1)]. However, it requires enormous computation time because it needs a sufficiently small time step to follow high fluctuations in the contact dynamic model between particles. To overcome the deficit of conventional DEM, speeding up DEM is proposed in this study. There are several approaches to speeding up DEM, such as promoting efficiency in the algorithm to detect contact between particles, increase in the time step and limitation of the number of particles to calculate. In this study, we report a method to increase the time step.

In DEM calculation, the time step must be set smaller than the particle size and the density becomes smaller or the spring constant becomes larger, in order to obtain a stable numerical solution. Several methods to increase the time step have been reported, such as methods to set the spring constant smaller[2)-4)] and the particle size larger[5)] than the real value. This method is an effective method of increasing the time step, but it must be used after careful examination of the influence on the phenomenon to which DEM calculation is applied, because delays in contact detection cannot be avoided.

The purpose of this study is to develop an original DEM in which a large time step is possible by improving the algorithm needed to obtain the numerical solution to the contact dynamic equation between particles. We propose a Contact Force Prediction Method in which predicted values of contact force at every contact point are calculated by a more stable method than the conventional DEM and used to solve particle velocity and location. The packing (**Fig. 1**) and discharge (**Fig. 2**) system is chosen here as an example

---

[*] 3-4-1, Okubo, Shinjuku-ku, Tokyo, 169-8555, Japan
[1] Corresponding author
TEL: +81-3-5286-3327 FAX: +81-3-5286-3491
E-mail: tokoro@aoni.waseda.jp

[†] This report was originally printed in J. Soc. Powder Technology, Japan, **40**, 236-245 (2003) in Japanese, before being translated into English by KONA Editorial Committee with the permission of the editorial committee of the Soc. Powder Technology, Japan.

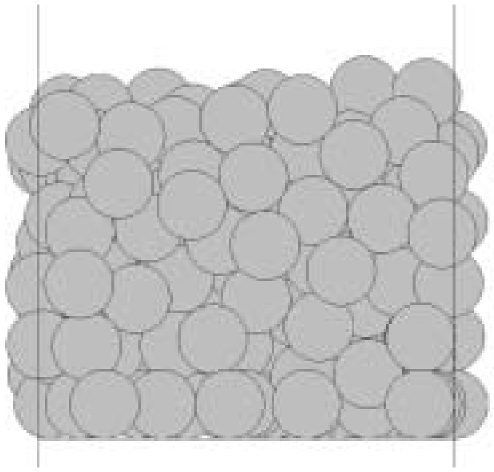

Fig. 1 An example of packing simulation

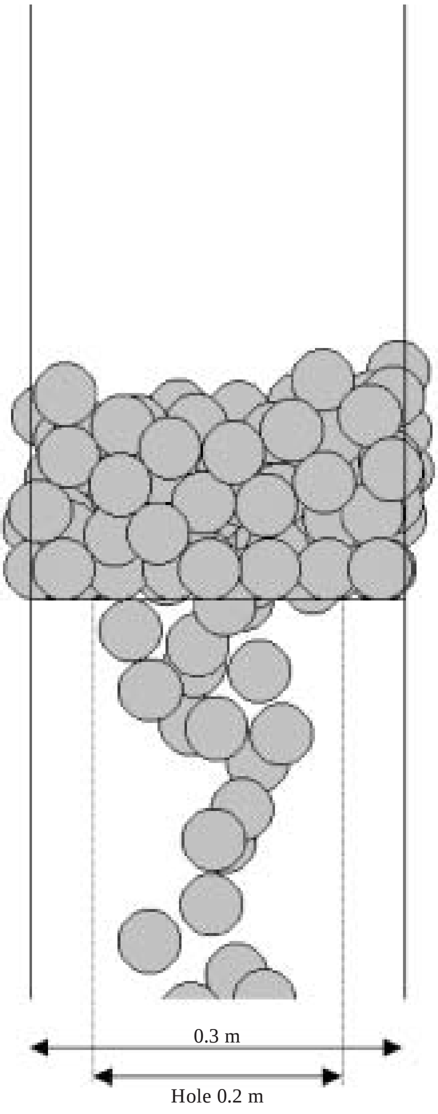

Fig. 2 An example of discharge simulation

of a phenomenon in which contact between many particles is important, and it is shown that the proposed method is effective for calculating the packing ratio or the discharge rate.

2. Delays in contact search and stability of calculation

When the time step is increased, DEM calculation may become incapable of reproducing a real phenomenon for the following reasons: one is delays in the contact detection and another is the error of the differential method. In the following, the effects of these factors with the conventional method are examined.

2.1 Outline of DEM

Contact force $\mathbf{f}_{cij}$ in DEM is calculated by projecting on the normal direction ($\mathbf{f}_{nij}$) and the tangential direction ($\mathbf{f}_{sij}$) as shown below:

$$\mathbf{f}_{cij}(t)=\mathbf{f}_{nij}(t)+\mathbf{f}_{sij}(t), \tag{1}$$

where (t) means a function of time t. The normal direction force is calculated from the following equations:

$$\mathbf{f}_{nij}(t)=-k_{nij}\delta_{nij}^{\alpha_1}(t)\mathbf{n}_{ij}(t)-\eta_{nij}\delta_{nij}^{\alpha_2}(t)\mathbf{v}_{nij}(t) \tag{2}$$

$$\delta_{nij}(t)=(r_i+r_j)-\left|\mathbf{x}_i(t)-\mathbf{x}_j(t)\right| \tag{3}$$

$$\mathbf{v}_{ij}(t)=\mathbf{v}_i(t)-\mathbf{v}_j(t) \tag{4}$$

$$\mathbf{v}_{nij}(t)=\left(\mathbf{v}_{ij}(t)\cdot\mathbf{n}_{ij}(t)\right)\mathbf{n}_{ij}(t), \tag{5}$$

where k is the spring constant, η is the damping constant, r is the radius of the particle, δ is the overlap between particles, $\mathbf{n}$ is the normal unit vector, $\mathbf{v}$ is the velocity vector, and $\mathbf{x}$ is the location vector. Subscript i denotes the physical values of particle i; j denotes particle j; ij denotes between particles i and j, n denotes the normal direction value, and r denotes the relative value. α_1 and α_2 are constants that depend on the type of contact dynamic model: $\alpha_1=1$ and $\alpha_2=0$ for the linear spring model and $\alpha_1=1.5$ and $\alpha_2=0.25$ for the Hertz model[6)].

The tangential direction force is calculated from the following equations:

$$\mathbf{f}_{sij}(t)=-k_{sij}\delta_{nij}^{\alpha_3}(t)\delta_{sij}(t)\mathbf{s}_{ij}(t)-\eta_{sij}\delta_{nij}^{\alpha_4}(t)\mathbf{v}_{sij}(t) \tag{6}$$

$$\delta_{sij}(t)=\left|\int\mathbf{v}_{sij}(t)dt\right| \tag{7}$$

$$\mathbf{s}_{ij}(t)=\frac{\mathbf{v}_{sij}(t)}{\left|\mathbf{v}_{sij}(t)\right|} \tag{8}$$

$$\mathbf{v}_{sij}(t)=\mathbf{v}_{ij}(t)-\mathbf{v}_{nij}(t)+\left(r_i\boldsymbol{\omega}_i(t)+r_j\boldsymbol{\omega}_j(t)\right)\times\mathbf{n}_{ij}(t), \tag{9}$$

where **s** is the tangential unit vector and **ω** is the angular vector velocity. α_3 and α_4 are constants that depend on the type of the contact dynamic model: $\alpha_3 = \alpha_4 = 0$ for the linear spring model and $\alpha_3 = 0.5$ and $\alpha_4 = 0.25$ for the Mindlin model[7), 8)]. The total tangential force is limited by the Coulomb frictional limit.

$$\mathbf{f}_{sij}(t) \leq \mu_{ij} \left| \mathbf{f}_{nij}(t) \right| \mathbf{s}_{ij}(t), \qquad (10)$$

where μ is the friction constant.

In the linear spring model, it is difficult to theoretically decide the spring constant value except when the particle shape is a disk, but it is usually used because of its convenience in the calculation[9)].

2.2 An error from delays in contact detection

Contact detection between particles may produce a maximum delay that equals the time step. This delay can be ignored when the time step is small, but the following two problems occur when the time step is large.

One is the large contact force between particles due to the large strain, which is not practical, because two particles that are in contact with each other continue to come close during a delay in contact detection without receiving contact force from each other. A method whereby the calculation time is returned to the starting point when two particles make contact with each other and where particle locations are recalculated, which overcomes this problem, has already been reported[5), 10)]. In this study, this problem is solved using the contact force prediction method described below.

Another problem is that several particles make contact with the same particle at same time. Two contacts with a small time lag may be misjudged as occurring at almost the same time because of the large time step. This phenomenon changes the behavior of particles after they make contact because the consumption of the collision energy is different.

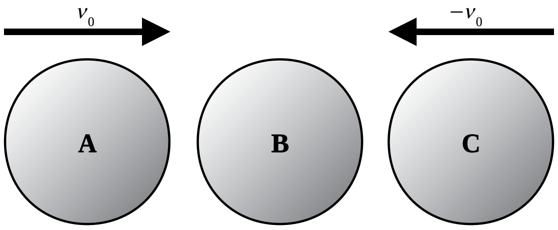

Fig. 3 3-particle contact problem

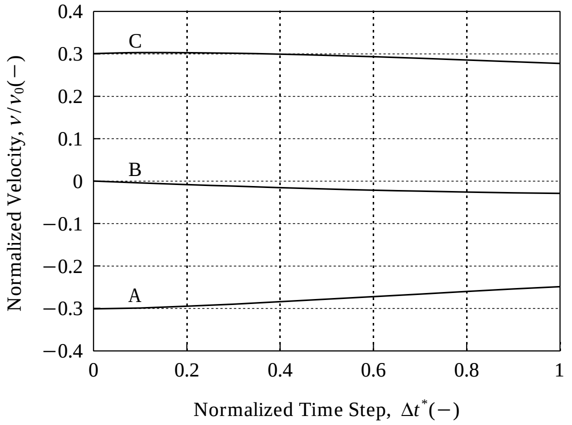

Fig. 4 Normalized velocity of the 3-particle problem

Table 1 Parameter settings for DEM simulation of ice pellets

Properties	Unit	Value
Density	[kg/m^3]	800
Linear Spring Constant	[N/m]	2.3×10^6
Young's Modulus	[N/m^2]	5.0×10^9
Poisson's Ratio	[−]	0.32
γ	[−]	1.0
Friction Coefficient	[−]	0.3

As an example, we consider a difference between a real phenomenon and calculation result using the three particles below. As shown in **Fig. 3**, there are three particles, A, B and C, without rotation in a one-dimensional line, and the particles of both ends, A and C, collide at the same velocity with the central particle, B, whose initial velocity is zero. **Fig. 4** shows the calculated velocity of each particle after contact when the beginning of the contact between particle C and B is after $\Delta\tau^*$ from the beginning of contact between particle A and B. Although natural gas hydrate pellets[11), 12)] have been chosen in this simulation, parameter values used in the simulation can be substituted for the physical properties of ice pellets[13)], as shown in **Table 1**. The particle diameter is 10 mm, and a linear model is used. The contact time between particles in this simulation is 3.7×10^{-5} seconds, and the time step is set up in 1/100 of the contact time, in which the calculation error becomes sufficiently small. $\Delta\tau^*$ in **Fig. 4** is the normalized value of $\Delta\tau$, the difference between the beginning of the contact between particles A and B and the beginning of the contact between particles C and B, divided by t_c, the contact time between two particles:

$$\Delta\tau^* = \frac{\Delta\tau}{t_c}. \tag{11}$$

The velocity is also normalized by the velocity of particle A and C before they make contact. **Fig. 5** is the simulation result of the normalized velocity error of particle A calculated from **Fig. 4**, when the contact detection between particle A and B is shifted by the time step in the system in which the contact between A and B and the contact between C and B take place at the same time. It can be concluded that DEM with a large time step is the method that allows the error shown in **Fig. 5** compared with DEM with a small time step so that the effect of the contact between the other particles can be ignored. Therefore, the appropriate numerical solution for DEM with a large time step is not a highly precise method, but its calculation is sufficiently fast and stable for a large time step.

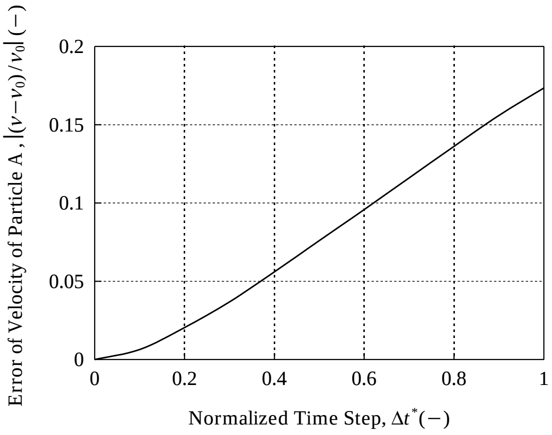

Fig. 5 Error of velocity of particle A

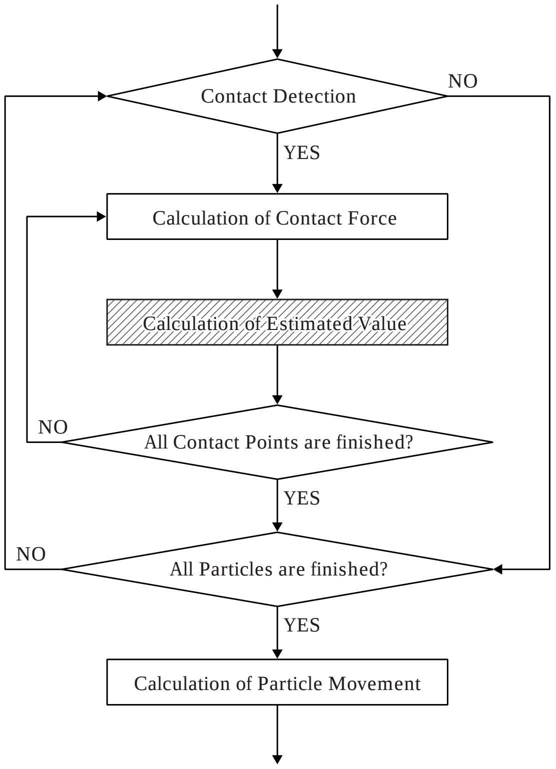

Fig. 6 Algorithm of calculation of contact force and movement in the conventional method and the new method

2.3 Stability of calculation

Fig. 6, except its shadowed area, is the general calculation procedure for DEM. The explicit method is used in DEM and particle i's velocity $\mathbf{v}_i(t+\Delta t)$, angular velocity $\boldsymbol{\omega}_i(t+\Delta t)$, location $\mathbf{x}_i(t+\Delta t)$ and angular location $\boldsymbol{\theta}_i(t+\Delta t)$ after time step Δt are calculated using contact force $\mathbf{f}_i(t)$ and torque $\mathbf{T}_i(t)$. In the following, several solutions with the conventional DEM are compared using the linear spring model in the system in which a particle without rotation makes contact with a wall in one dimension.

Although several numerical methods of solving the differential equation that represents the contact between two particles can be considered for the conventional DEM, the easiest with first-order accuracy is the explicit Euler method[14)]. On the other hand, the second-order Adams-Bashforth[15)], Leapfrog[16)] and predictor-corrector methods[10)] are used with the conventional DEM. Although the predicted value of the contact force in the second-order Adams-Bashforth method is calculated by linear extrapolation, there is the problem of second-order accuracy not being strictly guaranteed unless appropriate processing is performed at the discontinuous points, such as the beginning and end points of the contact. Neither is second-order accuracy guaranteed with the Leapfrog method, unless the value of the velocity during the contact is recalculated using an appropriate method, because the particle velocity is defined by only the middle point of a time step. Moreover, although the correction process is usually repeated until an error decreases enough in the predictor-corrector method, it is common to limit the correction process to 1 or 2 times to shorten the computational time in conventional DEM. It is necessary to store all contact states until the calculation of predicted values for the velocity and location are finished because predicted values are calculated after all contact forces are calculated with this method. This processing increases computational time.

Table 2 compares the 4 above-mentioned methods. One-dimensional collision of one particle is assumed, and subscript i and n are omitted. In addition, subscript κ is defined with $\kappa = t/\Delta t$ and Δt; time step, is simplified with h. The contact force is calculated assuming a linear spring model as follows:

$$f_\kappa = -k\delta_\kappa - \eta v_\kappa. \tag{12}$$

The analysis contents are explained as follows. In the case of the explicit Euler method, the explicit Euler method is expressed in the matrix description as follows:

$$\begin{bmatrix} v_{\kappa+1} \\ \delta_{\kappa+1} \end{bmatrix} = \mathbf{A} \begin{bmatrix} v_\kappa \\ \delta_\kappa \end{bmatrix} \tag{13}$$

$$\mathbf{A} = \begin{bmatrix} 1-h\dfrac{\eta}{m} & -h\dfrac{k}{m} \\ h & 1 \end{bmatrix}. \tag{14}$$

The determinant of $\mathbf{A}$ is as follows:

$$|\mathbf{A}| = 1 - \frac{\eta}{m}h + \frac{k}{m}h^2, \tag{15}$$

where m is the mass of the particle. From Equation (15), it is found that the eigenvalue of matrix A may be larger than 1. This shows the possibility of deviating from a stability domain of a calculation with the explicit Euler method. The calculation stability in **Table 2** is calculated in the same way as when $\eta = 0$. Δt^* in **Table 2** is defined as follows:

$$\Delta t^* = \frac{\Delta t}{t_c}, \tag{16}$$

where t_c is the contact time when $\eta = 0$.

$$t_c = \pi\sqrt{\frac{m}{k}} \tag{17}$$

The conservation of energy in the explicit Euler method is examined when $\eta = 0$ as follows:

Table 2 Comparison of 4 conventional methods ($\kappa = t/\Delta t$, $h = \Delta t$)

Method	Equations	Calculation Stability at $\eta=0$	Energy Conservation at $\eta=0$	Calculation Time
Explicit Euler	$\frac{v_{\kappa+1}-v_\kappa}{h} = \frac{f_\kappa}{m}$ $\frac{\delta_{\kappa+1}-\delta_\kappa}{h} = v_\kappa$	Unstable	$h^2\frac{k}{m}(mv_\kappa^2 + k\delta_\kappa^2)$ No Good	1
2-Order Adams-Bashforth	$\frac{v_{\kappa+1}-v_\kappa}{h} = \frac{1}{m}\left(\frac{3}{2}f_\kappa - \frac{1}{2}f_{\kappa-1}\right)$ $\frac{\delta_{\kappa+1}-\delta_\kappa}{h} = \frac{3}{2}v_\kappa - \frac{1}{2}v_{\kappa-1}$	Unstable	$hk(v_\kappa x_{\kappa-1} - v_{\kappa-1}x_\kappa) + h^2\frac{k}{m}(mv_{\kappa\cdot\kappa-1}^2 + k\delta_{\kappa\cdot\kappa-1}^2)$ No Good	1.46^+
Leap Frog	$\frac{v_{\kappa+1/2}-v_{\kappa-1/2}}{h} = \frac{f_\kappa}{m}$ $\frac{\delta_{\kappa+1}-\delta_\kappa}{h} = v_{\kappa+1/2}$	$\Delta t^* \leq \frac{2}{\pi}$	$-\frac{h^2}{4}\frac{k}{m}x_{\kappa+1}^2 + \frac{h^2}{4}\frac{k}{m}x_\kappa^2$ Good	1.01^+
Predictor-Corrector	$\frac{\hat{v}_{\kappa+1}-v_\kappa}{h} = \frac{1}{m}\left(\frac{3}{2}f_\kappa - \frac{1}{2}f_{\kappa-1}\right)$ $\frac{\hat{\delta}_{\kappa+1}-\delta_\kappa}{h} = \frac{3}{2}v_\kappa - \frac{1}{2}v_{\kappa-1}$ $\frac{v_{\kappa+1}-v_\kappa}{h} = \frac{1}{2m}(\hat{f}_{\kappa+1} + f_\kappa)$ $\frac{\delta_{\kappa+1}-\delta_\kappa}{h} = \frac{1}{2}(\hat{v}_{\kappa+1} + v_\kappa)$	$\Delta t^* \leq \frac{2\sqrt{\sqrt{2}-1}}{\pi}$	$h^2\frac{k}{m}(mv_\kappa v_{\kappa\cdot\kappa-1} + k\delta_\kappa\delta_{\kappa\cdot\kappa-1})$ $+h^2\frac{k}{m}\Big\{(mv_\kappa^2 + k\delta_\kappa^2) + h\frac{k}{2}(v_\kappa\delta_{\kappa-1} - v_{\kappa-1}\delta_\kappa)$ $+4h^2\frac{k}{m}(mv_{\kappa\cdot\kappa-1}^2 + k\delta_{\kappa\cdot\kappa-1}^2)\Big\}$ No Good	2.08

$$mv_{\kappa+1}^2+k\delta_{\kappa+1}^2=\left(1+h^2\frac{k}{m}\right)(mv_\kappa^2+k\delta_\kappa^2)>mv_\kappa^2+k\delta_\kappa^2, \tag{18}$$

Equation (18) shows that energy is not strictly conserved, but there is a conservative quality for a conversion when the eigenvalue of matrix A is 1. More concretely, this means that the calculated energy value shows the minute fluctuations up and down around the true energy value and does not greatly decrease or increase. The energy conservation in **Table 2** is examined in the same way as when $\eta=0$. "Good" shows the case where the energy is not conserved but the eigenvalue is 1.

Numerical equations in terms of the energy conservation in **Table 2** show the error of energy conservation, which is defined as follows:

$$\Delta e=(mv_{\kappa+1}^2+k\delta_{\kappa+1}^2)-(mv_\kappa^2+k\delta_\kappa^2). \tag{19}$$

$v_{\kappa\cdot\kappa-1}$ and $\delta_{\kappa\cdot\kappa-1}$ are defined as follows:

$$\begin{aligned} v_{\kappa\cdot\kappa-1}&=\frac{3}{2}v_\kappa-\frac{1}{2}v_{\kappa-1} \\ \delta_{\kappa\cdot\kappa-1}&=\frac{3}{2}\delta_\kappa-\frac{1}{2}\delta_{\kappa-1} \end{aligned} . \tag{20}$$

The calculation time in **Table 2** shows the time needed to calculate a one-dimensional collision of a particle when the calculation time in the explicit Euler method is 1. Adscript + in the second-order Adams-Bashforth method shows the calculation time increases when appropriate processing is performed at discontinuous points, such as the beginning and end points of the contact to guarantee second-order accuracy. With the Leapfrog method, the following formulae for the beginning and end points are used to guarantee second-order accuracy:

$$\frac{v_{\kappa+1/2}-v_\kappa}{h/2}=\frac{f_\kappa}{m}; \tag{21}$$

$$\frac{v_\kappa-v_{\kappa-1/2}}{h/2}=\frac{f_\kappa}{m}. \tag{22}$$

However, Equation (22) cannot be used for the explicit method when $\eta\neq0$, so more appropriate processing such as the multi-step method is needed to guarantee second-order accuracy. Adscript + with the Leapfrog method shows the calculation time increases for the reasons given above. However, it is necessary to note that the contact detection holds most of the calculation time rather than the calculation of contact force in a state of crowded particles.

Although the Leapfrog method has the above-mentioned problem, **Table 2** shows that it is the superior of the three methods with second-order accuracy in calculation stability and energy conservation.

With the above-mentioned consideration, a one-dimensional collision of one particle with a wall is assumed. It is necessary for the time step to set up a smaller value in the case of collision of many particles, because the frequency of the contact dynamic model becomes larger when the number of contact points increases. In the following section, we propose a method whereby a stable numerical solution can be found for a large time step in a system of multiple particle collisions.

3. Contact force prediction method

3.1 Outline of contact force prediction method

A predicted value of the contact force at the stage where two particles collide is solved by this method.

$$\hat{\mathbf{f}}_i(t+\Delta t)=\sum_j\hat{\mathbf{f}}_{cij}(t+\Delta t)+\hat{\mathbf{f}}_{oi}(t+\Delta t), \tag{23}$$

where "ˆ" denotes a predicted value. We refer to this method in which a predicted value of the contact force is used in this way as the "contact force prediction method" in this study. **Fig. 6** shows the calculation procedure for this method. As compared to the conventional calculation procedure, the procedure for predicting the contact force at every contact point, the shadowed area in **Fig. 6**, is added. Thus, it is necessary for the calculation time needed to obtain the predicted value to be small.

The meaning of using a predicted value of a two-particle collision for a multi-particle collision is examined here from the viewpoint of numerical analysis. As an example of a multi-particle collision, we assumed a one-dimensional collision of many particles without rotation. The dynamic equations of particle *i* and *j* in a one-dimensional collision system are as follows:

$$m_i\frac{dv_i(t)}{dt}=f_{ij}(t)+\sum f_i(t) \tag{24}$$

$$m_j\frac{dv_j(t)}{dt}=-f_{ij}(t)+\sum f_j(t), \tag{25}$$

where the second term of the right-hand side in each equation is a summation of forces acting on particles *i* and *j* except for the contact force between particles *i* and *j*.

For example, achieving second-order accuracy for the velocity of particle *i* depends on the following equation:

$$v_i(t+\Delta t)=v_i(t)+\Delta t\frac{dv_i(t)}{dt}+\frac{(\Delta t)^2}{2}\frac{d^2v_i(t)}{dt^2}, \tag{26}$$

where the terms above third-order accuracy for Δt are omitted. Equation (24) is substituted for Equation (26) as follows:

$$v_i(t+\Delta t)=v_i(t)+\frac{\Delta t}{2m_i}\left(f_{ij}(t)+\hat{f}_{ij}(t+\Delta t)+\sum f_i(t)+\sum \hat{f}_i(t+\Delta t)\right), \tag{27}$$

where

$$\hat{f}_{ij}(t+\Delta t)=f_{ij}(t)+\Delta t\frac{df_{ij}(t)}{dt} \tag{28}$$

$$\hat{f}_i(t+\Delta t)=f_i(t)+\Delta t\frac{df_i(t)}{dt}. \tag{29}$$

On the other hand, the following equation relates to Equation (28).

$$\begin{aligned}\frac{df_{ij}(t)}{dt}&=k_{ij}\left(v_j(t)-v_i(t)\right)+\eta_{ij}\left(\frac{dv_j(t)}{dt}-\frac{dv_i(t)}{dt}\right)\\&=k_{ij}\left(v_j(t)-v_i(t)\right)+\eta_{ij}\left(\frac{-f_{ij}(t)+\sum f_j(t)}{m_j}-\frac{f_{ij}(t)+\sum f_i(t)}{m_i}\right).\end{aligned} \tag{30}$$

From Equation (28) and Equation (30), it is found that second-order accuracy is not achieved unless the influence of the other contact forces, $\sum f_i(t)$ and $\sum f_j(t)$, is considered in the predicted value. However, it is not necessary to achieve second-order accuracy with this method because DEM with a large time step permits an error of a certain order for the calculation of the contact force, as mentioned in Section 2. Equation (27) shows that first-order accuracy is achieved even if the influence of the other contact forces, $\sum f_i(t)$ and $\sum f_j(t)$, is ignored. In the following, a method whereby the influence of other contact forces is ignored for the predicted value is considered.

Although various methods can be used to obtain the predicted value, four methods whereby stable solutions can be achieved in a large time step are selected and shown in **Table 3**. The manner of consideration is similar to that used in **Table 2**, and the stability of calculation and energy conservation are examined when $\eta=0$. "Exactly Good" in terms of energy conservation means that the particle energy is conserved strictly according to the examination similar to Equation (18). The modified Runge-Kutta method with second-order accuracy is as follows:

$$\frac{v_{\kappa+1/2}-v_\kappa}{h/2}=\frac{f_\kappa}{m} \tag{31}$$

$$\frac{\delta_{\kappa+1/2}-\delta_\kappa}{h/2}=v_\kappa \tag{32}$$

$$\frac{v_{\kappa+1}-v_\kappa}{h}=\frac{f_{\kappa+1/2}}{m} \tag{33}$$

$$\frac{\delta_{\kappa+1}-\delta_\kappa}{h}=\frac{1}{2}(v_{\kappa+1}+v_\kappa). \tag{34}$$

This differs from the conventional Runge-Kutta method with second-order accuracy in that Equation

Table 3 Comparison of 4 methods of calculating the estimated value of force ($\kappa=t/\Delta t$, $h=\Delta t$)

Method	**Calculation Stability at $\eta=0$**	**Energy Conservation at $\eta=0$**	**Application to the Hertz and Mindlin Model**	**Calculation Time**
Implicit Trapezoidal	Stable	0 Exactly Good	NO	1.22
Modified 2-Order Runge-Kutta	$\Delta t^*\leq\frac{2}{\pi}$	$-\frac{h^2}{4}\frac{k}{m}v_{\kappa+1}^2+\frac{h^2}{4}\frac{k}{m}v_\kappa^2$ Good	OK	1.77
4-Order Runge-Kutta	$\Delta t^*\leq\frac{2\sqrt{2}}{\pi}$	$\frac{k}{m}\left(h+\frac{h^2}{2}+\frac{h^3}{6}+\frac{h^4}{24}\right)^2(mv_\kappa^2+k\delta_\kappa^2)$ No Good	OK	2.61
Exact Solution	Stable	0 Exactly Good	NO	1.22

(34) is the trapezoid method. Although the calculation when $\eta=0$ is unstable with the conventional Runge-Kutta method with second-order accuracy, it is interesting that this method is stable even with such little modification. "Exact Solution" in **Table 3** means a method whereby an exact solution to the differential equation of the contact dynamic model is used for the predicted value.

"Stable" in terms of the stability of calculation in **Table 3** means that a stable solution for the predicted value of the contact force can be achieved with a large time step. However, there is another limit for the time step in DEM calculation, as mentioned in Section 2.2. The time step has to be set to less than the contact time t_c, i.e., $\Delta t^* \leq 1$.

From **Table 3**, the implicit trapezoid method and the exact solution method are superior to the other two methods in terms of the large time step and energy conservation, but these methods cannot be applied to the non-linear spring model. The method that can be applied to the non-linear spring model and permits a large time step is the fourth-order Runge-Kutta method. The calculation time is smallest with the implicit trapezoid method and the exact solution method. However, the effect of the time step that can be set larger is bigger for the total speedup of DEM calculation than the calculation time of the predicted value is small. This is because the calculation time of the contact detection is larger than that of the calculation of the contact force, as mentioned above.

A predicted value is calculated by projecting on the normal direction and the tangential direction similar to the contact force. $\hat{\delta}_{nij}(t+\Delta t)$ and $\hat{\delta}_{sij}(t+\Delta t)$ define the predicted value of the particle location in the normal and tangential direction, respectively; $\hat{v}_{nij}(t+\Delta t)$ and $\hat{v}_{sij}(t+\Delta t)$ define the predicted particle velocity in the normal and tangential direction, respectively. These values can be obtained by either method, as mentioned above, and the predicted value of the contact force in the normal direction, $\hat{f}_{nij}(t+\Delta t)$, is obtained as follows:

$$\hat{f}^*_{nij}=k_{nij}\hat{\delta}^{\alpha_1}_{nij}(t+\Delta t)+\eta_{nij}\hat{\delta}^{\alpha_2}_{nij}\hat{v}_{nij}(t+\Delta t), \tag{35}$$

where α_1 and α_2 are similar to the constants in Equation (2). With the conventional DEM, tension in the normal direction is not permitted by the no-tension joint, so the predicted value of the contact force in the normal direction is also not permitted as follows:

$$\text{when}\quad \hat{f}^*_{nij}>0,\quad \hat{f}_{nij}(t+\Delta t)=\hat{f}^*_{nij}$$

$$\text{when}\quad \hat{f}^*_{nij}\leq 0,\quad \hat{f}_{nij}(t+\Delta t)=0. \tag{36}$$

The predicted value in the tangential direction, $\hat{f}_{sij}(t+\Delta t)$, is obtained as follows:

$$\begin{aligned}&\text{when}\quad \Delta t\leq\Delta\hat{t}_{cij},\\ &\hat{f}_{sij}(t+\Delta t)=k_{sij}\hat{\delta}^{\alpha_3}_{nij}(t+\Delta t)\hat{\delta}_{sij}(t+\Delta t)\\ &\qquad\qquad+\eta_{sij}\hat{\delta}^{\alpha_4}_{nij}(t+\Delta t)\hat{v}_{sij}(t+\Delta t)\end{aligned} \tag{37}$$

$$\begin{aligned}&\text{when}\quad \Delta t>\Delta\hat{t}_{cij},\\ &\hat{f}_{sij}(t+\Delta t)=k_{sij}\hat{\delta}^{\alpha_3}_{nij}(t+\Delta\hat{t}_{cij})\hat{\delta}_{sij}(t+\Delta\hat{t}_{cij})\\ &\qquad\qquad+\eta_{sij}\hat{\delta}^{\alpha_4}_{nij}(t+\Delta\hat{t}_{cij})\hat{v}_{sij}(t+\Delta\hat{t}_{cij}),\end{aligned} \tag{38}$$

where α_3 and α_4 are similar to the constants in Equation (6). $\Delta\hat{t}_{cij}$ is the time when the two-particle collision finishes, i.e., $\hat{f}^*_{nij}=0$, and is obtained by the following linear approximation equation, for example:

$$\Delta\hat{t}_{cij}=\frac{f_{nij}(t)}{f_{nij}(t)-\hat{f}^*_{nij}}\Delta t. \tag{39}$$

Moreover, the predicted value of the contact force in the tangential direction is limited by the Coulomb frictional limit:

$$\left|\hat{f}_{sij}(t+\Delta t)\right|\leq\mu_{ij}\left|\hat{f}_{nij}(t+\Delta t)\right|. \tag{40}$$

3.2 Application examples of the contact force prediction method

Some examples of DEM calculation using the above-mentioned original method are introduced here. In this study, the packing and discharge system are used as an example of multi-particle collision.

The properties of the particles have already been shown in **Table 1**. The particle size is 50 mm, the number of particles is 200, and the calculation space is a quadratic column whose bottom is 0.3 m×0.3 m. The contact time between two particles in this calculation is 2.0×10^{-4} seconds. The periodic boundary condition is used in all side walls in order to moderate the wall effect. The linear spring model is used for the contact force model, and the spring constant is determined from the contact time by the Hertz spring model.

In all calculations, the exact solution method is used to obtain the predicted value of the contact force with the contact force prediction method.

3.2.1 Packing simulation

The packing simulation results produced by the free fall of particles are shown here. Particles fall freely from a height of 1 m.

Fig. 7 shows the time change of the energy summation of all particles in the case of the contact force

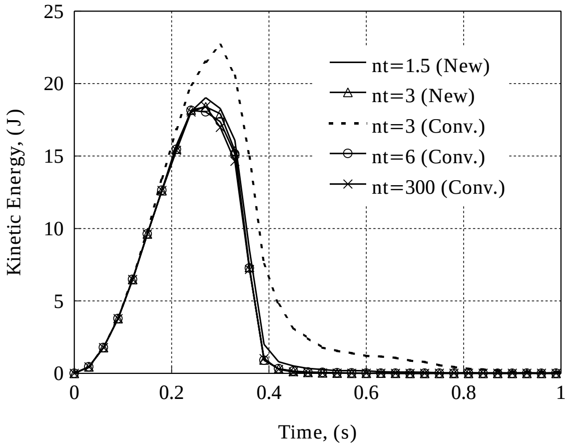

Fig. 7 Kinetic energy of total particles in packing simulation

prediction method or the conventional method, respectively. n_t is the number of partitions in the contact time as follows:

$$n_t=\frac{t_c}{\Delta t}, \tag{41}$$

where t_t is the contact time needed for one particle to contact a wall. Although the calculation is dispersed in $n_t<3$ with the conventional method, it is not dispersed in $n_t \leq 3$ with the proposed method.

Fig. 8 shows the comparison between the conventional method and the proposed method for the calculation results of the packing ratio. The calculated packing ratio becomes larger as the time step becomes larger. It is assumed that this is because the overlap at the beginning of contact between two particles is maintained. How fine the time step must be set with the proposed method depends on how much calculation error is permitted. In **Fig. 8**, although the packing ratio does not depend on the time step in $n_t>300$ with the conventional method, $n_t>30$ with the proposed method. In other words, the proposed method can set the time step 10 times larger than that of the conventional method. The calculation time of 1 step with the proposed method is 1.2 times larger than with the conventional method. Thus, the proposed method accelerates DEM calculation 8 times when the time step is set 10 times larger than conventionally.

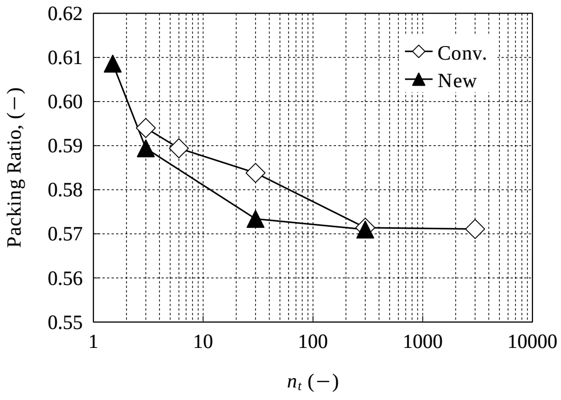

Fig. 8 Result of packing simulation

Incidentally, there have been various considerations regarding the random packing of mono-dispersed particles in the long term[17), 18)]. The random packing ratio should be between the closest packing ratio, 0.74, and the packing ratio in a simple cube lattice, theoretically 0.52. Moreover, experimental results of mono-dispersed spherical particles by Westman and White[17)] show that their packing ratio is between 0.553 and 0.63. Therefore, the packing ratio 0.57 obtained in this study is the appropriate value.

3.2.2 Discharge simulation

In order to simulate a system in which particle movement is more dynamic than in the packing system, a 0.2-m diameter circular outlet is opened at the bottom of the packed particles bed, and the particles are allowed to fall freely from the outlet to the floor, a distance of under 1 m.

Similar to **Fig. 7**, **Fig. 9** shows the time change of the energy summation of all particles. Although the calculation is dispersed in $n_t=3$ with the conventional method, it is not dispersed in $n_t \leq 3$ with the proposed method. **Fig. 10** shows a comparison between the conventional method and the proposed method for the calculation results of the number of discharged particles from the outlet. As for the discharge behavior, a big difference between the conventional method and the proposed method is not found, even with the large time step. It is believed that this is because the calculation error is canceled out due to the movement of all particles. In **Fig. 9**, the kinetic energy is not dispersed in $n_t=6$ with the conventional method and $n_t=1.5$ with the proposed method, so the proposed method can set the time step 4 times larger than that of the conventional method. When the calculation time of 1 step is considered, the proposed method accelerates DEM calculation 3 times.

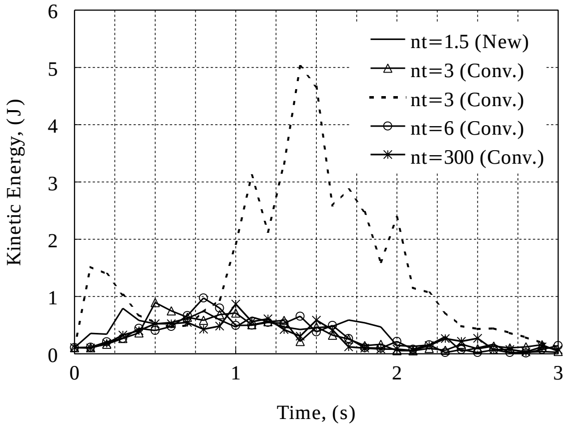

Fig. 9 Kinetic energy of total particles in discharge simulation

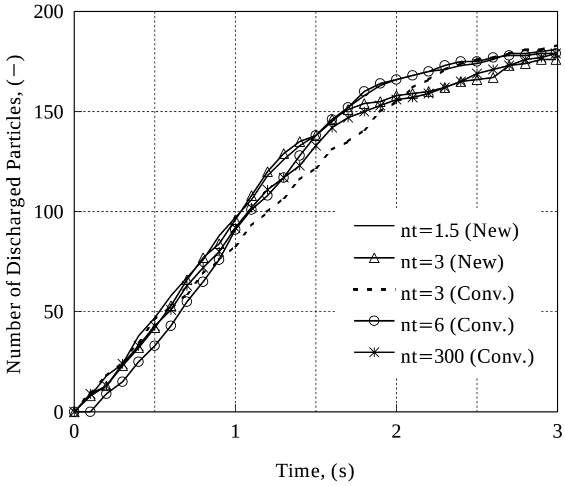

Fig. 10 Result of discharge simulation

4. Conclusion

DEM in which a large time step is possible is developed by improving the algorithm to solve the contact force between two particles. In general, the equations of motion of particles are solved by the second-order Adams-Bashforth method, which estimates the values of the contact force in the following calculation time by linear extrapolation, or by multi-step methods such as the predictor-corrector method. Inspired by these two conventional methods, we propose an original method called the contact force prediction method, which uses the predicted value of the contact force at each contact point of two particles. As for the method of obtaining the predicted value of the contact force with the proposed method, four methods in which a large time step can be set are examined, and their characteristics are shown. Moreover, the packing and discharge system is chosen as an example of the multi-particle collision, and the proposed method accelerates DEM calculation 3−8 times.

In this paper, some calculation results of mono-dispersed particles are introduced as an imminent example, but we have already confirmed that the contact force prediction method is useful for two sizes of particle at a number of approximately 10 million. Under the present parameters, it is expected that the number of particles calculated in DEM will be limited to 100 million, even if several techniques to accelerate DEM calculation, such as the method proposed here, are applied. Thus, an additional acceleration, such as parallel computation or combination with a continuous method, is needed for application to the general scale system. However, it is confirmed that the contact force prediction method proposed in this study is useful for DEM acceleration.

Nomenclature

$\mathbf{f}$	: Force Vector of Particle	(N)
$\hat{\mathbf{f}}$	: Estimated Value of $\mathbf{f}$	(N)
$\mathbf{f}_c$	: Contact Force Vector of Particle	(N)
$\hat{\mathbf{f}}_c$	: Estimated Value of $\mathbf{f}_c$	(N)
$\mathbf{f}_o$	: Force Vector of Particle except for Contact Force	(N)
$\hat{\mathbf{f}}_o$	: Estimated Value of $\mathbf{f}_o$	(N)
$\mathbf{g}$	: Acceleration of Gravity Vector	$(\mathrm{m}^2/\mathrm{s})$
h	: Time Step in **Table 2** and **3**	(s)
i	: Particle Index	(−)
I	: Moment of Inertia of Particle	$(\mathrm{kg}\cdot\mathrm{m}^2)$
j	: Particle Index	(−)
k	: Spring Coefficient	$(\mathrm{N/m}$ or $\mathrm{N/m}^{1.5})$
κ	: Time Index	(−)
m	: Mass of Particles	(kg)
$\mathbf{n}$	: Unit Vector from the Center of Particle to Contact Point	(−)
n_t	: Number of Steps in Contact Time	(−)
r	: Radius of Particle	(m)
$\mathbf{s}$	: Tangential Unit Vector	(−)
t	: Time	(s)
t_c	: Contact Time	(s)
$\mathbf{T}$	: Torque Vector of Particle	$(\mathrm{N}\cdot\mathrm{m})$
$\mathbf{v}$	: Velocity Vector of Particle	(m/s)
v	: Velocity of Particle	(m/s)

$\hat{v}$: Estimated Value of v (m/s)
$\mathbf{x}$: Position Vector of Particle (m)
δ : Displacement (m)
$\hat{\delta}$: Estimated Value of δ (m)
Δt : Time Step (s)
Δt^* : Normalized Time Step (−)
$\Delta \hat{t}_c$: Estimated Value of Contact Time (s)
$\Delta \tau$: Time Difference of Contact Start Points (s)
$\Delta \tau^*$: Normalized Time Difference of Contact Start Points (−)
γ : Constant Related to Restitution Coefficient (−)
η : Viscosity Coefficient (kg/s or kg/s/$m^{0.25}$)
$\boldsymbol{\theta}$: Angular Position Vector of Particle (rad)
μ : Friction Coefficient (−)
$\boldsymbol{\omega}$: Angular Velocity Vector of Particle (rad/s)

Subscripts
i : Particle i
ij : Between Particle i and j
j : Particle j
n : Normal Direction
s : Tangential Direction

References

1) Cundall, P. A.: "Rational Design of Tunnel Supports: A Computer Model for Rock Mass Behavior Using Interactive Graphics for the Input and Output of Geometrical Data," Technical Report MRD-2-74 Missouri River Division, US Army Corps of Engineers.
2) Kawaguchi, T., Tanaka, T. and Tsuji, Y.: "Numerical Simulation of Fluidized Bed Using the Distinct Element Method (the Case of Spouting Bed)," *Trans. Japan Soc. Mech. Eng.* (Series B), **58-551**, 2119-2125, (1992).
3) Asakura, K., Harada, S., Funayama, T. and Nakajima, I.: "Simulation of Descending Particles in Water by DEM," *Sigen to Sozai*, **112**, 219-224, (1996).
4) Watanabe, H.: "Critical Rotation Speed for Ball-Milling," *Powder Technol.*, **104**, 95-99, (1999).
5) Natsuyama, S. and Horio, M.: "Study of Dynamical Analysis for Scale Up of Fluidized-bed of Solid Dosage Forms by DEM Simulation," *Kagaku Souchi*, **9**, (2001).
6) Timoshenko, S. P. and Goodier, J. N.: "Theory of Elasticity, 3rd Edition," 380, McGraw-Hill Book Company, (1970).
7) Mindlin, R. D.: "Compliance of Elastic Bodies in Contact," *J. Appl. Mechanics*, **16**, 259-268, (1949).
8) Mindlin, R. D.: "Elastic Spheres in Contact Under Varying Oblique Forces," *J. Appl. Mechanics*, **20**, 327-344, (1953).
9) Taguchi, Y.: "Dynamics of Granular Matter from the Physical Point of View (I)," *J. Soc. Powder Technol., Japan*, **32**, 240-246, (1995).
10) Xu, B. H. and Yu, A. B.: "Numerical Simulation of the Gas-Solid Flow in a Fluidized Bed by Combining Discrete Particle Method with Computational Fluid Dynamics," *Chem. Eng. Sci.*, **52-16**, 2785-2809, (1997).
11) Okui, T.: "Expectation of Gas Hydrate Transport Technology," *J. Japanese Assoc. Petroleum Technol.*, 66, 168-174, (2001).
12) Nakajima, Y., Kawagoe, Y. and Takaoki, T.: "Transporting System of Natural Gas Hydrate in Pellet Form," *Proceedings of JSME Transportation and Logistics 2001*, Kawasaki, 315-316, (2001).
13) Maeno, N. and Fukuda, M.: "Seppyou no Kouzou to Bussei," 122, Kokon Shoin, (1986).
14) Hitotsumatsu, S.: "Suuchi Kaiseki," 103, Asakura Shoten, (1982).
15) The Society of Powder Technology, Japan: "Funtai Simulation Nyumon," p.29, Sangyo Tosho, (1998).
16) Moakher, M., Shinbrot, T. and Muzzio, J.: "Experimentally Validated Computations of Flow, Mixing and Segregation of Non-Cohesive Grains in 3D Tumbling Benders," *Powder Technol.*, **109**, 58-71, (2000).
17) Cumberland, D. J. and Crawford, R. J.: "The Packing of Particles," p.14-39, Elsevier, (1987).
18) Mogami, T. (ed.): "Doshitu Rikigaku," p.893-933, Gihodo Shuppan, (1969).

Author's short biography

Chiharu Tokoro

Chiharu Tokoro is Research Associate at the Faculty of Science and Engineering of Waseda University. She received her B.E. from the Dept. of Science and Engineering in 1998 at Waseda University, and her M.E. from the Dept. of Geosystem Engineering in 2000 at the University of Tokyo. She received her Doctor of Engineering in 2003 from the University of Tokyo. Her research interests are resources processing and environmental technology.

Katsunori Okaya

Katsunori Okaya is Research Associate at the Department of Geosystem Engineering, Graduate School of Engineering, the University of Tokyo. He obtained his B.Sc. and M.Sc. degrees from the University of Tokyo in 1974 and 1976, respectively.

Okaya's current research interests are in the handling of particles and grains (grinding, classification, random packing, segregation, dispersion, etc.) and simulations using DEM (Discrete Element Method).

Jun Sadaki

Jun Sadaki received a master degree in geosystem engineering in 1987 and a Doctor of Engineering degree in geosystem engineering in 1990, both from the Department of Geosystem Engineering, Graduate School of Engineering, the University of Tokyo. The theme of his thesis was 'A Study of Control in Mineral Processing Plants.' He joined Nippon Steel Corporation (NSC) in 1990 and worked as a researcher and a senior researcher until 2000. His research subjects in NSC were modeling, simulation and the control of industrial plants, especially of steel making plants and energy plants. He moved to the Department of Geosystem Engineering, Graduate School of Engineering, the University of Tokyo, as a lecturer in 2000. His research interests include natural gas hydrate (NGH), transportation and/or storage of NGH, application of NGH to industrial processes as well as the modeling, simulation, control and optimization of processes. Ms. Chiharu Tokoro was his doctor course student from 2000–2003, and now is a co-worker. He is a member of the Mining and Materials Processing Institute of Japan, the Society of Instrument and Control Engineers, a member of the board of Japan Federation of Ocean Engineering Societies.

Fundamental Study on Particle Transportation by Pressure Waves in Pipes[†]

— The Characteristics of Particle Transportation —

M. Horie
Department of Mechanical Engineering,
*Faculty of Engineering, Setsunan University**
H. Kado[1] and H. Ide
Department of Mechanical Engineering,
*Faculty of Engineering, Kagoshima University***

Abstract

This study investigates the development of new technology for particle transportation in pipes with cyclic pressure waves. The flow is not steady because progressive and reflective pressure waves do exist in pipes and as a result, the flow in pipes is a pulsating one. The particles are continuously supplied into a horizontal pipe and are transported by the cyclic pressure waves. In this experiment, the loading ratio corresponds to a general high-pressure force feed system, and as a result the main flow pattern is plug flow. The properties of the plug are clarified by measuring the characteristic length and velocity of the plug, and the mean number of pressure waves between successive plug passages. Then, the properties of particle transportation are explained using the calculated apparent loading ratio.

Key words: Pneumatic Transport, Compressible Flow, Unsteady Flow, Multi-phase Flow, Pressure Wave, Plug Flow

Introduction

In recent years, pneumatic transportation methods using the force of pressure, such as plug transportation, which is called a high-pressure transportation system, are often used. However, choking is caused by a variety of transportation conditions, i.e., particle shape and material, piping arrangement, etc. in the pipeline. Therefore, methods of preventing choking[1-4] and the breaking-up of particles accumulated in pipes[5-7], have been studied for better transportation efficiency. It is essential to obtain the best transportation conditions, because the behavior of particles is remarkably different depending on the condition of the particles. In general, the pipe flow is steady in pneumatic transport of particles[8]. The particles are supplied to the pipe periodically to make the particles form plugs.

The unsteady flow in pipes has been researched with focus on oscillating flow[9, 10] and pulsating flow[11-13], where oscillating flow is superimposed on a mean flow. In pneumatic transportation, experimental research on the behavior with pulsating flow[14] was clarified, but it seems that there has been no research on pulsating flow or oscillation flow using pressure waves.

This investigation is basic, new research on solid particle transportation using pressure waves. It is assumed that this method is suitable for plug transportation and is effective against the choking problem. In the previous report[15], the unsteady drag coefficient of single spherical particles slipping or tumbling on the pipe wall was estimated by the correlation of experimental particle behavior and the loci calculated from the equation of motion. However, in practical pneumatic transportation, the theoretical elucidation of the behavior of the particles is very dif-

---

* 17-8 Ikeda Nakamachi, Neyagawa, Osaka 572-8508, Japan
** 1-21-40, Koorimoto, Kagoshima 890-0065, Japan
[1] Corresponding author
TEL: 81-99-285-8271 FAX: 81-99-285-8271
E-mail: kado@mech.kagoshima-u.ac.jp

[†] This report was originally printed in Japanese J. Multiphase Flow, **17**, 276-284 (2003) in Japanese, before being translated into English by KONA Editorial Committee with the permission of the editorial committee of the Society of Multiphase Flow.

ficult because of friction, collision, rebound, and pressure loss. Therefore, in this report, the behavior of a lump of particles (plug) was experimentally investigated.

In this investigation, a cyclic pressure wave was generated in the horizontal pipe, and the downstream end of the pipe was allowed to remain open. Therefore, the flow in the pipe was unsteady where progressive, reflective waves existed simultaneously. The feeder continuously supplied the particles into a pipe, and the behavior of the lump of particles was analyzed. As a result, it appears that the loading ratio ranged from the low-pressure transportation system to the high-pressure one in this experiment, and the state of flow differed according to the air and particle mass flow rate. Moreover, by measuring plug behavior in pipes, the characteristics of plug transportation were clarified by the experimental and the apparent loading ratios.

Experimental equipment and method

Fig. 1 shows an outline of the experimental equipment. A cyclic pressure wave generated by the pulsating pressure generator ① was discharged into a horizontal pipe ④, and particles were supplied into a pipe by a feeder ⑤. The pressure at the referential position was measured by a pressure probe ②, and the velocity at any cross-section of a pipe was measured by using I-probe hot wire anemometry ③. Since the downstream side of a pipe was open, progressive, reflective waves existed in pipes.

Fig. 2 shows the detailed structure of the pulsating pressure generator. The compressed air supplied from the compressor ⑥ was adjusted with the regulator ⑦. Thereafter, an electromagnetic valve ⑧-A was opened, and the compressed air was stored in a tank ⑨ with a capacity of 400 cm^3. An electromagnetic valve ⑧-B was opened just after the valve ⑧-A was shut, then the compressed air was discharged into a pipe. This operation was periodically repeated by a sequencer at 0.7s intervals. The pressure in the tank was measured with a Bourdon tube.

The particle feeder is shown in **Fig. 3**. The feeder was mounted at right angles to a pipe axis on a horizontal plane. The particles were put in a bucket ⑫ with a capacity of approximately 3,900 cm^3, and pushed into the pipe by the screw ⑪. The screw whose pitch is 28 mm was connected with a shaft of a DC motor, and its rotational speed was set within the range of 50-300 rpm. By using a bearing ⑬ and a spring ⑭, the particles were smoothly supplied into a pipe. The properties of the feeder are described in the following chapter.

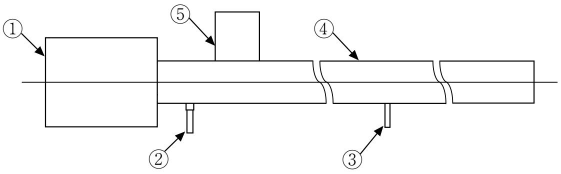

Fig. 1 Outline of experimental equipment

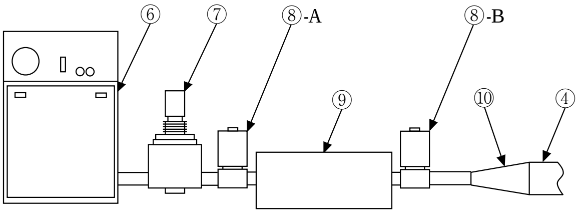

Fig. 2 Details of pulsating pressure generator

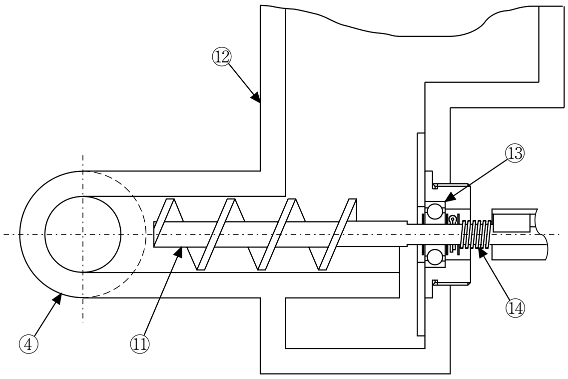

Fig. 3 Details of particle feeder

Fig. 4 shows the details of the pipe. Inside diame-

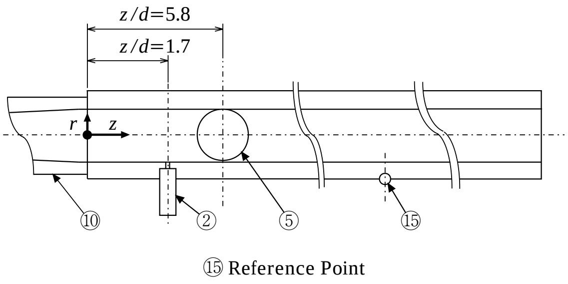

Fig. 4 Details of test pipe

ter d of this pipe, which was made of transparent acrylic, was 30 mm. The origin was set at the pipe entrance, and the direction of the pipe axis and radius were z and r, respectively. The pressure probe was set up at the referential position of $z/d=1.7$, and all pressure waves were measured at this position. The pressure probe was of the semiconductor type, and the space between the pressure measurement hole on the pipe wall and the sensor diaphragm of the pressure probe was filled with silicone oil to prevent the damping of pressure and phase delay. With the transportation experiment, the feeder was mounted at the position of $z/d=5.8$, and behavior of the particles in the pipe was taken by a video camera over the range of approximately 1500 mm downstream from the reference point ⑮ ($z/d=29.3$). The length of the test pipe was 125 d. When measuring the pressure and velocity, only the pressure probe and I-probe hot wire anemometer were set on the pipe whose length was 140 d.

The flow in a pipe

In this investigation, the downstream edge of the pipe was open, thereby the flow in a pipe was composed of progressive and reflective waves. We first considered the flow field where there were only progressive waves. The flow in pipes was assumed to be compressible, and the solution of the velocity $v(z,t)$ and pressure $p(z,t)$ with only progressive waves was derived in the previous research$^{15)}$. The solutions are obtained from the following formulas:

$$v(z,t)=\sum_{n}\left[A_n\cos\left\{\frac{2\pi n}{T}\left(t-\frac{z}{a}\right)\right\}+B_n\sin\left\{\frac{2\pi n}{T}\left(t-\frac{z}{a}\right)\right\}\right] \tag{1}$$

$$p(z,t)=\rho a v(z,t) \tag{2}$$

where T is the period of the pressure wave, t is time, A_n and B_n are arbitrary constants, ρ is the density of air, and a is the propagation velocity of the pressure. When there are only progressive waves in a pipe, the phase of pressure and velocity becomes the same, and the pressure is equal to the product of the velocity, the density, and the propagation velocity.

Fig. 5 shows the pressure waves over one period at $z/d=1.7$ when there are only progressive waves. P is the pressure value, and the value of the first pressure peak is defined as P_1. t^* is non-dimensional time as

$$t^*=\frac{t}{T} \tag{3}$$

where the period of pressure wave T is 0.7 s. This time is sufficient for the response time of the electromagnetic valve and for accumulating the compressed air into a tank and discharging it. In measuring the pressure with the progressive waves, the pressure absorber was set on the downstream end of the pipe. In this case, the measured pressure has only a positive value, and the values of P_1 range between 3.5 kPa and 7.7 kPa.

Fig. 6 shows velocity v on pipe axis $r/R=0.0$ at

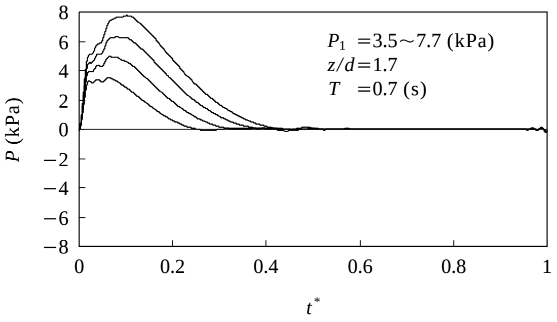

Fig. 5 Pressure waves without reflection

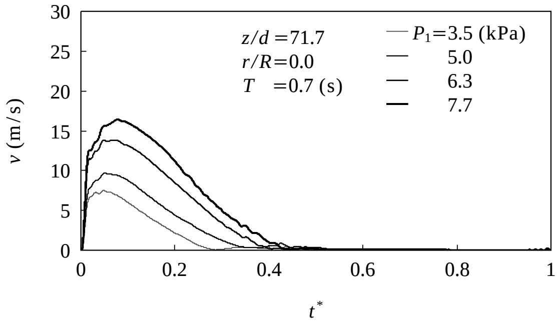

Fig. 6 Velocity on pipe axis without reflection

$z/d=71.7$, where R is the radius of the pipe. It can be seen from **Fig. 5** and **Fig. 6** that the shapes of the pressure waves and the velocity are almost the same.

Next, we considered the flow field where there were both progressive and reflective waves. The solution of the pressure and the velocity with progressive and reflective waves is given as follows.

$$v(z,t)=\sum_n\left[A_n\cos\left\{\frac{2\pi n}{T}\left(t-\frac{z}{a}\right)\right\}+B_n\sin\left\{\frac{2\pi n}{T}\left(t-\frac{z}{a}\right)\right\}\right]$$
$$+\sum_n\left[C_n\cos\left\{\frac{2\pi n}{T}\left(t+\frac{z}{a}\right)\right\}+D_n\sin\left\{\frac{2\pi n}{T}\left(t+\frac{z}{a}\right)\right\}\right] \tag{4}$$

$$P(z,t)=\rho a\sum_n\left[A_n\cos\left\{\frac{2\pi n}{T}\left(t-\frac{z}{a}\right)\right\}+B_n\sin\left\{\frac{2\pi n}{T}\left(t-\frac{z}{a}\right)\right\}\right]$$
$$-\rho a\sum_n\left[C_n\cos\left\{\frac{2\pi n}{T}\left(t+\frac{z}{a}\right)\right\}+D_n\sin\left\{\frac{2\pi n}{T}\left(t+\frac{z}{a}\right)\right\}\right] \tag{5}$$

The first terms on the right-hand side of Eq. (4) and (5) are progressive waves, and the second terms are reflective waves. Moreover, the phase of the reflective waves of the pressure and the velocity shifted by 180 deg.

Fig. 7 shows the pressure waves with the progressive and reflective waves. They were measured without the pressure absorber so that the downstream end of the pipe was opened. In this case, the supplied air pressure in the tank was equal to that in the previous experiment. As a result, the discharged pressure waves from the pulsating pressure generator were the same as in the case of **Fig. 5**. The progressive waves that reached the downstream end produced reflective waves with a value of the reverse sign, and the latter propagated upstream. Next, the reflective waves was reflected at the device on the upstream end and then proceeded downstream as a new progressive wave, and so on. Therefore, the progressive waves and the reflective waves overlapped in a complex manner in a pipe. As a result, the pressure waves oscillated between positive and negative values, in spite of having the same pressure conditions in **Fig. 5**. The first peak values P_1 ranged between 3.5 kPa and 5.8 kPa, and were smaller than this when there were only progressive waves. Vibration of the particles due to pressure fluctuation seems to be effective in the case of particle transportation, because the pressure fluctuation and pressure gradient are larger than when there are only progressive waves.

Fig. 8 shows the velocity with the progressive and reflective waves on a pipe axis at $z/d=71.7$. The reflective pressure wave with a negative value accompanies the reflective velocity wave with a positive value, and as a result, the peak value of the velocity is larger than that in **Fig. 6**, and there are no negative values.

As mentioned above, when progressive waves and reflective waves co-exist in a pipe, there is a better effect for particle transportation. When there are a lot of particles in a pipe, it is difficult to specify the pressure wave because of the mutual interference between the flow and the particles. Therefore, the pressure with no particles shown in **Fig. 7** is treated as proxy for the pressure with particles in a pipe.

Fig. 9 shows the velocity profile on a cross-section at $z/d=71.7$, when P_1 is 4.4 kPa. The maximum velocity in a pipe axis is expressed by $v_{\max}$. The velocity profile is nearly uniform over the test section except near the wall, and similar results were obtained in all instants. **Table 1** shows mean velocity v_{mean} and mass

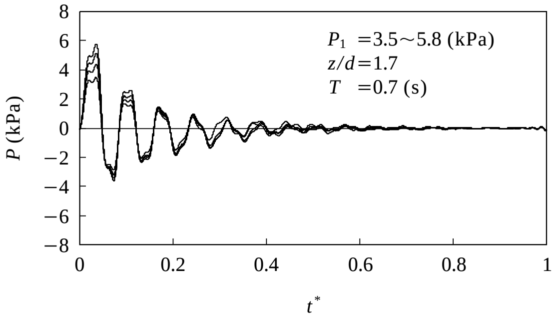

Fig. 7 Pulsating pressure waves with reflection

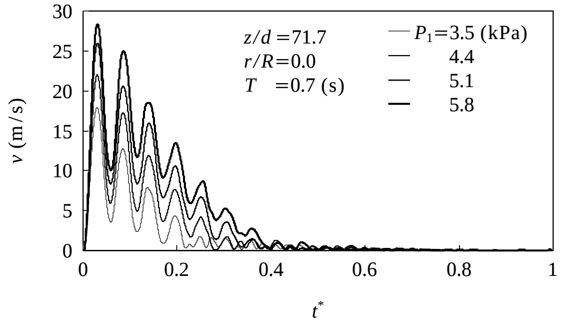

Fig. 8 Pulsating velocity on a pipe axis with reflection

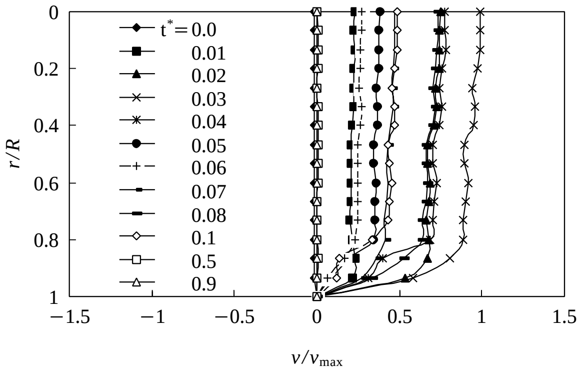

Fig. 9 Velocity profile over a cross-section (P_1=4.4 kPa, z/d=71.7)

Table 1 Mean velocity and mass flow rate of air

P_1 (kPa)	v_{mean} (m/s)	W_a (kg/s)
3.5	1.23	1.03×10^{-3}
4.4	1.80	1.50×10^{-3}
5.1	2.60	2.17×10^{-3}
5.8	3.14	2.65×10^{-3}

(20℃, 101.3 kPa)

flow rate W_a in a pipe, calculated by measuring the amount of air in the tank.

A general pulsating flow is composed of the oscillation and mean flows, and consequently so its velocity is not zero. In this investigation, there is a time average velocity and the flow looks like the pulsating flow because of the cyclic pressure waves. Since there is no steady flow, this flow has the feature of the velocity becoming zero over the latter half of the period.

Properties of the feeder

Two kinds of particle shown in **Table 2** were used in this investigation. The diameter and the density of the particles are designated d_s and ρ_s in this table, respectively, and 'PS' stands for polystyrene. Since the amount of mixing of the stone powder is different, the densities of these two kinds of particle differ. As the surface of the particles was round, the roughness of the particle surface was almost the same value.

Table 2 Condition of particles

Particle	d_s (m)	ρ_s (kg/m^3)
PS A	5.93×10^{-3}	1027
PS B	5.93×10^{-3}	2697

The feeder was mounted at right angles to the pipe axis on a horizontal plane. The performance of the feeder filled with particles was tested by changing the screw rotational speed N from 50 to 300 rpm, and supplying the particles into the pipe. The particles were transported downstream by the pressure waves generated by the pulsed pressure generator, and the volume flow rate of particle Q_s was measured at the end of the pipe. Measurements were made four times for the same conditions. The measurement time ranged from about 30 seconds to 2.5 minutes according to the screw rotation speed, and was sufficient compared with one time period (0.7 s) of the pressure wave. With flow pattern Type A described later, the error of Q_s was about 1% or less. When Q_s was less and the plug formation was irregular, or when Q_s was large and the flow pattern was just before choking, the error of Q_s was about 25% or less. When the plug was almost regularly formed, the error of Q_s was about 8% or less.

The properties of the feeder are shown in **Fig. 10**. It is clear that the feeder supplies the particles in proportion to the rotational speed of the screw. The particles stagnated at the outlet of the feeder in the pipe when the particle supply exceeded transportation ability by the pressure wave. For this reason, as P_1 becomes less or N becomes larger, Q_s shifts downward slightly from the line. In addition, when the particle supply increased drastically, i.e. when N is extremely large, choking occurred in the pipe near the outlet of the feeder.

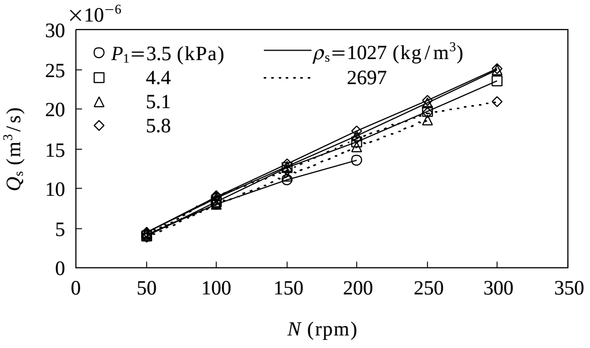

Fig. 10 Properties of the particle feeder

Properties of transportation

Loading ratio

Loading ratio χ_s is defined as follows:

$$\chi_s = \frac{W_s}{W_a} \tag{6}$$

where W_s is the mass flow rate of the particles measured at the pipe end, and W_a is the mass flow rate of air calculated according to **Table 1**. χ_s ranged from 2 to 23 in this investigation (**Fig. 11**). This value corresponds to the range of the low-pressure transportation system (χ_s=1~10) and the high-pressure transportation system (χ_s=10~40). χ_s decreases with increasing P_1, and increases with increasing ρ_s. Moreover, it is clear that when ρ_s is constant, optimum pressure P_1 exists according to the volume flow rate of particles Q_s to obtain the same loading ratio value. In this investigation, when ρ_s was 2697 (kg/m^3) and P_1 is 5.1 (kPa), χ_s obtained a maximum of approximately 23.

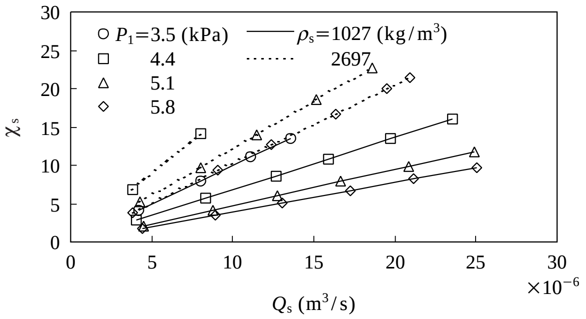

Fig. 11 Loading ratio

Flow pattern

The behavior of the particles was recorded using a video camera from the reference point (z/d=29.3) to the range of 1500 (mm) on the downstream side. The following flow pattern was observed in this investigation (**Fig. 12**)[8].

Type A: The particle is transported without stagnating in the pipe bottom.

Type B: Unstable state of transportation in which particles alternately repeat stagnation, accumulation, and movement.

Type C: The particles accumulate in the pipe bottom. In addition, the upper part of the accumulating particles is transported irregularly by the flow of air.

Type D: The accumulating particles that are close together in a cross-section over some length of the pipe are transported by the pressure force. This type of flow is called plug transportation.

Type E: The particles choke a pipe, and cease to move. Generally, this state is called choking.

These flow patterns are demonstrated in **Fig. 13** and **Fig. 14**. It is clear that the flow pattern differs

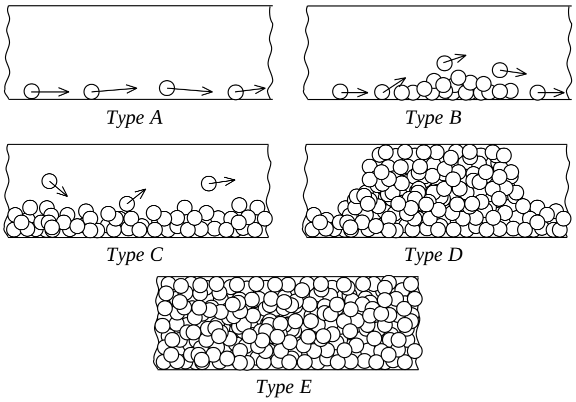

Fig. 12 Flow pattern

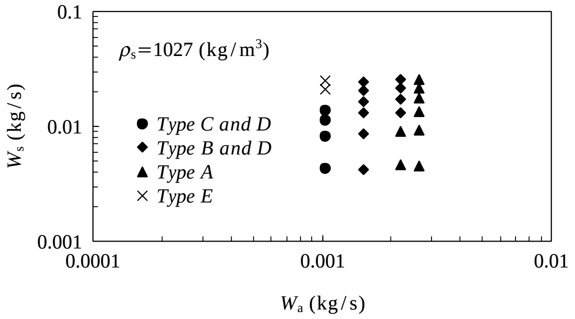

Fig. 13 Experimental range and flow pattern (ρ_s=1027 kg/m^3)

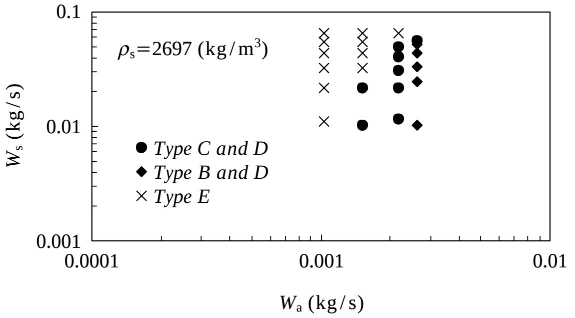

Fig. 14 Experimental range and flow pattern (ρ_s=2697 kg/m^3)

depending on difference in ρ_s and W_a and W_s. The flow pattern in the pipe can be divided roughly into Type A, Type D, and Type E. The plug flow (Type D) is main transportation state and accompanies Type B and Type C.

Properties of plug flow

To clarify the mechanism of plug formation, the behavior of particles in a pipe was recorded using a video camera. Photographs of the plug from generation to disintegration are shown in **Fig. 15**. They were taken every 0.2 seconds. The height of each photograph is equal to the inside diameter of the pipe. This example is the plug flow of Type D. The first photograph shows the particles accumulating on the pipe bottom, at the pressure of zero. In the second photograph, the pressure wave reaches the particles, the accumulated particles are pushed up and a plug is formed. The next photograph shows that the plug moves on, rolling up the accumulating particles in front of it. The last photograph shows the particles when the pressure wave vanishes again. They keep moving for a little while according to inertia force, and the upper part of the plug disintegrates gradually in front of and behind it. Finally, the plug disintegrates completely and does not move. This process from generation to disintegration is similar to the flow of Type B.

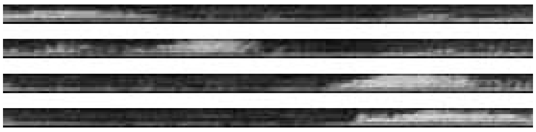

Fig. 15 Behavior of the plug in a pipe (ρ_s=2697 kg/m^3, P_1=5.1 kPa)

The loci of the plug are traced, and one example is shown in **Fig. 16**. t^* is non-dimensional time and z is the distance from the reference point (z/d=29.3). The coordinates of the downstream and upstream points where the plug touches the upper pipe wall are $z_{p1}(t^*)$ and $z_{p2}(t^*)$, respectively. Then, the coordinate at the center of the plug is given as follows.

$$z_p(t^*)=\frac{z_{p1}(t^*)+z_{p2}(t^*)}{2} \tag{7}$$

Moreover, the length of plug $l_p(t^*)$ and the velocity of plug $u_p(t^*)$ are given by:

$$l_p(t^*)=z_{p1}(t^*)-z_{p2}(t^*) \tag{8}$$

$$u_p(t^*)=\frac{d}{dt^*}z_p(t^*) \tag{9}$$

A plug does not always exist in a pipe. So, a plug is generated at t_1^* and disintegrates at t_2^* in one period of pressure wave, and its generation and disintegration are similar with all of the plugs in this investigation.

Fig. 17 shows an example of the relation between l_p and u_p, and each curve corresponds to one plug. The value of u_p is largest at the moment the plug is formed, and decreases afterwards. On the other hand, l_p shows several patterns of change. One decreases after an increase, one increases after a decrease, and one increases monotonically, decreases monotonically, or nearly preserves itself. These changes are related to the plug formation processes that depend on the state of the particles accumulating in the pipe in front of and behind the plug.

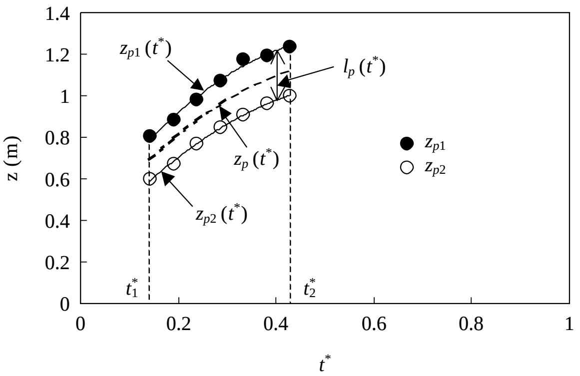

Fig. 16 Locus of plug

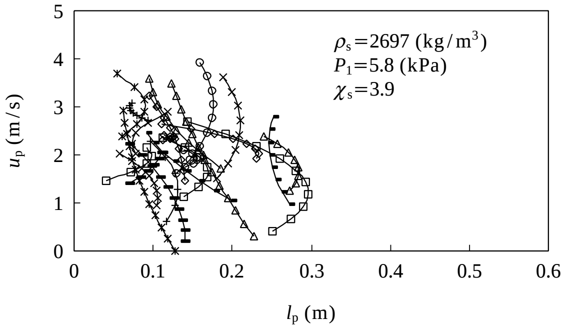

Fig. 17 Relation between u_p and l_p

Characteristic length L_p and velocity U_p of the plug are defined by:

$$t_p^* = t_2^* - t_1^* \tag{10}$$

$$L_p = l_p(t_1^* + t_p^*/2) \tag{11}$$

$$U_p = u_p(t_1^* + t_p^*/2) \tag{12}$$

where t_p^* is non-dimensional plug-existing time, and L_p and U_p are the length and velocity of plug at the mid-point of the existence of the plug, respectively. After calculating L_p and U_p for all plugs, it is clear that their tendencies vary according to the pressure wave, density of particles, and loading ratio χ_s. The mean values of L_p and U_p are calculated as $L_{p\ mean}$ and $U_{p\ mean}$, and their relations to χ_s are shown in **Fig. 18** and **Fig. 19**, respectively. In **Fig. 18**, the dispersion of $L_{p\ mean}$ becomes large when P_1 is small, but it becomes small and the value of $L_{p\ mean}$ decreases when P_1 is large. In the case of P_1=3.5 (kPa), $L_{p\ mean}$ increases as χ_s increases, and the dispersion becomes large. However, even if P_1 becomes larger, this remarkable tendency cannot be seen. In **Fig. 19**, it is clear that the dispersion of $U_{p\ mean}$ and the value of $U_{p\ mean}$ increases when P_1 is large, and $U_{p\ mean}$ remains virtually unchanged against χ_s. Although the result of ρ_s=2697 (kg/m^3) is omitted in this report, the above-mentioned tendency of $L_{p\ mean}$ is not found in this case. The value of $L_{p\ mean}$ becomes approximately 0.18 (m) regardless of the P_1 and χ_s values, and its dispersion remains virtually unchanged. Moreover, the value of $U_{p\ mean}$ becomes smaller than that in former case when P_1 is the same value, but their overall tendencies are almost the same.

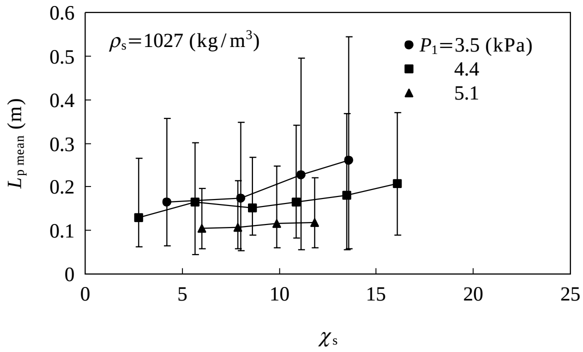

Fig. 18 Relation between $L_{p\ mean}$ and χ_s

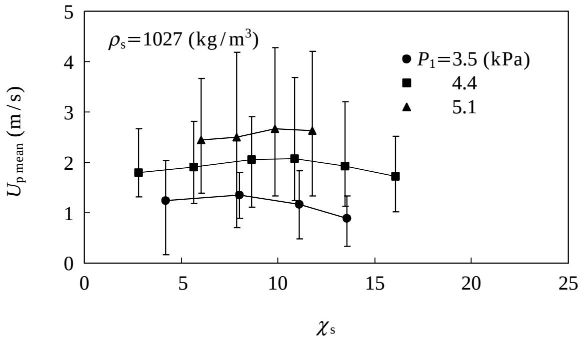

Fig. 19 Relation between $U_{p\ mean}$ and χ_s

Frequency histogram of plug passage

A number of pressure waves between successive plug passages at a position (z/d=58.3) of the pipe were measured as N_c. An example of the frequency histogram of the plug passage for each χ_s is shown in **Fig. 20**. n_p is the plug passage frequency, and N_p is the total plug passage frequency. When χ_s is small, N_c is distributed over a wide range up to large value. With increasing χ_s, N_c comes to be distributed over a narrow range on the small value side. This tendency is similar to that in the other condition of P_1 and ρ_s. Moreover, it was observed that two or more plugs were formed at the same time in the pipe when χ_s was large (N_c is small).

The mean number of pressure waves, $N_{c\ mean}$, was defined as follows:

$$N_{c\ mean} = \sum \left[N_c \frac{n_p}{N_p} \right] \tag{13}$$

Fig. 21 shows the calculated result. In all condi-

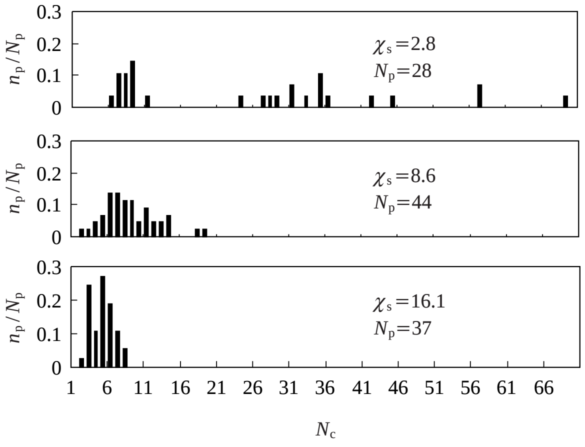

Fig. 20 Frequency histogram of plug passage (P_1=4.4 kPa, ρ_s=1027 kg/m^3, z/d=58.3)

tions of P_1, $N_{c\,mean}$ decreases with increasing χ_s and grows with increasing ρ_s when ρ_s is large. In this investigation, the minimum value of $N_{c\,mean}$ was about 4.5. From the above-mentioned observation, it becomes clear that the frequency of plug passages in cyclic pressure waves is closely related to P_1, ρ_s, and χ_s.

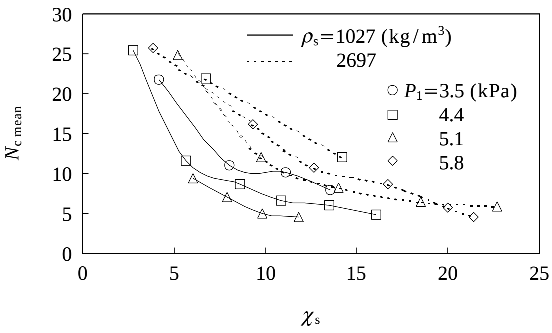

Fig. 21 Relation between $N_{c\,mean}$ and χ_s

Apparent loading ratio

To elucidate the role of the plug in particle transportation, assuming that the plug transports the particles, apparent loading ratio χ_{as} is given as follows:

$$\chi_{as}=\frac{\rho_b L_{p\,mean}\frac{\pi}{4}d^2}{N_{c\,mean}\,T\,W_a} \tag{14}$$

where ρ_b is the real bulk density of the particles in the pipe. To calculate ρ_b, a cylindrical container (V=3.28×10^{-4}m^3), which has the same inside diameter (d=30.0mm) as the pipe used in the experiment, was filled with particles, and the mass was measured. ρ_b is given by:

$$\rho_b=\frac{\rho_s W}{V(\rho_s-\rho)} \tag{15}$$

where W is the mass of the particle and ρ is the density of air. Real porosity ϕ is given as follows:

$$\phi=1-\frac{\rho_b}{\rho_s} \tag{16}$$

Moreover, theoretical bulk density $\rho_{b\,th}$ and porosity ϕ_{th} in a hexagonal closed-packed structure are given as follows:

$$\rho_{b\,th}=\frac{\sqrt{2}}{6}\pi\rho_s \tag{17}$$

$$\phi_{th}=1-\frac{\rho_{b\,th}}{\rho_s} \tag{18}$$

Table 3 indicates the real and theoretical values of the bulk density and porosity of the particles. Real porosity is approximately 1.5 times greater than theoretical porosity. This is because, near the wall of the container, there are insufficient particles. As a result, the bulk density is less than the theoretical density. However, it appears that these values are almost equal to the actual density and porosity of the plug formed in the pipe.

Fig. 22 shows the relation between experimentally obtained loading ratio χ_s and apparent loading ratio χ_{as}. The oblique straight line shows the case in which χ_s and χ_{as} are equal. A plotted point on a straight line means that the plug formed in the pipe transports the particles efficiently. Plotted points above the straight line mean that the plug transports only a portion of the particles. Therefore, it is thought that the moving particles in the plug are only in the upper part, except for the bottom part (Type C), and that the bottom part of the plug does not assist transportation. When the plotted points are below the straight line, the particles are transported not only by the plug but also by accumulating particles (state of Type B). These results correspond well with the observation of plug behavior.

Table 3 Bulk density and porosity

Particle	$\rho_{b\,th}$ (kg/m^3)	ϕ_{th}	ρ_b (kg/m^3)	ϕ
PS A	760	0.26	601	0.41
PS B	1997	0.26	1554	0.42

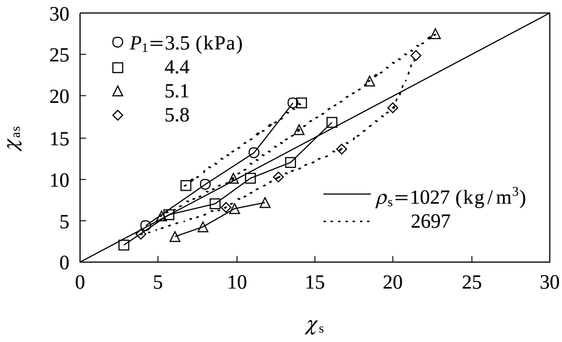

Fig. 22 Apparent loading ratio

Conclusion

1. When cyclic pressure waves are generated upstream the pipe, transportation using both progressive and reflective waves is more effective than using only progressive waves.
2. The loading ratio ranges from 2 to 23 in this investigation. These values range from low-pressure transportation to high-pressure one.
3. The flow pattern in the pipe is divided roughly into Type A, plug flow, and choking. Plug flow usually accompanies Type B or Type C.
4. The plug in the pipe is generated and disintegrates for one period of pressure wave. The characteristics of the plug are clarified by measuring its length and velocity in relation to the pressure waves, the density of the particles, and the loading ratio.
5. The number of pressure waves between successive plug passages decreases as the loading ratio increases, and its minimum value is 4.5 in this investigation.
6. The properties of transportation by the plug becomes clear from a comparison between the experimental and apparent loading ratios.

Principal nomenclature

a	: propagation velocity of pressure	(m/s)
d, d_s	: diameter of pipe and particle	(m)
l_p	: length of plug	(m)
L_p	: characteristic length of plug	(m)
$L_{p\ mean}$	: averaged characteristic length of plug	(m)
n_p	: plug passage frequency	
N	: rotating speed of screw	(rpm)
N_c	: number of pressure waves between plug passages	
$N_{c\ mean}$	: mean number of pressure waves	
N_p	: total plug passage frequency	
P	: pressure	(kPa)
P_1	: peak value of pressure	(kPa)
Q_s	: volume flow of particles	(m^3/s)
r	: radial coordinate	(m)
R	: radius of pipe	(m)
t	: time	(s)
t^*	: non-dimensional time, t/T	
t_p^*	: non-dimensional plug-existing time	
T	: period of pressure	(s)
u_p	: velocity of plug	(m/s)
U_p	: characteristic velocity of plug	(m/s)
$U_{p\ mean}$	: averaged characteristic velocity of plug	(m/s)
v	: velocity of air	(m/s)
$\mathrm{v}_{\mathrm{max}}$	: maximum instantaneous velocity	(m/s)
$\mathrm{v}_{\mathrm{mean}}$	: mean velocity of air	(m/s)
W	: mass of particles	(kg)
W_a	: mass flow of air	(kg/s)
W_s	: mass flow of particles	(kg/s)
z	: axial coordinate	(m)
ϕ	: real porosity $(\rho_s-\rho_b)/\rho_s$	
ϕ_{th}	: theoretical porosity	
ρ	: density of air	(kg/m^3)
ρ_s	: density of particles	(kg/m^3)
ρ_b	: real bulk density of particles in pipe	(kg/m^3)
$\rho_{b\ th}$	: theoretical bulk density	(kg/m^3)
χ_s	: loading ratio W_s/W_a	
χ_{as}	: apparent loading ratio	

References

1) Barth, W., Chem. Ing. Techn., 26-1 (1954-1), 29
2) Ochi, M., and Ikemori, K., Trans. JSME, 43-374 (1977-10), 3816
3) Matsumoto, S., Hara, M., et al., J. Chem. Eng. Japan, 7-6 (1975-1), 425
4) Morikawa, Y., Tsuji, Y., et al., Trans. JSME, 45-399 (1979-11), 1642
5) Lippert, A., Chem. Ing. Techn., 38-3 (1966-3), 350
6) Flatt, W., and Allenspach, W., Chem. Ing. Techn., 41-21 (1969-11), 1173
7) Morikawa, Y., Tsuji, Y., et al., Trans. JSME, 46-407 (1980-7), 1273
8) Karino, T., “Funryutai yusou souchi,” Nikkan-Kogyo, (1971)
9) Edwards, M.F., and Wilkinson, M.A., Trans. Inst. Chem. Eng., 49 (1971), 85
10) Ohmi, M., Iguchi, M., et al., Trans. JSME, 47-419 (1981-7), 1214
11) Mizushina, S., Maruyama, T., et al., J. Chem. Eng. Japan, 6-2 (1973), 152
12) Patel, R.D., Mcfeeley, J.J., and Jolls, K.R., AIChE J., 21-2 (1975), 259
13) Ohmi, M., Iguchi, M., et al., Trans. JSME, 46-404 (1980-4), 619
14) Marcus, R.D., Dickson, A.J., and Rallis, C.J., Powder Tech., 15 (1976), 107
15) Horie, M., Kado, H., and Ide, H., Japanese J. Multiphase Flow, Vol. 16, No. 4, 404

Author's short biography

Horie, Masaaki

Dr. Horie has been at the Department of Mechanical Engineering, Faculty of Engineering, Setsunan University. He obtained his B.Eng. and M.Eng. degrees from Kagoshima University. In 2003, he obtained his D.Eng. from Kagoshima University. 1996-1999, he worked in TOTO LTD. In 2004, he accepted a post as a lecturer at Setsunan University. His current research interests are a fundamental study on pneumatic transportation using pulsating pressure waves and a research on magnetically suspended centrifugal blood pumps.

Kado, Hisayoshi

Professor Kado has been at the Department of Mechanical engineering, Kagoshima University. He obtained his B.Eng. and M.Eng. degrees from the University of Osaka Prefecture. In 1986, he obtained his D.Eng. from Osaka University. Since 1987, he has been working in the Department of Mechanical Engineering at Kagoshima University. His current research interests are pneumatic transportation using pulsating pressure waves, flow-rectifying technology, and research and development on natural energy & the environment.

Ide, Hideo

Dr. Ide has been Associate Professor at the Department of Mechanical engineering, Kagoshima University. He obtained his B.Eng. and M.Eng. degrees from Kagoshima University. Then, he obtained his D.Eng. from Kyushu University. His current research interest is gas-liquid two-phase flow in narrow channels.

Photo-Functionalized Materials Using Nanoparticles: Photocatalysis[†]

K. Mori
Surface Finishing R&D Center
Central Research Laboratories
Nihon Parkerizing Co., Ltd.[*]

Abstract

Among photo-functionalized materials, photocatalysts in particular have been researched and developed by many researchers in various fields. After the discovery of the Honda-Fujishima effect, their effectiveness became apparent, not only in water decomposition but also in sanitation and purification of the environment, for example, through antibacterial, self-cleaning, and deodorizing effects as well as NOx removal. Recently, novel nano-size photocatalysts, with performance superior to that of conventional types, have been developed, and examples include nitrogen-doped photocatalysts responsive to visible light and brookite-type photocatalysts with higher photocatalytic activity.

Moreover, when applying a photocatalyst, it must be fixed to a substrate and blocking of the latter avoided. When photocatalysts with high photocatalytic performance are fixed to plastics, papers and textiles, the substrate can be decomposed and may be prone to peel off when exposed to irradiation with light, owing to the oxidation action of the photocatalysts. To prevent damage to the substrate resulting from photocatalytic oxidation, we have developed a photocatalyst whose particles are coated with inorganic compounds that can be blended with organic substances.

Key words: Photocatalyst, Environment, Antibacterial, Self-cleaning, Deodorizing

1. Introduction

Among photo-functionalized nanoparticle materials, photocatalysts in particular are expected to provide a useful environment conserving technology. This technical field has recently been developing rapidly as active efforts have been made for research and development and commercial applications; in particular in Japan. Following research into the utilization of photocatalysis, beginning with the discovery of the TiO_2-based Honda-Fujishima effect, it has been reported that the photocatalysis of photo-functionalized nanoparticle photocatalysts is effective not only for the photodecomposition of water but also for sanitation and environmental purification applications such as antibacterial, self-cleaning and deodorizing operations, as well as the removal of NOx. Thus, researchers in various technical fields have been studying the potential applications of photocatalysts. TiO_2 is mainly used as a photocatalyst because of its strong photo-oxidation power, chemical stability and safety for the human body, and its most common form is an anatase type powder with particles measuring several to tens of nm in crystal size. However, as development in photocatalyst applications progresses, demand is mounting for those that are capable of effective photocatalysis in weak light or in the absence of ultraviolet radiation. To address this problem, laboratories and manufacturers of ceramics materials in Japan have been actively researching higher functions with TiO_2-based photocatalytic materials.

Consequently, novel nanoparticle photocatalysts with functions more advanced than those of conventional photocatalysts have been commercialized, and examples include visible light-responsive photocatalysts, prepared by doping TiO_2 particles with a dissimilar element such as nitrogen, and brookite type TiO_2

---

[*] 2784, Ohgami, Hiratsuka, Kanagawa 254-0012, Japan
TEL: 81-463-55-4431, FAX: 81-463-54-7328
E-mail: kmori@parker.co.jp

[†] This report was originally printed in J. Soc. Powder Technology, Japan, **41**, 750-756 (2004) in Japanese, before being translated into English by KONA Editorial Committee with the permission of the editorial committee of the Soc. Powder Technology, Japan.

photocatalysts, featuring high photocatalytic activity.

Incidentally, to allow photocatalyst particles to be applied to final products, the particles must be fixed to a substrate and at the same time deterioration of the latter must be avoided. However, if a highly active photocatalyst material is carried by an organic substrate, such as resin, paper or cloth, the oxidizing power of the photocatalyst will lead to decomposition of the substrate, causing the photocatalyst particles to come off. To prevent this problem, a unique powder photocatalyst to be mixed with organic material has been developed, wherein the particles of this photocatalyst are of a core-shell structure; prepared by allowing inert particles of silica, hydroxyapatile or similar to be deposited on the surface of photocatalyst particles. Photocatalysts with a surface layer of inert particles are generally high-performance photocatalysts. It is also possible to enhance the adsorption of bacteria and NOx by choosing appropriate inert particles to be deposited on the surface of TiO_2 particles.

2. Operating Principle and Types of Photocatalysts

When a given photosemiconductor is irradiated with light of energy greater than the band gap energy of the photosemiconductor, charge separation occurs. Then, utilizing the electrons and holes generated by the charge separation, the photocatalyst triggers an oxidation-reduction reaction. In particular, TiO_2, with a relatively large band gap energy of 3.0 to 3.2 eV as shown in **Fig. 1**$^{1)}$, can achieve a powerful oxidation-reduction reaction with the ultraviolet rays present in our living environment.

It is known that active oxygen and radical species existing in the presence of oxygen and water take part in the oxidation-reduction reaction, and that various functions of the photocatalysts are realized by this reaction. Various types of TiO_2 are listed in **Table 1**$^{2)}$ as representative photocatalysts. Ordinary TiO_2 for pigment is of the rutile type and its crystal size mea-

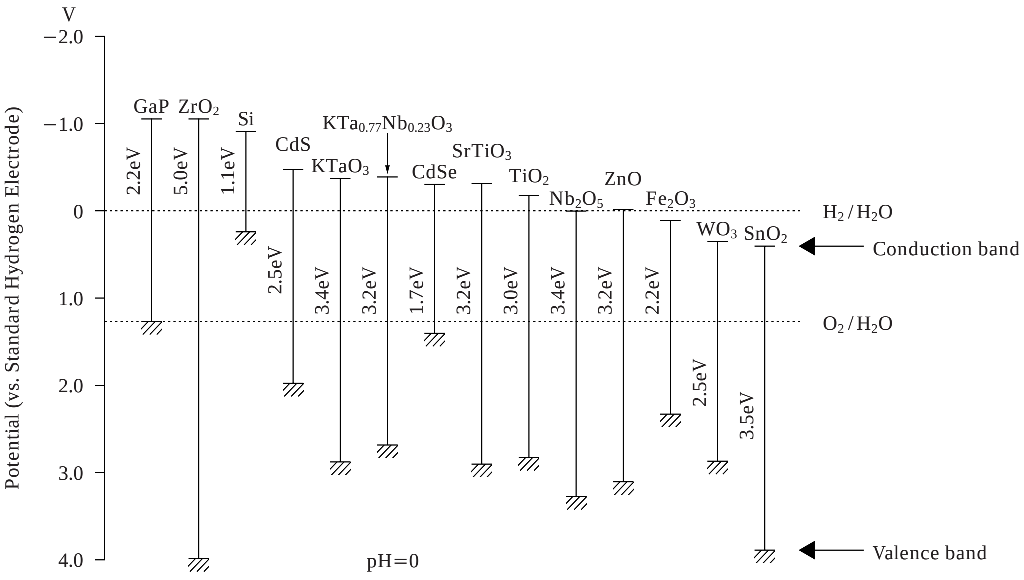

Fig. 1 Energy structures of various photosemiconductors$^{1)}$

Table 1 Types and physical properties of titanium oxide

Properties	Rutile	Anatase	Brookite
Crystalline form	Tetragonal system	Tetragonal system	Orthogonal system
Density (g/cm^3)	4.27	3.90	4.13
Refractive index	2.72	2.52	2.63
Mohs' hardness	7.0～7.5	5.5～6.0	5.5～6.0
Permittivity	114	48	78
Melting point (℃)	1825	Transformation to rutile	Transformation to rutile

sures several hundreds of nm in size. TiO_2 for photocatalysts, meanwhile, is of the anatase type with very small crystal size, measuring several to 20 nm. For this reason, TiO_2 for photocatalysts is more transparent than conventional TiO_2 for white pigment, and a colorless transparent photocatalytic layer may be obtained if the layer thickness measures 1 μm or less. Various manufacturing processes for titanium oxides for photocatalysts have recently been investigated, and the rutile, brookite and amorphous types (for precursors) of TiO_2 for photocatalysts have been developed, other than the anatase type.

Studies on photocatalysts began with research on the decomposition of water into hydrogen and oxygen by irradiation with light, and are still underway. No photocatalyst for the photodecomposition of water has yet been commercialized because of a lack in efficiency, high production cost, etc. Nevertheless, the progress attained in photocatalysts to date is based on the results of these studies. Various photocatalysts for water decomposition have been disclosed and developed, many of which utilize TiO_2, and the examples of which comprise TiO_2 particles carrying a metal such as Pt or Rh[3) 4)] as shown in **Fig. 2** or an oxide such as RuO_2.

Recently, there are many studies concerning TiO_2 photocatalysts that feature higher efficiency and that are capable of responding to visible light. Certain examples of such photocatalysts already disclosed include a TiO_2 photocatalyst, whose response to visible light is improved with TaON[5)], a TiO_2 photocatalyst that utilizes $In_{1-X}Ni_XTaO_4$[6)], and a TiO_2 photocatalyst, whose quantum yield is improved with La-doped $NaTaO_3$[7)]. Though these examples have photocatalysts with relatively large particle sizes, ranging from 0.1 to several μm, they still boast excellent functions by controlling their crystal structure.

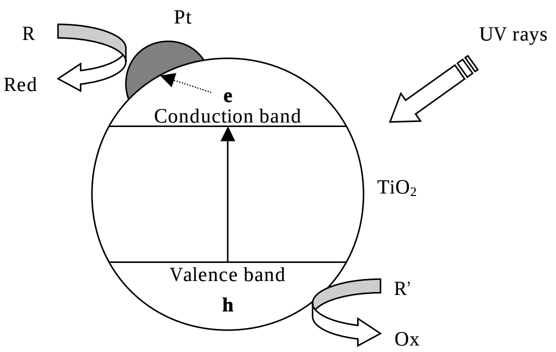

Fig. 2 Structure of Pt-carrying TiO_2 particles

3. Functions and Features of Photocatalysts

3.1 Self-cleaning, hydrophilic, and antibacterial characteristics

Titanium oxide particles decompose organic matters when irradiated with ultraviolet rays. This fact has long been known as a choking phenomenon that occurs with a paint containing a TiO_2 pigment. During a self-cleaning process with a photocatalyst, contaminants on a substrate are photodecomposed, wherein radicals and active oxygen generated by ultraviolet irradiation on a photocatalyst decompose the organic contaminants into carbon dioxide, thereby allowing the surface of the substrate to remain clean.

It has been reported that a positive hydrophilic effect appears when a TiO_2 photocatalyst is irradiated with ultraviolet rays. This characteristic is widely applied to glasses, mirrors and building materials.

If a TiO_2 photocatalytic coating material is used in an outdoor location exposed to rainwater, organic contaminants on the surface of coating are decomposed by light irradiation and the residual inorganic particles are readily washed away by the rainwater, hence the coated surface exhibits the expected self-cleaning effect. **Fig. 3** schematically illustrates a self-cleaning model with an outdoor application, and **Fig. 4** shows an example of a self-cleaning effect with an exterior wall consisting of tiles coated with a TiO_2 photocatalytic material.

Radicals and active oxygen generated by the activity of a TiO_2 photocatalyst are effective in decomposing and preventing the propagation of bacteria and fungi. Because of their small selectivity against bacteria species and their ability to decompose the toxins produced by bacteria, TiO_2 photocatalysts have been increasingly used for interior finishing materials in hospitals and medical equipment.

On the other hand, the intensity of ultraviolet rays available indoors is one digit lower compared with that available outdoors, as shown in **Fig. 5**, and it is difficult to offer sufficient photocatalytic effect with ultraviolet rays in a room alone. In addition, there are many places where the intensity of ultraviolet rays is lower than expected − such as in cars that are equipped with UV-cut glasses. To operate effectively in these locations, novel photocatalysts responsive to visible light, and capable of performing within the visible light spectrum in the region of 500-600 nm wavelength as well as the UV band have been developed

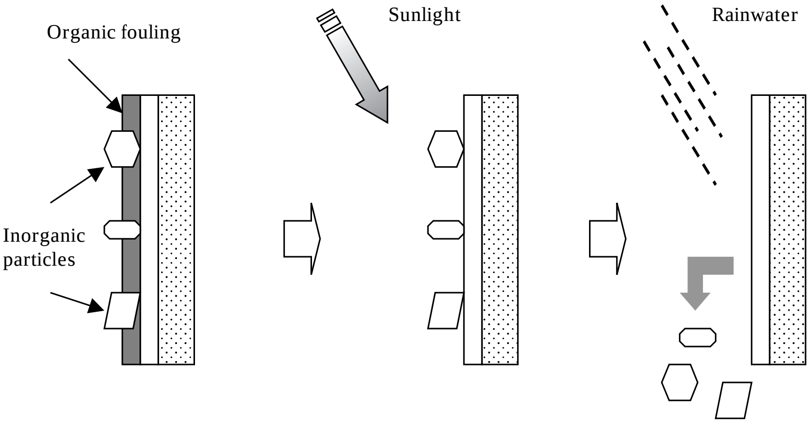

Fig. 3 Model of fouling removal by self-cleaning effect (outdoor)

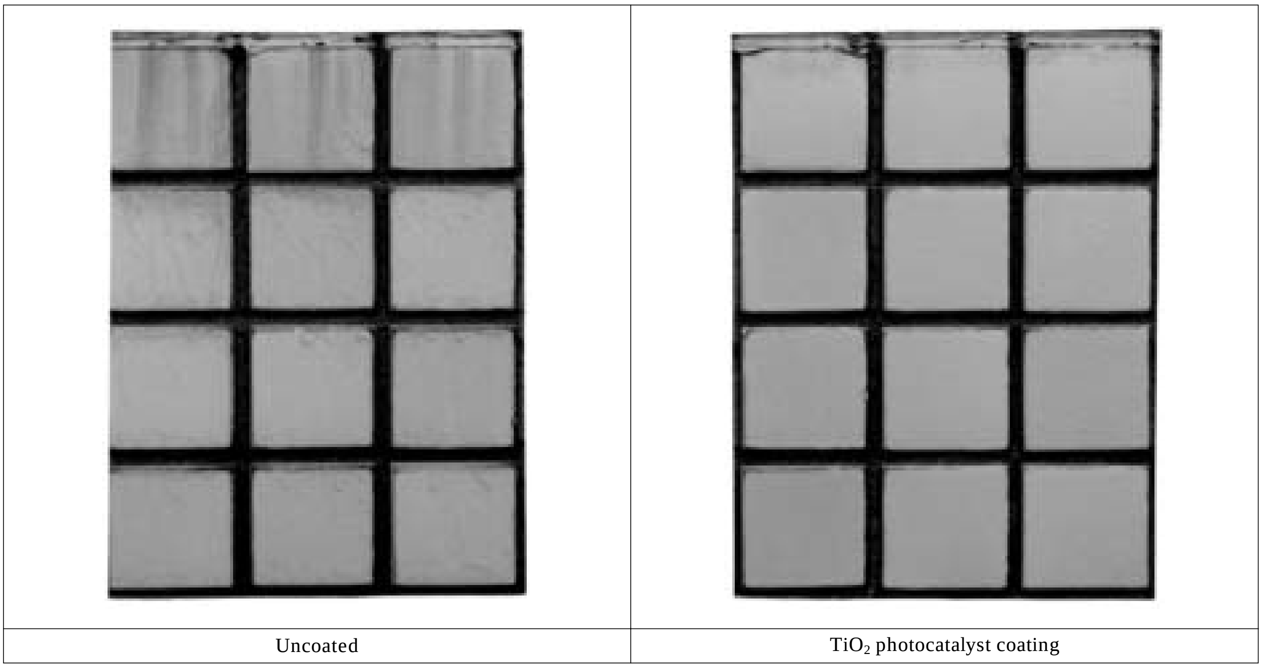

Uncoated | TiO_2 photocatalyst coating

Fig. 4 Self-cleaning effect of wall tiles coated with TiO_2 photocatalyst (1 year after installation: top joint is filled with silicone sealant)

and commercialized. It should be understood from the spectra of sunlight[8)] in **Fig. 6** that the energy efficiency of photocatalysts under sunlight will be improved with expansion of the effective wavelength to 500-600 nm.

Visible light-responsive photocatalysts can be produced, for example, through change in the band structure with the addition of new energy levels resulting from the presence of impurities by doping a TiO_2 photocatalyst with another element such as nitrogen or sulfur[9) 10)]. The photocatalyst thus obtained is yellowier compared with conventional anatase-type photocatalysts, and capable of absorbing a portion of the visible light. Usually, the crystal size of the visible light-responsive photocatalysts is designed to be somewhat larger than that of conventional anatase-type photocat-

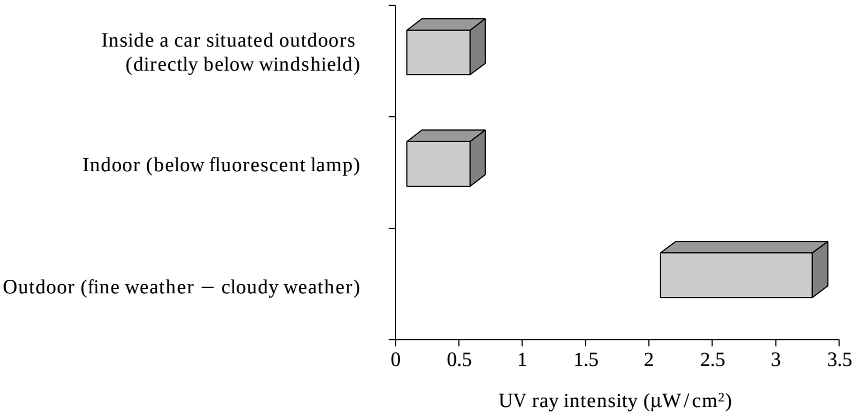

Fig. 5 Amounts of UV light in living environments

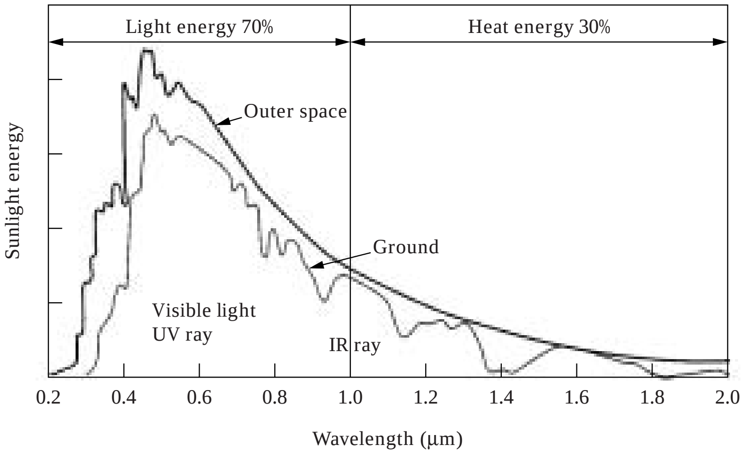

Fig. 6 Sunlight spectra

alysts. One reason for this arrangement is to avoid a shift of the optical absorption edge to a shorter wavelength side, resulting from the quantum size effect occurring when the crystal size is less than 10 nm. In order to investigate the photocatalytic activity of a visible light-responsive photocatalyst, a dye (Methylene Blue) was allowed to be adsorbed onto a layer of visible light-responsive photocatalyst, and was then decomposed with a white fluorescent lamp. The result is shown in **Fig. 7**. From this illustration, we can presume that decolorization is minor on the irradiated area (upper half of the photo in the left) of the anatase TiO_2 (diameter: 7 nm) layer and that the dye in the irradiated area (upper half of the photo in the right) of the visible light-responsive photocatalyst (diameter: 11 nm) layer has been virtually completely decomposed following irradiation with a fluorescent lamp.

Furthermore, a fingerprint was printed on a glass substrate coated with a visible light-responsive photocatalyst and decomposed by irradiation with a fluorescent lamp. The result is visually illustrated in **Fig. 8**. Components in fingerprints comprise organic contaminant matters, such as fatty acids, as well as inorganic contaminant particles, such as those of salts. The organic contaminants, which form the major constituents of fingerprints, were found to have been decomposed, and it was visually apparent that the fingerprints had disappeared. In addition, the antibacterial performance of the visible light-responsive photocatalyst (a property important in indoor appli-

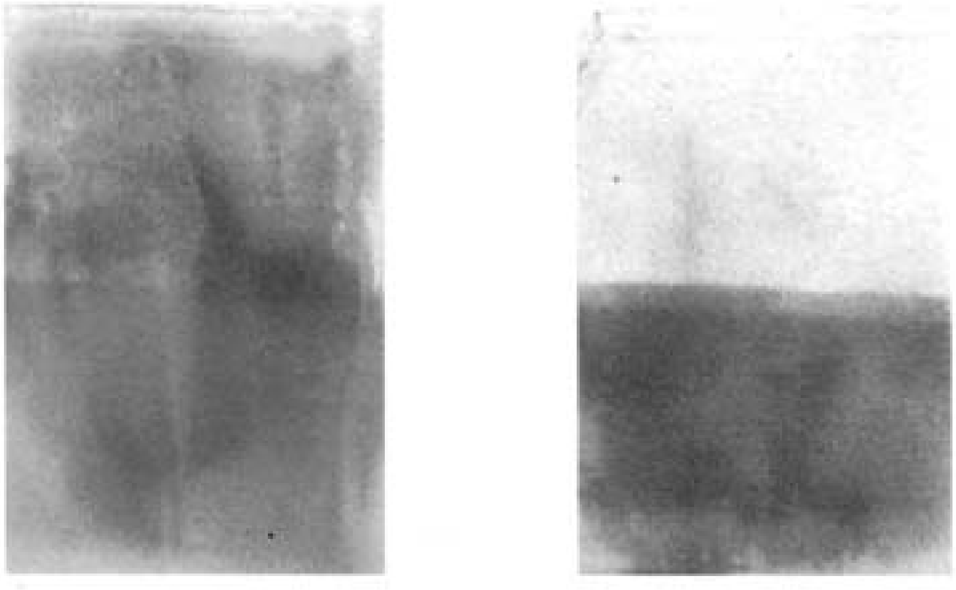

Anatase type (conventional)

Visible light-responsive type

Fig. 7 Dye decomposing ability of visible light-responsive photocatalyst coating layer (after 12 hours of irradiation onto the upper half with a white fluorescent lamp)

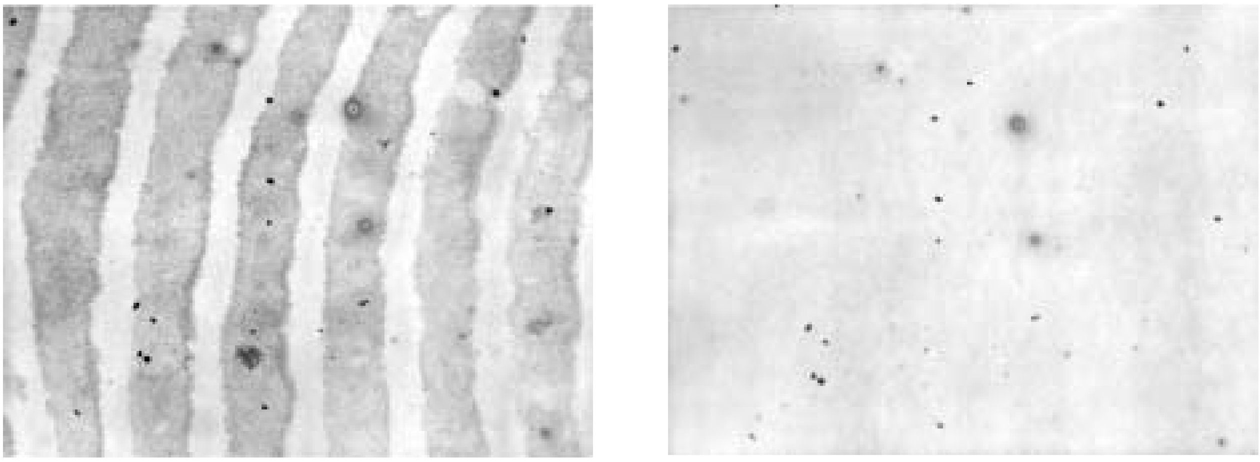

Before irradiation

After irradiation

Fig. 8 Fingerprint decomposing ability of visible light-responsive photocatalyst
Evaluated with an optical microscope [magnifying power: ×50]
Substrate: glass (12 hours of irradiation with a white fluorescent lamp, 3,000 lx)

cations) was tested and the results are summarized in **Fig. 9**. As can be understood from this figure, antibacterial performance is obtained with a white fluorescent lamp rated at about 1000 lx. Examples of commercialized applications of antibacterial visible light-responsive photocatalyst include window blinds and wallpapers. To be able to form a photocatalyst layer on the surface of these resin-coated products, a

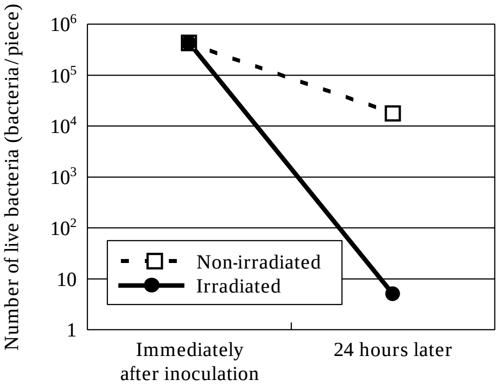

Fig. 9 Antibacterial performance of visible light-responsive coating material (MRSA)
Light irradiation: white fluorescent lamp, 1,000 lx
Method: film contact method
Executed by: Japan Food Research Laboratories

transparent primer coating agent, composed principally of inorganic components, is applied to form an intermediate layer to improve durability, and then a coating solution, containing photocatalyst particles, is applied to form the top layer.

3.2 Fog-proofing

Since the expression of super-hydrophilicity with TiO_2 photocatalyst was presented in 1997 by Hashimoto et al.[11], research into this feature has been active. Consequently, it has been increasingly applied to fog-proofing and self-cleaning applications for mirrors, including road mirrors (curve mirrors) and door mirrors on cars, as well as window glass panels. Since the hydrophilicity of TiO_2 photocatalysts is more positively maintained by the addition of SiO_2 or a more porous structure of TiO_2 particles, improvement in the composition and layer forming method for TiO_2 photocatalysts is now underway.

Additionally, in order for TiO_2 photocatalysts to be effective under weak indoor lighting, tungstic oxide may be joined with TiO_2[12], or TiO_2 surface may be provided with a nanoporous structure[13] by a photoetching technique.

3.3 Air purification

Air purification is one example of the most advanced applications of photocatalysts. For example, photocatalysts are used in deodorizing filters in air-purifiers incorporating UV lamps to eliminate aldehyde or VOC in indoor air. Such filters are used in the form of a honeycomb or porous substrate; hence allowing UV rays to penetrate their deeper portions. Currently, these filters are required to have higher performance under weak light, to be more responsive to visible light and to have a boosted decomposition ability against various indoor pollutants including VOC. **Fig. 10** summarizes the acetaldehyde decomposition rate of a visible light-responsive photocatalyst (mean diameter: 11 nm) exposed to sunlight transmitted through a UV-cut glass (car windshield), by comparing the acetaldehyde decomposition rate with that of a conventional anatase type photocatalyst (mean diameter: 7 nm).

Furthermore, interior finishing materials and textile products capable of air purification can be manufactured by blending photocatalyst particles into organic materials such as wallpapers, *shouji* (Japanese paper screen doors) and floor panels during their production processes or by finishing the interior of buildings with a resin coating containing photocatalysts. With this type of application, however, the substrate may be gradually degraded owing to irradiation with light. Moreover, the strength of the substrate can decrease or the adhesion of the photocatalyst-containing material to the substrate may decrease, rendering the material prone to drop off. To address this problem, there have been new developments in photocatalysts: muskmelon-like TiO_2 particles produced by coating TiO_2 photocatalyst particles with inert porous silica and thus preventing them from coming into contact with the substrate[14] and surface-coated TiO_2

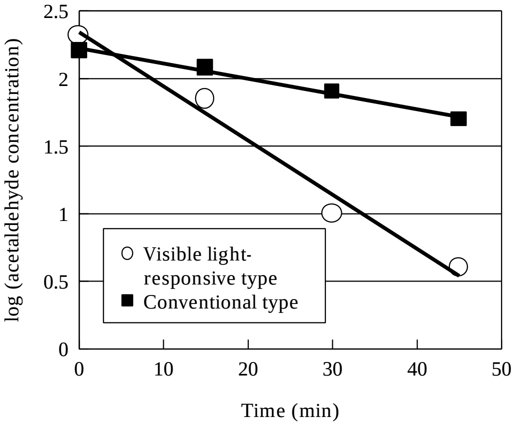

Fig. 10 Acetaldehyde decomposition rate in a car
Fine weather: under sunlight, sample size: 100 cm^2
(A 3-L glass cell was placed directly below the windshield.)

particles, prepared by depositing hydroxyapatite on the surface of TiO_2 particles[15]. These products are already commercially used for plastics and textile products and electron-microscopic photos of the latter are shown in **Figs. 11 (a)** and **(b)**. Note that with these TiO_2 photocatalyst particles types, individual particles are not fully covered and their coating layers are gas-permeable.

These coated TiO_2 photocatalyst particles are formed through the aggregation of primary TiO_2 particles whose particles size measures from several nm to 20 nm and a coating of aggregated particles. Consequently, despite their relatively large particle size, they can be treated like pigment particles. 20% of each of these particle types was mixed in an acrylic resin, and each mixture was applied to a glass substrate to a thickness of 100 µm. Subsequently, each specimen was irradiated with UV rays with black light and the resin decomposition inhibition effect provided by the coated TiO_2 photocatalyst particles was compared with that of conventional anatase-type TiO_2 photocatalyst particles. The result is summarized in **Fig. 12**.

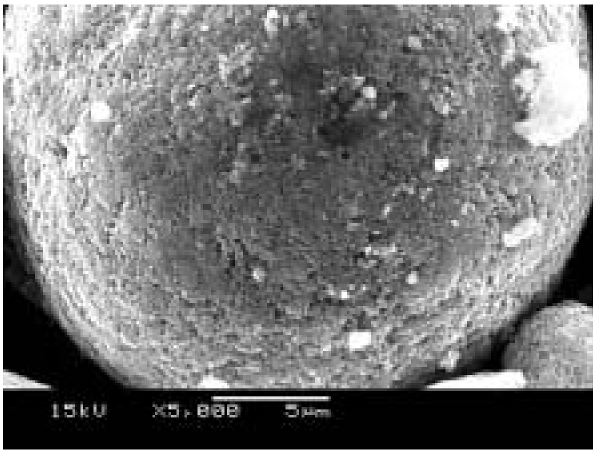

a) Muskmelon-like substance-coated TiO_2

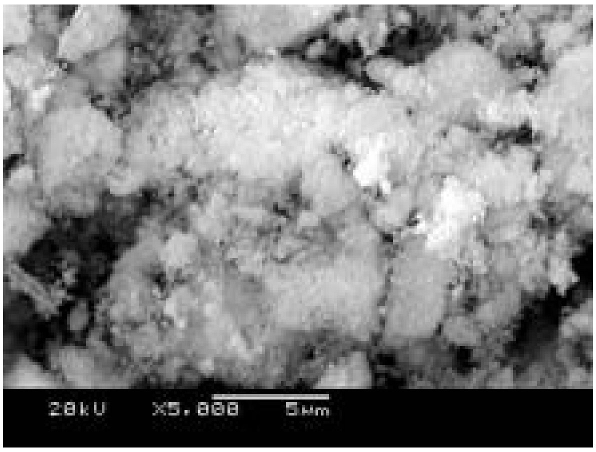

b) Hydroxyapatite-coated TiO_2

Fig. 11 Surface-coated photocatalyst particles

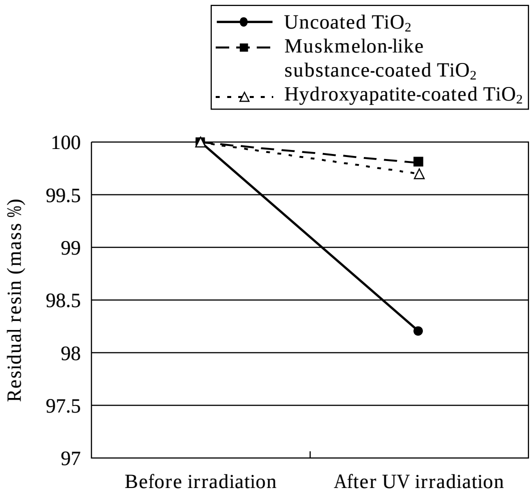

Fig. 12 Resin substance decomposition inhibition effect with coated TiO_2 photocatalyst particles

3.4 Elimination of NOx

Since the report concerning the successful elimination of low-concentration NOx in outdoor environments by Dr. Ibusuki, Dr. Takeuchi et al., expectations for photocatalysts as environmental cleaning materials have been mounting, and air purification-capable paving materials and soundproof wall materials for roads have been developed, while research efforts for the application of NOx-eliminating equipment in road tunnels are underway.

A TiO_2 photocatalyst oxidizes NO into NO_2 and eventually into NO_{3-}, hence removing NO from the air. Since the nitric acid ions generated are adsorbed and accumulated in the surface of the photocatalyst, the latter must be rinsed at regular intervals with water to prevent deterioration in performance due to an increase in adsorbed nitric acid ions. When used in outdoors, a TiO_2 photocatalyst will be cleaned by sunlight and rainwater, and its NOx elimination effect will be guaranteed without any maintenance work required.

One potential problem when NO is eliminated with a TiO_2 photocatalyst is that if the NO_2 adsorption power of the photocatalyst type is low, the reaction only progresses to NO_2 (an intermediate product) stage and the resultant NO_2 concentration on the TiO_2 photocatalyst will be higher than before adsorption. The known methods and means to avoid this problem include a TiO_2 photocatalyst particle type that carries another metal or metal oxide or a method involving mixing the TiO_2 photocatalyst particles with adsorptive particles such as active carbon[16] or blending them into mortar.

3.5 Water purification and soil decontamination

Various researches have been conducted for the purification of water with titanium oxide photocatalysts, wherein the examples of water being purified include effluent water from factories and sewage and environmental water such as ground and river water. Much research is associated with low concentration chlorinated organics in effluent water from factories and in groundwater. Such research has helped to prove that titanium oxide photocatalysts can decompose endocrine disrupting chemicals such as bisphenol A[17], meaning commercial water purification applications involving this type of photocatalyst are expected, although progress in water purification applications is lagging behind that of air purification equivalents. This is because the reaction efficiency of a titanium oxide photocatalyst decreases in water and the performance of a titanium oxide photocatalyst easily deteriorates when the surface of photocatalyst particles becomes fouled up. To overcome these problems, certain methods have been commercialized, wherein air is bubbled into groundwater or soil water and volatile organic chemicals, which are taken into the air phase, are eliminated using a photocatalyst filter similar to an air purifying photocatalyst filter[18]. The examples of photocatalysts developed for water treatment include a water purifying substance that is prepared by allowing an inorganic adsorbent consisting of silica gel particles carrying photocatalyst particles to enhance pollutant adsorbing performance[19]. This substance, however, has the disadvantage of the tendency of the photocatalyst particles to peel off or be damaged by water flow. To solve this problem, a high-strength titania fiber material[20] boasting sufficient strength and durability, and capable of withstanding a high-speed water flow, has been developed.

3.6 Other applications

Other potential applications for the photocatalyst powder include corrosion prevention by metal cathodes, and utilization in dye-sensitized solar cells.

Photocathode corrosion prevention is a unique technique where if a photocatalyst layer consisting of a n-type semiconductor forms on the surface of metal, the potential on the metal surface drops as the surface is irradiated with light, promoting a non-sacrificial cathode corrosion prevention effect[21]. Currently, research is in progress for the commercial utilization of this effect.

The dye-sensitized solar cells (Graetzel cells) are wet-type solar cells that use electrodes comprising photocatalyst particles, such as TiO_2 particles, that have adsorbed dye. This solar cell type has been developed as a type of next-generation solar cell; since it will realize higher efficiency and lower cost.

4. Conclusion

As discussed above, photocatalysts boast many unique functions among photo-functionalized materials and satisfy the environmental conservation and energy saving requirements. Therefore, they will be utilized in a diversity of industrial fields familiar to us.

The current market size for photocatalysts in Japan is estimated at tens of billions yen per year, and will dramatically expand as photocatalyst technology is increasingly recognized as a typical key technology; indispensable for environmental conservation and energy saving following progress in research and development work associated with this technology. We hope this paper will assist in the further development and creation of a new market for photo-functionalized materials.

References

1) A. Fujishima, K. Hashimoto, T. Watanabe: “TiO_2 Photocatalysis Fundamentals and Applications,” p. 128, BKC, Inc. (1999)
2) M. Kiyono: “Sankatitan,” Gihodo-shuppan, Japan, p. 52 (1991)
3) S. Sato, J. M. White, *Chem. Phys. Lett.*, 72, p. 83 (1980)
4) K. Yamaguchi et al., *JCF Faraday Trans.* 1, 81, p. 1237 (1985)
5) G. Hitoki, A. Ishikawa, T. Takata, J. N. Kondo, M. Har, and K. Domen: “Ta_3N_5 as a Novel Visible Light-Driven Photocatalyst ($\lambda<600$ nm),” *Chem. Lett.*, p. 736 (2002)
6) Z. Zou, J. Ye, H. Arakawa: “Photocatalytic behavior of a new series of $In_{0.8}M_{0.2}TaO_4$ (M=Ni, Cu, Fe) photocatalysts in aqueous solutions,” Catal. Lett., 75, 209 (2001)
7) H. Kato and A. Kudo: “Highly Efficient Water Splitting into H_2 and O_2 over Lanthanum-Doped $NaTaO_3$ Photocatalysts with High Crystallinity and Surface Nanostructure,” *J. Am. Chem. Soc.*, 125, 3082 (2003)

8) A. Fujishima: Kagaku-sosetsu "Muki-Hikarikagaku," No. 39, Gakkai Shuppan Center, Japan, p. 98 (1983)
9) R. Asahi, T. Morikawa, T. Ohwaki, K. Aoki, Y. Tage: "Visible-Light Photocatalysis in Nitrogen-Doped Titanium Oxides," *SCIENCE*, Vol. 293, 269 (2001)
10) Y. Sakatani, K. Okusako, H. Koike, H. Ando: "Development of a Visible Light Responsive TiO_2 Photocatalyst," *Kaiho Hikari Shokubai*, Vol. 4, p. 51 (2001)
11) T. Watanabe: "Super-hydrophilic TiO_2 Photo-Catalyst and Its Application," *Bull. Chem. Soc. Jpn.*, 31, 837-840 (1996)
12) M. Miyauchi, A. Nakajima, K. Hashimoto, T. Watanabe: "A Highly Hydrophilic Thin Film under 1 $\mu W/cm^2$ UV Illumination," *Adv. Mate*r, 12, 1923 (2000)
13) T. Shibata, A. Nakajima, T. Watanabe, K. Hashimoto: "Sensitization for photo-induced hydrophilicity of TiO_2," *Kaiho Hikari Shokubai*, Vol. 4, p. 45 (2001)
14) N. Yamashita, K. Hayashi, S. Imaizumi, H. Nimura, T. Umemura, H. Sakurai, M. Takahashi: "Development of muskmelon-like photocatalyst," *JETI*, Vol. 49, No. 2, p. 97 (2001)
15) T. Nonami et al: "Apatite formation on TiO_2 photocatalyst in a pseudo body solution," *Material Research Bulletin*, 33, 125-131 (1998)
16) T. Ibusuki, S. Kutsuna, and K. Takeuchi: "Removal of low-concentration NOx from ambient air by the photocatalytic oxidation of NOx using TiO_2 active carbon mixture," Proc. Fukuoka Int. Symp. '90, pp. 253-254 (1990)
17) I. Ando, Y. Ohko, T. Nakashima, Y. Kubota, T. Yamamura, T. Tatsuma, A. Fujishima: "Degradation of bisphenol-A in water by TiO_2 photocatalysis," Proceedings of the 6th Symposium on Recent Development in Photocatalysis (Photo-Functionalized Materials Society), p. 134 (1999)
18) H. Tomioka, H. Yamazaki, K. Okamoto, K. Ito, M. Murabayashi: "Purification of underground water contaminated with organic chloride by the gas-phase photocatalytic reaction," Proceedings of the 6th Symposium on Recent Development in Photocatalysis (Photo-Functionalized Materials Society), p. 122 (1999)
19) Y. Zhang et. al.: "Fixed-Bed Photocatalysts for Solar Decontamination of Water," *Environ. Sci. Technol.*, 28, 435 (1994)
20) H. Yamaoka: "Development of Strong Photocatalytic Fiber and Environmental Purification," Proceedings of the 9th Symposium on Recent Development in Photocatalysis (Photo-Functionalized Materials Society), p. 206 (2002)
21) T. Imokawa, R. Fujisawa, T. Shinohara, S. Tsujikawa, A. Suda: Proceedings of the 39th Japan Conference on Corrosion and Protection, p. 277 (1992)

Author's short biography

Kazuhiko Mori

K. Mori graduated in industrial chemistry from the Nagoya Institute of Technology, Japan, in 1980 and has been developing material surface treatments for over 20 years. His expertise spans a range of surface treatment and coating technologies, including photocatalytic coating, ceramic composite plating, and sol-gel coating. He is currently a research manager in surface treatment and functionalized coating technologies in laboratories at Nihon Parkerizing Co., Ltd.

Information Articles

The 39th Symposium on Powder Technology

The 39th Symposium on Powder Technology was held on August 29, 2005 at the Senri Hankyu Hotel in Osaka under the sponsorship of the Hosokawa Powder Technology Foundation and with the support of Hosokawa Micron Corporation. The symposium in this year was also very successful with the attendance of 205 including 41 academic people. The main subject of this year was "Beginning of Era for the Practical Use of Nano-particles".

The 39th Symposium on Powder Technology

Subject: "Beginning of Era for the Practical Use of Nano-particles"

Session 1 Chairperson: Prof. Yutaka Tsuji (Osaka Univ.)

• Design of Functional Materials Related to Particles Using Computer Simulation (KONA Award Commemorative Lecture)	Prof. Jusuke Hidaka (Doshisha Univ.)
• Fabrication of Advanced Materials by Powder Processing (KONA Award Commemorative Lecture)	Prof. Shuji Hanada (Tohoku Univ.)

Session 2 Chairperson: Prof. Kiyoshi Nogi (Osaka Univ.)

• Nanoparticles Synthesis and Functionalization Technology towards Industrial Applications: Recent Research in NEDO-Nanoparticle Project	Prof. Kikuo Okuyama (Hiroshima Univ.)
• Development of Carbon Nanotube Doped High Performance Ceramics	Prof. Katutoshi Komeya (Yokohama National Univ.)
• The state of Solid Oxide Fuel Cell Development Using Nano-particle Processing	Dr. Takehisa Fukui (Hosokawa Powder Technology Research Institute)

Session 3 Chairperson: Prof. Makio Naito (Osaka Univ.)

• Development of Nano-composite Materials	Dr. Norio Tobori (Lion Corporation)
• Functional Cosmetics Designed by Nano-particles, Including the Application of New Hair Growth Tonic Development etc	Dr. Hiroyuki Tsujimoto (Hosokawa Powder Technology Research Institute)

The 13th KONA Award

The 13th KONA Award sponsored by Hosokawa Powder Technology Foundation and given to the scientists or groups who have achieved excellence in the researches related to the basic powder technology, was presented to Professor Jusuke Hidaka of Doshisha University and to Professor Shuji Hanada of Tohoku University by Masuo Hosokawa, President of the Foundation on January 26, 2005 at the R&D Center of Hosokawa Micron Corporation in Hirakata, Osaka Prefecture.

Prof. Hidaka received his M.S. and Ph.D in Chemical Engineering from Doshisha University in 1972 and 1989. After he worked as a researcher at Showa Denko Co. Ltd., 1972 to 1976, he joined Doshisha University and became a full professor in 1990. The major focus of his current research work is to establish the design method of functional materials related to particles by using computer simulation. He has proposed a new method to design the microstructure of polycrystalline $BaTiO_3$ ceramics based on the mathematical model which represents the relation between the microstructure of $BaTiO_3$ ceramics and dielectric or piezoelectric characteristics. The KONA Award was given to his achievement on the development of design method of functional ceramics and powder industrial processes to produce precisely the microstructure of the ceramics using computer simulation.

Prof. Hanada graduated from Graduate School of Engineering (Materials Science), Tohoku University, and received a Ph.D degree in 1971. Then he worked at Institute for Materials Research (IMR), Tohoku University, and became a full professor in 1987 at IMR. His major research activities have been novel powder processing for advanced functional materials such as porous, biocompatible Ti alloys with low elastic modulus close to that of human cortical bone and very high temperature structural materials based on Mo/silicide and Nb/silicide in-situ composites with good oxidation resistance. He has revealed a hydrogen pulverization mechanism of Nb and Ta and their alloys. The KONA Award was given to his such a remarkable achievement.

Prof. Hidaka

Prof. Hanada

Academic publication concerning powder technology in Japan (2004)

JOURNAL OF THE SOCIETY OF POWDER TECHNOLOGY, JAPAN VOL. 41 (2004)

- Preparation of Barium Titanate/Solder Composite Particles by Rotating Drum Method and PTCR Property of the Composite Particles
  M. Kobayashi, K. Saito, M. Egashira and N. Shinya ······ 4
- Direct Observation of Agglomerated Powder Structure in Slurry Using an Optical Microscopy
  H. Abe, M. Naito, K. Okamoto, Y. Hotta, S. Ohara and T. Fukui ······ 10
- Possibility of Particle Transportation with Vibrating Parallel Saw-tooth Plates under Microgravity
  Y. Ohyama, H. Takeuchi, A. T. Pyatenko, S. Chiba, I. Uchidate and K. Shinohara ······ 15
- Estimation of Dielectric Property for $BaTiO_3$ Nano-particles by Raman Scattering
  T. Ohno, D. Suzuki, H. Suzuki and T. Ida ······ 86
- Strength of Granules Prepared by Binderless Granulation in Spouted Bed and Observation of Granulation Process
  S. Hatano, S. Osawa, R. Yamazaki and S. Mori ······ 92
- Synthesis of Calcium Phosphate-Mullite Composite Powders by Ultrasonic Spray Pyrolysis and the Sintering Properties
  K. Myoujin, T. Ogihara, K. Nakane and N. Ogata ······ 99
- Particle Shape Measurement Using X-ray Micro Computed Tomography
  M. Suzuki, K. Kawabata, K. Iimura and M. Hirota ······ 156
- Adhesion Force between Particle and Substrate in Humid Atmosphere Studied by Atomic Force Microscope
  A. Fukunishi and Y. Mori ······ 162
- Evaluation of Pharmaceutical Glidant with Atomic Force Microscope and Mechanism of Flowability Enhancement
  K. Machida, Ohta, K. Toyoshima, M. Fuji, T. Takei and M. Chikazawa ······ 169
- Evaluation of Uniformity of Powder Mixture with a Local Analysis Method
  − Minimum Number of Measurements Required for Sampling −
  Y. Nakahara, A. Tsuge, T. Uchida, Y. Uwamino and H. Morikawa ······ 177
- Preparation of Au/Ag Alloy Particles by Spray Pyrolysis and Its Applications
  N. Iida, K. Nakayama, I. W. Lenggoro and K. Okuyama ······ 246
- Mechanism and Rate of Composition by the Rotating Drum Method
  M. Kobayashi, T. Konno, M. Egashira, K. Saito and N. Shinya ······ 252
- Production of Polymeric Nanocomposites Using Mechanochemical Polymerization
  M. Kimata, I. Takahashi and M. Hasegawa ······ 259
- Analysis for Flow and Feed Rate Characteristics of Injection Feeder with Bleeding Holes
  H. Ueda, K. Horii and Y. Tomita ······ 266
- Fluidized Bed Medium Separation (FBMS) for Dry Coal Cleaning
  J. Oshitani, K. Tani, K. Takase and Z. Tanaka ······ 334
- Characterization of Titanium-Apatite Dental Implant Prepared Using Metal Injection Molding Technique
  H. Mori, H. Furusawa and M. Mizuno ······ 342
- Constrained Sintering of the Sandwich Substrate with Inner-constraining Fine Particles Layer
  S. Nakao, M. Kojima and K. Tanaka ······ 350
- Contact Angle of Bridging Liquid in Wet Spherical Agglomeration
  H. Takase and U. Shimazaki ······ 356
- Generation of Nanodroplets and Nanoparticles by Ion-Induced Nucleation
  M. Adachi, M. Kusumi and S. Tsukui ······ 424
- The Influence of Habit Modifiers of Particle Shape in a Crystallization Process
  K. Kadota, K. Takase, A. Shimosaka, Y. Shirakawa and J. Hidaka ······ 431
- Sonochemical Synthesis and Characterization of Magnetic Composite Nanoparticles
  Y. Mizukoshi, K. Okitsu, H. Nitani, S. Seino, T. Nakayama, K. Niihara, T. Nakagawa and T. Yamamoto ······ 440
- Synthesis of Spherical BST Powder via Polymer Templating Method
  S. Shibamoto and T. Kinoshita ······ 445
- Size Effect for Lead Zirconate Titanate Nanoparticles with $Pb(Zr_{0.4}Ti_{0.6})O_3$ Composition
  T. Ohno, D. Suzuki, H. Suzuki and K. Ishikawa ······ 451
- Effect of Small Size Beads of Dispersion of Nanometer-sized Silica Particle by Wet Beads Mill Process
  H. Yoden and N. Itoh ······ 457

KAGAKU KOGAKU RONBUNSHU VOL. 30 (2004)

- Effects of Filtering Velocity and Dust Concentration on Pressure Drop Parameters in a Bag Filter
  H. Ikeno, Y. Tada, S. Hiraoka, M. Ikei and Y. Shuto ······ 7
- Study of Pressure Drop in Bag Filter Based on Patched Cleaning Model
  H. Ikeno, Y. Tada, S. Hiraoka, M. Ikei and Y. Shuto ······ 14
- Adding Effect of Saccharides to Microsuspension Particle Sizes of Griseofulvin-Lipid Mixtures Subjected Freeze-drying and Rehydration
  Y. Nozawa, S. Kamiya, Y. Sadzuka, A. Miyagishima and T. Sonobe ······ 43
- Controlled Release of Structural Bed of Coated Particles Filled with Wax Dispersing Starch
  H. Nunoko, R. Ito, B. Golman and K. Shinohara ······ 102
- Effect of Blade Angle on Pulverizing Characteristics in a Mechanical Impact Mill: Calculation of Particle Trajectory for a Long Simulation Time
  S. Akiyama, K. Kozawa and H. Yoshida ······ 108
- Clarification of Soot Formation Mechanism by Experiment and DSM
  T. Yamamoto, N. Omoto, F. Shishido, H. Aoki and T. Miura ······ 36
- Effect of Physical Properties on Droplet Formation in Microchannel Emulsification
  S. Sugiura, N. Kumazawa, S. Iwamoto T. Oda, M. Satake and M. Nakajima ······ 129
- Prediction of Particle Adhesion to the Wall in a Coal Gasifier: Application to Pre-analysis of Coal Combustion in the Coal Combustor
  Y. Harada, T. Yamashita, T. Yamamoto, H. Aoki and T. Miura ······ 217
- Upward Transport of Solid Particles from a Fluidized Bed with a Cone-Type Freeboard
  Y. Ikeda, M. Tashiro and Y. Fujiyama ······ 267
- Dispersion of Nanoparticles in Water Using a High Pressure Wet-type Jet Mill
  K. Tanaka and H. Kumazawa ······ 325
- Gas-Phase Synthesis of Fine Silica Particles from Tetramethoxysilane
  T. Kojima, T. Uchiyama, S. Katou, H. Shibuya and S. Uemiya ······ 306
- Powder Automaton Simulation for Flow Behavior of Particles under Gravity
  N. Katsura, A. Shimosaka, Y. Shirakawa and J. Hidaka ······ 332
- Preparation of Hydrophobic Mika Particles for Use as an Emulsifying Agent
  T. Aita, R. Kanbayashi, T. Toude, K. Iha, T. Higuchi and S. Sato ······ 372
- Estimation of Void Fraction inside Granules Prepared by Spray Drying
  H. Minoshima, K. Matsushima and K. Shinohara ······ 381
- Preparation of Biodegradable Microcapsules Encapsulating Activated Carbon Impregnated with Potassium Nitrate by Solvent Evaporation
  K. Shiomori, J. Taniguchi, M. Kodama, S. Kiyoyama, H. Yoshizawa, Y. Hatate and Y. Kawano ······ 532
- Analysis of pressure Drop in a Multi-Compartment Bag Filter Based on the Patched Cleaning Model
  H. Ikeno, Y. Tada, S. Hiraoka, Y. Shuto and M. Ikei ······ 413
- Development of a Heat-Balance Model for a Fluidized Bed Waste Gasification Furnace
  T. Marumoto, N. Fujiwara, N. Ohyatsu and T. Iwase ······ 447
- Filtration Behaviors in Microfiltration with Cyclic Backwashing of Sewage Secondary Effluent under Constant Rate and Constant Pressure Condition
  M. S. Jami, T. Ohn and E. Iritani ······ 561
- Enhancement of Settling Tank Capacity with Inclined Tube Settlers
  K. Fujisaki ······ 568
- Separation Properties of Various Activated Sludges by Dynamic Filtration
  T. Hamada and S. Nakatsuka ······ 574
- The Effect of Operating Conditions on the Filtration Resistances of Microfiltration Type Hollow Fiber Membrane in Submerged Membrane Activated Sludge Process
  K. Kawasaki, A. Matsuda, K. Nakayama, C. P. Bhatta, Y. Noma and D. Omori ······ 581
- The Effect of Freezing and Thawing Treatment on the Solid Liquid Separation Characteristics of Bulking Activated Sludge
  K. Kawasaki, A. Matsuda and H. Yamashita ······ 587
- Particulation of Copper Sulfides Produced by Sulfurization of Cu-Plating Wastewater and Its Effect on Filtration Characteristics
  T. Fukuta, Y. Kojima, H. Matsuda, F. Seto and K. Yagishita ······ 592

- Removal of Contaminated Zn from Consolidated soil by Electrokinetic Method Employing Ion-Exchange Reaction
  K. Hayashi, N. Katagiri, E. Iritani and M. Iwata ······ 598
- Analysis of Separation Mechanism of Non-woven Metallic Filter Media Based on Probability Model
  S. Ishikawa, A. Shimosaka, Y. Shirakawa and J. Hidaka ······ 604
- Improving the Collection Performance of the Cyclone Scrubber with Surfactant
  K. S. Yang and H. Yoshida ······ 640
- Process Development to Obtain Agglomerate Crystals Suitable for Powder Filling
  T. Mukuta ······ 745
- A Study on Supersonic Pulverization of Fine Particles: Use of Rectangular Nozzle
  H. Morimoto, T. Shakouchi, T. Fujii and Y. Ichiminami ······ 802
- Collection of Electrified Submicron Particles by Packed Bed with Applied Electric Field
  C. Kasai, Y. Nakajima and K. Shinohara ······ 815
- Estimation of Temperature of Coated Particles in a Fluidized Bed
  R. Ito, A. Mukai, B. Golman and K. Shinohara ······ 840
- Formation Characteristics of Seamless Macro-Capsule in Liquid Phase
  S. Sakai, B. Golman and K. Shinohara ······ 844

JOURNAL OF AEROSOL RESEARCH VOL.19 (2004)

- A Moment Method of an Extended Log-Normal SizDistribution(ELND): Application to Brownian Aerosol Coagulation
  M. Yamamoto ······ 41
- Measurement of Cigarette Side-stream Smoke Using In-situ 2-D Polarization-Sensitive Laser Light Scatteing Method
  K. Katayama, S. Kitao, M. Shimada and K. Okuyama ······ 50
- A New Method for Measuring the Deposition Flux of Small-sized Water Droplets with a Polymeric Water Absorbent
  K. Izumi, H. Ghilajidin, M. Utiyama, T. Fukuyama, S. Yamagata and S. Ohta ······ 142
- Surface Contamination and Corrosion of HDD Media in the Existence of SO_2 Gas
  A. Komatsu, J. Yamamoto, Y. Ogawa, N. Namiki and Y. Otani ······ 181
- Removal of Organic Gaseous Contaminants by the Reaction of Labile Species Using Different Wavelengths of Radiation from a Single UV Source
  K. Sekiguchi, J. Y. Jeong and K. Sakamoto ······ 188
- Contribution of Aerosol Taking Account of Condensation to Heat Island in Japan during Summer Night
  M. Tomosada and M. Tamura ······ 197
- A Statistical Derivation of the Basic Equation in REA Method and the Properties of the Coefficient b
  Y. Matsumoto and M. Utiyama ······ 266
- Influence of Electrical Charge of PTFE Filter on Weighing of Filter with Electric Microbalance
  H. Yoshiyama ······ 274

HOSOKAWA MICRON “Clean-Sphere” Air Shower

Improvement of Working Environment Eliminates dusts into a canteens or rest rooms.

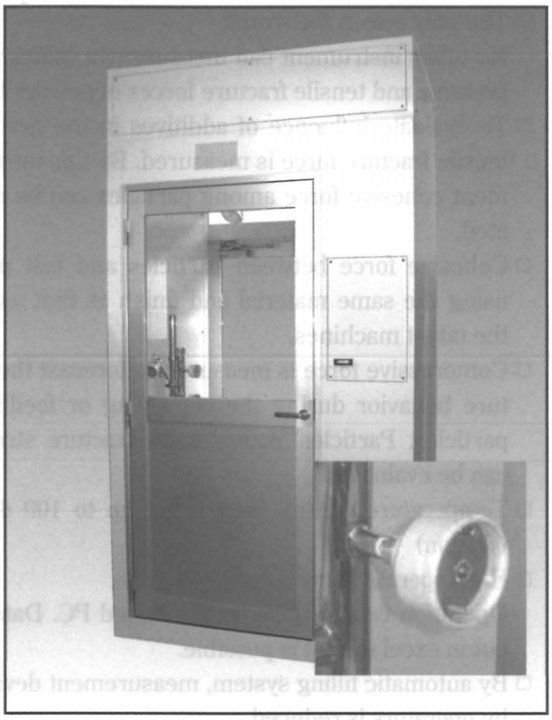

It is best to install at following places.

Doorways of the room where dusting is generated.

Doorways of the area where toxic material is handled.

General

In any working area where dusty powder products are handled.
It is a nuisance to remove dusts adhered on the working clothes.
Commonly seen air showers do not clean the dusts off completely and furthermore, dusts will fly away into human breathing area. (Inside of the air shower room is in turbulent situation.) Workers are forced to inhale the re-spattered dusts. Therefore air blowing power and method for cleaning is re-engineered and the air flow direction is fixed from the ceiling to the floor. In this way problems of spattering, adhering and inhalation are resolved instantly.

Application

It is best to install at doorways in the following places.
- Chemical factories such like carbon, toner, ceramics, etc.
- Dusty plants pigment
- Food plants
- Pharmaceutical plants
- Environmental and recycling facilities

Features

1. Multi Air Nozzles are adopted. The washing air (100m/s speed, 5 times compared to standard case) will hit the clothes and remove dusts efficiently.
2. Re-scattering of dusts is prevented by the down flow.
3. Blow-off by high pure air is possible using HEPA filters.
4. Structure is simple and maintenance is easy.

Instrument for Powder Characteristics Evaluation
AGGROBOT AGR-2

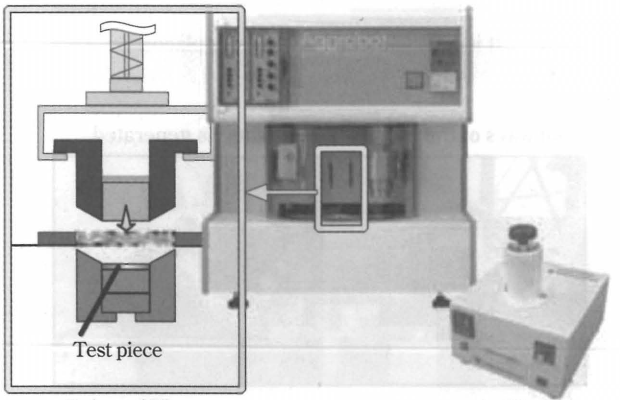

Enlarged View

automatic filling system

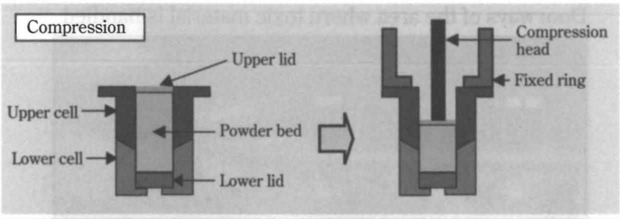

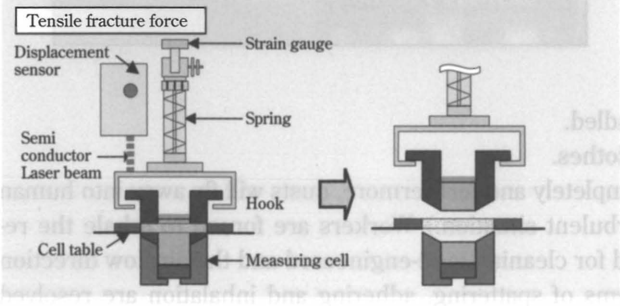

☐ The only one in the world!
No other instrument can measure two values, compressive and tensile fracture forces of powder beds.

☐ To evaluate influence of additives in the granules, tensile fracture force is measured. By this measurement cohesive force among particles can be evaluated.

☐ Cohesive force between particles and test pieces using the same material and finish as that used in the tablet machines.

☐ Compressive force is measured to forecast the fracture behavior during the conveying or feeding of particles. Particles' compressive fracture strength can be evaluated.

☐ Temperature control is possible up to 100 deg C (Option)

☐ High operationality
Operation can be done by the linked PC. Data output in excel format is possible.

☐ By automatic filling system, measurement deviation by operators is reduced.

<Main Application Area>

☐ Pharmaceutical: Increase yield rates and stabilization of the tabletting process.
(Molding formability and breaking strength)

☐ Battery materials: Improvement of battery performance (compressive force)

☐ Troubleshooting of powder processing (cohesive and adhesive property)

HOSOKAWA MICRON USP TAPPING DENSITY TESTER

General

The USP Tapping Tester conforms to USP (United State Pharmacopeia) measurement method. Just by feeding a sample to a specified quantity the unit will automatically measure the height of the tapped powder layer to get the tapped density. Besides, it is also possible to make evaluation of powder characteristics by use of parameters from the Kawakita's method. The unit can be attached to the Powder Tester.

Advantages

The unit can measure Tapped Densities automatically, conforming to following methods;
USP, ASTM Tapped Density Measurement
Kawakita's assessment: Evaluation of filling property of powder layer

Applications

Pharmaceuticals, Toner, Battery Materials, Metallic powders

Specification

Power: AC100V 50/60Hz
Power Consumption: 15W
Weight: 16kgs
Data communication (Modular cable) for External PC communication
(1) USP Type
Tapping stroke: 14 +/−2mm
Vibration Frequency: 300rpm
Tapping: initial 500times, the 2nd 750times, the third or later 1250times
Finishes when the displacement before the tapping is less than 2%.
(2) ASTM Type
Tapping stroke: 3 +/−0.3mm
Vibration Frequency: 250rpm

Kawakita's assessment can base on either condition.

HOSOKAWA MICRON SUPER MICRON MILL® E

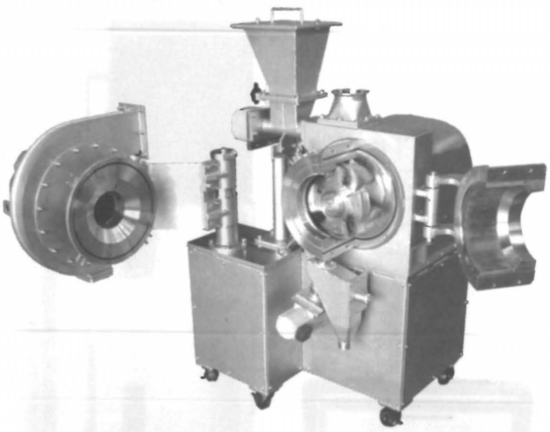

Ultra fine milling system for wide applications Fibrous materials, Foodstuffs, Polymers, Inorganic materials.... Compact & Energy Saving & Low noise & Separating foreign material Attritional Ultra Fine Mill

Principle & Inner Structure

New model was the complete renewal of Hosokawa's Super Micron Mill.
The mill is based on the attrition grinding and is integrated with the unique nozzle extraction mechanism which can separate the foreign material/ungrindable material from the grinding chamber.
This unique combination offers the grinding of fibrous material which has been difficult to grind in room temperature.

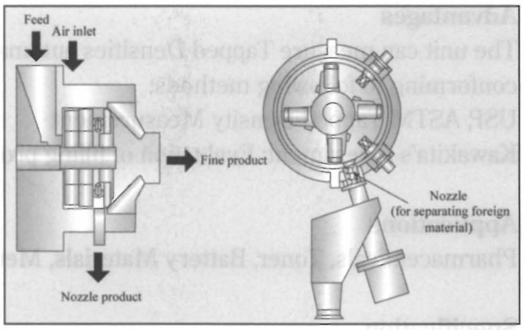

Features

☐ Saving space & Saving Energy
  - The installation area required is approx 65% of the conventional Super Micron Mill
  - The total energy required is approx 60% of the conventional.
  - Noise level is low (85 dB) at operation

☐ To meet wide range of application, the unit is constructed in Stainless steel as standard and easy assembling/cleaning structure (for small amount/various types of material processing)
  - No dead zone for easy cleaning
  - Option for wearing protection

☐ Nozzle extraction mechanism for separating foreign material
  - Possibility of grinding bi-component material (grain and husk etc)
  - To improve the product quality, ungrindable material can be discharged from the grinding chamber

☐ Easy assembling and Easy adjustment of grinding parameter realize the optimized plant management
  - The simplest set-up consists feeder, mill, (integrated) blower. No bag filter may be required

☐ The high rotor speed with attrition type mill is realized

HOSOKAWA MICRON

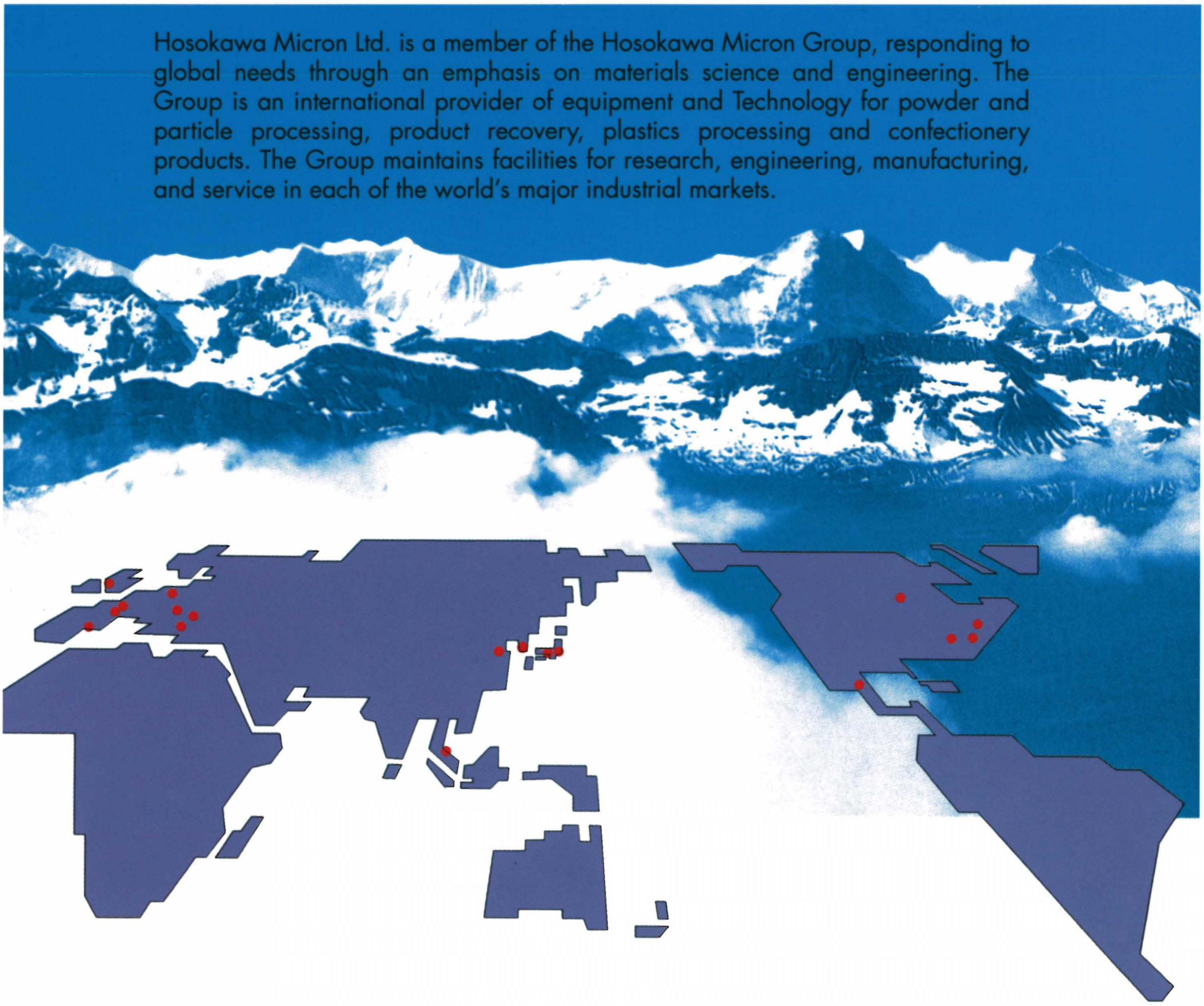

Hosokawa Micron Ltd. is a member of the Hosokawa Micron Group, responding to global needs through an emphasis on materials science and engineering. The Group is an international provider of equipment and Technology for powder and particle processing, product recovery, plastics processing and confectionery products. The Group maintains facilities for research, engineering, manufacturing, and service in each of the world's major industrial markets.

Process Technologies for Tomorrow

HOSOKAWA MICRON

Headquarter Locations;
HOSOKAWA MICRON CORPORATION
http://www.hosokawamicron.co.jp